

# **Emplacement of sub-volcanic cone sheet intrusions**

by

Craig Magee

A thesis submitted to  
The University of Birmingham  
For the degree of  
DOCTOR OF PHILOSOPHY

Department of Earth Sciences  
School of Geography, Earth and  
Environmental Sciences  
The University of Birmingham  
September 2011

UNIVERSITY OF  
BIRMINGHAM

**University of Birmingham Research Archive**

**e-theses repository**

This unpublished thesis/dissertation is copyright of the author and/or third parties. The intellectual property rights of the author or third parties in respect of this work are as defined by The Copyright Designs and Patents Act 1988 or as modified by any successor legislation.

Any use made of information contained in this thesis/dissertation must be in accordance with that legislation and must be properly acknowledged. Further distribution or reproduction in any format is prohibited without the permission of the copyright holder.

---

## ABSTRACT

---

Sub-volcanic intrusive networks, of which cone sheets are recognised as a major constituent, control volcano growth and eruption style. The accepted cone sheet model is that these confocally dipping intrusions originate from an unexposed central magma chamber through dip-parallel magma flow. However, the emplacement mechanism of cone sheets has remained poorly understood. The classic ~58 Ma cone sheet swarm of Ardnamurchan, NW Scotland, offers an excellent opportunity to further resolve the emplacement dynamics of cone sheets through studying their magma flow. Structural measurements and anisotropy of magnetic susceptibility (AMS) analyses have constrained a lateral magma flow regime, consistently oriented NW-SE, in the majority of the Ardnamurchan cone sheets. This is not consistent with previous emplacement models. In this thesis, it is suggested that emplacement of the Ardnamurchan cone sheets occurred through the deflection of laterally propagating, NW-SE trending regional dykes, sourced from laterally adjacent magmatic systems (likely the Palaeogene Mull central complex). Field observations highlight the importance of host rock structure and interference between locally compressional and regional extensional stress fields in controlling intrusion geometry. Implicitly, edifice construction and potential eruption precursors observed at a volcano may instigate, or result from, magmatic activity in laterally adjacent volcanic systems.

---

## ACKNOWLEDGEMENTS

---

Where to begin. The time spent doing my PhD has been the best three years of my life and although PhD's are supposed to be stressful, I feel I have escaped rather lightly thanks to the wealth of support I have received from all my family and friends. One day I hope that I can return the favour to each and every one of you. Although the list is too long to mention everybody, I would like to pay special thanks to several groups of people.

First and foremost, I would like to say a massive thankyou to my brother (David Magee), mum (Wendy Magee) and dad (Ray Magee), without whom I would not be where I am today. David has always been there to put a smile on my face when I have needed it and to pass on words of infinite wisdom when I get bogged down in my work. You are right Dave, one of my next tasks is to follow in your footsteps and chat up the ladies! My parents have provided constant support (both moral and financial) and encouragement to me, which I hope to one day repay; starting with a signed copy of my thesis! All three have aided me in the field, either by taking up the hammer and chisel (Ray Magee) or by supervising (David and Wendy Magee), for which I am truly grateful. Although, it must be said that walking up a 'well marked, easy-going mountain path' proved tricky.

A particular thanks to my supervisors and people who have unofficially supervised me, without whom this PhD would not have been completed. My principal supervisor, Dr. Carl Stevenson, deserves a special thankyou for all the knowledge and support he has passed on, as well as introducing me to whisky. In thanking Carl, I would also like to pass on my gratitude to his wife, Ruth Stevenson. I wish the both of you, and little Nonín, all the best in the future. Dr. Brian O'Driscoll has also been a major help, both as a supervisor and as a friend, providing lots of valuable advice and observations. I guess I should also thank my third supervisor, Prof. Tim Reston, here...though for what I'm not entirely sure. We've certainly had a few good laughs and nips of whisky, although I fear I have failed to convince Tim on the potential use of AMS. In this section I would also like to thank Dr. Nick Schofield and Dr. Mike Petronis who have been invaluable non-supervisors. Nick has been a great friend to me over the years and introduced me to the legacy of Room 116, which following a few pranks (some to be mentioned later) and an award for Best Postgraduate presentation at TSG I hope I can now be accepted into. I thank Mike for showing me how fieldwork should truly be conducted and protecting me from fenians whilst block sampling. Don't worry gents, these papers will get published eventually!

A special thanks go to Andy Chambers and Ben van Vyk de Vries for examining (and passing!) this thesis, as well as Steve Jones for chairing the viva. It was a surprisingly enjoyable experience.

Having mentioned Room 116, I am now brought to the task of thanking my fellow PhD compatriots. My friend Ken McDermott has been with me since the beginning and it's safe to say it has been a good ride. I would like to thank Yvonne McGillicuddy for allowing Ken to come out and play so much. It has also been a pleasure to know Mr. Anderson (Paul), who I maintain thoroughly deserved to get parcel-taped to his chair and wheeled into his supervisors office; Plamen Andreev; Edward Fleming; Phil Jardine and Babangida Jibrin. Thanks also to the other PhD students of the department and fleeting visitors for lots of good, and occasionally disturbing times (that means you Mr. Rees): Andy Rees, Sarah King, Ben Slater, Andrew Storey, William McCarthy and Emanuelle Roni. Driven by curiosity, we have collectively and courageously chased that capricious and often cryptic creature, the PhD, to a point of (near) completion whilst thankfully circumventing too many catastrophies and cannily combating certain cantankerous academics. I would also like to take this opportunity to thank all of the support staff within the department.

Penultimately, I would like to thank my group of six close friends from 'back home', with whom I have had some much needed short-breaks and a great few laughs. Stuart and Laura Perkins are thanked for their hospitality and alcohol. Robert Johnson and Emily James (soon to be Mrs Johnson) are also thanked for alcohol provision. I'm not quite sure I've laughed so much as I have watching Steve Churchill loose at things consecutively; some great memories Steve. And last but not least, thanks to Adam Turner for all the stimulating discussions, which have inevitably culminated in further alcohol consumption.

Finally I would like to pass on my thanks to the VMSG, TSG and LASI communities, particularly the magnetic mafia, for many helpful discussions and enjoyable moments. It was also remiss of me to forget thanking my good friend Dan Welch (and his wife Jess), in a previous version of these acknowledgements, for all their help and support. Well, Dan, you've forced your way in and I'm hoping this earns me a few more sips of your growing whisky collection.

All that is left is for me to say is that, "the ferries going out".

This Thesis is dedicated to:

The memory of 'Grandpa' Alan Henry Smith  
1923–2006

who encouraged the scientist in me and sadly on his passing taught me the importance of not  
taking things for granted.

*“Oooh ya beaut”*

and to

'Nan', Amy Catherine Magee  
1919–

who has shown me the true meaning of vitality.

*It is the mark of an educated  
mind to be able to entertain a  
thought without accepting it.*

Aristotle (384 – 322 BC)

---

## TABLE OF CONTENTS

---

<b>Chapter 1: INTRODUCTION</b>	<b>1</b>
<b>1.1 Development of the original cone sheet emplacement model</b>	<b>2</b>
1.1.1 Field observations and initial considerations on emplacement mechanism	2
<b>1.2 Emplacement model variations</b>	<b>9</b>
1.2.1 Shear fracture intrusion	9
1.2.2 Deflection of vertically propagating dykes by acid diapirs	13
1.2.3 Deformation of the volcanic edifice	15
1.2.4 Magma chamber shape and local stress field variability	17
<b>1.3 Discussion</b>	<b>20</b>
1.3.1 Cullin cone sheets, Skye	21
1.3.2 Otoge cone sheet swarm, Japan	22
1.3.3 Summary	22
<b>1.4 Thesis structure</b>	<b>23</b>

## **Chapter 2: ANISOTROPY OF MAGNETIC SUSCEPTIBILITY** **25**

### **2.1 Rock magnetism and its anisotropy** **25**

2.1.1 Physics of grain scale magnetism 25

2.1.2 The magnetic response of grains 26

2.1.3 Magnetic responses of key minerals and mineral groups in igneous rocks 30

### **2.2 Application of anisotropy of magnetic susceptibility (AMS) to determining igneous petrofabrics** **32**

2.2.1 Mineral fabric description 32

2.2.2 Determination of the magnetic fabric using anisotropy of magnetic susceptibility (AMS) 33

2.2.3 Comparing magnetic fabrics to petrofabrics in igneous rocks 36

2.2.4 Primary magma flow determination using AMS 39

### **2.3 The AMS method used within this thesis** **42**

2.3.1 Sample collection and analysis 42

2.3.2 Distinguishing magnetic carriers and their influence on AMS 43

## **Chapter 3: THE GEOLOGY OF ARDNAMURCHAN** **46**

### **3.1 Precambrian host rocks** **47**

3.1.1 Lewisian Gneiss basement 47

3.1.2 Neoproterozoic Moine metasedimentary rocks 48

<b>3.2 Mesozoic metasedimentary rocks</b>	<b>53</b>
<b>3.3 The British and Irish Palaeogene Igneous Province (BIPIP)</b>	<b>55</b>
3.3.1 Regional setting of the North Atlantic Igneous Province (NAIP)	55
3.3.2 Components of the BIPIP	57
3.3.2 The Ardnamurchan central complex	63

## **Chapter 4: ANALYSIS OF FIELD OBSERVATIONS AND STRUCTURAL MEASUREMENTS OF CONE SHEETS**

<b>4.1 The controls of pre-existing structure and host rock lithology on cone sheet intrusion</b>	<b>72</b>
4.1.1 Relationships between host rock lithology and cone sheet structures	72
<b>4.2 Data collection and results</b>	<b>80</b>
4.2.1 Differentiating individual cone sheets	81
4.2.2 Cone sheet abundance variation	85
4.2.3 Cone sheet orientation and dip	85
4.2.4 Modes of opening and thickness variations of cone sheets	90
<b>4.3 Stress field conditions during intrusion</b>	<b>92</b>
4.3.1 Derivation of emplacement conditions	92

4.3.2 Model of the active stress field during cone sheet intrusion	97
--	----

<b>4.4 Summary</b>	<b>101</b>
--------------------	------------

## **Chapter 5: ANISOTROPY OF MAGNETIC SUSCEPTIBILITY**

<b>OF THE ARDNAMURCHAN CONE SHEETS</b>	<b>102</b>
--	------------

---

<b>5.1 Characterising the magnetic mineralogy</b>	<b>104</b>
---	------------

5.1.1 Mean susceptibility	104
---------------------------	-----

5.1.2 High-temperature, low-field susceptibility experiments	107
--	-----

5.1.3 Petrographic observations	111
---------------------------------	-----

<b>5.2 AMS strength and shape</b>	<b>113</b>
-----------------------------------	------------

5.2.1 Strength of anisotropy (H)	113
----------------------------------	-----

5.2.2 Strength of anisotropy ( $\mu$ )	115
--	-----

<b>5.3 Orientation of magnetic fabrics</b>	<b>119</b>
--	------------

5.3.1 Correlation of the magnetic fabric to primary magma flow	120
--	-----

5.3.2 Expected flow regime based on previous emplacement models	121
---	-----

5.3.2 Magnetic lineation trends	124
---------------------------------	-----

5.3.2 Magnetic foliations	129
---------------------------	-----

<b>5.4 Interpretation and summary of the AMS fabrics</b>	<b>132</b>
--	------------

## **Chapter 6: EMPLACEMENT OF THE ARDNAMURCHAN**

<b>CONE SHEETS</b>	<b>134</b>
--------------------	------------

---

<b>6.1 Suitability of previous cone sheet emplacement models</b>	<b>135</b>
--	------------

6.1.1 A comparison to the traditionally accepted model for the Ardnamurchan cone sheets developed by Richey and Thomas (1930) and Anderson (1936)	135
6.1.2 Shear fracture intrusion (Robson and Barr, 1964; Durrance, 1967; Phillips, 1974)	136
6.1.3 Deformation of the volcanic edifice (Walker, 1992; 1993)	137
6.1.4 Variations in magma chamber conditions (Gautneb et al., 1989; Gautneb and Gudmundsson, 1992; Gudmundsson, 1995; 1998; Schirnack et al., 1999)	139
6.1.5 Local stress field and host rock control	141
6.1.6 Source position of the Ardnamurchan cone sheets	142

<b>6.2 Magma source</b>	<b>145</b>
-------------------------	------------

6.2.1 Viability of laterally propagating regional dyke magma source	146
6.2.2 Geochemistry of the Ardnamurchan cone sheets	148

<b>6.3 Influence of the regional stress field</b>	<b>162</b>
---	------------

6.3.1 Cone sheet abundance variations	164
---------------------------------------	-----

6.3.2 Stress field interference	165
---------------------------------	-----

<b>6.4 Summary</b>	<b>170</b>
--------------------	------------

## **Chapter 7: EMPLACEMENT OF THE BEN HIANT DOLERITE**    **171**

<b>7.1 Previous emplacement models of the Ben Hiant Dolerite</b>	<b>172</b>
--	------------

<b>7.2 Field relationships and petrography</b>	<b>175</b>
--	------------

7.2.1 South-west of the Ben Hiant summit	175
--	-----

7.2.2 Stallachan Dubha and Sròn Mhor	177
--------------------------------------	-----

7.2.3 Northern margin	179
-----------------------	-----

7.2.4 Overall structure of the Ben Hiant Dolerite	181
---	-----

<b>7.3 Magnetic fabric analysis</b>	<b>181</b>
-------------------------------------	------------

<b>7.4 Structural emplacement of the Ben Hiant Dolerite</b>	<b>186</b>
---	------------

7.4.1 Construction of the Ben Hiant Dolerite	186
--	-----

7.4.2 Controls on Emplacement position	195
--	-----

7.4.3 Magma flow regime and source	198
------------------------------------	-----

7.4.4 Intrusion of the Ben Hiant Dolerite and implications for the emplacement of the Ardnamurchan cone sheets	202
---	-----

## **Chapter 8: DISCUSSION AND CONCLUSIONS** **204**

### **8.1 Summary of Ardnamurchan sheet intrusion emplacement mechanisms** **204**

8.1.1 The Ardnamurchan cone sheets 204

8.1.2 The Ben Hiant Dolerite Intrusion 205

8.1.3 Controls on regional dyke emplacement 206

### **8.2 Insights into the emplacement of other sub-volcanic complexes** **207**

8.2.1 The British and Irish Palaeogene Igneous Province 208

8.2.2 Cone sheet-bearing complexes in regional extensional settings similar to  
the BIPIP 215

8.2.3 Cone sheet-bearing complexes in regional compressional settings 220

8.2.4 Major intrusions laterally fed by regional dykes 221

### **8.3 Conclusion** **222**

## **APPENDICES** **224**

## **LIST OF REFERENCES** **229**

---

## LIST OF FIGURES

---

### **Chapter 1: INTRODUCTION**

Fig. 1.1: Map of the north-west BIPI and a representation of a sub-volcanic system.	3
Fig. 1.2: Initial model of cone sheet emplacement.	5
Fig. 1.3: Map of igneous intrusions on Ardnamurchan.	7
Fig. 1.4: Anderson's (1936) mathematical models.	8
Fig. 1.5: Spiral cone sheet strike after Durrance (1967).	11
Fig. 1.6: Phillips (1974) model of cone sheet emplacement.	13
Fig. 1.7: Cone sheet emplacement models associated with acid diapirs.	14
Fig. 1.8: Cone sheet emplacement models associated with Walker (1992; 1993).	16
Fig. 1.9: Numerically modelled magma chambers and associated local stress fields.	19
Fig. 1.10: Proposed laccolithic source of the Miocene Tejada cone sheets.	20
Fig. 1.11: Maps and emplacement mechanism of sheet intrusions in the Otoge igneous centre, Japan.	23

### **Chapter 2: ANISOTROPY OF MAGNETIC SUSCEPTIBILITY**

Fig. 2.1: Various magnetic response to applied magnetic fields.	27
Fig. 2.2: Possible magnetic domain configurations.	29
Fig. 2.3: Ternary diagram of common Fe-Ti oxide solid-solution series.	31

Fig. 2.4: Magnetic lattice structure of magnetite and ilvospinel and an example of ilmenite exsolution in magnetite.	32
Fig. 2.5: Petrofabric ellipsoids and their magnetic susceptibility.	34
Fig. 2.6: Strain associated with magma flow of variable rheologies.	41

### **Chapter 3: THE GEOLOGY OF ARDNAMURCHAN**

Fig. 3.1: Map of major terrane boudaries in Scotland.	47
Fig. 3.2: Geological map of Ardnamurchan.	49
Fig. 3.3: Construction of cross-sections to determine Moine Thrust depth beneath Ardnamurchan.	52
Fig. 3.4: The NAIP presently and 60 Ma.	56
Fig. 3.5: Map and relative ages of the components within the BIPI.	58
Fig. 3.6: Field photographs of variable cone sheet geometries and chilled margins.	67

### **Chapter 4: ANALYSIS OF FIELD OBSERVATIONS AND STRUCTURAL MEASUREMENTS OF CONE SHEETS**

Fig. 4.1: Map and structural measurements of the Ardnamurchan cone sheets.	71
Fig. 4.2: Xenoliths.	73
Fig. 4.3: Intrusive step and broken bridge formation.	75
Fig. 4.4: Host rock fluidisation adjacent to cone sheets.	77
Fig. 4.5: Formation of magma fingers.	79

Fig. 4.6: 1:1000 map and photographs of variability in individual cone sheets.	82
Fig. 4.7: Fe-sulphide populations in the Ardnamurchan cone sheets.	84
Fig. 4.8: Ramp-flat cone sheet morphologies.	88
Fig. 4.9: Cone sheet dip data.	89
Fig. 4.10: Cone sheet opening vectors and thickness ranges.	91
Fig. 4.11: Comparison of cone sheet orientations to bedding and fracture planes.	93
Fig. 4.12: Mohr circle construction.	96
Fig. 4.13: Local stress field development during emplacement of the Ardnamurchan cone sheets.	100

## **Chapter 5: ANISOTROPY OF MAGNETIC SUSCEPTIBILITY**

### **OF THE ARDNAMURCHAN CONE SHEETS**

---

Fig. 5.1: AMS sample positions.	103
Fig. 5.2: Mineral magnetic susceptibilities.	105
Fig. 5.3: $K_{\text{mean}}$ distribution.	106
Fig. 5.4: High-temperature, low-field susceptibility experiment results.	108
Fig. 5.5: Titanomagnetites in the Ardnamurchan cone sheets.	112
Fig. 5.6: $K_{\text{mean}}/H$ .	114
Fig. 5.7: Distribution of H values.	116
Fig. 5.8: Magnetic fabric ellipsoid shape data.	117
Fig. 5.9: AMS stereographic projections.	118

Fig. 5.10: Magnetic lineation and visible magma flow indicator axes.	122
Fig. 5.11: Expected magma flow within cone sheets.	123
Fig. 5.12: Magnetic lineations in the Ardnamurchan cone sheets.	125
Fig. 5.13: Magnetic lineation plunge data.	128
Fig. 5.14: Magnetic foliation data.	130
Fig. 5.15: Magnetic foliations compared to magnetic lineation and cone sheet orientations.	131

## **Chapter 6: EMPLACEMENT OF THE ARDNAMURCHAN**

### **CONE SHEETS**

---

Fig. 6.1: 3D model of cone sheets and expected magma flow patterns.	135
Fig. 6.2: Magma flow predicted by Durrance's (1967 model).	138
Fig. 6.3: Regional dyke dilation axes.	139
Fig. 6.4: Lateral magma flow in regional dykes.	144
Fig. 6.5: Geochemistry of the Ardnamurchan cone sheets.	151
Fig. 6.6: Major element and rare earth element plots comparing the Ardnamurchan cone sheets to intrusions and extrusions throughout the BIPIP.	154
Fig. 6.7: $^{87}\text{Sr}/^{86}\text{Sr}$ against $^{143}\text{Nd}/^{144}\text{Nd}$ .	155
Fig. 6.8: Determination of a central source depth to the Ardnamurchan cone sheets.	158

Fig. 6.9: Block diagram of the possible sub-surface relationships beneath Ardnamurchan.	161
Fig. 6.10: Magma source positions beneath Mull defined by Kerr et al., (1999).	162
Fig. 6.11: Cone sheet abundance variations related to regional principal stress axes.	165
Fig. 6.12: Regional dyke geometries around central complexes.	167
Fig. 6.13: Interpreted deflection traces of regional dykes around Ardnamurchan.	168
Fig. 6.14: Host rock foliation patterns around the Merrimac and Ardara plutons.	169

## **Chapter 7: EMPLACEMENT OF THE BEN HIANT DOLERITE**

Fig. 7.1: Map of Ardnamurchan.	172
Fig. 7.2: Detailed map of the Ben Hiant Dolerite.	174
Fig. 7.3: Field relationships and petrography of the Ben Hiant Dolerite.	177
Fig. 7.4: Sròn Mhor petrographical variations.	179
Fig. 7.5: Internal contact within the Ben Hiant Dolerite.	180
Fig. 7.6: AMS sample positions, $\mu$ distribution and L/F plot.	182
Fig. 7.7: High-temperature, low-field susceptibility experiment results.	184
Fig. 7.8: Magnetic lineation and foliation orientations.	187
Fig. 7.9: Magma lobes within the Ben Hiant Dolerite.	189
Fig. 7.10: Magnetic fabric deflection and faulting.	190
Fig. 7.11: Magma lobes.	192
Fig. 7.12: Position of the Ben Hiant Dolerite relative to stress field interference patterns.	197

Fig. 7.13: Emplacement of the Ben Hiant Dolerite from a central source.	200
Fig. 7.14: Model of regional dykes feeding the Ben Hiant Dolerite.	201

## **Chapter 8: DISCUSSION AND CONCLUSIONS**

---

Fig. 8.1: Mapped geometries and magma flow patterns of the Cuillin cone sheets.	210
Fig. 8.2: Distribution of the Mull cone sheets.	212
Fig. 8.3: The Carlingford cone sheets.	214
Fig. 8.4: Regional stress field of the Canary Islands and sheet intrusion form on La Gomera.	218
Fig. 8.5: Regional dykes feeding laccoliths in the Adel Mountains (Montana) and analogue models.	222

---

**LIST OF TABLES**

---

**Chapter 3: THE GEOLOGY OF ARDNAMURCHAN**

Table. 3.1: Range of possible Moine Thrust depths beneath Ardnamurchan. 54

**Chapter 4: ANALYSIS OF FIELD OBSERVATIONS AND STRUCTURAL  
MEASUREMENTS OF CONE SHEETS**

Table. 4.1: Angular ranges of pre-existing fractures potentially reactivated during  
cone sheet intrusion. 98

---

## CHAPTER 1

### INTRODUCTION

---

The emplacement of interconnected sub-volcanic intrusions partially controls the growth of volcanic edifices and may influence subsequent eruptive styles (Gudmundsson, 1995; Annen et al., 2001; Sparks, 2003; Corazzato et al., 2008). Sub-volcanic networks consist of major plutonic bodies (i.e. magma chambers), of variable form, interconnected by a complex series of sheet intrusions, which effectively act as magma transport conduits. Developing and testing models for the emplacement mechanisms of sheet intrusions is therefore key to understanding the transport and accommodation of magma in the upper crust, which contributes towards volcanic hazard assessment (Sparks, 2003; Tibaldi and Pasquarè, 2008; Kervyn et al., 2009; Mathieu and van Wyk de Vries, 2009). Primarily, research into sheet intrusions has focused on the emplacement mechanisms of dykes and, to a lesser extent, sills. Inwardly inclined conical sheet intrusions (cone sheets) are closely associated with ring dykes (outward inclinations) and are recognised as important elements in the intrusive framework of many volcanic systems (central complexes) in the geological record (e.g. Mull central complex, Scotland, Bailey et al., 1924; Zarza ring complex, Mexico, Johnson et al., 1999; Tejeda complex, Gran Canaria, Schirnick et al., 1999; Messum igneous complex, Namibia, Ewart et al., 2002; Thverartindur igneous centre, Iceland, Klausen, 2004; Otoge igneous complex, Japan, Geshi, 2005). Reconstructing the growth and temporal evolution of these conical intrusions is therefore an important step in understanding volcanic behaviour and deformation (Le Bas, 1971; Pasquarè and Tibaldi, 2007; Tibaldi and Pasquarè, 2008; Burchardt et al., 2011). For example, Sigmundsson et al., (2010) attributed a component of the measured ground deformation associated with the Eyjafjallajökull eruption (Iceland, April 14<sup>th</sup> 2010) to the intrusion of a 3–6 km long ‘tilted dyke’; potentially a cone sheet.

Traditionally, magmatic networks of a volcano are viewed as vertically stacked

systems with an eruption site directly overlying the melt generation area located at depth (Hall, 1996; Best, 2003; Acocella and Neri, 2009). Magma is transported through dyke complexes from an upper mantle or lower crustal source and stored in upper crustal reservoirs composed of a series of sills, laccoliths, lopoliths or other pluton morphologies interconnected by further dykes (Fig. 1.1) (Hall, 1996; Best, 2003). Sheet intrusion from these upper crustal reservoirs, as either dykes or conical intrusions (i.e. cone sheets and ring dykes), significantly influences host rock deformation of the volcano (Richey and Thomas, 1930; Le Bas, 1971) and may provide conduits for magma to reach the surface (Gudmundsson, 1995; 1998; Tibaldi et al., 2011). The propagation and geometry of sheet intrusions within the upper crust is controlled by the local and regional stress regimes, magma behaviour and the pre-existing host rock structure (Pollard, 1987; Rubin, 1995; Gudmundsson and Phillip, 2006; Acocella and Neri, 2009; Siler and Karson, 2009; Schofield et al., 2010). However, recent studies have also suggested significant volumes of magma can be transported laterally ( $\sim <1000$ 's km) through extensive sill complexes (Thomson and Hutton, 2004; Cartwright and Hansen, 2006; Leat, 2008) or dyke swarms (Macdonald et al., 1988, 2009; Ernst and Baragar, 1992; Ernst et al., 1995). The British and Irish Palaeogene Igneous Province (BIPIP) and the central complexes it contains, which represent the deeply eroded roots of ancient volcanic edifices, offer an excellent opportunity to study cone sheet emplacement mechanisms and their importance to sub-volcanic networks (Fig. 1.1).

## **1.1 Development of the original cone sheet emplacement model**

### **1.1.1 Field observations and initial considerations on emplacement mechanisms**

Harker (1904) first described numerous, thin, inclined sheet intrusions arranged in a concentric manner with a disposition towards inward inclinations from the Cuillin igneous complex, as part of the encompassing Skye central complex (Fig. 1.1). Similar inclined sheet geometries were mapped on Mull (Bailey et al., 1924) and Ardnamurchan (Richey and Thomas, 1930) following an initiative by the British Geological Survey to map the volcanic

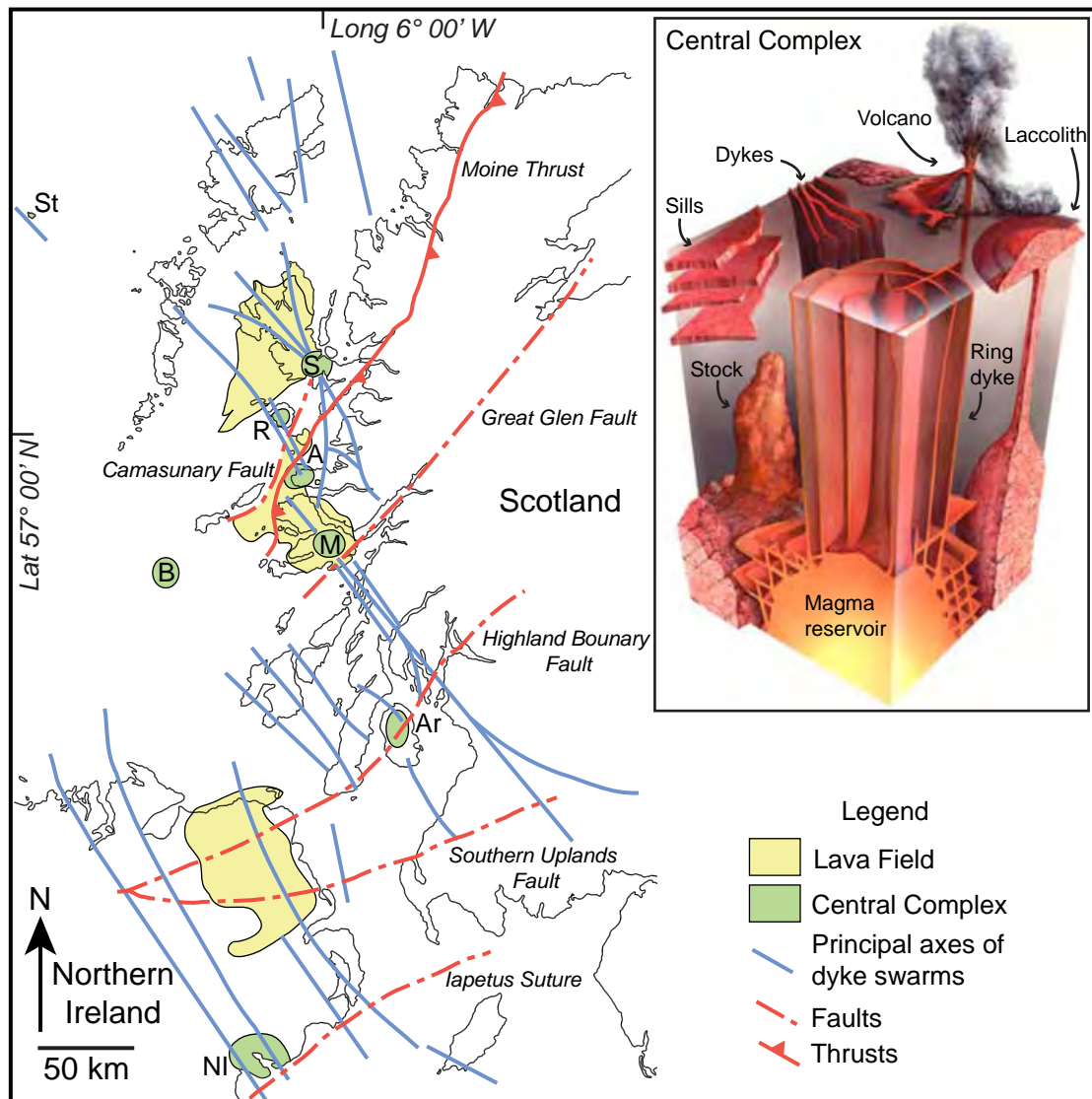


Fig. 1.1: Map of the distribution of flood basalt lavas, NW-SE regional dykes and central complexes in the British and Irish Palaeogene Igneous Province (BIPIP) (redrawn from Emeleus and Bell, 2005). The central complexes are: St, St Kilda; S, Skye; R, Rum; A, Ardnamurchan; M, Mull; B, Blackstones; Ar, Arran; NI, Northern Ireland central complexes including Slieve Gullion, Carlingford and the Mourne. Major Caledonian faults are also displayed. Inset: A central complex intrusive network (Hincks, 2004).

complexes and surrounding areas of the Scottish west coast (Fig. 1.1). Extrapolation of the inclined sheets straight down-dip suggested most sheets converge at a common apex at depth, describing an inverted conical geometry, from which the term ‘cone sheet’ originated (Bailey et al., 1924). Appendix A provides additional information on the structure and interpretations of the various cone sheet complexes, and others, mentioned in this chapter.

### 1.1.1:1 *Mull, NW Scotland: Bailey et al., (1924)*

The cone sheets on Mull have inward inclinations of 40°–45° on average and sub-concentric (horseshoe) strikes displaying a slight elongation about a NW-SE axis (Bailey et al., 1924). Bailey et al., (1924) noted that the cone sheets could be sub-divided into four distinct swarms (the early acid, early basic, late acid and late basic cone sheet swarms) from their con-focal source disposition and lithology. Bailey et al., (1924), Richey and Thomas (1930) and Anderson (1936) observed considerable variation between the strike and dip of individual cone sheets within a single swarm but noticed that the swarm itself always displayed the idealised inverted conical geometry and was restricted to the confines of the central complex. Within swarms, individual cone sheets often increase in dip towards the inner margin of a swarm (Harker, 1904) and dip variability decreases towards the outer margin (Gudmundsson, 2002). It was from the overall swarm morphology that emplacement models were developed.

Cone sheet swarms are often found in association with ring dykes, arcuate intrusions with moderate to steep outward dips (occasionally with a flat roof) that are significantly thicker than cone sheets (Bailey et al., 1924; Richey, 1928; Richey and Thomas, 1930; Anderson, 1936). Comparing the interpreted cone sheet swarm geometries and mapped cross-cutting relationships with major intrusions (predominantly ring dykes) allowed Bailey et al., (1924) to define two spatially and temporally separate centres of igneous activity, with an apparent NW migration, on Mull. The early cone sheet intrusion phases were attributed to the Beinn Chàisgidle centre and the later cone sheets to the younger Loch Bà centre (Bailey et al., 1924). Three centres of intrusive activity are now recognised on Mull, still maintaining the proposed NW migration route, classified as Glen More (the oldest centre, Centre 1), Beinn Chàisgidle (Centre 2) and Loch Bà (Centre 3) (Emeleus and Bell, 2005). The cone sheet swarm dispositions have been modified with some of the early cone sheets being attributed to Centre 1, despite their inclination towards Centre 2, and the later cone sheets accredited to the latter phases of Centre 2 and to Centre 3 (Emeleus and Bell, 2005). After further analysis of the mapped relationships between the cone sheets and ring dykes of each Centre, Bailey et al., (1924) identified a spatial and temporal correlation connecting the two, a feature later

observed by Richey and Thomas (1930) on Ardnamurchan, implying an affiliation of the respective emplacement processes (Fig. 1.2). The ring dykes cyclically interrupted periods of cone sheet intrusion, cross-cutting them, and were themselves cut by later cone sheet swarms often originating from a younger Centre (Bailey et al., 1924; Richey and Thomas, 1930).

A succinct model of dynamic cone sheet and ring dyke emplacement was provided in the Mull memoir (Fig. 1.2; Bailey et al., 1924) and later in more detail by Anderson (1936). Assuming a horizontal free surface and a magma reservoir at depth, it was suggested that if the density of magma within a reservoir was in equilibrium with the host rock then no further intrusion or deformation would occur (Bailey et al., 1924). However, any increase in the magma pressure would superimpose a tensional regime on the host rock and favour the formation of inverted conical fractures, the intrusion of which produces cone sheets (Fig. 1.2) (Bailey et al., 1924). Bailey et al., (1924) suggested that cone sheet trajectory may vary with distance from the magma reservoir, potentially forming dyke or sill morphologies (Fig. 1.2). In contrast, a decrease in magma pressure (created by evacuation of magma into cone sheets) would instigate instability in the roof rock resulting in subsidence along outward dipping fractures (Fig. 1.2), which themselves are intruded with magma to form ring dykes (Bailey et al., 1924).

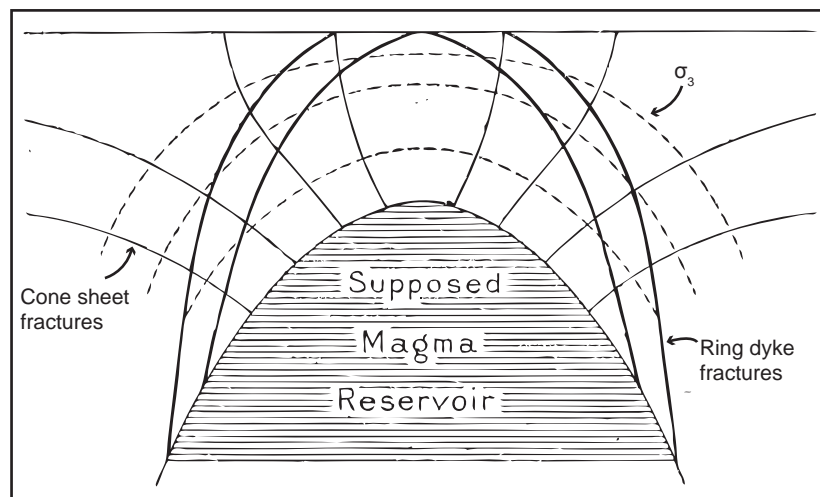


Fig. 1.2: Initial model of cone sheet emplacement proposed by E. M. Anderson in Bailey et al., (1924).

### 1.1.1:2 *Ardnamurchan, NW Scotland: Richey and Thomas (1930)*

The cone sheets of Ardnamurchan, though predominantly mafic, were divided by Richey and Thomas (1930) into three swarms based on their dip foci and age relationships with major intrusions of the central complex (Fig. 1.3). The oldest cone sheets, which define Centre 1 (Fig. 1.3), have shallow inward inclinations of  $10^{\circ}$ – $20^{\circ}$ . Interruption of the Centre 2 swarm by ring dyke intrusions and a minor migration of dip foci further sub-divides the swarm into the Outer and Inner sets (Fig. 1.3) (Richey and Thomas, 1930). Whilst the Outer set has an average dip of  $40^{\circ}$ , the Inner set dips much more steeply at  $\sim 70^{\circ}$  (Richey and Thomas, 1930), describing an overall increase in cone sheet dip towards the centre *sensu* Harker (1904). The Centre 3 cone sheets, only exposed in a restricted area to the S of the Centre 3 foci, dip at  $\sim 50^{\circ}$  N (Fig. 1.3) (Richey and Thomas, 1930). No cone sheets are observed directly above any of Richey and Thomas' (1930) defined Centre foci. From these observations Richey and Thomas (1930) commented on the importance of localised crustal stresses to cone sheet intrusion and suggested that they were sourced from cupolas on the roof of a large magma reservoir. Focusing of excess magmatic pressure within the cupola, simulates a point source and applies stress to the host rock in an upwards direction, producing inverted conical fractures (Richey and Thomas, 1930). Implicitly, Richey and Thomas (1930) stressed the potential of cone sheet intrusion to instigate significant uplift, considerably influencing edifice construction.

### 1.1.1:3 *Anderson's (1936) model of cone sheet and ring dyke emplacement*

Anderson (1936) developed a mathematical model for the dynamic emplacement of cone sheets and ring dykes based on field observations from the geological surveys of Mull, Ardnamurchan, Skye and Richey's (1928) paper on the Mourne (N. Ireland) granite ring dykes. Essentially expanding the original hypotheses presented in Bailey et al., (1924), Anderson (1936) applied centre of dilation (radial displacement) and point-push (upwards directed) strain models to a homogeneous and semi-infinite (a horizontal plane represents the free surface) solid in order to model the local stress field during intrusion (Fig. 1.4). Both

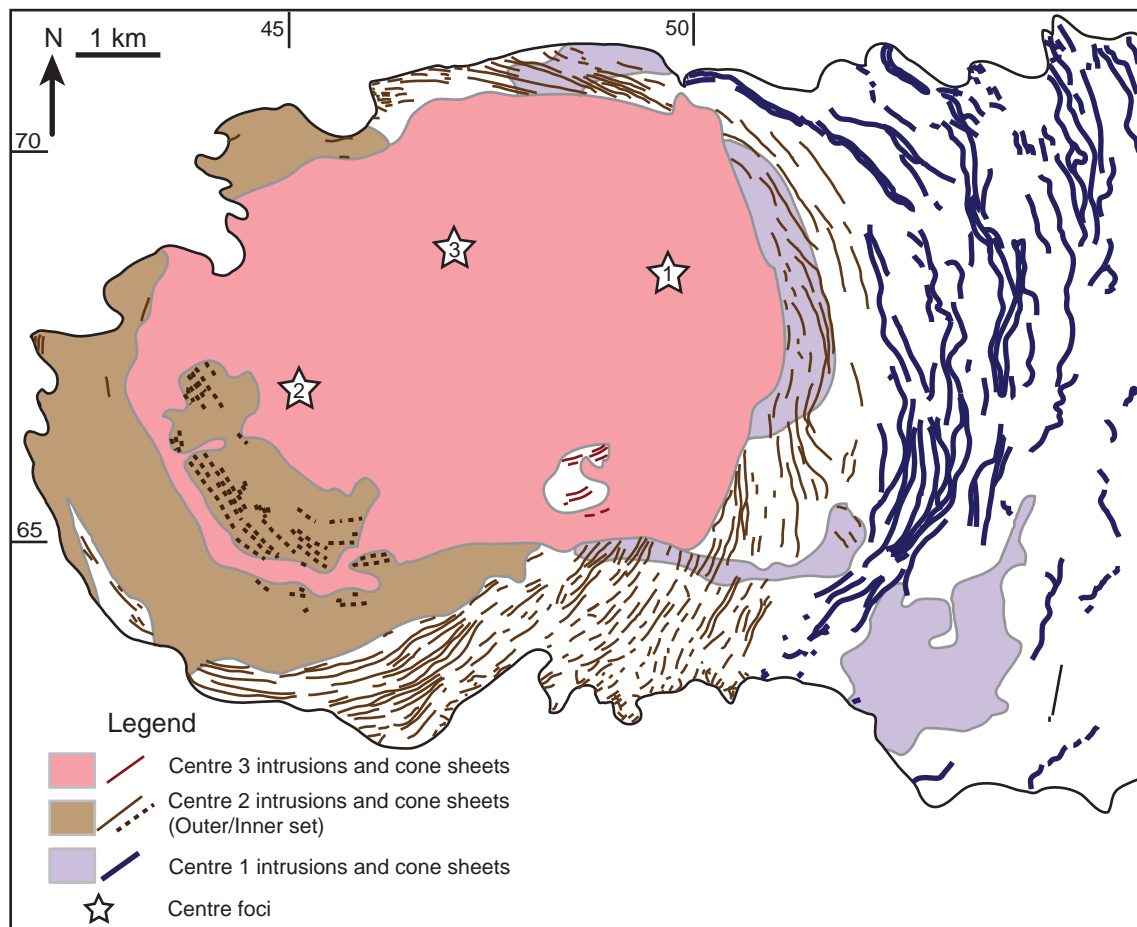


Fig. 1.3: Simplified geological map of Ardnamurchan highlighting the three intrusive centres and their associated cone sheet swarms (after Richey and Thomas, 1930; Emeleus, 2009). Co-ordinates correspond to the UK National Grid.

models contain a set of isostatic surfaces (equivalent to  $\sigma_3$  *sensu* Anderson, 1951), defining a pressure gradient, orthogonal to the principal pressure and therefore parallel to the roof of the source reservoir (Fig. 1.4). Anderson (1936) suggested that the centre of dilation experiments, which require a spherical magma chamber fed by a volumetrically insignificant feeder dyke, are unrealistic compared to the point-push model. Within the point-push model, inwardly inclined, concentric fractures are generated by the release of magmatic overpressure and are subsequently intruded to form cone sheets that steepen towards the centre (Anderson, 1936). Cone sheet intrusion is accommodated by the dilatational (i.e. tensional) opening of the fractures (Anderson, 1936). Beyond the reservoirs radius of influence the cone sheets flatten to form sills or steepen into dykes (Fig. 1.4) (Anderson, 1936). Roberts (1970) suggested tangential stresses across the magma–host rock interface would be variable in Anderson’s

(1936) model and reduced to a minimum at the shoulders of the chamber. Tensile failure would be promoted in these sectors of the magma chamber surface, restricting intruded cone sheets to a concentric belt with an inner area free from intrusion (Roberts, 1970). Anderson (1936) notes that variations in the shape of the source reservoir, influence of a regional stress field, and erosion level will dictate the exposed cone sheet structure and potentially produce radial dykes if the tangential stress dominates. Importantly, the model implies magma flow in cone sheets is likely radially upwards and outwards from the central source reservoir (Fig. 1.4) (Palmer et al., 2007).

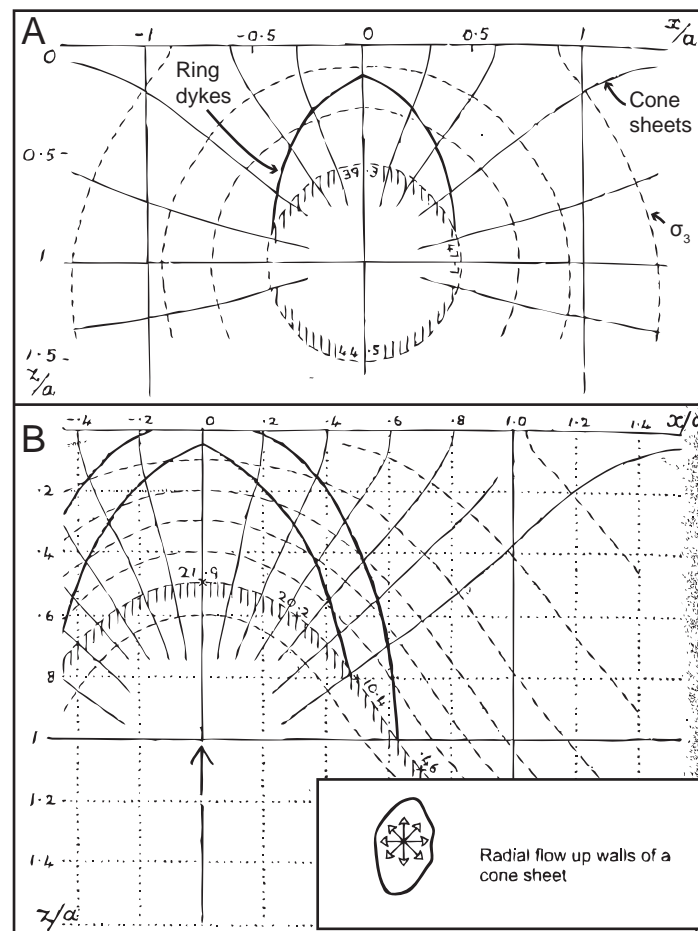


Fig. 1.4: The centre of dilation (A) and upwards point-push (B) mathematical models used by Anderson (1936) to model cone sheet emplacement. Note that in both models the cone sheets rotate into dykes or sills with distance from the centre. *Inset*: Plan view of the radial up and out magma flow regime (Palmer et al., 2007) implied from Anderson's (1936) models.

To model a ring dyke, Anderson (1936) applied a downward point-push to represent the instability and subsidence of the central roof block following evacuation of magma along cone sheets. Anderson (1936) considered ring dykes to be emplaced into shear fractures that have an outward inclination ( $\sim 60\text{--}70^\circ$  dip) and which become shallower as the surface is approached (Fig. 1.4). The thickness of the ring dyke is proportional to the subsidence of the central block, a potential issue considering the ring dykes of Ardnamurchan are  $\sim 7$  km diameter (Anderson, 1936).

## **1.2 Emplacement model variations**

Many subsequent alternative models of cone sheet emplacement have been proposed over the last 90 years. They can be divided into four groups, each focusing on a specific control or mechanism of cone sheet emplacement. These groups are: 1) shear fracture intrusion, 2) deflection of vertically propagating dykes by acid diapirs, 3) edifice deformation and 4) magma chamber shape and local stress field variability.

### **1.2.1 Shear fracture intrusion**

Dilatational opening vectors of cone sheets implies a component of horizontal displacement, which given the proximity of the free surface will require more energy than pure vertical (shear) uplift (Phillips, 1974). Intrusion of shear fractures offers an alternative explanation and predicts cone sheets are restricted to a concentric swarm with an inner and outer margin as magma is only injected from the shoulders of a magma chamber (see Phillips, 1974).

The amount of uplift induced by cone sheet intrusion may have significant implications for edifice construction, volcanic hazards and eruption pre-cursors (Le Bas, 1971). For example, Richey and Thomas (1930) calculated the uplift associated with intrusion for the Outer Centre 2 Ardnamurchan cone sheet swarm as 1200 m, assuming pure vertical (shear) opening, an aggregate cone sheet thickness of 1000 m and an average dip of  $35^\circ$ . However, in their memoir Richey and Thomas (1930) note that virtually all cone sheets display dilatational

opening (Keunen, 1937), which produces a significantly lower value (800 m) of uplift. Le Bas (1971) noted that many of the Carlingford cone sheets exploit pre-existing fractures, which may have formed as shear fractures prior to intrusion, potentially complicating determination of opening vectors and uplift amounts (Halsall, 1974).

#### 1.2.1:1 *Robson and Barr (1964)*

Robson and Barr (1964) argued that a magma chamber surface orthogonal to a principal stress axis required to reduce the shear stress at the magma–rock interface to zero, cannot be satisfied because the magnitude of the principal stress will vary with depth. From modelling variable regional stress fields around cylindrical holes (representing magma chambers) in isotropic mediums, Robson and Barr (1964) calculated that a vertical  $\sigma_1$  (an upward point-push) would instigate the propagation of inwardly inclined shear fractures from a magma chamber at  $\geq 4.7$  km depth. The sense of shear Robson and Barr (1964) calculated suggests the hangingwall (central roof block) subsided (Phillips, 1974) into the magma source. At shallower depths, a zone of tension dominates with modelled fracture planes oriented either moderately outwardly inclined (ring dykes) or vertical (Robson and Barr, 1964). The results imply greater excess magma pressures are required to intrude cone sheets compared to ring dykes and dykes (Robson and Barr, 1964).

#### 1.2.1:2 *Durrance (1967)*

Following suggestions that cone sheets intrude shear fractures (Robson and Barr, 1964) with a spiral geometry produced from point source percussion coning (Jeffrey, 1936; Hills, 1963), Durrance (1967) re-evaluated the Ardnamurchan cone sheets using a comparison between photoelastic stress studies and mapped field relationships. From a diametric compressive stress regime, Durrance (1967) showed that resultant sheet intrusions would exploit conjugate shear fractures formed orthogonal to the free surface and obtain similar vertical forms to previously described cone sheets. This predicts an outcrop disposition strongly defining a spiral arrangement centred on, and symmetrical about, the axis of the conical form (Fig. 1.5)

(Durrance, 1967). Application of this model to the Ardnamurchan cone sheets assumes they all belong to one central source, which indicates an apparent asymmetry in cone sheet dip from east ( $\sim 20^\circ$ ) to west ( $\sim 70^\circ$ ) (Durrance, 1967). Durrance (1967) argues this asymmetry and the apparent spiral strike (Fig. 1.5) of the cone sheets can be attributed to a point-source, below Sanna (NW Ardnamurchan; NM 44 69 using UK National Grid co-ordinates), with the conical axis inclined at  $\sim 65^\circ$  to the present land surface. This may be supported by the location of a gravity high beneath Sanna (Bott and Tuson, 1973). The bilateral symmetry of the cone sheets and ring dykes are parallel, suggesting both are sourced from a single magmatic system with alternation between a regional compressive (cone sheet) and extensional (ring dyke) regime controlling intrusive form (Durrance, 1967).

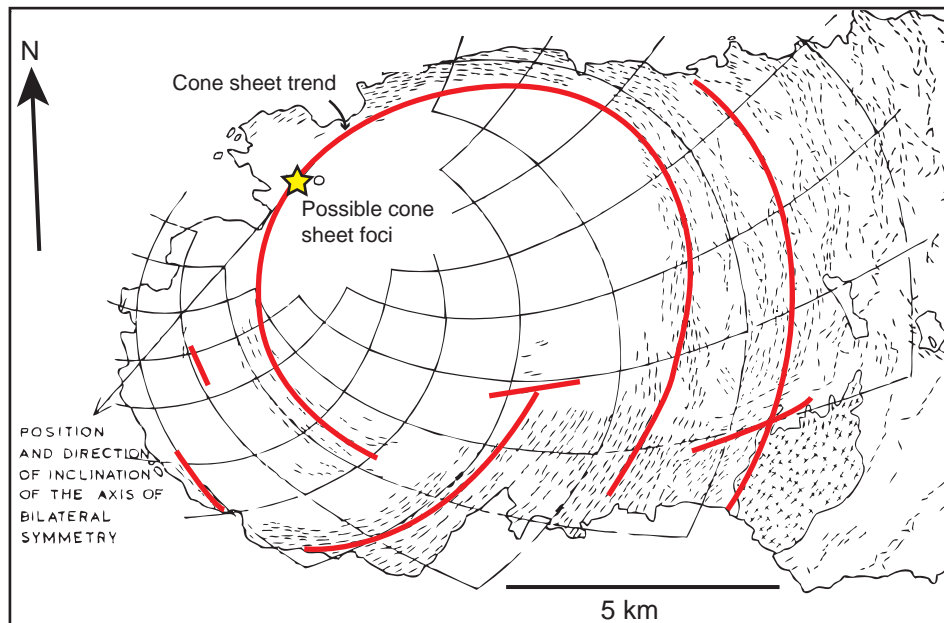


Fig. 1.5: Map of the apparent spiral strike of the Ardnamurchan cone sheets and their potential foci suggested by Durrance (1967).

#### 1.2.1:3 Phillips (1974)

Previous structural observations of cone sheets indicated it was unlikely that their intrusion was facilitated by the absence of a local stress field and subsidence of a central block along inwardly inclined fractures as proposed by Robson and Barr (1964), as there are space accommodation issues (Phillips, 1974). Phillips (1974) also noted that for conjugate shear fractures to form orthogonal to the surface, as suggested by Durrance (1967), it required

$\sigma_2$  to be vertical. Additionally it should be noted that the Durrance (1967) model relies on cone sheet intrusion within a compressive regional stress regime to be active during the emplacement of the cone sheets. However, throughout the evolution of the BIPIP the regional stress regime was extensional (cf. England, 1988). Considering Robson and Barr (1964) and Durrance (1967) to be incorrect, Phillips (1974) developed the model of Anderson (1936) to incorporate geomechanical aspects of magma intrusion.

Phillips (1974) notes that host rock deformation around an abruptly expanding spherical magma body produces similar magnitudes of compressional stress above and to the sides but that intermediate to these areas, the shoulders of the magma chamber, rotational strain occurs (Fig. 1.6). Rotational strain produces inwardly inclined shear fracturing as the roof uplifts relative to the immobile side regions (Phillips, 1974). After the initial injection of magma into the shear fractures, magma will propagate according to the deviatoric stress ( $\sigma_n - \sigma_h$ ; principal stress axes - hydrostatic stress) and host rock tensile strength ( $T$ ) conditions, which can significantly affect the type and longevity of fractures produced in any system (Phillips, 1974). Low deviatoric stress conditions where fluid pressure is sufficient to overcome  $\sigma_3 + T$  result in the formation of hydraulic tensile fractures orthogonal to  $\sigma_3$  (Phillips, 1974). In contrast, high porosity rocks under a high deviatoric stress but relatively low fluid pressures promote shear fracture formation. The inclination of these fractures relative to  $\sigma_1$  increases with pore fluid pressure at the time of fracture (Phillips, 1974). Therefore, depending on the deviatoric stress, cone sheets could extend in shear fractures steepening upwards to the surface (bowl-like geometry; cf. Gautneb et al., 1989) or if the deviatoric stress decreases they may curve into sub-horizontal sills (trumpet-shape; Klausen, 2004) and propagate as hydraulic tension fractures (Fig. 1.6) (Phillips, 1974).

Although Phillips' (1974) model appears more feasible than those of Robson and Barr (1964) and Durrance (1967), many field studies conducted on cone sheet swarms have reported that the majority of intrusions exhibit dilatational opening vectors and do not occupy shear fractures (e.g. Gaunteb et al., 1989; Gudmundsson, 2002; Pasquarè and Tibaldi, 2007). The only notable exceptions to this are Johnson et al., (1999) and Schirnack et al., (1999).

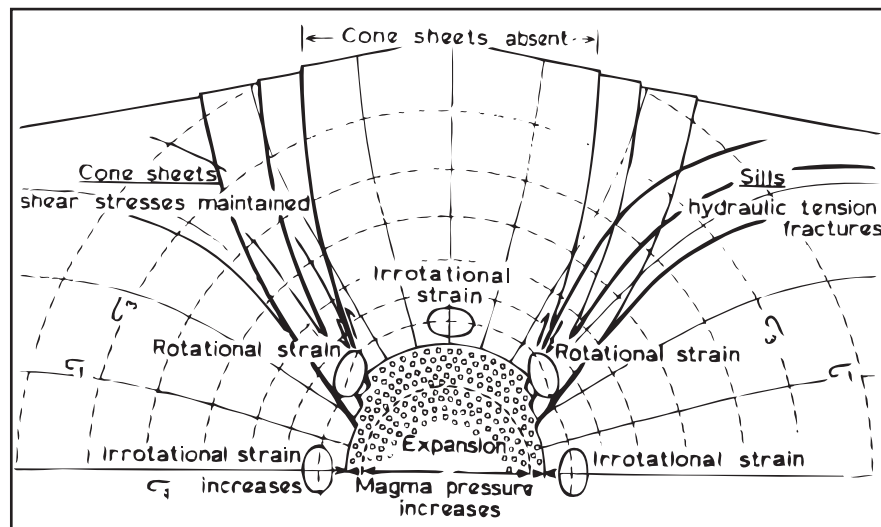


Fig. 1.6: Phillips (1974) cone sheet emplacement model (see text for details).

### 1.2.2 Deflection of vertically propagating dykes by acid diapirs

#### 1.2.2:1 Walker (1975)

Out of the five BIIP central complexes that contain cone sheet swarms, four (i.e. Ardnamurchan, Mull, Rum and Carlingford) display a strong correlation between the areal extent of the swarms and that of preceding host rock doming, potentially induced by an ascending acidic diapir (Walker, 1975a). The Cuillin cone sheets, Skye, are offset with respect to doming (Walker, 1975a). Walker (1975a) proposed magma preferentially intrudes along planes of increasing excess hydrostatic pressure ( $P_{He}$ ), derived from hydrostatic pressure ( $P_H$ ) and lithostatic pressure ( $P_L$ ) as  $P_{He} = P_H - P_L$ , which are depressed from their normal horizontal trend around acidic diapirs due to the lateral density variations imposed (Fig. 1.7a). Basaltic magma ascending below the acid diapir will be trapped beneath it, or if intrusion occurs slightly outside the diapir the magmatic sheet will be deflected along the inwardly inclined  $P_{He}$  surfaces (Fig. 1.7a) (Walker, 1975a). Nested cone sheet intrusion will occur when the acidic diapir reaches shallower crustal levels, instigating doming, and continued diapiric ascent modifies the  $P_{He}$  pathways (Walker, 1975a). With distance from the diapir the cone sheets are inferred to become sub-horizontal, potentially producing sill complexes genetically linked to cone sheet swarms (e.g. Loch Scridain cone sheet swarm, Mull; Walker, 1975a).

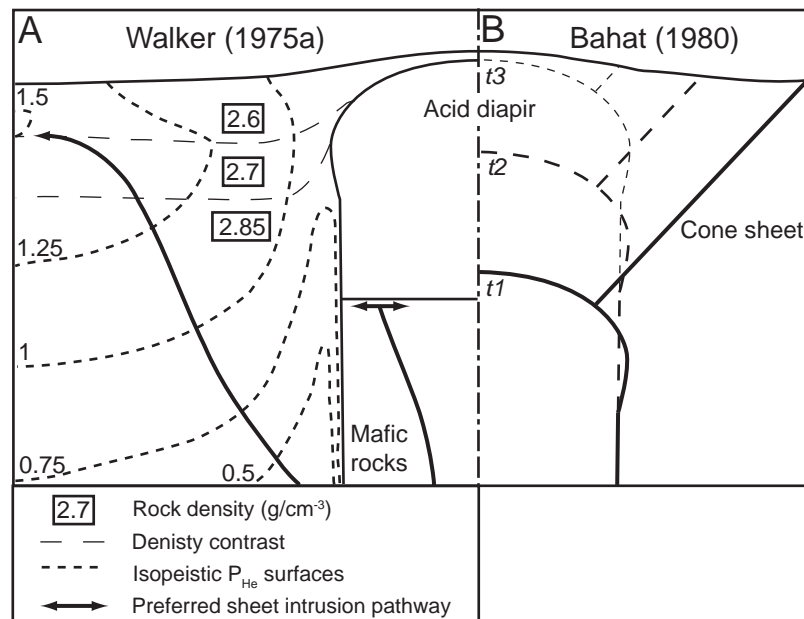


Fig. 1.7: A) Deflection of the  $P_{He}$  and density gradient surfaces, favouring cone sheet intrusion, produced by the ascent of an acidic diapor (Walker, 1975a). B) Incremental ascent of an acidic diapor producing Hertzian fractures intruded to form a swarm of nested, parallel cone sheets (Bahat, 1980).

#### 1.2.2.2 Bahat (1980)

Bahat (1980) suggested a Hertzian stress field, describing deformation initiated by the impact of a point source indenter (e.g. a rising acid diapor), controlled cone sheet emplacement.

A fracture generated in a Hertzian stress field will propagate orthogonally to the radial  $\sigma_1$  in a concentric (parallel to  $\sigma_2$ ) and inwardly inclined (parallel to  $\sigma_3$ ) manner; producing an overall inverted conical fracture (Fig. 1.7b) (Bahat, 1980). Incremental ascent of an acid diapor periodically indents the crust above forming new Hertzian conical fractures, which are potentially intruded (Bahat, 1980). The ascent rate and size of the diapor will determine the size of the Hertzian fractures and the intrusion rate of subsequent basaltic magma will control age relationships between the cone sheets, major intrusions (including those related to the acid diapor) and doming (Bahat, 1980). Bahat (1980) proposed cone sheets intrude tensile fractures at shallow depths but shear fractures at greater depths.

### 1.2.2:3 *Diapirism*

Both models, although significantly different in determining how cone sheets adopt their inverted conical form, require an ascending acidic diapir to drive the deflection of originally vertically ascending dykes. The geometry of granitic plutons, particularly circular intrusions (e.g. Ardara, Ireland; Arran, W Scotland), is traditionally viewed as a reflection on how the melt ascended; essentially as a cylindrical or tear-drop shape body with similar dimensions to the currently exposed outcrops (cf. Paterson and Vernon, 1995; Petford and Clemens, 2000). However, work in the last 20 years has highlighted that most granitic intrusions are tabular in form, often incrementally intruded and therefore represent emplacement mechanisms, not ascent processes (Petford and Clemens, 2000; Cruden and McCaffrey 2001; Stevenson et al., 2007a). As such, it appears there are few, if any, granitic diapirs and that tabular granites do not necessarily ascend as large bodies but rather as small pulses along crustal weaknesses (e.g. faults and shear planes) (Molyneux and Hutton, 2000; Cruden and McCaffrey 2001). The ability of ascending acidic melt to influence the local crustal stress field (depressing  $P_{He}$ ; Walker, 1975a) or structure (production of Hertzian fractures; Bahat, 1980) is therefore seriously questioned. Furthermore, Ardnamurchan contains negligible quantities (~2 %) of felsic intrusions that may be related to an acidic diapir (Bell, 1982).

### 1.2.3 Deformation of the volcanic edifice

#### 1.2.3:1 *Walker (1992; 1993)*

Walker (1992) proposed the term ‘coherent intrusion complexes’ to describe mafic cone sheet and dyke swarms that contain closely spaced, parallel sheet intrusions whose intensity reduces rapidly towards its outer margins. The model attributes both forms of coherent sheet swarm, which although temporally separate may have similar sources (e.g. a central magma chamber), to different emplacement styles controlled by intrusion rate and local tectonic structure (Walker, 1992). Accommodation of dyke complexes predominantly requires horizontal displacement, which can be satisfied where a decollement is developed at the

base of a volcanic edifice allowing lateral slip or where the extension rate at rift zones is  $\geq$  emplacement rates (Fig. 1.8a and b) (Walker, 1992). If, however, the volcanic edifice resists widening or the emplacement frequency is sufficiently higher, then a coherent sheet complex (cone sheets) will intrude from a central magma chamber (Fig. 1.8c and d) (Walker, 1992). Increased subsidence in the centre of the edifice, where the 'wedge' is greatest, will impart a stronger downbowed stress field resulting in steeper cone sheet dips towards the centre (Walker, 1992).

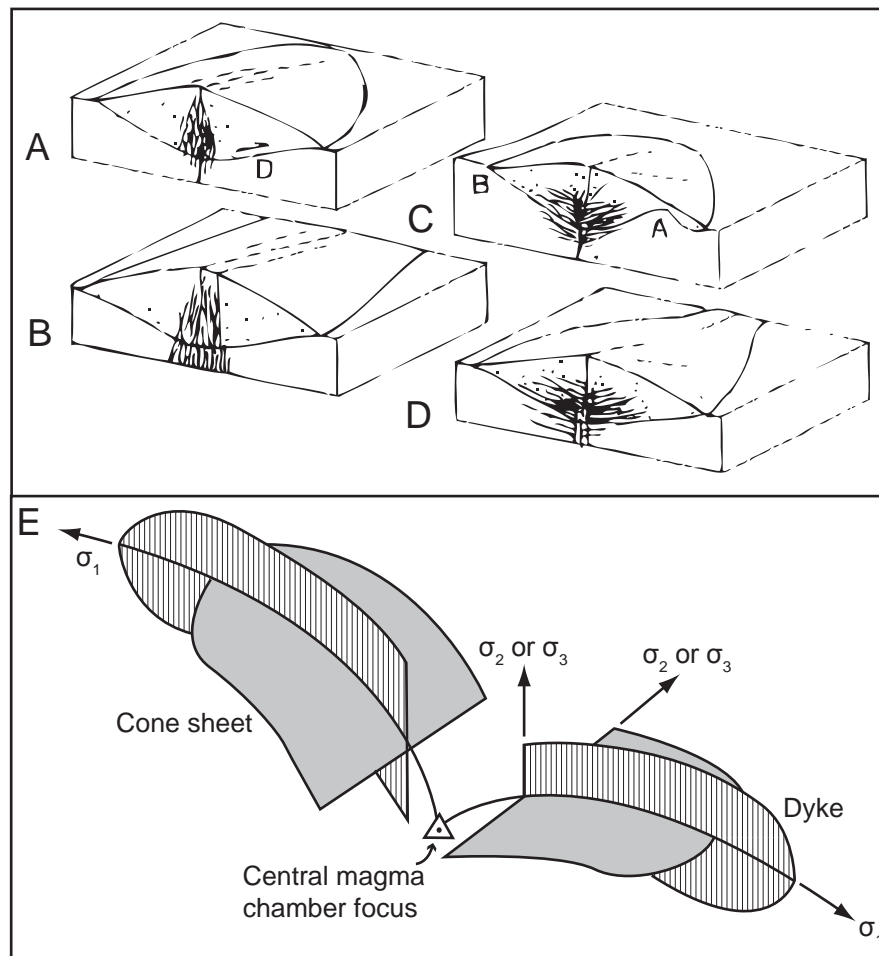


Fig. 1.8: A, B, C and D) Potential geometries of coherent igneous sheet complexes suggested by Walker (1992) to form in volcanic edifices (see text for details). E) Alternate intrusion of dykes and cone sheets from a central source dependent on fluctuations in the orientation of the local  $\sigma_2$  and  $\sigma_3$  principal stress axes (Walker, 1993).

Walker (1993) applied this model to the cone sheets and regional dykes associated with the Cuillin igneous complex, Skye. The dykes, predominantly oriented NW-SE, occur towards the margins of the Cuillin igneous complex and extend laterally for 10's of

kilometres (Walker, 1993). The cone sheets are laterally restricted to the igneous complex and show an increased intensity in the NW-SE quadrants (Walker, 1993). Walker (1993) suggested the regional stress field controlled the lateral propagation of linear dykes from the Cuillin igneous complex with  $\sigma_1$  oriented NW-SE and  $\sigma_3$  horizontally oriented NE-SW (Fig. 1.8e). Walker (1993) postulated  $\sigma_3$  would occasionally switch to vertical in response to an excursion of emplacement rate above spreading rate, favouring the intrusion of coherent cone sheet complexes with dips decreasing further from the source reservoir as deformation is significantly vertical (Fig. 1.8e) (Walker, 1993). From a vertical reconstruction of the planar cone sheets, Tibaldi et al., (2011) defined two potential central magma sources located at variable depths.

#### **1.2.4 Magma chamber shape and local stress field variability**

##### *1.2.4:1 Icelandic cone sheet swarms*

Gudmundsson (1995) and Klausen (2004) note that numerous cone sheets in Iceland feed lava flows and are therefore important to constrain in terms of their emplacement. The predominantly mafic cone sheet swarms observed in Iceland (e.g. Hafnarfjall volcanic complex) often display bimodal dip distributions and a dominance of strikes parallel to the volcanic rift zone, suggesting local and regional stress fields influenced emplacement (e.g. Gautneb et al., 1989; Gudmundsson, 1995). Gudmundsson (2002) suggests the bimodal dip distribution, observed in many cone sheet swarms in Iceland (Hafnarfjall, Gautneb et al., 1989; Reykjadalur, Gautneb and Gudmundsson, 1992; Hvalfjörður, Gudmundsson, 1995; Geitafell, Burchardt and Gudmundsson, 2009), reflects the position of cone sheet injection from the magma chamber source, with steeper sheets originating from the roof and shallower dipping sheets intruded from the margins. A central source for all Icelandic cone sheets is assumed, following their close proximity to central gabbro intrusions and their inward increase in intensity (Gudmundsson, 1998). As the majority of the cone sheets occupy dilatational fractures, Gautneb et al., (1989) suggested that as  $\sigma_3$  was likely perpendicular

to the fracture plane during opening (cf. Anderson, 1951), the magmatic overpressure ( $P_E$ ) combined with the lithostatic pressure ( $P_L$ ) must exceed  $\sigma_3 + T$  for intrusion to occur. Once intrusion occurs, the cone sheets will propagate according to the local stress field, itself controlled by the regional stress field,  $P_E$  and the shape of the magma chamber (Gautneb et al., 1989). Siler and Karson (2009) also highlight the importance of the mechanical properties of the host rock, such as Young's modulus, on the local stress field. From these parameters, many authors (e.g. Gautneb et al., 1989; Gautneb and Gudmundsson, 1992; Gudmundsson, 1998) numerically modelled cone sheet morphologies generated from geometrically variable magma chambers considered to be a centre of dilation (Fig. 1.4a); a model Anderson (1936) considered less realistic compared to an upward point-push model. Figure 1.9 presents two numerical models showing the tendency of cone sheets to revert to sub-vertical dykes or sub-horizontal sills as they approach the surface from a spherical (or prolate) or sill-like magma chamber source, respectively. The cone sheet morphologies define distinctive bowl-shape (Fig. 1.9a) and trumpet-like (Fig. 1.9b) geometries (see Chadwick and Dieterich, 1995; Gudmundsson, 1998; Klausen, 2004). Gautneb et al., (1989) suggested that inflation, or deflation, of the central magma chamber simultaneous to cone sheet swarm emplacement may modify the local stress field enough to alter preferred cone sheet trajectories and potentially produce the observed variability in strike, dip and cross-cutting relationships.

There is a prominent rift-parallel (NW-SE) regional dyke swarm throughout Iceland, which often displays a marked absence in many volcanic centres (Gautneb and Gudmundsson, 1992; Klausen, 2006). Gautneb and Gudmundsson (1992) and Gudmundsson (1998) attribute this spatial variation to the entrapment of vertically ascending regional dykes by upper crustal magma chambers; a process which may trigger cone sheet intrusion. Theoretically the local stress field controls both the distribution of cone sheets intruded and regional dykes that are trapped. Gautneb and Gudmundsson (1992) calculated that the magnitude of the local stress field decreased inversely as the cube of the distance from the central magma chamber, implying that local stresses could only influence emplacement pathways close to the magma chamber. Klausen (2004) indicated such a decrease in the magnitude of the local stress field

may be manifested in a fanning arrangement of cone sheets within a swarm.

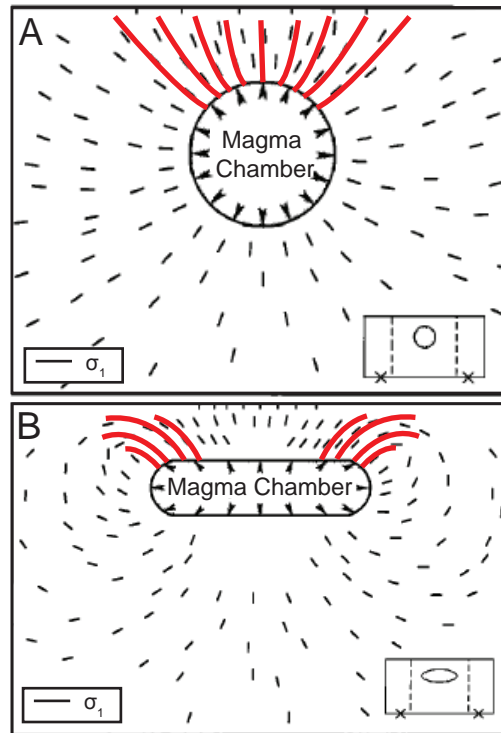


Fig. 1.9: Numerically modelled orientations of local  $\sigma_1$  principal stress axes associated with overpressured spherical (A) and sill-like (B) magma chambers, which favour the intrusion of bowl-like and trumpet-like cone sheets, respectively (Gudmundsson, 2006).

#### 1.2.4:2 *Gran Canaria*

The cone sheet complex of the Miocene (16 Ma) Tejeda complex, Gran Canaria, is predominantly felsic, 20 km in diameter and divided into two swarms showing no systematic age distribution. Individual sheets dip consistently at  $\sim 45^\circ$ , measured over 1200 m of relief, suggesting cone sheets are parallel and converge on a central axis rather than a point source (Schirnick et al., 1999). This contrasts with models of decreasing outward dips (cf. Harker, 1904; Bailey et al., 1924; Richey and Thomas, 1930) or bimodal dip distributions observed elsewhere (cf. Gautneb et al., 1989; Gautneb and Gudmundsson, 1992; Gudmundsson, 1998) and implies that there is not a single focus point. Schirnick et al., (1999) proposed episodic replenishment of a laccolith magma source (at  $<2$  km depth) was too voluminous to be accommodated purely by host rock deformation (i.e. doming) and instead resulted in

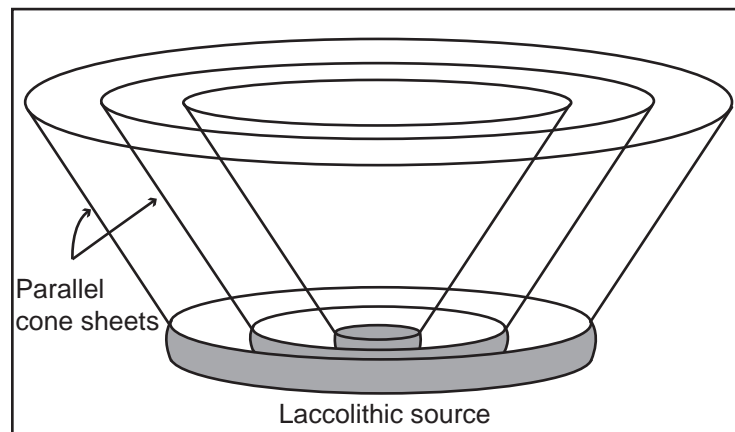


Fig. 1.10: Nested parallel cone sheets of Miocene Tejeda complex, Gran Canaria, attributed to the inflation and deflation of a central source laccolith (Schirnack et al., 1999).

cone sheet intrusion from the laccolith periphery (Fig. 1.10). Consequently, dilation was predominantly vertical as lateral growth was restricted (Schirnack et al., 1999). Although cone sheet structure was controlled by the laccolithic source, this model bears similarities to that of Phillips (1974) and Walker (1992).

### 1.3 Discussion

It can be seen from the sections above and Appendix A that many descriptions of cone sheet swarms and their proposed emplacement mechanisms often incorporate elements from numerous models, highlighting the variability between cone sheet-bearing complexes (Burchardt et al., 2011). However, a series of fundamental assumptions and observations, that originate from Anderson's (1936) model and are common to virtually all subsequent models, can be elucidated (cf. Siler and Karson, 2009):

1. Cone sheet strike is roughly concentric around a central complex.
2. Cone sheets within a swarm dip inwards towards a common focus.
3. Excess magmatic overpressure within the central source produced a local stress field which instigated the formation of new inverted conical fractures.
4. Magma flow is required to radiate upwards and outwards from the central source (Fig.

1.4b *inset*).

These fundamental parameters have been tested and corroborated by analogue experiments (e.g. Mathieu et al., 2008; Galland et al., 2009). It is important to note that many authors have dispensed with the term ‘cone sheets’, to avoid its genetic connotations (Tibaldi et al., 2011), in favour of descriptive terms such as ‘centrally inclined sheets’ (Walker, 1975b; Walker, 1993), ‘inclined sheets’ (e.g. Gautneb et al., 1989) and ‘coherent intrusive-sheet complexes’ (e.g. Walker, 1992). However, as all emplacement models are generally based on the fundamental components of Anderson’s (1936) mathematical model, the term ‘cone sheet’ is adopted throughout this thesis.

In light of recent advances in understanding lateral magma migration, it is important to re-evaluate cone sheet emplacement, the focus of this PhD thesis, which has widely been assumed to be dominantly vertical from a central magma source (e.g. Gudmundsson, 1995; Schirnick, 1999; Palmer et al., 2007). Little evidence, if any, is usually provided as to why a central source is adopted apart from the inwardly inclined disposition and proximity of the sheet intrusions. The exceptions to this are the studies of Herrero-Bervera et al., (2001; 2003) and Geshi (2005), which are summarised below and are seemingly compatible with a central magma source. Several other studies have suggested a central source based on rare flow lines (comparable to slickenlines) on cone sheets, which need to be interpreted with caution (Gautneb and Gudmundsson, 1992; Siler and Karson, 2009); the increase in cone sheet intensity towards the swarm inner margin and that some cone sheets may be traced back towards a central gabbro intrusion (Gudmundsson, 1998; 2002).

### 1.3.1 Cuillin cone sheets, Skye

Herrero-Bervera et al., (2001) conducted an anisotropy of magnetic susceptibility (AMS) study, utilised to measure primary magmatic flow fabrics, on cone sheet and regional dyke swarms focused on the Cuillin igneous complex. Although several errors were made in their data presentation (Aubourg et al., 2003), which were later corrected, Herrero-Bervera et al.,

(2001; 2003) identified a strong sub-horizontal magma flow regime in both the cone sheets and the dykes, apparently radiating outwards from the central focus but concentrated in a NW-SE direction. From these results Herrero-Bervera et al., (2001) proposed sheet intrusions propagated in the direction of maximum  $P_{He}$  (cf. Walker, 1975a) with either cone sheets or linear dykes favoured depending on the dynamics of the local stress field (cf. Walker, 1993).

### **1.3.2 Otoge cone sheet swarm, Japan**

The cone sheets of the Otoge central complex dip inwards at  $\sim 30^{\circ}$ – $60^{\circ}$ , decreasing towards the outer margin, and exhibit very rare cross-cutting relationships (Geshi, 2005). From this, Geshi (2005) proposed the individual cone sheets had a planar form (cf. Schirnack et al., 1999) and overall described a slight fanning arrangement (cf. Klausen, 2004). Cone sheet intensity is greatest to the E and W of the central complex with a geochemically similar, younger linear dyke swarm developed along a N-S axis (Geshi, 2005). Magma flow indicators, such as elongated bubbles, enclaves and imbricated phenocrysts describe a radial, upward magma flow in the cone sheets and a sub-horizontal flow regime in the linear dyke swarm with both focusing on the main Otoge central complex (Fig. 1.11; Geshi, 2005). The model for their emplacement therefore contains aspects of upward, radial flow (cf. Anderson, 1936); an alternation between cone sheet and dyke emplacement attributed to  $\sigma_2$  and  $\sigma_3$  fluctuations (cf. Walker, 1993) and planar cone sheet geometries (cf. Schirnack et al., 1999).

### **1.3.3 Summary**

Cone sheets are integral components of sub-volcanic systems and may provide conduits to the surface and influence host rock deformation. A review of previous emplacement models highlights several common fundamental processes. Although the model of Geshi (2005) strongly supports a central source and therefore provides an ideal example of cone sheet intrusion, other evidence of magma flow in cone sheets is found to be severely lacking. In this thesis, it will be argued that cone sheets do not require a central source and may instead be fed laterally from adjacent magmatic systems.

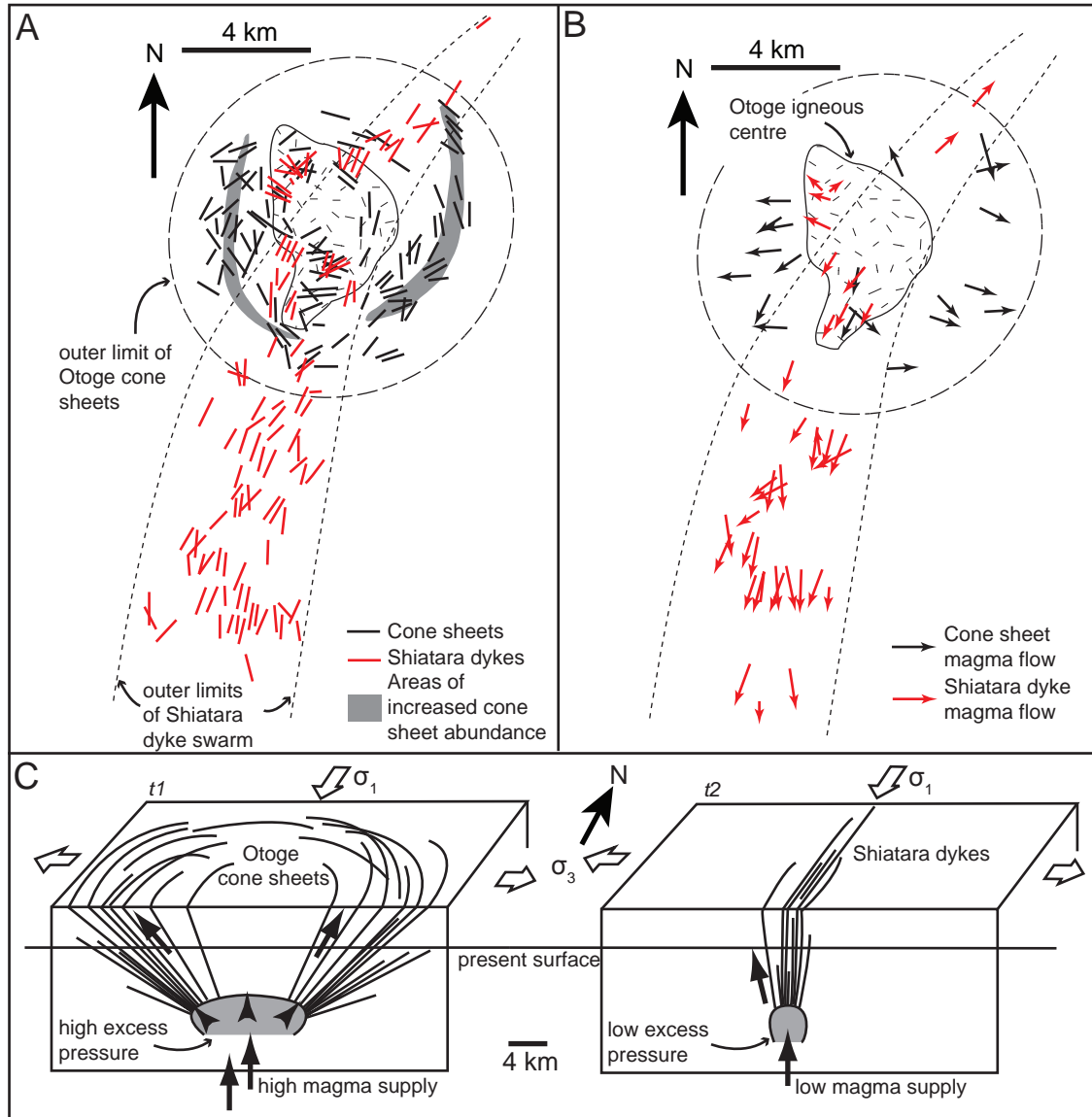


Fig. 1.11: Individual cone sheet and dyke swarm surface traces (A) and magma flow directions (B) within the Otoge igneous centre, Japan (Geshi, 2005). C) Form of the sheet intrusions is controlled by the magma supply rate and subsequent magmatic overpressure within a central chamber (Geshi, 2005).

## 1.4 Thesis structure

The thesis examines the emplacement of sub-volcanic sheet intrusions, particularly cone sheets, observed in the Ardnamurchan central complex, NW Scotland.

**Chapter 2** - provides a brief introduction to the theory and application of anisotropy of magnetic susceptibility (AMS) with respect to determining magma flow regimes in igneous

sheet intrusions.

**Chapter 3** - discusses previous studies of the geology of Ardnamurchan and places it within a regional context.

**Chapter 4** - presents field observations and structural measurements of the Ardnamurchan cone sheets and discusses controls on their emplacement.

**Chapter 5** - details and discusses the AMS results of the Ardnamurchan cone sheets, providing an interpretation of their magma flow regime.

**Chapter 6** - considers both the field and AMS data collected from the Ardnamurchan cone sheets to identify potential emplacement models, which are then discussed to highlight caveats.

**Chapter 7** - contains a succinct description and interpretation of the emplacement of the Ben Hiant Dolerite intrusion (Ardnamurchan, NW Scotland), which is used to test hypotheses generated in Chapter 6.

**Chapter 8** - provides a discussion and concluding remarks on the implications of the results and emplacement models presented in this thesis to other cone sheet complexes.

---

## CHAPTER 2

### ANISOTROPY OF MAGNETIC SUSCEPTIBILITY

---

A review of previous cone sheet emplacement models highlights that cone sheets are often assumed to be fed from a central source, implying a radial upwards and outwards magma flow regime. However, few studies have attempted to corroborate this premiss despite the important constraints and controls on emplacement that may be elucidated from an understanding of magma flow in cone sheets. In this thesis, magma flow of the classic Ardnamurchan cone sheets has been quantitatively evaluated using anisotropy of magnetic susceptibility (AMS), a powerful tool in analysing subtle petrofabrics. This chapter presents an introduction to the theory of AMS and its application to defining primary magma flow fabrics within sheet intrusions.

## **2.1 Rock magnetism and its anisotropy**

### **2.1.1 Physics of grain scale magnetism**

Each electron has a distinctive spin and angular momentum, which controls an atoms magnetic moment (the measured intensity of magnetisation) (Dunlop and Özdemir, 1997). To reduce the magnetostatic energy generated by the motion of electrically charged particles, electrons are paired and organised into shells of variable electron capacity (Tarling and Hrouda, 1993). However, application of an external magnetic field to any substance (above 0K) imparts a preferred orientation to the spin and angular momentum of all electrons, producing an increase in magnetic moment (Tarling and Hrouda, 1993). If an atom contains virtually complete atomic shells, perhaps missing one electron, the net magnetic moment will be negligible (Dunlop and Özdemir, 1997). In contrast, first transition series elements (Fe, Mn, Co, Cr and Ni) have significantly more unpaired electrons in their 3d shell, which

promotes the development of an electrostatic charge (i.e. an alignment of angular momentum and spin of electrons) through the interaction of electrons within neighbouring ions (Tarling and Hrouda, 1993; Dunlop and Özdemir, 1997). When an external magnetic field is applied a strong net magnetic moment results (Dunlop and Özdemir, 1997). The strength of magnetisation ( $M$ ; measured in  $\text{Am}^{-1}$  SI units) is also dependent on the strength of the applied field ( $H$ ; measured in  $\text{Am}^{-1}$  SI units) and the grains susceptibility ( $K$ ; how easy it is to magnetise), which is dimensionless (Tarling and Hrouda, 1993):

$$M = KH$$

From this equation and the principles of magnetism described above it can be understood how the quantity of first transition series ions in a grain will control its susceptibility and how an organised crystal structure will focus the magnetic moment along specific crystallographic ‘easy’ axes (magnetocrystalline anisotropy; Tarling and Hrouda, 1993) by controlling cation positioning. The shape of a grain may also control susceptibility as the alignment of electrons creates poles on the crystal surface, which form at either end of the grain’s long axis (shape anisotropy) to minimize magnetostatic forces (Tarling and Hrouda, 1993). Susceptibility to magnetisation of a grain will consequently depend on the relative orientation of the applied field to the magnetocrystalline ‘easy’ axes or shape axes, as well as the grain composition. Importantly, the crystal lattice of most minerals influences grain shape and consequently the shape anisotropy; i.e. there is a general relationship between susceptibility and crystallography (Borradaile and Jackson, 2004).

## **2.1.2 The magnetic response of grains**

### *2.1.2.1 Diamagnetism and Paramagnetism*

If a grain contains complete electron shells, an induced magnetisation will cause electron spins to precess in an antiparallel direction to that of the applied magnetic field, resulting in a weak, negative magnetic moment (Fig. 2.1) (Tarling and Hrouda, 1993). This behaviour

is termed diamagnetism (O'Reilly, 1984; Tarling and Hrouda, 1993; Dunlop and Özdemir, 1997). As magnetisation is directly linked to magnetic susceptibility, diamagnetic minerals (e.g. quartz and calcite) have a weak, negative magnetic susceptibility ( $< -10^{-6}$  SI; Dunlop and Özdemir, 1997).

All other grains, those containing atoms with incomplete electron shells, are paramagnetic (O'Reilly, 1984; Tarling and Hrouda, 1993; Dunlop and Özdemir, 1997). The partial alignment of magnetic moments parallel to the applied magnetic field (Fig. 2.1) produces a relatively weak ( $\sim 10\text{--}100 \times 10^{-6}$  SI), positive magnetic susceptibility (Tarling and Hrouda, 1993). Paramagnetism, the alignment of isolated and non-interacting first transition series elements (Dunlop and Özdemir, 1997), is therefore predominantly observed in ferromagnesian silicates (e.g. biotite, pyroxene and amphibole) as well as some Fe-Ti oxides (e.g. ilmenite) and iron sulphides (e.g. pyrite) (Tarling and Hrouda, 1993).

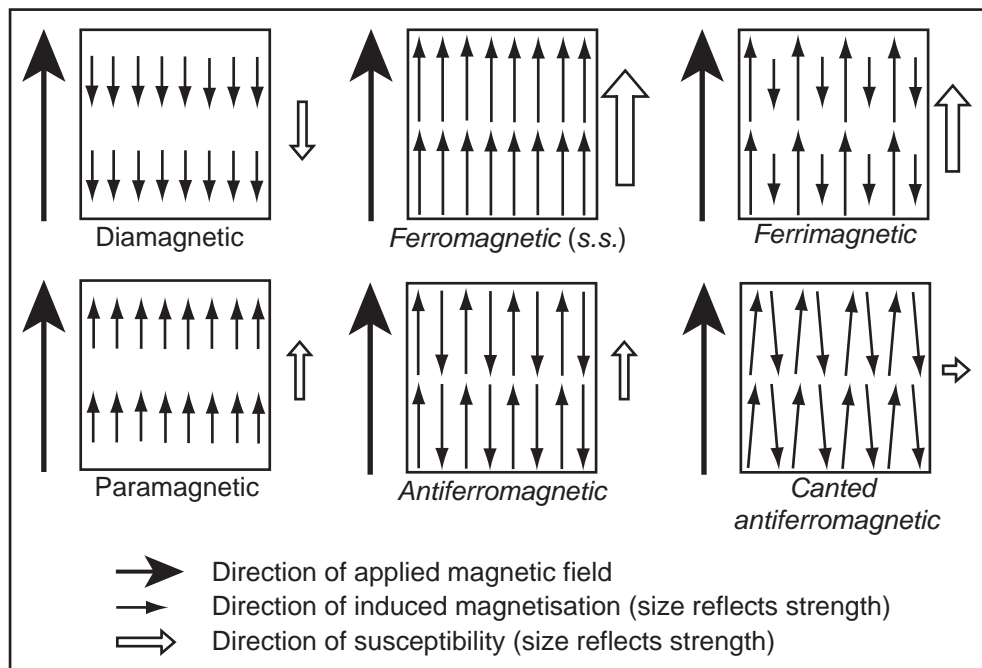


Fig. 2.1: The magnetic susceptibility to an applied field of materials with various magnetic behaviours (after Tarling and Hrouda, 1993; Dunlop and Özdemir, 1997).

The difference in susceptibility values for diamagnetic and paramagnetic minerals implies that paramagnetism is dominant. However, temperature fluctuations can alter the alignment of electron spins within paramagnetic minerals to an extent that susceptibility is

inversely proportional to increasing temperature; the Curie-Weiss law (Dunlop and Özdemir, 1997). In contrast, the magnetic susceptibility of diamagnetic minerals is temperature independent (Tarling and Hrouda, 1993), implying diamagnetic behaviour may be important at high temperature. Characteristically, both diamagnetic and paramagnetic grains do not hold a magnetisation after the applied external field is removed (Butler, 1992).

#### 2.1.2:2 *Ferromagnetism*

Ferromagnetic (*sensu lato*) grains generally produce a strong, positive susceptibility (up to three orders of magnitude greater than paramagnetic grains) in response to an applied external field due to a significant abundance of first transition series elements (Tarling and Hrouda, 1993). As such, only a small quantity of ferromagnetic (*s.l.*) grains is required to dominate the magnetic signature of a sample. Removal of the external field leaves ferromagnetic (*s.l.*) grains with a remanent magnetisation for a variable period of time dependent on grain size (Dunlop and Özdemir, 1997). Although rare in nature, true *ferromagnetic (sensu stricto)* substances (e.g. pure iron) adopt a strong magnetisation consistently parallel to the applied magnetic field through direct exchange coupling of electrons between adjacent cations, which induces a common spin direction (Fig. 2.1) (Borradaile and Jackson, 2004). However, most minerals are complex structures comprising of cations and anions (Borradaile and Jackson, 2004). Magnetisation is instead controlled by the crystal lattice structure through the formation of magnetic sub-lattices, which instigates superexchange (indirect) coupling of electrons between cations across an intervening anion (Dunlop and Özdemir, 1997). The magnetic moments of the two cations within the magnetic sub-lattice are directionally opposite, with one parallel to the external field and the other antiparallel (Tarling and Hrouda, 1993). If the net magnetic moments of each direction in the sub-lattice are equal, the grain behaves *antiferromagnetically* and produces a weak, positive susceptibility (Fig. 2.1) (Tarling and Hrouda, 1993). Occasionally some grains display *canted antiferromagnetism*, whereby the induced magnetic moments, although still equal, deviate from exact (anti-)parallelism with the external field and result in a slight, positive susceptibility orthogonal to the applied

field (Fig. 2.1) (Tarling and Hrouda, 1993; Borradaile and Jackson, 2004). A significant difference in the amount of first transition series cations in adjacent magnetic sub-lattices results in a strong, positive susceptibility parallel to the external magnetic field and is termed *ferrimagnetic* behaviour (Fig. 2.1) (Tarling and Hrouda, 1993). Ferromagnetism (*s.l.*) is superimposed onto paramagnetic behaviour and may be removed by increasing the applied field strength or heating above a grains Curie (*ferrimagnetic*) or Néel (*antiferromagnetic*) Temperature ( $T_C$  and  $T_N$  respectively).

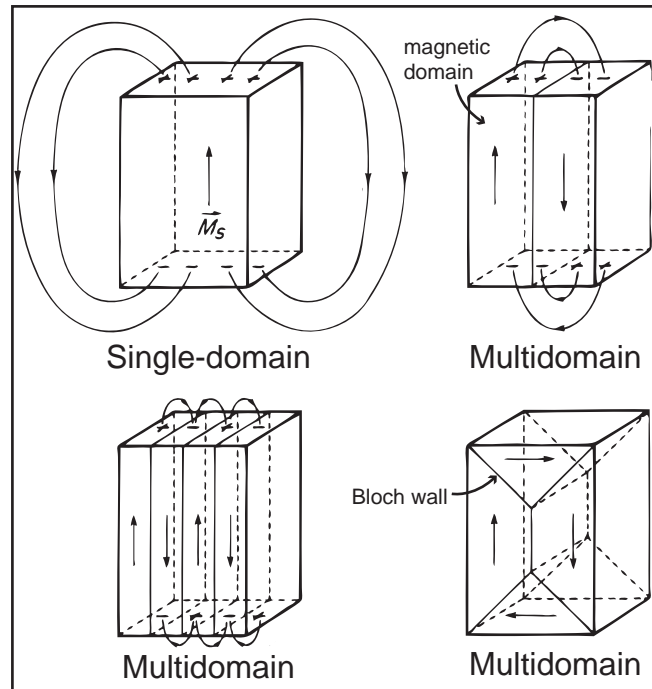


Fig. 2.2: Potential imposed configurations of magnetic moments, to reduce the magnetostatic energy, in ferromagnetic (*s.l.*) grains of variable sizes in the absence of an applied magnetic field (Dunlop and Özdemir, 1997).

The magnetic response of ferromagnetic (*s.l.*) grains to an applied field is strongly dependent on grain size (Butler, 1992). Grains  $\sim >10 \mu\text{m}$  are divided into discrete volumes of atoms, with a specific net magnetic moment parallel to one of several crystallographic ‘easy’ axes, by Bloch walls and are termed magnetic domains (Fig. 2.2) (Butler, 1992; Dunlop and Özdemir, 1997). Under zero field conditions the magnetic domains and their associated magnetic moment will orient themselves to minimize the internal magnetostatic energy (Fig. 2.2). If a weak magnetic field is applied to a true multidomain (MD) grain (e.g.  $>100 \mu\text{m}$

for magnetite), the domains with magnetic moments sub-parallel to the external field will grow, by Bloch wall translation, at the expense of differently oriented domains and thus produce a net magnetic moment aligned parallel to the magnetic field (Tarling and Hrouda, 1993). A greater amount of domains oriented parallel to a specifically oriented external field will therefore result in a stronger magnetic susceptibility. The number of magnetic domains decreases with grain size until only one domain can be accommodated; single-domain (SD) grains for magnetite are  $< 1 \mu\text{m}$  (Butler, 1992). As SD grains only contain one domain, the orientation of its magnetic moment reflects its remanent magnetisation (Fig. 2.2). Application of an external magnetic field to an SD grain (anti-)parallel to the remanent magnetisation will generate no magnetic response (Tarling and Hrouda, 1993). Instead, if the applied magnetic field is oriented orthogonally to the original remanent magnetisation, a slight deviation will be induced (Fig. 2.2), i.e. SD grains display a stronger susceptibility along a plane orthogonal to its actual magnetisation (Tarling and Hrouda, 1993). Grains ranging from 1–100  $\mu\text{m}$  are termed pseudo-single-domain (PSD) as crystal lattice imperfections act to pin domain walls, effectively reducing their capability to translate under an applied magnetic field (Dunlop and Özdemir, 1997).

### 2.1.3 Magnetic responses of key minerals and mineral groups in igneous rocks

From a magnetic perspective, the most important minerals in igneous rocks are Fe-Ti oxides (Tarling and Hrouda, 1993). Figure 2.3 depicts the chemical relationships between the titanomagnetite, titanomaghaemite and ilmenohaematite solid solution series on a ternary diagram (Tarling and Hrouda, 1993). The shaded areas represent the common Fe-Ti oxide components of mafic igneous rocks and show that the *ferrimagnetic* titanomagnetites tend to dominate in abundance (Tarling and Hrouda, 1993). The high intrinsic susceptibility of *ferrimagnetic* minerals increases their importance (Tarling and Hrouda, 1993).

#### 2.1.3:1 Titanomagnetites

At high temperatures ( $>560^\circ\text{C}$ ) there is complete solid-solution series between pure

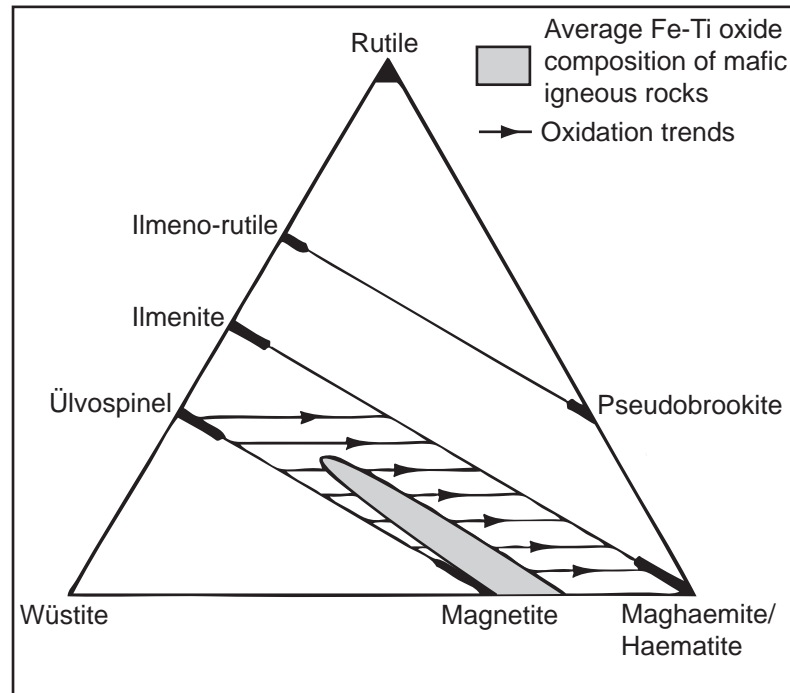


Fig. 2.3: Ternary diagram highlighting the solid-solution series of magnetite–ülvöspinel and ilmeno–haematite (Tarling and Hrouda, 1993). Oxidation trends and the typical Fe-Ti oxide composition of igneous rocks are also displayed.

magnetite ( $\text{Fe}_3\text{O}_4$ ) and ulvöspinel ( $\text{Fe}_2\text{TiO}_4$ ) following crystallisation from  $>1200\text{--}800\text{ }^\circ\text{C}$  (Tarling and Hrouda, 1993; Dunlop and Özdemir, 1997). The two magnetic lattices developed (A = tetrahedral; B = octahedral) are not equal in magnetites, resulting in a *ferrimagnetic* behaviour (Fig. 2.4). Substitution of  $\text{Fe}^{3+}$  by  $\text{Ti}^{4+}$ , to form ulvöspinel, makes the lattices magnetically equal and produces an *antiferromagnetic* behaviour (Fig. 2.4). Superexchange coupling forces are also weakened by  $\text{Ti}^{4+}$  substitution, lowering the Curie Temperature ( $T_C$ ) from  $578^\circ\text{C}$  (pure magnetite) to a Néel Temperature ( $T_N$ ) of  $-153^\circ\text{C}$  (ulvöspinel) (Tarling and Hrouda, 1993). Inherently, ulvöspinel behaves paramagnetically at room temperature. As only single phases can exist at lower temperatures, equilibration of titanomagnetites often results in the exsolution of paramagnetic ilmenite along specific  $\{111\}$  crystallographic lamellae (Fig. 2.4) (Tarling and Hrouda, 1993). This may alter the shape and size of the *ferrimagnetic* component and may produce rods of SD titanomagnetite (Fig. 2.4) (Dunlop and Özdemir, 1997).

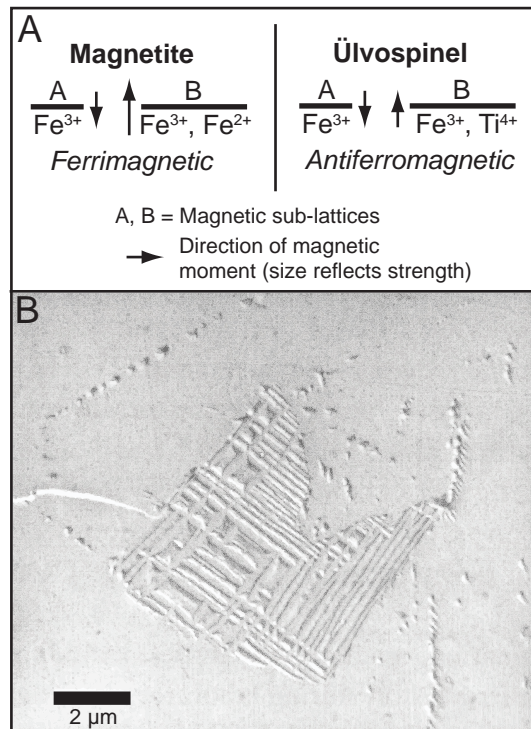


Fig. 2.4: A) Schematic diagram highlighting the control of the magnetic lattice composition on the magnetic response of magnetite and ülvospinel (Dunlop and Özdemir, 1997). B) Magnetite-ilmenite intergrowth following high temperature oxidation (Dunlop and Özdemir, 1997).

### 2.1.3.2 Titanomaghaemites

Crystallisation of titanomagnetite in an oxygen rich magma  $>1000^{\circ}\text{C}$  or the low temperature oxidation of titanomagnetite produces titanomaghaemites ( $\gamma\text{Fe}_2\text{O}_3$  to  $\text{FeTiO}_3$ ) (Dunlop and Özdemir, 1997). Titanomaghaemites are magnetically similar to titanomagnetites (e.g.  $T_c$  of pure maghaemite is  $590\text{--}675^{\circ}\text{C}$ ), although they often display slightly weaker susceptibilities (Tarling and Hrouda, 1993). On heating to  $200\text{--}350^{\circ}\text{C}$  titanomaghaemites typically invert to ilmenohaematite (Dunlop and Özdemir, 1997).

## 2.2 Application of anisotropy of magnetic susceptibility (AMS) to determining igneous petrofabrics

### 2.2.1 Mineral fabric description

A petrofabric is defined as the arrangement and distribution of minerals into a common

orientation following anisotropic stress (Hirt and Almqvist, 2011). As petrofabrics are anisotropic, they may be described by three mutually orthogonal principal axes of variable magnitude; the maximum ( $A_1$ ), secondary ( $A_2$ ) and minimum ( $A_3$ ) axes (Correa-Gomes et al., 2001). This allows mineral fabrics to be characterised by an ellipsoid, the shape of which directly relates to the coeval strain field and may range from prolate ( $A_1 > A_2 = A_3$ ) to triaxial ( $A_1 > A_2 > A_3$ ) to oblate ( $A_1 = A_2 > A_3$ ) (Fig. 2.5a). For example, prolate fabrics primarily result from the stretching and extension of minerals to define a strong lineation, whilst oblate fabrics typically form due to flattening (constriction) and are expressed by a planar foliation (Callot and Guichet, 2003; Féménias et al., 2004; Horsman et al., 2005; Twiss and Moores, 2007; Morgan et al., 2008). In igneous rocks, a petrofabric may be acquired during intrusion (e.g. magma flow, Bouchez, 1997; coeval tectonic shear, Correa-Gomes et al., 2001) or post-emplacement (e.g. *in situ* crystallisation; post-cumulus modification, O'Driscoll et al., 2008; tectonic strain, Borradaile and Henry, 1997). Additionally, multiple fabrics (sub-fabrics) may be present in a single rock (Hirt and Almqvist, 2011). Analysing petrofabrics can therefore provide important information on strain processes (e.g. including orientation and strength) and the evolutionary history of an intrusion.

### **2.2.2 Determination of the magnetic fabric using Anisotropy of Magnetic Susceptibility (AMS)**

Within igneous rocks, mineral fabrics are often not visible at outcrop (Martín-Hernández et al., 2004). Graham (1954) was the first to utilise AMS as a technique to provide quick, cheap and accurate analyses of weak/subtle fabrics in rocks. Subsequently, the AMS theory and technique has constantly been refined through its wide application to a plethora of geological studies (e.g. magma flow, palaeocurrent reconstruction and diagenetic processes).

The AMS of a rock sample is determined by the cumulative response of all constituent grains and is dependent on the orientation of their shape anisotropies and/or crystallographic lattice configurations with respect to a systematically varied direction of an applied magnetic field. Any common alignment of individual grains within a sample (i.e. a petrofabric) will act

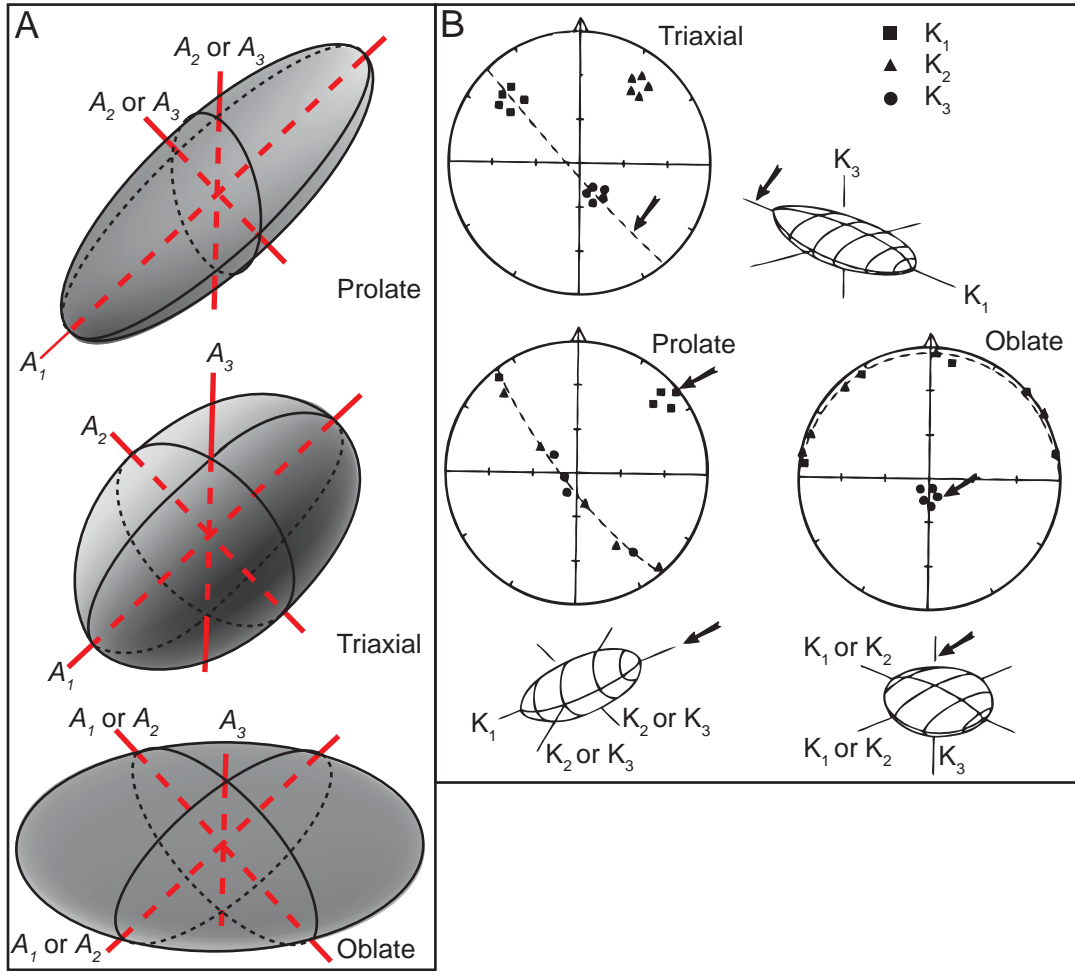


Fig. 2.5: A) Idealised petrofabric ellipsoids described by three mutually orthogonal axes;  $A_1$ ,  $A_2$  and  $A_3$ . B) Magnetic susceptibility tensor ellipsoids defined by the  $K_1$ ,  $K_2$  and  $K_3$  principal susceptibility axes (Tarling and Hrouda, 1993). Hypothetical equal area stereographic projections of triaxial, prolate and oblate magnetic fabrics are also provided (Tarling and Hrouda, 1993).

to focus the susceptibility anisotropy into specific directions and thus form a magnetic fabric. The magnetic fabric is described by the magnetic susceptibility tensor, which may be pictured as an ellipsoid comprising of three principal susceptibility magnitudes and a corresponding set of three orthogonal principal axis directions ( $K_1 \geq K_2 \geq K_3$ ) (Tarling and Hrouda, 1993) typically presented on an equal area, lower-hemisphere stereographic projection (Fig. 2.5b). As two principal susceptibility axes are virtually identical in magnitude for prolate ( $K_2$  and  $K_3$ ) and oblate ( $K_1$  and  $K_2$ ) ellipsoids, they plot as a girdle on the stereographic projection (Fig. 2.5b). The magnitude parameters are traditionally reported in terms of ‘size’ ( $K_{\text{mean}}$ ), ‘strength’ ( $P_j$ ) and ‘shape’ ( $T$ ) of the ellipsoid (Jelinek, 1978):

$$K_{\text{mean}} = (K_1 + K_2 + K_3)/3$$

$$P_j = \exp\sqrt{\{2[(\eta_1 - \eta)^2 + (\eta_2 - \eta)^2 + (\eta_3 - \eta)^2]\}}$$

and

$$T = [2\ln(K_2/K_3) / (\ln(K_1/K_3))] - 1$$

where  $\eta = (\eta_1 + \eta_2 + \eta_3)/3$ ,  $\eta_1 = \ln K_1$ ,  $\eta_2 = \ln K_2$ ,  $\eta_3 = \ln K_3$ . A  $P_j$  (degree of anisotropy) value of 1 describes a perfectly isotropic fabric whilst a  $P_j = 1.15$  describes a sample with 15% anisotropy and so on. Although these strength and shape parameters are widely used, Borradaile and Jackson (2004) highlight that for low anisotropies (<10 %), such as those of magmatic fabrics (Tarling and Hrouda, 1993), the significance of the ellipsoid shape is disproportionately represented compared to higher anisotropies. Owens (1974) and Stevenson et al., (2007a) advocate use of the following parameter set, in conjunction with  $K_{\text{mean}}$ , to allow easier visualisation with respect to the susceptibility ellipsoid:

$$H = (K_1 - K_3)/K_{\text{mean}}$$

$$L = (K_1 - K_2)/K_{\text{mean}}$$

$$F = (K_2 - K_3)/K_{\text{mean}}$$

$$m = (K_1 - K_2)/(K_2 - K_3)$$

and

$$\mu = \tan^{-1} m.$$

The strength of anisotropy is defined by the parameter H (%). Plotting L (lineation) against F (foliation) graphically displays the fabric shape, which is quantified by  $m$ , the slope of the line from the point through to the origin, and by  $\mu$ , the angle from the x axis to the line (Stevenson et al., 2007a).

### 2.2.3 Comparing magnetic fabrics to petrofabrics in igneous rocks

From the two previous sub-sections it is evident that the AMS ellipsoid size ( $K_{\text{mean}}$ ), shape ( $m$ ), strength ( $H$ ) and the orientations of its principal axes, referred to as the magnetic fabric, may parallel the mineral petrofabric (i.e.  $K_1 = A_1$ ;  $K_2 = A_2$ ;  $K_3 = A_3$ ) (Knight and Walker, 1988). Several studies have supported this assumption through combined AMS and petrographical analysis (e.g. Khan, 1962; Launeau and Cruden, 1998; Abelson et al., 2001; Callot et al., 2001; Féménias et al., 2004; Horsman et al., 2005; O'Driscoll et al., 2008). Even in weakly anisotropic igneous rocks, it is now widely accepted (e.g. Bouchez, 1997) that the magnetic lineations and foliations potentially reflect the magmatic fabric and can provide information on magma migration, flow geometries, and regional strain (King 1966; Owens and Bamford 1976; Hrouda, 1982; Borradaile 1987, 1988; Rochette 1987; Rochette et al., 1992; Tarling and Hrouda 1993; Petronis et al., 2004; Horsman et al., 2005; O'Driscoll et al., 2006; Stevenson et al., 2007a;). However, some magnetic fabrics, particularly the magnetic lineation, have been measured that significantly deviate from the mineral petrofabric (e.g. Geoffroy et al., 2002; Callot and Guichet, 2003; Aubourg et al., 2008; Creixell et al., 2009). Although processes responsible for sub-fabric formation have been suggested to account for these disparities (discussed further in section 2.2.4), there are several potential explanations related to the magnetic mineralogy that first need to be contemplated. An awareness of these possible caveats is further supported following a consideration of the broad range of mineralogical compositions and crystallisation histories that igneous rocks may have (section 2.1.3).

### 2.2.3:1 *Magnetic fraction composition*

The magnetic fraction of igneous rocks is typically dominated by either Fe-bearing silicate phases or by magnetite. In Fe-bearing silicate dominated rocks, the magnetocrystalline anisotropy of paramagnetic silicates such as olivine, biotite or amphibole will control the AMS fabric when magnetite is absent or of very low volume percent. Comparatively, for magnetite-bearing rocks (>0.1 vol. % magnetite) the contribution of Fe-Mg silicates is negligible due to the high intrinsic magnetic susceptibility of magnetite (Tarling and Hrouda, 1993). Stacey (1960) postulated the magnetic fabric of magnetite-bearing rocks (e.g. most mafic igneous rocks), therefore results primarily from the shape anisotropy of the grains of magnetite. This effect has been examined and corroborated by microscopic observations on various rock types (Khan, 1962; Uyeda et al., 1963; Ellwood and Whitney, 1980; Grégoire et al., 1995). However, some mineral phases (e.g. haematite, Tarling and Hrouda, 1993; tourmaline, Borradaile and Jackson, 2004) produce a magnetic fabric that is geometrically inverse to its petrofabric (i.e.  $K_1 = A_3$ ). For haematite, this occurs because its basal plane (parallel to its magnetocrystalline ‘easy’ axis) commonly defines an oblate crystal shape (Tarling and Hrouda, 1993) and haematite displays *canted antiferromagnetic* behaviour (Dunlop and Özdemir, 1997). In contrast, paramagnetic tourmaline has a minimum susceptibility axis parallel to its longest crystallographic axis (Borradaile and Jackson, 2004). Identification of potential exsolution or alteration products is also important. Kissel et al., (2010) report ilmenite laths exsolved parallel to the short axis of coarse titanomagnetite crystals in dykes in E Iceland have divided the host crystal into small MD titanomagnetite laths with long axes orthogonal to the magma flow fabrics.

### 2.2.3:2 *Controls on magnetite petrofabrics*

Magnetic fabrics measured in magnetite-bearing rocks are at times difficult to interpret because of the unknown relationship between the magnetite fabric and the mineral fabrics of the volumetrically dominant silicate phases (e.g. feldspars, amphibole and biotite).

When attempting to interpret magma flow fabrics this issue is compounded as magnetite frequently crystallises late. The shape of magnetite crystallised in association with K-feldspar, hornblende, and biotite is often observed to be controlled by the crystalline faces of the dominant silicate phases (Hrouda et al., 1971; Borradaile, 1994). Stacey (1960) originally suggested the primary silicate framework may control the growth and orientation of later crystallising magnetic mineral phases. Therefore, the magnetic fabric likely reflects the petrofabric of the silicate phases. This “template” behaviour has been demonstrated with quantitative image analysis of thin sections (e.g. Cruden and Launeau, 1994; Archanjo et al., 1995; Launeau and Cruden, 1998). Hargraves et al., (1991), suggest that the primary silicate framework control on magnetite distribution may also create a network of closely spaced magnetites that are able to magnetically interact to an extent where shape anisotropy may be replaced or accentuated by a distribution anisotropy. Cañón-Tapia (2001) concluded shape anisotropy should dominate, unless the magnetite grains were equant and/or clustered.

#### 2.2.3:3 *Grainsize influence on AMS*

The magnetic response of titanomagnetites is controlled by its grainsize as well as its shape anisotropy (Tarling and Hrouda, 1993). MD titanomagnetites ( $>100\ \mu\text{m}$ ) have a strong shape preferred anisotropy, thus the maximum susceptibility axis will parallel the long axis of the grain. In contrast, SD magnetites ( $<1\ \mu\text{m}$ ) are more susceptible to magnetization along the magnetocrystalline ‘easy’ axis, orthogonal to the shape long axis (Hrouda, 1982; O’Reilly, 1984; Potter and Stephenson, 1988; Dunlop and Özdemir, 1997). From the dependence of principal susceptibility axis orientation on grainsize, titanomagnetite populations consisting purely of MD or SD grainsizes are interpreted as producing normal and inverse magnetic fabrics respectively (Rochette et al., 1999; Ferré, 2002). A normal magnetic fabric implies that the magnetic fabric reflects the mineral fabric and that the magnetic foliation in sheet intrusions is parallel to the dyke plane. Distinguishing the presence and proportion of magnetic domain states is an important distinction as inverse magnetic fabrics orthogonal to the actual petrofabric and likely perpendicular to the dyke plane (Potter and Stephenson,

1988; Hargraves et al., 1991; Rochette et al., 1992; Dragoni et al., 1997; Rochette et al., 1999; Aubourg et al., 2002; Ferré, 2002; Cañón-Tapia and Chávez-Álvarez, 2004). A mixture of SD and MD titanomagnetites may yield intermediate fabrics, where two of the principal susceptibility axes are switched (Rochette et al., 1999; Ferré, 2002).

#### **2.2.4 Primary magma flow determination using AMS**

Interpretation of magnetic fabrics as pertaining to primary magma flow fabrics in tabular sheet intrusions (and lava flows) has a strong historical founding, which has allowed various models to be evaluated and refined. Stacey (1960) provided important insights into the acquisition of AMS fabrics in flowing magma, highlighting that crystals rotated into alignment during magma flow. Initially, magma flow axes were interpreted to parallel  $K_2$ , providing the susceptibility axis was statistically valid and oriented within the plane of the dyke (Khan, 1962; Ellwood, 1978). Cañón-Tapia (2004) explains that the particle transport dynamics incorporated to support magma flow parallel to  $K_2$  are restricted in their application and likely do not occur frequently. Knight and Walker (1988) presented the first empirical study of AMS and suggested that  $K_1$ , the magnetic lineation, could be equated to the primary magma flow axis with  $K_3$  orthogonal to the intrusion margins (i.e. magnetic foliation is parallel to the dyke plane). Subsequently, many authors have either assumed this relationship is correct (Cañón-Tapia, 2004) or substantiated it through correlations to visible magma flow indicators (e.g. Callot et al., 2001; Aubourg et al., 2002; Liss et al., 2002; Horsman et al., 2005; Morgan et al., 2008). However, several studies have provided examples where magnetic lineations do not correlate to the inferred magma flow trend (e.g. Geoffroy et al., 2002; Cañón-Tapia, 2004; Bascou et al., 2005; Philpotts and Philpotts, 2007; Aubourg et al., 2008). Whilst these may be attributed to variations in magnetic mineralogy (see section 2.2.3), Cañón-Tapia and Chávez-Álvarez (2004) suggest that processes occurring during magma flow may also produce spurious magnetic fabrics. This section provides a brief account of the dynamics of magma flow within sheet intrusions and the potential magnetic fabrics created.

### 2.2.4:1 *Generation of magmatic flow fabrics in sheet intrusions and lavas*

Magma flow fabrics in sheet intrusions may be attributed to the hydrodynamic alignment of suspended crystal populations by non-coaxial simple shear or coaxial pure shear, dependent on variations in magma-velocity gradients across the intrusion (Fig. 2.6a) (Correa-Gomes et al., 2001; Callot and Guichet, 2003; Cañón-Tapia and Chávez-Álvarez, 2004). The geometry of the magma-velocity gradients, which define the velocity profile, in a sheet intrusion is dependent on the rheological behaviour (i.e. Newtonian, pseudo-plastic or Binghamian) of magma and friction with the wall rocks (Correa-Gomes et al., 2001). Velocity gradients are greatest at the intrusion margins and impart a simple shear stress, whereas towards the interior of the intrusion the velocity gradient decreases and pure shear dominates (Fig. 2.6) (Correa-Gomes et al., 2001; Callot and Guichet, 2003; Cañón-Tapia and Chávez-Álvarez, 2004; Féménias et al., 2004).

Cañón-Tapia and Chávez-Álvarez (2004) suggest that cyclical rotation of crystals during magma flow may produce a multitude of possible fabric orientations as  $K_1$ ,  $K_2$  and  $K_3$  systematically switch. This seems to contradict the consistency in magma flow fabric orientations often observed. Importantly, Cañón-Tapia and Chávez-Álvarez (2004) incorporated no crystal-crystal interaction into their models. Arbaret et al., (1996) showed that >15 % crystallinity, mechanical interactions between crystals prevents cyclicity and promotes alignment parallel to the shear direction. Regardless of magma rheology, the magma velocity-profile at sheet margins and crystal interactions causes fabrics to become imbricated (<30° from the dyke planes; Tauxe et al., 1998) parallel to the symmetrical inclination of the magma velocity profile (Fig. 2.6a) (Knight and Walker, 1988; Correa-Gomes et al., 2001; Geoffroy et al., 2002; Callot and Guichet, 2003; Féménias et al., 2004; Morgan et al., 2008; Philpotts and Philpotts, 2008). This relationship is demonstrated by sheet intrusions containing magnetic fabrics parallel to bulbous sheet terminations, which reflect and preserve the magma-velocity profile (e.g. Horsman et al., 2005). Importantly, the closure direction of the imbricated fabrics coincides with the magma flow direction (Fig. 2.6a). Geoffroy et al., (2002) suggested imbricated magnetic foliations provide a more reliable sense of magma flow

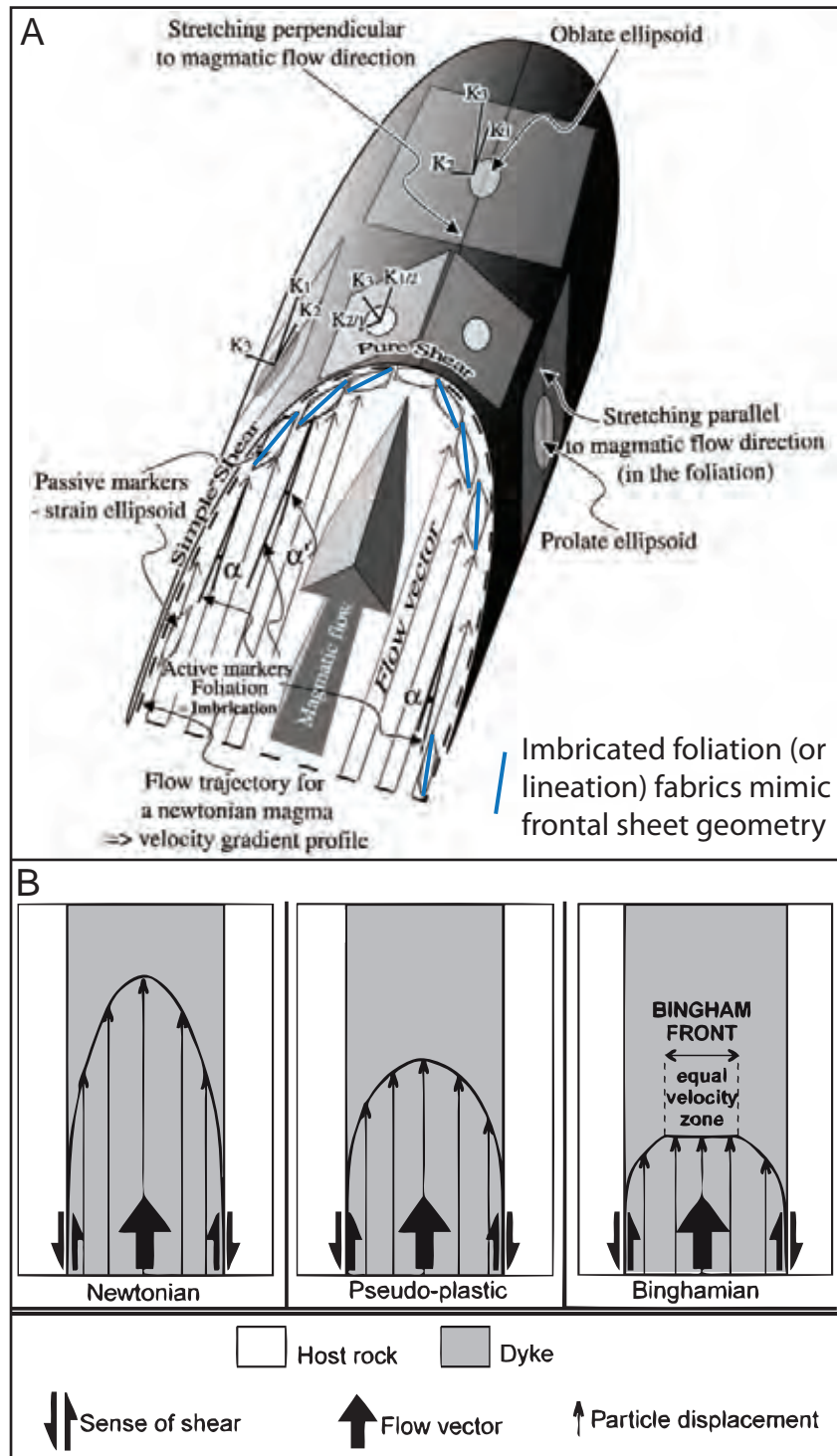


Fig. 2.6: Deformation of flowing magma within a constricted conduit (see text for details) (Féménias et al., 2004). B) Potential velocity profiles for magmas of differing rheology (Correa-Gomes et al., 2001).

direction compared to imbricated magnetic lineations as image analysis, field observation and AMS study of dykes in E Greenland highlighted a strong consistency between imbricated magnetic foliation and other magma flow indicators but a discrepancy in the orientations of magnetic lineations and magma flow interpretations for >50 % of dykes measured. The disparity in magnetic lineation and magma flow direction was attributed to the formation of a strong lineation formed by the intersection between two foliations; a fabric composed of an imbricated foliation sub-fabric and magma flow coaxial sub-fabric (Geoffroy et al., 2002; Callot and Guichet, 2003). These results suggest samples acquired from intrusion margins, to measure imbricated fabrics, provide the most reliable estimates of magma flow. However, consideration of the study by Philpotts and Philpotts (2007) highlights a potential caveat to this method. Philpotts and Philpotts (2007) measured vesicle and magnetic fabrics from the chilled margin of a camptonite dyke significantly different to those within the sheet core, suggesting two magma flow regimes are recorded (Tauxe et al., 1998).

From a brief consideration of magma flow dynamics, it is apparent that magnetic fabrics can provide good indicators of magma flow and that  $K_1$  may be interpreted as (sub-) parallel to the magma flow axis if there is independent evidence to corroborate it. The imbrication of fabrics may be analysed in an attempt to determine magma flow direction, although samples should be collected from the chilled margins (if present) and in the normal sheet groundmass for comparison.

## **2.3 The AMS method used within the thesis**

### **2.3.1 Sample collection and analysis**

In this study, AMS samples were collected in the field as oriented blocks following permission from Scottish Natural Heritage as several areas of Ardnamurchan are designated Sites of Special Scientific Interest (SSSI). The aim of this study is to provide an analysis of magma flow within the cone sheets of Ardnamurchan, requiring samples to be collected from representative areas of cone sheet outcrop spanning the whole intrusion time-frame.

Consequently, due to time restrictions, only one or two blocks were retrieved per cone sheet sampled. Owing to poor exposure quality and sheet thickness it was often difficult to define the sample position with respect to the top, middle and base of the sheet. Chilled margins in the Ardnamurchan cone sheets are typically <2 cm so were not individually sampled. The block samples were oriented in the lab and, using a drill-press, a series of 2.5 cm diameter cores were obtained (cf. Owens, 1994). All drill cores were prepared, using a diamond-tipped, non-magnetic saw blade, into 3 to 16 (typically 7) 2.2 by 2.5 cm right-cylindrical specimens. The AMS fabrics for these specimens were measured on an AGICO KLY-3S Kappabridge (an induction bridge that operates at a magnetic field of 300 A/m and a frequency of 875Hz) at the University of Birmingham (UK). The results for each specimen were combined and averaged using software modified by W.H.Owens after Jelínek (1978). This statistical analysis also reorients the results with respect to the original field position of the block. Each block is assumed to represent a multinormal homogeneous population with within block variability accounted for by calculation of 95% confidence ellipses. The AMS magnitude parameters advocated by Stevenson et al., (2007a) have been used; i.e.  $K_{\text{mean}}$ ,  $H$  and  $\mu$ . Appendix B provides an explanation of the software used to reorient the block samples collected in this thesis, as well as all the raw AMS data.

### **2.3.2 Distinguishing magnetic carriers and their influence on AMS**

It has been established that prior to the interpretation of AMS fabrics, a full characterisation of the magnetic phase(s) that contribute to the magnetic fraction and their intrinsic properties is required. The techniques employed to characterise the magnetic mineralogy and its relation to the petrofabric in this study are discussed below.

#### *2.3.2.1 High-temperature, low-field magnetic susceptibility*

Stepwise heating/cooling of a sample from 40°C to 680°C to 40°C was conducted on powdered samples, using a CS-3 furnace attachment for the AGICO KLY-3S Kappabridge, in order to evaluate the magnetic composition. All the raw high-temperature, low-field

magnetic susceptibility data and a description of its manipulation are presented in Appendix C. Ferromagnetic (*s.l.*) minerals are highly sensitive to temperature (T) fluctuations as heating causes superexchange coupling forces to breakdown, resulting in the development of a Curie Point (Dunlop and Özdemir, 1997). In comparison, paramagnetic minerals always display an inverse slope with susceptibility proportional to  $1/T$  and the susceptibility of diamagnetic grains is T independent (Dunlop and Özdemir, 1997). The overall morphologies of the heating-cooling curves therefore allow these three magnetic behaviours to be distinguished. The Curie Temperature ( $T_C$ ) estimates, which represent the transition from ferromagnetic (*s.l.*) to paramagnetic behaviour, are inferred using the inflection point or Hopkinson Peak method (Tauxe, 1998; Petrovský and Kapička, 2006). It is important to note that although most ferromagnetic (*s.l.*) minerals described in the literature are attributed a single unique  $T_C$ , this will strongly depend on mineral phase composition. Titanomagnetites with variable Ti contents ( $x$ ) of 0–0.6 will range in  $T_C$  from 578–150°C respectively (Tarling and Hrouda, 1993).

Curie Points are often preceded by an increase in susceptibility (the Hopkinson effect; Hopkinson, 1889), either represented by a shallow positive slope and/or by the development of a convex-upwards ‘bump’ in susceptibility, termed a Hopkinson Peak (Liss et al., 2004). The morphology of an Hopkinson Peak is dictated by the size and shape of the respective mineral phase grains. Remanent magnetisations of ferromagnetic (*s.l.*) minerals are often thermally locked in between the  $T_C$  and the Blocking Temperature ( $T_B$ ) (Dunlop and Özdemir, 1997). Note that a remanent magnetisation does not affect the measurement of the *anisotropy* of magnetic susceptibility. On heating above the  $T_B$ , but below the  $T_C$ , the remanence disappears allowing SD grains to behave superparamagnetically (i.e. the magnetic moment is easily reoriented and relaxes immediately after removal of the applied field). This produces an increase in susceptibility up to two orders of magnitude greater than values below the  $T_B$  (Dunlop and Özdemir, 1997). An internal demagnetising field in MD grains, derived from opposing orientations of domains, subdues the increase in susceptibility above the  $T_B$  (Dunlop and Özdemir, 1997). A further distinction between SD and MD grainsizes, aside from the

relative increase in susceptibility, is the width of the Hopkinson Peak, which is a function of the  $T_B$ – $T_C$  range. In SD grains the  $T_B$  is directly proportional to the grain size, whereas for MD grains the presence of numerous internal movable Bloch walls produces a spectrum of  $T_B$  values that extends to lower temperatures (Dunlop and Özdemir, 1997). Hopkinson Peaks of SD grains are therefore typically narrow and higher compared to MD grains and may therefore provide a proxy for magnetic grain size (Orlický, 1990; Liss et al., 2004) as well as magnetic mineralogy.

#### 2.3.2:2 *Reflected light microscopy*

Once the mineral phases contributing to the AMS fabric have been identified, reflected light microscopy may be used to qualitatively examine the textural relationship of the magnetic fraction and the primary silicate framework. For example, magnetite phenocrysts have been observed to mantle altered olivines producing a magnetic fabric parallel to the olivine petrofabrics (Tarling and Hrouda, 1993). Similarly, magnetite growth and elongation along tabular plagioclase-plagioclase grain boundaries is evocative of a mimetic relationship (e.g. Bascou et al., 2005). Additionally, reflected light microscopy may provide useful information on the alteration state (if any) of the magnetic fraction (Butler, 1992).

---

## CHAPTER 3

### THE GEOLOGY OF ARDNAMURCHAN

---

Ardnamurchan is considered as one of the classic areas of igneous geology in the UK, following the pioneering studies of Judd (1874), Geikie (1897) and the extensive British Geological Survey mapping initiative (e.g. Richey and Thomas, 1930) from which many fundamental concepts of sub-volcanic intrusion and evolution were developed. This chapter provides an overview of the geology of Ardnamurchan and its regional setting through a review of previous studies but also develops several ideas pertinent to subsequent chapters.

The Ardnamurchan peninsula is situated in the Northern Highlands Terrane (Fig. 3.1), which primarily consists of Neoproterozoic Moine Supergroup metasedimentary rocks (Emeleus and Bell, 2005) and is bounded by major Caledonian faults; the Moine Thrust Belt to the NW and the Great Glen Fault to the SE (Trewin, 2002). During the Caledonian orogeny the Northern Highlands Terrane was thrust north-westwards over the foreland Hebridean Terrane through the development of the Moine Thrust Belt (Fig. 3.1) (Trewin, 2002; Emeleus and Bell, 2005). Thus, the Hebridean Terrane, comprising predominantly of Archean Lewisian Gneisses (*ca.* 2400 Ma) with a minor proportion of Torridonian sedimentary rocks, forms the basement of the Northern Highlands and Grampian Terranes (Fig. 3.1) (Trewin, 2002; Emeleus and Bell, 2005). Following the Caledonian orogeny, several extensive sedimentary basins developed, in which deposition of various Palaeozoic and Mesozoic successions occurred. These are represented on Ardnamurchan by Mesozoic shallow marine sedimentary rocks (Emeleus and Bell, 2005). Emplacement of the Ardnamurchan igneous rocks ~58 Ma, during an extensive period of magmatic activity in Greenland and NW Europe associated with the opening of the North Atlantic (~62–53 Ma; White and McKenzie, 1989), therefore occurred in a structurally complex and lithologically variable setting.

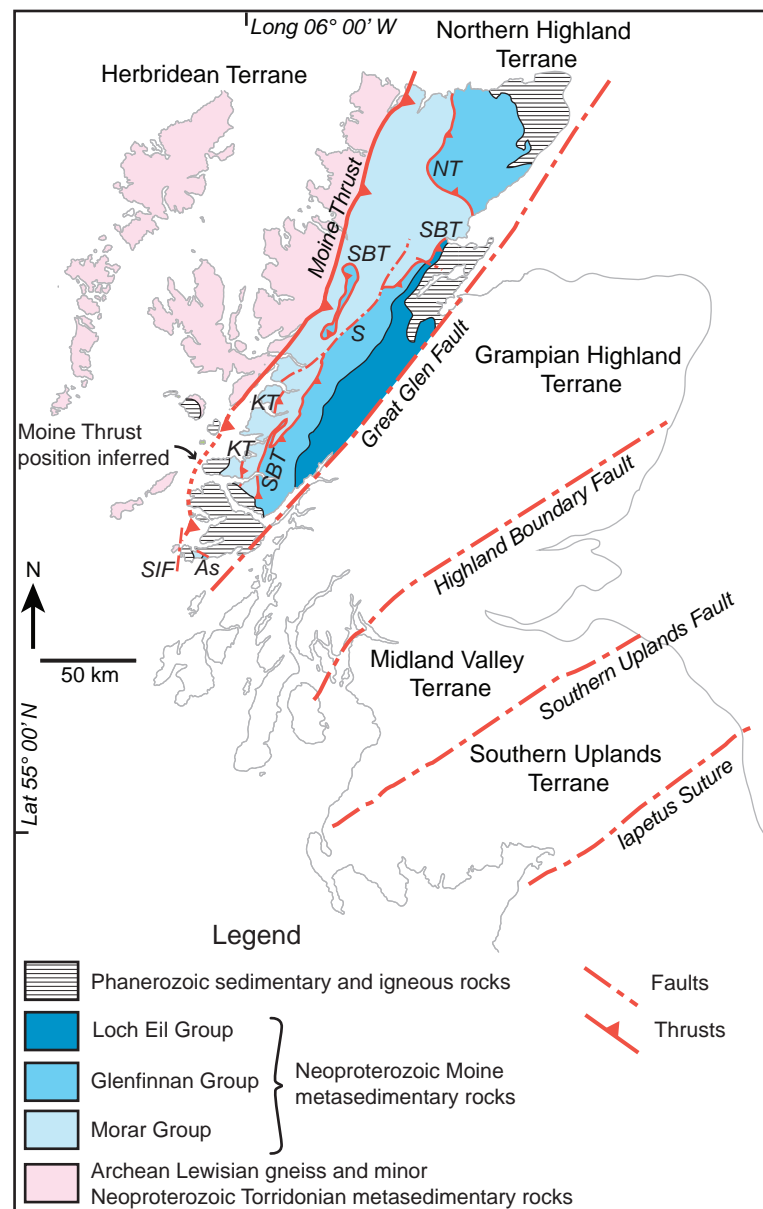


Fig. 3.1: Division of the geological terranes of Scotland by major Caledonian structures (after Soper et al., 1998; Trewin, 2002). Ardnamurchan is situated within the Northern Highlands Terrane, the simplified internal structure of which is also shown. The minor faults displayed are: *NT*, Naver Thrust; *SBT*, Sgurr Beag Thrust; *KT*, Knoydart Thrust; *S*, Strathconon Fault; *As*, Assapol fault; *SIF*, Sound of Iona Fault.

### 3.1 Precambrian host rocks

#### 3.1.1 Lewisian Gneiss Basement

The Lewisian Gneiss of the Hebridean Terrane is not exposed on Ardnamurchan, although it does form the basement rock (cf. Geldmacher et al., 1998; Trewin, 2002; Emeleus and Bell,

2005). Elsewhere, outcrops of Lewisian Gneiss are observed to be a highly deformed complex of variable grade metamorphic rocks, which originated from heterogeneous protoliths of felsic, basic and ultrabasic igneous rocks, as well as some sedimentary rocks (Trewin, 2002; Wheeler et al., 2010). Although the Lewisian Gneiss can be separated into numerous subdivisions dependant on protolith or tectonic history (cf. Trewin, 2002; Wheeler et al., 2010), a simplified geophysical and geochemical division can be made into amphibolite- and granulite-facies metamorphic rocks (Bamford et al., 1977; Meyer et al., 2009). Outcrops of Lewisian Gneiss on Coll, Tiree (Richey and Thomas, 1930; Park, 2005) and Rum (Meyer et al., 2009; Nicoll et al., 2009), as well as Lewisian Gneiss crustal xenoliths incorporated in igneous intrusions (e.g. Mull, Faithful and Upton, 2006) observed in the Inner Hebrides (Fig. 3.1) suggest a simplified stratification to the deep crust beneath the British and Irish Palaeogene Igneous Province with the lower crust suggested to be granulite-facies and the middle–upper crust inferred as amphibolite-facies Lewisian Gneiss. Seismic velocity studies support this interpretation and suggest a transition from mid-crustal amphibolite facies to deep-crustal granulite facies occurs at 6–14 km (Bamford et al., 1977).

### **3.1.2 Neoproterozoic Moine metasedimentary rocks**

The oldest rocks exposed on Ardnamurchan are part of the Neoproterozoic Moine Supergroup (*ca.* 1000 Ma), which is divided lithostratigraphically, from oldest to youngest, into the Morar, Glennfinnan and Loch Eil Groups (Soper et al., 1998). On Ardnamurchan, the Neoproterozoic Moine metasedimentary rocks belong to the Morar Group and consist of low-grade greenschist-facies psammites and pelites (Day, 1989; Trewin, 2002). The Morar Group itself, dominated by fluvial deposits, is divisible into the Lower Morar Psammite (~1 km thick), the Morar Pelite and the Upper Morar Psammite (~5 km thick) (Soper et al., 1998; Bonsor and Prave, 2008; Strachan et al., 2010).

Around Kilchoan, on the southern shore of Ardnamurchan, Moine metasedimentary rocks of low-grade greenschist facies crop out (Fig. 3.2). Their shallow dips and weak folding suggest they have undergone little deformation (Day, 1989). Metre thick psammitic beds,

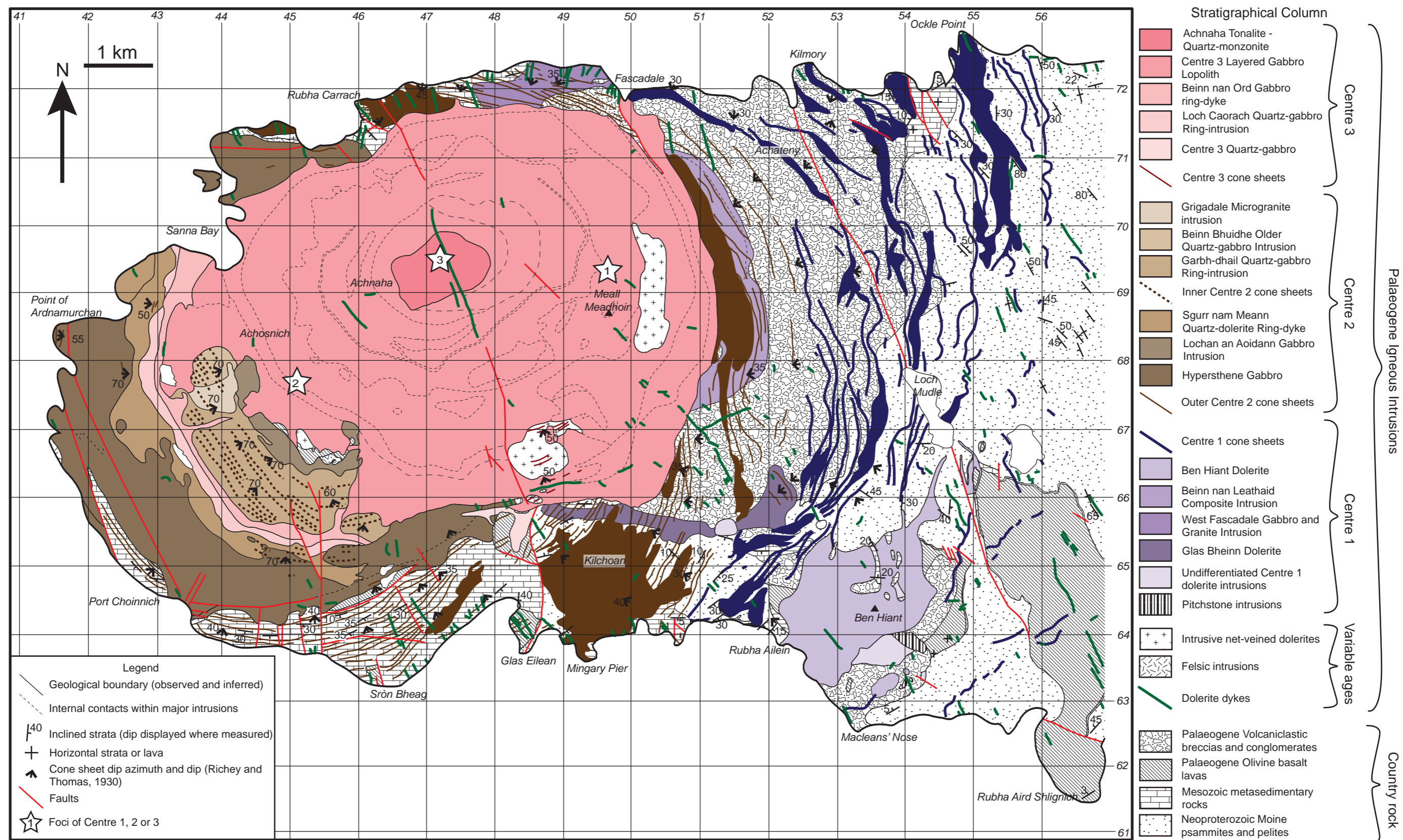


Fig. 3.2: Geological map of Ardnamurchan (after Richey and Thomas, 1930; Emeleus, 2009). Co-ordinates refer to the UK National Grid.

dominated by recrystallised quartz and alkali feldspar with minor muscovite and Fe-oxides also present, are interbedded with thin pelitic bands (Richey and Thomas, 1930). The pelitic beds display a schistose fabric composed of wavy muscovite crystal aggregates enveloping occasional quartz grains (Richey and Thomas, 1930). Additionally, small quantities of fine biotite and garnets have been observed in the pelites, both indicative of low-grade regional metamorphism (Richey and Thomas, 1930). This succession, although its base is not exposed, is interpreted as part of the Lower Morar Psammite (see Soper et al., 1998, their Figure 5).

Bonsor and Prave (2008) interpreted the Moine metasedimentary rocks along the northern coast of Ardnamurchan, near Ockle Point, (Fig. 3.2) as forming the lower *c.* 2.5 km of the Upper Morar Psammite. Significant proportions of porphyroblastic garnets in the Upper Morar Psammite indicate they have been regionally metamorphosed to a higher metamorphic grade relative to the Lower Morar Psammite in the west (Richey and Thomas, 1930). This increase in metamorphic grade is quite abrupt and can be defined by an approximate N-S line just to the west of Loch Mudle, potentially highlighting the trace of a thrust fault (Fig. 3.2) (Richey and Thomas, 1930). Soper et al., (1998) imply that the Morar Pelite, which separates the Lower and Upper Morar Psammites elsewhere in the NW Highlands, is exposed on Ardnamurchan. However, there are few descriptions of the Morar Pelite in the literature and its thickness and potentially its presence are hard to validate (cf. Richey and Thomas, 1930; Day, 1989; Soper et al., 1998; Bonsor and Prave, 2008). The Morar Group and the base of the Glenfinnan Group are well exposed in SW Mull (Holdsworth et al., 1987). The sedimentary units observed in the Morar Group of SW Mull, which correlate to those in Ardnamurchan, are considerably deformed and thinner than their relatively undeformed counterparts (Holdsworth et al., 1987). Given that the Lower Shiaba Psammite, comparable to the ~1 km thick Lower Morar Psammite, is now 250 m thick; it is here suggested that the 130 m thick Shiaba Pelite on Mull is equivalent to a ~500 m thick Morar Pelite unit on Ardnamurchan (cf. Holdsworth et al., 1987; Soper et al., 1998).

To the east of the Ardnamurchan peninsula, the Moine metasedimentary rocks of the Morar Group display a moderate granulitized texture (Richey and Thomas, 1930), suggesting

the metamorphic grade increases to an epidote-amphibolite facies (Trewin, 2002). The boundary between the Morar Group and the stratigraphically higher Glenfinnan Group is defined by the Sgurr Beag Thrust located ~19 km to the east of the Ardnamurchan central complex (Fig. 3.1) (Trewin, 2002). Overall, a gradual westwardly decrease in metamorphic grade is observed and correlates to an increasing proximity to the Moine Thrust (Richey and Thomas, 1930).

### 3.1.2:1 *The Moine Thrust*

Juxtaposition of the Moine Supergroup on top of Archean Lewisian Gneiss basement occurred during the Caledonian orogeny through the development of the Moine Thrust Belt (Fig. 3.1), which consists of three E/SE dipping major thrusts; the Sgurr Beag Thrust (oldest), the Knoydart Thrust and the Moine Thrust (youngest and stratigraphically lowest). The decreasing metamorphic grade of the Moine metasedimentary rocks to the west on Ardnamurchan is consistent with an increased proximity to the Moine Thrust (Richey and Thomas, 1930). From the extrapolation of the Moine Thrust strike, which onshore is exposed for ~200 km between N Scotland and S Skye, it has been postulated that its surface intersection trace is ~5–10 km offshore Ardnamurchan to the west (Fig. 3.1) (Trewin, 2002; Woodcock and Strachan, 2004; Emeleus and Bell, 2005). Late Palaeozoic–Mesozoic tectonic tilting rotated the Moine Thrust from an original ~30° SE dip (Anderson, 1951) to a shallower 8–25° SE inclination (Coward, 1983; Smythe, 1987; Geldmacher et al., 1998; 2002; Woodcock and Strachan, 2004). The combined strike and dip approximations of the Moine Thrust suggests it forms a major upper crustal boundary beneath Ardnamurchan (Richey and Thomas, 1930; Geldmacher et al., 2002; Emeleus and Bell, 2005; Dobson et al., 2010), which may have influenced the volcano-tectonic evolution of the Ardnamurchan central complex.

The vertical depth ( $V_1$ ) of the Moine Thrust beneath Ardnamurchan can be calculated trigonometrically from the dip ( $\alpha$ ) of the Moine Thrust, assuming it remains constant, and the distance ( $W_1$ ) between an arbitrarily defined central point within the Ardnamurchan central complex and the surface intersection of the Moine Thrust along a NW-SE cross-section

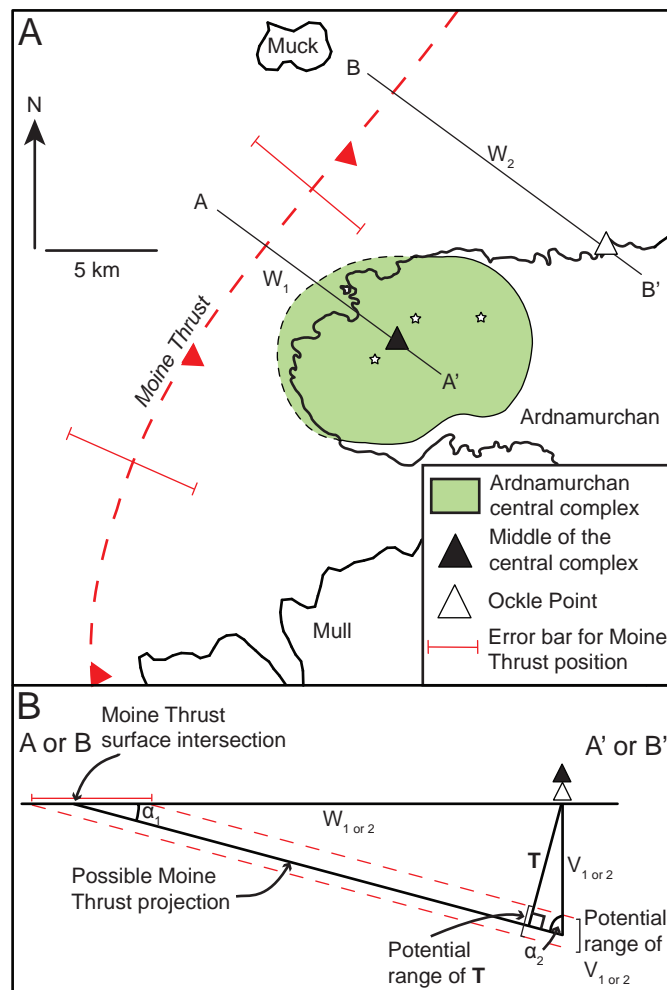


Fig. 3.3: A) The potential variation in distance of the Moine Thrust surface intersection from the centre of the Ardnamurchan central complex ( $W_1$ ) and from Ockle Point ( $W_2$ ). B) Simplified cross-section constructed along the profiles marked in (A) orthogonal to the strike of the Moine Thrust. By varying  $W_{1 \text{ or } 2}$  and  $\alpha_1$ , a range of  $V_{(1 \text{ or } 2)}$  and  $T$  values may be calculated that can be compared to the maximum  $T$  of the Neoproterozoic Moine metasedimentary rocks on Ardnamurchan in order to constrain the likely parameters of the Moine Thrust.

constructed orthogonal to strike (Fig. 3.3). This further assumes the Moine Thrust may be represented as a single fault plane, as it is observed to behave as in some areas (Krabbendam and Leslie, 2010).

$$V_1 = W_1 \times \tan \alpha_1$$

Stratigraphical observations at Ockle Point, which is a further 5 km from the Moine Thrust

( $W_2$ ) compared to the arbitrary centre of Ardnamurchan (Fig. 3.3), suggest the Morar Group has a maximum true thickness ( $T$ ) of ~4 km (1 km Lower Morar Psammites; 0.5 km Morar Pelite; 2.5 km Upper Morar Psammite; cf. Soper et al., 1998; Bonsor and Prave, 2008). It is important to note this predicted  $T$  is a maximum limit as folding and potential removal of hangingwall material during faulting may overestimate the observed thickness (cf. Bonsor and Prave, 2008). Calculating the  $T$  of the Moine metasedimentary rocks from the vertical depth ( $V_2$ ) of the Moine Thrust at Ockle Point can therefore be used to refine the position and dip of the Moine Thrust.

$$T = V_2 \times \sin \alpha_2$$

Table 3.1 shows the results for these two calculations using variable dips ( $\alpha_1$ ) and surface intersection distances ( $W$ ) of the Moine Thrust. For example, a true thickness of 4.15 km of Moine metasedimentary rock at Ockle Point is calculated for a Moine Thrust dip of  $15^\circ$ , which therefore constrains the maximum surface intersection distance at 11 km ( $W_1$ ). If this dip is maintained but the intersection distance is increased, the calculated true thickness would exceed the maximum true thickness predicted from stratigraphical observations. Overall a negative correlation is observed between  $\alpha_1$  and  $W_{(1 \text{ and } 2)}$ . Regardless of the parameter value used, the maximum vertical depth of the Moine Thrust beneath the centre of the Ardnamurchan central complex is ~3 km (Table 3.1a).


### 3.2 Mesozoic metasedimentary rocks

A succession of Triassic and Jurassic metasedimentary rocks, resting unconformably on the Neoproterozoic Moine rocks, is observed around the S and NE coast of Ardnamurchan (Fig. 3.2). The small thickness (6 m) of Triassic metasedimentary rocks consists of sandstones, chemically-formed limestones and sedimentary breccias containing clasts of Moinian rocks (Richey and Thomas, 1930; Day, 1989; Emeleus and Bell, 2005). Lower to Middle Jurassic

Table 3.1: A) Calculated vertical depths (V) of the Moine Thrust beneath Ardnamurchan for variable surface intersection distances and dips. B) True thickness (T) of the Moine metasedimentary rocks calculated from vertical depths in (A).

(A)		Moine Thrust dip - $\alpha_1$ (°)												
		8	9	10	11	12	13	14	15	16	17	18	19	20
Distance to Moine Thrust surface intersection - $W_{1 \text{ and } 2}$ (km)	5	0.70	0.79	0.88	0.97	1.06	1.15	1.25	1.34	1.43	1.53	1.62	1.72	1.82
	6	0.84	0.95	1.06	1.17	1.28	1.39	1.50	1.61	1.72	1.83	1.95	2.07	2.18
	7	0.98	1.11	1.23	1.36	1.49	1.62	1.75	1.88	2.01	2.14	2.27	2.41	2.55
	8	1.12	1.27	1.41	1.56	1.70	1.85	1.99	2.14	2.29	2.45	2.60	2.75	2.91
	9	1.26	1.43	1.59	1.75	1.91	2.08	2.24	2.41	2.58	2.75	2.92	3.10	3.28
	10	1.41	1.58	1.76	1.94	2.13	2.31	2.49	2.68	2.87	3.06	3.25	3.44	3.64
	11	1.55	1.74	1.94	2.14	2.34	2.54	2.74	2.95	3.15	3.36	3.57	3.79	4.00
	12	1.69	1.90	2.12	2.33	2.55	2.77	2.99	3.22	3.44	3.67	3.90	4.13	4.37
	13	1.83	2.06	2.29	2.53	2.76	3.00	3.24	3.48	3.73	3.97	4.22	4.48	4.73
	14	1.97	2.22	2.47	2.72	2.98	3.23	3.49	3.75	4.01	4.28	4.55	4.82	5.10
	15	2.11	2.38	2.64	2.92	3.19	3.46	3.74	4.02	4.30	4.59	4.87	5.16	5.46
	16	2.25	2.53	2.82	3.11	3.40	3.69	3.99	4.29	4.59	4.89	5.20	5.51	5.82

(B)														
		8	9	10	11	12	13	14	15	16	17	18	19	20
Distance to Moine Thrust surface intersection - $W_{1 \text{ and } 2}$ (km)	5	0.68	0.76	0.85	0.94	1.03	1.12	1.20	1.29	1.38	1.48	1.57	1.66	1.76
	6	0.81	0.92	1.02	1.13	1.23	1.34	1.44	1.55	1.66	1.77	1.88	2.00	2.11
	7	0.95	1.07	1.19	1.31	1.44	1.56	1.69	1.81	1.94	2.07	2.20	2.33	2.46
	8	1.09	1.22	1.36	1.50	1.64	1.78	1.93	2.07	2.22	2.36	2.51	2.66	2.81
	9	1.22	1.38	1.53	1.69	1.85	2.01	2.17	2.33	2.49	2.66	2.82	2.99	3.16
	10	1.36	1.53	1.70	1.88	2.05	2.23	2.41	2.59	2.77	2.95	3.14	3.33	3.52
	11	1.49	1.68	1.87	2.07	2.26	2.45	2.65	2.85	3.05	3.25	3.45	3.66	3.87
	12	1.63	1.84	2.04	2.25	2.46	2.68	2.89	3.11	3.32	3.54	3.77	3.99	4.22
	13	1.76	1.99	2.21	2.44	2.67	2.90	3.13	3.36	3.60	3.84	4.08	4.32	4.57
	14	1.90	2.14	2.38	2.63	2.87	3.12	3.37	3.62	3.88	4.13	4.39	4.66	4.92
	15	2.04	2.29	2.55	2.82	3.08	3.35	3.61	3.88	4.15	4.43	4.71	4.99	5.27
	16	2.17	2.45	2.73	3.00	3.29	3.57	3.85	4.14	4.43	4.73	5.02	5.32	5.63

 Probable maximum V and T values, and their associated Moine Thrust dips and surface intersection distances, as constrained by the predicted T of the Moine metasedimentary succession at Ockle Point.

metasedimentary rocks form the majority of outcrops and are comprised of decimetre to metre scale bedded limestones and sandstones, often with mudstones interbedded. They can be attributed to the Blue Lias, Pabay Shale, Scalpay Sandstone, Portree Shale and Berreraig Sandstone Formations (Emeleus and Bell, 2005). The limestones typically are pale

blue in colour. The sandstones are white or pale yellow in colour and resemble the Moine metasedimentary rocks; although the two can be distinguished by the presence of muscovite and the development of a granulitized texture in the Moine psammities. Due to the abundance and distribution of Palaeogene intrusions many of the Mesozoic sedimentary rocks are contact metamorphosed to some extent, as evidenced by their crystallinity and occasional high-temperature, low-pressure mineral assemblages (Day, 1989).

### 3.3 The British and Irish Palaeogene Igneous Province (BIPIP)

#### 3.3.1 Regional setting of the North Atlantic Igneous Province (NAIP)

The BIPIP formed through extensive igneous activity between *ca.* 61–55 Ma and is a subsidiary component of the *ca.* 62–53 Ma North Atlantic Igneous Province (Fig. 3.4a) (White and McKenzie, 1989; Emeleus and Bell, 2005; Hansen et al., 2009). During the Cretaceous and Early Palaeogene, NW-SE extension resulted in the northwards propagation of sea-floor spreading into the Labrador Sea and stretching of the continental lithosphere linking Greenland–NW Europe, which eventually led to the opening of the North Atlantic *ca.* 55 Ma (Trewin, 2002; Woodcock and Strachan, 2004; Hansen et al., 2009). It is traditionally believed that lithospheric extension was coupled with the impingement of a mantle plume on the base of the continental lithosphere towards the end of the Cretaceous (White and McKenzie, 1989; Jones et al., 2002), which instigated regional thermal uplift (Kent and Fitton, 2000; Woodcock and Strachan, 2004; Saunders et al., 2007) and provided a high magma flux (Storey et al., 2007). However, following the absence of a discernible hotspot track, several other interpretations to the origin of magmatism have been suggested. For example, the delamination of eclogitic rocks and their subsequent adiabatic melting have been suggested as a source of voluminous fertile magma (Lundin and Doré, 2005).

The NAIP consists of two volcanic rifted margins; the conjugate E Greenland–NW European and the W Greenland–Baffin Bay margins (Hansen et al., 2009). The igneous rocks ( $\sim 6.6 \times 10^6 \text{ km}^2$ ) attributed to this event are observed both onshore and offshore in the BIPIP,

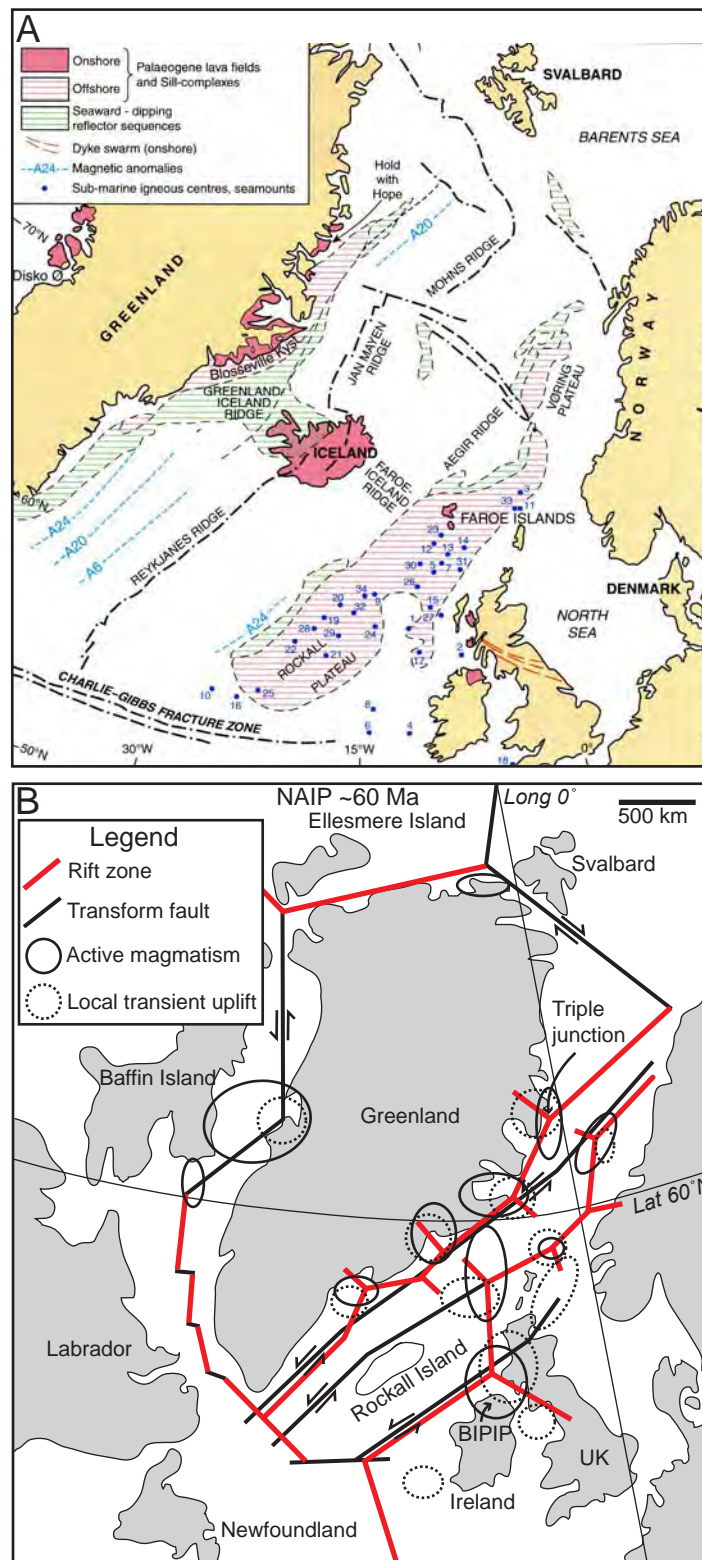


Fig. 3.4: A) Areal extent of component intrusions and extrusions of the NAIP (Emeleus and Bell, 2005). B) Palaeogeographic (60 Ma) reconstruction of the North Atlantic highlighting the correlation between the positions of plate triple junctions, zones of transient uplift and areas of active magmatism (redrawn from Hansen et al., 2009).

Rockall Trough, Rockall–Hatton area, Faroe–Shetland basin, Faroe Islands, Møre margin, Vøring margin and SE–NE Greenland (Fig. 3.4a) (Hansen et al., 2009). Active magmatism on Iceland is the modern manifestation of the NAIP (Emeleus and Bell, 2005). The igneous rocks are compositionally variable, although predominantly basaltic, and their form ranges from extrusive lavas, tuffs and volcanoclastic rocks (up to 6 km thick) to intrusive sill complexes, linear regional dyke swarms and sub-volcanic networks (Trewin, 2002; Woodcock and Strachan, 2004; Storey et al., 2007; Hansen et al., 2009).

Age relationships and radiometric dating suggest the NAIP can be divided into two main phases of magmatic activity; one from c. 62–58 Ma (e.g. W Greenland, BIPIP) and the other (e.g. E Greenland) spanning 57–53 Ma (Saunders et al., 1997). This differentiation has been ascribed to pre-thinned continental crust at the margins the magma source (e.g. the impinging plume head) providing a quicker route for magma to reach the upper crust (England, 1992). Focusing of continental extension and rifting at the E Greenland margin at ~56 Ma then instigated a shift in the location of magmatic activity (Storey et al., 2007). Plate reconstructions further suggest the position of igneous activity, within the two phases, was locally centred on zones of transient uplift and associated plate triple junctions (Fig. 3.4b) (Hansen et al., 2009). These triple junctions were interconnected during the embryonic stages of rifting, with many of the currently onshore intrusive remnants of the NAIP situated along failed rift arms (Hansen et al., 2009). For example, the central complexes of the BIPIP are located in a roughly NNW-SSE line and the regional dyke swarms are typically oriented NW-SE (Fig. 3.5a), both of which are sub-parallel to the NW-SE trending failed rift arm developed during the Palaeocene (Hansen et al., 2009).

### **3.3.2 Components of the BIPIP**

Within the BIPIP, much of the voluminous flood basalt lavas have eroded away exposing a shallow (<5 km depth) intrusive network of sills, central complexes (e.g. Ardnamurchan) and NW-SE oriented regional dykes (Fig. 3.5a) (Emeleus and Bell, 2005). The central complexes, which represent the deeply eroded roots of ancient volcanic edifices (Harker, 1904), provide

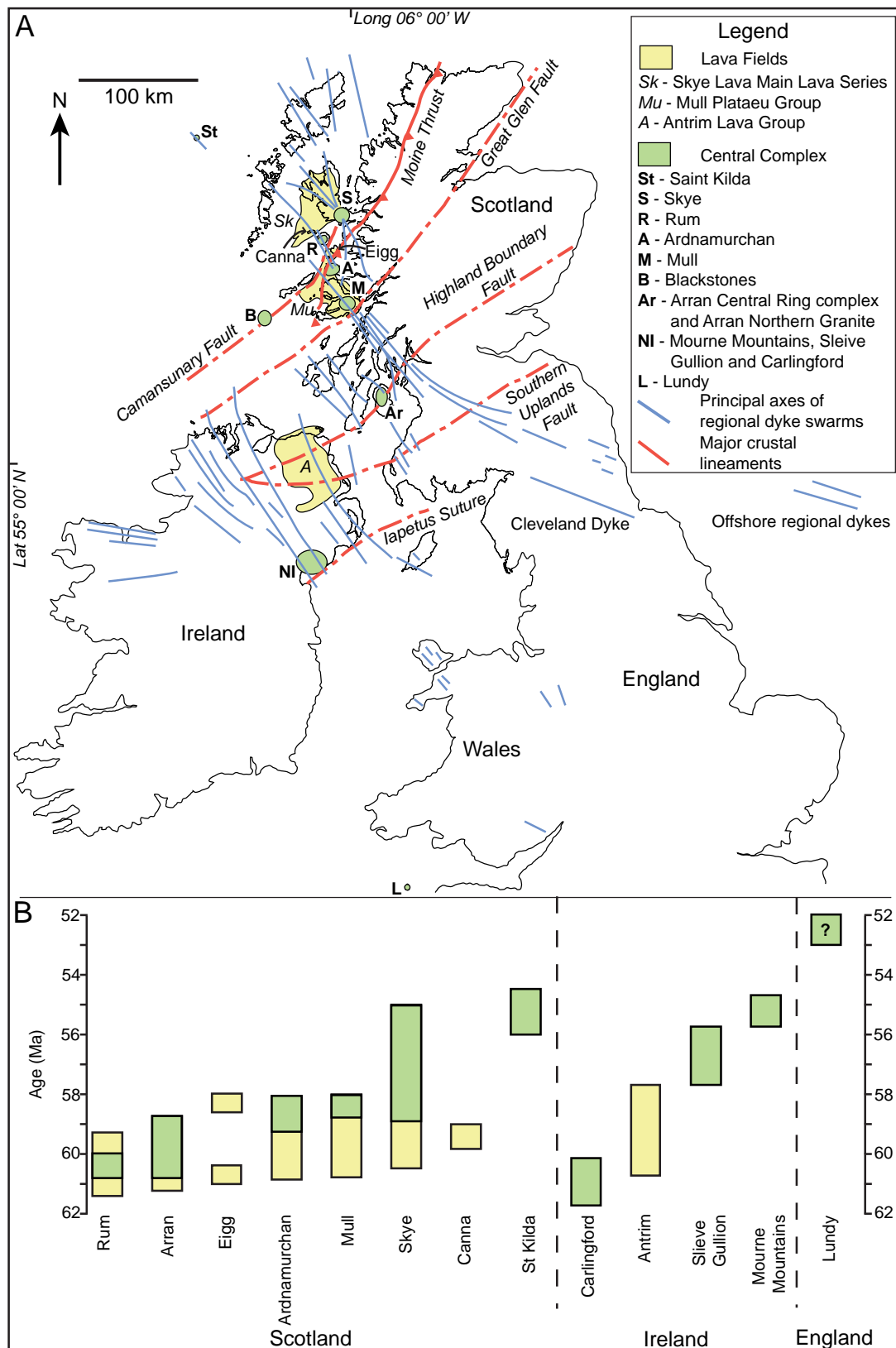


Fig. 3.5: A) Map of the BIPIP (after Ernst et al., 1995; Emeleus and Bell, 2005; Wall et al., 2009). B) Relative ages of components of the BIPIP determined from field relationships, radiometric dating, palynology and palaeomagnetism (after Mitchell, 2004; Emeleus and Bell, 2005).

direct access to the major intrusions (e.g. laccoliths, lopoliths, ring dykes) and minor sheet intrusions (e.g. cone sheets) that constitute sub-volcanic networks, allowing magma linkages, storage and accommodation to be studied. Field relationships, radiometric dating and palaeomagnetic studies have allowed relative ages to be defined and a stratigraphical series to be developed for the BIPIP (Fig. 3.5b) (Emeleus and Bell, 2005). Regional dyke emplacement occurred throughout the BIPIP (*ca.* 61–55 Ma), although intrusion intensity decreased with time (England, 1988; Emeleus and Bell, 2005). Some of the early regional dykes are observed to have fed fissure eruptions, from which flood basalt lavas were extruded (*ca.* 61–59 Ma; Emeleus and Bell, 2005). Extrusive igneous activity likely coincided with the initial development of the central complexes (Brown and Bell, 2006) but age relationships and radiometric dating suggests that the majority of basalts are older (Fig. 3.5b) (Emeleus and Bell, 2005; Tibaldi et al., 2011). The exception to this is the Rum central complex (60.5 Ma), which was rapidly emplaced (over ~1 Ma) between the extrusion of the Eigg Lava Formation and the development Canna Lava Formation (Fig. 3.5b) (Emeleus and Bell, 2005).

### 3.3.2:1 *Flood basalt lavas*

Voluminous flood basalt activity 60.5–54.5 Ma (Jolley and Bell, 2002), is represented by the coeval extrusions of the 2–6 km thick Middle Lava Series, E Greenland (Tegner et al., 1998); the offshore lava sequence (<6 km thick) of the North Atlantic and the BIPIP tertiary plateau lavas (Emeleus and Bell, 2005). In the BIPIP, the flood basalt lavas are broadly divided into the Skye Lava Group, of which the Canna Lava Formation is a component, and the Mull Lava Group, to which the Eigg Lava Formation is attributed (Emeleus and Bell, 2005). Extrusion was predominantly sub-aerial with palaeosol horizons and thin sedimentary rock units often developed during eruption hiatuses (Emeleus and Bell, 2005; Dobson et al., 2010). Lavas are typically basaltic variants (e.g. tholeiitic, alkali) and can be subdivided geochemically (Emeleus and Bell, 2005). Importantly, these sub-divisions have been interpreted as representative of variable parental magma-types, allowing comparisons with younger intrusions to determine magma source and contamination trends. For example, the

Mull lavas are divided, from oldest to youngest, into the Mull Plateau Group, the Coire Gorm lavas and the Central Mull Tholeiite (Kerr et al., 1995; 1999). Geochemical analyses of the Skye Lava Group have identified two dominant magma types; the Skye Main Lava Series and the Preshal More Magma-type (Emeleus and Bell, 2005). The most primitive basalts in the Skye Main Lava Series attained their final composition at 1700 MPa in the asthenospheric mantle (~60 km), whilst other magmas represented in the Skye Main Lava Series and the Mull Plateau Group fractionated at 900 MPa, equivalent to a depth consistent with the base of the crust (Emeleus and Bell, 2005). The Central Mull Tholeiite and Preshal More Magma-type apparently fractionated at low pressures corresponding to upper crustal levels (Emeleus and Bell, 2005).

### 3.3.2:2 *Regional dykes*

The numerous Palaeogene dykes attributed to the regional linear dyke swarms are extensive in their areal coverage and can be observed in the Outer Hebrides, Scotland, Ireland, Wales, Lundy (Bristol Channel), N England and the North Sea (Fig. 3.5a) (Harker, 1904; Bailey et al., 1924; Speight et al., 1982; Macdonald et al., 1988; Jolly and Sanderson, 1995; Mitchell, 2004; Emeleus and Bell, 2005; Wall et al., 2009). Lithologically, the regional dykes are typically tholeiitic and alkali basalts (Emeleus and Bell, 2005). A pronounced NW-SE trend is evident for the vast majority of regional dykes, although dyke strike is generally rotated towards E-W in the west of the Republic of Ireland and in NE England (Fig. 3.5a). Some N-S striking dykes are also observed (Fig. 3.5a) (England, 1988). The NW-SE striking, sub-vertical geometry of the regional dykes, which were intruded contemporaneously to central complex construction (Emeleus and Bell, 2005), indicate emplacement was tectonically controlled by the regional extensional stress regime ( $\sigma_3$  sub-horizontally oriented NE-SW) active throughout the formation of the BIIP (Richey and Thomas, 1930; England, 1988). England (1988) suggests that the absence of regional uplift may indicate  $\sigma_1$  was oriented sub-horizontally NW-SE and that the regional stress field contained a minor dextral shear component to account for N-S oriented dykes. Other authors have suggested this deflection

relates to the central complexes or deep-seated zones of crustal weakness (see Jolly and Sanderson, 1995 and references therein).

Figure 3.5a highlights a prominent correlation between the major NW-SE axes of the regional dykes and the positions of central complexes. Based on the observation that regional dyke intensity increases toward the central complexes, Speight et al., (1982) subdivided the regional dykes into major swarms (e.g. the Skye Main swarm and the Mull dyke swarm). Sub-swarms, often oriented N-S or E-W are developed on a local scale around the central complexes (Fig. 3.5a) (Emeleus and Bell, 2005). Very few regional dykes are actually observed within the central complexes themselves (Emeleus and Bell, 2005). Crustal extension, associated to regional dyke dilation, has a regional mean of ~9 %, although locally it is calculated to be greater around the central complexes (Speight et al., 1982; Emeleus and Bell, 2005). Furthermore, towards the central complexes the regional dykes decrease in average thickness (from ~4 m to ~1 m); strike orientations deviate more from the regional trend (Fig. 3.5a) and the dykes are compositionally more variable, ranging from ultrabasic to felsic (Jolly and Sanderson, 1995; Emeleus and Bell, 2005). These data imply the central complexes significantly influenced regional dyke morphology through modifying the active stress field to allow the preferential intrusion of the pre-existing host rock structures (Jolly and Sanderson, 1995; Dagley et al., 2008). Influence of the central complexes is exemplified by the contrasting forms of the Mull regional dyke swarm to the SE of the Mull central complex (Jolly and Sanderson, 1995; Emeleus and Bell, 2005). The regional dykes extending into southern Scotland and NE England (e.g. Cleveland dyke, Eskdalemuir dyke) are fewer, thicker (<25 m) and more laterally continuous (<600 km) compared to those observed adjacent to the Mull central complex (Macdonald et al., 1988, 2009, 2010; Jolly and Sanderson, 1995).

Speight et al., (1982) proposed the regional dykes were sourced from a NW-SE laterally extensive ridge of magma, at a depth of 20–50 km, and thereby dominated by a vertical magma flow regime. Dagley et al., (2008) supported this hypothesis by suggesting the *en échelon* segmentation of the Cleveland dyke prohibited lateral magma flow and must

therefore have emplaced vertically. Contrastingly, based on geochemical and petrological correlations with lavas and intrusions associated with the Mull central complex, Macdonald et al., (2009, 2010) suggested the Cleveland dyke and other regional dykes in NE England were laterally fed from the Mull central complex. Segmentation is attributed to fault displacement and the development of intrusive offsets, commonly observed in dykes (Rickwood, 1990; Gudmundsson, 2002), and therefore not restrictive of a lateral magma flow regime (Macdonald et al., 2010). Similarly, anisotropy of magnetic susceptibility studies of regional dykes on Skye suggested they were probably laterally fed from the Skye central complex (Herrero-Bervera et al., 2001; 2003).

### 3.3.2:3 *Sill complexes*

The majority of sills and sill complexes within the BIPIP post-date flood basalt eruption and are likely associated to central complex formation (Emeleus and Bell, 2005). The two major sill complexes, the Little Minch (N Skye) and Loch Scridain (SW Mull) Sill Complexes are on average basaltic in composition, whilst minor sill complexes range from basaltic (e.g. Fair Head Sill and Portrush Sill, Northern Ireland; Mitchell, 2004) to felsic (S Arran sills; Emeleus and Bell, 2005).

### 3.3.2:4 *Central complexes*

Pre-existing crustal structures are inferred to play a significant role in the positioning of central complexes given that they occur in a conspicuous N-S line, with the exception of St. Kilda, and frequently coincide with major Caledonian fault traces (Fig. 3.5a) (Richey and Thomas, 1930; England, 1988; Emeleus and Bell, 2005; Brown et al., 2009). For example, the Mull central complex is adjacent to the Great Glen Fault, which may have acted as a preferential magma pathway (Fig. 3.5a) (Mathieu and van Wyk de Vries, 2009). Often, central complexes display evidence of multiple phases of igneous activity (e.g. Skye, Ardnamurchan, Mull, and Carlingford-Slieve Gullion), which often describe either a linear (e.g. Mull) or rotational (clock-wise; e.g. Ardnamurchan) migratory pathway (England, 1988). These

spatially and temporally separate phases of magmatism are typically defined by cross-cutting relationships and the dip foci of cone sheet swarms, which delineate a central source (e.g. Skye, Tibaldi et al. 2011; Ardnamurchan, Richey and Thomas, 1930; Mull, Bailey et al., 1924; Carlingford, Le Bas, 1971; Rum, Emeleus and Bell, 2005). Hence, a complex history of fluctuating extensional and compressional stress regimes associated with the regional tectonics and magma chamber dynamics is inferred (Bailey et al., 1924; Richey and Thomas, 1930; England, 1988; Day, 1989; Emeleus and Bell, 2005). England (1988) suggested the migratory pattern described by the different phases of intrusive activity resulted from a localisation of tensional stresses in the host rock adjacent to an ascending magma batch, which favoured subsequent intrusion.

### **3.3.3 The Ardnamurchan central complex**

The first significant attempt at mapping and interpreting the emplacement history of the Ardnamurchan central complex, including the exposed cone sheets, is presented in the geological survey memoir of Richey and Thomas (1930). A series of successive intrusion components, classified as either major intrusions (i.e. laccoliths, lopoliths and ring dykes) or minor intrusive sheets (i.e. dykes, sills and cone sheets), were recognised (Fig. 3.2) (Richey and Thomas, 1930; Emeleus and Bell, 2005). They typically have gabbroic compositions, (sub-)annular geometries and appear to be successively nested within previous intrusions (Fig. 3.2) (Richey and Thomas, 1930; Walker, 1975; Emeleus and Bell, 2005). Similarly, the cone sheets, which are generally equigranular tholeiitic basalts or dolerites, have a concentric strike and dip inwards (Richey and Thomas, 1930; Holland and Brown, 1972; Day, 1989; Emeleus and Bell, 2005). Some cone sheets are composite or felsic, whilst others display variolitic or porphyritic textures (Richey and Thomas, 1930; Geldmacher et al., 1998).

Richey and Thomas (1930) further divided the Ardnamurchan central complex into three spatially and temporally separate phases of intrusive activity (Fig. 3.2) (Centres 1, 2 and 3 respectively) from the disposition of the (sub-)annular major intrusions and the assumed central source of the cone sheets (see Chapter 1). By inferring the central magma

reservoir was roughly equivalent to a point source and that the cone sheets could be directly traced down-dip, Richey and Thomas (1930) further calculated the depth of each Centre to be approximately 5 km below the present surface. Temporal variation in the emplacement of each Centre is considered to be minor as palaeomagnetic analyses, which suggest intrusions of the three Centres are reversely magnetized (Dagley et al., 1984), and radiometric dating imply intrusion of the Ardnamurchan central complex lasted c. 1–2 Ma (Mitchell and Reen, 1974; Chambers et al., 2005).

### 3.3.3:1 *Centre 1*

The oldest Palaeogene rocks of the Ardnamurchan central complex, defined by cross-cutting relationships, are a series of fragmental rocks (Brown and Bell, 2006) that rest unconformably on the Neoproterozoic and Mesozoic country rock as well as the remnant Early Palaeogene olivine basalt lavas associated with the Mull Plateau Lavas (Fig. 3.2) (Richey and Thomas, 1930; Emeleus and Bell, 2005; Brown and Bell, 2006). In the field, these fragmentary rocks are typically poorly lithified breccias and conglomerates with fragment sizes ranging from ~1 cm–100 m. Richey and Thomas (1930) interpreted the fragmental rocks as vent agglomerates based on their moderately to steeply inwardly inclined contacts and the high proportion of angular felsic igneous clasts identified. From this interpretation, Richey and Thomas (1930) inferred the position of two volcanic vents on Ardnamurchan; one at Ben Hiant and the other at Achateny. However, Brown and Bell (2006) re-interpreted the vent agglomerates as high energy debris flows, not pyroclastic in origin, deposited in a topographic depression after recognising the presence of pollen spores, various sedimentary structures and a much greater proportion of country rock clasts to igneous clasts than previously recorded. The generation of debris flows is ascribed to contemporaneous shallow intrusions instigating uplift and increased erosion rates (Brown and Bell, 2006; Brown et al., 2006). Similarly, the generally radial outward dip of the host rocks (<30° dip) around the Ardnamurchan central complex was formed by intrusion-induced doming (Fig. 3.2) (Richey and Thomas, 1930; Walker, 1975; Brown and Bell, 2006).

Minor andesitic pitchstone, displaying well defined columnar jointing, was intruded into the volcanoclastics at Ben Hiant (Fig. 3.2) soon after their deposition, suggesting emplacement occurred at shallow levels (Richey and Thomas, 1930). A number of major intrusions, also emplaced at a shallow depth ( $\sim <3$  km) into the olivine basalt lavas and volcanoclastics, are associated with Centre 1. The major Centre 1 intrusions include the Glas Bheinn Porphyritic Dolerite, interpreted as a dyke-like intrusion; the steeply inclined intrusive sheets of quartz gabbro and granophyre west of Fascaidale; the composite, gently inclined Beinn nan Leathaid sheet intrusion and the Ben Hiant Dolerite (Fig. 3.2) (Richey and Thomas, 1930). The Ben Hiant Dolerite has been suggested to represent either a volcanic plug with lavas radiating out (Judd, 1874), an amalgamation of inclined sheets (Geikie, 1897; Gribble, 1974) or a single homogeneous mushroom-shaped intrusion (Richey and Thomas, 1930). The Centre 1 intrusions are not well exposed and have poorly defined geometries compared to the intrusions of Centres 2 and 3 (Emeleus and Bell, 2005).

Contemporaneous to the formation of the Ben Hiant Dolerite was the emplacement of the Centre 1 cone sheets, now preserved only to the east of the central complex in an arcuate belt of country rock  $\sim 8$  km long and  $\sim 4$  km wide (Fig. 3.2). Individually, cone sheets of Centre 1 are typically 6–15 m thick, widely spaced and form well defined topographic scarps (Richey and Thomas, 1930). On average, the Centre 1 cone sheets dip  $\sim 20^\circ$  inwards, defining the proposed foci of Centre 1 (Richey and Thomas, 1930), although there is an increase in inclination (to  $\sim 40^\circ$ ) towards inner margin of the swarm (Fig. 3.2) (Emeleus and Bell, 2005). There are no exposures preserved detailing cross-cutting relationships between the Centre 1 cone sheets and igneous intrusions attributed to purportedly younger Centres (Richey and Thomas, 1930; Day, 1989).

### 3.3.3:2 *Centre 2*

Intrusive activity within Centre 2 can be sub-divided into four simplified stages based on cross-cutting relationships: (1) initial intrusion of abundant, thin cone sheets dipping inwards at  $\sim 40^\circ$  belonging to the Outer Centre 2 set; (2) emplacement of several major intrusions,

originally interpreted by Richey and Thomas (1930) as ring dykes, including the Hypersthene Gabbro; (3) intrusion of the steeper ( $\sim 70^\circ$ ) Inner Centre 2 cone sheet set and (4) the formation of incomplete ring intrusions (Fig. 3.2) (Richey and Thomas, 1930; Emeleus and Bell, 2005). From the dip and strikes of the cone sheets, as well as the nested disposition of the major intrusions (interpreted as ring dykes), the foci of Centre 2 is suggested to be located to the S of Achosnich (Fig. 3.2) (Richey and Thomas, 1930; Emeleus and Bell, 2005). The down-dip extrapolation of the Inner Centre 2 cone sheet set highlights a slight offset in their foci, compared to that of the Outer Centre 2 cone sheet set (Richey and Thomas, 1930).

The Outer Centre 2 cone sheet set is the best cone sheet set exposed on Ardnamurchan and displays the concentric strike disposition of the swarm (Fig. 3.2) (Richey and Thomas, 1930), although individual cone sheets are often discontinuous along strike (Keunen, 1937). Overall, the cone sheet set has an inward dip ( $\sim 35\text{--}45^\circ$ ) with variation observed within individual cone sheets (Fig. 3.6a) (Richey and Thomas, 1930). Some outward dipping cone sheets also occur (Fig. 3.6b). Richey and Thomas (1930) noted the Outer Centre 2 cone sheets are restricted to an arcuate belt 4 km wide, with an outer and inner margin situated 7.2 km and 3.2 km from Centre 2 respectively, that coincides with an area of pre-domed country rock (Fig. 3.2). Within this belt, joints parallel to the cone sheets were described by Richey and Thomas (1930) as unfilled cone sheet fractures but Keunen (1937) noted their conjugate nature and suggested cone sheet magma exploited pre-existing cracks (Fig. 3.6a). Compared to the Centre 1 cone sheets, the Outer Centre 2 cone sheets are geochemically and compositionally indistinguishable (Richey and Thomas, 1930; Holland and Brown, 1972; Emeleus and Bell, 2005). Within the Outer Centre 2 cone sheet set some porphyritic dolerites and composite intrusions may be observed (Richey and Thomas, 1930). All cone sheets have well developed chilled margins, whether they are in contact with the country rock or earlier cone sheet intrusions (Fig. 3.6c), implying individual intrusion was relatively rapid and successive (cf. Richey and Thomas, 1930).

The first phase of major intrusion emplacement in Centre 2 was dominated by the development of the Hypersthene Gabbro, the most complete ring intrusion of Centre 2 and



Fig. 3.6: A) Photograph of a cone sheet (locality 25, Area 1) displaying a ramp-flat morphology. Note the 'flat' cone sheet section is sub-parallel to the Mesozoic limestone and shale bedding whereas the 'ramp' is sub-parallel to inwardly inclined fractures belonging to a conjugate fracture set (dashed orange lines). B) A photograph of a classic inward dipping cone sheet (i) presented in the Geological Memoir of Richey and Thomas (1930, top left of Plate IV). Note that Robert Johnson is standing on a cone sheet (ii) that dips away from the Ardnamurchan central complex. C) Chilled margins (~1–2 cm thick) developed in cone sheets. Presumably cone sheet (i) intruded first, chilling against the volcanoclastic host rock, and cone sheet (ii) was subsequently emplaced along the contact and becoming chilled against both the country rock and early cone sheet.

interpreted as a classic ring dyke (Fig. 3.2) (Richey and Thomas, 1930). However, following the identification of some inward dipping contacts and layering and the pioneering work of Wells (1953), Skelhorn and Elwell (1966) and Walker (1975a), the Hypersthene Gabbro was re-interpreted as a laccolith by Day (1989). Cone sheet intrusions, belonging to the Outer Centre 2 set, bordering the Hypersthene Gabbro record a complex history of intermittent intrusion throughout its emplacement history (Day, 1989). Some cone sheets are cut by the

Hypersthene Gabbro (Fig. 3.2), whilst others display specific contact metamorphic mineral assemblages linked to discrete phases in the growth of the Hypersthene Gabbro (Day, 1989). Furthermore, adjacent to the Hypersthene Gabbro, field relationships indicate cone sheet intrusion was associated with thrust faulting, whilst extensional, inward dipping concentric normal faults developed during periods of cone sheet quiescence (Day, 1989). These observations suggest cone sheet emplacement overlapped temporally with and occurred laterally adjacent to the development of some major intrusions (Day, 1989).

The Inner Centre 2 set of cone sheets, intruded after the solidification and post-cumulus modification of the earlier Centre 2 major intrusions, outcrop in a restricted arcuate belt extending along strike for approximately 90° (Fig. 3.2) (Richey and Thomas, 1930). They cross-cut the major gabbroic intrusions of the Hypersthene Gabbro, the Sgurr nam Meann ring dike and the Garbh-dhail ring intrusion (Fig. 3.2) (Emeleus, 2009). In contrast to the Outer Centre 2 cone sheets, the Inner Centre 2 cone sheets have a steeper average dip (70°) and compositionally are plagioclase-phyric (Richey and Thomas, 1930; Geldmacher et al., 1998). However, there is no geochemical distinction between the Outer and Inner Centre 2 cone sheet sets (Holland and Brown, 1972; Geldmacher et al., 1998).

Geldmacher et al., (1998; 2002) suggested the Centre 2 cone sheet magma initially fractionated at ~10 km depth, during which time 5% crustal assimilation of the granulite-facies Lewisian Gneiss occurred. The magma is then suggested to have ascended and ponded in an upper crustal magma reservoir (Geldmacher et al., 1998). A high percentage of crustal assimilation of the Neoproterozoic Moine sedimentary rocks suggests the upper crustal magma chamber was situated above, or at, the Moine Thrust structural boundary (Geldmacher et al., 1998; 2002).

### 3.3.3:3 *Centre 3*

Centre 3 is dominated by annular gabbroic major intrusions (Fig. 3.2), originally interpreted as ring dykes (Richey and Thomas, 1930). A recent re-evaluation of the majority of the Centre 3 ring intrusions by O'Driscoll et al., (2006), incorporating field mapping, petrographical

analysis and anisotropy of magnetic susceptibility techniques questioned the ring dyke interpretation. Instead, identification of inward dipping contacts and petrofabrics suggests many of the nested annular intrusions represent discrete layers within a single lopolithic intrusion (O'Driscoll et al., 2006; O'Driscoll, 2007), termed the Centre 3 Layered Gabbro Lopolith (Fig. 3.2) (Emeleus, 2009). Mathieu et al., (2008) suggest the cup-shape of the lopolith is a primary feature (i.e. no central sagging; cf. O'Driscoll et al., 2006), a geometry which may also be applicable to many of the other major intrusions on Ardnamurchan. The Centre 3 foci, near Achnaha (Fig. 3.2), is predominantly defined by the disposition of the major annular intrusions as few cone sheets attributable to Centre 3 are observed (Richey and Thomas, 1930; Gribble, 1974; Emeleus and Bell, 2005). Centre 3 cone sheets that are exposed generally crop out in a small area to the S of the proposed foci where they intrude an intrusive net-veined dolerite (Brown et al., 2006) and the outer layer of the Centre 3 Layered Gabbro Lopolith (Fig. 3.2) (Emeleus, 2009). Typically, the cones sheets are thin and plagioclase-phyric with inward dips of  $\sim 50^\circ$  N (Richey and Thomas, 1930; Emeleus and Bell, 2005).

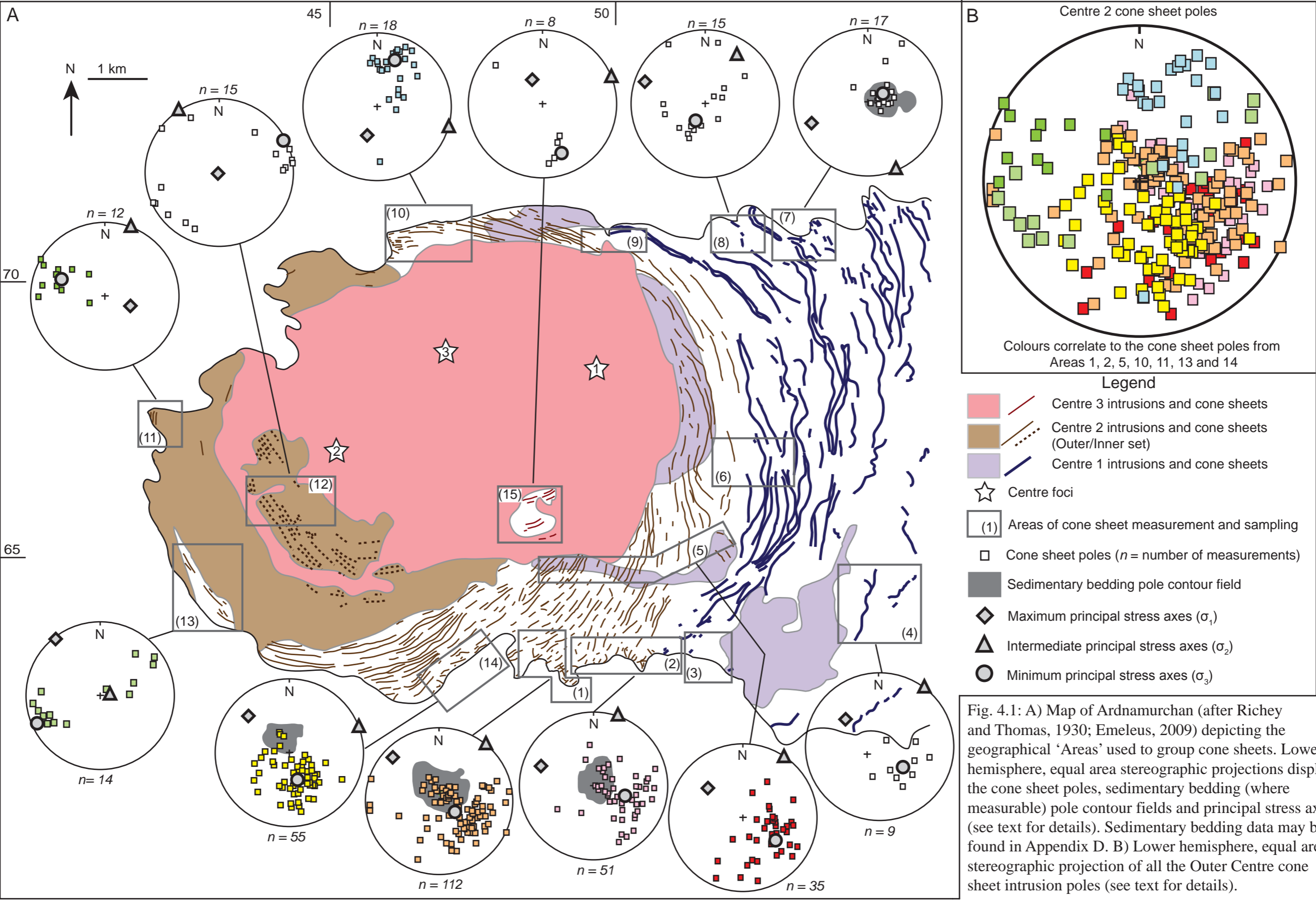
---

## CHAPTER 4

### ANALYSIS OF FIELD OBSERVATIONS AND STRUCTURAL MEASUREMENTS OF CONE SHEETS

---

Structural studies of sub-volcanic sheet intrusions are key to understanding the relationships between stress fields (local and regional), local geology and the position and emplacement of intrusions in order to establish controls on eruption dynamics and volcano growth (Corazzato et al., 2008; Tibaldi et al., 2011). Measurements were collected from the complete variety of the Ardnamurchan cone sheets so that all ages, geometries and dip dispositions were analysed (Fig. 4.1a). Over 500 structural data were collected from 265 cone sheets, with multiple readings from single cone sheets often recorded along strike or up/down the dip azimuth if local variations were observed (Appendix D). Although the Palaeozoic host rocks display evidence of intrusion related doming, the Early Palaeogene volcanoclastic and basalt lava unconformity is typically sub-horizontal, suggesting post-intrusion tilting is negligible and may be ignored (cf. Klausen, 2004; 2006; Tibaldi et al., 2011). The cone sheets of the Outer Centre 2 set form the majority of the studied cone sheets (209 in total) as they are the best and most widely exposed cone sheets on Ardnamurchan. Cone sheet outcrops are divided into 15 Areas (Fig. 4.1a), defined by their geographical proximity and relative ages, to allow easier data correlation. For each cone sheet, the strike and dip were measured using a Suunto compass clinometer (with an accuracy of  $1\pm 2^\circ$ ) and where both contacts were visible, sheet thickness was measured (Appendix D). A Garmin extrex GPS unit with an accuracy of 10 m was used to position outcrops (see Appendix D for locality positions).



## 4.1 The controls of pre-existing structures and host rock lithology on cone sheet intrusion

Emplacement of magma within the upper crust is facilitated by the development or reactivation of brittle fractures (e.g. bedding plane anisotropies, faults) ahead of a propagating magma tip (Pollard et al., 1973; Delaney et al., 1986; Rickwood, 1990; Rubin, 1995; Kavanagh et al., 2006; Menand, 2008). Magma propagation under a brittle regime involves: 1) opening of the fracture ahead of the leading edge of magma; 2) propagation of tip fluids and 3) magma flow within the body (Baer, 1995). Magmatic sheets emplaced in a brittle regime primarily intrude orthogonally to the least compressive principal stress axis (i.e.  $\sigma_3$ ; Anderson, 1951; Baer, 1995) when the internal magma pressure exceeds the magnitude of  $\sigma_3$  (Delaney et al., 1986; Rubin, 1995). The orientation of the principal stress axes during intrusion therefore controls the orientation of new fractures or which, if any, pre-existing fractures may be reactivated (Delaney et al., 1986). However, an increasing amount of evidence also demonstrates that in upper crustal magmatic systems, intrusion may occasionally instigate non-brittle behaviour of the host rocks (e.g. Liss, 2004; Thomson, 2007; Mathieu et al., 2008; Schofield et al., 2010). The morphology of intrusions exploiting non-brittle weaknesses in the host rock is distinct compared to those facilitated by brittle processes alone (Schofield et al., 2010). Determining intrusion mechanisms of the Ardnamurchan cone sheets and their relation to the host rock lithology (cf. Baer, 1995) is therefore an important step in analysing structural measurements and producing an encompassing emplacement model. Once the host rock behavior during cone sheet intrusion has been characterised, the relationships and relative orientations of sheet intrusions can be assessed to resolve the stress regime active during emplacement.

### 4.1.1 Relationships between host rock lithology and cone sheet structures

#### 4.1.1:1 *Xenoliths*

Xenoliths are occasionally observed in the Ardnamurchan cone sheets and consist

predominantly of Neoproterozoic Moine metasedimentary rocks, although Mesozoic metasedimentary rock and Palaeogene gabbro xenoliths are also observed. Typically, xenoliths are compositionally similar to the country rock the host cone sheet is observed to intrude (Fig. 4.2). They are often elongated (5–60 cm in length), sub-angular to angular (Fig. 4.2a and b) and exhibit no preferred orientation with respect to the host cone sheet geometry. One exception to this is a cone sheet intruding Mesozoic limestones and shales in Area 1 [NM 49334 62597], which contains numerous clusters (~20 cm–5 m long) of  $\sim \leq 10$  cm long tabular xenoliths of Neoproterozoic Moine psammite within its core (Fig. 4.2c and d). Traditionally, xenoliths are considered to form through magma-driven brittle fracturing or thermal erosion of intrusion walls, separating minor blocks, which then become entrained in the magma

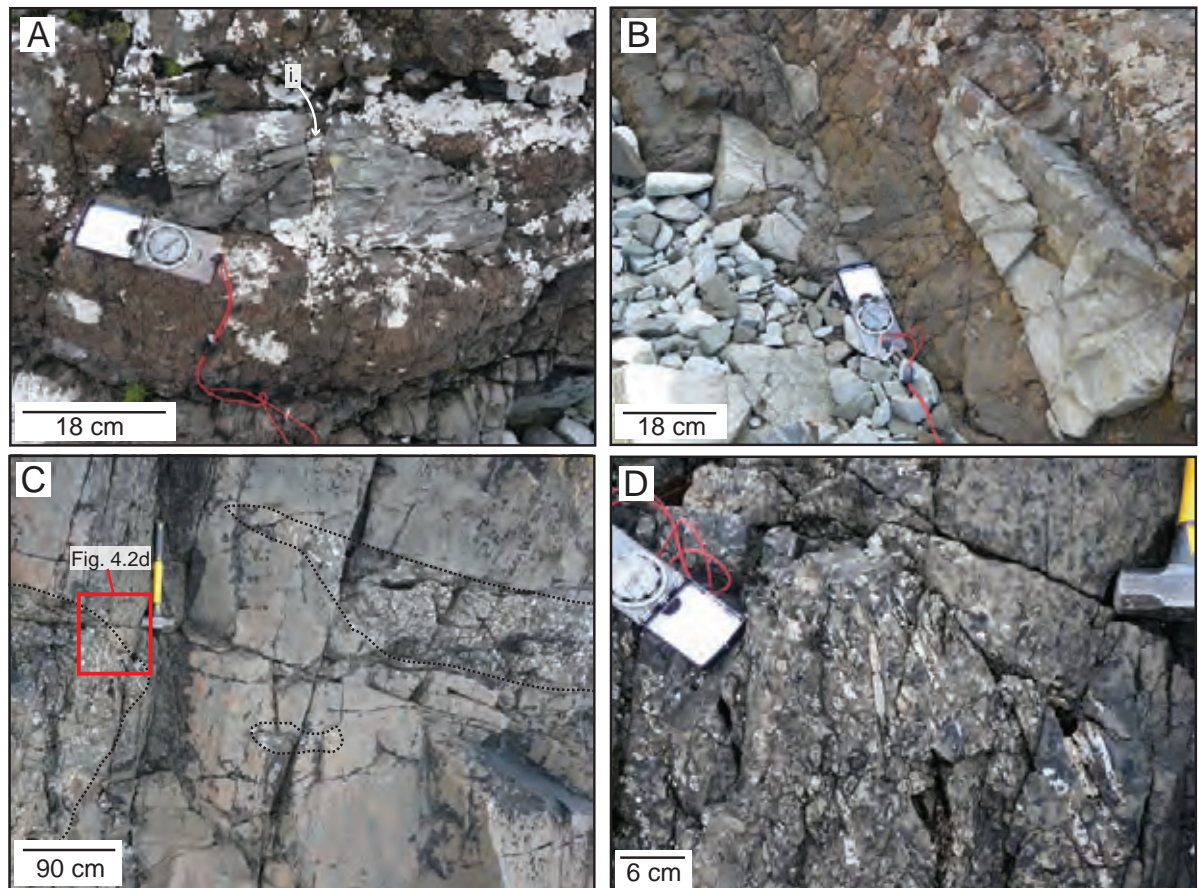


Fig. 4.2: A and B) Field photographs of sub-angular Moine psammite xenoliths within cone sheets intruding Neoproterozoic Moine metasedimentary rocks. In (A), the Moine xenolith has been split by an offshoot (i) of the host cone sheet. C) Laterally and vertically restricted zones of clustered Neoproterozoic Moine psammite xenoliths within a single cone sheet. D) Towards the edges of the clusters the xenoliths are typically aligned parallel to the outer margins and perhaps show some imbrication.

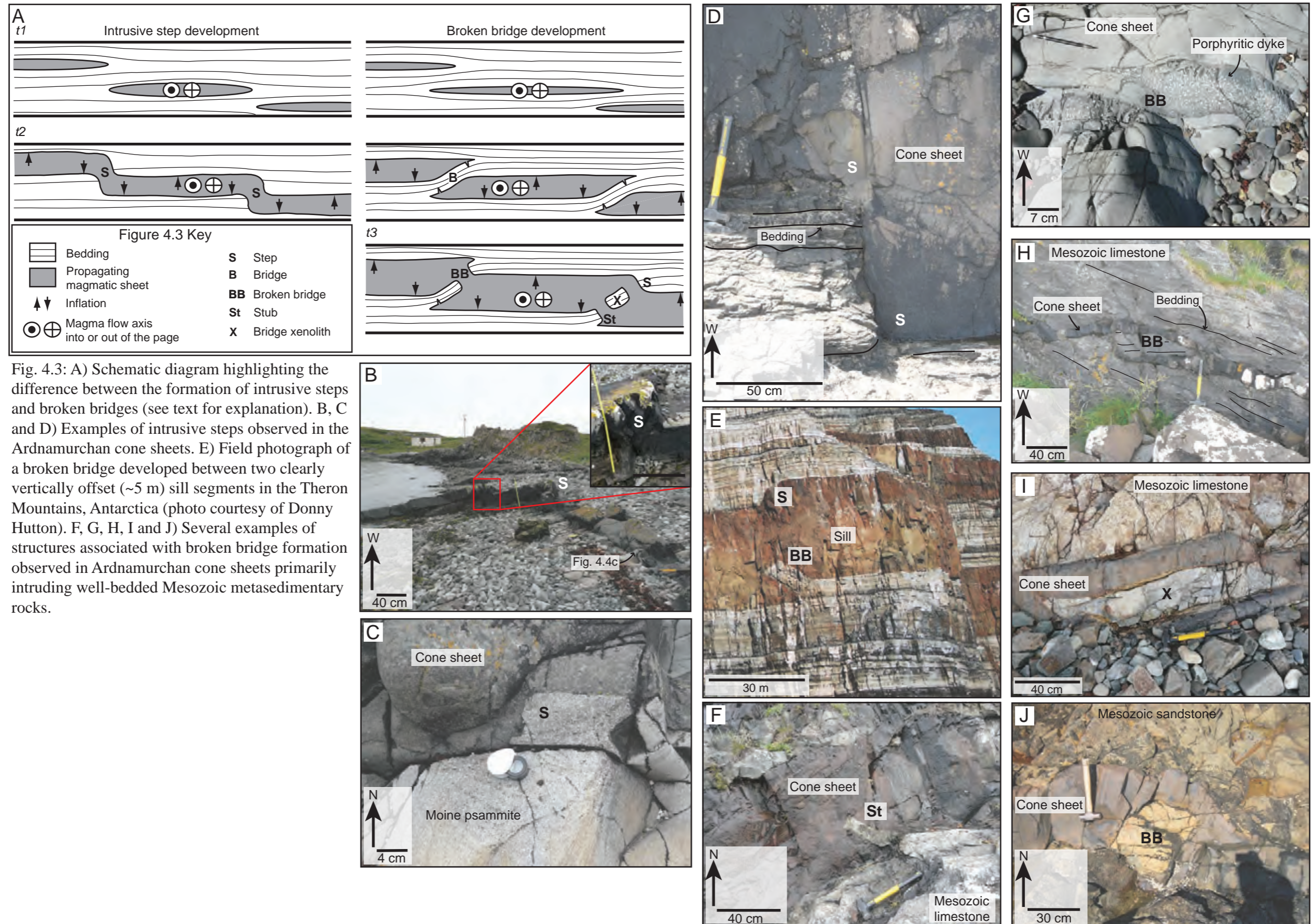
(McLeod and Sparks, 1998). The angularity and close proximity to country rock of a similar lithology suggests the xenoliths observed in the Ardnamurchan cone sheets were locally derived and entrained by brittle processes.

#### 4.1.1:2 *Intrusive steps and broken bridges*

Intrusive steps and broken bridges are observed in many forms of intrusions, including dykes (Rickwood, 1990), sills (Hutton, 2009; Schofield, 2009), cone sheets (Day, 1989), hydrothermal veins (Delaney and Pollard, 1981) and sand injectites (Vétel and Cartwright, 2010). They are distributed throughout Ardnamurchan and are observed in all host rock types, although they are more abundant in the Mesozoic metasedimentary rocks and, to a lesser extent, the Neoproterozoic metasedimentary units. Formation occurs predominantly through brittle processes and results from the division of intrusion tips into contemporaneously propagating segments that exploit slightly offset horizons (Fig. 4.3a) (Hutton, 2009; Schofield, 2009). As the individual sheet segments inflate, they impinge on each other and coalesce through the development of an intrusive connection oriented normal to the plane of intrusion (Fig. 4.3a) (Rickwood, 1990; Hutton, 2009). The geometry of the connecting structure, whether it is an intrusive step or broken bridge, is determined by the initial overlap between individual segments (Fig. 4.3a).

Step features are commonly observed in cone sheets on Ardnamurchan emplaced within the Neoproterozoic Moine metasedimentary and Mesozoic metasedimentary host rocks, although some also occur in cone sheets intruding the Early Palaeogene volcanoclastics. Typically, intrusive step structures are sharp and occur along sections of cone sheets exploiting bedding plane anisotropies (Fig. 4.3b, c and d). The size of the step ranges from ~2–50 cm (Fig. 4.3b, c and d) and is likely controlled by the thickness of the cone sheet and the scale of the bedding.

Broken bridges develop when the inflation of two overlapping segments bends the separating bridge of host rock strata until eventually fractures form in one or both of the zones of maximum flexure (Fig. 4.3a). Implicitly, the bedding of broken bridges (if visible) is



inclined to that of the surrounding host rock (Fig. 4.3a, e and h) (cf. Hutton, 2009). Tensional fractures developed in the host rock bridges at either end (Fig. 4.3a) may be infilled with magma, possibly detaching the bridge from the host rock at one end (i.e. a broken bridge; Fig. 4.3f, g and h) or both (i.e. bridge xenoliths; Fig. 4.3i and j) (Hutton, 2009). Resultantly, broken bridges and bridge xenoliths are associated with steps in the intrusion walls, which may preserve bridge stubs (Fig. 4.3a, e and f), and often contain evidence of partial melting (Hutton, 2009). On Ardnamurchan, broken bridges ( $\leq 3$  m wide) are primarily observed in cone sheets intruding the Mesozoic metasedimentary strata (Fig. 4.3). Occasionally, broken bridges of dolerite were also encountered.

#### 4.2.1:3 *Non-brittle behaviour of the host rock*

On Ardnamurchan, morphological features of several cone sheets and associated host rock structures are suggestive of intrusion facilitated by non-brittle fluidisation processes (Fig. 4.4). It is suggested that heated fluids, derived either from the cone sheet magma or the host rock pore fluid, infiltrated the coherent host rock (e.g. Mesozoic shale) resulting in grain disaggregation and fluidisation (Kokelaar, 1992; Schofield, 2009; Schofield et al., 2010). Fluidisation may occur if the respective fluid undergoes rapid expansion through a drop in fluid pressure; potentially instigated through fluid flow into either the relatively unconfined fracture tip (ahead to the propagating magma sheet) or a cross-cut pre-existing fracture (Kokelaar, 1982; Curtis and Riley, 2003). Evidence of the former process is provided by the observation of remobilised shale, containing fragments of brecciated limestone and *Gryphaea* fossils (Fig. 4.4a and b), and back-veins of melted and rapidly recrystallised sandstone (Fig. 4.4c) adjacent to cone sheet contacts. Some remobilised shale, often displaying conspicuous convoluted laminations, is restricted to fractures in the host rock proximal to a cone sheet (Fig. 4.4d and e), thus providing evidence of the activity of localised hydrothermal fluids during emplacement.

Non-brittle host rock behaviour may also be instigated during magma intrusion into poorly lithified and unconsolidated host rocks if the low mechanical strength, inherent due

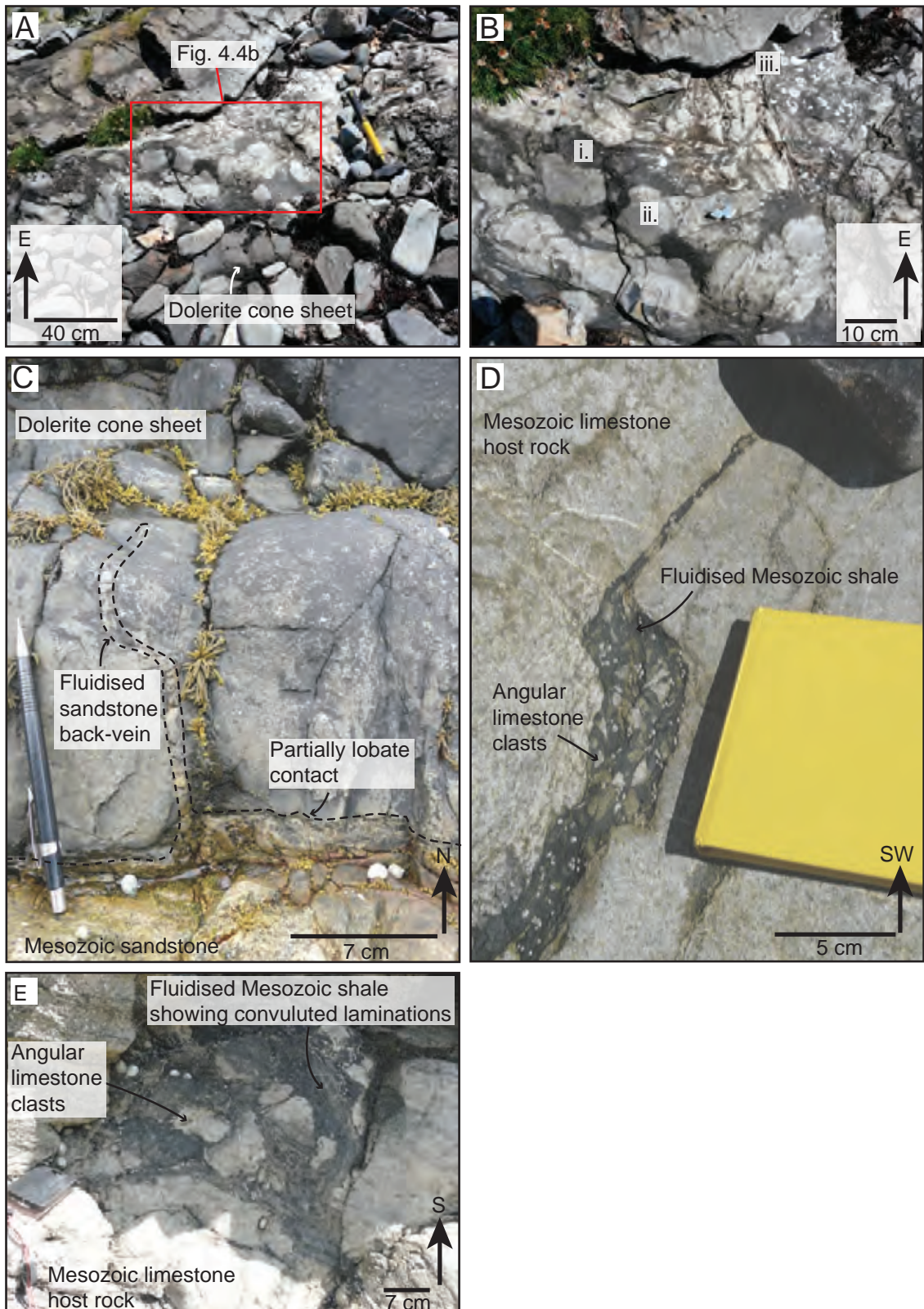


Fig. 4.4: A and B) Photographs of fluidised Mesozoic shale (B i), containing brecciated Mesozoic limestone clasts (B ii) and *Gryphaea* fossils (B iii), adjacent to a cone sheet. C) Back-vein of fluidised sandstone injected into a cone sheet. D) Fluidised Mesozoic shale injected along a pre-existing fracture in the Mesozoic limestone, which has been brecciated. E) Convoluted laminations in fluidised Mesozoic shale.

to reduced grain cohesion, promotes ductile deformation (Schofield, 2009). Infiltration of fluids through the host rock may enhance this effect. Several cone sheets intruded into the Early Palaeogene poorly consolidated volcanoclastics and olivine basalt lavas display magma fingers; relatively long, thin tubes of magma that are elliptical in cross-section (Fig. 4.5) (Pollard et al., 1975; Schofield et al., 2010). Magma fingers develop through the initiation of a viscous-viscous contact, due to ductile deformation processes (i.e. fluidisation or ductile flow of unconsolidated grains), between the propagating edge of an intrusive sheet and the host rock (Fig. 4.5a) (Pollard et al., 1975; Schofield et al., 2010). Lobate irregularities at the viscous-viscous contact serve to focus magma flow and preferentially propagate ahead of the main magmatic sheet (Fig. 4.5a) (Pollard et al., 1975). Towards the source, magma fingers coalesce as continued magma inflow promotes lateral inflation (Fig. 4.5a). Expansion of the magma fingers deforms and expels the intervening host rock eventually resulting in the coalescence of magma fingers, potentially forming magmatic lobes (Fig. 4.5a) (Schofield et al., 2010). On Ardnamurchan, magmatic lobes comprised of magma fingers are well developed in two cone sheets observed to the east of Ben Hiant at NM 548 639 (locality 208-215) and NM 553 642. The first cone sheet can be seen to transgress up stratigraphy through Neoproterozoic Moine metasedimentary rocks, at which point the cone sheet appears planar, and into the poorly lithified Early Palaeogene volcanoclastics and basalt lavas where it can be separated into magma lobes sub-divided into magma fingers (Fig. 4.5b). The magma fingers are elliptical in cross-section and well defined by the fanning arrangement of cooling joints (Fig. 4.5c). Although the host rock contacts are poorly exposed, where present, the Early Palaeogene host rock is unstructured and can occasionally be seen to pinch out between two fingers (Fig. 4.5d). Identification of magma fingers in the second cone sheet, to the east of the Loch Mudle Fault, is complicated by the degradation of the exposure but the cone sheet may reflect increased levels of inflation and coalescence of magma fingers. Six spatially separate magma lobes, which dip moderately northwards and display a distinct fanning arrangement, are recognised (Fig. 4.5e and f). Textural variations are observed between the magma lobes, which each display a marked chilled margin containing amygdalae. Another cone sheet, ~50

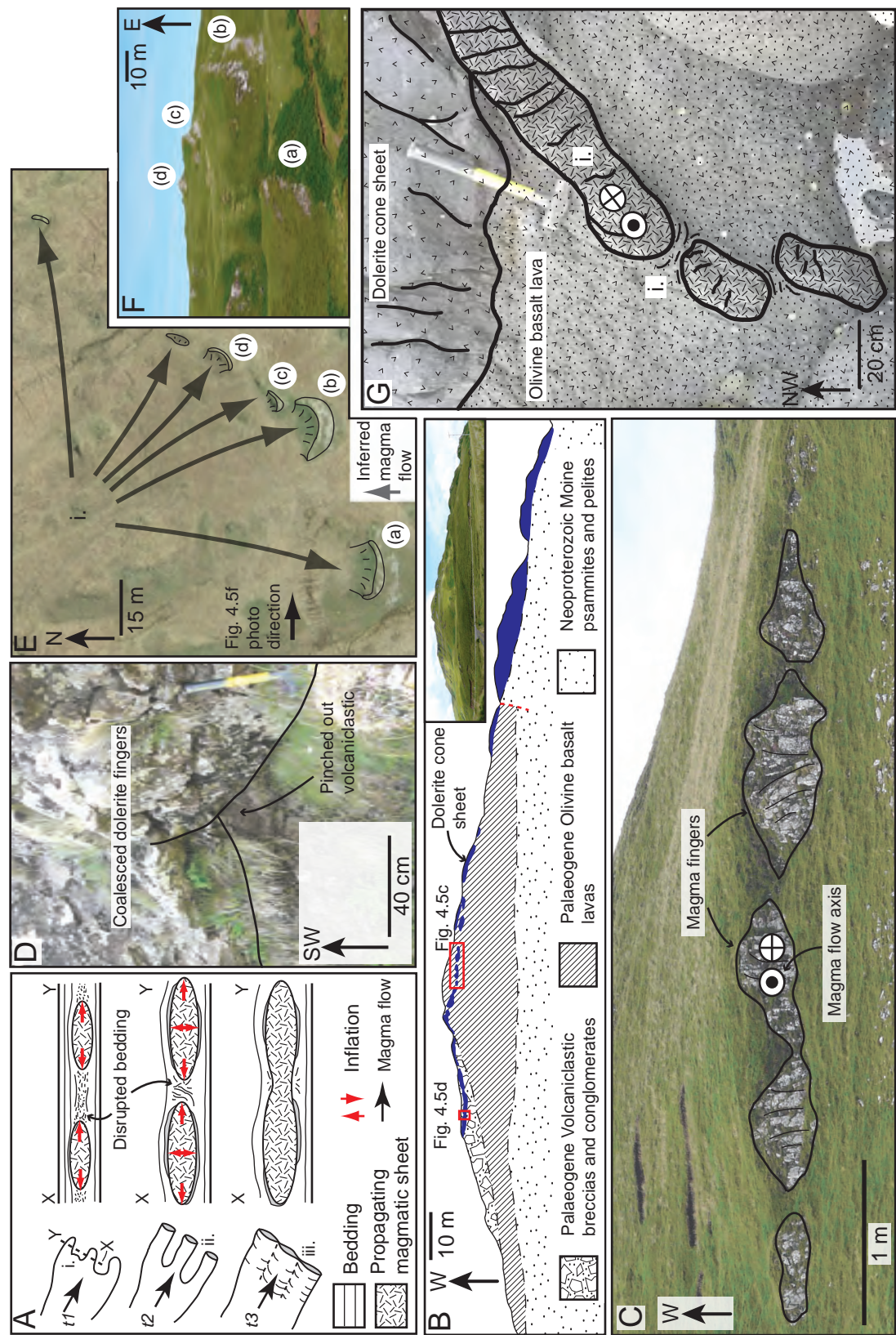


Fig. 4.5: A) Formation of magma fingers (redrawn from Schofield et al., *in press*). B, C, D, E, F and G) Magma lobes and magma fingers observed in cone sheets on Ardnamurchan. See text for details.

cm thick, intruding Early Palaeogene basalt lavas in Area 1 at Glas Eilean [NM 48339 62730] is observed to contain magma fingers (Fig. 4.5g). The adjacent basalt host rock contains apparent flow lines that are consistent with the lateral expansion of the magma fingers towards each other (Fig. 4.5g i).

Whilst there is evidence that the emplacement of some cone sheets was facilitated by non-brittle processes, they are volumetrically minor and spatially restricted. Brittle processes can therefore be considered to dominate. This allows the observed and measured geometries of the cone sheets to be interpreted in a straightforward manner.

## 4.2 Data collection and results

Gautneb et al., (1989), Gautneb and Gudmundsson (1992), Schirnack et al., (1999) and Tibaldi et al., (2011) highlighted the potential effects of variations in cone sheet outcrop elevation when analysing sheet dip, as local stress fields in sub-volcanic systems vary in orientation and magnitude with depth. Thus, cone sheets may have a curved profile in cross-section (cf. Anderson, 1936; Phillips, 1974), complicating dip correlations if significant variations in height above sea level are recorded for separate outcrops. Cone sheets on Ardnamurchan are predominantly exposed along the coast or within topographical depressions and occasionally on mountain flanks. Overall, the variation in altitude of cone sheet outcrops is typically <200 m, so they are considered to represent a single level within the ~5 km deep (Richey and Thomas, 1930) Ardnamurchan sub-volcanic system. Discerning between steep to sub-vertical cone sheets and dykes is also of particular importance as the two sheet intrusion types are traditionally considered to develop under different stress conditions (Walker, 1993; Chadwick and Dieterich, 1995; Tibaldi et al., 2011). Gautneb et al., (1989) argued that there is no tectonic justification for an arbitrary cut-off between cone sheet and dykes and instead suggested cross-cutting relationships should instead be utilised. Within the BIPIP, contemporaneous regional dykes and cone sheets are compositionally similar and proximal to the central complexes are morphologically (e.g. thickness, intrusion structures) comparable

(Richey and Thomas, 1930; Emeleus and Bell, 2005; Tibaldi et al., 2011). Within central complexes, the regional dykes and cone sheets may be differentiated as the regional dykes are typically more continuous along strike, often extending beyond the limits of a central complex (Tibaldi et al., 2011), and have a consistent NW-SE (infrequently N-S) orientation (Speight et al., 1982) typically at high angles to the local cone sheet strikes. The exception to this is in areas where the expected cone sheet strike is similarly oriented NW-SE (i.e. to the SW and NE of the Ardnamurchan central complex). Therefore, where no structural or petrological basis to differentiate adjacent dykes and cone sheets at outcrop was defined, both were measured. Note that published geological maps of Ardnamurchan (i.e. Richey and Thomas, 1930; Emeleus, 2009) present a diagrammatic representation of the cone sheets, as their size and abundance is not transferable to large scales. All data discussed in the following section is tabulated in Appendix D.

#### **4.2.1 Differentiating individual cone sheets**

To determine the volcano-tectonic conditions active during cone sheet emplacement, structural trends and local morphological variations both need to be considered. Identifying and mapping the extent of individual cone sheets is therefore vital and also provides a context for the data collected. Where the Ardnamurchan cone sheets are well exposed along several coastal sections, particularly along the southern shore, they collectively and individually display highly variable dips, anatomising strike trends and complex cross-cutting relationships (cf. Richey and Thomas, 1930; Keunen, 1937; Day, 1989). Figure 4.6 is a 1:1000 scale map of Mingary Pier (part of Area 1), which highlights the local variation in cone sheet strike and dip. As the majority of cone sheets are equigranular dolerites, that consistently weather to an orange–brown or pale grey colour (depending on whether they are located below the storm line or not), they are often difficult to differentiate from both field observations and hand specimens. Mapping discrete cone sheets inland ( $\sim > 50$  m from the coast) is further complicated as outcrops are sporadic and the host rock, as well as contact relationships, are often unexposed. Tracing chilled margins and identification of subtle variations in dolerite

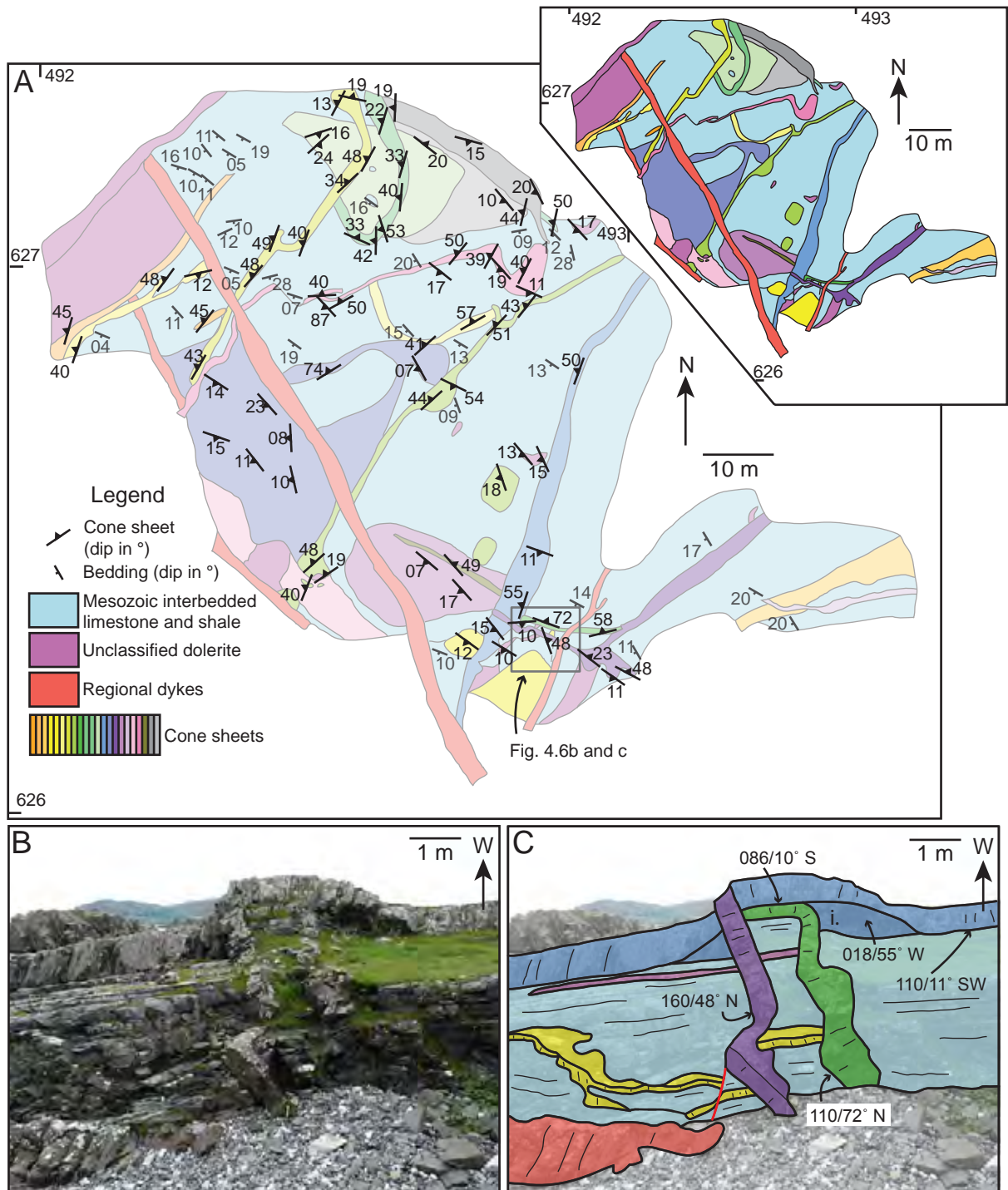


Fig. 4.6: A) Detailed 1:1000 scale map of small area at Mingary Pier (Area 1) highlighting the variation in cone sheet strike and dip as well as the complex cross-cutting relationships they exhibit. *Inset*: A full colour map provided to allow individual cone sheets to be better distinguished. B and C) A photograph and interpreted photograph (including cone sheet strike and dips), respectively, of a gully wall exposed in the mapped area that clearly portrays the numerous local variations in cone sheet behaviour that are often encountered. For example, one dyke is observed to abruptly rotate into a sill where it seemingly deflects part of a sill into an inclined sheet (i). The geology in (C) is colour coded to the legend in (A).

grainsize may allow separate cone sheets to be distinguished. However, the paucity of exposure and internal grainsize variations often nullifies these techniques. To map the cone sheets a method of correlating individual sheet segments without relying on subtle textural variations is therefore required.

Many cone sheets (69 in total; ~26 %) analysed in the field throughout this study, and also noted by Day (1989), were observed to contain a volumetrically minor (<5 vol. %) population of Fe-sulphides; identified through reflected light microscopy to consist of pyrite and minor chalcopyrite (Fig. 4.7a). The grainsize of pyrite ranges from ~0.1–2 mm, whilst chalcopyrite is restricted to grainsizes <0.2 mm. Typically, the coarse-grained pyrite has a euhedral cubic crystal habit, although some irregular crystal aggregates occur, compared to the finer grainsize Fe-sulphides, which are anhedral and interstitial (Fig. 4.7a and b). Within individual cone sheets the distribution of Fe-sulphides is seemingly random, although they are occasionally arranged into layers (~1.5 cm thick) or associated with amygdales containing chlorite, zeolite, quartz and calcite (Fig. 4.7b). In one cone sheet in Area 1 [locality 447, NM 49362 62606], cooling fracture surfaces are coated with oxidised iron and sporadic, coarse ( $\leq 2$  mm) cubic pyrite crystals (Fig. 4.7c and d). Importantly, significant textural variation is observed between the Fe-sulphide populations of distinct cone sheets but is remarkably consistent within single cone sheets. This suggests the characteristics of Fe-sulphide populations are unique to each host cone sheet.

Assuming that the cone sheets have a common source (e.g. Anderson, 1936; Phillips, 1974; Schirnack et al., 1999), the observed variation in distribution and abundance of Fe-sulphides may reflect changes in the source evolution of the magma or injection of cone sheets from different sections of a stratified magma chamber. However, the majority (68 %) of the cone sheets observed to contain Fe-sulphides were intruded into Mesozoic metasedimentary successions whilst those within the Neoproterozoic Moine metasedimentary rocks, Early Palaeogene volcanoclastics, the Glas Bheinn Dolerite and older cone sheets accounted for only 23 %, 4 %, 2 % and 5 % respectively. No Fe-sulphides were observed in cone sheets emplaced into the major intrusions of Centre 2 and 3. This correlation between

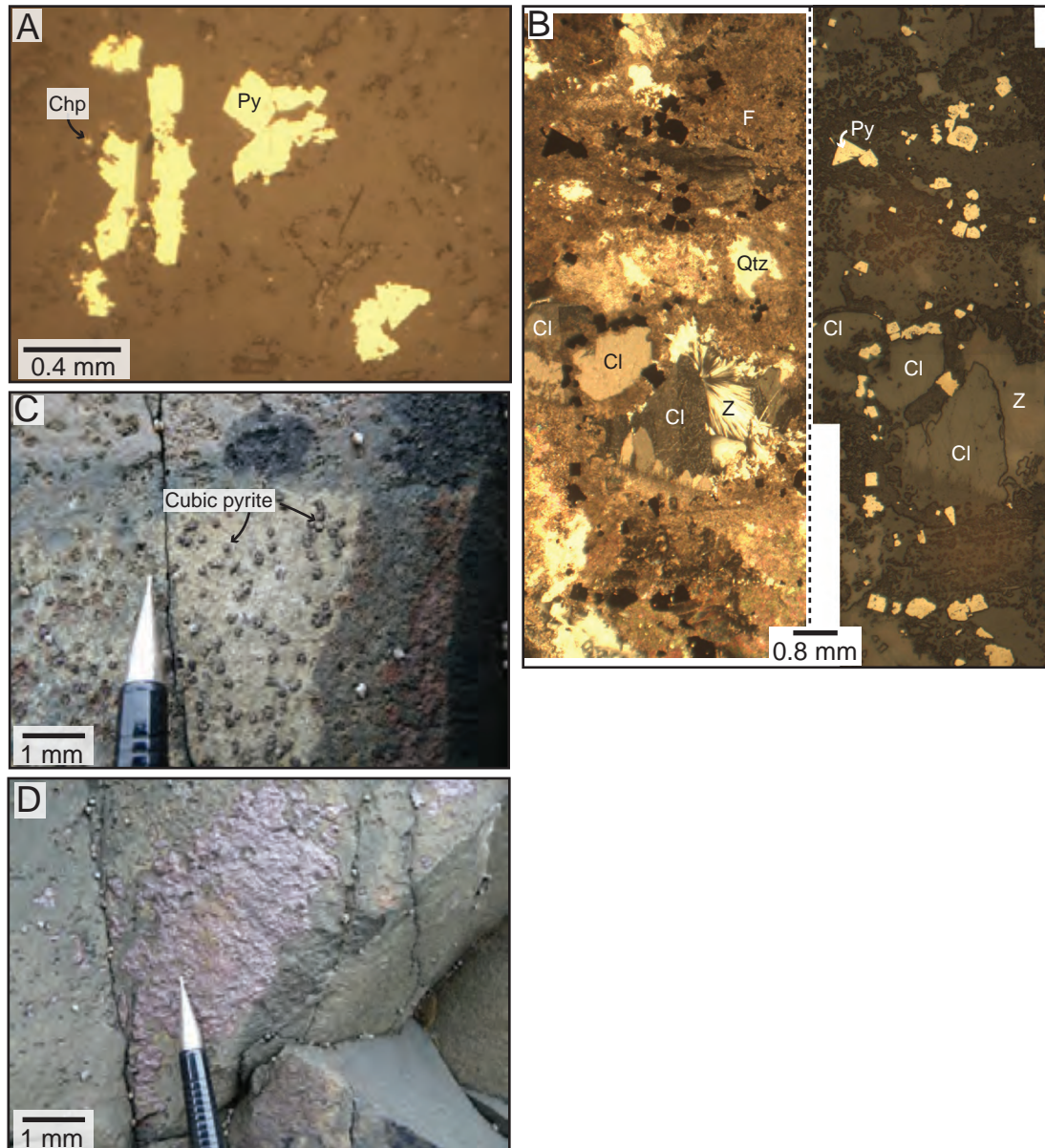


Fig. 4.7: A) Reflected light photomicrograph from locality 95 (Area 2) showing the range of pyrite (Py) grainsize and the propensity towards subhedral to euhedral crystal habits of coarser pyrite crystals. A small bleb of chalcopyrite (Chp) is also highlighted. B) A plane polarised light (left) and reflected light (right) photomicrograph mosaic of a section through an amygdale within a cone sheet observed at locality 17 (Area 14). Fine to medium, subhedral to euhedral pyrite is disseminated throughout the amygdale and is spatially associated with calcite (Cl), quartz (Qtz) and zeolite (Z). C and D) Cooling joint planes within a cone sheet (locality 447; Area 1) are often observed to contain precipitated cubic pyrite crystals (C) or be coated in weathered iron oxide.

Fe-sulphide presence and host rock type cannot be explained if a magmatic origin to the Fe-sulphides is assumed. Instead, it is suggested that the Fe-sulphides are secondary mineral phases (Day, 1989) that were incorporated into the magma during cone sheet propagation

or post-emplacement, following either the partial melting of country rock or hydrothermal leaching. This is supported by the identification of a biological signature within pyrite through geochemical analyses (e.g. standard mass spectrometry and *in situ* laser combustion; Prof. John Parnell, pers. comm.) and the association of some Fe-sulphides with amygdales. The majority of the Fe-sulphides likely originated from the Mesozoic successions, given the correlation between Fe-sulphide presence and host rock type as well as the observation of occasional minor pyrite within the limestones and shales. As the Fe-sulphide populations appear texturally unique to the host cone sheet and are likely secondary mineral assemblages acquired from the host rock (i.e. not from the source reservoir), it is suggested that comparison between adjacent cone sheet outcrops allows the exposed extent of most cone sheets to be identified. For example, correlation of Fe-sulphide populations was used to produce the map displayed in Fig. 4.6a.

#### **4.2.2 Cone sheet abundance variations**

Although the concentric disposition of the Ardnamurchan cone sheets is incomplete, with the majority of cone sheets located offshore or obscured by later major intrusions, there is an apparent increase in cone sheet abundance to the south and south-east of the Ardnamurchan central complex (Richey and Thomas, 1930). Out of the 209 cone sheets analysed in this study, 147 were observed to the south and south-east of the Ardnamurchan central complex (between Sròn Bheag and Mingary Castle). Whilst this distribution may not be definitive and possibly a result of poor exposure or measurement bias, similar geographically restricted areas of increased cone sheet intensity have been observed at other central complexes (e.g. Skye, Walker, 1993; Hvalfjörður, Iceland, Gudmundsson, 1995; Thverartindur, Iceland, Klausen, 2004; Otoge, Japan, Geshi, 2005).

#### **4.2.3 Cone sheet orientation and dip**

Field observations reveal individual cone sheets are often discontinuous along strike on a decametre scale (Fig. 4.6), consistent with the observations of Keunen (1937). A few cone

sheets inland at Sròn Bheag (Day, 1989) and on the east flank of Beinn nan Leathaid may be traced along strike for 0.1–1 km. Along strike, cone sheets may be observed to either be cut by later intrusions; gradually decrease in thickness to a tip point; anatomise with other cone sheets or develop horn-like geometries (cf. Rickwood, 1990).

A concentric strike is apparent from the general cone sheet trend, although further (>2 km) to the east and north-east the cone sheets display a partial elliptical strike, elongated NW-SE (Richey and Thomas, 1930), and appear to wrap around the Ardnamurchan central complex (Fig. 4.1a). These observations are supported by the inward convergence and concentric disposition of the poles to cone sheet planes, for the Outer Centre 2 and Centre 1 cone sheet sets (Fig. 4.1b) (cf. Tibaldi et al., 2011). Whilst the average cone sheet dip azimuths for most areas are oriented radially towards the Ardnamurchan central complex, they often do not correlate to the Centre foci (particularly Centre 1) which they were suggested by Richey and Thomas (1930) to define (Fig. 4.1a). Out of all the cone sheet dip azimuths measured (Centre 1  $n = 46$ ; Centre 2  $n = 320$ ; Centre 3  $n = 8$ ), only 50 % from Centre 1 and Centre 2 and 86 % from Centre 3 may be projected to within  $30^\circ$  (to either side) of the respective foci positions. Using the average cone sheet swarm dip azimuths, for selected areas, reduces the difference between the Centre foci position and the dip azimuth trajectories, although there is still some discrepancy (Fig. 4.1a).

Cone sheet dips range from  $0^\circ$ – $90^\circ$ . Figure 4.1a also highlights locally developed deviations from the concentric cone sheet strike trend implied by Richey and Thomas (1930). Primarily these deviations are represented by relatively small clusters of gently-dipping ( $\sim < 15^\circ$ ), outwardly inclined (with respect to the Ardnamurchan central complex) cone sheet poles, attributed to the Centre 1 and Outer Centre 2 sets, and are more conspicuous where the host rock is well-bedded (i.e. Mesozoic metasedimentary rocks) (Fig. 4.1a). Plotting sedimentary bedding poles and the cone sheet poles for each geographically defined Area indicates the deviatory cone sheet cluster is roughly coincident with the sedimentary bedding cluster (Fig. 4.1a). This implies the majority of outward dipping cone sheets are parallel to bedding although field observations indicate a significant proportion deviate slightly ( $\leq 5^\circ$ )

from this bedding-parallel trend (Day, 1989). Field relationships reveal the inward-dipping and outward-dipping cone sheets do not represent two separate intrusion populations as numerous cone sheets observed (sub-)parallel to bedding abruptly transgress up stratigraphy along inwardly inclined (25–65°) ramps (Fig. 4.8) (Day, 1989). Outward dipping cone sheets (sub-)parallel to bedding are predominantly observed  $\geq 1$  km from the outer margins of the Ardnamurchan central complex and generally increase proportionally with distance away from the central complex to the furthest limits of significant Mesozoic metasedimentary rock outcrops (Fig. 4.1a). Areas closer to the Ardnamurchan central complex also contain outward-dipping cone sheets, although their abundance is significantly diminished and their inclination is often steeper ( $\sim 56^\circ$ ) (Fig. 4.1a). For example, re-investigation of the Inner Centre 2 cone sheet set, which intrudes the major gabbroic intrusions of Centre 2 (Fig. 4.1), reveals that although a few sheets ( $\sim 13\%$ ) dip inwards between  $50^\circ$ – $70^\circ$  (cf. Richey and Thomas, 1930), the majority of sheets are sub-vertical ( $71^\circ$ – $90^\circ$ ) with both inward and outward inclinations suggesting they are dykes *sensu lato*.

The mean dips calculated for the Centre 1 ( $34^\circ$ ), Outer Centre 2 ( $42^\circ$ ), Inner Centre 2 ( $77^\circ$ ) and Centre 3 ( $59^\circ$ ) cone sheet sets are similar to those presented by Richey and Thomas (1930) ( $10$ – $20^\circ$ ,  $35$ – $45^\circ$ ,  $70^\circ$ ,  $50^\circ$  respectively) for Ardnamurchan, elsewhere in the BIPIP (e.g.  $40$ – $50^\circ$ , Skye, Tibaldi et al., 2011) and globally (e.g.  $41^\circ$ , Gran Canaria, Schirnack et al., 1999;  $30$ – $60^\circ$ , Japan, Geshi, 2005). These calculated means are corroborated by plotting frequency against dip angle, which for the Centre 1, Inner Centre 2 and Centre 3 cone sheet sets reveals a Gaussian distribution (Fig. 4.9a, b and d). The bimodal distribution of the Outer Centre 2 cone sheet set (Fig. 4.9b), with peaks at  $10$ – $20^\circ$  and  $40$ – $50^\circ$ , is similar to that observed in data from cone sheet swarms in Iceland and is typically interpreted to reflect cone sheet intrusion from different levels of a central magma reservoir (cf. Gautneb et al., 1989; Gudmundsson, 1995; Burchardt and Gudmundsson, 2009). Whilst this may be the case for the Outer Centre 2 cone sheet set, it is most likely the peak at  $10^\circ$  represents the significant proportion of cone sheets intruded sub-parallel to bedding.

Plots of dip angle against distance from the respective Centre foci indicate the Outer

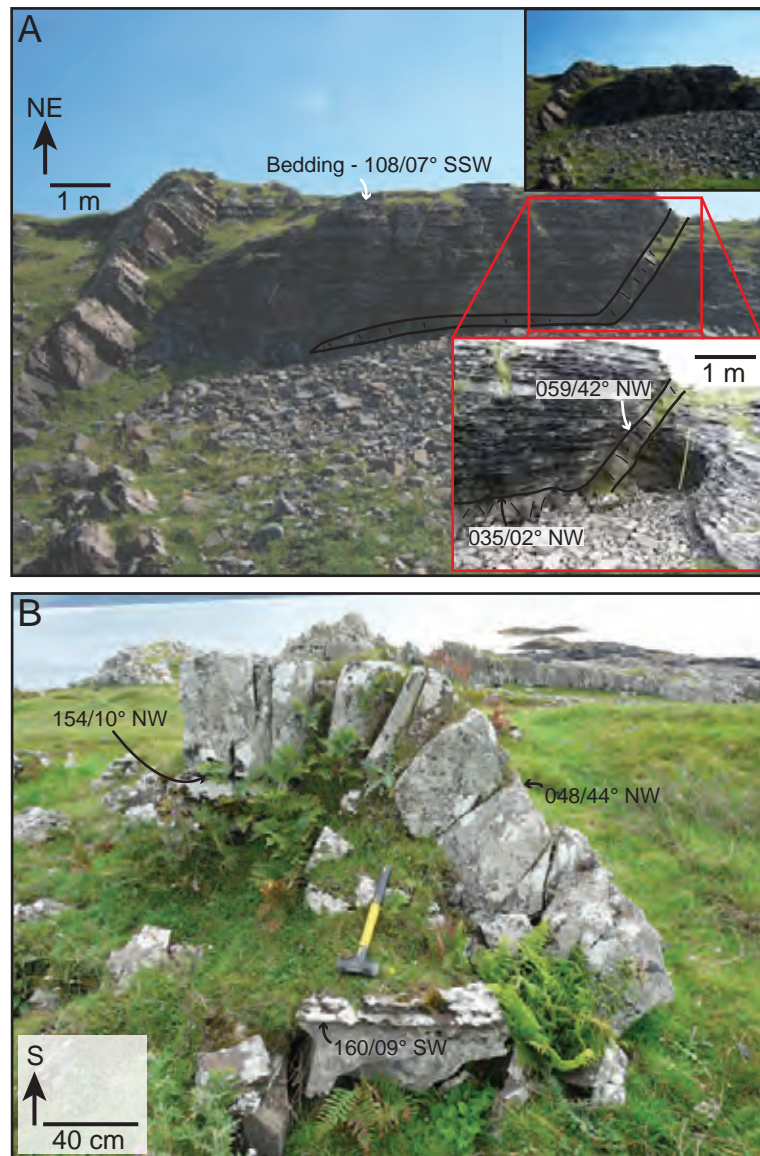


Fig. 4.8: A and B) Field photographs of two cone sheets in Area 1 (localities 25 and 52) with ramp-flat morphologies.

Centre 2 cone sheets increase in dip inwards towards Centre 2, supporting Richey and Thomas's (1930) original observations (Fig. 4.9f i). However, the Centre 1 cone sheets appear to increase in dip away from the Centre 1 foci (Fig. 4.9e i), contrary to suggestions by Richey and Thomas (1930). This variation in dip implies that the Ardnamurchan cone sheets are not planar and so cannot be simply extrapolated linearly down-dip to define the source reservoir (cf. Richey and Thomas, 1930; Geldmacher et al., 1998; Burchardt and Gudmundsson, 2009; Siler and Karson, 2010; Tibaldi et al., 2011; Burchardt et al., 2011).

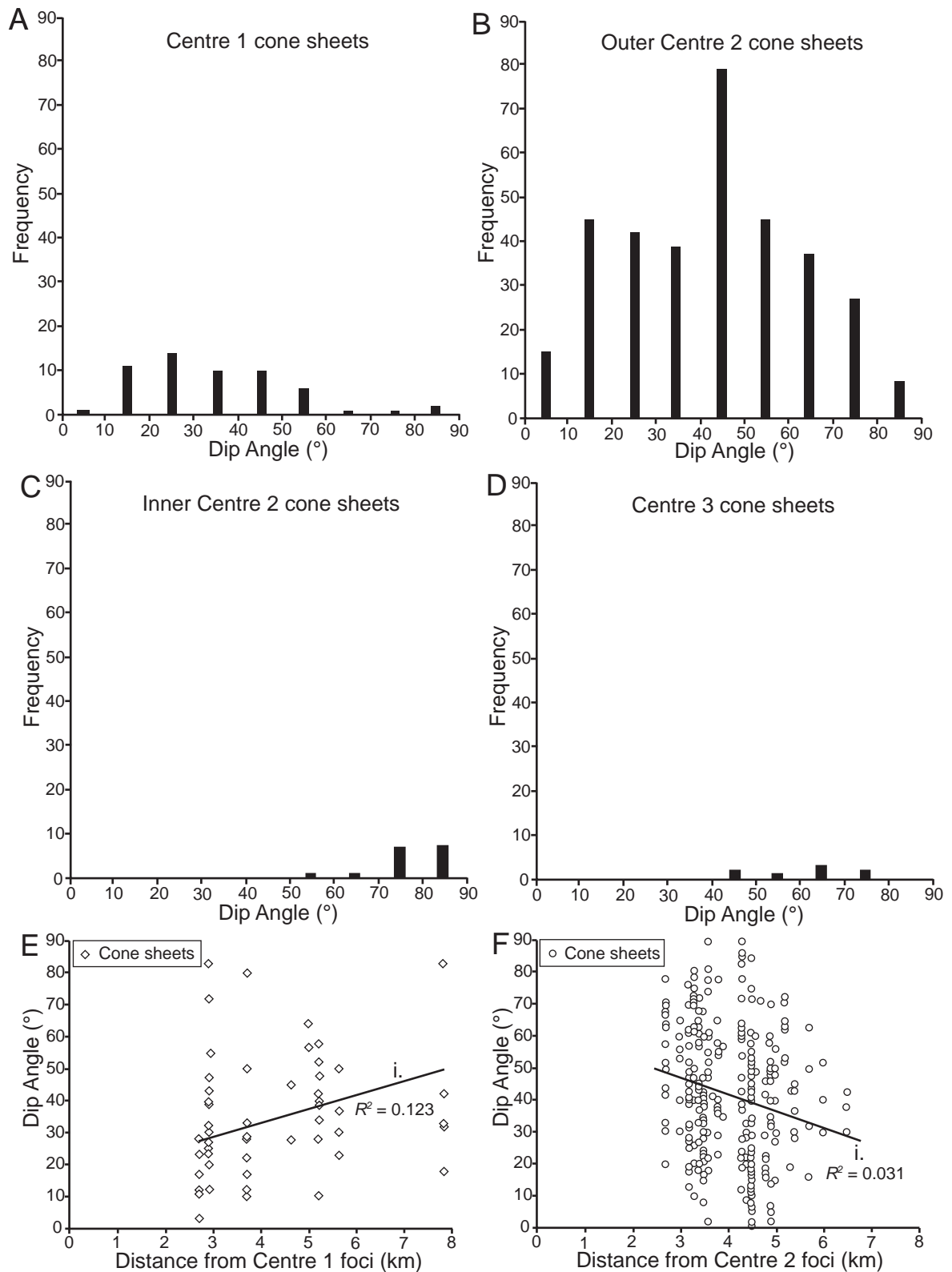


Fig. 4.9: A, B, C and D) Dip angle against frequency graphs for the four cone sheet sets defined on Ardnamurchan by Richey and Thomas (1930). E and F) Plots of cone sheet dip angle, for Centre 1 and 2, against outcrop distance from the respective Centre foci.

#### 4.2.4 Modes of opening and thickness variations of cone sheets

As intrusive sheets are often opened orthogonal to  $\sigma_3$  (Anderson, 1951), establishing the opening vectors of sheet intrusions therefore determines whether the local stress field conditions active during emplacement promoted development and intrusion of dilatational (tensile; mode I) or shear (mode II and III) fractures (Pollard, 1987; Rubin, 1995). Describing the opening vector of the cone sheets was achieved through correlating marker horizons on either side of the cone sheet intrusion (Fig. 4.10). If the cone sheets occupy dilatational fractures, the offset of the marker horizons may be accounted for purely by the thickness of the cone sheet (Fig. 4.10a to c) (Pollard, 1987). Conversely, if the marker horizons are displaced by a distance greater than the thickness of the cone sheet it is typically assumed shearing accompanied intrusion (Pollard, 1987). Rotation of the principal stress axes during intrusion may potentially create hybrid dyke morphologies whereby mixed mode I and mode II or III fracturing occurs (e.g. Fig. 4.10d) (Pollard, 1987; Rubin, 1995).

Field observations are consistent with Keunen's (1937) suggestion that the majority of cone sheets on Ardnamurchan predominantly exhibit dilatational opening (e.g. Fig. 4.10a). For cone sheets exhibiting a ramp-flat geometry, the opening vector of the inwardly inclined ramps is dilatational (Fig. 4.10c). Implicitly, the opening vector of the 'flat' sections (sub-) parallel to bedding must therefore contain some component of shear (Fig. 4.10e). In Area 2, one cone sheet [NM 50618 62002] is observed to contain sinistrally displaced *en échelon* segments, each terminating laterally in a horn (Rickwood, 1990), which is suggestive of mixed mode I and III fracturing resulting in a change in principal stress axes orientations (Fig. 4.10d) (cf. Pollard, 1987; Rubin, 1995).

Cone sheet thickness was measured orthogonally to intrusion walls and ranges from 0.05 m to 2.5 m, with an average of 0.6 m. However, many sheets with none or only one margin exposed up to 10 m thick were observed (Richey and Thomas, 1930). A plot of thickness against the distance of the cone sheets from their respective Centre foci may highlight an apparent positive correlation with cone sheet thickness increasing with distance (Fig. 4.10f). No statistically valid correlation is observed between cone sheet thickness and

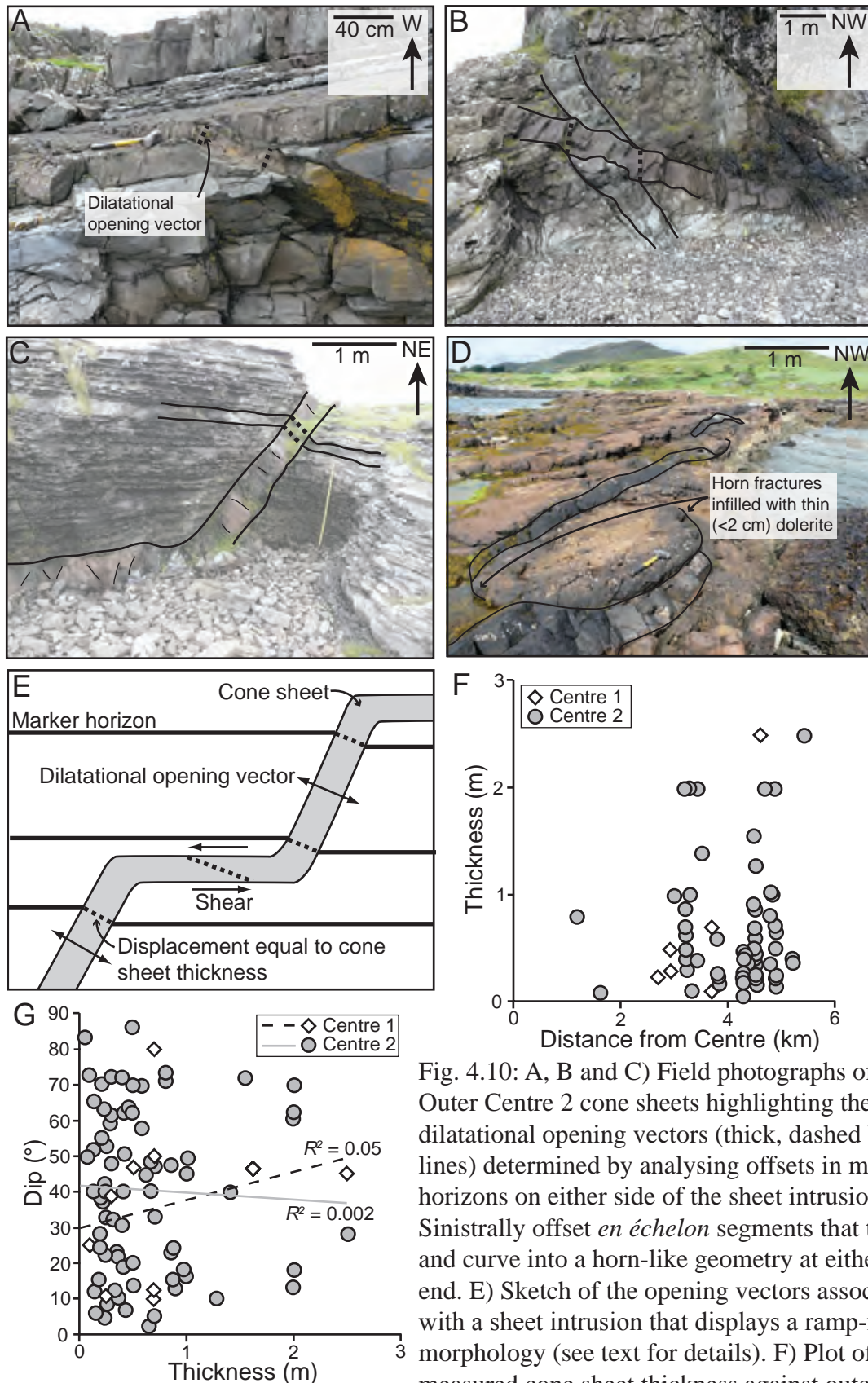


Fig. 4.10: A, B and C) Field photographs of Outer Centre 2 cone sheets highlighting their dilatational opening vectors (thick, dashed black lines) determined by analysing offsets in marker horizons on either side of the sheet intrusion. D) Sinistrally offset *en échelon* segments that thin and curve into a horn-like geometry at either end. E) Sketch of the opening vectors associated with a sheet intrusion that displays a ramp-flat morphology (see text for details). F) Plot of measured cone sheet thickness against outcrop distance from the respective Centre foci. G) A graph displaying the relationship between the measured dip and thickness of cone sheets belonging to the Centre 1 and Centre 2 swarms.

dip (Fig. 4.10g).

## 4.3 Stress field conditions during intrusion

### 4.3.1 Derivation of emplacement conditions

Having established that cone sheets predominantly opened by dilation and that brittle processes accompanied intrusion, the relationships between cone sheets and other fractures may be used to reconstruct the stress field conditions active during emplacement (Delaney et al., 1986; Pollard, 1987) by developing the methods employed by Jolly and Sanderson (1997), André et al., (2001) and McKeagney et al., (2004). Furthermore, the influence of pre-existing fractures on cone sheet intrusion may be evaluated. To illustrate the methodology utilised, the following section presents a detailed analysis of data collected from the well exposed Area 1 cone sheets and Mesozoic metasedimentary host rock.

In Area 1, two fracture sets with sub-parallel strikes, oriented tangentially to the Ardnamurchan central complex, and moderate inward and outward dips are common in the Mesozoic metasedimentary rocks. On average the inwardly and outwardly inclined fractures are oriented 311/53° (dip azimuth and dip) and 117/68° (dip azimuth and dip) respectively (Fig. 4.11a). Plotting the poles to the fracture planes on an equal area, lower hemisphere stereographic projection highlights two clusters, for which the average fracture planes suggest an inter-fracture angle of 59° (Fig. 4.11b ii); consistent with them being a conjugate fracture set (Twiss and Moores, 2007). Comparison of the poles to sedimentary bedding, fractures planes and cone sheets reveal that the cone sheets intruded either (sub-)parallel to bedding or to the set of inwardly inclined fractures (Fig. 4.11b). No cone sheets parallel to the outward-dipping fracture set were encountered (Fig. 4.11b). Similar observations were made at Areas 2 and 14, though the variable orientation of other fracture sets and poorer exposure complicated analysis. It is important to determine whether the observed conjugate fracture set developed prior to or as a result of cone sheet intrusion in order to further interpret emplacement conditions.

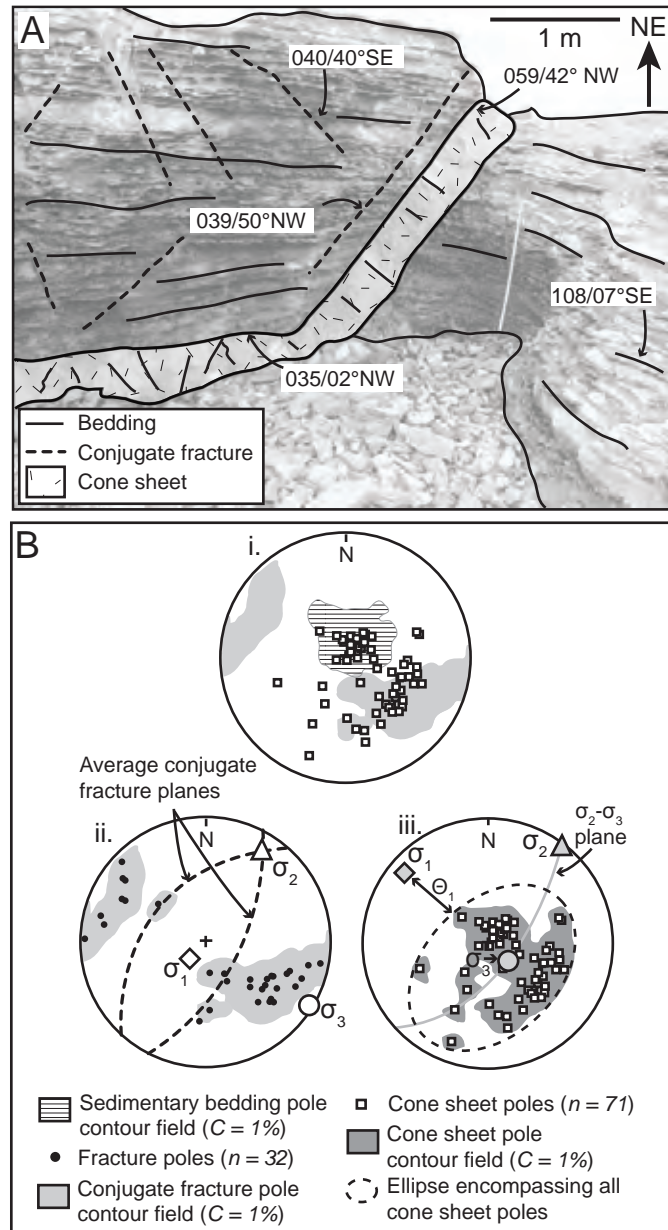


Fig. 4.11: A) Transgressive cone sheet intruding bedding and also ramping up stratigraphy parallel to a series of inward dipping fractures, one half of a conjugate fracture set. B) Lower hemisphere, equal area stereographic projections of cone sheet poles, conjugate fracture poles (and contours) and bedding poles (and contours) from Area 1 (i). ii) Resolved formational principal stress axes orientations for conjugate fractures and (iii) cone sheet intrusion. Fracture data is presented in Appendix D.

Principal palaeostress axes calculated from the conjugate fracture set suggest that they formed in an extensional stress field, with  $\sigma_1$  sub-vertical and  $\sigma_3$  horizontal (Fig. 4.11b ii). Dilatational opening vectors of the cone sheets suggests the intrusive planes were orthogonal to  $\sigma_3$  (Anderson, 1951) allowing dyke attitude to be used to determine the principal stress trajectories (Pollard, 1987). Considering cone sheets with gentle outward dips (sub-)parallel

to bedding and moderate to steep inward dips parallel to the NW-dipping fractures were intruded contemporaneously, whilst the outward dipping conjugate fractures remain closed, the orientation of all cone sheets may be used to define the average stress field active during emplacement. Hence, the eigenvector of the gross cluster of the cone sheet poles, located within an ellipse encompassing the poles, may be taken to represent  $\sigma_3$  (128/73°; Fig. 4.11b) (Jolly and Sanderson, 1997). It is important to note that it is not just the cone sheet orientation that is used to determine the principal stress axes, as host rock anisotropies may allow deviations in sheet orientation relative to the contemporaneous stress axes (Delaney et al., 1986). Rather, it is a combination of cone sheet orientation and dilatational opening vectors, oriented parallel to the cone sheet poles, which are used. Fracture opening is easier closer to  $\sigma_2$  than  $\sigma_1$ , suggesting the axis of symmetry that bisects the encompassing ellipse long axis and the  $\sigma_3$  eigenvector represents the  $\sigma_2$ – $\sigma_3$  plane (Fig. 4.11b **iii**) (Jolly and Sanderson, 1997; McKeagney et al., 2004). The pole to the  $\sigma_2$ – $\sigma_3$  plane is therefore equivalent to  $\sigma_1$  (308/17°; Fig. 4.11b). Calculating the orientation of the principal stress axes active during intrusion of the cone sheets throughout Ardnamurchan suggests the stress regime was compressional, with  $\sigma_3$  sub-vertical, becoming shallower towards the central complex, and  $\sigma_1$  radially inclined inwards, steepening towards the central complex (Fig. 4.1a). The two stress regimes active during fracture formation (extensional) and cone sheet intrusion (compressional) contrast, indicating the events were not coeval. It is likely the conjugate fractures formed first, either in relation to regional extension prior to the development of the central complex (cf. England, 1988) and/or during periods of major local intrusion deflation (cf. Day, 1989). Reactivation of the conjugate fractures in a compressive stress field may then have accommodated cone sheet intrusion (Mathieu et al., 2008). The scatter of cone sheet poles around  $\sigma_3$  (Fig. 4.11b) supports this hypothesis as, considering the dilatational opening of the sheets, the observed distribution of cone sheet poles is suggestive of pre-existing fracture reactivation rather than intrusion of newly formed fractures (McKeagney et al., 2004). One cone sheet in Area 1 [locality 65, NM 4928 6263] may also be observed to intrude along an inward dipping conjugate fracture and is then chilled against the outward dipping conjugate fracture,

supporting reactivation of pre-existing fractures.

Mohr circles may be derived from the principal stress axes, active during cone sheet emplacement, and their orientation relative to intrusion planes to further establish whether or not pre-existing fractures were reactivated or new fractures formed and to constrain the magma pressure and emplacement depth (Jolly and Sanderson, 1997). To calculate the Mohr diagrams it is assumed  $\sigma_3$  (sub-vertical) is equal to lithostatic load (26.46 MPa/km, derived from an average crustal density of 2700 kg/m<sup>3</sup>, Allen and Allen, 2005) and magma pressure (Pf) is equivalent to pore fluid pressure (Jolly and Sanderson, 1997). Here, only the Mohr diagrams for Areas 1, 2, 5, 7 and 14 (Fig. 4.1a) are calculated as field observations indicate the cone sheets intruded dominantly through brittle processes. The failure envelope, derived from the limestone shear strength (24.5 MPa) and angle of internal friction (30°) parameters of Jaeger (1969), constrains the position and size of the Mohr circle, allowing the angle of new fractures formed relative to  $\sigma_1$  to be measured (Fig. 4.12). For variable magma pressures (e.g. 20 MPa, 30 MPa) and emplacement depths (e.g. 0.5 km, 1 km) the effective minimum principal stress ( $\sigma_3 - Pf$ ),  $\sigma_3'$ , may be calculated and fixed on the normal stress ( $\sigma_n$ ) axis of the Mohr diagram (Fig. 4.12). The  $\Theta_1$  angle, measured off the equal area, lower hemisphere stereographic projections as the angle between the defined  $\sigma_1$  and the bounding edge of the ellipse encompassing the cone sheet poles along the  $\sigma_1$ – $\sigma_3$  plane (Fig. 4.11b iii), can be incorporated into equation 4.1 to calculate the maximum shear stress (radius) of the Mohr circle (Jolly and Sanderson, 1997):

$$\tau_{\max} = (Pf - \sigma_3') / (1 + \cos 2\Theta_1). \quad (4.1)$$

Equation 4.1 may also be used to fix  $\sigma_1'$  onto the  $\sigma_n$  axis, allowing the Mohr circle to be plotted (André et al., 2001). The size of the Mohr circle can be tuned to establish the first point of contact with the failure envelope by adjusting the Pf, whilst maintaining the emplacement depth (André et al., 2001). The  $2\theta$  angle between this point and the centre of the Mohr circle defines the angle at which new fractures will form, with respect to  $\sigma_1$ , under the

stress regime and magma pressure modelled (Fig. 4.12).

Addition of a Byerlee friction envelope (i.e. criteria for failure in fractured rock) to the Mohr circle diagram allows the angular range of pre-existing fractures (relative to  $\sigma_1$ )

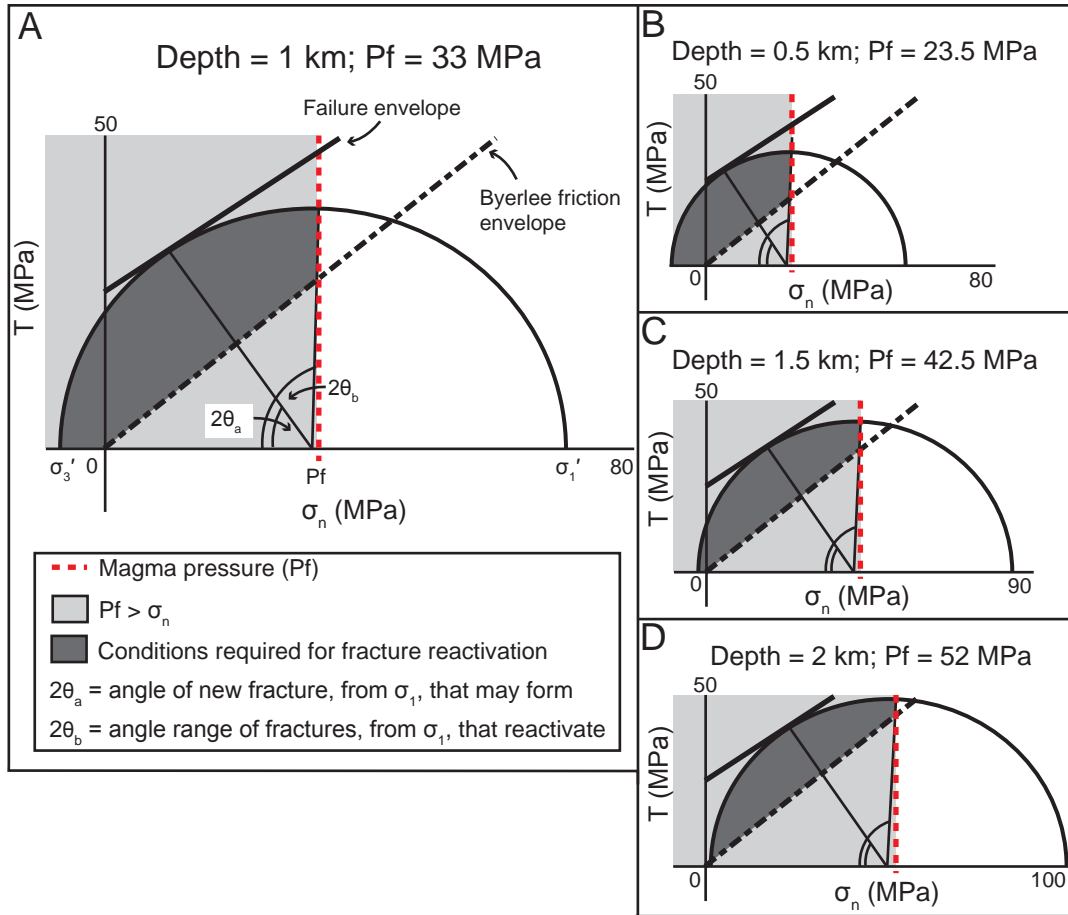


Fig. 4.12: Mohr circles for Area 1 calculated for (A) 1 km depth and a magma pressure of 33 MPa to demonstrate how the stress regime active during intrusion is calculated. Note that the  $2\theta$  angles are relative to  $\sigma_1$ , not  $\sigma_3$ . Mohr circles for emplacement depths of B) 0.5 km, C) 1.5 km and D) 2 km are also displayed from Area 1.

that may be reactivated (Byerlee, 1978), given the conditions modelled, to also be calculated.

For intrusion of a pre-existing or new fracture to occur the  $P_f$  must exceed the compressive stress normal to the fracture. Hence, pre-existing fractures may only be reactivated if their orientation, relative to  $\sigma_1$ , places them within the  $P_f > \sigma_n$  zone and above the Byerlee friction envelope (Fig. 4.12). Table 4.1 provides the calculated results for variable  $P_f$  and emplacement depths. The maximum depth this occurs at for the Ardnamurchan cone sheets ranges from 1.5–2 km with magma pressures of 42.5–58 MPa respectively (Table. 4.1).

Under these conditions new fractures would form at angles ranging from  $24^\circ$ – $30^\circ$  relative to

$\sigma_1$  (Table. 4.1). However, the Byerlee friction envelope is cut by the Mohr circle before the failure envelope is reached, implying pre-existing fractures within a certain angular range (e.g.  $0^\circ$ – $52.5^\circ$ ; Fig. 4.12) from  $\sigma_1$  may be reactivated. Overall, cone sheets are likely to have exploited pre-existing fractures within  $<67^\circ$  of  $\sigma_1$ . Bedding planes and pre-existing inward dipping fractures (of the conjugate set) fall within this range as attested to by the position of their pole contour fields within the encompassing ellipse of the cone sheet poles (Fig. 4.11b).

#### 4.3.2 Model of the active stress field during cone sheet intrusion

Throughout the evolution of the BIPIP the regional stress field maintained an extensional regime (England, 1988). As the cone sheets were intruded during compression, it is suggested the active stress field was localised and likely initiated through the development of the Ardnamurchan central complex. This is evidenced by the initial doming of the country rock (i.e. outward dipping bedding planes) and the deposition of Early Palaeogene volcanoclastics, which likely formed in relation to the intrusion of a currently unexposed shallow ( $\sim <5$  km) magma reservoir prior to the emplacement of the cone sheets and the major intrusions of Centres 1, 2 and 3 (Richey and Thomas, 1930; Emeleus and Bell, 2005). Local stress fields associated with magma chambers vary temporally and are controlled by the shape, depth and internal magma pressure of the magma reservoir (Gudmundsson, 1998, 2006; Corazzato et al., 2008). It is therefore important to attempt to characterise the evolving geometry of the unexposed upper crustal source reservoir to the central complex. The local stress field active during cone sheet intrusion appears to have been compressional, with  $\sigma_1$  radially inclined inward and  $\sigma_3$  sub-vertical (Fig. 4.1a), and comparable to the stress fields suggested to accompany intrusion of other cone sheet swarms from modelled spherical or elliptical magma chambers (e.g. Anderson, 1936; Phillips, 1974; Gautneb et al., 1989; Chadwick and Dieterich, 1995; Gudmundsson, 1998; 2006; Tibaldi and Pasquarè, 2008). However, the majority of previous models consider a homogeneous and isotropic crust, ignoring the potential for sheet deflection at local discontinuities (Gudmundsson, 2002).

The following model attempts to qualitatively incorporate a realistic magma source

Table 4.1: Calculated angular range of reactivated pre-existing fractures

Area*	Depth (m)	$\sigma_3$ (MPa)	Maximum magma pressure (MPa)	Reactivated fracture angles from $\sigma_1$		Angle of new fractures (°)
				Minimum (°)	Maximum (°)	
Area 1 (Mingary Pier)	500	13.23	23.5	0	47.5	25.5
	1000	26.46	33	0	48	25.5
	1500	39.69	42.5	0	48	27.5
	2000	52.92	52	1	48.5	27
Area 2 (Mingary Castle)	500	13.23	23.5	0	47.5	25.5
	1000	26.46	33	0	48	25.5
	1500	39.69	42.5	0	48	27.5
	2000	52.92	52	1	48.5	27
Area 5 (Glas Bheinn)	500	13.23	28	0	67	24
	1000	26.46	38	0	50	28
	1500	39.69	48	0	51	26
	2000	52.92	58	0	50	26
Area 7 (Garbh Rubha)	500	13.23	27	0	63	24
	1000	26.46	36	0	62	28
	1500	39.69	46.5	0	63	26
	2000	52.92	56.5	0	62.5	26
Area 14 (Sròn Bheag)	500	13.23	27.5	0	66	24
	1000	26.46	38	0	62.5	26
	1500	39.69	48	0	62	27
	2000	52.92	58	0	62.5	26

\* Areas refer to those depicted in Fig. 4.2

geometry and a simplified host rock structure. The central complexes of the Henry Mountains (Utah, USA), which consist of several major laccoliths and minor sheet intrusions (i.e. sills and dykes) emplaced throughout their evolution (Jackson and Pollard, 1988), are excellently exposed at a sub-volcanic level and may provide a suitable analogue to the central complexes of the BIPIP. Jackson and Pollard (1988) proposed the Henry Mountains central complexes initially developed as sills that then thickened to form laccoliths. Mathieu et al., (2008) suggested cone sheet intrusion on Ardnamurchan was related to the intrusion and inflation of a sill into a laccolith, which instigated host rock doming and fracturing, resulting in a final cup-shaped lopolithic intrusion. The stress regime highlighted here by the analysis of the

cone sheets and the host rock doming is consistent with, but not exclusive to, the expansion of a laccolith (cf. Jackson and Pollard, 1988). Assuming the Ardnamurchan central complex originated through the development of an upper crustal laccolith, a simplified model of the evolving local stress field and its influence on cone sheet intrusion may be deduced. Many major intrusions, such as laccoliths, are now recognised as having assembled from discrete magma pulses emplaced incrementally (Pitcher, 1979; Glazner et al., 2004; Stevenson et al., 2007a; Zellmer and Annen, 2008; Annen, 2009). Implicitly, the laccolith likely grew from an initial sill, with dominantly sub-vertical  $\sigma_1$  and sub-horizontal  $\sigma_3$  principal stress axes (Fig. 4.13a) (Gautneb et al., 1989; Gudmundsson, 1998, 2006), through inflation or stacking of subsequent sheet intrusions. Doming of the host rock associated with the expansion and growth of a sill into a laccolith would be restricted to a belt of country rock coincident to the lateral margins of the intrusion (Fig. 4.13b) (Pollard and Johnson, 1973; Jackson and Pollard, 1988). Deformation of the host rock is consequently focused into two zones of flexure where contraction and extension occurs (Pollard and Johnson, 1973), similar to monocline development (Fig. 4.13b). Extensional conjugate fractures formed in these areas would obtain inward and outward dips and strikes concentric about the central intrusion (cf. Gray and Monaghan, 2004). This fracture geometry is very similar to those measured in the field, suggesting at least some of the conjugate fractures likely formed during doming and prior to any cone sheet intrusion. Within the BIPIP, the spatial distribution of cone sheet swarms into restricted concentric belts coincident with zones of intrusion-induced flexure supports the doming control on intrusion (Walker, 1975a). Continued growth of the laccolith would have resulted in the progressive rotation of pre-existing structures (i.e. bedding and fracture planes) and the principal axes of the local stress field (Fig. 4.13c) (cf. Jackson and Pollard, 1988). Inherently, the  $\sigma_1$  principal stress axes are inwardly inclined and steepen with proximity to the centre of the laccolith roof, whereas the  $\sigma_3$  principal stress axes are parallel to the magma reservoir and host rock contact (Fig. 4.13c). Eventually, bedding and pre-existing fracture planes may have been rotated into, or formed at orientations, that relative to the  $\sigma_1$  principal stress axes allowed their reactivation and intrusion (Fig. 4.13c).

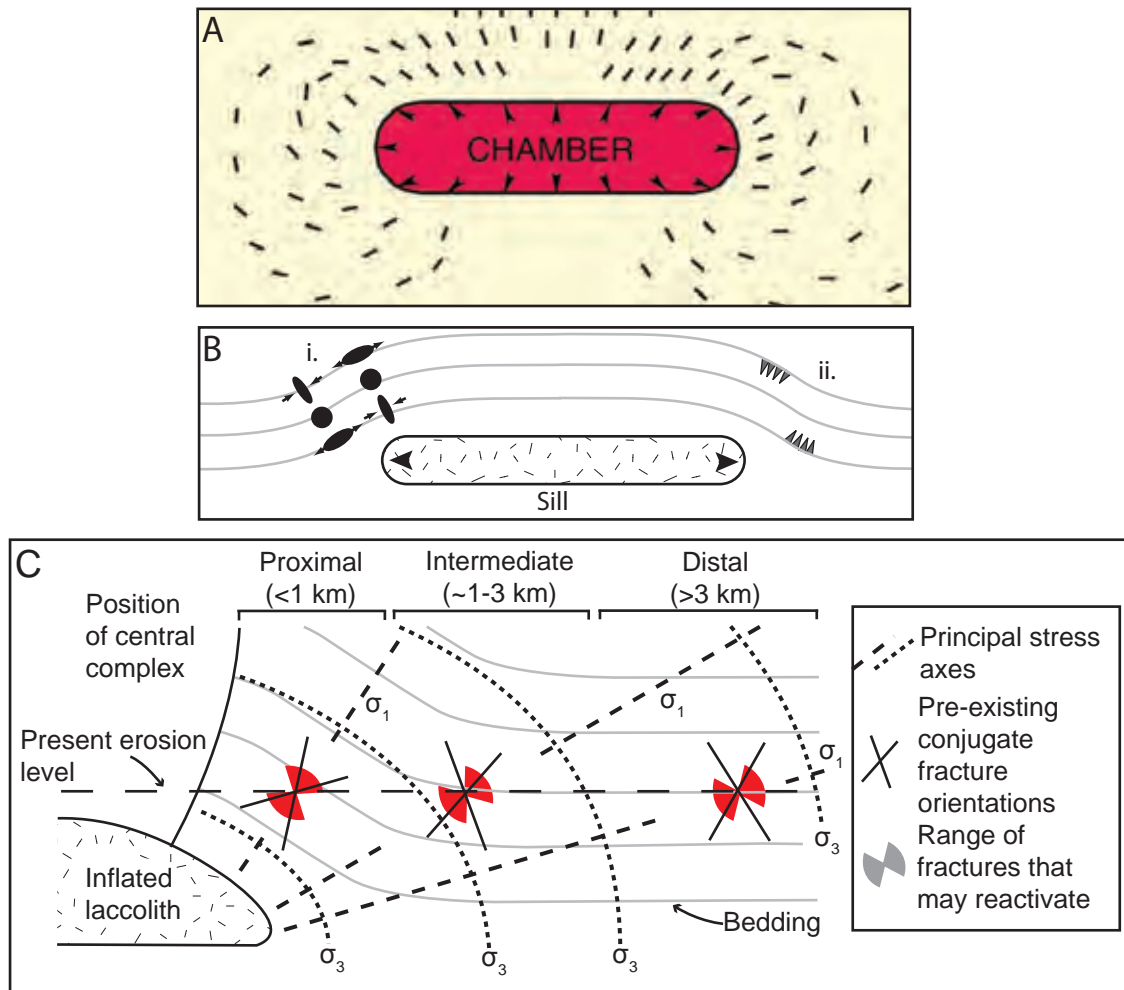


Fig. 4.13: A) Numerical model of a local stress regime generated by magmatic overpressure within a sill or laccolith (Gudmundsson, 2006). B) Simplified sketch of the strain ellipsoids (i) and fractures (ii) associated with host rock flexure induced by doming. Inwardly inclined fractures form in areas of tension. C) Sketch of local principal stress axes orientations formed in response to an inflating laccolith and the resultant fracture/bedding planes that may be reactivated (see text for details).

Figure 4.13c highlights that cone sheets proximal to the laccolith may exploit moderate to steep inward dipping fractures whilst with distance away from the central complex the proportion of bedding planes that may be intruded increases. Bedding plane intrusion correlates to a decrease in dip of the inwardly inclined conjugate fractures, a result of uplift and rotation associated with doming (Fig. 4.13). This is supported by the steepening inwards trend of the Centre 2 cone sheet set (Fig. 4.9f). Furthermore, the exploitation of pre-existing fractures by cone sheets may also explain the restriction of cone sheets to belts about their proposed Centre foci. However, the model also predicts that with increasing distance from the laccolithic source of the local stress field, cone sheets should predominantly only

exploit bedding plane anisotropies as the conjugate fractures have not been rotated into a sufficient orientation, relative to  $\sigma_1$ , to allow reactivation. The Loch Scridain sill-complex on Mull, which apart from dip is indistinguishable from the cone sheets, may reflect this predicted scenario. Conversely, the Ardnamurchan Centre 1 cone sheets display a steepening outwards trend (Fig. 4.9e). This implies  $\sigma_1$  had a steeper orientation, which although inconsistent with the simplified model presented may have been produced by interference between the local compressional stress field and the ambient regional stress field in a transitional zone (cf. Guglielmo, 1993; 1994).

Field relationships suggest the intrusion of cone sheets, and formation of associated thrust faults, occurred intermittently to the formation of normal faults (Day, 1989). Cyclical inflation and deflation of the laccolith or subsequent major intrusions within the central complex may result in the fluctuation of the active stress field between localised compressional and extensional regimes (Day, 1989; Mathieu and van Wyk de Vries, 2009); thus instigating the alternating formation of extensional faults/fractures and intrusion of cone sheets. Subsequent phases of cone sheet intrusion may be facilitated by local compressive stress fields associated with the formation of the major intrusions.

## 4.4 Summary

Structural observations indicate that the host rock structure and lithology played an important role in determining cone sheet geometry, orientation and distribution. Primarily intrusion occurred through the brittle opening of pre-existing inwardly inclined fractures and gently outwardly inclined bedding plane anisotropies. Occasionally, intrusion appears to have been facilitated by non-brittle processes such as host rock fluidisation and ductile flow of unconsolidated grains. Expansion of a shallow ( $\sim < 5$  km) laccolith, likely to be the source of the Ardnamurchan central complex, is suggested to have initiated the local compressional stress field active during cone sheet emplacement and rotated the pre-existing host rock structures into suitable orientations to allow their intrusion.

---

## CHAPTER 5

### ANISOTROPY OF MAGNETIC SUSCEPTIBILITY OF THE ARDNAMURCHAN CONE SHEETS

---

Anisotropy of magnetic susceptibility (AMS) allows the visualization of subtle petrofabrics, reflecting the preferred orientation and alignment of Fe-bearing minerals, and is here used to evaluate primary magmatic flow of the Ardnamurchan cone sheets. To assess the AMS of the cone sheets, 113 oriented block samples were collected from 69 widely distributed cone sheets representing examples of all ages, dip dispositions and geometries. For comparison, several ( $n = 8$ ) regional dykes were also analysed for AMS. Individual sample locations are presented in Fig. 5.1, as well as the respective cone sheet traces, with the majority of samples partitioned into the same Areas utilised for structural measurements. Appendix E presents locality and AMS data for all cone sheet and regional dyke samples as well as assigned sheet intrusion identification numbers. Due to the range of cone sheet and regional dyke thickness and paucity of exposure, block samples were collected from variable positions (e.g. contact adjacent or central) within the sheets.

From each block sample, assumed to represent a homogeneous multi-normal population (Owens, 2000), approximately 4–15 sub-specimens with volumes of  $\sim 10 \text{ cm}^3$  were prepared according to the procedure described in Stevenson et al., (2007a). An AGICO KLY-3S Kappabridge (an induction bridge operating at a field of 300 A/m and a frequency of 875 Hz) was used to measure the AMS of the sub-specimens, which were then averaged in order to calculate each block sample's magnetic susceptibility tensor. The magnetic susceptibility tensor presented for each sample comprises the  $K_{\text{mean}}$ ,  $H$  (strength of anisotropy),  $\mu$  (shape of anisotropy) and three principal axis directions (Owens, 1974; 2000; Stevenson et al., 2007b). From the principal susceptibility axes (i.e.  $K_1$ ,  $K_2$  and  $K_3$ ), magnetic lineations and foliations may be inferred (e.g. Khan, 1962; Ellwood, 1978; Tarling and Hrouda, 1993; Tauxe

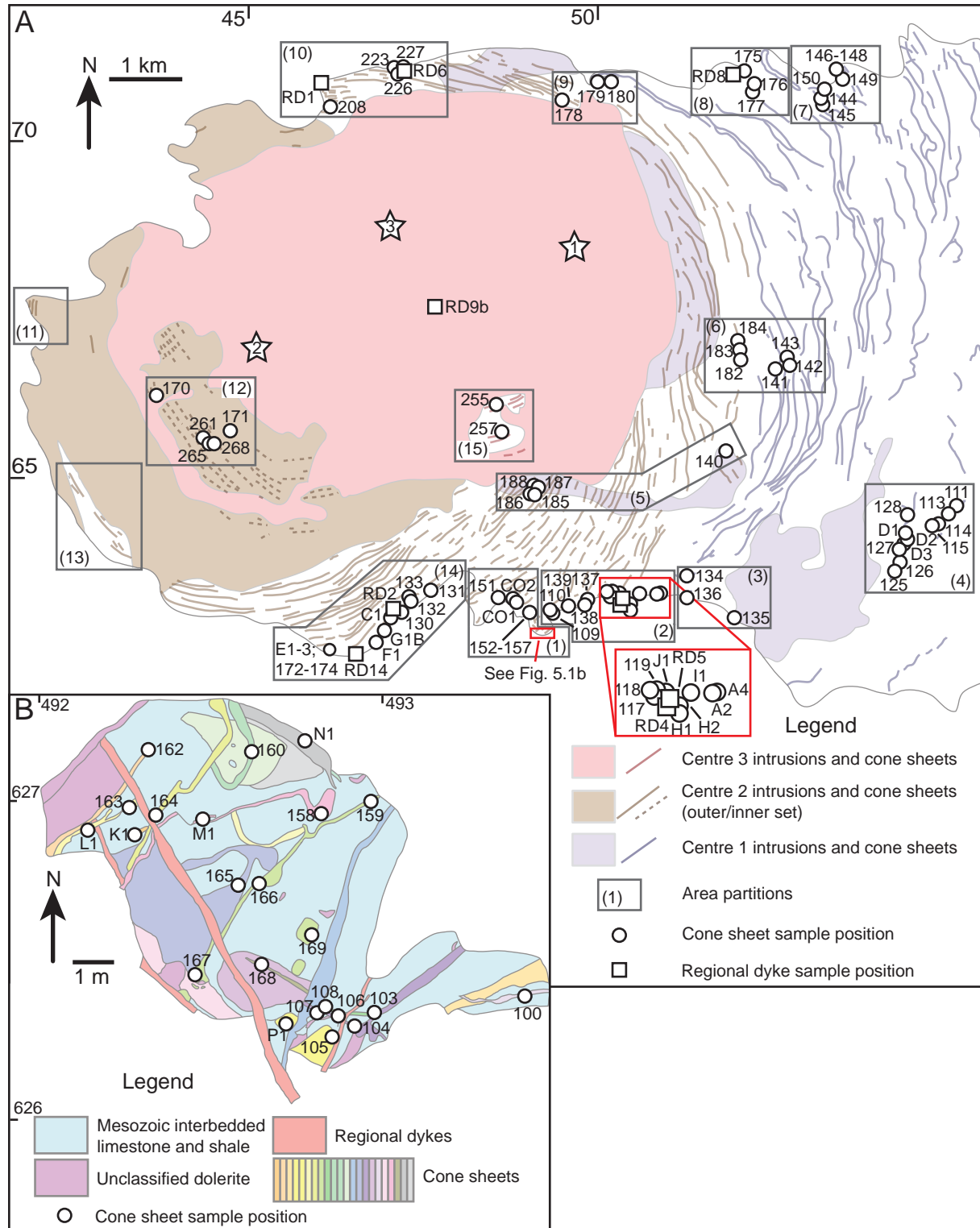


Fig. 5.1: A and B) Geological maps of Ardnamurchan (after Richey and Thomas, 1930; Emeleus, 2009) and a small area of Mingary Pier displaying cone sheet and regional dyke AMS sample locations. The areal groupings defined are consistent with those in Figure 4.1.

et al., 1998; Martín-Hernández et al., 2004). Variation within a block is accounted for by the calculation of 95% confidence ellipses for both the directional and magnitude parameters (Jelínek, 1978).

## 5.1 Characterising the magnetic mineralogy

The magnetic response of a sample to an externally applied magnetic field is dependent on two variables; the orientation of the specimen (and hence the petrofabric), with respect to the applied field, and the mineral phases contributing to the magnetic signature (Tarling and Hrouda, 1993). As AMS is utilised to determine the petrofabric of a sample, through the application of an external magnetic field in three orthogonal orientations (Tarling and Hrouda, 1993), the magnetic mineralogy of the sample first needs to be constrained before magnetic fabrics may be correlated to the rock petrofabric (see Chapter 2, section 2.2.3). The texture of the magnetic mineralogy is also important to study as it provides information on how the petrofabric formed (e.g. through primary magmatic flow) and if it has since been modified; perhaps through the supposition of a syn- or post-intrusion tectonic fabric (e.g. Tauxe et al., 1998; Correa-Gomes et al., 2001; Féménias et al., 2004) or post-cumulus modification processes (e.g. O'Driscoll et al., 2008). Here, a combination of rock magnetic experiments and petrographical observations are used to determine the mineralogy and texture of the magnetic fraction, in order to identify possible problems with fabric interpretation and to delineate the origin of the magnetic fabric (i.e. magmatic or tectonic).

### 5.1.1 Mean susceptibility

The mean susceptibility ( $K_{\text{mean}}$ ) may be correlated to the intrinsic susceptibility (i.e. diamagnetic, paramagnetic and ferromagnetic) and abundance of the dominant magnetic mineral phase(s) present in a sample (Tarling and Hrouda, 1993). The  $K_{\text{mean}}$  values of the Ardnamurchan cone sheets ( $0.1\text{--}23.49 \times 10^{-2}$  (SI)) and regional dykes ( $0.05\text{--}9 \times 10^{-2}$  (SI)) (Appendix E) indicate the rocks are strongly magnetic, consistent with a titanomagnetite

carrier of 0.1–10 vol. % (Fig. 5.2) (Tarling and Hrouda, 1993). A potential exception to this are those samples with  $K_{\text{mean}}$  values ranging from  $0.05\text{--}0.99 \times 10^{-2}$  (SI), in which paramagnetic haemo-ilmentite may also contribute if present in abundances  $\sim >5\%$  (Fig. 5.2) (Tarling and Hrouda, 1993).

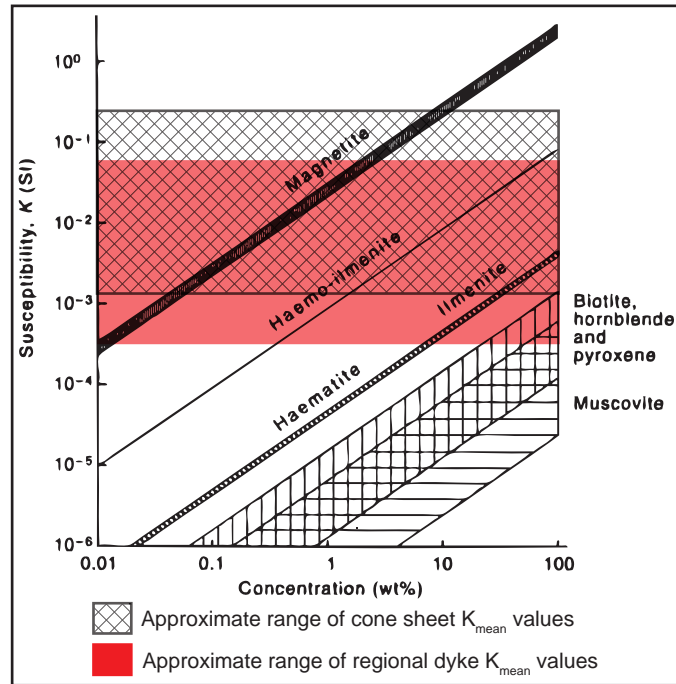


Fig. 5.2: The contribution of various minerals to magnetic susceptibility dependent on their concentration (after Tarling and Hrouda, 1993). The approximate range of the cone sheet and regional dyke  $K_{\text{mean}}$  values has also been plotted.

There is a seemingly irregular distribution of  $K_{\text{mean}}$  values throughout the Ardnamurchan cone sheets and regional dykes, with significant variation observed between neighbouring intrusions and occasionally internally within individual sheets (Fig. 5.3). Cone sheets exhibiting intra-intrusion  $K_{\text{mean}}$  variability are sometimes composed of discrete magmatic segments (e.g. Sheet 3 contains magma fingers and Sheet 20 consist of magma lobes; Fig. 5.3a **i** and **ii**), which may relate to numerous magma pulses of slightly variable composition. On closer inspection of Figure 5.3, the stronger  $K_{\text{mean}}$  values are often located adjacent to (e.g. CS226) or within (e.g. CS257, CS261, CS265 and CS268) the Ardnamurchan central complex. A cluster of low  $K_{\text{mean}}$  values occurs in cone sheets to the south of the Ardnamurchan central complex in Area 14 (Fig. 5.3).

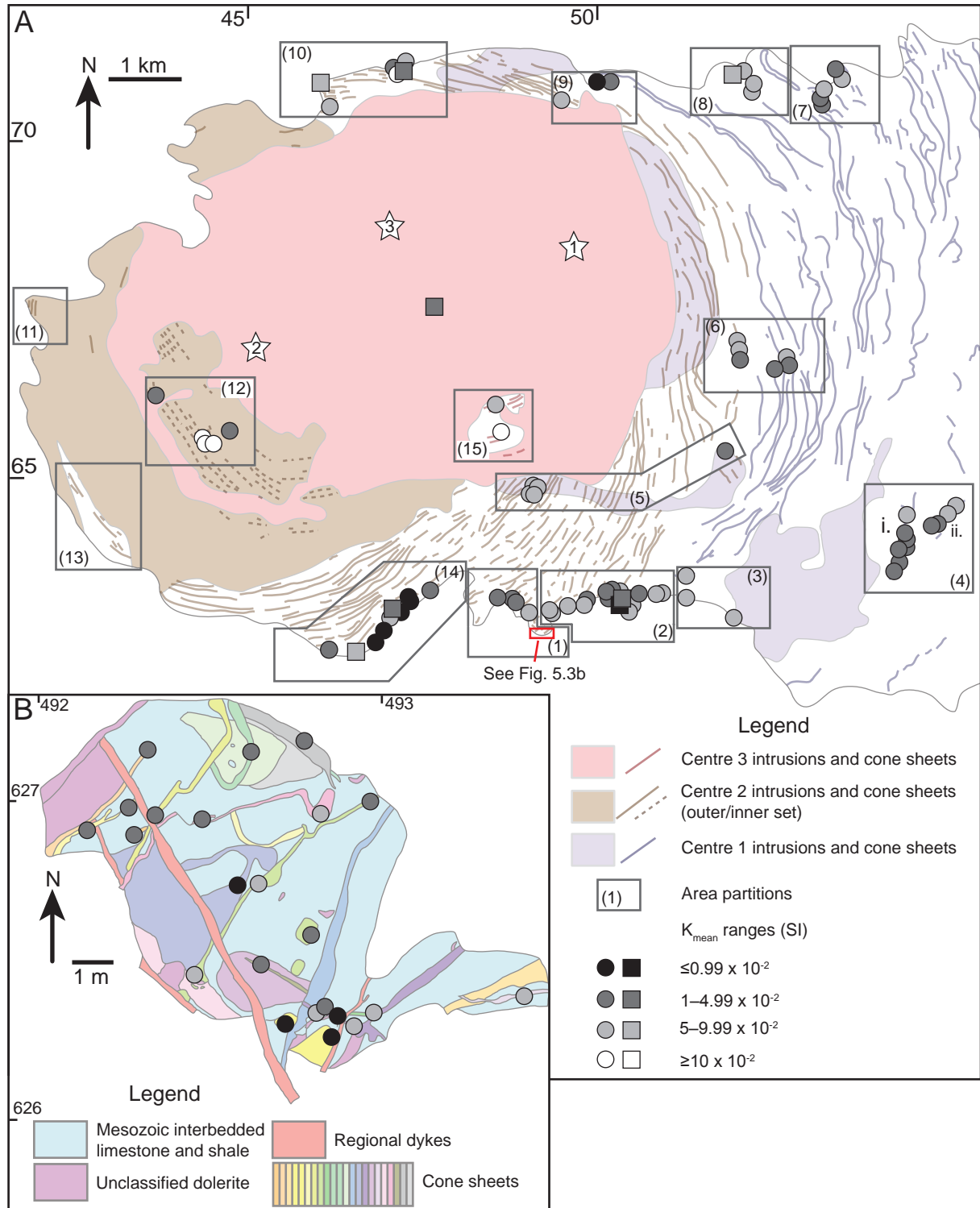


Fig. 5.3: A and B) Geological maps of Ardnamurchan (after Richey and Thomas, 1930; Emeleus, 2009) and a small area of Mingary Pier displaying the distribution of cone sheet and regional dyke AMS  $K_{\text{mean}}$  values.  $K_{\text{mean}}$  values are divided into four groups for clarity.

### 5.1.2 High-temperature, low-field susceptibility experiments

Whilst petrographical analyses may identify Fe-bearing mineral phases present within a sample, rock magnetic experiments are required to determine the relative contributions. High-temperature, low-field susceptibility experiments were conducted, by heating ( $\sim 30^\circ\text{C}$  to  $650^\circ\text{C}$ ) and cooling ( $\sim 650^\circ\text{C}$  to  $30^\circ\text{C}$ ) a powdered sample, to evaluate the magnetic mineral composition based on Curie Point ( $T_C$ ) estimates and assist with identifying mixtures of magnetic phases within a given sample (Orlický, 1990; Tauxe, 1998; Petrovský and Kapička, 2007). The shape and reversibility (or irreversibility) of these curves reflect variation in magnetic mineralogy (e.g. Lattard et al., 2006). Ferromagnetic minerals (*sensu lato*) are particularly responsive to temperature variations as the exchange and superexchange forces, that couple electron spin and govern the ferromagnetic (*s.l.*) behaviour, are overcome thermally (Curie Point) dependent on the grain composition (Tarling and Hrouda, 1993; Dunlop and Özdemir, 1997). This is marked by a sudden reduction in susceptibility (Fig. 5.4a i) (Petrovský and Kapička, 2007). Often associated with this transition is a brief enhancement in susceptibility over a narrow temperature range, a Hopkinson Peak, relating to induced superparamagnetic behaviour (Fig. 5.4c i) (Clark and Schmidt, 1982; Dunlop and Özdemir, 1997; Liss et al., 2004). High-temperature, low-field susceptibility curves may therefore provide a proxy for magnetic grain size (Orlický, 1990; Liss et al., 2004). All inferred  $T_C$  estimates are determined either from a well developed Hopkinson Peak (Moskowitz, 1981; Petrovský and Kapička, 2007) or by the inflection point, defined as the start of paramagnetic behaviour, method (Fig. 5.4) (Petrovský and Kapička, 2007).

A suite of representative samples were selected for high-temperature, low-field susceptibility experiments to cover the broad range of cone sheet morphologies, compositions and  $K_{\text{mean}}$  values (Fig. 5.1; Appendix C). The two representative Centre 1 cone sheet samples, obtained from Area 6 (CS143) and Area 9 (CS180), have a moderate ( $6.57 \times 10^{-2}$  (SI)) and strong ( $11.92 \times 10^{-2}$  (SI))  $K_{\text{mean}}$  value (Appendix E), respectively. Samples CS151, CS162 and CS187 were randomly selected from those samples collected from the Outer Centre 2 cone

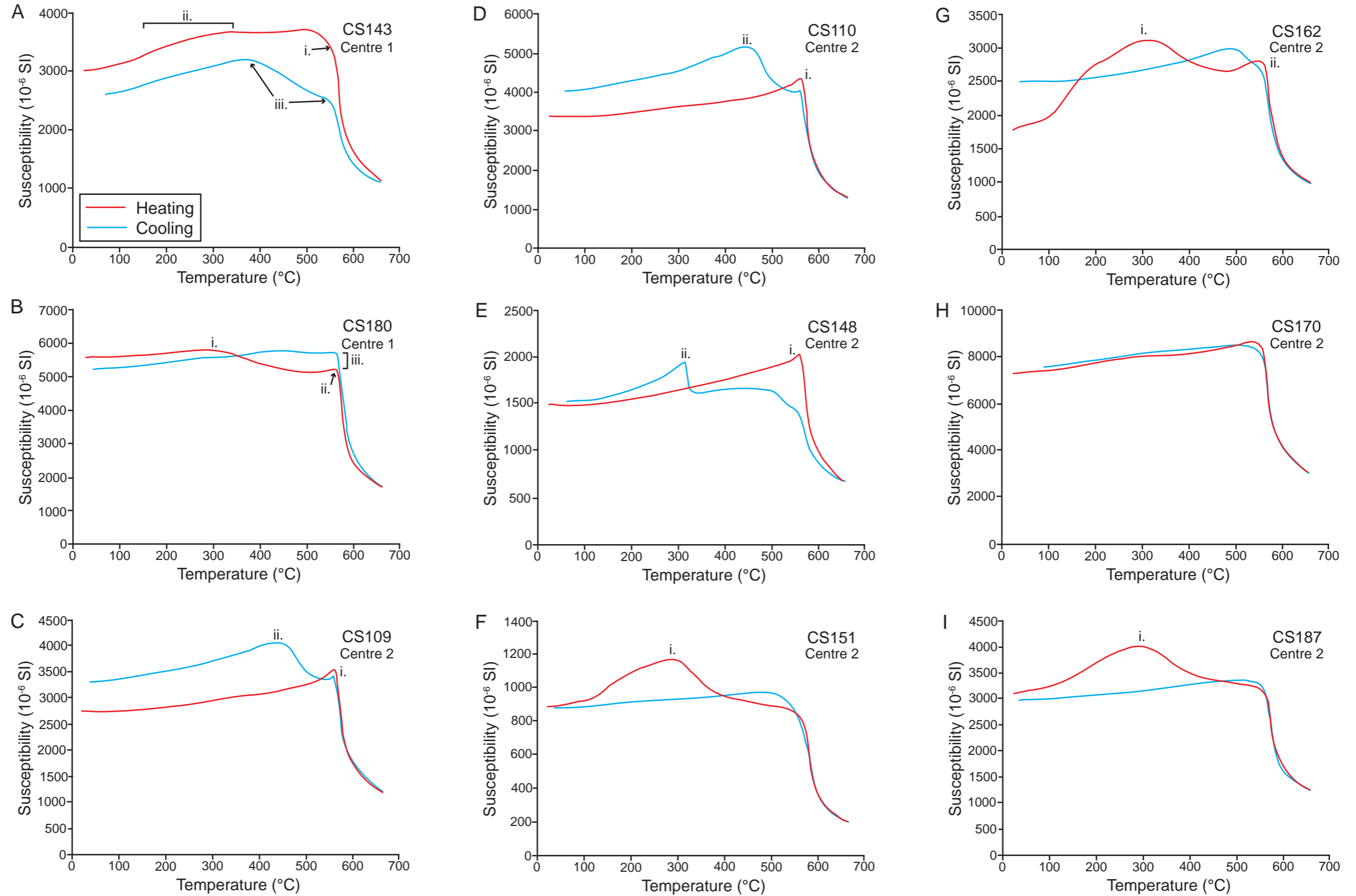


Fig. 5.4: High temperature, low-field susceptibility curves for numerous cone sheet samples (see text for explanation).

sheets and sample CS170 was analysed from the Inner Centre 2 cone sheet set. To test if there is any internal variation of magnetic mineralogy within the cone sheets, two closely spaced samples (CS109 and CS110) from a single Outer Centre 2 cone sheet from Area 2 were selected for analysis (Fig. 5.1). Many of the Ardnamurchan cone sheets contain a population of Fe-sulphides consisting primarily of pyrite ( $\text{FeS}_2$ ). Sample CS148 (Area 7), an Outer Centre 2 cone sheet containing a  $\sim 1.5$  cm layer of pyrite, was analysed to establish if the Fe-sulphides contribute to the magnetic fabric.

The samples analysed yield a spectrum of results that vary from fully reversible curves with a single  $T_C$  estimate to more complex irreversible curves with two or more inferred  $T_C$  estimates (Fig. 5.4). On heating, sample CS143 displays a steady increase in susceptibility with temperature until a sharp decrease, correspondent to the  $T_C$ , at  $545^\circ\text{C}$  (Fig. 5.4a **i**). Although pure magnetite has a  $T_C$  of  $578^\circ\text{C}$ , there is an inverse relationship between the Ti-content ( $x$ ) of magnetite and its  $T_C$  (e.g.  $x = 0.6$  correlates to a  $T_C$  of  $150^\circ\text{C}$ ) (Dunlop and Özdemir, 1997; Lattard et al., 2006). The behaviour of CS143 and lack of a Hopkinson Peak is therefore typical of low-Ti multidomain magnetite. Superimposed onto the heating curve is a broad, shallow ‘bump’ in susceptibility from  $\sim 150$ – $350^\circ\text{C}$  (Fig. 5.4a **ii**). This feature, though poorly understood (Hrouda, 2003), is often interpreted to reflect the homogenization of two exsolved Fe-Ti oxide phases into a single titanomagaemite phase during the experiment (Özdemir and O’Reilly, 1981; 1982). The amplitude of the ‘bump’ approximately correlates with the abundance of titanomagaemite, which in CS143 is minor (Fig. 5.4a **ii**). The  $T_C$  at  $545^\circ\text{C}$  and the broad peak in susceptibility, at  $380^\circ\text{C}$ , on the cooling curve of CS143 (Fig. 5.4a **iii**) likely indicates a mixture of remnant primary titanomagnetite and secondary (produced during heating) titanomagaemite. Susceptibility of sample CS180 on heating is relatively independent of temperature up until the  $T_C$  with no Hopkinson Peak, at  $570^\circ\text{C}$ , although a suppressed ‘bump’ at  $\sim 200$ – $350^\circ\text{C}$  is suggestive of a small volume of titanomagaemite (Fig. 5.4b **i**). The  $570^\circ\text{C}$   $T_C$  of CS180 (Fig. 5.4b **ii**) correlates to a very low-Ti magnetite phase. On cooling, the CS180 curve initially ascends to a higher susceptibility than the heating curve at high temperatures, implying new titanomagnetite was generated (Fig. 5.4b **iii**). This suggests

maghaemite was lost during heating and possibly was converted to titanomagnetite.

The heating curves of samples CS109, CS110 and CS148 show a monotonous increase in susceptibility with temperature until a  $T_C$  at 558°C, defined by a relatively narrow, minor Hopkinson Peak (Fig. 5.4c, d and e **i**). These curves are consistent with a low-Ti titanomagnetite phase dominating the magnetic mineralogy with the Hopkinson Peak morphology perhaps suggesting grainsizes down to pseudo-single-domain (see Liss et al., 2004). No discernible effect from the Fe-sulphide population in CS148 is observed (Fig. 5.4c and d **ii**). During cooling, the ‘bump’ in susceptibility, peaking at 441°C, observed in both CS109 and CS110 (Fig. 5.4c and d) likely correlates to a new titanomagnetite phase grown during heating. The greater susceptibility of the cooling curve, compared to the heating run, at room temperature supports the generation of a new magnetic phase (titanomagnetite) by low-temperature oxidation of a less magnetic phase (Irving, 1970; Marshall and Cox, 1972; Johnson and Atwater, 1977). There is no apparent variation in the magnetic mineralogy between samples CS109 and CS110 collected from the same cone sheet (Fig. 5.4c and d). On the cooling curve for CS148 there is a prominent Hopkinson Peak and  $T_C$  at 330°C (Fig. 5.4e **ii**), which may represent the growth of a new Fe-sulphide phase during the experiment.

The Outer Centre 2 cone sheet samples of CS151, CS162 and CS187 have heating and cooling curves that are geometrically similar, with the broad peaks in susceptibility at ~200–350°C likely correlating to titanomaghaemite (Fig. 5.4f, g and i **i**). Compared to CS143 and CS180, the ‘bump’ in susceptibility is more readily defined, implying a greater quantity of titanomaghaemite (Fig. 5.4). No similar ‘bump’ at 200–350°C is observed on the cooling curve, suggesting titanomaghaemite was lost during heating (Fig. 5.4f, g and i). For samples CS151 and CS187, no Hopkinson Peak is associated with the  $T_C$  at 556°C and 563°C respectively (Fig. 5.4f and i). A relatively suppressed Hopkinson Peak occurs in CS162 just prior to the  $T_C$  at 556°C (Fig. 5.4g **ii**). These heating and cooling curves are suggestive of low-Ti multidomain magnetite dominating the AMS. Similarly, the fully reversible heating and cooling curves of CS170, with a  $T_C$  at 555°C (Fig. 5.4h), are consistent with a single low-Ti multidomain magnetite phase.

High-temperature, low-field susceptibility experiments suggest that low-Ti titanomagnetites dominate the magnetic mineralogy of the cone sheets. Hopkinson peaks are typically absent or suppressed, suggesting the titanomagnetite grainsize is predominantly multidomain, with some samples (e.g. CS109, CS110 and CS148) potentially containing a population of pseudo-single-domain grainsizes.

### 5.1.3 Petrographic observations

In magnetic studies, the opaque mineral fraction is important as it typically contains Fe-bearing ferromagnetic (*s.l.*) mineral phases. Having established titanomagnetite as the dominant carrier of AMS in all analysed samples, a detailed petrographical analysis of titanomagnetite shape and relationship to other mineral phases is required to determine the origin of the petrofabrics (i.e. does it relate to primary magmatic flow?). Reflected light microscopy confirms that magnetite (0.1–0.5 mm), in typical abundances of 3–5 vol. % (10 % maximum), dominates the Fe-oxide population of the fine-grained equigranular dolerites (Fig. 5.5), consistent with the  $K_{\text{mean}}$  values. The magnetite is moderately reflective and is typically grey in colour with subtle brown or pink tinges. The brown colouration suggests that the magnetite contains titanium whereas the pink tinges are indicative of pure magnetite (Craig and Vaughan, 1981). Importantly, observed titanomagnetite grainsizes of 0.1–1 mm (Fig. 5.5) is consistent with a multidomain configuration suggested by the high-temperature, low-field susceptibility experiments. Titanomagnetites are generally either elongated or have a euhedral to subhedral equant crystal habit, depending on whether they are observed along two primary crystal grain boundaries or at triple junctions (Fig. 5.5a). Other growth forms of titanomagnetite include acicular crystals in very fine (~0.1 mm) grained dolerites.

In some titanomagnetites, a poorly reflective blue-grey mineral occurs around the grain boundaries (Fig. 5.5d and e) and likely reflects alteration of the original titanomagnetite to a very fine aggregate of  $\text{TiO}_2$  minerals (Craig and Vaughan, 1981). Within these altered titanomagnetites, an unaltered pale pink birefractant mineral is exsolved along specific crystallographic axes (Fig. 5.5d and e). It is suggested the exsolved mineral is ilmenite,

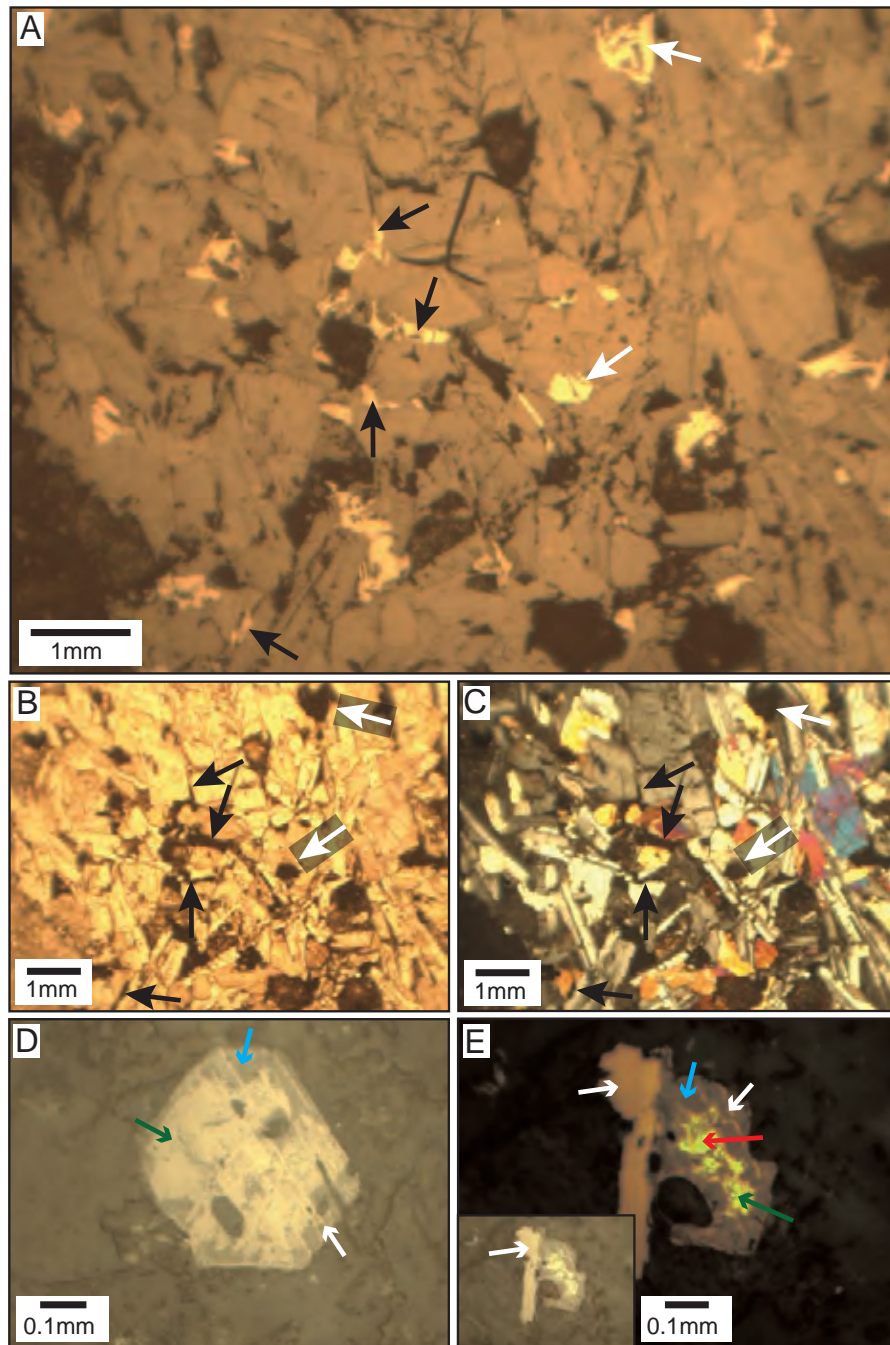


Fig. 5.5: A) Reflected light photomicrograph highlighting titanomagnetite forms commonly observed within the cone sheets. Comparison with plane polarized (B) and cross-polarized (C) light images of the same section shows elongated, tabular titanomagnetite crystals grown along crystal-crystal boundaries (black arrows) and coarser, subhedral titanomagnetite crystals grown at crystal triple-junctions (white arrows). D) Reflected light image of titanomagnetite (green arrow) partially replaced with a poorly reflective blue-grey mineral (blue arrow), likely a  $\text{TiO}_2$  aggregate. Exsolved lamellae of pinkish ilmenite (white arrow) also occur. E) Reflected light photomicrograph that has been edited (brightness reduced and contrast increased) to highlight the colour variations between titanomagnetite (green arrow), the  $\text{TiO}_2$  aggregate (blue arrow) and ilmenite (white arrow). The editing also highlights a small, bright white area that may correspond to secondary maghaemite (red arrow).

which also infrequently occurs as single lobate-lath shaped crystals, based on its reflected light characteristics and resistance to alteration (Nesse, 2004). Exsolution of ilmenite within titanomagnetites effectively separates the host crystal into smaller sub-crystals, potentially creating a very fine aggregate of paramagnetic ilmenite and (pseudo-)single-domain titanomagnetite (Dunlop and Özdemir, 1997). Within the Ardnamurchan cone sheets, exsolved ilmenite is predominantly observed in only the coarser titanomagnetite populations so the sub-crystal titanomagnetites remain multidomain. Areas of white within the titanomagnetites (Fig. 5.5e) potentially represent secondary maghaemite (Craig and Vaughan, 1981).

The Ardnamurchan dolerite cone sheets and regional dykes are dominated by a cumulus framework of tabular plagioclase and clinopyroxene, occasionally containing olivine, with interstitial quartz and alkali feldspar (Richey and Thomas, 1930). Titanomagnetites are interstitial, their orientation and shape controlled by the primary silicate framework. There is little evidence of deformation (e.g. fracturing) or postcumulus modification (e.g. textural equilibration) within the cone sheets. Therefore, titanomagnetite growth, and likely the magnetic fabric, is controlled by an apparently unmodified primary silicate framework, suggesting a primary magma flow may be interpreted (e.g. Callot and Guichet, 2003; Stevenson et al., 2007a).

## 5.2 AMS strength and shape

### 5.2.1 Strength of anisotropy (H)

The strength, or degree, of anisotropy (H) for the Ardnamurchan cone sheets ranges from 0.2–10.8 % (Appendix E), with a mode of 2 % and a median of 2.3 %. For the regional dykes, H ranges from 0.8–5.5%, with a median of 3.2 %. Throughout the literature, corrected anisotropy degree ( $P_j$ ) values are often used to describe a samples degree of anisotropy in place of H. The H value is utilised here as it best correlates to the deviatoric components of the susceptibility tensor measured by a KLY-3S Kappabridge compared to  $P_j$ , which instead is derived from less precise axial susceptibility measurements (Stevenson et al., 2007a). A  $P_j$

value of 1.03 is equivalent to an anisotropy of 3 % and so on. Whilst not directly comparable, the anisotropy percent obtained from each method are approximately equivalent below ~20 %. For example, the cone sheet samples with H values of 0.2 % and 10.8 % have calculated  $P_j$  values of 1.002 (0.2 %) and 1.119 (12 %) respectively (Appendix E). The H values of the Ardnamurchan sheet intrusions indicate the magnetic fabrics are weakly anisotropic, consistent with similar measurements obtained from other magnetite dominated mafic sheet intrusions (e.g. 0.4–7.1 % anisotropy strength for the Okavango dyke swarm, South Africa, Aubourg et al., 2008; 0.6–17 % anisotropy strength for Icelandic Palaeogene dykes, Kissel et al., 2010). Borradaile and Jackson (2004) highlight that in many rock magnetic studies there is a strong correlation ( $R^2 = \sim 0.72$ ) between  $K_{\text{mean}}$  and H (or  $P_j$ ), implying that rock composition controls the degree of anisotropy. Contrary to this suggestion, Figure 5.6 displays a very weak positive correlation ( $R^2 = 0.005$ ) between  $K_{\text{mean}}$  and H. Inherently, magnetic mineralogy appears to be only a minor component, compared to mineral alignment, in determining the degree of anisotropy of the Ardnamurchan sheet intrusions (i.e. a high  $K_{\text{mean}}$  value indicative of significant proportion of titanomagnetite does not necessarily denote a high H value).

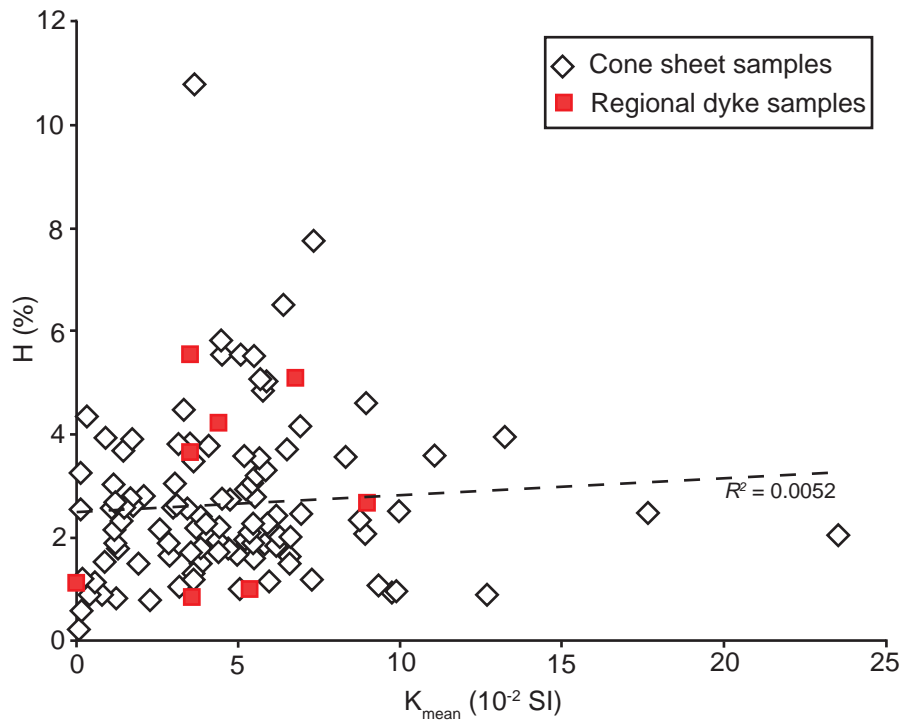


Figure 5.6: Plot of cone sheet and regional dyke  $K_{\text{mean}}$  values plotted against H values.

There is no discernible pattern to the spatial distribution of  $H$ , although the majority of samples with  $H$  values  $>5\%$  were collected from cone sheets to the SE of the Ardnamurchan central complex (Fig. 5.7). Occasionally, within individual cone sheets a range of  $H$  values are observed (Fig. 5.7). For example, two cone sheets to the east of Ben Hiant [Sheet 3, NM 547 637 and Sheet 20, NM 555 645] in Area 4, that are divisible into discrete magmatic lobes and/or magma fingers, contain variable  $H$  values ranging from 0.77–2.22 % and 2.21–10.8 % respectively (Fig. 5.7a **i** and **ii**). This variation may reflect sampling of individual lobes and fingers that are representative of magma pulses with differing variable compositions or crystallisation histories, as the strength of anisotropy is dependent on mineral alignment as well as mineralogy. Implicitly, apparently continuous cone sheets exhibiting variations in  $H$  (e.g. Sheet 58) may contain internal divisions. A further possibility is that differing  $H$  values within a single sheet intrusion record subtle variations in petrofabric development resulting from differing conditions of magma flow at the contact and in the centre of the intrusion.

### 5.2.2 Shape of anisotropy ( $\mu$ )

The shape of anisotropy may be represented by plotting the linear ( $L$ ) and planar ( $F$ ) components of the magnetic fabric against each other (Fig. 5.8a). From this, the  $\mu$  value is equal to  $\tan^{-1}(L/F)$  and ranges from 0–90°. Prolate fabrics are defined by  $\mu$  values  $>60^\circ$  with triaxial fabrics 30°–60° and oblate fabrics  $<30^\circ$ . The  $\mu$  values for the Ardnamurchan cone sheets range from 0.9–87.5° (Appendix E), with a mode of 79.6° and a median of 51.4°. Regional dyke  $\mu$  values are mainly triaxial, ranging from 15.6–70.8° (Appendix E). There is a wide distribution in fabric shapes observed, although a plot of  $\mu$  against frequency suggests prolate fabrics are dominant (Fig. 5.8b). Spatially there is an irregular distribution of  $\mu$  (Fig. 5.8c). The Inner Centre 2 cone sheets (Area 12) are characterised by only prolate fabrics (strong to weak) (Fig. 5.8c). Similar to the  $H$  values,  $\mu$  is observed to vary significantly within individual cone sheets (e.g. Sheets 3, 15, 20, 44) (Fig. 5.8c and d). Whilst there is generally no correlation with  $K_{\text{mean}}$ , Figure 5.8e suggests the highest  $K_{\text{mean}}$  values correlate to strongly prolate samples. Conversely, a plot of  $\mu$  against  $H$  suggests the more strongly anisotropic

samples have an oblate fabric (Fig. 5.8f).

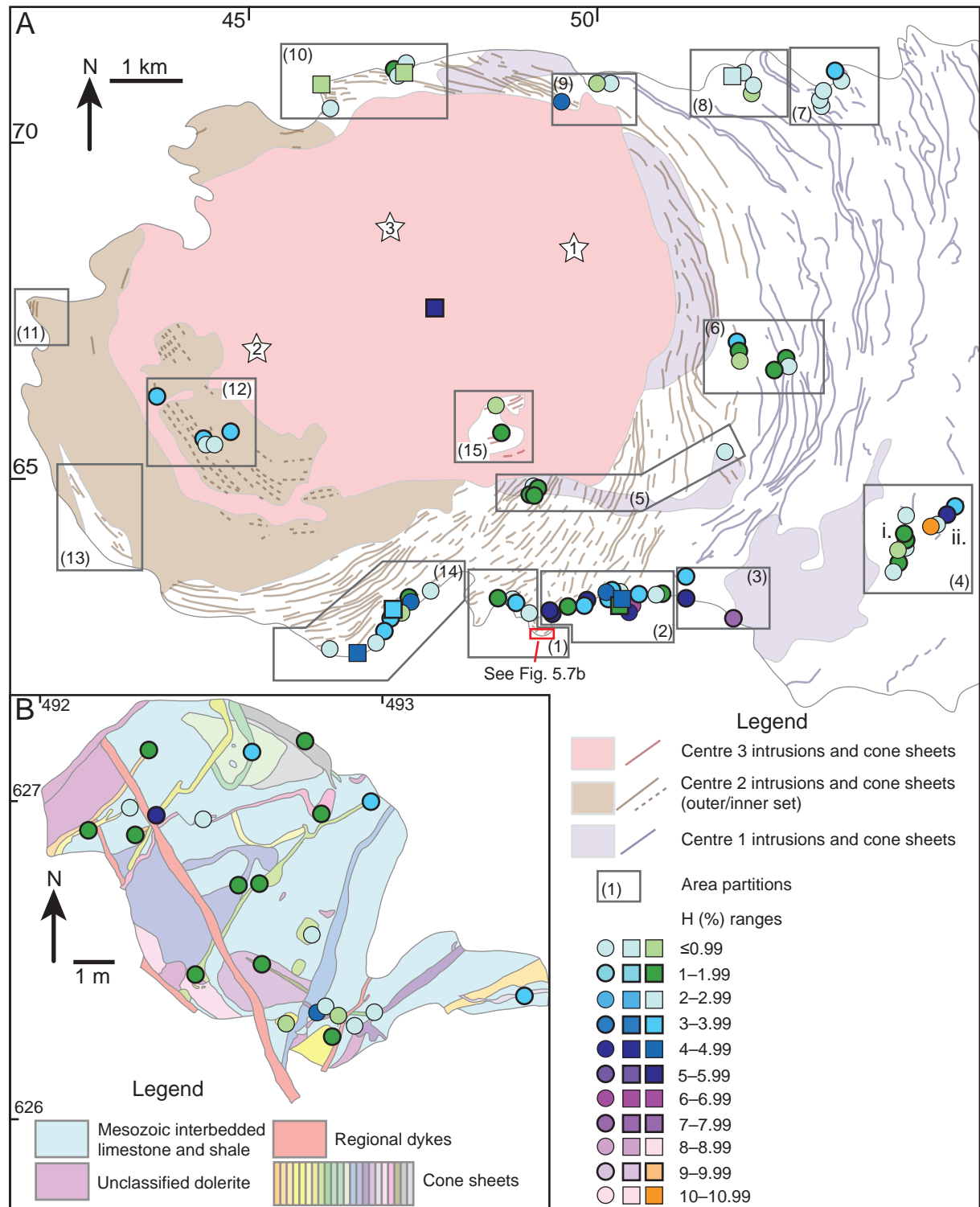


Fig. 5.7: A and B) Geological maps of Ardnamurchan (after Richey and Thomas, 1930; Emeleus, 2009) and a small area of Mingary Pier displaying the distribution of cone sheet and regional dyke H values.

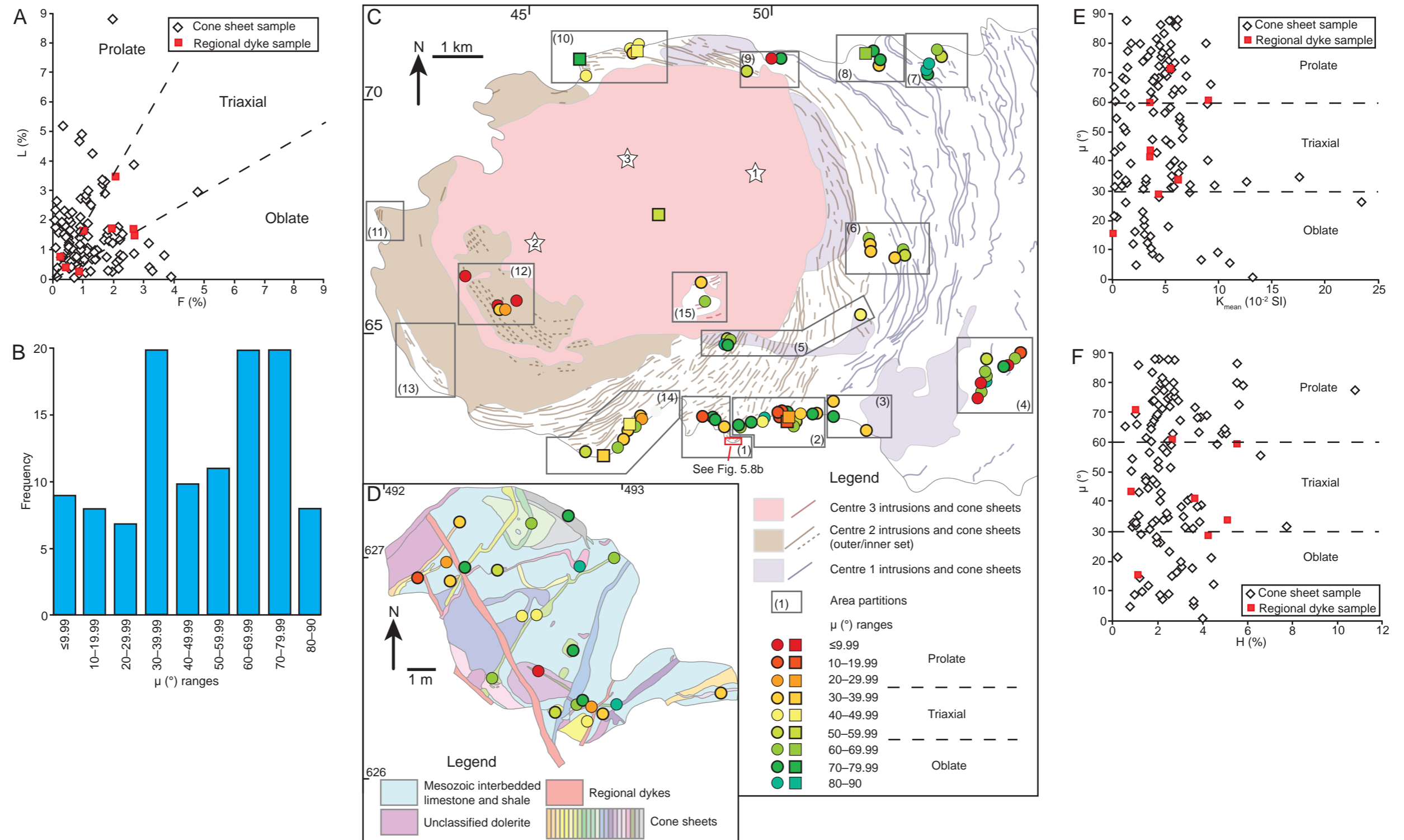


Fig. 5.8: A) L/F plot for the Ardnamurchan cone sheets and regional dykes. There is a slight predominance of prolate fabrics compared to oblate fabrics, which is supported by the plot of  $\mu$  (shape) value frequency (B). C and D) Geological maps of Ardnamurchan (after Richey and Thomas, 1930; Emeleus, 2009) and a small area of Mingary Pier displaying the distribution of cone sheet and regional dyke  $\mu$  values. E) A plot of  $\mu$  against  $K_{\text{mean}}$ . F) Plot of  $\mu$  against H.

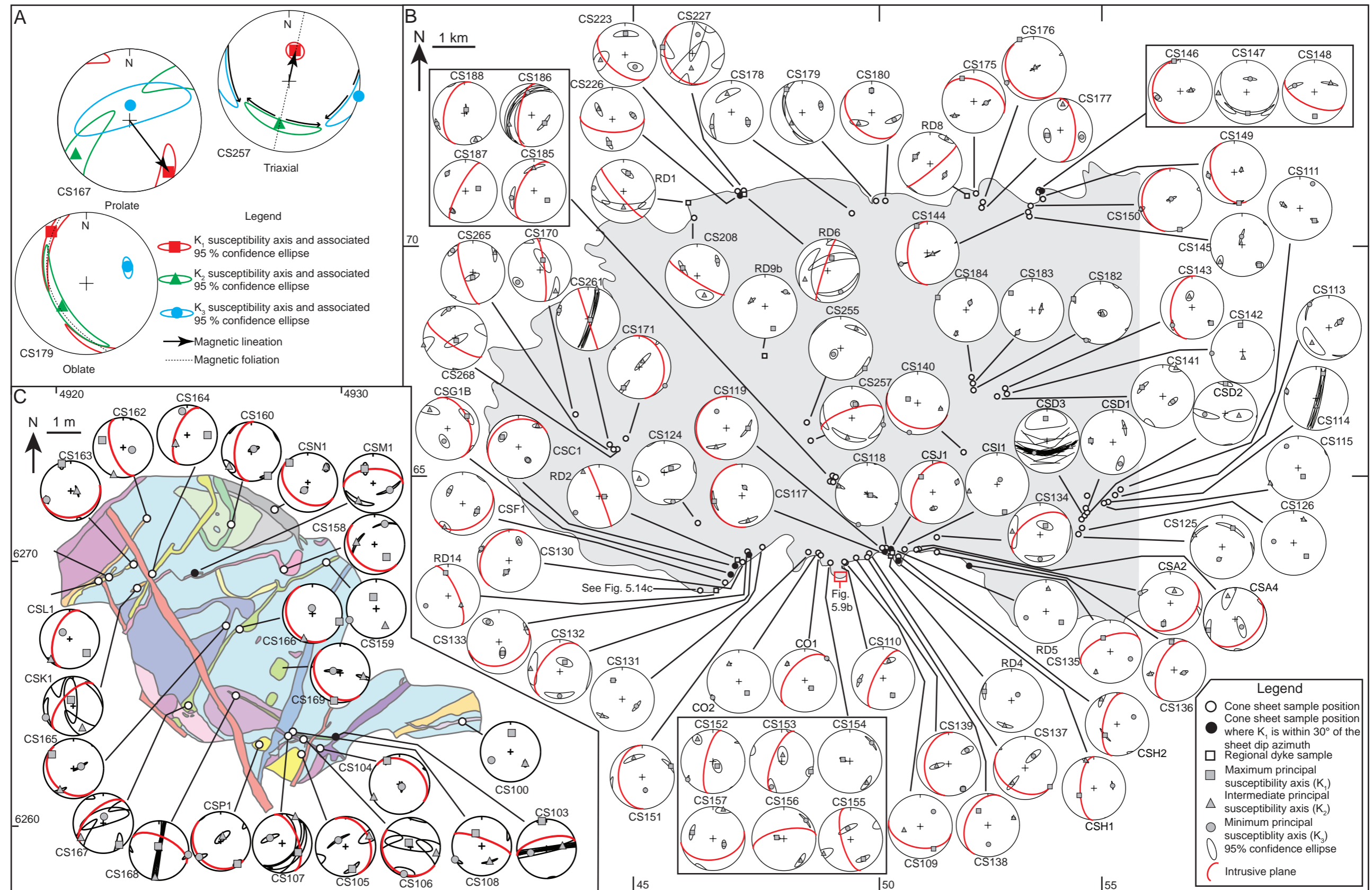


Fig. 5.9: A) Three examples of AMS lower hemisphere, equal area stereographic projections that correspond to the three main fabric shapes; prolate, oblate and triaxial (see text for explanation). B and C) Outline map of Ardnamurchan (after Richey and Thomas, 1930; Emeleus, 2009) and geological map of a small area of Mingary Pier displaying the normalised AMS stereoplots for all cone sheets and regional dykes measured. Great circles denoting the intrusive plane of the cone sheets and regional dykes have been incorporated where measured. The locality 89 (Area 14) cone sheet AMS stereoplots are present later in Figure 5.14.

### 5.3 Orientation of the magnetic fabrics

High-temperature low-field susceptibility experiments and  $K_{\text{mean}}$  values suggest the AMS fabrics measured may be interpreted as equivalent to the titanomagnetite petrofabric. Importantly, the subdued Hopkinson Peaks observed in Figure 5.4 further implies the titanomagnetites are multidomain and that their magnetic fabric is parallel to the petrofabric. Petrographical observation of anhedral intercumulus magnetite occupying the interstices of a plagioclase and clinopyroxene primocryst ‘framework’ suggest the titanomagnetite petrofabric itself is controlled by the fabric of the primary silicate mineralogy. These observations mean the measured AMS fabrics can be interpreted and presented in a straightforward manner as primary magmatic flow fabrics. Thus, the long axis of the susceptibility tensor ellipsoid ( $K_1$ ) equates to the magnetic lineation (L) and the magnetic foliation plane (F) may be defined by the  $K_1$ - $K_2$  plane, the pole to which is represented by the  $K_3$  axis (Tarling and Hrouda, 1993), and these reflect the actual lineation and foliation.

The susceptibility axes, defined by a plunge azimuth and plunge, are plotted onto an equal-area, lower-hemisphere stereographic projection along with 95 % confidence ellipses to account for within block variation (Fig. 5.9) (Jelínek, 1978). The shape and relationships of the confidence ellipses may then be used to determine the magnetic fabric (Fig. 5.9a). Figure 5.9a describes the three main examples of AMS stereoplot geometries, using samples measured from the Ardnamurchan cone sheets. A strongly prolate fabric has a well defined  $K_1$  axes whilst the  $K_2$  and  $K_3$  axes are poorly constrained with their respective confidence ellipses overlapping (Fig. 5.9a). In this scenario a magnetic foliation may not be interpreted. Conversely, a magnetic lineation may not be determined if the magnetic fabric is strongly oblate and the  $K_1$  and  $K_2$  axes overlap (Fig. 5.9a). The majority of samples are, at least, partially triaxial and may be used to infer magnetic lineation and magnetic foliation. All cone sheet and regional dyke AMS stereoplot data are presented in Figure 5.9b and c on a simplified geological map of Ardnamurchan. Raw AMS data is contained in Appendix B.

### 5.3.1 Correlation of the magnetic fabric to primary magma flow

Examining the magnetic fabrics and their relation to the sheet intrusion orientation may provide information on local magma flow dynamics and help to delineate source regions. It is inherently assumed there is coaxiality between magma flow and the generated petrofabric (Callot and Guichet, 2003). In igneous rocks, the magnetic lineation is often interpreted as parallel to the primary magma flow direction (e.g. Knight and Walker, 1988; Ernst and Baragar, 1992; Tauxe et al., 1998); although several caveats summarised by Aubourg et al., (2008) exist: (1) the potential development of magnetic lineations perpendicular to magma flow, (2) uncertainty of principal axes directions associated with inverse and intermediate magnetic fabrics and (3) the possible generation of an intersection magnetic lineation from two foliations. In response to these concerns, many authors have instead advocated the use of imbricated magnetic foliations as a more accurate indicator of magma flow (e.g. Geoffroy et al., 2002; Callot and Guichet, 2003; Aubourg et al., 2008), although many caveats (e.g. inverse fabric development) are still applicable. These caveats may largely be circumvented by a detailed magnetic mineralogy study and correlation of magnetic fabrics to other magma flow indicators (e.g. aligned phenocrysts). Determining the application of magnetic lineation to analyse primary magma flow in the Ardnamurchan cone sheets is paramount here as the sampling strategy adopted (i.e. block sampling to cover all cone sheet variants and to account for the paucity of exposure) is not ideal for imbricated magnetic foliation study, which generally requires drilling multiple transects across the width of a sheet intrusion (e.g. Féménias et al., 2004; Aubourg et al., 2008).

To independently evaluate the accuracy of the magnetic lineations record of primary magma flow, a comparison of  $K_1$  orientation and visible field flow indicators was conducted. For example, the long axes of broken bridge and intrusive step structures, flow lines on intrusive sheet walls or flow-aligned phenocrysts may all be used in the field to approximate the primary magma flow axis (Rickwood, 1990; Correa-Gomes et al., 2001; Liss et al., 2002; Hutton, 2009). On Ardnamurchan, these features are often ambiguous and poorly exposed, making accurate measurements difficult. Nevertheless several locations provided sufficient

constraint on magma flow to test the magnetic data. Figure 5.10 highlights several examples of AMS fabrics correlated to measured field flow indicators. Comparison between the visible field flow indicator axes and  $K_1$  of 16 cone sheets and two regional dykes, reveals 72 % of the  $K_1$  lineation azimuths are within  $30^\circ$  (i.e. to either side) of the measured field flow axes (Appendix E). It is probable that the ambiguity associated with measurement of visible field flow axes has contributed to this error. The broad correlation to visible field flow indicators further suggests the magnetic fabric can be interpreted as a primary flow fabric and that the magnetic lineation correlates to the magma flow axis (Correa-Gomes et al., 2001; Liss et al., 2002). The magnetic foliation of 27 % ( $n = 5$ ) of the samples is sub-parallel to the visible flow axes.

### 5.3.2 Expected flow regime based on previous emplacement models

Magnetic lineations may be used to identify primary magma flow trends in the Ardnamurchan cone sheets and regional dykes, providing important information on magma flow dynamics and constraints on source position. Previous cone sheet emplacement models imply magma originates from a commonly unexposed, centralised source reservoir at depth (e.g. Anderson, 1936; Phillips, 1974; Schirnack et al., 1999; Tibaldi et al., 2011). Few investigations have applied petrofabric and/or geochemical analyses to corroborate the inherently assumed central source (e.g. Cuillin central complex, Skye, Herrero-Bervera et al., 2001; Otoge igneous centre, Japan, Geshi, 2005). Magma flow regimes in cone sheets are therefore poorly understood. Following the intrusion conditions and central source position defined by previous emplacement models, two main potential magma flow regime end member hypotheses for cone sheets may be envisaged. From these hypotheses, expected magnetic lineation trends may be inferred (Fig. 5.11).

Palmer et al., (2007) suggested magma intruding cone sheet fractures flowed radially out from the central source up along the inclined plane of the cone sheet (Fig. 5.11a). This hypothesis implies cone sheet magnetic lineations around the Ardnamurchan central complex should describe a radial pattern, with a positive correlation between magnetic lineation plunge

azimuth and cone sheet dip azimuth (i.e. they should be sub-parallel; Fig. 5.11a). A similar radial, inwardly inclined magma flow regime is apparent in the Ootoge cone sheet swarm (Japan) from study of elongated vesicles and enclaves (Geshi, 2005).

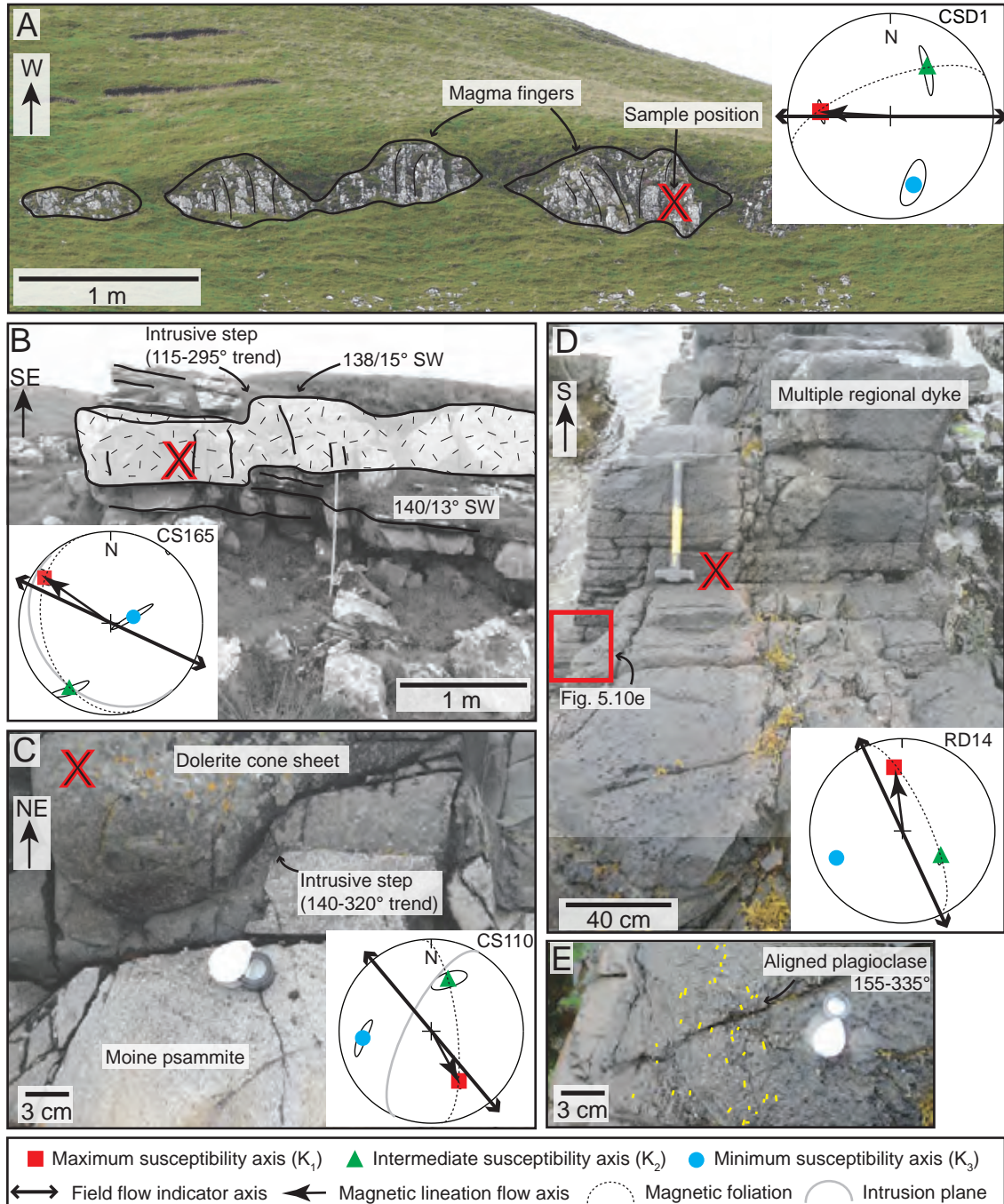


Fig. 5.10: A selection of photographs that depict various magma flow indicators measured in the field, including the axes of magma fingers (A) and intrusive steps (B and C) as well as phenocryst alignments (D and E), which correlate closely to  $K_1$  trends measured from the same sheets. Note that in all four examples,  $K_1$  is contained within the intrusive plane and plunges at a gentle to moderate angle.

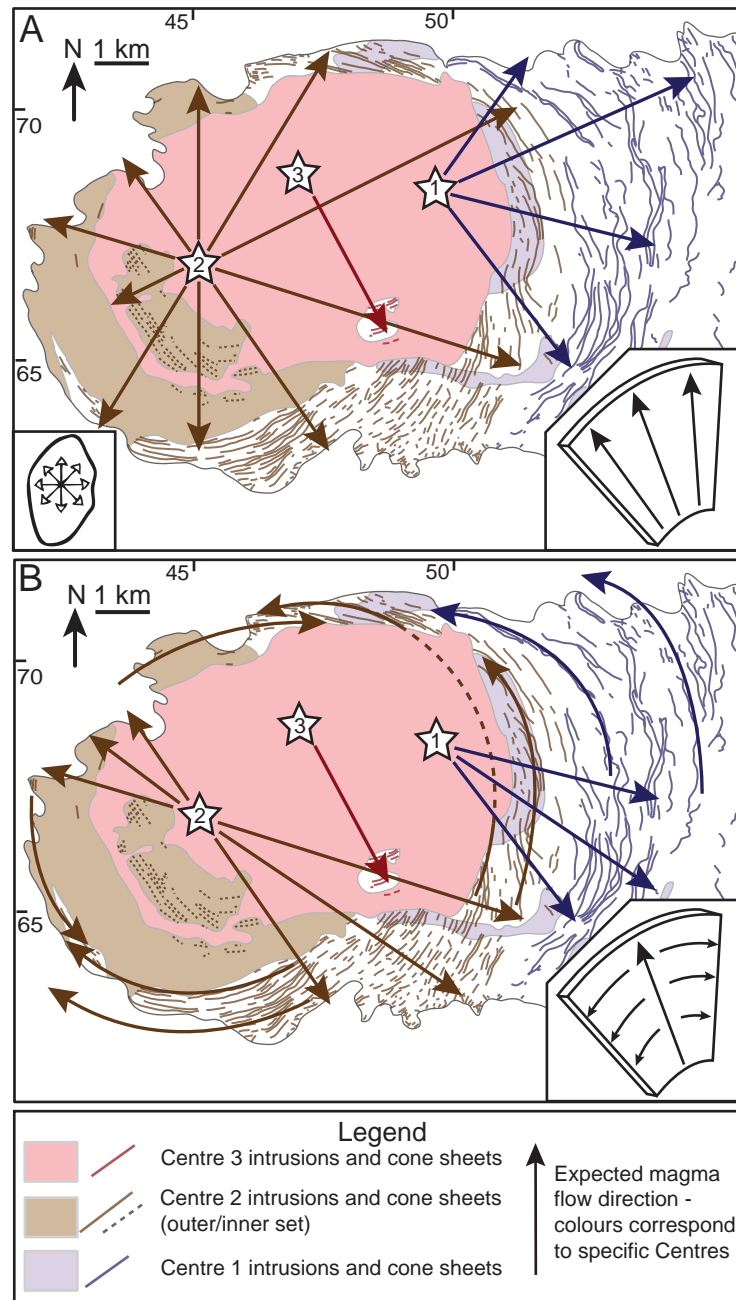


Fig. 5.11: Plan view of expected magma flow trends of the Ardnamurchan cone sheets. A) If magma flow is oriented radially up and out (Palmer et al., 2007; *inset* bottom left), measured magnetic lineations should parallel the cone sheet dip azimuth (*inset* bottom right). B) However, it may also be considered that radial up and out magma flow is geographically restricted (e.g. to the SE and/or NW of the Ardnamurchan central complex) and that from these areas cone sheets propagate laterally and concentrically around the central complex. This may result in a  $K_1$  correlation with either the cone sheet dip or strike azimuth (*inset* bottom right).

An alternative hypothesis similarly involves magma flow parallel to cone sheet fracture dip azimuth (*sensu* Anderson, 1936), albeit restricted to specific geographic quadrants

around the central complex (Fig. 5.11b). The relative position of the quadrants would likely be controlled by the regional stress field active during intrusion. This may be exemplified by the greater abundances of cone sheets, for example, to the NW and SE of the Cuillin igneous complex, Skye (Harker, 1904; Walker, 1993) and to the E and W of the Thverartindur igneous centre, Iceland (Klausen, 2004). If magma continued to intrude up the cone sheets in these quadrants, lateral propagation concentrically around the central complex (Fig. 5.11b) and parallel to the local compressive  $\sigma_3$  trajectory may be instigated by the inhibition of dip-parallel flow (e.g. due to sheet arrest; Gudmundsson, 2002) or an intrusion rate greater than an eruption rate. Consequently, magnetic lineations may be expected to vary in their plunge azimuth, potentially ranging from cone sheet dip parallel to cone sheet strike parallel. However, distinct zones of predominantly cone sheet dip-parallel and cone sheet strike-parallel magnetic lineations should be defined (Fig. 5.11b). In both models, magnetic foliation may be expected to generally mimic the cone sheet orientation (i.e. concentric and inwardly inclined).

### 5.3.3 Magnetic lineation trends

In order to improve clarity, the magnetic lineations and magnetic foliations are initially considered separately and later collated during the interpretation. The magnetic lineation is defined by the  $K_1$  principal susceptibility axis. In total, 66 cone sheets (106 samples) are represented in the magnetic lineation analysis and the results displayed on a simplified geological map of Ardnamurchan (Fig. 5.12). Seven AMS samples (Appendix E) proved unusable for magnetic lineation interpretation as the  $K_1$  and  $K_2$  confidence ellipses overlapped, implying the magnetic fabric only has a planar component (i.e. no lineation may be derived).

#### 5.3.2:1 Plunge azimuth

Magma flow axes inferred from previous cone sheet emplacement models suggest  $K_1$  plunge azimuths should predominantly radiate out from the respective central foci (Palmer et al., 2007), with some potentially oriented tangentially to the central complex (Fig. 5.11). Figure

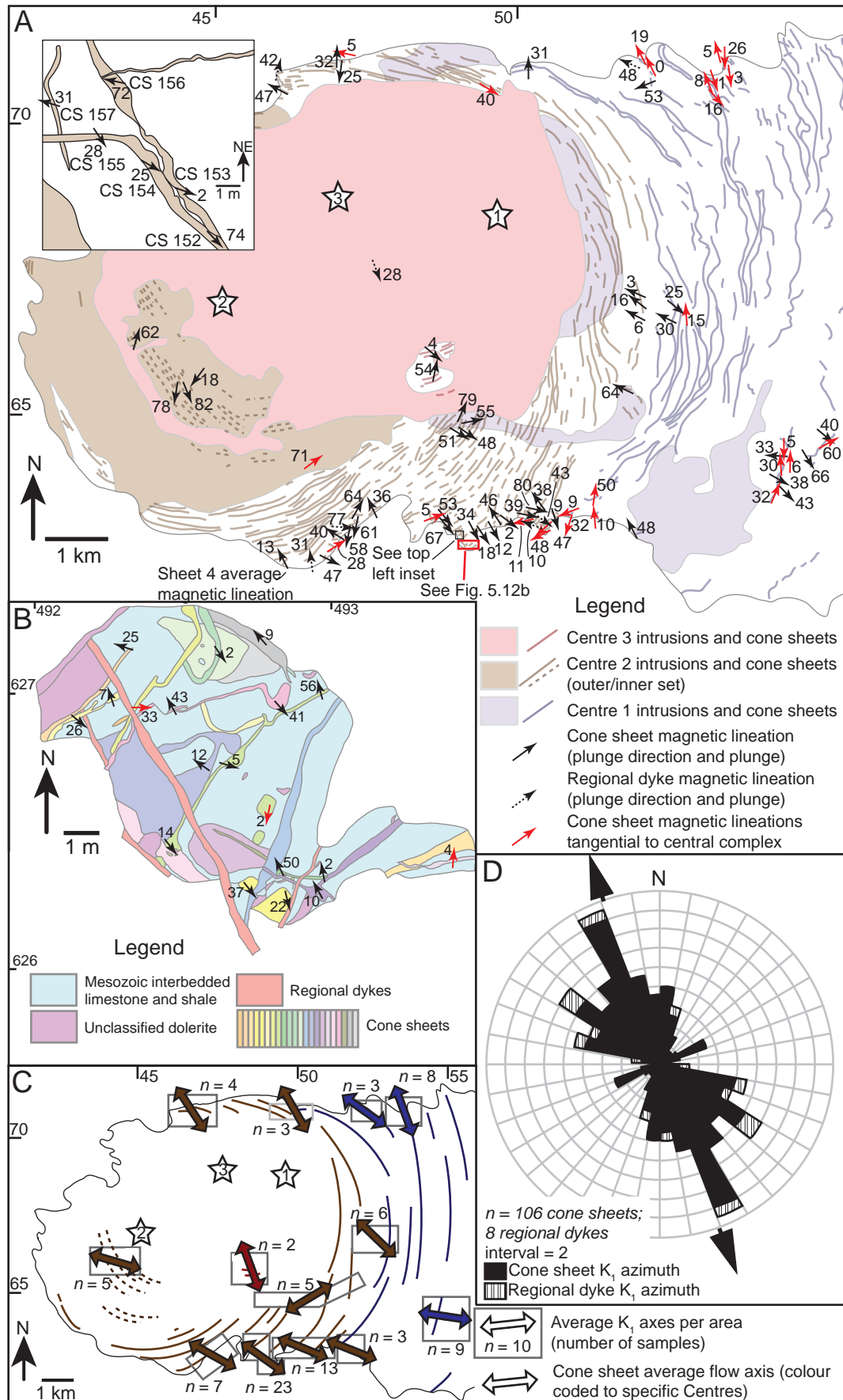


Fig. 5.12: A and B) Geological maps of Ardnamurchan (after Richey and Thomas, 1930; Emeleus, 2009) and a small area of Mingary Pier displaying magnetic lineations measured from cone sheets and regional dykes. *Inset*: Small map of AMS samples CS152–CS157. The bottom right of the square is at NM 49148 62826 and the bottom left is at NM 49146 62887. C) Simplified geological map of Ardnamurchan (after Emeleus, 2009) with the average  $K_1$  trends of each Area plotted on. A dominant NW-SE trend is apparent and importantly only a few may be traced directly to the Centre foci they are inferred to originate from (cf. Richey and Thomas, 1930). D) Rose diagram of the cone sheet and regional dyke magnetic lineations to highlight the predominance of a NW-SE trend.

5.12a and b displays a map of all magnetic lineations, from which no definitive radial trend may be described.  $K_1$  plunges oriented towards and away from the central complex are common (Fig. 5.12a and b). Extrapolating the  $K_1$  axes along the plunge azimuth indicates that, whilst the majority (73 %) intersect the Ardnamurchan central complex, 27 % ( $n = 29$ ) of magnetic lineations are oriented tangentially to the central complex margins. These tangential magnetic lineations are more abundant to the east and north-east of the Ardnamurchan central complex (Fig. 5.12a and b). Out of the  $K_1$  axes that may be traced into the central complex, many do not correlate to the specific Centre foci defined by Richey and Thomas (1930). These observations are further highlighted by compartmentalising the  $K_1$  axes into the defined geographical and age specific Areas and averaging the plunge azimuths (Fig. 5.12c). Overall, a dominant NW-SE trend is apparent in the Ardnamurchan cone sheets (Fig. 5.12d). A similar NW-SE trend is observed in the regional dyke  $K_1$  azimuths (Fig. 5.12d).

### 5.3.2.2 *Plunge*

Magnetic lineation plunges range from 0–82°. An equal-area, lower-hemisphere stereographic projection of the  $K_1$  axes indicate that 70 % of samples exhibit plunges ranging from sub-horizontal (0°–20°;  $n = 40$ ) to moderate ( $\leq 45^\circ$ ;  $n = 33$ ) (Fig. 5.13a). The remaining 30 % ( $n = 30$ ) of the magnetic lineations are steeper ( $\geq 45^\circ$ ) (Fig. 5.13a). Accounting for samples collected from the same intrusion, 38 cone sheets contain purely sub-horizontal to moderate plunges and 17 cone sheets contain steep plunges ( $\geq 45^\circ$ ). Seven cone sheets contain both shallow and steep  $K_1$  plunges, measured from separate block samples, often display a ramp-flat morphology in the field (e.g. Sheets 15, 17, 21 and 44). Within cone sheets of a ramp-flat

morphology, no spatial correlation is observed between sample position (i.e. collected from the ‘ramp’ or ‘flat’ section) and  $K_1$  plunge values. Magnetic lineations within the regional dykes are generally moderately inclined ( $42^\circ$  mean) but range from  $10\text{--}77^\circ$  (Fig. 5.13a).

### 5.3.2:3 *Correlation between $K_1$ and cone sheet orientation*

Figure 5.13b and c display a plot of  $K_1$  plunge azimuth against cone sheet dip azimuth and cone sheet strike. Figure 5.13b indicates there is little correlation observed between  $K_1$  plunge azimuth and cone sheet dip azimuth, in contrast to the projections of the inferred magma flow trends from a central source (Fig. 5.11a), with only 12 cone sheets (16 samples) containing a  $K_1$  plunge azimuth within  $30^\circ$  of the dip azimuth (Fig. 5.13b). With respect to the central complex, these 12 cone sheets are variably distributed (Fig. 5.9) to the SE ( $n = 6$ ), S ( $n = 3$ ), N ( $n = 1$ ), NE ( $n = 1$ ) and within the Centre 3 cone sheet swarm ( $n = 1$ ). Instead, a greater positive correlation is observed between cone sheet strike and  $K_1$  azimuth (corrected to a value  $<180^\circ$  removing the plunge direction) (Fig. 5.13c). Twenty cone sheets (21 samples), widely distributed throughout Ardnamurchan, contain a  $K_1$  azimuth within  $30^\circ$  of the cone sheet strike. The plunge of these tangential lineations ranges from  $0\text{--}66^\circ$ , with a mean of  $23^\circ$ , a mode of  $5^\circ$  and a median of  $16^\circ$ . The majority of cone sheets appear to display no correlation between  $K_1$  and cone sheet orientation, suggesting oblique magma flow dominated.

In one of the seminal studies applying AMS to determining magma flow in sheet intrusions, Khan (1962) measured several samples from the Ardnamurchan cone sheets. Using  $K_2$  as the magma flow indicator, Khan (1962) suggested magma flow within the cone sheets was dip-parallel (Fig. 5.13d). Although Cañón -Tapia (2004) dismissed the applicability of  $K_2$  to defining a magma flow axis, Khan’s (1962) results highlight that the  $K_1$  axes are located within the dyke plane and are oriented at a moderate angle to sheet dip (Fig. 5.13d); corroborating the magnetic lineation relationships described in this thesis.

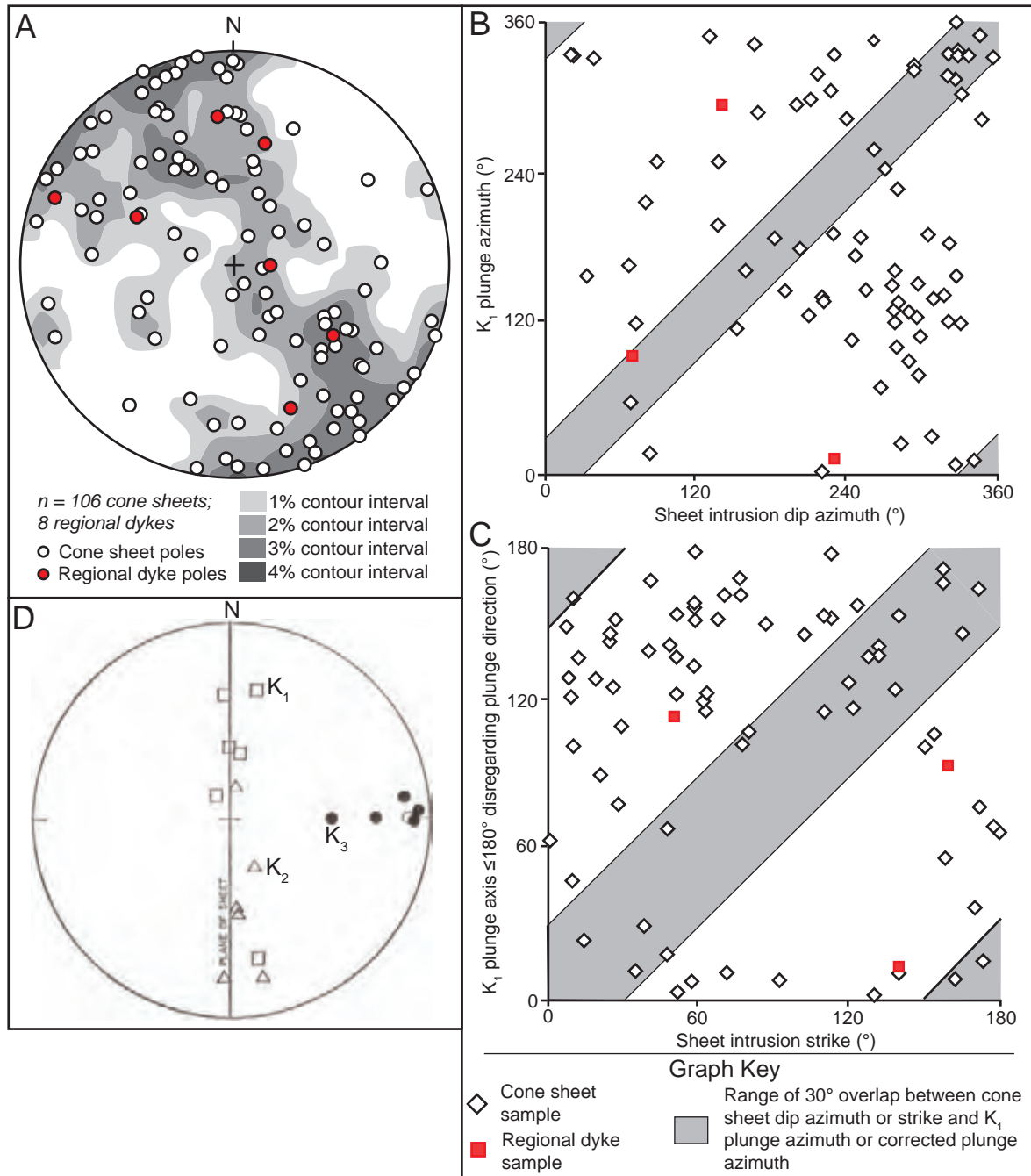


Fig. 5.13: A) Equal area stereographic projection of  $K_1$  lineations showing a NW-SE trend and preponderance of sub-horizontal to moderately inclined plunges. B and C) Plot of  $K_1$  plunge azimuth against sheet intrusion dip azimuth and sheet intrusion strike. Note that in (C), the  $K_1$  trend is corrected to  $<180^\circ$  as lateral magma flow within cone sheets may occur in two directions. D) Lower hemisphere, equal area stereographic projection of the Ardnamurchan cone sheet AMS measurements presented by Khan (1962). The plane of intrusion and the principal susceptibility axes have been rotated to correspond to a vertical intrusive plane.

### 5.3.4 Magnetic foliations

The preponderance of prolate fabrics suggests oblate fabrics, and hence magnetic foliations, are not as well defined as the magnetic lineation (Fig. 5.8a). From the original cone sheet emplacement model, and subsequent adaptations, the magnetic foliations within the Ardnamurchan cone sheets may be expected to have strikes tangential to the central complex (overall describing a concentric trend) with inward dips. Magnetic foliations plotted onto a simplified map of Ardnamurchan display no obvious trend (Fig. 5.14). Approximately 18 % of samples ( $n = 19$ ), representing 17 cone sheets, contain a tangential inwardly inclined magnetic foliation plane, with respect to the Ardnamurchan central complex (Fig. 5.14). Instead, the majority of magnetic foliations dip outwards and/or are oriented obliquely to the central complex (Fig. 5.14). Significant variation of foliation trends is observed within individual cone sheets (Fig. 5.14), which may partially correlate to the position the sample was collected from. Magma velocity profiles vary, due to friction with the wall rock, and often result in imbricated fabrics close to the host rock contact (Correa-Gomes et al., 2001). A detailed magnetic study of Sheet 4 (Area 14; [NM 46007 62320]) highlights that despite significant variations in magnetic foliation, the magnetic lineation remains relatively constant (Fig. 5.14c). This suggests magnetic foliations record local magma flow perturbations whereas the magnetic lineations correlate to the overall magma flow regime active during emplacement. This may potentially explain the lack of correlation between magnetic foliation strike and  $K_1$  plunge azimuth (Fig. 5.15a). No correlation is observed between the magnetic foliation strike and the strike of the cone sheets (Fig. 5.15b). A minor and strong negative correlation is apparent in Figure 5.15c between the cone sheet dip values and the magnetic foliation dips ( $K_3$  plunge) of the cone sheets and regional dykes respectively, implying magma flow was oriented obliquely to the plane of intrusion.

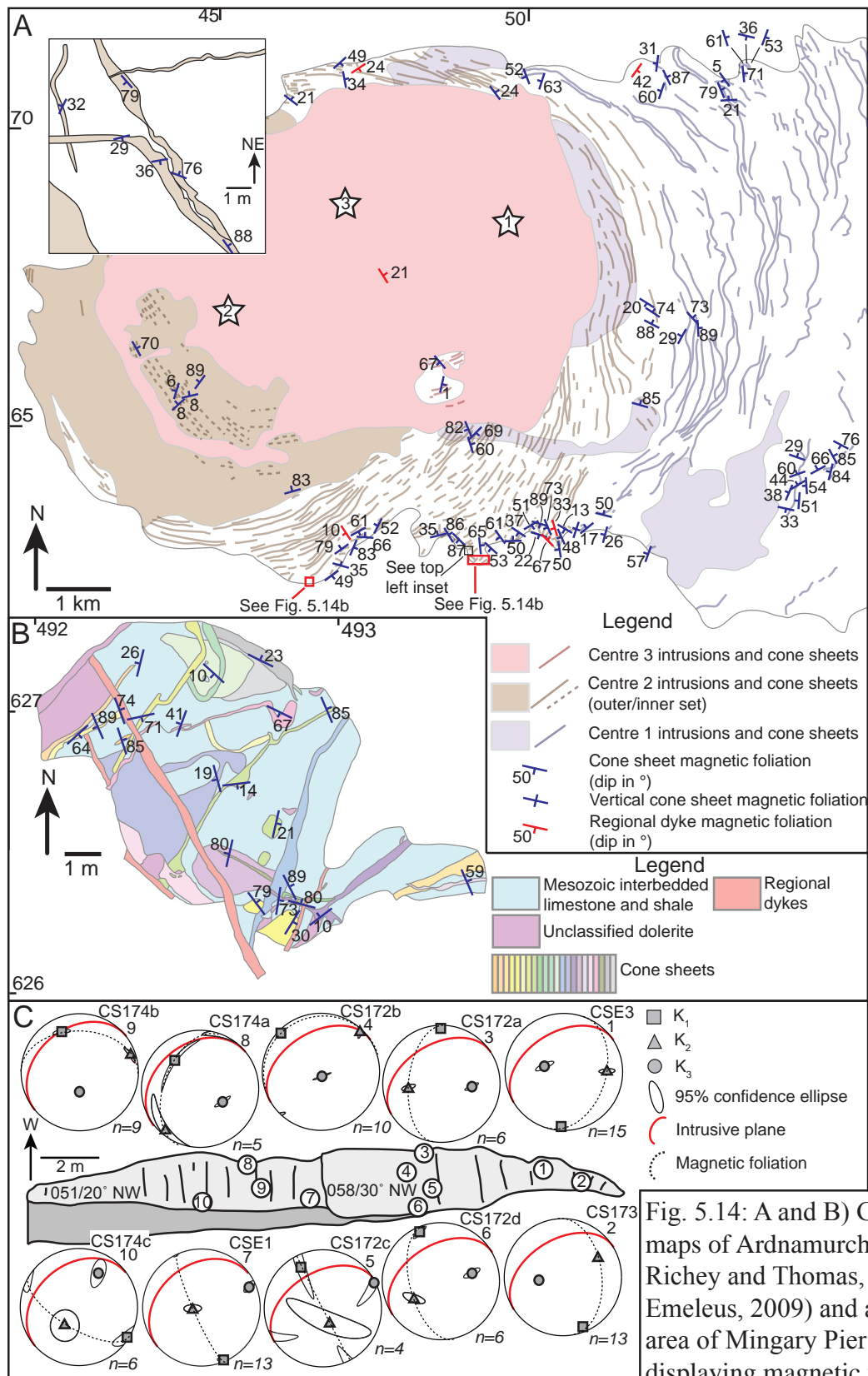


Fig. 5.14: A and B) Geological maps of Ardnamurchan (after Richey and Thomas, 1930; Emeleus, 2009) and a small area of Mingary Pier displaying magnetic foliations

measured from cone sheets and regional dykes. *Inset*: See Figure 5.12 for sample numbers and map co-ordinates. C) Block sample positions and associated AMS stereoplots for a cone sheet in Area 14. The intrusive plane and magnetic foliation great circles are also plotted.

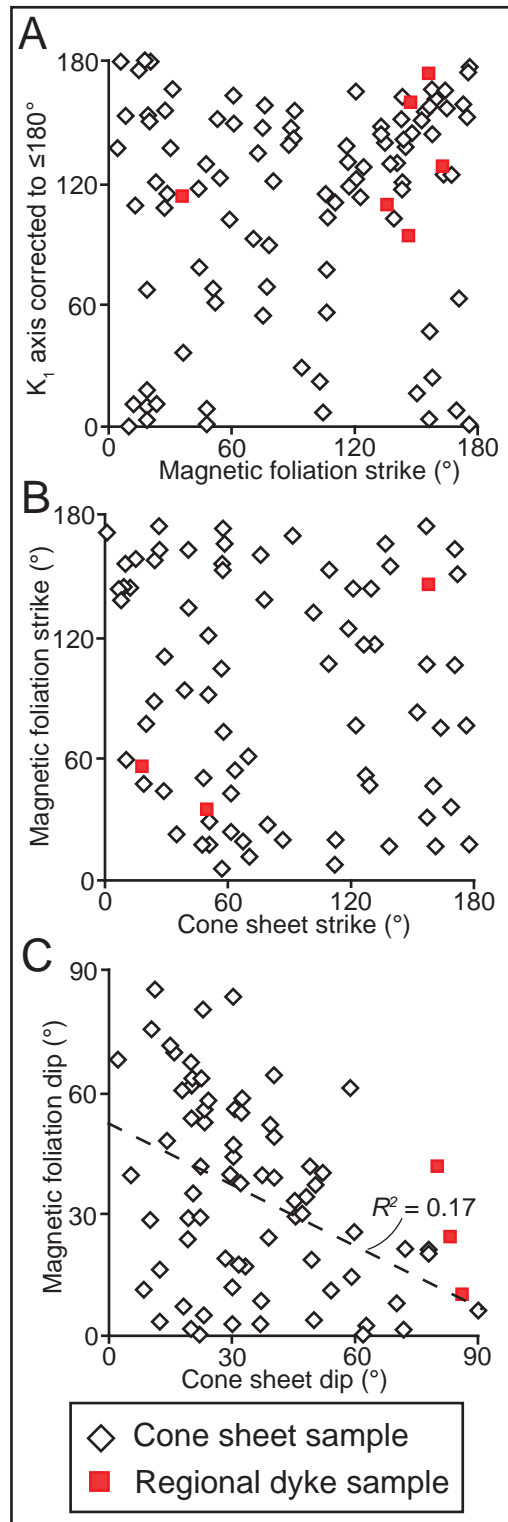


Fig. 5.15: A) Plot of corrected  $K_1$  axes against magnetic foliation strikes. B) Magnetic foliation strikes plotted against cone sheet strike. C) Magnetic foliation dip and cone sheet dip. See text for details.

## 5.4 Interpretation and summary of the AMS fabrics

Traditionally, magma flow within cone sheets is expected to be radially up and out from a central source (Fig. 5.11a) (Palmer et al., 2007). An alternative to this hypothesis, whilst maintaining a central source, involves spatially restricted cone sheet dip-parallel magma flow, which then laterally propagate around a concentric path (Fig. 5.11b). Anisotropy of magnetic susceptibility has been successfully applied in this thesis to analyse subtle mineral alignments (i.e. the petrofabric) within the cone sheets relating to primary magma flow. This is corroborated by the correlation between magnetic lineations and visible field flow indicators (e.g. broken bridge axes and aligned phenocrysts) as well as the lack of petrographical evidence for significant postcumulus textural modification or deformation. It has been established that the magnetic fabrics measured are equivalent to the petrofabric of the multidomain titanomagnetite fraction within each sample. Although the titanomagnetite may have crystallised following emplacement, its growth and distribution was likely controlled by the primary silicate framework that formed during magma flow. Overall, the magnetic lineation is interpreted to be parallel to the primary magma flow axis and used to test the predicted magma flow regimes of the two hypotheses discussed.

Analysis of the magnetic lineations and magnetic foliations presented here and those described by Khan (1962) suggest magma flow within individual cone sheets was predominantly oriented obliquely to the intrusive plane, with few displaying cone sheet dip-parallel ( $n = 12$ ) or strike-parallel ( $n = 21$ )  $K_1$  axes. Variations in magnetic fabrics within individual intrusions likely reflect differing strain amounts, possibly produced by a heterogeneous magma flow regime (Dragoni et al., 1997; Wartho et al., 2001). Furthermore, the magnetic lineations do not describe a radial trend (Fig. 5.12). These observations together suggest the radial up and out magma flow regime implied by Palmer et al., (2007) cannot be attributed to the Ardnamurchan cone sheets. Instead, the magnetic lineations predominantly describe a NW-SE trend with sub-horizontal to moderate plunges consistent with a significant proportion of lateral magma flow (Fig. 5.13a). This trend may be synthesised with the

alternative magma flow hypothesis proposed (Fig. 5.11b), if magma flowed up and out from a central source in a south-easterly (and potentially north-westerly) direction and then propagated laterally around the central complex. Inherently, this implies the vast majority of cone sheet dip-parallel  $K_1$  axes should be located to the SE of the Ardnamurchan central complex, with those  $K_1$  azimuths that are parallel to cone sheet strike predominantly situated to the NE and SW. No such spatial correlation is observed (Fig. 5.9). Neither magma flow regime, assuming a central source, considered can satisfactorily explain the orientation and distribution of the measured magnetic fabrics.

---

## CHAPTER 6

### EMPLACEMENT OF THE ARDNAMURCHAN CONE SHEETS

---

Field observations and mapping of cone sheet swarms in the BIPIP (e.g. Harker, 1904; Bailey et al., 1924; Richey and Thomas, 1930) defined the essential cone sheet geometries that Anderson (1936) mathematically modelled. Subsequent studies have developed our understanding of cone sheet emplacement (e.g. Phillips, 1974; Gautneb et al., 1989; Walker, 1993; Schirnack et al., 1999; Klausen, 2004; Tibaldi et al., 2011), but are still fundamentally based on Anderson's (1936) tenet that a centrally subjacent overpressured magma reservoir imparts a local stress field on the host rock, favouring the formation of inwardly inclined concentric fractures. Several criteria may be extracted from previous emplacement models to characterise cone sheet swarms (Fig. 6.1): 1) cone sheet strike should be roughly concentric; 2) cone sheets should dip inwards towards a central magma source and 3) magma flow should radiate upwards and outwards from the central source, either throughout the entire cone sheet swarm or within a restricted zone beyond which (i.e. along sheet strike) lateral propagation occurs.

Field observations and magnetic fabric analyses of the Ardnamurchan cone sheets reveal that: 1) cone sheet strikes are roughly concentric proximal to the central complex but further away (~2 km) to the east and north-east the strike curvature appears reduced and a prominent NW-SE trend is apparent; 2) cone sheet dip angles and azimuths are locally highly variable (e.g. some dip outwards), although on average there is a tendency towards inward inclinations; 3) cone sheets display dilatational opening vectors and 4) primary magmatic field flow indicators (within error) and AMS fabrics are consistently oriented NW-SE with predominantly sub-horizontal to moderate plunges. This chapter discusses the applicability of previous emplacement models, in light of new observations and data, to the Ardnamurchan cone sheets.

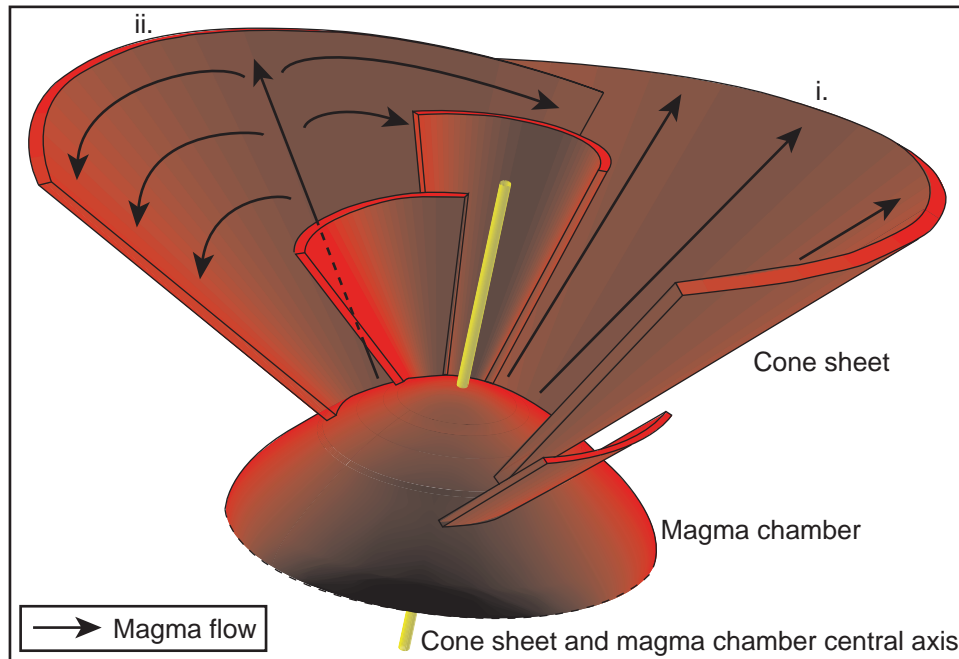


Fig. 6.1: Schematic 3D representation of a cone sheet swarm fed from a central source and highlighting two possible magma flow regimes. Magma is expected to flow radially up and out, either throughout cone sheets (i) or restricted to an ascent zone from which it then propagates laterally (ii).

## 6.1 Suitability of previous cone sheet emplacement models

The following section compares new field observations and magnetic fabric data with various components of previous models, divided into the main groups distinguished in Chapter 1. The models of Walker (1975a) and Bahat (1980) are not considered as they rely on an ascending acid diapir, a process questioned by many authors as an effective intrusion mechanism (e.g. Molyneux and Hutton, 2000; Petford et al., 2001). Furthermore, there is no evidence on Ardnamurchan for an early felsic diapir.

### 6.1.1 A comparison to the traditionally accepted model for the Ardnamurchan cone sheets developed by Richey and Thomas (1930) and Anderson (1936)

The field observations and structural measurements collected during this study generally conform to those presented in the Geological Memoir of Richey and Thomas (1930). Overall, cone sheets are observed to be roughly concentric with the majority displaying inward dips

towards the Ardnamurchan central complex. A proportion of the cone sheets were observed to dip outwards (i.e. away from the central complex), also noted by Richey and Thomas (1930). An important observation of Richey and Thomas (1930) is the increasing inclination of the cone sheets with proximity to the central complex, as this is consistent with the predicted principal stress axes orientations and cone sheet dip dispositions surrounding an inflating central magma chamber (Anderson, 1936; Gautneb et al., 1989; Gautneb and Gudmundsson, 1992). New data suggests that although the Centre 2 cone sheet swarm follows this trend (i.e. displays a trumpet-like morphology), the Centre 1 cone sheets instead decrease in dip towards the central complex describing a bowl-like geometry (cf. Gautneb et al., 1989; Gudmundsson, 1998). Gautneb et al., (1989) have ascribed such dip distribution patterns to variable magma source geometries (see section 6.1.4). This suggests the Centre 1 and Centre 2 cone sheets may be attributed to differing magma source geometries, supporting a multiple centre hypothesis (*sensu* Richey & Thomas, 1930). However, this thesis has highlighted a significant discrepancy between the projected cone sheet dip azimuths (down-dip) and the Centre foci positions (see Chapter 4, section 4.2.3 and Appendix D), which appears to question the migratory centre hypothesis of Richey and Thomas (1930), at least in terms of the defined Centre foci positions. O'Driscoll et al., (2006) and O'Driscoll (2007) have previously questioned the separate migratory intrusive centres model following their re-evaluation of the originally defined multiple Centre 3 ring dykes as a single intrusion (i.e. the Centre 3 Layered Gabbro Lopolith). Although local variations in cone sheet orientation are observed, these may be at least partially attributed to a significant host rock influence on local cone sheet geometry identified through field observations and calculations determining the angular range of pre-existing fractures (from  $\sigma_1$ ) that may have been reactivated during cone sheet intrusion.

### **6.1.2 Shear fracture intrusion (Robson and Barr, 1964; Durrance, 1967; Phillips, 1974)**

As an alternative to Anderson's (1936) model of cone sheets intruded into tensile fractures, Robson and Barr (1964) proposed cone sheets were emplaced into shear fractures generated by the collapse of a central roof block into an underlying magma chamber. However, as

Phillips (1974) demonstrated, subsidence of a central block along inward dipping fractures is unable to accommodate sufficient space. Ideas pertaining to cone sheet exploitation of shear fractures were further developed by Durrance (1967), who proposed the Ardnamurchan cone sheets originated from a central source and were intruded into a spiral shear fracture. Phillips (1974) also considered that cone sheets intruded shear fractures, suggesting the rotational strain imparted on the host rock adjacent to the shoulders of an overpressured magma chamber favoured shear fracture formation. Contrary to Robson and Barr (1964), Durrance (1967) and Phillips (1974) suggested space for intrusion was created by uplift of the central block above the source reservoir.

Initially, the lateral and partially oblique magma flow regime, identified from AMS analysis of the Ardnamurchan cone sheets, may appear to support the model of Durrance (1967), which implies magma intruded obliquely around a set of spiral shear fractures from a central source (Fig. 1.5). However, this magma flow regime would require the magnetic lineations to describe an *en échelon* arrangement that defines an overall concentric pattern (Fig. 6.2). Instead, this thesis has revealed a preponderance of NW-SE oriented magnetic lineations measured (Fig. 5.12). Furthermore, the compressive stress regime that Durrance (1967) invokes to generate the spiral fractures, requires a sub-vertical  $\sigma_2$  principal stress axes. Assuming the cone sheets intrude orthogonally to  $\sigma_3$  (Anderson, 1951; Rubin, 1995), an analysis of the Ardnamurchan cone sheet pole dispositions suggest either  $\sigma_1$  or  $\sigma_3$  was sub-vertical during intrusion (see Chapter 4, section 4.3.1). The principal argument against emplacement models reliant on shear fracture intrusion, for Ardnamurchan and other areas (e.g. the Thverartindur igneous centre, Iceland, Klausen, 2004), is that the vast majority of cone sheets observed are congruent with the dilatational opening of tensile fractures (Richey and Thomas, 1930; Keunen 1937; Gautneb et al., 1989; this study).

### **6.1.3 Deformation of the volcanic edifice (Walker, 1992; 1993)**

Walker (1992) suggested that the local inhibition of crustal extension favoured the intrusion of cone sheet swarms, rather than vertical dyke swarms, from a central magma source.

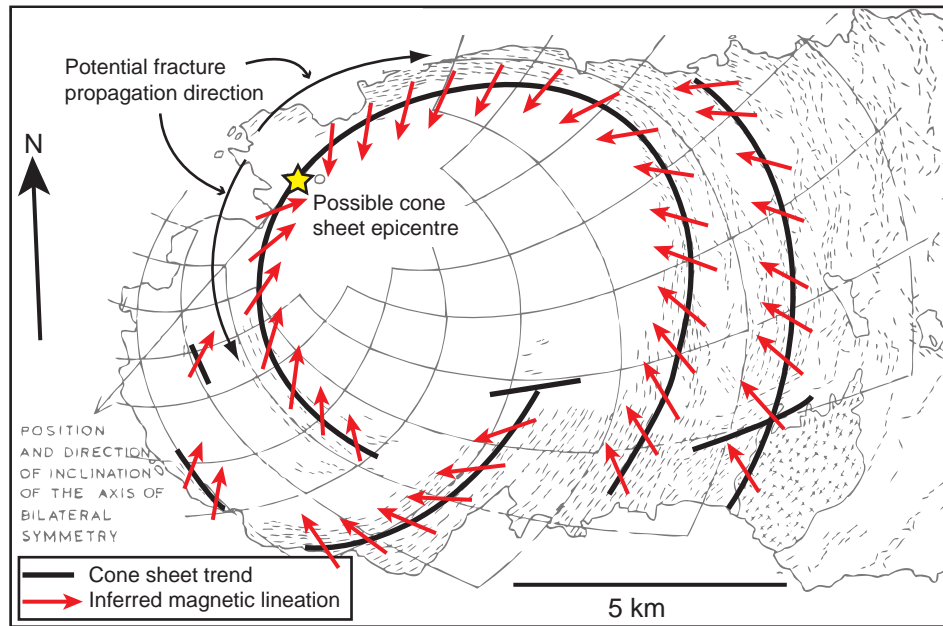


Fig. 6.2: Predicted magnetic lineation trends for the cone sheet emplacement model of Durrance (1967).

Inhibition of crustal extension may be attributed to the host volcanic edifice resisting widening (e.g. if the volcano is buttressed by an adjacent edifice; Walker, 1992) or an emplacement rate greater than extension (Fig. 1.8). Walker (1993) further developed this hypothesis, suggesting centrally fed dykes and cone sheets may be emplaced intermittently during periods of extension and compression respectively; perhaps instigated by cyclical inflation and deflation of the source reservoir (Day, 1989). A local reduction in regional dyke dilation percentage around Ardnamurchan (Fig. 6.3) (Speight et al., 1982) may reflect a resistance to crustal extension due to the development of the Ardnamurchan volcanic edifice, potentially promoting cone sheet intrusion. Cross-cutting relationships are consistent with alternating periods of cone sheet emplacement, coupled with thrust fault development, and normal faulting on Ardnamurchan. This is supported by the compressional stress regime, active during intrusion, resolved from the principal stress axes of the Ardnamurchan cone sheets. Fluctuations in the active stress field are attributed to temporal variations in inflation (i.e. associated with compression) and deflation (i.e. associated with extension) of the major intrusions of the Ardnamurchan central complex. It is apparent from these models (i.e. Walker, 1992; 1993) and from field observations and structural measurements of the cone sheets that

the local stress field, itself controlled by the evolution of the Ardnamurchan central complex, significantly affected sheet intrusion geometry and disposition.

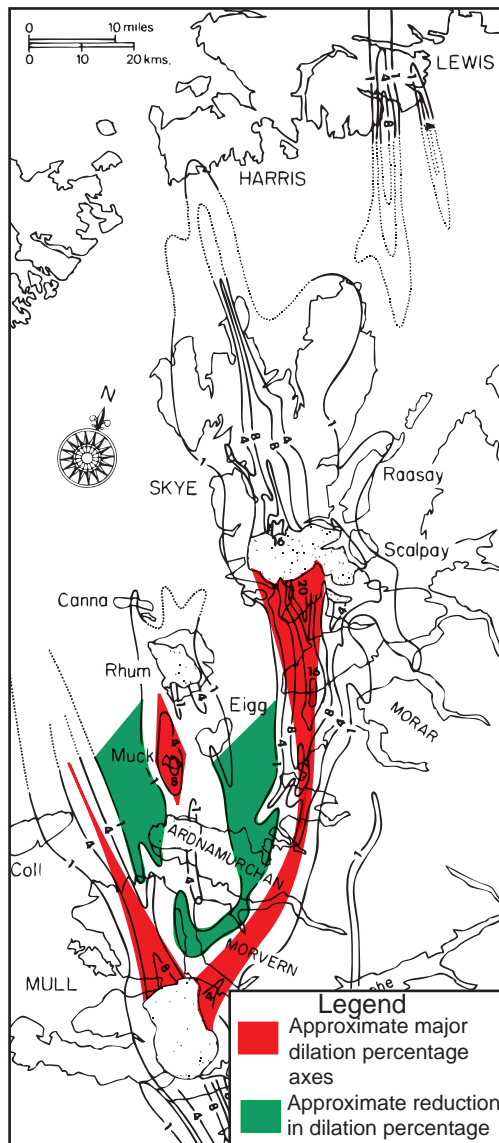


Fig. 6.3: Map of regional dyke percentage dilation axes within the BIPIP (Speight et al., 1982). The shaded areas highlight areas where crustal extension was approximately focused (red) or reduced (green). With the exception of Muck, the absence of significant dyke dilation surrounding Ardnamurchan may imply crustal extension was locally inhibited.

#### 6.1.4 Variations in magma chamber conditions (Gautneb et al., 1989; Gautneb and Gudmundsson, 1992; Gudmundsson, 1995; 1998; Schirnick et al., 1999)

The influence of the local stress field on cone sheet emplacement is further highlighted by Gautneb et al., (1989), Gautneb and Gudmundsson (1992), Gudmundsson (1995; 1998) and

Schirnack et al., (1999). As the cone sheets of the Hafnarfjall volcanic complex (Iceland) predominantly intrude tensile fractures, Gautneb et al., (1989) suggested the  $\sigma_1$  and  $\sigma_3$  principal stress axes associated with magmatic overpressure in a central magma chamber may be modelled and correlated to observed cone sheet dispositions in order to characterise source reservoir geometry. Cone sheets emplaced in a local stress field, superimposed onto a regional extensional regime, related to a spherical or prolate central magma source are expected to steepen towards the surface defining a bowl-like geometry (Gautneb et al., 1989; Mathieu et al., 2008). In contrast, cone sheets originating from sill-like (oblate) magma chambers are predicted to obtain a trumpet-like geometry (Gudmundsson, 1998). As the Ardnamurchan cone sheets essentially crop out at similar elevations, the difference in dip angle and distance from the central complex relationships observed between the Centre 1 and Centre 2 cone sheets may be construed as evidence for separate magma chamber sources of variable geometry. Dips of the Centre 1 cone sheets decrease in inclination with distance from the Centre foci, suggestive of a bowl-like geometry, whereas the Centre 2 cone sheets display a trumpet-like geometry with inclinations increasing towards the central complex. If the cone sheets do originate from a central source, the dip dispositions indicate intrusion from a spherical/prolate (Centre 1) or oblate (Centre 2) source. However, this characterisation of the central magma chamber geometries relies upon two assumptions: 1) intrusion of pre-existing fractures only accentuates an underlying geometrical preference for cone sheet dip and 2) that the Centre 1 and Centre 2 cone sheets are separate suites, although there are no cross-cutting relationships exposed and the two sets are geochemically indistinct (Holland and Brown, 1972).

Schirnack et al., (1999) proposed that a cyclically expanding and deflating central laccolith fed a series of nested, parallel cone sheets in the Miocene Tejada Complex, Gran Canaria. Similarly, resolved principal stress axes active during cone sheet intrusion and a correlation to other central complexes (e.g. the Henry Mountains, Utah, USA; Jackson and Pollard, 1988), suggests the Palaeogene local stress field and Ardnamurchan central complex may originate from a central, shallow ( $\sim 5$  km) laccolithic magma chamber (see Chapter

4, section 4.3.2). Although there is evidence of cyclical inflation and deflation of major intrusions within the Ardnamurchan central complex, which likely reflects similar processes in the inferred source laccolith, the cone sheets are not parallel and instead have highly variable dips.

### 6.1.5 Local stress field and host rock control

The following common components in each cone sheet model reviewed above have been identified: 1) cone sheet swarms have an overall inverted conical geometry but individual cone sheets are strongly influenced by local host rock heterogeneities and 2) cyclical inflation and deflation of a central laccolith (*sensu* Schirnick et al., 1999), as well as other major intrusions of the Ardnamurchan central complex, modified the local stress field sufficiently to promote dyke intrusion during extension and cone sheet emplacement, as well as thrust faulting (cf. Day, 1989; Mathieu and van Wyk de Vries, 2009), during compression (*sensu* Walker, 1992; 1993). These results and interpretations are consistent with recent studies of other intrusive forms, which highlight the importance of local stress field and host rock characteristics (e.g. Pollard, 1987; Rubin, 1995; Geshi, 2005; Gudmundsson and Phillip, 2006; Corazzato et al., 2008; Acocella and Neri, 2009; Siler and Karson, 2009; Schofield et al., 2010) in controlling emplacement dynamics. The specific local stress field and host rock conditions determined to have actively influenced Ardnamurchan cone sheet intrusion are summarised here to provide a context for subsequent discussion (see Chapter 4 for more detail).

Assuming cone sheet intrusion occurred orthogonally to  $\sigma_3$ , corroborated by the dilatational opening vectors of the cone sheets, the poles to the cone sheet intrusion planes were used to determine the contemporaneous principal stress axes active during emplacement. Overall,  $\sigma_1$  was radially inclined inwards and increased in inclination towards the central complex, whereas  $\sigma_3$  decreased in inclination towards the central complex. The compressional stress regime defined is similar to those inferred for other magma chambers (e.g. Anderson, 1936; Gautneb et al., 1989; Gudmundsson, 1998). This stress regime is interpreted as

originating from an expanding central laccolith at a depth of  $\sim < 5$  km, likely the source of the currently exposed components of the Ardnamurchan central complex, which is consistent with the doming of the country rocks. The subsequent orientation of the principal stress axes favoured the intrusion of magma along reactivated fractures (i.e. the inward dipping fractures of a conjugate fracture set) and bedding planes. The ratio of fractures to bedding planes intruded is a function of distance from the Ardnamurchan central complex and the amount of local doming. Importantly, this explains the dominant inwardly inclined disposition of the Ardnamurchan cone sheets and the vast majority of local deviations from this trend. Another control on cone sheet emplacement and morphology was the lithology of the host rock. Predominantly brittle processes are interpreted to have facilitated magma intrusion (e.g. from intrusive step and broken bridge development), although a few examples of non-brittle emplacement may be derived from field observations of cone sheets intruding into the Early Palaeogene volcanoclastics and olivine basalt lavas.

#### **6.1.6 Source position of the Ardnamurchan cone sheets**

Although some aspects of previous emplacement models may be applied to various characteristics of the Ardnamurchan cone sheets, the measured dominant NW-SE, sub-horizontal to moderately plunging magma flow regime is inconsistent with the generally assumed radial upwards and outwards magma flow regime for cone sheets (see Palmer et al., 2007). There are two principal hypotheses to be considered that may account for the dominant NW-SE lateral magma flow regime.

##### *6.1.6:1 Potential emplacement model for the Ardnamurchan cone sheets pertaining to a central source*

Magma intruded from a central source into cone sheets is expected to flow upwards and outwards at some point (Fig. 5.11), implying that derived magma flow axes (e.g. magnetic lineations) should correlate to the respective cone sheet dip azimuth and dip angle. This is exemplified by the work of Geshi (2005) who noted magma flow was sub-parallel to cone

sheet dip in the Otoge igneous centre (Japan), which in conjunction with a strong geochemical (major and trace element) similarity to other local intrusions supported derivation from a central source. However, out of the 69 Ardnamurchan cone sheets analysed for AMS, only 12 contain magnetic lineations that are sub-parallel to the cone sheet dip angle and dip azimuth (Fig. 5.13b). Instead, the majority of Ardnamurchan cone sheets (73 %) contain AMS fabrics suggestive of a lateral magma flow. To maintain a central source for the Ardnamurchan cone sheets, the hypothesis presented in Chapter 5 (section 5.3.2), involving geographically restricted cone sheet dip-parallel flow (*sensu* Anderson, 1936) followed by concentric lateral magma flow, requires further consideration (Fig. 5.11b). To account for the dominant NW-SE magma flow trend, initial cone sheet intrusion from the central source (i.e. producing cone sheet dip-parallel  $K_1$ ) is suggested to have occurred to the SE and/or NW of the central complex. Lateral magma flow within cone sheets to the NE and SW of the central complex may then augment the NW-SE flow trend. Although 50 % ( $n = 6$ ) of cone sheet containing dip-parallel magnetic lineations are distributed to the SE of the Ardnamurchan central complex, this is a relatively minor quantity considering 27 cone sheets to the SE of the Ardnamurchan central complex display evidence of lateral magma flow. This disparity may potentially be explained cone sheet dip-parallel magnetic lineations are overprinted by secondary lateral magma flow (cf. Tauxe et al., 1998; Philpotts and Philpotts, 2007).

#### 6.1.6:2 Regional dyke lateral propagation and deflection around the Ardnamurchan central complex

A novel alternative to centrally fed cone sheets is that cone sheets may have intruded from a laterally adjacent source, independent of the Ardnamurchan central complex. The NW-SE magnetic lineation trend (150–330°) of the cone sheets is indistinguishable from the magnetic lineations (NW-SE trend and shallow to moderate plunge; Herrero-Bervera et al., 2001; this study) and strike (160–340°; Speight et al., 1982) of the regional dyke swarm (Fig. 6.4a). This common, predominantly lateral, magma flow regime suggests the cone sheets and regional dykes may be related. It is proposed that the Ardnamurchan cone sheet may represent

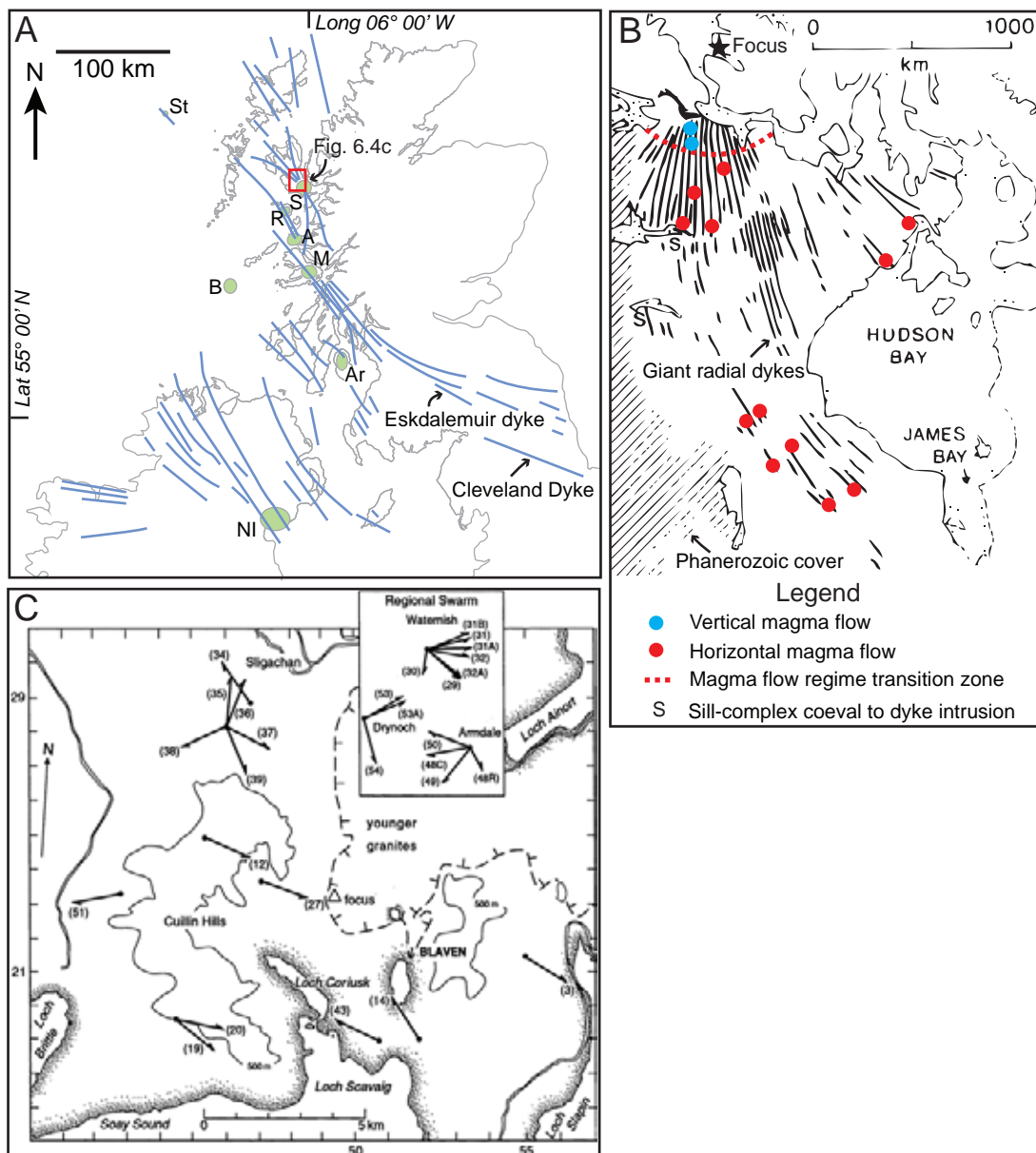


Fig. 6.4: A) Map of the BIIP highlighting the traces of the regional dyke swarm (after Ernst et al., 1995; Emelius and Bell, 2005). The central complexes are: St, St Kilda; S, Skye; R, Rum; A, Ardnamurchan; M, Mull; B, Blackstones; Ar, Arran; NI, Northern Ireland central complexes including Slieve Gullion, Carlingford and the Mourne. B) The MacKenzie dyke swarm, Canada, and magma flow regimes measured through AMS analysis (after Ernst and Baragar, 1992; Ernst et al., 1995). C) Magma flow directions of regional dykes proximal to and distal to (*inset*) the Cuillin igneous complex, Skye, determined from AMS analysis (Herrero-Bervera et al., 2003).

laterally propagating regional dykes. As magmatic sheets preferentially intrude orthogonal to  $\sigma_3$ , transition of the regional dykes to a cone sheet-like geometry may be facilitated by their deflection around the central complex upon entering the Ardnamurchan local stress field,

where the  $\sigma_3$  principal stress axis is oriented differently compared to the regional  $\sigma_3$  principal stress axis.

If this hypothesis is to be developed, the implications of the measured dip-parallel  $K_1$  lineations first need to be considered. Cone sheet dip-parallel magnetic lineations conform to the magma flow regimes predicted for centrally fed cone sheets, suggesting that at least a small minority of the Ardnamurchan cone sheets were intruded from a central source contemporaneous to the lateral propagation and deflection of regional dykes into a ‘cone sheet’ geometry. The significantly lower intrusive volume of centrally fed sheets, compared to the proposed laterally propagating regional dykes, may imply they either had a reduced magma supply or that their injection was temporally restricted. For sheet intrusion from a central magma chamber to occur, the magmatic overpressure must exceed the minimum principal stress and tensile strength of the wall rock and the mechanical properties of the heterogeneous host rock must allow magma propagation (Gautneb and Gudmundsson, 1992; Gudmundsson and Phillip, 2006). There are two processes which may inhibit centralised cone sheet intrusion. Firstly, cone sheet emplacement is suggested to alleviate the magmatic overpressure (Anderson, 1936). However, magmatic overpressure may not necessarily be accommodated by sheet intrusion (Gautneb and Gudmundsson, 1992) as is often assumed, but can also be reduced by magma chamber growth instead (Schirnack et al., 1999). Secondly, significant mechanical variation in the host rock within the close vicinity of the magma chamber may promote sheet arrest until stress field homogenization occurs (Gudmundsson and Phillip, 2006). Either of these processes, or a combination of both, may have acted to restrict cone sheet intrusion from the Ardnamurchan central complex. These localised controls on cone sheet intrusion may also explain the absence of cone sheets from some BIPIP central complexes (e.g. Slieve Gullion).

## 6.2 Magma source

Both geochemical and physical (fabrics that record magma flow pathways) methods may help

to constrain magma source. The following section summarises the relevant AMS results and provides a review of published geochemical data and their implications to the two models presented in section 6.1.6.

### **6.2.1 Viability of a laterally propagating regional dyke magma source**

The approximately 1000 km long BIPIP regional dyke swarm (Fig. 6.4a) is a giant dyke swarm (>300 km in length; Ernst et al., 1995) and may be divided into several swarms associated with specific central complexes (e.g. Mull and Skye) (Speight et al., 1982; Emeleus and Bell, 2005). Giant dyke swarms, predominantly mafic in composition, identified on Earth are typically associated with Large Igneous Provinces and interpreted to relate to an upwelling mantle plume (Ernst et al., 1995). Several studies focused on elucidating the magma flow regime of giant dyke swarms have highlighted a substantial proportion of individual dykes display evidence of lateral magma flow (Ernst et al., 1995). For example, magnetic fabric analyses of the MacKenzie dyke swarm, Canada (Ernst and Baragar, 1992); the Sudbury dyke swarm, Canada (Ernst, 1994); the Abitibi dyke swarm, Canada (Ernst et al., 1995); and the Okavango dyke swarm, Botswana (Aubourg et al., 2008) have identified that vertical magma ascent is localised to the lithospheric impingement zone of the associated mantle plume with lateral magma flow dominating beyond this area. Approximately 1600 km of lateral magma flow, within individual dykes, is interpreted from sub-horizontal to moderately plunging  $K_1$  lineations in the MacKenzie dyke swarm (Fig. 6.4b; Ernst and Baragar, 1992). Similarly, lateral magma flow regimes active during the emplacement of the BIPIP regional dyke swarms (Fig. 6.4a and c) have been suggested at Ardnamurchan (this study), Skye (Herrero-Bervera et al., 2001) and for the Eskdalemuir and Cleveland dykes ( $\leq 600$  km of lateral flow, southern Scotland-NE England; Macdonald et al., 1988, 2009).

Figure 6.4a displays the mapped pattern of the regional dykes that extend  $\sim \leq 600$  km into the western part of the North Sea off NE England, which may be projected along strike to the Mull central complex (Macdonald et al., 1988; 2009; 2010; Jolly and Sanderson, 1995; Dagley et al., 2008). Mafic compositions are dominant in the southern Scotland-

NE England regional dyke swarm, with many containing distinctive rare earth element trends comparable to the Mull lavas (Kerr et al., 1999; Macdonald et al., 1988; 2009). The Cleveland dyke (on average ~7 m thick), divisible into a series of *en échelon* segments (Macdonald et al., 1988; Dagley et al., 2008), is perhaps the most well studied dyke from this swarm of regional dykes. From geochemical similarities with lavas attributed to the Mull central complex and numerical modelling of intrusion dynamics, Macdonald et al., (1988) suggested the Cleveland dyke was rapidly emplaced (<5 days) laterally as a single pulse (~85 km<sup>3</sup>) originating from a small overpressured magma chamber in the Mull central complex. Conversely, Dagley et al., (2008) interpreted the *en échelon* segmentation, along-strike chemical heterogeneity and local dyke widths of <2 m as diagnostic of a vertical emplacement mechanism from numerous high-level, local magma reservoirs. Several hypotheses have been suggested for the development of the *en échelon* segmentation, which remain consistent with a dominantly lateral emplacement mechanism (e.g. localised post-emplacement vertical magma flow, Macdonald et al., 1988; near-surface stress field perturbations, Ernst et al., 1995). Establishment of a lateral magma flow regime within the Cleveland dyke implies other regional dykes within the southern Scotland-NE England swarm, such as the Eskdalemuir dyke, may be sourced from the Mull central complex (cf. Macdonald et al., 2009). Pinel and Jaupart (2004) and Kervyn et al., (2009) suggest that the effect of a large volcanic edifice load and presence of a lithological discontinuity (defined by a significant density contrast) in the shallow sub-surface may instigate magma storage (i.e. if the height of the volcanic edifice is relatively small) or promote development of extensive horizontal dykes (if the edifice is of a sufficient size). Using the constraints provided by Pinel and Jaupart (2004), Macdonald et al., (2009; 2010) suggested the large size of the Mull volcanic edifice (~25 km diameter; Mathieu and van Wyk de Vries, 2009) and the Neoproterozoic to Mesozoic unconformity promoted the lateral intrusion of regional dykes into southern Scotland and NE England.

It is apparent from these studies that lateral magma flow in the BIPIP regional dykes was possible. Although numerous studies have identified regional dykes which likely propagated laterally from the Mull central complex toward the SE (e.g. Macdonald et

al., 1988; 2009; 2010; Jolly and Sanderson, 1995), no dykes propagating to the NW have previously been correlated and the magma source for the BIPIP regional dykes remains uncertain. The areal coverage and positive 50 mGal Bouguer gravity anomaly determined for both the Mull central complex and the Skye central complex, suggest remnant intrusive volumes ( $<3600 \text{ km}^3$ ) significantly greater compared to Ardnamurchan ( $237\text{--}509 \text{ km}^3$ ) (Bott and Tuson, 1973). Using this volume as a proxy for the size of the volcanic edifice, it may be suggested that the Skye central complex is also a viable source for laterally propagating regional dykes. This may be supported by the fanning arrangement of the regional dykes (including the Glenbrittle and Scalpay sub-swarms) surrounding the Skye central complex (Speight et al., 1982). Regardless of whether regional dykes originated from Ardnamurchan, it is likely that some laterally propagating regional dykes were sourced from Mull ( $\sim 30 \text{ km}$  SE of Ardnamurchan) and/or Skye ( $\sim 50 \text{ km}$  N of Ardnamurchan). Alternative models for the magma source of the regional dykes have suggested emplacement from an extensive subsurface ridge-like source, implying a vertical magma flow regime (Speight et al., 1982) or from an associated plume head source (e.g. MacKenzie dike swarm, N America, Ernst and Baragar, 1992; Ernst et al., 1995). The regional dykes on Ardnamurchan therefore potentially derive from multiple and spatially separate sources.

### **6.2.2 Geochemistry of the Ardnamurchan cone sheets**

A means of distinguishing between centrally fed and laterally fed cone sheets might be to examine the geochemical characteristics of the Ardnamurchan intrusions and compare these with the intrusive products of other central complexes. Broad spatially controlled compositional groupings of BIPIP igneous lithologies, corresponding to proximity to specific central complexes, are observed (Emeleus and Bell, 2005). Centrally fed cone sheets should therefore be characteristically similar to other intrusions on Ardnamurchan whilst laterally fed cone sheets may display geochemical trends attributable to their specific source (e.g. the Mull central complex). However, caution is required when interpreting major and trace element geochemical trends as significant localised compositional variation exists within all of the

BIPIP intrusions and extrusions (Kerr et al., 1999; Emeleus and Bell, 2005). A more reliable method of differentiating the potential source of the Ardnamurchan cone sheets might be through the analysis of radiogenic isotope ratios (e.g. Sr, Nd and Pb), which are sensitive to crustal contamination (Geldmacher et al., 1998; 2002; Emeleus and Bell, 2005). It is beyond the scope of this project to carry out a detailed isotopic study of the Ardnamurchan intrusions, but some work has already been carried out that has direct relevance to the problem of interest. Isotope systematics (e.g.  $^{143}\text{Nd}/^{144}\text{Nd}$ ,  $^{87}\text{Sr}/^{86}\text{Sr}$ ,  $^{208}\text{Pb}/^{204}\text{Pb}$  and  $^{206}\text{Pb}/^{204}\text{Pb}$ ) indicate that the three major host rocks underlying the NW Scotland BIPIP section (i.e. granulite-facies Lewisian Gneiss, amphibolite-facies Lewisian Gneiss and the Neoproterozoic Moine metasedimentary rocks) are readily distinguishable (Dickin, 1981; Emeleus and Bell, 2005). During magma transport and storage in the lithosphere, magma inevitably interacts with and potentially assimilates surrounding country rock, incorporating an isotopic signature of the respective host rock (Kerr et al., 1995; Geldmacher et al., 1998; Emeleus and Bell, 2005). Therefore, magma pathways, likely unique to each central complex due to the variable crustal configurations, might be derived from the isotopic analysis of the percentage and assemblage of assimilated host rocks. The following section presents a summary of some of the relevant geochemical and isotopic studies on Ardnamurchan and elsewhere, comparing the compositions of the cone sheets from Ardnamurchan with those from Skye, Rum, Mull and southern Scotland-NE England to assess whether the magma sources for the Ardnamurchan cone sheets can be constrained.

The geochemical and isotopic data utilised here is collated from a comprehensive review of previous studies. Geldmacher et al., (1998; 2002) provide a comprehensive series of major and trace element chemical data, along with isotopic data (i.e.  $^{143}\text{Nd}/^{144}\text{Nd}$ ,  $^{87}\text{Sr}/^{86}\text{Sr}$ ,  $^{208}\text{Pb}/^{204}\text{Pb}$  and  $^{206}\text{Pb}/^{204}\text{Pb}$ ), for a selection of Ardnamurchan Centre 2 cone sheets. There is no apparent compositional distinction between the Centre 1 and Outer Centre 2 cone sheets (Holland and Brown, 1972) or the Outer and Inner Centre 2 (Geldmacher et al., 1998) cone sheet populations. In the absence of isotopic data for the Centre 1 and the volumetrically negligible Centre 3 cone sheets, it is assumed that the Centre 2 cone sheet geochemical data of

Geldmacher (1998; 2002) are representative of the Ardnamurchan cone sheets. See Appendix F for a table of the collated major, trace element and isotopic data referenced, together with the data sources.

#### 6.2.2:1 *Geochemistry of the Ardnamurchan cone sheets*

Tholeiitic basalts dominate the cone sheet lithologies on Ardnamurchan, with major and trace element geochemistry allowing the distinction of high (>4.6 wt. %) and low (<4.6 wt. %) MgO types; these subgroups are also distinguishable based on their  $^{87}\text{Sr}/^{86}\text{Sr}$  and  $^{143}\text{Nd}/^{144}\text{Nd}$  isotopic compositions and from rare earth element (REE) trends (Geldmacher et al., 1998). Geldmacher et al., (1998) defined the two MgO type cone sheets as basaltic (>4.6 wt. %) and evolved (<4.6 wt. %), a classification also utilised here. From a total alkalis vs.  $\text{SiO}_2$  (TAS) diagram, the evolved cone sheets may compositionally be classed as basaltic ( $n = 1$ ) or trachy-andesite to rhyolite ( $n = 4$ ) and display an enriched REE profile, particularly with respect to the light rare earth elements (LREE), compared to the basaltic sheets (Fig. 6.5) (Geldmacher et al., 1998). Geldmacher et al., (1998; 2002) attribute this difference in REE values, as well as distinguishable variations on  $^{143}\text{Nd}/^{144}\text{Nd}$  against  $^{87}\text{Sr}/^{86}\text{Sr}$ ,  $^{208}\text{Pb}/^{204}\text{Pb}$  against  $^{206}\text{Pb}/^{204}\text{Pb}$  and  $^{207}\text{Pb}/^{204}\text{Pb}$  against  $^{206}\text{Pb}/^{204}\text{Pb}$  plots, to a greater percentage of crustal contamination in the evolved cone sheets by a host rock rich in incompatible LREE (i.e. La to Sm).

Overall, the basaltic cone sheets appear contaminated by lower crustal granulite-facies Lewisian Gneiss, similar to the evolved cone sheets, which also display evidence of Neoproterozoic Moine metasedimentary rock assimilation (Geldmacher et al., 1998; 2002). No assimilation of amphibolite-facies Lewisian Gneiss is apparent in any of the Ardnamurchan cone sheets (Geldmacher et al., 1998; 2002). From these observations Geldmacher et al., (1998; 2002) suggested a basaltic cone sheet magma that fractionated in a magma chamber at ~10 km depth (i.e. hosted in the granulite-facies Lewisian Gneiss) was transported vertically to an upper crustal magma chamber within the Neoproterozoic Moine metasedimentary rocks, bypassing with little or no interaction the amphibolite-facies Lewisian Gneiss. The contamination trends imply the basaltic cone sheets were emplaced virtually

immediately after ponding in the upper crust, before interacting with the host rock, whilst some magma (i.e. the evolved cone sheets) had a greater residence time allowing further fractionation and assimilation of the Moinian wall rocks (Geldmacher et al., 1998; 2002). Importantly, Geldmacher et al., (1998; 2002) highlighted that the sustained temperatures required for partial fusion of the crustal rocks could only be generated by a major magma reservoir and not by thin (<10 m thick) cone sheets or regional dykes.

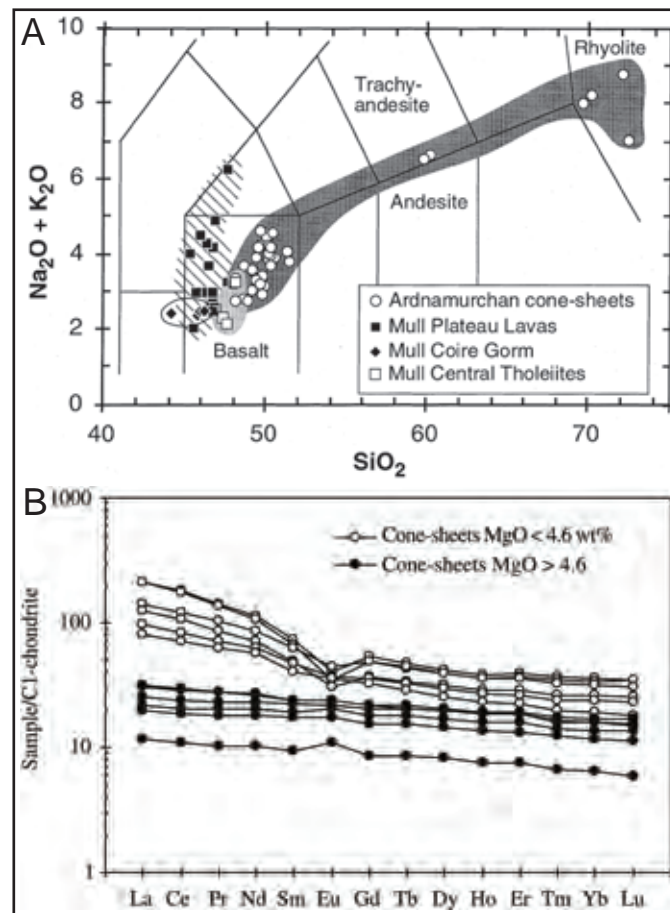


Fig. 6.5: A) A total alkalis vs. silica plot of the Ardnamurchan cone sheets and the three geochemical divisions of the basalt lavas associated with the Mull central complex (Geldmacher et al., 1998). B) Rare earth element plot highlighting the difference between the basaltic and evolved Ardnamurchan cone sheets.

#### 6.2.2:2 Geochemical trends and correlations with other BIPIP intrusions/extrusions

1.  $\text{SiO}_2$  vs.  $\text{Na}_2\text{O} + \text{K}_2\text{O}$ : A TAS diagram reveals that the Ardnamurchan cone sheets may typically be classified as tholeiitic basalts (Geldmacher et al., 1998) and overall describe a similar range in composition to the Mull cone sheets (Fig. 6.6a). Minor

overlap is also observed with the Mull Central Tholeiite lavas, regional dykes and the Hypersthene Gabbro of Ardnamurchan (Fig. 6.6a).

2. *MgO wt. % vs. TiO wt. %*: The relationship between these two major elements potentially allows fractionation and mixing processes to be defined (Kerr et al. 1999). An overlapping positive correlation is initially observed in the Ardnamurchan, Mull and Skye cone sheets and is comparable to similar ranges for the Mull regional dykes, Mull Plateau Group (MPG) lavas and the Marginal Border Group of the Hypersthene Gabbro (Fig. 6.6b). At ~4 wt. % MgO there is a marked downwards deflection to a negative slope of the MPG lavas (Fig. 6.6b). Between 0–4 MgO wt. % the Ardnamurchan cone sheets and Mull cone sheets and regional dykes display a vague negative slope parallel to that of the MPG lavas (Fig. 6.6b). Kerr et al., (1999) interpreted this convex-upwards pattern as representative of the initial fractionation of a Fe-Ti oxide or apatite mineral phase. Ranging from ~3–7 MgO wt. % and occurring at ~1 TiO wt. % some of the Ardnamurchan and Mull cone sheets, as well as the Loch Scridain sill-complex of Mull and southern Scotland-NE England regional dykes, describe a horizontal line that bypasses the apex of the fractionation trend (Fig. 6.6b). This relationship has been attributed cryptic magma mixing (Kerr et al., 1999), which is evidenced in the field by the composite nature of some cone sheets (e.g. Bailey et al., 1924; Richey and Thomas, 1930) and regional dykes (e.g. Macdonald et al., 2009).
3. *Feldspar compositions*: Figure 6.6c, a ternary Ab-An-Or diagram, displays groundmass plagioclase composition ranges for the Ardnamurchan cone sheets, the Sithean Mor intrusion (part of the Centre 3 Layered Gabbro Lopolith), the Loch Scridain sill-complex and the Eskdalemuir regional dyke. As might be expected from rocks of all broadly basaltic composition, significant overlap is observed between all intrusions represented (Fig. 6.6c).
4. *Rare earth element (REE) patterns*: All REE values presented are chondrite normalised (Sun and McDonough, 1989). Comparison of the REE trends reveals that the various sheet intrusion suites analysed and the MPG lavas display a greater

variability in the LREE compared to the heavy rare earth elements (HREE) (Fig. 6.6d). The ranges for the Ardnamurchan cone sheets and Centre 3 gabbros, Mull cone sheets, the Loch Scridain sill-complex and the regional dykes all overlap and display a negative slope (Fig. 6.6d). In contrast, the Skye cone sheets, although partially overlapping with other intrusive/extrusive ranges for the LREE, display a sub-horizontal trend with significantly increased HREE values (Fig. 6.6d). On closer inspection, the basaltic Ardnamurchan cone sheets display sub-horizontal slopes, comparable to those of the representative Coire Gorm type and Central Mull Tholeiite type lavas of Mull, as well as the Skye cone sheets (Fig. 6.6d).

5.  *$^{87}\text{Sr}/^{86}\text{Sr}$  and  $^{143}\text{Nd}/^{144}\text{Nd}$  isotopic compositions:* Isotopic ratio comparisons, particularly those of Sr and Nd, can provide important information on magma sources and crustal contamination (Dickin, 1981; Emeleus and Bell, 2005). It is assumed all magmas originated with a primitive mantle melt composition (Meyer et al., 2009) and through assimilation of different crustal components, obtained distinctive radiogenic isotope ratio trends. The forward projection of individual intrusive suite trends identifies the principal crustal contaminant. Geldmacher et al., (1998) showed that the Ardnamurchan basaltic cone sheets (>4.6 wt. % MgO) exhibit an overlap with the MPG compositions with respect to initial  $^{143}\text{Nd}/^{144}\text{Nd}$  isotopic compositions (Fig. 6.7). The overall range of initial (60 Ma)  $^{87}\text{Sr}/^{86}\text{Sr}$  and  $^{143}\text{Nd}/^{144}\text{Nd}$  isotopic compositions of 0.70528–0.71096 and 0.51185–0.51220, respectively, reported by Geldmacher et al., (1998) for the Ardnamurchan cone sheets overlaps with the field of the Mull cone sheet data (Fig. 6.7). The Ardnamurchan and Mull cone sheets with MgO contents >4.6 wt. % both describe a steep negative slope, which may be projected forward to the granulite-facies Lewisian Gneiss range (Fig. 6.7). Geldmacher et al., (1998) suggest this trend and the low Nd isotopic ratios observed in the Ardnamurchan cone sheets reflect >5 % contamination by lower crustal granulite-facies Lewisian Gneiss; a similar conclusion to that reached for the Mull magmas (cf. Kerr et al., 1995). In contrast, the slope of the Rum intrusions and the

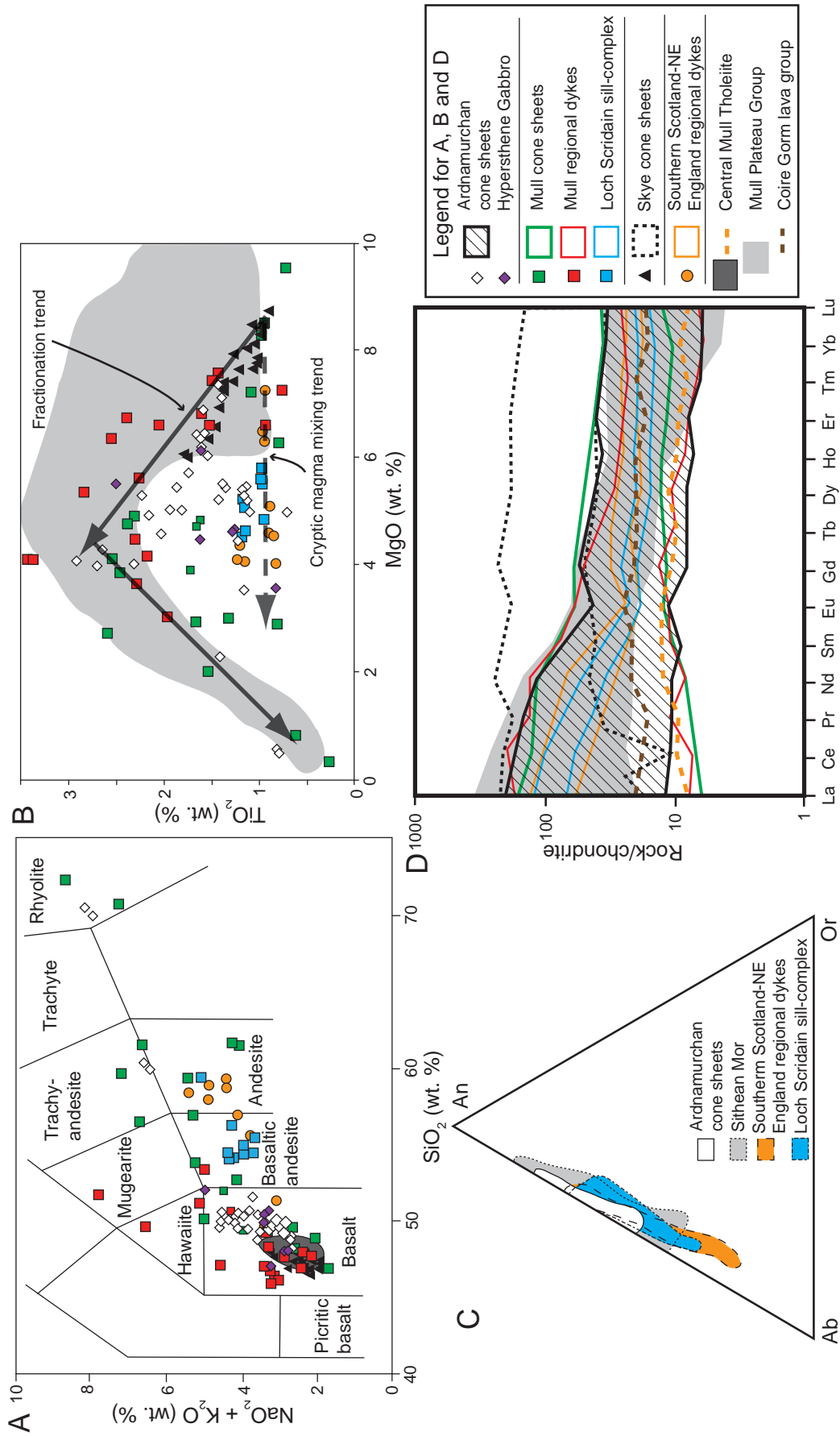


Fig. 6.6: A series of major and rare earth element geochemical plots, comparing data obtained from the Ardnamurchan cone sheets and other intrusions and extrusions within the BIIP (see Appendix F for raw data and references). The Central Mull Tholeiite and Mull Plateau Group ranges are from Kerr et al., (1999). A) A total alkalis vs. silica plot. B) A plot of TiO<sub>2</sub> (wt %) against MgO (wt %). C) Ternary Ab-An-Or diagram. D) Rare earth element diagram. See text for explanations.

initial portion of Loch Scridain sill-complex project towards the amphibolite-facies Lewisian Gneiss range (Fig. 6.7). At  $\sim 0.512$   $^{143}\text{Nd}/^{144}\text{Nd}$ , the Ardnamurchan and Mull cone sheet trend, defined by samples with MgO contents  $< 4.6$  wt. %, along with the Loch-Scridain sill-complex curve becomes horizontal and may be traced into the Neoproterozoic Moine metasedimentary rock range (Fig. 6.7). There is no apparent compositional relationship between the Ardnamurchan and Skye cone sheets (Fig. 6.7). Unfortunately no Sr–Nd isotopic data is available for the BIPIP regional dykes.

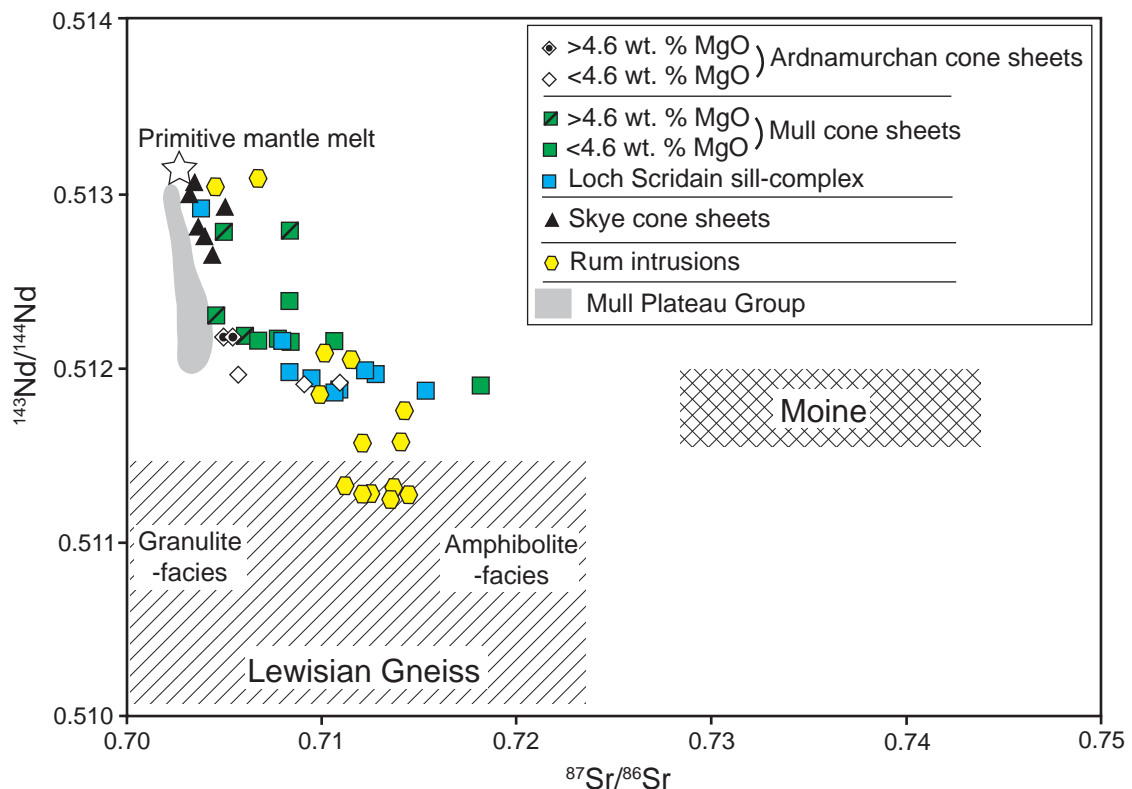


Fig. 6.7: Plot of  $^{87}\text{Sr}/^{86}\text{Sr}$  and  $^{143}\text{Nd}/^{144}\text{Nd}$  radiogenic isotopic compositions. The Lewisian and Moine metasedimentary rock composition ranges are taken from Kerr et al., (1999) and the primitive mantle melt composition is from Meyer et al., (2009).

### 6.2.2.3 Implications of the geochemical correlations between separate intrusions

The collated geochemical data reveals significant overlap between the data ranges of the Ardnamurchan cone sheets, major intrusions of the Ardnamurchan central complex (i.e. the Hypersthene Gabbro and the Centre 3 Layered Gabbro Lopolith) and the intrusive and extrusive products of the Mull central complex (Fig. 6.6 and 6.7). It is important to note that the similarities in major and trace element data ranges observed may simply

reflect regional BIPIP trends dictated by similar parental magma compositions, melt generation depths, fractionation processes and central complex evolution (Emeleus and Bell, 2005), rather than a close genetic link attributable to a common upper crustal source reservoir. However, correlations between the Ardnamurchan cone sheets and the Mull cone sheets and Loch Scridain sills are also importantly observed on a plot of  $^{87}\text{Sr}/^{86}\text{Sr}$  against  $^{143}\text{Nd}/^{144}\text{Nd}$ . As radiogenic isotopes, particularly  $^{87}\text{Sr}/^{86}\text{Sr}$  and  $^{143}\text{Nd}/^{144}\text{Nd}$ , are sensitive to crustal contamination they provide a record of magma ascent pathways and storage sites (Geldmacher et al., 1998; 2002). The overlap observed in Figure 6.7 between the variable intrusive forms therefore provides a compelling suggestion of a genetic link between magma emplaced in Mull and Ardnamurchan, which may also be reflected in the major and trace element similarities. From the geochemical data comparisons presented, neither the Ardnamurchan nor Mull central complexes can be dismissed as potential magma sources for the Ardnamurchan cone sheets. As only a minor degree of correlation is observed between the Ardnamurchan and Skye cone sheets, it is suggested that the corresponding differences reflect fundamental variations in magma evolution (i.e. fractionation trends and contamination processes) and that the Ardnamurchan cone sheets were not likely sourced from the Skye central complex.

#### *6.2.2:4 Integration of crustal contamination trends with the derived sub-surface geology of Ardnamurchan*

Geldmacher's et al., (1998; 2002) interpretation of the Ardnamurchan cone sheet crustal contamination trends relies on a series of assumptions pertaining to upper crustal structure: 1) the Moine Thrust, inferred to dip at 20–25° dip and intersecting the surface ~6 km from the Ardnamurchan central complex (Geldmacher et al., 2002), is located at a shallow depth (~3 km; calculated trigonometrically following the procedure outlined in Chapter 4, section 3.1.2:1) beneath Ardnamurchan (Geldmacher et al., 1998); 2) the common focal points of the Ardnamurchan cone sheets converge on an upper crustal central source at ~2.5 km depth and 3) the magma source of the Ardnamurchan cone sheets was situated fully within the

Neoproterozoic Moine host rock to explain the lack of amphibolite-facies Lewisian Gneiss contamination. Whilst Geldmacher et al., (1998) adopt the two-tiered Lewisian Gneiss structure (i.e. basal granulite-facies overlain by amphibolite-facies) of Dickin (1981), it is important to highlight that this is probably highly oversimplified (Wheeler et al. 2010). However, as there is no new information on the structure of the Lewisian Gneiss beneath Ardnamurchan and to maintain context with previous models (i.e. Geldmacher et al., 1998; 2002), the following discussion assumes a two-tiered Lewisian Gneiss *sensu* Dickin (1981).

A principal issue arising from these inferences concerns the wall rocks in contact with the upper crustal magma reservoir. The evolved cone sheets display geochemical trends consistent with crustal assimilation and concomitant fractional crystallisation (AFC) (Geldmacher et al., 1998), whereby the latent heat of crystallisation released from a fractionating magma in a major reservoir partially melts the wall rock (Kerr et al., 1995). Therefore, any country rock in contact with the magma chamber is likely to be partially assimilated. From the arguments of Geldmacher et al., (1998; 2002), the upper crustal magma reservoir (~2.5 km depth) was situated close to the Moine Thrust (~3 km depth). Recent field and experimental studies of igneous intrusions have highlighted a tendency for magma to exploit major structural and lithological discontinuities (e.g. Horsman et al., 2005; Kavanagh et al., 2006; Burchardt, 2008; Menand, 2008; Morgan et al., 2008; Thomson and Schofield, 2008; Schofield et al., 2010). If a similar structural control on the position of the Ardnamurchan cone sheet source is envisaged, the magma chamber may have been located at the Moine Thrust in contact with both amphibolite-facies Lewisian Gneiss and Neoproterozoic Moine metasedimentary rocks. Hence, it is important to further delineate the potential magma chamber and host rock configuration. This may be achieved through combining the sub-surface geological constraints identified in Chapter 3 and cone sheet structural measurements presented in Chapter 4.

Figure 6.8 shows a schematic cross-section through Ardnamurchan, constructed to determine the approximate range of host rock interactions for the Ardnamurchan Centre 2 cone sheet source. Along the horizontal axis representing distance from the Centre 2 foci

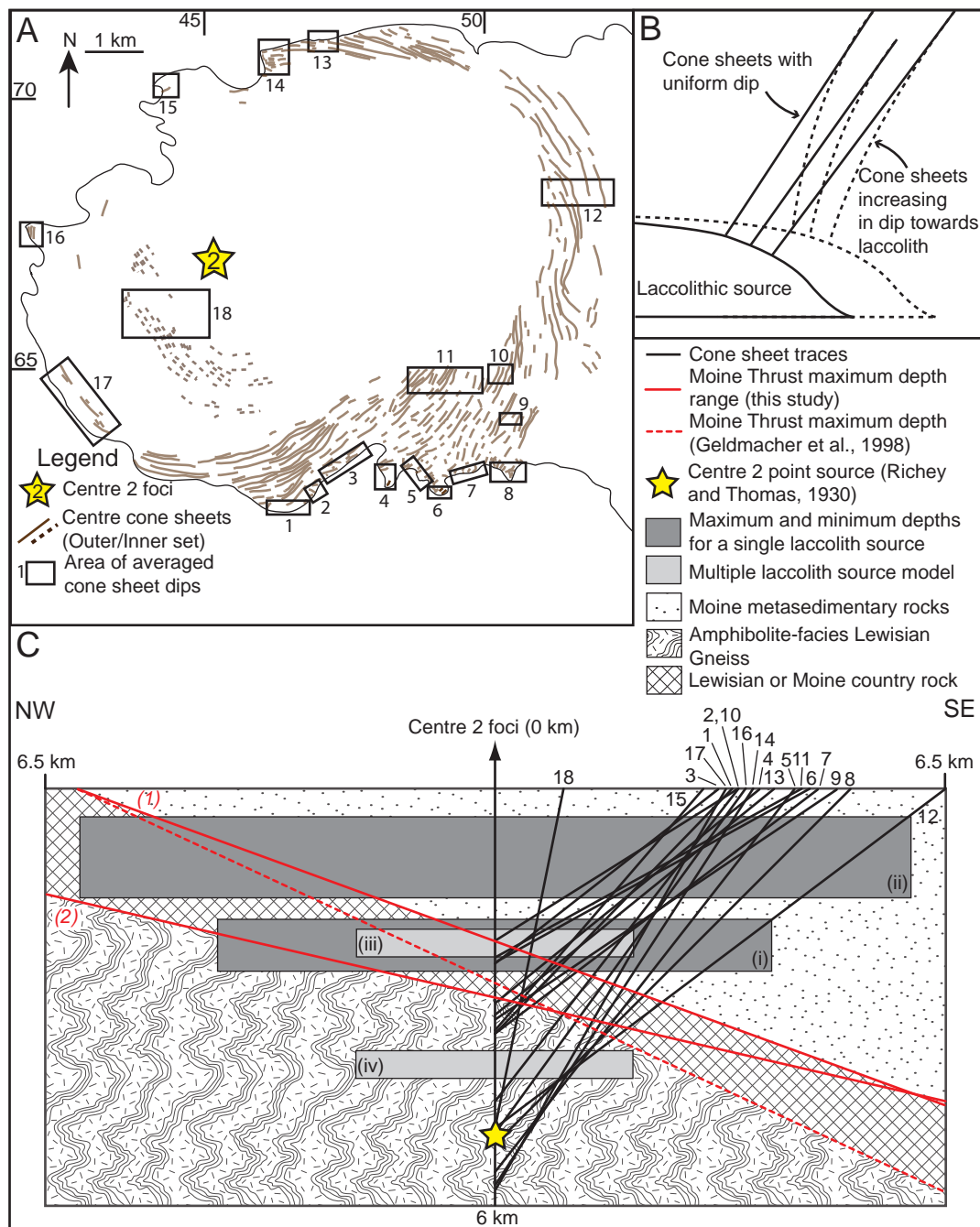


Fig. 6.8: A) Map of areas used to calculate average cone sheet dip angles for (C). B) Schematic diagram highlighting how extrapolating the trumpet-like Centre 2 cone sheets as straight lines for simplicity may underestimate the width of a modelled source laccolith. C) Schematic cross-section through Ardnamurchan, oriented orthogonally to the Moine Thrust strike and passing through the Centre 2 foci of Richey and Thomas (1930). The areas defined in (A) have been transposed onto the cross-section at a point equal to their distance from the Centre 2 foci. Potential Moine Thrust projections calculated in Chapter 3 (section 3.2.1:1) for the steepest dip (1; 25°) and furthest surface intersection distances (2; 13 km) relative to the Ardnamurchan central complex have also been incorporated to constrain the likely range of the maximum depth of the Moine Thrust beneath Ardnamurchan and the sub-surface geology. See text for explanation.

(Richey and Thomas, 1930), specific areas are plotted where an average Centre 2 cone sheet dip angle has been calculated (Fig. 6.8a). The average dips of the inwardly inclined cone sheets have been extrapolated straight down-dip, for each area, until they intersect with the vertical central axis (Fig. 6.8c). Following Richey and Thomas (1930), Anderson (1936), Phillips (1974), Gautneb et al., (1989) and Walker (1993), amongst others, the central axis is inferred to also define the central axis of the proposed upper crustal magma source. The majority of cone sheet emplacement models suggest intrusion occurs primarily from the shoulders of a central source (e.g. Phillips, 1974; Gautneb et al., 1989; Schirnack et al., 1999); implying cone sheet trajectories may be employed to constrain the approximate width of the central magma reservoir from the central axis (Fig. 6.8c). Assuming a central laccolith beneath Ardnamurchan was the source of the Centre 2 cone sheets, the empirical power law describing the scale invariant relationship between laccolith width (L) and thickness (T) (Petford et al., 2000) may be used to constrain the source extent. The empirical power law is expressed as:

$$T = bL^a$$

where  $a$  and  $b$  are constants equal to 0.88 and 0.12 respectively (Cruden and McCaffrey, 2001). It is important to note that although several studies have utilised planar down-dip projections of cone sheets to define central source positions (e.g. Ancochea et al., 2003; Burchardt and Gudmundsson, 2009; Siler and Karson, 2009; Burchardt et al., 2011; Tibaldi et al., 2011), it is assumed individual cone sheets have a uniform dip and that there is no variation in cone sheet dip with distance from the central complex (see Burchardt et al., 2011). The Ardnamurchan Centre 2 cone sheet swarm however displays a trumpet-like morphology (cf. Gautneb et al., 1989; Gudmundsson, 1998; Burchardt et al., 2011), with dip decreasing from the central complex (Chapter 4). Therefore, from the planar cone sheets, adopted for simplicity and as the curvature of the cone sheets is not known, the source reservoir width will likely be underestimated (Fig. 6.8b) (Burchardt et al., 2011). Finally, the addition of two

Moine Thrust projections spanning the range of maximum depths (2.18–3 km), calculated for variable dip and surface intersection configurations (Chapter 3, section 3.1.2), allows the amphibolite-facies Lewisian Gneiss and Neoproterozoic Moine metasedimentary rock areas to be constrained.

Although individual area cone sheet projections are variable in terms of where their central axis intersects, two poorly constrained clusters may be identified at depths of ~3 km and ~5 km (Fig. 6.8c). There are two overarching models, which may explain the inferred sub-surface cone sheet dispositions; a single laccolith source (*sensu* Schirnick et al., 1999), supported by the geochemical homogeneity of the cone sheets, or multiple laccolithic sources (*sensu* Burchardt and Gudmundsson, 2009; Siler and Karson, 2009; Burchardt et al., 2011). The maximum depth of a single laccolithic reservoir is calculated to be at ~2–2.5 km (where  $L = 8$  km and  $T = 0.75$  km) (Fig. 6.8c i). A laccolith at a greater source depth would not intersect some cone sheets before they reach the central axis; inconsistent with all previous emplacement models. A shallower reservoir depth may be applied as long as there is a proportionate increase in  $L$  and  $T$ . For example, a source laccolith at a current depth of ~1 km would require a minimum diameter of 12 km (Fig. 6.8c ii). It should be noted that none of the major intrusions of the Ardnamurchan central complex currently exposed at the surface are considered to be sources for the cone sheets (Richey and Thomas, 1930). To maintain intrusion of cone sheets from the shoulders of the reservoir, a model of inflation and deflation *sensu* Schirnick et al., (1999) may be envisaged. Alternatively, two laccolith sources may be modelled at depths of 2 km and 4 km, both with widths of ~4 km (Fig. 6.8c iii and iv).

Although the relationships modelled in Figure 6.8c suggest that the central source laccolith developed at <3 km depth (*sensu* Geldmacher et al., 1998), its lateral extent and the dip and proximity of the Moine Thrust would likely result in partial contact with the amphibolite-facies Lewisian Gneiss (Fig. 6.8c and 6.9). The exception to this, for the model at least, may be a shallow (<1 km) source reservoir ( $L = >10.6$  km and  $T = >1.2$  km) with a Moine Thrust configuration of ~<13° dip and ~>13 km surface intersection (Fig. 6.8c). However, as only the maximum Moine Thrust depths are plotted and accounting for the actual

trumpet-like morphology of the cone sheets, which will either increase the depth or width of the source reservoir, it is likely that the degree of contact between the laccolith and the amphibolite-facies Lewisian Gneiss, assuming a two-tiered Lewisian Gneiss structure (*sensu* Dickin, 1981), is underestimated by the schematic model. The question therefore arises as

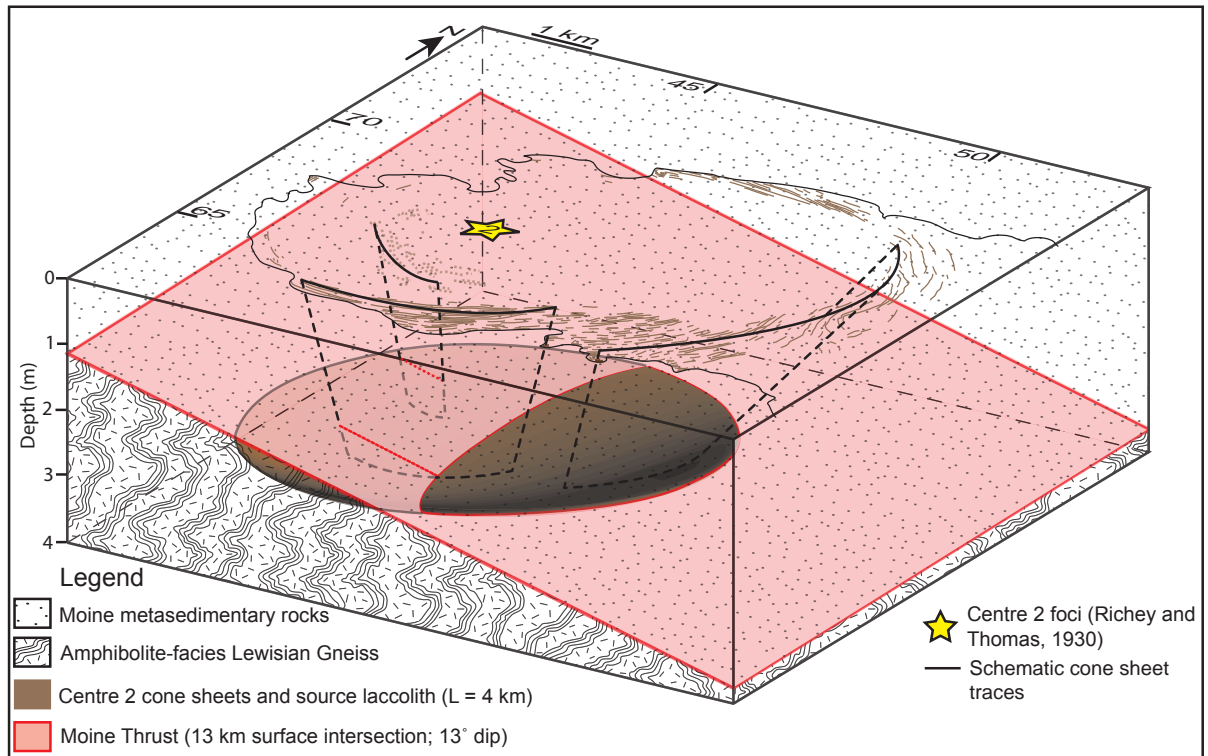


Fig. 6.9: Schematic 3D block diagram of the sub-surface geology and possible position of a central source laccolith to the Centre 2 cone sheets defined in Figure 6.8c i. Although the laccolith has been depicted as horizontal, it may also be inclined along the plane of the Moine Thrust. Importantly, the central laccolith is in contact with both the Neoproterozoic Moine metasedimentary rock and the amphibolite-facies Lewisian Gneiss.

to why no evidence of amphibolite-facies Lewisian Gneiss assimilation is observed in the evolved cone sheets yet contamination from the Moinian host rock is apparent.

The observed contamination trends of the Ardnamurchan cone sheets may perhaps be better reconciled with a source in the Mull central complex. Although the sub-surface geology of Mull is not as tightly constrained as that of Ardnamurchan, it is likely the Moine Thrust is vertically deeper beneath the central complex as its surface intersection is ~30 km NW (Fig. 6.10). This is supported by Kerr et al., (1999) who suggested the shallow magma reservoirs of Mull were situated fully within the Moine host rock (Fig. 6.10). Furthermore, Sr–Nd of

the Ardnamurchan cone sheets correlates to and overlaps with the range of the Mull cone sheets. It therefore seems permissible, on isotopic grounds as well as structural constraints on

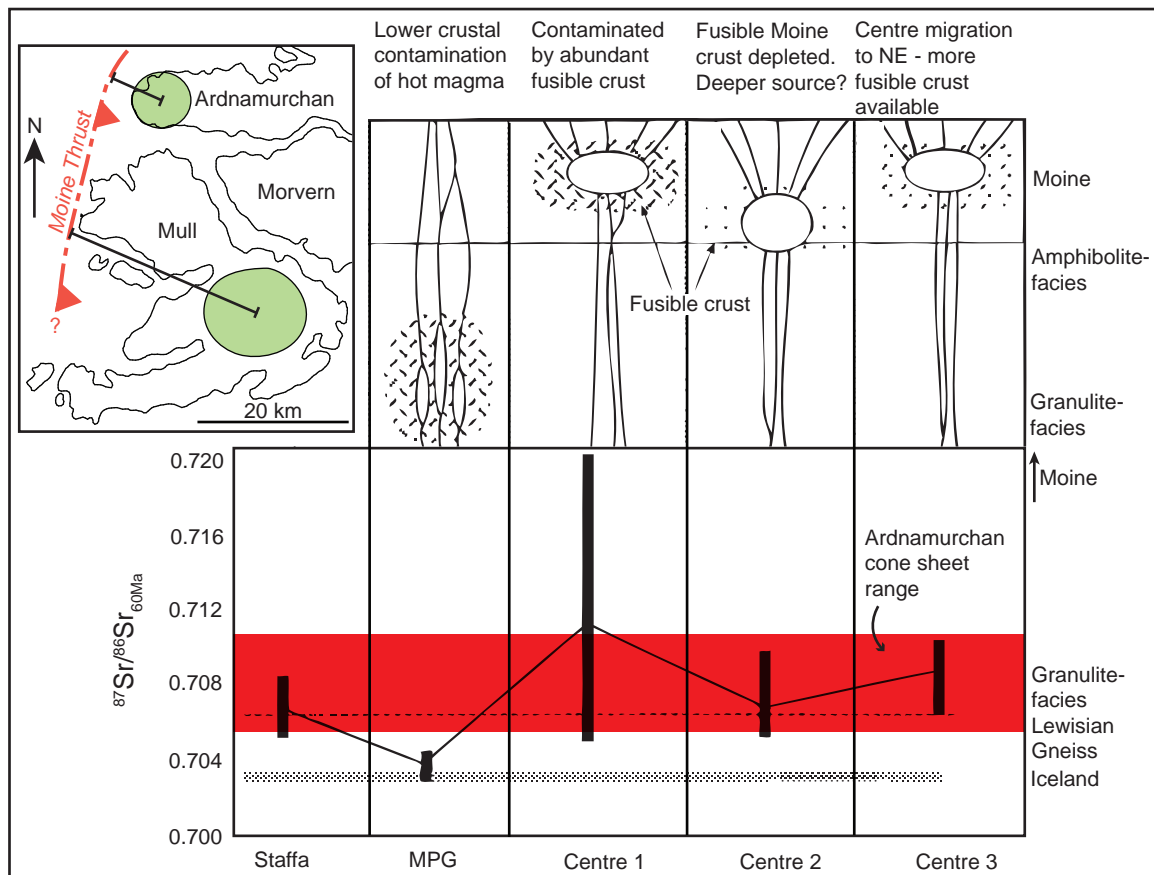


Fig. 6.10: Inferred evolution and upper crustal magma source position of the Mull central complex (Kerr et al., 1999). Note the position of the upper crustal reservoirs relative to the host rock for Centres 1 and 3. The range of the Ardnamurchan  $^{87}\text{Sr}/^{86}\text{Sr}$  values is also shown. *Inset:* Map showing the relative distances between the Moine Thrust surface intersection and the Ardnamurchan and Mull central complexes (after Emeleus and Bell, 2005).

the underlying crustal rocks, that the Ardnamurchan cone sheet magma was derived from the Mull central complex.

### 6.3 Influence of the regional stress field

It has already been established that the orientation of the principal stress axes during intrusion may significantly affect sheet geometry and disposition. Numerous studies have highlighted the importance of the regional stress field, as well as the local stress field, to

sheet emplacement (Anderson, 1936; Anderson, 1951; Gautneb et al., 1989; Gautneb and Gudmundsson, 1992; Gudmundsson, 1998; Schirnick et al., 1999; Gudmundsson, 2002; Geshi, 2005; Paquet et al., 1997; Pasquarè and Tibaldi, 2007; Acocella and Neri, 2009). The majority of these studies consider the two stress fields independently, implying that there is an abrupt division between the two. For example, Gautneb and Gudmundsson (1992) and Gudmundsson (1998) interpreted the marked change between cone sheet and regional dykes, 9 km from the Reykjadalur central volcano (Iceland), as evidence for a division between the local and regional stress fields. Realistically, there is likely a gradational transition zone between the contemporaneous local and regional stress fields (e.g. Geshi, 2005; Klausen, 2006; Pasquarè and Tibaldi, 2007; Kervyn et al., 2009). The influence each stress field exerts on sheet emplacement will depend on their relative magnitudes (Pasquarè and Tibaldi, 2007) and the proximity of the intrusion site to the source of the local stress field. Gautneb and Gudmundsson (1992) calculated the magnitude of a local stress field, associated with an overpressured magma chamber, inversely decreases to the cube of the distance from the source. When the local stress field is relatively weak (e.g. distal to its source), the regional stress field will strongly influence intrusion resulting in a preponderance of regional dykes. In contrast, if the local stress field is dominant, the regional stress field will have a minimal effect on emplacement dynamics (Geshi, 2005), potentially resulting in cone sheet intrusion. Sheet geometry is consequently also controlled by the timing of emplacement relative to fluctuations in the stress fields. Evidence on Ardnamurchan of fluctuation between extensional and compressional regimes (see Chapter 4) suggests a dynamic interplay between the regional and local stress fields occurred (cf. Richey and Thomas, 1930), with the sub-vertical regional dykes intruded when the local stress field was weaker and the regional stress field was dominant. This may possibly be exemplified by the Inner Centre 2 cone sheet set, which may have intruded under a dominant regional stress field following relaxation of the local stress field, thus resulting in NW-SE oriented sub-vertical intrusions. The emplacement of the Ben Hiant Dolerite (discussed in Chapter 7) derived from field observations and AMS analysis also provides evidence of stress field fluctuations and interference.

Various aspects of local and regional stress field interaction are discussed in the following sub-sections pertaining to the identification of potentially viable magma sources for the Ardnamurchan cone sheets.

### 6.3.1 Cone sheet abundance variations

The majority of cone sheet complexes described are interpreted to have intruded in magmatic systems associated with contemporaneous regional extension (e.g. the BIPIP, England, 1988; Iceland, Gautneb et al., 1989; Gran Canaria, Schirnick et al., 1999). Within individual central complexes in these areas, cone sheet distribution is often observed to be disproportionately greater in particular geographical quadrants (e.g. N, NE, E) with respect to the central complex and the regional principal stress axes orientations (Walker, 1975b). Cone sheets are most abundant in quadrants aligned with either the regional  $\sigma_1$  axis (e.g. Ardnamurchan, Richey and Thomas, 1930; Skye, Walker, 1993) or the regional  $\sigma_3$  axis (e.g. La Gomera, Canary Islands, Ancochea et al., 2003; Thverartindur, Iceland, Klausen, 2004; Otoge, Japan, Geshi, 2005) intersection with the central complex. This relationship may potentially be attributed to the influence of the regional stress field. Dilatational opening of cone sheets requires both uplift and crustal extension, which assuming intrusion orthogonal to the  $\sigma_3$  axis occurs (Anderson, 1951), suggests centrally fed cone sheets should preferentially intrude in a direction equivalent to the regional  $\sigma_3$  axis, so that their strike is parallel to  $\sigma_1$ . This suggestion is supported by the distribution of the centrally sourced cone sheets of the Otoge igneous complex (Japan), which are more abundant to the E and W of the igneous complex and were intruded during regional extension where  $\sigma_3$  was oriented sub-horizontally E-W (Fig. 6.11a) (Geshi, 2005). In contrast, lateral propagation of regional dykes towards, and deflected around, a central complex should result in the concentration of cone sheets in one or both geographical sectors that contain the intersection between the regional  $\sigma_1$  axis and the central complex (Fig. 6.11b). Throughout the evolution of the BIPIP,  $\sigma_3$  was oriented NE-SW, as indicated by the NW-SE strike of the regional dyke swarms (Speight et al., 1982; England, 1988). Given the regional  $\sigma_3$  axis, cone sheets derived from a central source

should therefore be more abundant to the NE and SW of the Ardnamurchan central complex. However, the Ardnamurchan cone sheets are more abundant to the SE of the central complex (the NW quadrant is offshore). The observed distribution and abundance of the Ardnamurchan cone sheets, in quadrants containing the regional  $\sigma_1$ –central complex intersection (i.e. SE), therefore does not conform to the expected distribution for centrally fed cone sheets but supports a regional dyke origin.

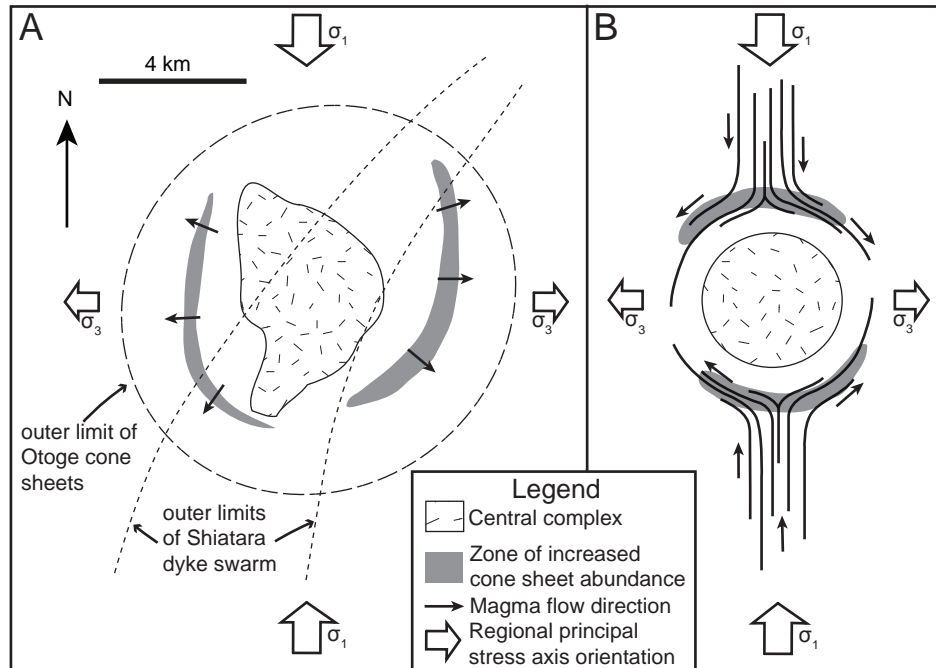


Fig. 6.11: A) Zones of increased cone sheet intensity in the Otoge igneous centre, Japan, relative to the regional  $\sigma_3$  principal stress axis (after Geshi, 2005). B) Hypothetical map depicting inferred areas of increased cone sheet intensity if they are fed by laterally propagating regional dykes.

### 6.3.2 Stress field interference

The magma flow regime and spatial abundance variations of the Ardnamurchan cone sheets suggests the majority were fed by laterally propagating regional dykes, rather than from a central source. This implies a significant number of regional dykes had trajectories that intersected Ardnamurchan. However, Jolly and Sanderson (1995) determined that regional dykes sourced from Mull that propagated laterally SE, decreased in intensity and increased in spacing with distance from Mull (Fig. 6.12a). There is a significant difference between regional dyke numbers adjacent to the Mull central complex and ~30 km to the SE

(Ardnamurchan is located ~30 km to the NW of the Mull central complex). This suggests an insufficient number of regional dykes, to produce the abundance of cone sheets observed, had a trajectory that aligned with Ardnamurchan. It is important to note the curvature of the regional dykes proximal to the Mull central complex and their transition into a more planar geometry further away (Fig. 6.12a) (Jolly and Sanderson, 1995). A similar geometrical relationship is observed in the radial dykes originating from the West Spanish Peak volcanic centre, Colorado (Fig. 6.12b) (Odé, 1957). This curvilinear, symmetrical form has been attributed to the gradual change between the principal stress axes of a local and regional stress field (Odé, 1957). Whilst these two examples are concerned with lateral propagation away from the source reservoir, several studies have suggested vertically propagating dyke swarms may converge on and become entrapped by the curving principal stress axes associated with a local stress field about an upper crustal magma chamber (Gautneb and Gudmundsson, 1992; Gudmundsson, 1998; Klausen, 2006). It is therefore plausible that laterally propagating dykes might also be preferentially deflected towards central complexes, explaining the observed cone sheets and regional dyke density distributions.

Crucial to the model of a regional dyke origin for the Ardnamurchan cone sheets is operation of a mechanism to deflect the sub-vertical, NW-SE trending regional dykes into an inverted conical geometry. Intrusion of sub-vertical regional dykes in the BIPIP was controlled by the extensional regional stress field ( $\sigma_1$  vertical and a NE-SW oriented horizontal  $\sigma_3$ ; England, 1988). Lateral propagation of these dykes into the Ardnamurchan central complex local stress field, with different principal stress axes orientations, may have instigated reorientation of the intrusion plane to maintain an orthogonal relationship to  $\sigma_3$  (e.g. Anderson, 1951; Pollard, 1973; England, 1988; Klausen, 2006). Consequently, the regional dykes would have been deflected around the central complex into reactivated pre-existing inward dipping fractures and/or outward dipping bedding planes  $<67^\circ$  from  $\sigma_1$ . As previously mentioned, there is a gradual transition between two overlapping stress fields. Whilst sheet dip is predominantly controlled by the orientation of pre-existing host rock structures, the fractures are laterally discontinuous so cannot significantly influence cone sheet strike. The

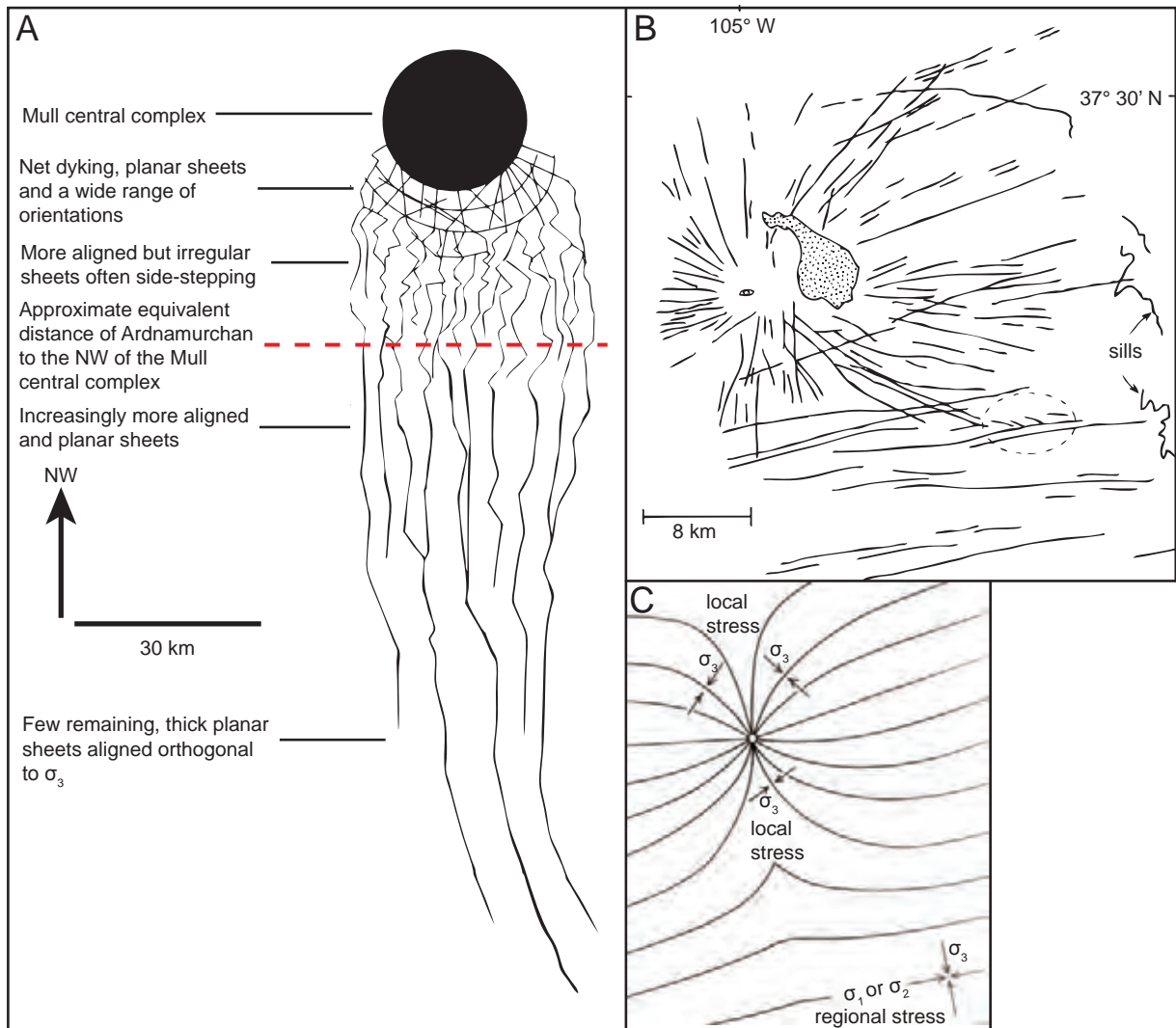


Fig. 6.12: A) The geometry and distribution of regional dykes that propagated laterally to the SE of the Mull central complex (Jolly and Sanderson, 1995). B) Map of the curvature of the radial dykes surrounding and laterally propagating from the Spanish Peaks volcanic centre, which appear to follow the locally deflected  $\sigma_1$  or  $\sigma_2$  principal stress axes (C).

strike of each cone sheet, whether they are concentric or just weakly deflected around the central complex, is therefore dependent on the strain ratio of the local and regional stress fields (see Guglielmo, 1994). Close to the Ardnamurchan central complex the local stress field is dominant (i.e. during local compression), resulting in a preponderance of concentric sheets (as  $\sigma_3$  is concentric in plan view) (Fig. 6.13). With distance from the central complex the magnitude of the local stress field decreases (Gautneb and Gudmundsson, 1992) and cone sheet strikes may only be weakly deflected from the regional NW-SE trend (Fig. 6.13). Outside the zone of influence of the local stress field, the regional dykes will maintain a NW-

SE striking, sub-vertical planar geometry (e.g. similar to the increasing inclination of the Centre cone sheets with distance from the central complex). This transition zone between

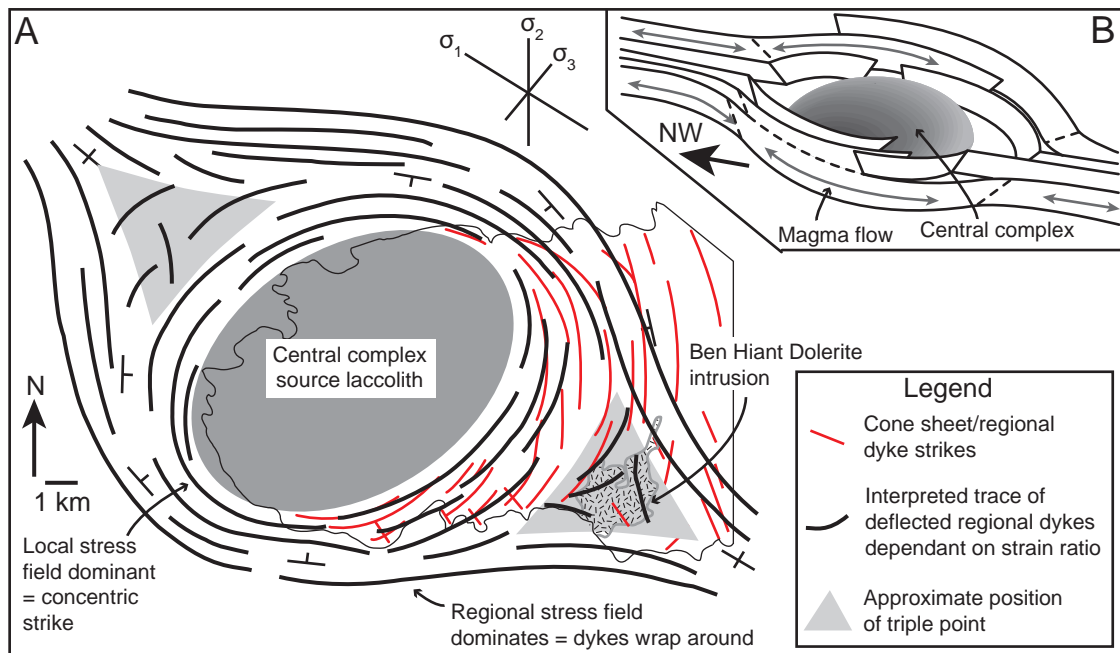


Fig. 6.13: A) Map of Ardnamurchan depicting the general and interpreted cone sheet and regional dyke strikes and the proposed zones tending towards lithostatic stress. B: Conceptual model of 'cone sheets' representing an inclined form of laterally propagating regional dyke.

concentric sheets and regional dykes will vary, in terms of distance from the central complex, with fluctuations in the local stress field.

Host rock foliations define similar deflected traces, from a regional trend, around major igneous bodies (e.g. Merrimac pluton, California, USA, Guglielmo, 1993; Ardara pluton, Ireland, Molyneux and Hutton, 2000). Around the Merrimac pluton, California, the pre-existing NW-SE trending host rock foliation is observed to proximally parallel intrusion margins but distally they are only weakly deflected (Fig. 6.14) (Guglielmo, 1993). Although host rock foliation deflection described by Guglielmo (1993) is associated with ductile deformation involving a single stress field, numerical models presented by Guglielmo (1994) suggest inflating intrusions in regional compressional or extensional stress regimes may produce similar deflection patterns. Deflection of host rock foliation may occur if the pluton was emplaced pre-, syn- or post-tectonic deformation. Importantly, Guglielmo (1994) showed

intrusion expansion in a uniaxial extensional stress regime, similar to that active during the BIPI (England, 1988), may rotate foliations to parallel the intrusion margins. Therefore, it is suggested that local compression, associated with emplacement and inflation of intrusive components of the Ardnamurchan central complex, contemporaneous with regional extension may have promoted deflection of the regional dykes around the central complex and into pre-existing inwardly inclined fractures; essentially obtaining a cone sheet-like geometry. Interference of two simultaneously active but contrasting stress fields potentially produces diagnostic conical 'low strain' zones on opposite sides of the central intrusion/complex (Guglielmo, 1994), which on Ardnamurchan are predicted to be situated offshore to the NW and along the coast to the SE of the central complex due to the orientation of the regional  $\sigma_1$  principal stress axis (Fig. 6.13 and 6.14) (Guglielmo, 1993). These zone essentially represent areas where the two competing stress fields (i.e. local and regional stress fields) cancel each other out and tend towards lithostatic stress (i.e.  $\sigma_3$  is sub-vertical). Within these zones, the variability of cone sheet strike and dip should increase, perhaps with a preponderance of sub-

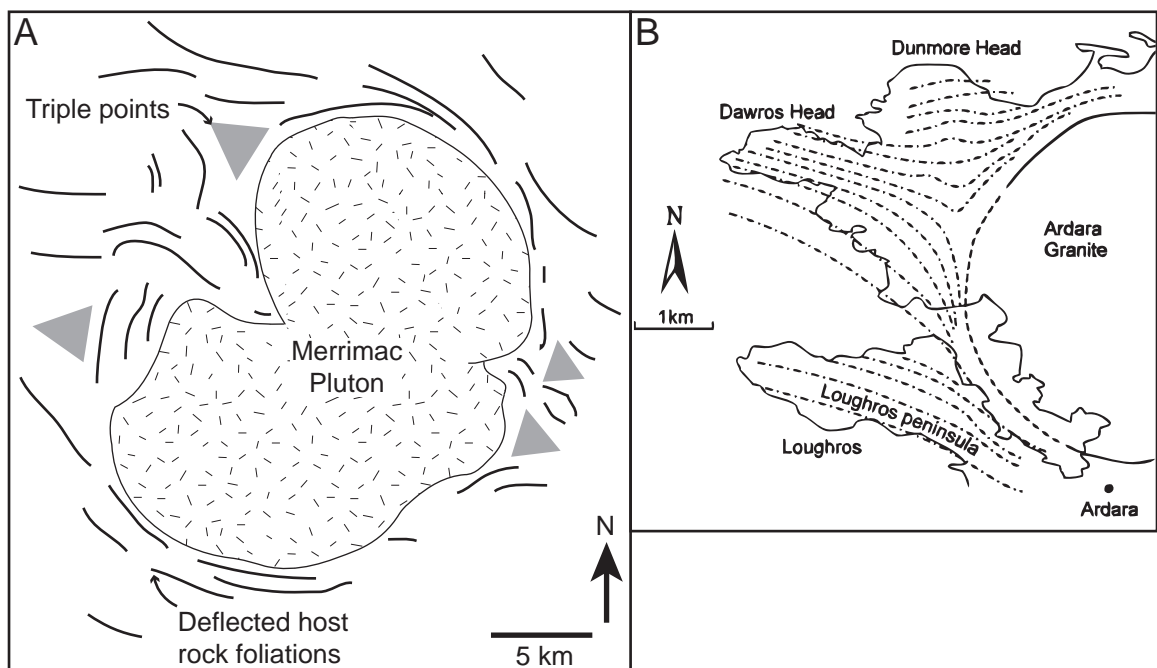


Fig. 6.14: A) Deflection of pre-existing host rock foliation patterns around the Merrimac pluton in California (Guglielmo, 1993). Note the positioning of triple points, defined by the curvature of the host rock foliations, to the NW and SE of the pluton. B) Host rock foliation patterns deflected by the intrusion of the Caledonian Ardnara Granite (Molyneux and Hutton, 2000).

horizontal inclinations as  $\sigma_3$  is sub-vertical. Analysis of these potential diagnostic lithostatic stress zones provides an opportunity to test stress field interference and consequently the plausibility of the regional dyke deflection hypothesis. However, the exposure of cone sheets in the suggested onshore SE lithostatic stress zone is restricted by the presence of the major Ben Hiant Dolerite intrusion (Fig. 6.13), which is discussed in Chapter 7 in the context of the ideas presented here.

## 6.4 Summary

The measured NW-SE oriented, sub-horizontal to moderately plunging lateral magma flow regime, obtained from AMS analysis, and observed distribution of cone sheets primarily to the SE of the Ardnamurchan central complex are inconsistent with previous models for the emplacement of the Ardnamurchan cone sheets (e.g. Richey and Thomas, 1930; Anderson, 1936; Durrance, 1967), which rely on a central source. Some cone sheets distributed throughout Ardnamurchan contain dip-parallel magnetic lineations, suggestive of a central source. The majority of the Ardnamurchan cone sheets are however interpreted to represent laterally propagating regional dykes, likely originating from the Mull central complex, that upon entering the local stress field at Ardnamurchan were deflected around the central complex (i.e. developing a concentric strike) and into inwardly inclined, pre-existing fractures and outwardly dipping bedding planes. Estimation of the sub-surface disposition of the Ardnamurchan central source reservoir, probably partially located within the amphibolite-facies Lewisian Gneiss, supports a distal magma source, as the Ardnamurchan cone sheets contain no evidence of contamination from the amphibolite-facies Lewisian Gneiss. There is also a significant geochemical and isotopic correlation between the Ardnamurchan and Mull cone sheets permitting a common origin for both. Consideration of all the relevant measured data (i.e. field observations, AMS analysis and a review of geochemical results) leads to the proposal that the majority of the Ardnamurchan cone sheets represent deflected laterally propagating regional dykes originating from the Mull central complex.

---

## CHAPTER 7

### EMPLACEMENT OF THE BEN HIANT DOLERITE

---

Satellite intrusions typically constitute a stacked series of laterally emplaced ( $\leq 10$  km from the source) laccolithic and sill-like intrusions (Petronis et al., 2004; Stevenson et al., 2007b) that often precede the main intrusive phase of a central complex (Horsman et al., 2005; Morgan et al., 2008). For example, the Trachyte Mesa, Black Mesa and Maiden Creek satellite intrusions crop out 8–10 km from the associated Mt Hillers central complex in the Henry Mountains, Utah (Horsman et al., 2005; Morgan et al., 2008). As satellite intrusions are generally emplaced during the early development of a central complex and are spatially removed from subsequent volcano-tectonic processes, they may provide important information pertaining to the initial stress field interactions and magma flow regimes. The Centre 1 Ben Hiant Dolerite is a satellite intrusion located 2 km to the SE of the main Ardnamurchan central complex (Fig. 7.1), commonly interpreted as the magma source (Judd, 1874; Geikie, 1897; Richey and Thomas, 1930; Gribble, 1974; Emeleus and Bell, 2005), coincident with the proposed zone of lithostatic stress potentially initiated by interference between the local and regional stress fields. As petrographic analyses suggest that there is a mineralogical similarity between the Ben Hiant Dolerite and Ardnamurchan cone sheets, potentially indicative of a common source (Geikie, 1897; Gribble, 1974), understanding the emplacement and spatial position of the Ben Hiant Dolerite may allow the cone sheet emplacement model proposed in Chapter 6 to be tested. Accordingly, a field mapping and an AMS study was conducted to elucidate the controls on the intrusion site (e.g. does its geometry correlate to formation in a zone of lithostatic stress?) and its relationship to the cone sheets (e.g. its magma source).

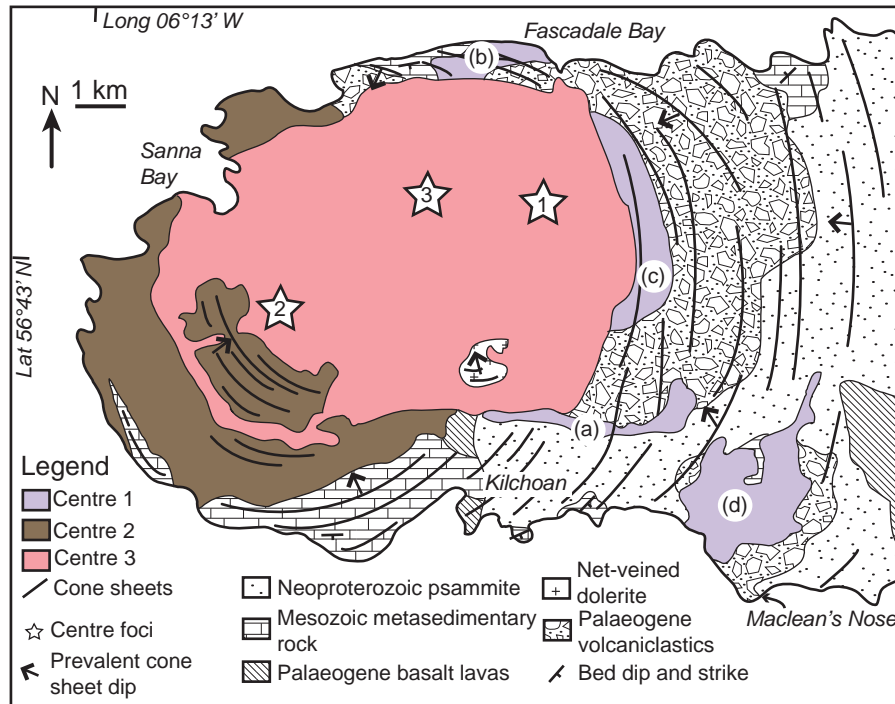


Fig. 7.1: Geological overview of the Ardnamurchan central complex highlighting the positions of the proposed intrusive centres and the relative positions of the individual Centre 1 intrusions: a) Glas Bheinn Porphyritic Dolerite, b) steep, sheet intrusions west of Fascaidale, c) Beinn nan Leathaid composite intrusion and d) the Ben Hiant Dolerite (redrawn from Richey and Thomas, 1930; Emeleus, 2009).

### 7.1. Previous emplacement models of the Ben Hiant Dolerite

On Ardnamurchan, the major intrusions of Centre 1 are not well exposed and include the Glas Bheinn Porphyritic Dolerite, interpreted as a dyke-like intrusion; the steeply inclined intrusive sheets of quartz gabbro and granophyre west of Fascaidale; the composite, gently inclined Beinn nan Leathaid sheet intrusion and the Ben Hiant Dolerite, the focus of this chapter (Fig. 7.1) (Richey and Thomas, 1930; Emeleus and Bell, 2005). The lithology of the largely equigranular Ben Hiant Dolerite ranges from an olivine-dolerite to a quartz-dolerite. From the coast, the intrusion margins can be traced vertically upward to altitudes of 120 m (NW margin) and ~200–300 m (SE margin) where they then become sub-horizontal, resulting in an apparent mushroom-shaped geometry (Fig. 7.2) (Richey and Thomas, 1930). This geometry and lateral extension of the margins is well demonstrated by the outlier of Ben Hiant Dolerite at Sròn Mhor and Stallachan Dubha which rests sub-horizontally on the Early Palaeogene

volcaniclastic host rock (Fig. 7.2). To the NE the Ben Hiant Dolerite becomes more irregular (Fig. 7.2) and is considered to be an amalgamation of multiple inclined sheets gently dipping NW (Geikie, 1897; Richey and Thomas, 1930). Interpretations of the geometry of the Ben Hiant Dolerite have led to the proposition of three emplacement mechanisms:

1. From the prevalent well developed columnar jointing and stepped topography of the Ben Hiant Dolerite, Judd (1874) proposed the summit of Ben Hiant represents a volcanic intrusive plug from which a series of lava flows radiate.
2. Geikie (1897) identified that the Ben Hiant Dolerite consists of several sills, inclined approximately N or NW. Some of these transgress up through the Neoproterozoic Moine stratigraphy and exhibit variable grainsizes (Geikie, 1897). From the mineralogical similarity of the Ben Hiant Dolerite with thinner adjacent dykes and sills (later identified as cone sheets; Richey and Thomas, 1930), Geikie (1897) proposed that magma from NE-SW oriented fissures fed both the Ben Hiant sills, in which magma was principally concentrated, and the surrounding inclined sheets. Petrographical analyses do not reveal a systematic progression in the compositional evolution of the Ben Hiant Dolerite from the base to the top of the intrusion but rather define a series of compositional 'steps' of variable thickness, which has been used to further suggest that the Ben Hiant Dolerite consists of a series of separate sheets (Gribble, 1974). The latter work further suggested that the Ben Hiant Dolerite sills were actually amalgamated cone sheets emplaced within the Ben Hiant volcanic vent, which provided space for sheet inflation and coalescence.
3. The apparent absence of intrusive contacts and a mushroom-shaped cross-sectional geometry (Fig. 7.2) led Richey and Thomas (1930) to propose the Ben Hiant Dolerite is a single intrusion emplaced vertically (from a dyke) into the separate Ben Hiant volcanic vent (Fig. 7.2). The intrusive sheet extensions to the NE of the Ben Hiant summit were suggested to be produced by some of the magma being diverted laterally into un-intruded cone sheet fractures (Richey and Thomas, 1930).

All three emplacement models imply that the Ben Hiant Dolerite was sourced from the Ardnamurchan central complex and was intruded into a volcanic vent, originally inferred

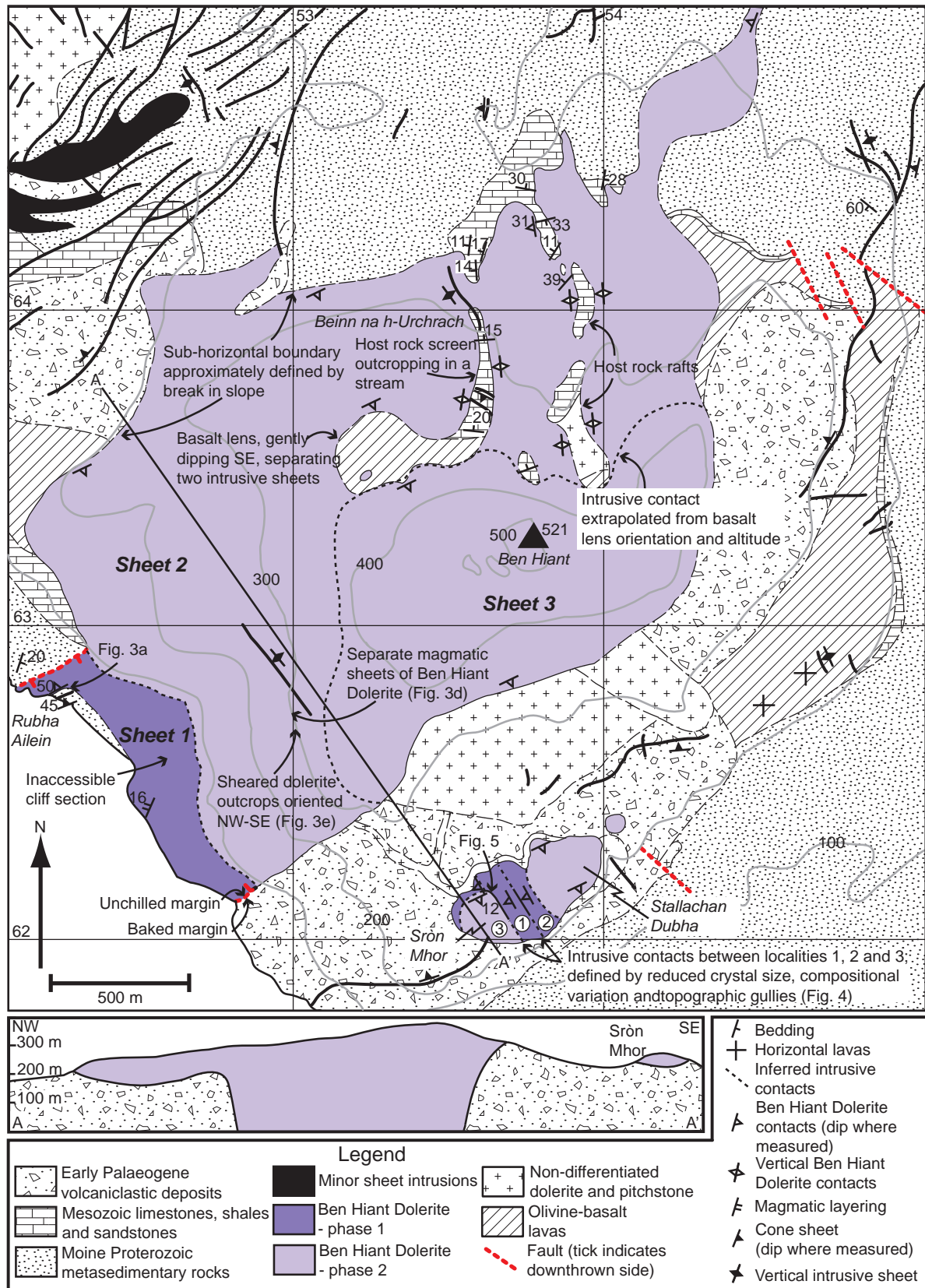


Fig. 7.2: Geology of the Ben Hiant Dolerite and the surrounding host rock, combining new observations and previous work by Richey and Thomas (1930) and Emeleus (2009). The cross-section is after Richey and Thomas (1930).

from the moderately to steeply inwardly inclined contacts and an abundance of acidic igneous clasts in the Early Palaeogene agglomerates (cf. Richey and Thomas, 1930). Brown and Bell (2006) re-interpreted the agglomerates as high energy debris flows deposited in a topographic depression after recognising a much greater proportion of country rock clasts to igneous clasts than previously recorded, the presence of pollen spores and various sedimentary structures. This latter work suggests the Ben Hiant area was not a volcanic vent and provides additional evidence that the Ben Hiant Dolerite was emplaced at a relatively shallow depth ( $<3$  km).

## **7.2 Field Relationships and Petrography**

Field and petrographical observations are described here with respect to their geographical location, following a similar distinction made by Richey and Thomas (1930), due to the variation observed between different areas and the importance of correlating both observation sets. In broad terms, the equigranular Ben Hiant Dolerite is medium-grained, texturally poorly equilibrated and is composed of cumulus plagioclase, clinopyroxene, ilmenite and occasionally olivine along with interstitial magnetite, alkali feldspar, quartz, calcite and apatite (cf. Richey and Thomas, 1930). New observations are synthesised with those recorded by Richey and Thomas (1930) in their memoir that are pertinent to the present study.

### **7.2.1 South-west of the Ben Hiant summit**

The contacts between the Ben Hiant Dolerite and the host rock are poorly exposed. At the SE end of the coastal outcrop, towards Maclean's Nose, the Ben Hiant Dolerite displays no chilled margin and an irregular contact, steeply inclined to the NW, with the exposed thermally baked volcanoclastic country rock (Fig. 7.1 and 7.2) (Richey and Thomas, 1930). The Ben Hiant Dolerite is also locally cross-cut by minor felsic veins (Richey and Thomas, 1930). The inferred contact zone can be traced topographically upwards from the exposures of Ben Hiant Dolerite and volcanoclastics. Similarly, adjacent exposures of Neoproterozoic Moine metasedimentary rocks and Ben Hiant Dolerite in the cliff section at Rubha Ailein

distinguish the NW margin, likely steeply inclined to the SE, of the coastal exposure although the contact itself is not visible (Fig. 7.2). There is no evidence of a chilled margin to the Ben Hiant Dolerite adjacent to the inferred NW contact. Throughout the cliff face, including adjacent to the inferred contacts, columnar jointing is sub-vertical. Approximately 10 m to the SE of the NW margin, a contact between the Ben Hiant Dolerite and the Neoproterozoic Moine metasedimentary rock is oriented 062/50° NW (strike and dip; Fig. 7.3a) [NM 52234 62816] sub-parallel to a cone sheet (068/45° NW; strike and dip). At the contact (Fig. 7.3a), the Ben Hiant Dolerite is chilled (with typically <1 mm grainsize) and contains plagioclase laths (40 vol.%), often enclosed within coarse (<3 mm) ophitic clinopyroxene (20 vol.%) and serpentinised subhedral olivine (<0.5 mm; 20 vol.%). A gradational increase from a medium-grained chill zone to the coarser (Fig. 7.3b) interior is observed in the Ben Hiant Dolerite over the marginal 2 m. The Ben Hiant Dolerite texturally is poorly equilibrated and consists of normally zoned plagioclase laths (<7 mm; 50 vol.%), subhedral clinopyroxene (<3 mm; 40 vol.%) and anhedral magnetite and ilmenite (<3 mm; 10 vol.%). Interstitial magnetite is commonly elongated along cumulus plagioclase and clinopyroxene grain boundaries (Fig. 7.3c). Within the middle of the coastal extent of Ben Hiant Dolerite [NM 52558 62380], sub-horizontal mineral layering (040/16° W; strike and dip), defined by the relative proportions of coarse-grained clinopyroxene and plagioclase phenocrysts, is developed on a decametre scale (Fig. 7.2).

At higher altitudes on the coastal cliff section of the Ben Hiant Dolerite, the NW and SE contacts with the host rock become sub-horizontal (at 120 m and ~200–300 m respectively). Along a small, pronounced topographic step on the south flank (at ~300 m altitude) of Ben Hiant [NM 53117 62647], a sheet (~2 m thick) of Ben Hiant Dolerite is defined by thin columnar joints (~20 cm wide), displaying a slight curvature from top (288/60°; dip azimuth and dip) to base (236/49°; dip azimuth and dip), bounded by apparently structureless Ben Hiant Dolerite (Fig. 7.2 and 7.3d). Approximately 20 m SE along strike [NM 53121 62608] the Ben Hiant Dolerite is heavily sheared in a brittle manner (Fig. 7.2 and 7.3e).

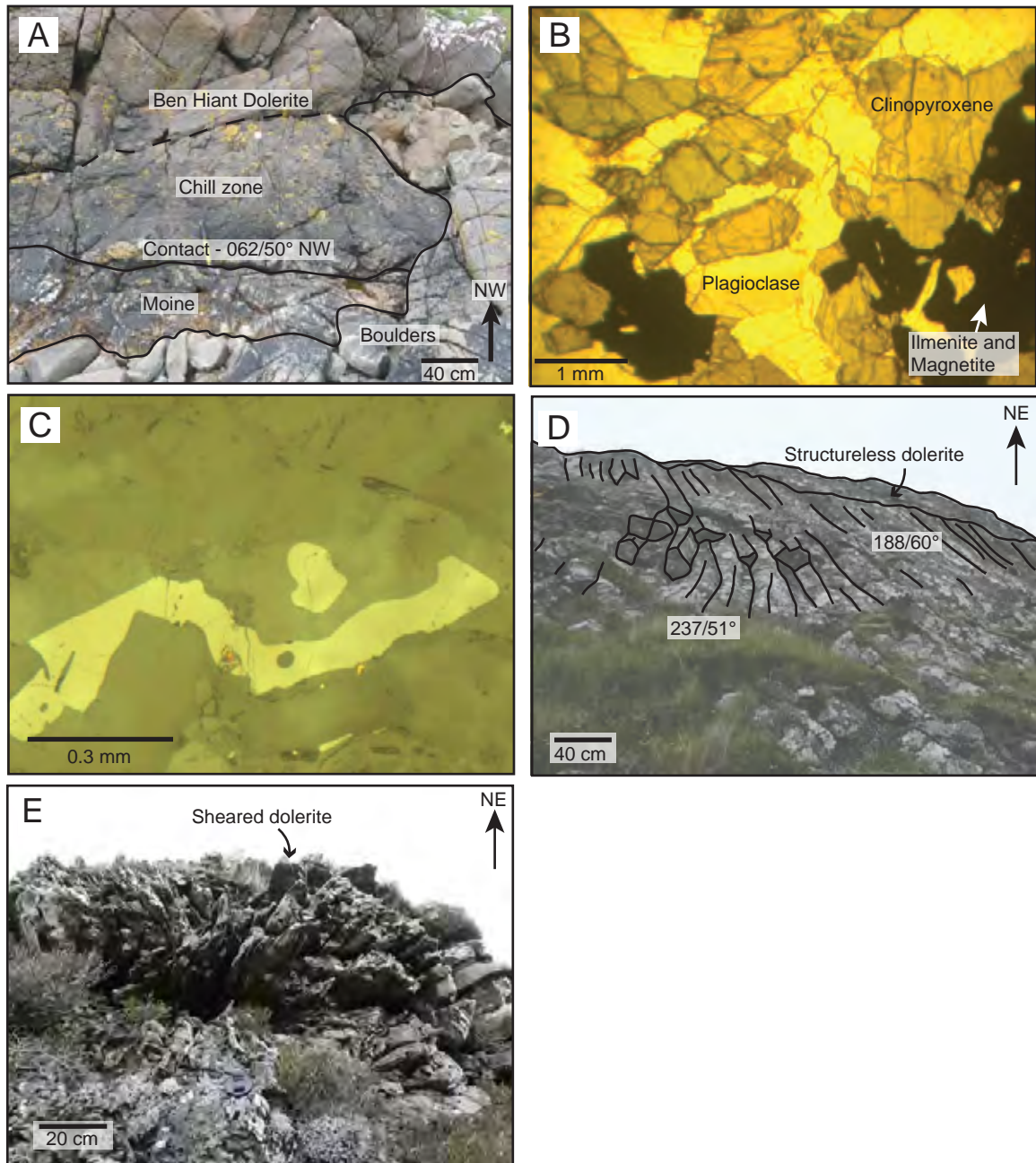


Fig. 7.3: A) Host rock contact between the chilled Ben Hiant Dolerite and Neoproterozoic Moine psammite observed along the coast [NM 52234 62816]. B) Plane polarized light photomicrograph of the typical coarse, nearly gabbroic, Ben Hiant Dolerite observed in Figure 7.3a. C) Reflected light photomicrograph showing titanomagnetite shape controlled by grain boundaries. D) Thin sheet of Ben Hiant Dolerite, consisting of relatively thin, curving columnar joints bounded by Ben Hiant Dolerite devoid of structures. Azimuth and plunge of the columnar jointing is presented. E) Heavily sheared Ben Hiant Dolerite.

### 7.2.2 Stallachan Dubha and Sròn Mhor

The mapped and topographical expression of the Ben Hiant Dolerite outlier of Sròn Mhor and

Stallachan Dubha suggests a gentle eastward dip of the basal contact with the volcanoclastics. Steeply inclined columnar jointing (~1 m wide) is well developed. The Ben Hiant Dolerite mass of Stallachan Dubha and the small hill outcrop to its NE are apparently uniform in both composition and texture throughout. In contrast, wide variation is observed on Sròn Mhor where two gullies, oriented ~147–327° and defined by a prominent topographic step on their SE side, containing heavily weathered and fractured Ben Hiant Dolerite separate distinct lithologies (Fig. 7.2 and 7.4). The Ben Hiant Dolerite observed at Localities 1 and 2 (Fig. 7.2 and 4a; [NM 53635 62198] and [NM 53646 62208]), is typically medium to coarse-grained and contains cumulus tabular plagioclase (~60 vol.%; <3 mm), clinopyroxene (~15 vol.%; <4 mm), heavily altered olivine (~13 vol.%) and fine to medium opaque crystals (~8 vol.%) (Fig. 7.4b). At Locality 3 (Fig. 7.2 and 7.4a; [NM 53615 62186]) the columnar joints are narrowly spaced (10 cm) and contain vugs (<20 mm) infilled with quartz. Petrographically, the Ben Hiant Dolerite at Locality 3 displays a porphyritic texture consisting of a variolitic groundmass of very fine acicular clinopyroxene, plagioclase and opaque minerals and some coarse-grained phenocrysts (<2 mm; <1 vol.%) of euhedral plagioclase and anhedral clinopyroxene. Numerous amygdales (<1.5 mm) infilled with cryptocrystalline silica, probably of similar origin to the infilling vuggy quartz, are also observed (Fig. 7.4c). Within the two gullies separating Localities 1, 2 and 3 (Fig. 7.2 and 7.4a), the equigranular Ben Hiant Dolerite is much finer-grained (<0.5 mm) and contains spherulitic amygdales (<0.3 mm) of very fine radiating acicular chlorite (Fig. 7.4d). Midway down the south-eastern gully [NM 53607 62217] an intrusive contact (064/12° SE strike and dip) is observed, defined by the decreasing width and increasing curvature of the columnar jointing particularly above the contact (Fig. 7.5). A decrease in grain size of the Ben Hiant Dolerite is also observed towards the contact. No brittle deformation was observed associated with the finer-grained Ben Hiant Dolerite. It is therefore suggested that the reduced grain sizes observed within the gullies represent chilled margins delineating separate sheets of Ben Hiant Dolerite. No palaeosol horizons or other evidence of sub-aerial exposure were observed between individual sheets.

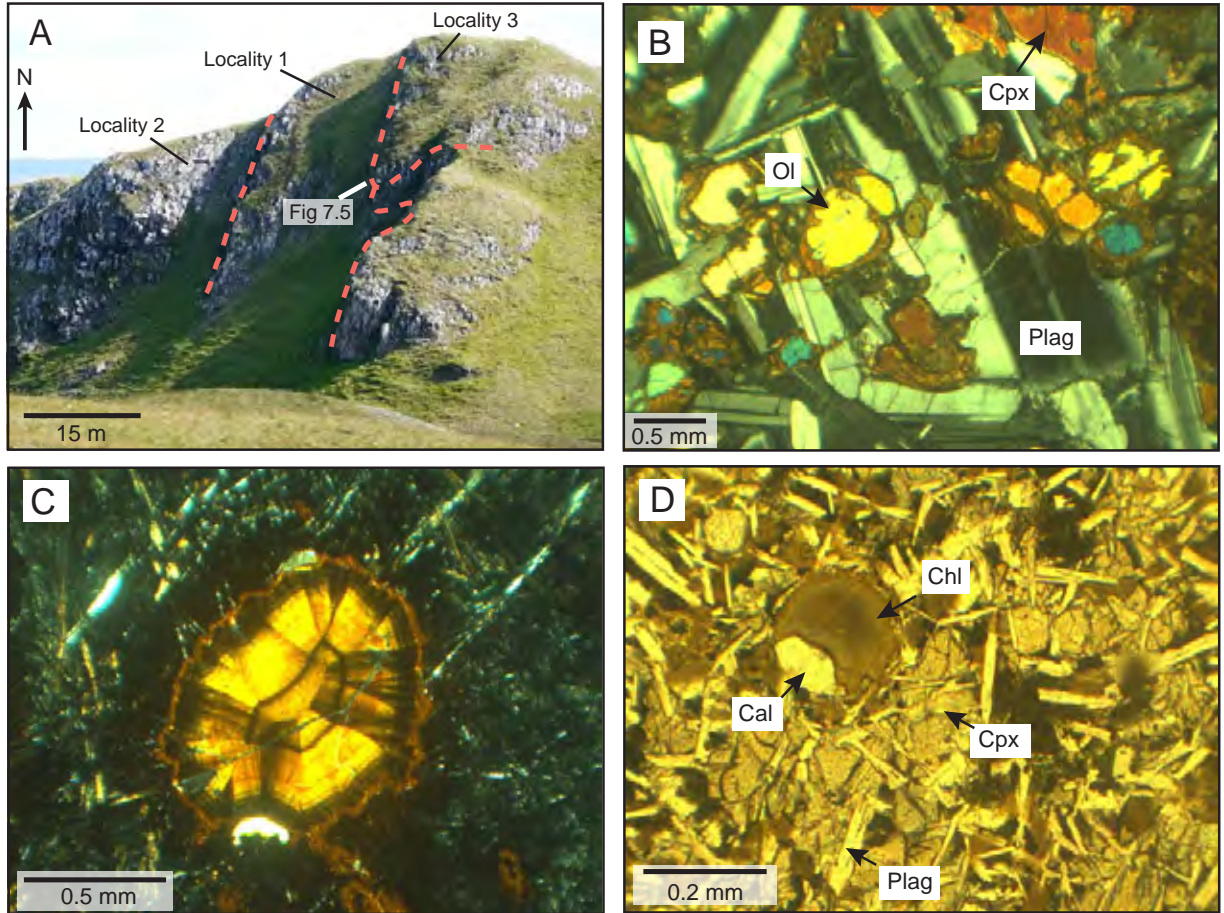


Fig. 7.4: A) View of Sron Mhor depicting locality positions and the intrusive contacts (dashed lines) between individual magmatic sheets. B) Photomicrograph, taken under cross-polars, of Ben Hiant Dolerite from Locality 1 showing coarse subhedral plagioclase (Plag) laths and the rounded olivines (Ol) with altered rims. Clinopyroxene (Cpx) is also present. (c) Variolite photomicrograph, taken under cross-polars, from Locality 3 showing an amygdale infilled with cryptocrystalline silica. D) Photomicrograph of fine acicular plagioclase (Plag), within a medium ophitic clinopyroxene (Cpx), and an amygdale of radiating chlorite (Chl) and a calcite (Cal) crystal from the gully between Localities 1 and 2.

### 7.2.3 Northern margin

The northern boundary is irregular with finger-like extensions of Ben Hiant Dolerite protruding into the Neoroterozoic and Mesozoic host rock (Fig. 7.2). North of the Ben Hiant summit, numerous isolated outcrops, of Mesozoic metasedimentary rocks (predominantly exposed in stream sections), olivine basalt lava or an older porphyritic dolerite occur (Fig. 7.2). Their mapped relationship with the topography suggests sub-vertical N-S boundaries between the host rock and Ben Hiant Dolerite (Fig. 7.2). One well exposed example, along a stream [NM 535 643 to NM 536 638], shows a thin (~10–50 m wide) outcrop of Mesozoic

limestone and shale, with sub-vertical longitudinal contacts, extending from an altitude of ~270 m to the top of the stream at ~310 m altitude (Fig. 7.2). At the top of the stream the Mesozoic host rock is unconformably overlain by a thin, shallowly SE dipping, lens of olivine basalt lava (Fig. 7.2). Towards the base of the stream the host rock outcrop is interrupted by a sub-horizontal sheet of Ben Hiant Dolerite connecting the two masses on either side (Fig. 7.2).

The topography and outer contacts of the Ben Hiant Dolerite on Beinn na h-Urchrach is suggestive of a gentle SE dipping sheet, bounded at the top by the olivine basalt lava screen, with a thickness of ~70 m (Fig. 7.2). The orientation and altitude (~350 m) of the shallowly SE dipping olivine basalt lava screen, which separates two medium-grained sheets of Ben Hiant Dolerite, is used to infer the intrusive contact elsewhere (Fig. 7.2).



Fig. 7.5: Intrusive contact between two sheets of Ben Hiant Dolerite defined by the thinning and curving of columnar jointing. See Figure 7.4a for location.

#### 7.2.4 Overall structure of the Ben Hiant Dolerite

Although several inferences are made here, defining the intrusive structure provides an important context for description of anisotropy of magnetic susceptibility results. Several internal contacts (i.e. boundaries between separate dolerite sheets) within the Ben Hiant Dolerite have been identified from the curvature and thinning of columnar jointing, grain size reductions (chilled margins) and amygdale development. Within the main body of the intrusion, three major intrusive sheets (Sheet 1, Sheet 2 and Sheet 3; Fig. 7.2), >70 m thick, can be inferred. The Sheet 1 and Sheet 2 contact is suggested to correlate to the sub-vertical to lateral outer margin transition of the Ben Hiant Dolerite observed towards the top of the cliff section to the SW of the Ben Hiant summit (Fig. 7.2). The Sheet 2 and Sheet 3 contact is partially constrained to the NW of the Ben Hiant summit by the presence of a shallowly SE dipping basalt lava lens, the altitude and dip of which allows the remaining contact trace to be suggested (Fig. 7.2). As columnar jointing usually forms orthogonal to the cooling front, which parallels the intrusion margins (Ryan and Sammis, 1978), the sub-vertical columnar jointing observed throughout the Ben Hiant Dolerite is consistent with broadly sub-horizontally oriented sheets.

### 7.3 Magnetic fabric analysis

To determine the magma flow regime of the Ben Hiant Dolerite, 41 oriented block samples were collected in the field (Fig. 7.6a) and drilled and cut in the laboratory (following the methods of Owens, 1974), using non-magnetic equipment, to obtain 4–15 (typically 8) 10 cm<sup>3</sup> right cylindrical sub-specimens. An AGICO KLY-3S Kappabridge (an induction bridge operating at a field of 300 A/m and a frequency of 875 Hz) at the University of Birmingham was used to measure the AMS of the sub-specimens, which were then averaged for each block sample assuming that the block sample represents a homogeneous multi-normal population (Owens, 2000). Variation within a block is accounted for by the calculation of 95 %

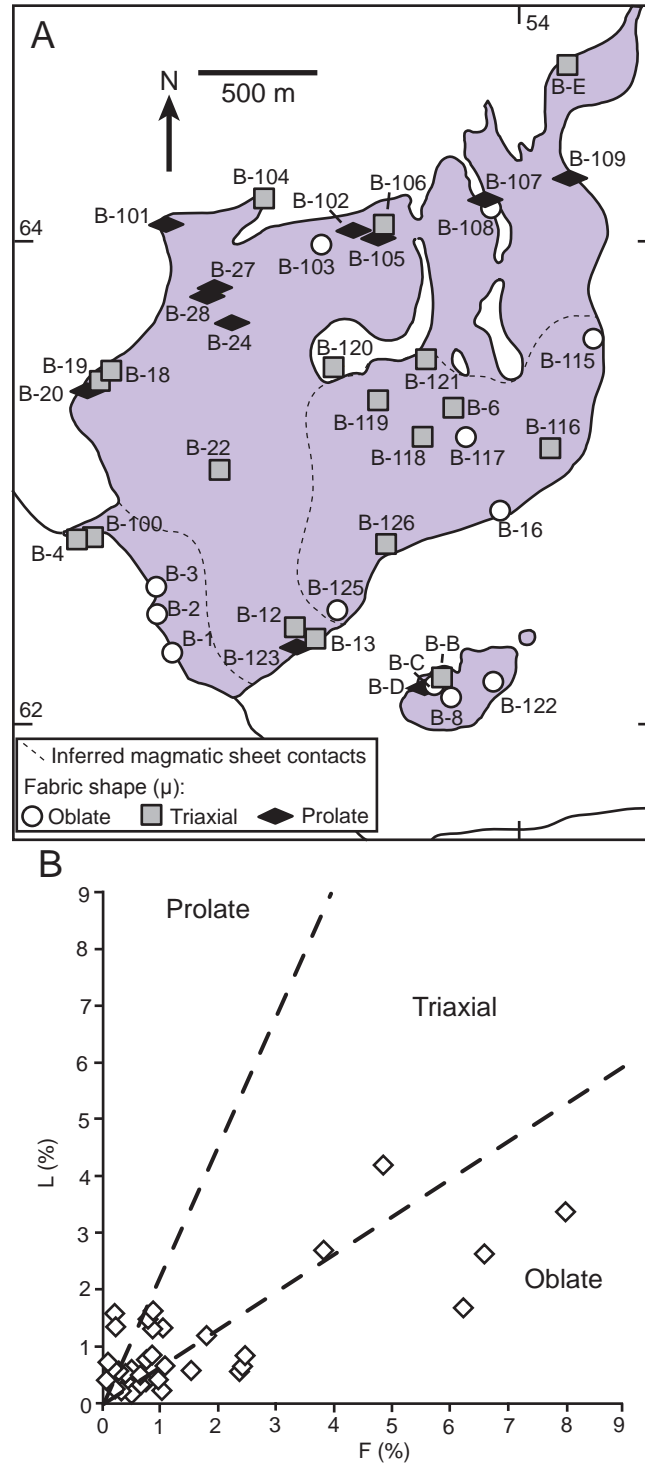


Fig. 7.6: A) Plot of  $\mu$  (ellipsoid shape) distribution and sample positions. There is a distinct absence of prolate fabrics around the summit and a notable NW-SE trend in strong prolate fabrics to the SW of the summit. Where magmatic layering is developed along the coast (Figure 7.2), oblate fabrics dominate. B) L against F plot showing the range in fabric shapes, from prolate to oblate, with a preponderance towards oblate fabrics.

confidence ellipses for both directional and magnitude parameters (Jelínek, 1978). Consistent with the AMS analysis of the Ardnamurchan cone sheets, the magnitude parameters  $K_{\text{mean}}$ ,  $H$  and  $\mu$  are used in conjunction with  $L$  and  $F$  to describe the magnetic susceptibility tensor (see Stevenson et al., 2007a). High-temperature magnetic susceptibility experiments were conducted to distinguish the magnetic phase(s) contributing to the AMS of six representative samples (B-4, B-18, B-100, B-103, B-116 and B-117; Fig. 7.6a and 7.7). Experiments on the temperature dependence of low-field susceptibility of selected samples were conducted using a CS3 furnace attachment for the Kappabridge. Stepwise heating/cooling of the samples from 40 °C to 680 °C to 40 °C in air allows the magnetic composition to be evaluated from the Curie point temperature estimates, inferred using the inflection point method on the heating-cooling curves (Tauxe, 1998). Appendix B contains all the raw AMS data and Appendix G presents the AMS results from the Ben Hiant Dolerite.

The  $K_{\text{mean}}$  values for the Ben Hiant Dolerite range from 1.85 to  $19.13 \times 10^{-2}$  (SI) and are consistent with the principal AMS carrier being a ferromagnetic (*sensu lato*) mineral phase, likely titanomagnetite as suggested by reflected light microscopy (Fig. 7.3c). This is further corroborated by high-temperature, low-field magnetic susceptibility experiments. In addition, these experiments also show that the three major component sheets of the Ben Hiant Dolerite may be chemically distinguished based on variable Ti-content of the titanomagnetites (Fig. 7.7). In general, on heating the low-field susceptibility curves are typically characterised by broad peaks in susceptibility followed by a rapid decrease in susceptibility. Samples B-4 and B-100 were collected from Sheet 1. Sample B-4 displays broad peak in susceptibility at 476 °C (Fig. 7.7a i) with a subsequent inflection (Curie point) at 550 °C (Fig. 7.7a ii), consistent with a relatively low-Ti magnetite population. A continued drop in susceptibility to ~680 °C suggests a minor amount of a subsidiary magnetic phases, likely fine-grained maghaemite or haematite, are also present. This is supported by the shift in the cooling curve, which reflects the oxidation and breakdown of a less magnetic phase during heating (Fig. 7.7a). Sample B-100 displays a minor Hopkinson Peak at 540 °C (Fig. 7.7b i), which also represents a principal contribution from low-Ti magnetite, likely of multidomain to

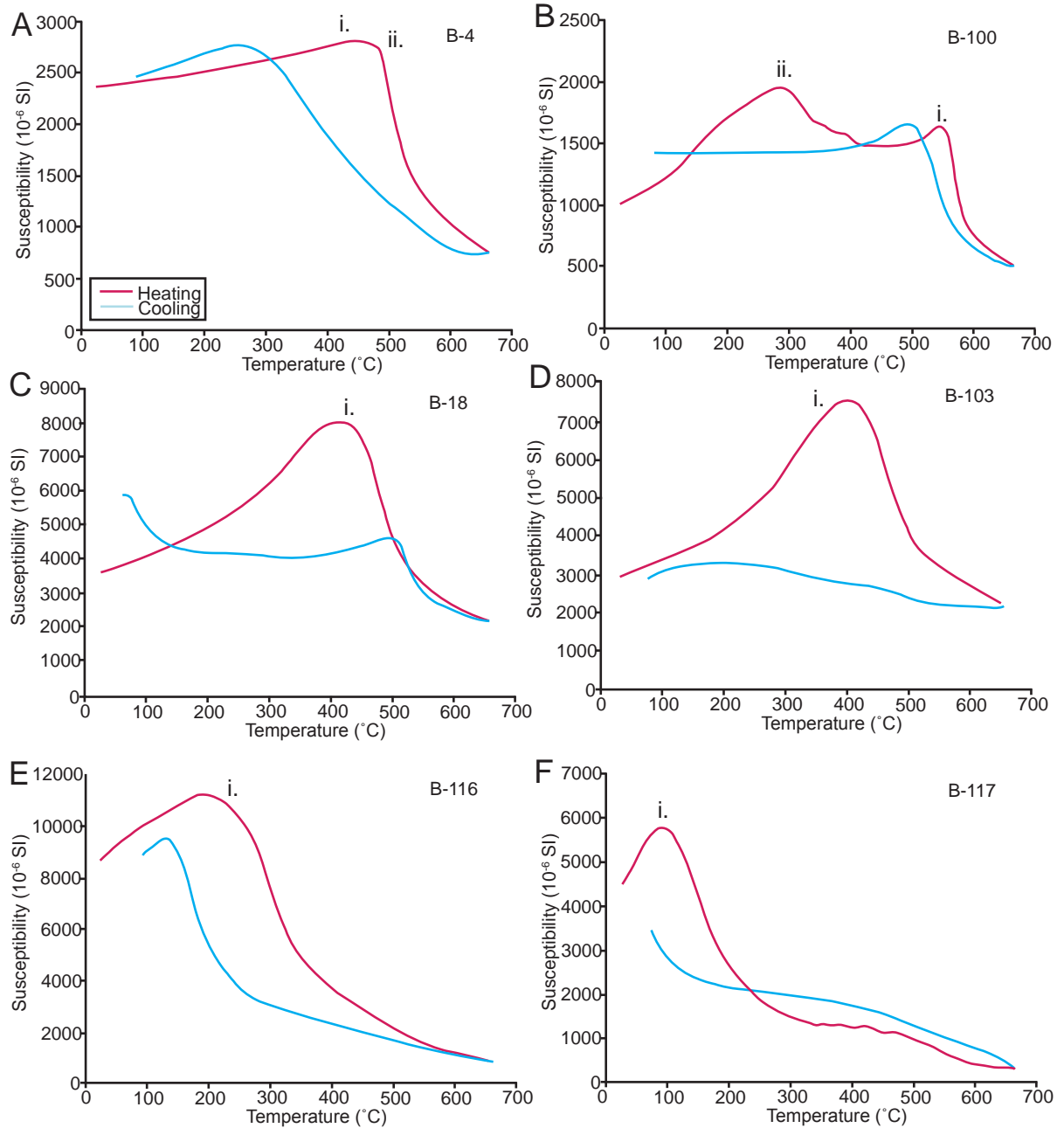


Fig. 7.7: High temperature, low-field susceptibility curves for several Ben Hiant Dolerite samples. See text for explanation.

pseudo-single-domain grainsize. The broad peak, on heating, at 300 °C (Fig. 7.7b ii) suggests the presence of pyrrhotite and/or a maghaemite phase (producing the irregularities on the downward slope), also contribute to the AMS. From Sheet 2, samples B-18 and B-103 display Curie point temperatures of 424 °C and 407 °C (Fig. 7.7c i and 7.7d i), respectively, suggestive of titanomagnetites with moderate-Ti contents. The significant reduction in susceptibility of the cooling curve for both samples suggests the titanomagnetites were

oxidised during heating to produce a less magnetic mineral phase. Susceptibility peaks at 88 °C and 194 °C on the heating curves of B-116 and B-117 (Fig. 7.7e i and 7.7f i), taken from Sheet 3, are representative of a Ti-rich magnetite phase. The continued drop in susceptibility to ~680 °C in both samples relates to the exsolution of Ti-poor magnetite and Ti-rich ilmenite on heating. This is reflected in the shift of the cooling curve.

A lack of a strong Hopkinson Peak in the high-temperature, low-field susceptibility experiments suggests that the titanomagnetite grains are of a multidomain grainsize (Liss et al., 2004), implying the AMS fabrics are ‘normal’ (Rochette et al., 1999; Ferré, 2002). Combined with the petrographical observation of anhedral intercumulus magnetite occupying the interstices of a plagioclase and clinopyroxene primocryst ‘framework’, the high-temperature, low-field susceptibility experiments suggest the AMS fabrics can be interpreted as the equivalent of the titanomagnetite petrofabric, itself controlled by the fabric of the primary silicate mineralogy (cf. Cruden and Launeau, 1994; Archanjo et al., 1995; Launeau and Cruden, 1998). These observations allow the measured AMS fabrics to be interpreted as primary magmatic flow fabrics.

The strength of the anisotropy (H) ranges from a very weak (0.35 %) to a strong (11.35 %) fabric. Figure 7.6b, a plot of lineation (L) versus foliation (F), indicates a wide range of fabric shapes from prolate to strongly oblate with a predominance of oblate fabrics. Some of the strongest oblate fabrics are located along the coast where mineral layering (040/16° NW) is developed in the Ben Hiant Dolerite, to which the AMS foliation (037/26° NW) is sub-parallel (Fig. 7.2 and 7.6a).

The magnetic fabric orientations for the Ben Hiant Dolerite are illustrated in Figure 7.8. Field relationships suggest the Ben Hiant Dolerite may be divided into a series of gently dipping intrusive sheets (Fig. 7.2 and 7.8). The identification of separate intrusive sheets of Ben Hiant Dolerite in the field requires that the magnetic fabrics be interpreted with caution, such that correlation of AMS fabrics at individual locations (i.e. Fig. 7.8b and c) can only be made if the samples are from the same magmatic sheet. Throughout the magmatic sheets identified there is a preponderance of  $K_1$  magnetic lineations with sub-horizontal to

moderate plunges (68 % are  $< 45^\circ$ ) and a NW-SE trend (Fig. 7.8a). In the north of the Ben Hiant Dolerite, the magnetic lineations are oriented more towards the N-S (Fig. 7.8b). Where strong prolate fabrics are developed, the lineation trend and foliation strike are often sub-parallel (Fig. 7.6a and 7.8a). The magnetic foliations, and to a lesser extent the magnetic lineations, in Sheet 1 are moderately inclined inwards proximal to the NW and SE margin and sub-horizontal in the centre of the coastal outcrop. In some areas of Sheet 2, convergent lineation trends are observed (Fig. 7.8a and b). Towards the NW margin of the Ben Hiant Dolerite (Sheet 2), the magnetic foliations define a convex-outwards (towards the NW) strike (Fig. 7.8c). Along the SE margin of the main Ben Hiant Dolerite body, within Sheet 2, a similar rotation in magnetic foliation strikes is present (Fig. 7.8c). The fabrics of Sròn Mhor and Stallachan Dubha are also slightly variable but define a sub-horizontal to moderately plunging NW-SE trend to the lineations (Fig. 7.8a). The Ben Hiant Dolerite above 300 m, ascertained through field observations to be an individual magmatic sheet (Sheet 3), contains magnetic fabrics that are more variable (Fig. 7.8a). Throughout the intrusion there appears to be little correlation between the AMS fabrics and the exposed Ben Hiant Dolerite boundaries, particularly adjacent to the steeply inclined Sheet 1 margins suggesting that the magma did not interact strongly with or flatten against the country rock margins (Fig. 7.8a).

## 7.4 Structural emplacement of the Ben Hiant Dolerite

### 7.4.1 Construction of the Ben Hiant Dolerite

#### 7.4.1:1 *Incrementally emplaced sub-horizontal sheets*

Previous emplacement models of the Ben Hiant Dolerite strongly rely on the interpretation of Ben Hiant as a volcanic vent complex, to provide space for intrusion, and suggest that magma originated from the Ardnamurchan central complex. However, this interpretation has been brought into question by the work of Brown and Bell (2006; 2007) who reclassified the volcanoclastic breccias as high energy debris flow deposits formed on the flanks of a central volcano. Within this study, several dolerite sheets of variable thicknesses (20 cm→70 m) have

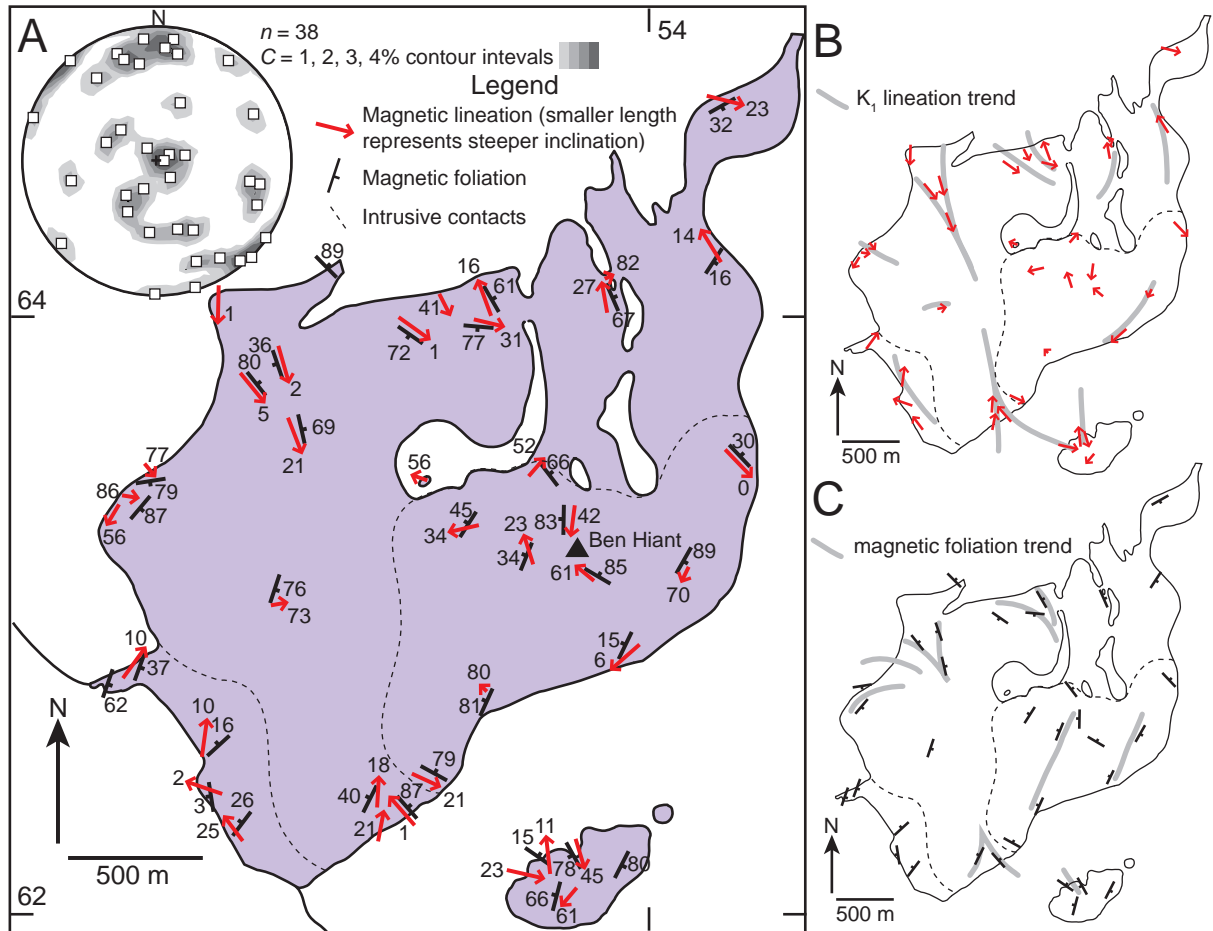


Fig. 7.8: A) Sketch map of the Ben Hiant Dolerite incorporating the magnetic lineation and magnetic foliation results. *Inset*: Lower hemisphere, equal area stereographic projection of  $K_1$  lineations displaying a pronounced NW-SE trend and shallow to moderate plunges. B) AMS lineations highlighting a general NW-SE trend with shallow plunges. C) Magnetic foliation, occasionally defining a convex outwards strike to the NW of the intrusion. Note that for both (B) and (C) the interpreted AMS trends can only be made between samples within the same intrusive sheet.

been defined structurally, rock magnetically and geochemically. The absence of palaeosol horizons between the observed dolerite sheets and the non-radial NW-SE sub-horizontal to moderately plunging magnetic lineation pattern suggest that the Ben Hiant Dolerite does not consist of a series of radiating lava flows as proposed by Judd (1874), but rather that it is an intrusive body. Identification of discrete sheets also implies that the Ben Hiant Dolerite is not a single homogeneous intrusion (cf. Richey and Thomas, 1930). Furthermore, the geometrical form of the stacked sheets, the gently plunging ( $2\text{--}25^\circ$ ; Fig. 7.8) magnetic lineations, sub-vertical columnar joints and the presence of underlying Neoproterozoic Moine metasedimentary host rock along the coast are not consistent with Sheet 1 representing a

vertical feeder zone as suggested by Richey and Thomas (1930). The findings favour the stacked intrusive sheet model proposed by Geikie (1897), although Geikie (1897) suggested the intrusive sheets dipped N–NW whereas field observations indicate an overall gentle eastward dip.

To strengthen the interpretation that the Ben Hiant Dolerite is constructed of vertically stacked, gently SE dipping intrusive sheets, a geologically valid explanation for the steeply inclined margins of Sheet 1 (Fig. 7.2 and 7.9a) is required. The Ben Hiant Dolerite adjacent to the lateral margins of Sheet 1 is unchilled (i.e. unlike all other exposed contacts throughout the intrusion where chilled margins are prevalent), contains AMS fabrics that are discordant at a moderate angle to the steeply inclined contact (Fig. 7.10a) and displays sub-vertical columnar joints (columnar jointing should be orthogonal to a primary contact and not sub-parallel; Ryan and Sammis, 1978). These observations suggest the contacts are not primary. On closer inspection, the moderately dipping, inwardly inclined magnetic foliations of marginal AMS samples (i.e. B-1, B-4 and B-100) appear to be deflected from the sub-horizontal magnetic foliation (Samples B-2 and B-4) and magmatic layering dips measured within the centre of the coastal outcrop (Fig. 7.10a). This concave-downwards geometrical relationship is reminiscent of fault drag and suggests the two lateral contacts are normal faults. The discrepancy in altitude of Ben Hiant Dolerite outcrops on either side of the two steeply, inwardly inclined margins are also congruent with normal fault displacement (Fig. 7.2, 7.10a). Interpreting the NW and SE lateral contacts as faults, implies that the marginal AMS fabrics reflect the interaction of a magmatic and a tectonic sub-fabric. This may be reflected by the 036/10° (plunge azimuth and plunge) magnetic lineation of B-100, which is oriented orthogonally to the overall NW-SE lineation trend of the Ben Hiant Dolerite, but within 10–20° of the magnetic foliation and fault plane (~045/70° SE; strike and dip) intersection. The observed error likely reflects the uncertainty of fault strike and dip. The B-100 magnetic lineation may therefore represent an intersection fabric developed between the magmatic strain field and the strain field associated with fault formation (Fig. 7.10b) (cf. Callot and Guichet, 2003; Žák et al., 2007). Development of two faults (i.e. at the current

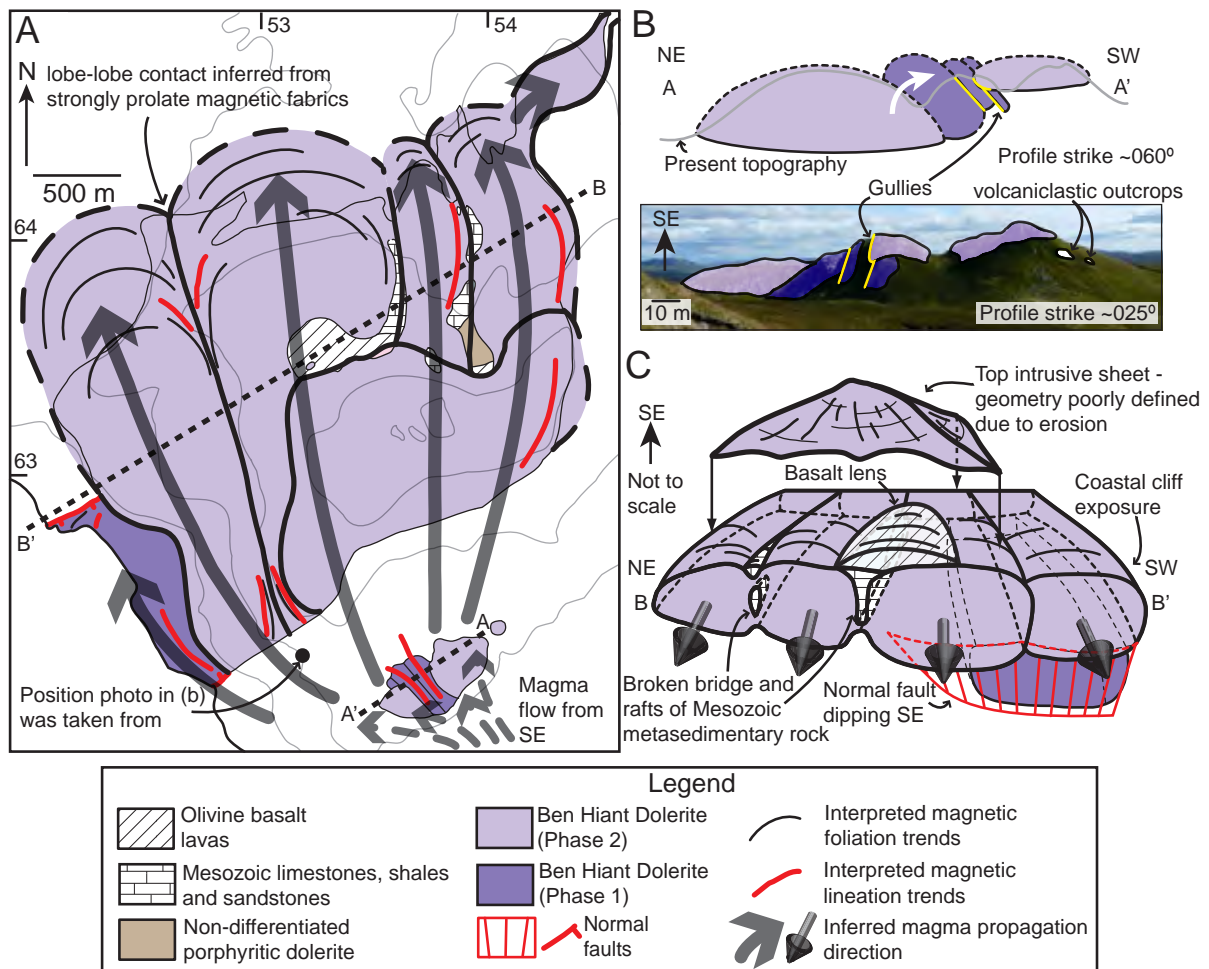


Fig. 7.9: A) Division of the most extensive magmatic sheet into magmatic lobes showing a NW flow direction. B) Section through the primary magma feeder tubes. Note the convex upwards geometry and tilting (white arrow) of the phase 1 magmatic sheets by phase 2 intrusions. C) Cross-section through the lobes detailing their inflated form and the geometry of the broken bridge and bridge xenoliths.

lateral margins) when Sheet 1 was still at a high (sub-solidus) temperature, immediately after solidification, may also explain why the dolerite is unchilled yet the adjacent country rock is thermally altered. These field observations and AMS data suggest the steep contacts are not primary and are instead normal faults. Although the cross-cutting felsic veining in the Ben Hiant Dolerite adjacent to the SE margin may be interpreted as evidence of country rock partial melting associated with a primary contact, the age relationship between the veining and potential faulting is unknown (see Richey and Thomas, 1930). The orientation of the two inferred NE-SW striking normal faults, which bound the Ben Hiant Dolerite in a graben, is orthogonal to the expected orientation of normal faults formed in an extensional regional

stress field where  $\sigma_3$  is oriented NE-SW (cf. Anderson, 1951; England, 1988). Instead, these two faults and some other normal faults observed on Ardnamurchan strike tangentially to the Ardnamurchan central complex, suggesting fault formation or reactivation was related to extensional volcano-tectonic processes, such as the deflation of a magma reservoir and caldera subsidence following a large eruption (cf. Day, 1989).

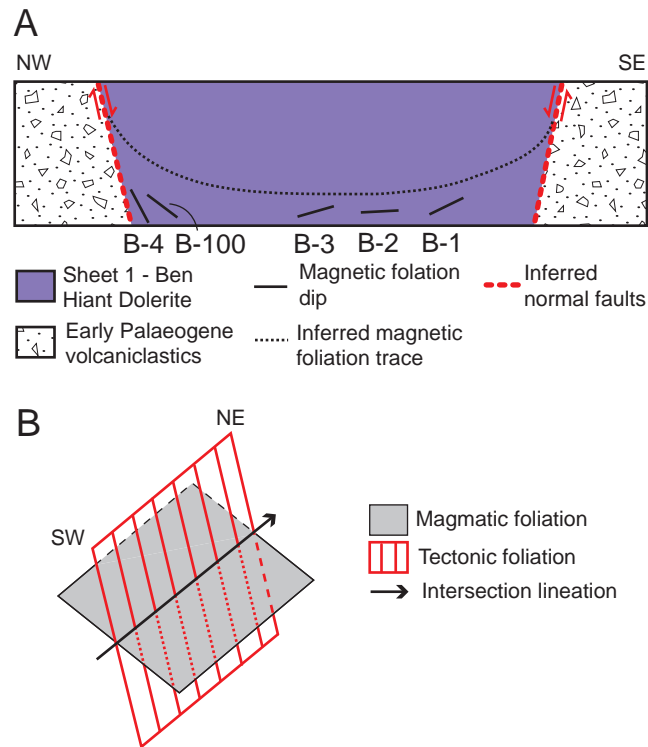


Fig. 7.10: A) Schematic cross-section through the vertical cliff exposure to the SW of the Ben Hiant summit. Magnetic foliations from the coastal AMS samples are transposed onto the section and an inferred trace extrapolated to highlight fabric deflection associated with the outer margins. B) Diagram showing how the intersection between the magmatic and tectonic (i.e. associated to faulting) foliations may produce a NE-SW oriented lineation similar to B-100.

Topographically higher intrusive sheets of Ben Hiant Dolerite are more laterally extensive and from field observations appear not to be affected by the normal faults, suggesting they were emplaced after fault movement (Fig. 7.9a). We argue that the Ben Hiant Dolerite was divided into two principal intrusive phases, phase 1 (Sheet 1) and phase 2 (Sheet 2 and 3) respectively, by an intervening period of extensional faulting. The temporal offset between extensional faulting and the intrusion of phase 2 implies the magnetic fabrics of Sheets 2 and 3 may purely be attributed to primary magmatic flow as suggested by the

rock magnetic data and petrographical observations. The spatial and temporal variation in titanomagnetite composition (i.e. Ti-content increases with topographic height in younger sheets) potentially reflects replenishment of the source reservoir or progressively increasing oxygen fugacity conditions in successive magma pulses associated with an evolving magma chamber. Given the overall silicate mineralogical similarities observed throughout the Ben Hiant Dolerite, it is unlikely the observed pattern of titanomagnetite composition variation is an indicator of magma differentiation; a similar conclusion reached for early Miocene Cieneguilla basanite in the northern Rio Grande Rift, New Mexico, USA (Lindline et al., 2011).

Gently plunging, NW-SE trending magnetic lineations measured in the Stallachan Dubha and Sròn Mhor are consistent with those in the main body of the Ben Hiant Dolerite to the NW, suggesting the two were once linked by a subsequently eroded section of Ben Hiant Dolerite. The minor intrusive sheets defined at Stallachan Dubha and Sròn Mhor, whilst thinner (~10–20 m) and more laterally restricted compared to the magmatic sheets observed within the main body of the Ben Hiant Dolerite, may also be temporally divided into phase 1 or 2 from their inferred geometries. Secondary to the overall gentle SE dip of the Stallachan Dubha and Sròn Mhor Ben Hiant Dolerite masses, the stepped topography of the gullies on Sròn Mhor (Fig. 7.4a) suggests three component sheets have a moderate SW dip (Fig. 7.9b). These sheets are cross-cut by a later intrusive sheet on Sròn Mhor inclined at 064/12° SE (strike and dip); similar to the orientation of the Stallachan Dubha mass (Fig. 7.2 and 7.9b). It is suggested that the moderately SW dipping sheets belong to the older phase 1 and were tilted, from an original gentle SE dip, to their current position by the intrusion of the later phase 2 Stallachan Dubha Ben Hiant Dolerite body. The cross-cutting sheet, oriented 064/12° SE (strike and dip), on Sròn Mhor is also attributed to phase 2.

#### 7.4.1:2 *Magmatic lobes*

Magmatic lobes (Fig. 7.11) have been identified in tabular intermediate-felsic intrusions (e.g. Dinkey Creek pluton, USA, Cruden et al., 1999; Maiden Creek Sill, USA, Horsman

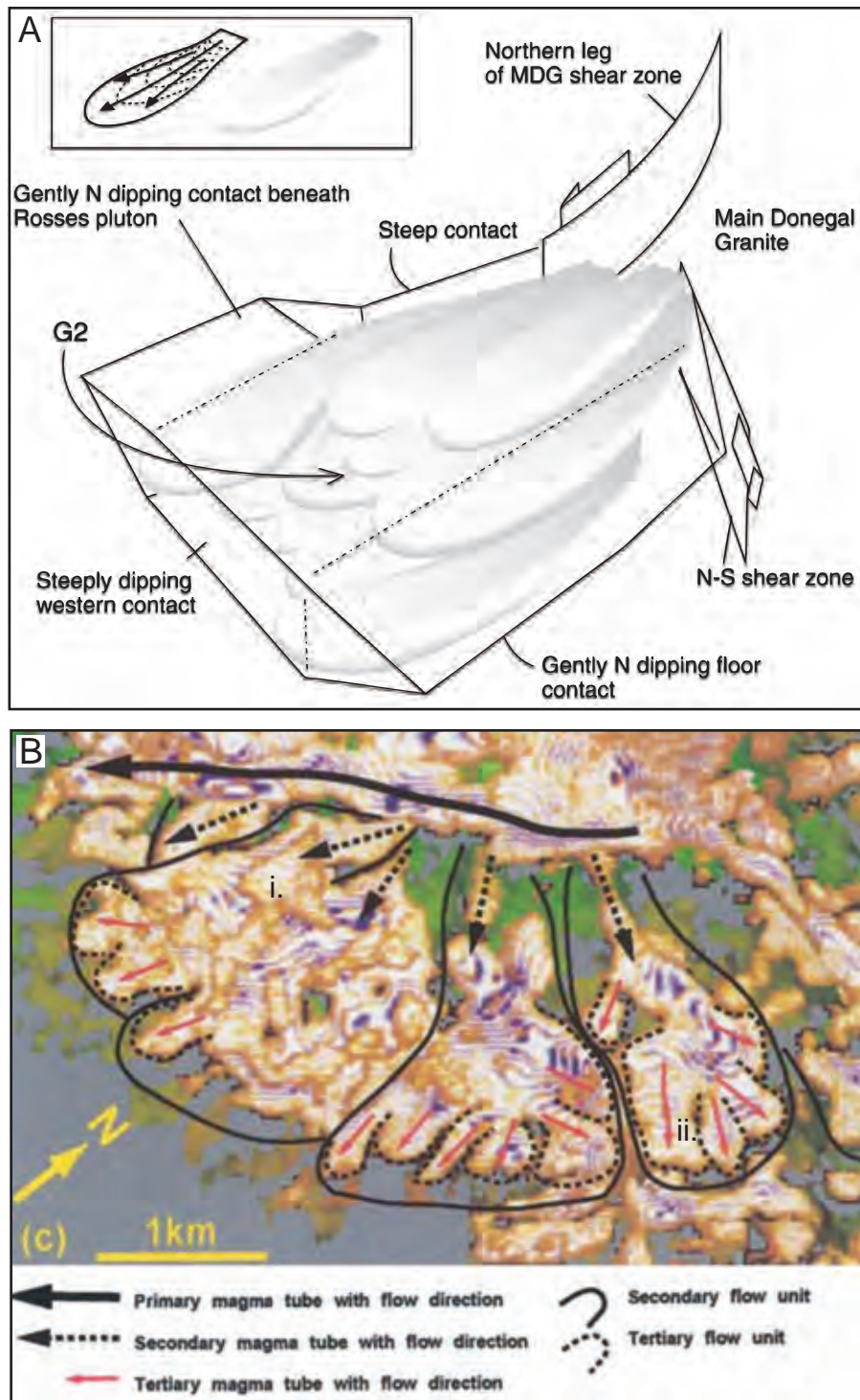


Fig. 7.11: A) Model of the magmatic lobes identified in the Trawenagh Bay Granite (Stevenson et al., 2007a). Fine dashed lines denote magnetic foliation strikes. B) Magmatic lobes (i) and potentially magma fingers (ii) identified in a high resolution seismic image of a sill in the Rockall Trough (Thomson and Hutton, 2004).

et al., 2005; Trawenagh Bay Granite, Ireland, Stevenson et al., 2007a) and in seismically imaged sills (e.g. Rockall Trough, Thomson and Hutton 2004; Solsikke lobate sill, Hansen and Cartwright, 2006). From a relatively confined magma feeder tube, magmatic lobes successively branch out laterally, gradually increasing in width as they propagate and developing a convex-outwards, bulbous end oriented parallel to the magma flow direction (Fig. 7.11) (Thomson and Hutton, 2004; Stevenson et al., 2007a; Morgan et al., 2008). Further focusing of magma into these flow units produces a second phase of growth as the lobe inflates vertically (similar to Rocchi et al., 2002). Incrementally intruded, expanding magmatic lobes often impinge on each other and may coalesce to form intrusive sheets with internal lobe-lobe contacts oriented normal to the intrusive plane (Thomson and Hutton, 2004); although discrete contacts between sheets are often not visible in the field they may be readily revealed with detailed AMS study.

A conspicuous zone, trending NW-SE, of convergent sub-horizontal magnetic lineations and foliation strikes, within Sheet 2 (Fig. 7.8) to the W of the Ben Hiant summit, is inferred as a sub-vertical lobe-lobe contact (Fig. 7.9a). The AMS fabrics close to the suggested internal boundary are strongly prolate (i.e. samples B-24, B-28, B-29, B-101 and B-123; Fig. 7.6a) with magnetic lineations and foliation strikes sub-parallel to the inferred contact (Fig. 7.8). Prolate fabrics typically develop from higher finite strains, compared to triaxial and oblate fabrics, and may reflect frictional drag of magma adjacent to the country rock (e.g. Horsman et al., 2005). Subsequently the maximum magma stretching direction, or flow direction, is parallel to the contact (Morgan et al., 2008). The NW-SE striking lobe-lobe contact interpreted from the magnetic fabrics coincides with the position and strike of several outcrops of highly sheared Ben Hiant Dolerite (Fig. 7.2 and 7.3e), supporting the inference that there was a higher finite strain near the conduit walls (Fig. 7.2 and 7.3e). Towards the interior of the two defined lobes, particularly towards the NW margin of the Ben Hiant Dolerite, the magnetic foliations are steeply inclined and, as they proceed towards the lobe interior, their strike progressively rotates to an orientation orthogonal (i.e. NE-SW) to the lobe-lobe contact describing a convex north-westwards geometry (Fig. 7.8c). Magnetic

foliation strikes rotate away from an orientation parallel to the lobe-lobe contact towards the SE margin of the main Ben Hiant Dolerite body, although no strikes orthogonal to the inferred NW-SE magma flow trend were observed. Similar curved, sub-vertical magnetic foliation geometries are observed near bulbous lobe terminations in field examples (Fig. 7.11a) (e.g. Cruden et al., 1999; Stevenson et al., 2007a; Morgan et al., 2008), as well as in analogue models (Kratinová et al., 2006), and are interpreted to form orthogonal to the magma flow direction from the development of a divergent magma flow regime that reflects the frontal lobe geometry (Cruden et al., 1999; Stevenson et al., 2007a; Morgan et al., 2008). The inward dip of the magnetic foliations is consistent with sampling in close proximity to the base of the interpreted lobes (cf. Cruden et al., 1999; Horsman et al., 2005). This further supports that AMS fabrics within each individual lobe reflect primary magmatic flow fabrics. Preservation of primary magmatic flow fabrics within individual lobes of Ben Hiant Dolerite suggest that internal boundaries were maintained after coalescence and no magma mixing or crystallisation processes occurred between lobes after emplacement.

Occasionally, a lobe-lobe contact may be defined by a bridge of host rock trapped between two inflating magmatic lobes (cf. Thomson and Hutton, 2004; Horsman et al., 2005; Hutton, 2009). An outcrop of Mesozoic sedimentary rock, observed in a stream to the NW of the Ben Hiant summit (Fig. 7.2), is vertically bounded by Ben Hiant Dolerite and is interpreted as a screen between two adjacent magmatic lobes. The screen is cut at its base by a sub-horizontal sheet of Ben Hiant Dolerite but at its top is attached to the stratigraphically younger olivine basalt lavas through a primary sub-horizontal unconformity (Fig. 7.2 and 7.9c), suggesting it may be defined as a broken bridge (cf. Hutton, 2009). Isolated host rock outcrops to the N of the summit (Fig. 7.2), which have a conspicuous linear arrangement and sub-vertical contacts along their length, may represent bridge xenoliths (both ends of the bridge are fractured and intruded; Hutton, 2009) from which another lobe-lobe contact may be inferred (Fig. 7.9). The long axes of broken bridges and bridge xenoliths can be used to roughly infer the primary magma flow axes (Rickwood, 1990; Hutton, 2009). Here, the bridges trend approximately N-S, sub-parallel to the local  $K_1$  lineations, further supporting

interpretation of magnetic fabric as a magma flow fabric.

Primary magma transport tubes feeding magma lobes are laterally thinner, compared to the lobes they feed, often elongated in the magma flow direction and convex-upwards in cross-section (cf. Pollard et al., 1975; Thomson and Hutton, 2004). The laterally restricted individual sheets described from Stallachan Dubha and Sròn Mhor possibly represent primary magma feeder tubes, assuming a SE to NW magma flow regime, or offshoots originating from the main Ben Hiant Dolerite body (i.e. magma flowed NW to SE).

## 7.4.2 Controls on emplacement position

### 7.4.2.1 *Stress field influence*

Intrusive sheets preferentially intrude orthogonally to the least compressive principal stress axis (i.e.  $\sigma_3$ ; Anderson, 1951) when the internal magma pressure exceeds the magnitude of  $\sigma_3$  (Rubin, 1995). Analysis of sheet geometry may inherently allow the stress field during emplacement to be reconstructed (Jolly and Sanderson, 1997). The approximate sub-horizontal orientation of the Ben Hiant Dolerite sheets suggests, during intrusion,  $\sigma_3$  was oriented sub-vertically. Traditionally, either a local or regional stress field may be envisaged to have controlled emplacement (Anderson, 1936; Anderson, 1951; Gautneb and Gudmundsson, 1992; Gudmundsson, 1998; Gudmundsson, 2006; Geshi, 2005; Acocella and Neri, 2009).

Throughout the evolution of the BIPIP the regional stress field  $\sigma_3$  axis was sub-horizontal and oriented NE-SW (England, 1988). Neither of the two stress fields described correlate to the principal stress axes determined from the intrusion geometry. The distribution and nature of the Centre 1 intrusions (e.g. the major intrusions and the cone sheets) are consistent with a syn-intrusive local compressional stress regime generated by an inflating central major magma reservoir, 3–5 km below the present surface (Richey and Thomas, 1930; Anderson, 1936). Gudmundsson (1998; 2006) numerically modelled the local principal stress axes generated by overpressured magma chambers, with spherical or sill-like geometries, within a regional extensional setting similar to the BIPIP. From these models it is apparent that sub-vertical  $\sigma_3$  trajectories may only be developed adjacent to the upper margins of the

magma chamber (Gudmundsson, 1998; 2006). Given that the Ben Hiant Dolerite is a satellite intrusion located ~2 km laterally to the SE of Ardnamurchan and was emplaced at a higher stratigraphic level compared to the Centre 1 magma reservoir (Richey and Thomas, 1930), it is unlikely the local compressive  $\sigma_3$  principal stress axes during its intrusion were oriented sub-vertically. The  $\sigma_3$  axes of the local or regional stress fields, active during the emplacement of the Ben Hiant Dolerite, are therefore both inconsistent with the sub-horizontal sheet orientations observed. The horizontal, older basalt lavas adjacent to the Ben Hiant Dolerite (Fig. 7.2) suggest little or no tilting has occurred.

It is suggested that the interaction and interference between the local compressive stress field and the regional extensional stress field cancelled each other out (see Chapter 6, section 6.3.2), resulting in localised zones tending towards lithostatic stress (i.e. little or no horizontal deviatoric component) where  $\sigma_3$  was sub-vertical (Fig. 7.12) (cf. Guglielmo, 1993; 1994). Similar stress field interference patterns are observed around expanding intrusions, within regional extensional regimes, where pre-existing host rock foliations are deflected and the approximate lithostatic stress zones (also termed 'low strain zones'; Guglielmo, 1993; 1994) adopt a conical geometry pointing away from the intrusion (Guglielmo, 1993; 1994). The position and the direction of the approximate lithostatic stress zones is controlled by the relative magnitudes of the competing stress fields, the shape of the intrusion(s) instigating the local stress field and the respective orientation of the regional stress field (Guglielmo, 1993; 1994). During formation of the BIPIP the active regional NE-SW extensional regime (England, 1988) likely promoted the formation of lithostatic stress zones to the NW and SE of the Ardnamurchan central complex (Fig. 7.12) (cf. Guglielmo, 1994). Intrusion of Ben Hiant Dolerite sheets into this lithostatic stress zone, regardless of their original geometry, would result in their reorientation to maintain an intrusive plane orthogonal to  $\sigma_3$ .

None of the observed Ben Hiant Dolerite intrusive sheets are coeval to the extensional faulting, suggesting faulting either coincided with a reduction in magma supply or that the intrusion of Ben Hiant Dolerite magma occurred elsewhere. Development of extensional faults reflects a change in orientation, and possibly magnitude, of the local principal stress,

which may have shifted the lithostatic stress zone to the SE. Consequently, Ben Hiant Dolerite magma may have been emplaced within a lithostatic stress zone to the SE of Ben Hiant, now offshore. Relaxation of the local stress field, similar to its previous magnitude, possibly relocated the lithostatic stress zone back to its original position and allowed further growth of the Ben Hiant Dolerite. Fluctuations in the local stress field, associated to cyclical inflation (i.e. compression) and deflation (i.e. extension) of major central intrusions, have been described from numerous volcanic centres and appear to significantly influence emplacement position and intrusion geometry (e.g. Day, 1989; Acocella and Neri, 2009).

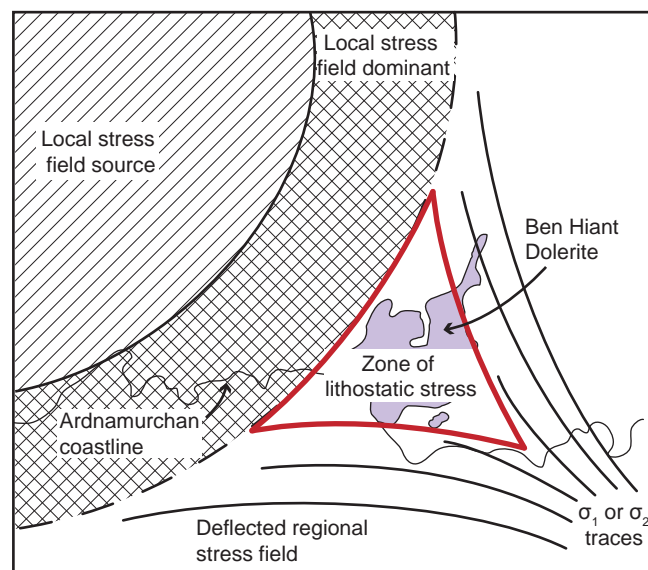


Fig. 7.12: Sketch of the interference between the local and regional stress field and possible position of a zone tending towards lithostatic stress, coincident with the location of the Ben Hiant Dolerite.

#### 7.4.2.2 Rigidity contrasts in the host rock succession

Several unconformities defining significant rigidity contrasts within the host rock occur in the region of Ben Hiant; the Proterozoic Moine metasedimentary rocks are overlain by Mesozoic limestones and shales as well as Early Palaeogene poorly consolidated volcanoclastics and weathered olivine basalt lavas (Fig. 7.2; Richey and Thomas, 1930; Emeleus and Bell, 2005; Brown and Bell, 2006). Numerous studies, based on field observations (Horsman et al., 2005; Morgan et al., 2008; Burchardt, 2008; Thomson and Schofield, 2008; Schofield et al., 2010) and analogue experiments (Kavanagh et al., 2006; Menand, 2008), have highlighted the

importance of such rigidity contrasts, whether developed between two country rock units or through the juxtaposition of country rock with a previous sheet intrusion, on controlling sheet intrusion position. The vertical stacking of the Ben Hiant Dolerite sheets is consistent with and provides further support for a rigidity contrast control on the successive emplacement of intrusive sheets.

#### **7.4.3 Magma flow regime and source**

The supposition that the Ben Hiant Dolerite magmas are derived from the Ardnamurchan central complex is central to the models of Geikie (1897) and Gribble (1974). The preponderance of NW-SE sub-horizontal to moderately plunging magnetic lineations and gently SE dipping sheeted form of the Ben Hiant Dolerite is suggestive of a lateral magma flow regime and, combined with field observations, does not define any potential vertical feeder. Although the NW-SE trending magnetic lineations are consistent with magma possibly being fed laterally from the Ardnamurchan central complex to the NW, this observation does not preclude a source to the SE. Magnetic lineation trends and sub-parallel broken bridge axes in the north of the Ben Hiant Dolerite are oriented more N-S compared to the general NW-SE trend, implying that the lobes are branching from a point in the SE (Fig. 7.9a) (cf. Thomson and Hutton, 2004). This is supported by the dimensions of the inferred magmatic lobes, which appear to increase in width towards the NW. The thinner intrusive sheets at Stallachan Dubha and Sròn Mhor are potentially primary magma feeder tubes. These observations, in conjunction with the convex north-westward closing geometry of the magnetic foliation strikes in the lobe interiors, suggest the Ben Hiant Dolerite magma propagated in a north-westwards direction from a source area located to the SE (Fig. 7.9). Overall, the data presented here is consistent with a magma source to the SE and lateral magma flow through primary magma transport tubes, preserved at Sròn Mhor and Stallachan Dubha, from which individual lobe buds diverged, and propagated for approximately 1.5 km before subsequently inflating.

This lateral magma flow regime and SE source is not consistent with previous

emplacement models for the Ben Hiant Dolerite (cf. Judd, 1874; Geikie, 1897; Richey and Thomas, 1930; Gribble, 1974; Emeleus and Bell, 2005). A source within the Ardnamurchan central complex may be maintained if it is envisaged that some of the transgressive Centre 1 cone sheets (cf. Palmer et al., 2007), observed to extend to the SE of Ben Hiant (Emeleus, 2009) and assumed to originate from a central source (Richey and Thomas, 1930), fed the Ben Hiant Dolerite. This implies the cone sheets were reoriented, upon entering the approximate lithostatic stress zone, into NW propagating sills or magma tubes (Fig. 7.13). Richey and Thomas (1930) highlight a geochemical similarity between the Ben Hiant Dolerite and the cone sheets, which may support this hypothesis, although they also note that there is a distinct mineralogical difference. Similar examples of inclined sheets feeding sills are observed in the field (e.g. Burchardt, 2008) and in seismic data (Smallwood, 2008). There are several issues with this interpretation. First, the relatively thin (~1 m) Ardnamurchan cone sheets often display chilled margins (Richey and Thomas, 1930) and lack internal variation, suggesting they did not form magma conduits capable of supplying a major intrusion such as the Ben Hiant Dolerite. Second, the prominent NW-SE trending lateral magma flow pattern identified within the majority of cone sheets may reflect a regional dyke source to the cone sheets, questioning the traditional assumption that cone sheets are centrally fed.

Alternatively, the Ben Hiant Dolerite may have been fed by the NW-SE striking regional dykes (Fig. 7.14). The regional dykes located in southern Scotland and northeast England (e.g. the Cleveland dyke) extend from the Mull central complex, with which they share a geochemical affinity and are interpreted to have laterally propagated from, for  $\leq 600$  km (Jolly and Sanderson, 1995; Macdonald et al., 2009; 2010). Speight et al., (1982) mapped in detail the distribution of the regional dyke swarm, identifying over 300 outcrops of NW-SE trending regional dykes that connect the Ardnamurchan and Mull central complexes. The regional dyke swarm associated with the Mull central complex, while locally compositionally variable, is dominated by tholeiitic basalts and, locally, alkali-olivine dolerites (Kerr et al., 1999). A detailed comparison between the Ben Hiant Dolerite and the Palaeogene regional dyke swarm is beyond the scope of this study. However, geochemical analyses (whole rock

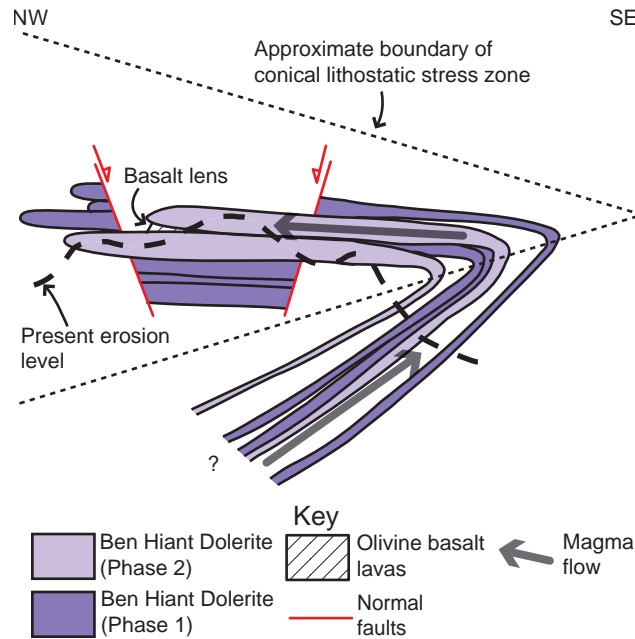


Fig. 7.13: Possible construction of the Ben Hiant Dolerite from cone sheets fed from a central source located at depth beneath Centre 1. Upon entering the zone of lithostatic stress, the cone sheets will likely reorient to sub-horizontal position (i.e. orthogonal to  $\sigma_3$ ) and may propagate back towards the Ardnamurchan central complex.

major and trace element) of rock glass within the Ben Hiant Dolerite, conducted to determine the composition of the primary magma, highlights a similarity in major element abundance with the 'Non-porphyritic Magma-type' of the Mull central complex (Gribble, 1974), now renamed the Central Mull Tholeiite Magma-type (Emeleus and Bell, 2005). In the absence of a detailed geochemical and isotopic study of the Ben Hiant Dolerite and the Mull regional dyke swarm, this is taken as permissible evidence that laterally propagating regional dykes from the Mull magmatic system may have sourced the Ben Hiant Dolerite (~35 km NW of the Mull central complex). This distance of lateral propagation is similar to that recorded for dyke intrusion (~30 km) associated with the 1975–1984 Krafla (Iceland) volcanic event (Paquet et al., 2007). Inherently, this model implies the regional dykes turned into a series of stacked sills, similar to the transition of intrusive forms observed in the field and particularly in analogue experiments (Hyndman and Alt, 1987; Rivalta et al., 2005; Kavanagh et al., 2006; Kervyn et al., 2009).

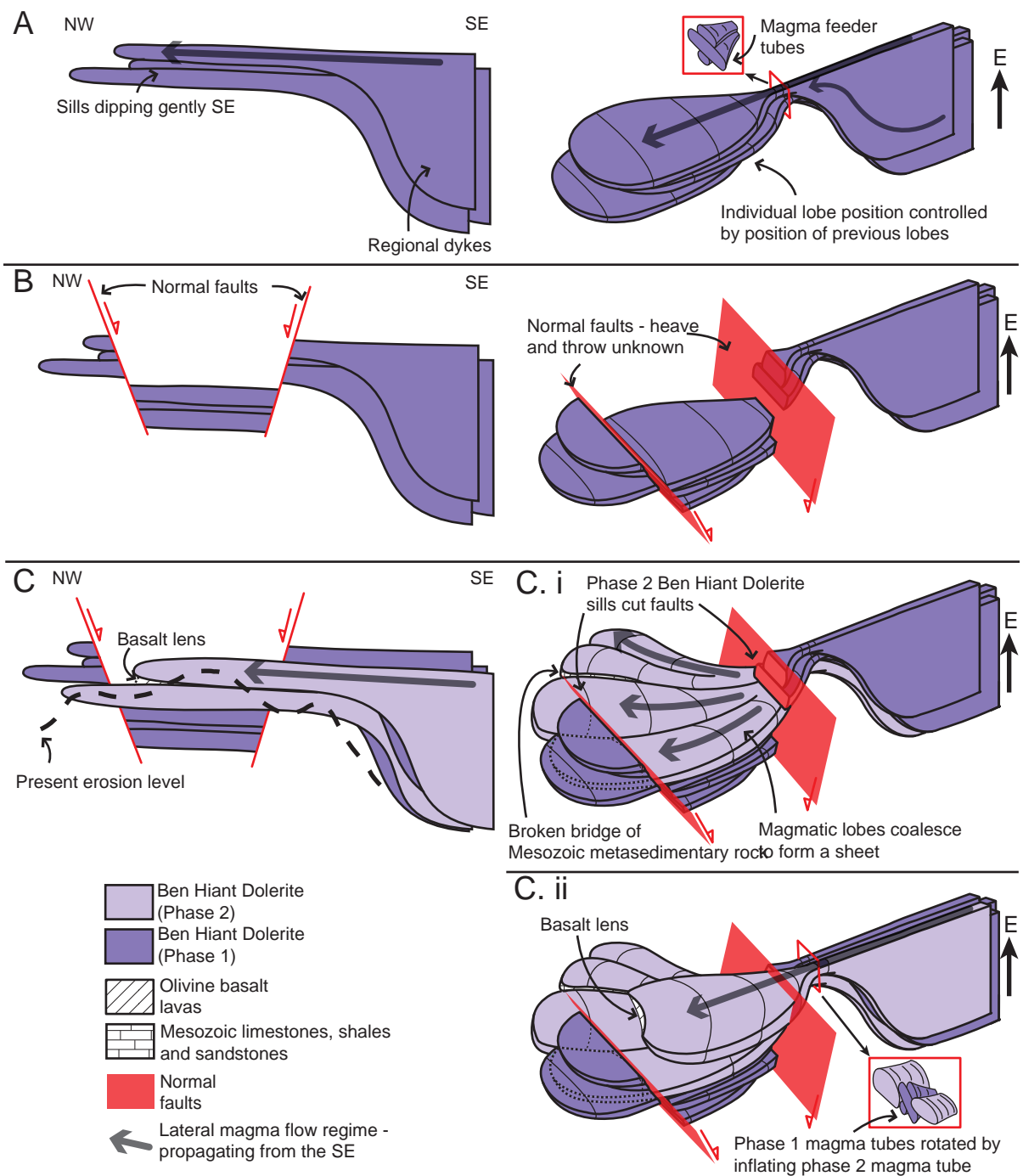


Fig. 7.14: Emplacement model of the Ben Hiant Dolerite if regional dyke feeders are assumed. A) Laterally propagating regional dykes become rotated, due to the reorientation of principal stress axes within the lithostatic stress zone, into sills through an intermediary magma tube. Initially sill growth is lateral. B) Normal faulting downthrows the central portion of the sills. C) A second phase of intrusion and inflation of magmatic sills, sourced from regional dykes and divided into discrete magmatic lobes, cuts through the faults.

#### **7.4.4 Intrusion of the Ben Hiant Dolerite and implications for the emplacement of the Ardnamurchan cone sheets**

Field observations reveal that the Ben Hiant Dolerite is constructed from incrementally emplaced magmatic sheets stacked vertically, in agreement with the emplacement models proposed by Geikie (1897) and Gribble (1974). Implicit in previous models is the assumption that the Ben Hiant Dolerite was fed from the Ardnamurchan central complex located ~2 km to the NW (Judd, 1874; Geikie, 1897; Richey and Thomas, 1930; Gribble, 1974). From AMS analyses, conducted to constrain the internal structure of the Ben Hiant Dolerite, a NW-SE trending, sub-horizontal–moderately plunging primary magma flow regime was identified. Several magmatic lobes, the primary component of the magmatic sheets, are defined by broken bridges, zones of high finite strain associated with frictional drag of magma and convex striking magnetic foliations. In contrast to previous models (cf. Judd, 1874; Geikie, 1897; Richey and Thomas, 1930; Gribble, 1974) the results suggest a magma source to the SE. This is supported by (1) the convex magnetic foliation strikes within the magmatic lobes, (2) the increase in width of the identified magmatic lobes to the NW (Fig. 7.9) and (3) the inferred branching nature of the lobes. The north-westerly, shallowly plunging primary magma flow regime identified from these data may be linked to either a centrally sourced cone sheet feeding a sill-like intrusion or to laterally propagating regional dykes fed from the Mull central complex located ~35 km to the SE. Local host rock (i.e. rigidity contrasts between unconformities) and stress field (e.g. instigating the normal faulting and the zone of lithostatic stress) conditions likely favoured and accommodated construction of a vertically stacked sheet intrusion rather than continued propagation.

The observed controls on emplacement of the Ben Hiant Dolerite, the host rock structure and local stress field, are consistent with similar conclusions derived from field studies (Geshi, 2005; Burchardt, 2008; Schofield et al., 2010) and experimental modelling (Gudmundsson, 1998; Gudmundsson, 2006; Kavanagh et al., 2006; Menand, 2008). Importantly, the interaction and interference between multiple, contemporaneous stress fields (e.g. the regional stress field and the local compressive stress field) appears to

have significantly influenced intrusion position. The derived emplacement models for the Ardnamurchan cone sheets and the Ben Hiant Dolerite, although possibly consistent with a central magma source, favour a laterally adjacent magma source connected to Ardnamurchan through laterally propagating regional dykes.

---

## CHAPTER 8

### DISCUSSION AND CONCLUSIONS

---

#### 8.1 Summary of Ardnamurchan sheet intrusion emplacement mechanisms

##### 8.1.1 The Ardnamurchan cone sheets

The broadly concentric, inwardly inclined Ardnamurchan cone sheets are locally highly variable in geometry and dip disposition. Field observations suggest cone sheet dip is strongly influenced by the pre-existing host rock structure. Inwardly inclined cone sheets are often observed to exploit inward-dipping fractures, that belong to a conjugate fracture set, whilst outward-dipping cone sheets ( $\sim < 15^\circ$ ) intrude roughly parallel to bedding plane (when bedding is present) or anisotropies that are sub-parallel to the local bedding trend (e.g. cleavage). Derivation of the principal stress axes active during fracture formation and cone sheet intrusion indicates a transition from an extensional to a compressional stress regime; related to the emplacement and inflation of component intrusions of the Ardnamurchan central complex. Intrusion-induced doming facilitated the rotation of fractures and bedding into orientations, which favoured their reactivation by propagating cone sheet magma. Host rock lithology also appears an important control on cone sheet morphology. Cone sheets intruding mechanically strong rocks (e.g. the Neoproterozoic and Mesozoic metasedimentary rocks) typically intruded offset brittle fractures and coalesced upon inflation through the development of intrusive steps and broken bridges. Several cone sheets emplaced into poorly consolidated Early Palaeogene volcanoclastics and olivine basalt lavas are observed to form magma lobes and magma fingers, indicative of intrusion accommodated by the non-brittle fluidisation of the host rock.

AMS measurements of the Ardnamurchan cone sheets and regional dykes highlight

a preponderance of NW-SE oriented, sub-horizontal to moderately plunging magnetic lineations, which following their correlation to visible field flow indicators, are interpreted to reflect the primary magma flow axis and is suggestive of a common origin. Although some cone sheets appear to be fed from a central magma source (i.e. magnetic lineation is sub-parallel to cone sheet dip and dip azimuth), as proposed by Richey and Thomas (1930) and Anderson (1936), the majority of cone sheets (~73 %) likely represent laterally propagating regional dykes.

The geometry and magma flow pattern of the archetypal Ardnamurchan cone sheets does not conform to previous emplacement models (e.g. Richey and Thomas, 1930; Anderson, 1936; Durrance, 1967; Phillips, 1974; Gautneb et al., 1989; Gautneb and Gudmundsson, 1992; Walker, 1993; Schirnack et al., 1999; Klausen, 2004; Geshi, 2005; Tibaldi and Pasquarè, 2008; Siler and Karson, 2009; Tibaldi et al., 2011), in that a central source is not supported. Instead, it is proposed that interference between the locally compressional and the regional extensional stress fields caused the deflection of laterally propagating regional dykes around the Ardnamurchan central complex and into pre-existing inwardly inclined fractures; thus producing a ‘cone sheet’ like geometry. It is suggested that the sheets that were emplaced laterally from an external source (i.e. independent of the Ardnamurchan central complex) are termed ‘deflected dykes’.

### **8.1.2 The Ben Hiant Dolerite intrusion**

Field observations and structural measurements integrated with new anisotropy of magnetic susceptibility (AMS) data have been utilised to re-assess the emplacement of the Ben Hiant Dolerite. Previous emplacement models have suggested the Ben Hiant Dolerite is an early satellite intrusion of the Ardnamurchan central complex (located ~2 km NW of Ben Hiant) and formed either as a single, homogenous intrusive mass (Richey and Thomas, 1930), an amalgamation of incrementally emplaced inclined sheets (Geikie, 1897; Gribble, 1974) or a series of lava flows (Judd, 1874). Shallowly dipping outer contacts with the host rock and predominantly gently plunging magnetic lineations suggest that the Ben Hiant Dolerite

consists of several incrementally emplaced sub-horizontal intrusive sheets, which in places may be further divided into magmatic lobes. Curved magnetic foliations and magmatic lobe geometries imply magma flow was directed north-westwards and did not originate from the Ardnamurchan central complex. The proposed emplacement model for the Ben Hiant Dolerite, involving laterally propagating regional dykes likely fed from the Mull central complex being reoriented into sub-horizontal sheets by intrusion into a zone tending towards lithostatic stress (i.e. a result of stress field interference), supports the intrusion mechanisms defined for the Ardnamurchan deflected dykes.

### **8.1.3 Controls on regional dyke emplacement**

Primary magma flow regimes from the Ardnamurchan deflected regional dykes, normal regional dykes and the Ben Hiant Dolerite are consistent with the magma flow regimes observed in BIPIP regional dykes on Skye (Herrero-Bervera et al., 2001; 2003) and in the southern Scotland-NE England regional dyke swarm (Macdonald et al., 1988; 2009; 2010). The north-westwards magma flow direction of the Ben Hiant Dolerite, inferred from the geometry of discrete magma lobes, suggests the Mull central complex situated ~35 km SE of Ardnamurchan is a potential source for the regional dyke magma. This is corroborated by geochemical similarities, particularly of radiogenic isotopes (e.g. Sr and Nd), between the Ardnamurchan deflected regional dykes and the Mull intrusions/extrusions. This may also preclude a magma source to the NW of the Ardnamurchan central complex and beyond the Moine Thrust terrane boundary as magmas from the NW should be geochemically distinctive (Prof. Val Troll, pers. comm.)

Cross-cutting relationships and radiometric dating indicate regional dyke emplacement occurred throughout the history of the BIPIP (Emeleus and Bell, 2005). On Ardnamurchan, the derived emplacement models for the deflected regional dykes and the Ben Hiant Dolerite suggest continuous regional dyke intrusion occurred during volcanic edifice construction, but that the intrusive geometries varied. The generation of a local compressive stress field, due to the emplacement and inflation of some currently unexposed part of the Ardnamurchan central

complex, produced an interference pattern with the regional extensional stress field, which resulted in the contemporaneous intrusion of the deflected regional dykes into a ‘cone sheet’ geometry and the Ben Hiant Dolerite stacked sheet intrusion, as well as the formation of thrust faults (Day, 1989). Extensional faulting, likely related to magma chamber deflation and/or caldera collapse in the Ardnamurchan central complex (Day, 1989), occurred intermittently with the formation of the deflected regional dykes and the Ben Hiant Dolerite. It is suggested that during phases of extension, the regional stress field predominantly controlled intrusive forms and led to the propagation of sub-vertical, NW-SE striking regional dykes into the Ardnamurchan central complex (cf. Geshi, 2005).

## **8.2 Insights into the emplacement of other sub-volcanic complexes**

Discerning the emplacement mechanisms of sheet intrusions is key to understanding the transport, delivery and accommodation of magma in the upper crust. Cone sheets, dyke swarms and stacked sheet intrusions are recognised as important elements in the intrusive framework of many volcanic systems in the geological record (e.g. Mull central complex, Scotland, Bailey et al., 1924; Tejeda complex, Gran Canaria, Schirnick et al., 1999; Thverartindur igneous centre, Iceland, Klausen, 2004; Otoge igneous complex, Japan, Geshi, 2005). Reconstructing the growth and temporal evolution of sheet intrusions is therefore an important step in understanding the sub-edifice behaviour of volcanic systems (e.g. Stardalur Volcano, Iceland, Pasquarè and Tibaldi, 2007; Tibaldi and Pasquarè, 2008). Distinguishing the magma source position is an integral part of this process. Traditionally, cone sheets have often been assumed to originate from a central source at depth. Although several studies have corroborated this relationship through field observations and geochemical analyses (e.g. Geshi, 2005), the results presented in this study suggest that the archetypal Ardnamurchan cone sheets were laterally emplaced from a source external to the Ardnamurchan central complex. This questions our current understanding of magmatic linkages between adjacent magmatic systems.

An important aspect in this study to delineate magma source position has been the utilisation of AMS to quantify primary magma flow fabrics to trace magma source position. However, few studies of cone sheets have applied AMS (e.g. Herrero-Bervera et al., 2001) or analysis of visible field flow indicators (e.g. Geshi, 2005) to determine magma flow patterns. The observed spatial relationship between areas of increased deflected regional dyke abundance and the intersection of the regional  $\sigma_1$  principal stress axis with the Ardnamurchan central complex may be applicable elsewhere to initially identify possible laterally fed cone sheet complexes. It is interesting to consider the application of this model to other central complexes throughout the geological record. Cone sheets emplaced during regional extensional regimes (e.g. the BIPIP, Iceland and the Canary Islands) are discussed first, as regional dykes are commonly developed in these settings, in an attempt to define the versatility of the emplacement model for the Ardnamurchan deflected regional dykes. In these tectonic settings it is hypothesised that increased cone sheet abundances in areas containing the central complex intersection with the regional  $\sigma_1$  (or  $\sigma_2$ ) and  $\sigma_3$  principal stress axes highlight a lateral and central source, respectively. Cone sheets intruded in compressional settings are also briefly considered and followed by insights into laterally fed stacked sheet intrusions.

### **8.2.1 The British and Irish Palaeogene Igneous Province**

#### **8.2.1:1 *Skye***

The cone sheet swarm associated with the Cuillin igneous complex is perhaps the most studied in the BIPIP. Similar to the Ardnamurchan cone sheets, the tholeiitic dolerite Cuillin cone sheets display an increase in abundance to the SE and NW of the Cuillin igneous complex, at its intersection with the NW-SE striking regional dyke swarm (Fig. 8.1a) (Speight et al., 1982; Walker, 1993; Emeleus and Bell, 2005). Cone sheet dips ( $\sim 40\text{--}50^\circ$ ) are uniform in both distance from the central complex and elevation, although no cone sheets are observed below 300 m (Harker, 1904; Walker, 1993; Tibaldi et al., 2011). In contrast to Ardnamurchan, the Cuillin cone sheets are offset from the area of local doming and intrude predominantly

Palaeogene gabbro (Walker, 1975a). As the orientation of cone sheets and gabbro layering are parallel (Walker, 1975a; Bell et al., 1994) and intrusive steps and broken bridges are observed (Walker, 1993), it is suggested that the pre-existing host rock structure influenced emplacement. Walker (1993) postulated that the regional dykes and cone sheets were intermittently emplaced (over 1 Ma; Bell et al., 1994) from a central source depending on the orientation of the local  $\sigma_2$  and  $\sigma_3$  principal stress axes (Fig. 1.8e). This is supported by Tibaldi et al., (2011) whom distinguished at least two alternating dyke and cone sheet emplacement phases. Dykes and normal faulting are proposed to have occurred during extension, locally related to magma chamber deflation, with cone sheets intruded during phases of compression (Walker, 1993; Tibaldi et al., 2011). Petrological and geochemical affinities between the regional dykes and cone sheets support a common origin (Bell et al., 1994; Tibaldi et al., 2011). Herrero-Bervera (2001; 2003) presented an AMS study of the Cuillin cone sheets and regional dykes in support of Walker's (1993) model, highlighting a preponderance (50–70%) of lateral magma flow vectors with a radial disposition (Fig. 8.1b). From extrapolating the planar sheets down-dip, Tibaldi et al., (2011) further suggested the cone sheet swarm may be divided into two sets, each derived from a separate shallow (~1 km and ~3 km) magma reservoir.

It is immediately apparent from a brief review of previous models applied to the Cuillin cone sheets that there are significant similarities with the Ardnamurchan deflected regional dykes (e.g. a lateral magma flow regime and pre-existing host rock structural control on intrusion). Although Herrero-Bervera et al., (2001; 2003) identified a lateral, radiating outwards magma flow regime (cf. Walker, 1993; Palmer et al., 2007), the spatial abundance of cone sheets coincident with the igneous complex and  $\sigma_1$  intersection suggests that the Cuillin cone sheets may be fed from an externally lateral source (Fig. 8.1c). Following a close scrutiny of the mapped AMS trends presented by Herrero-Bervera et al., (2003), it is difficult to determine a radial trend about the proposed foci (Fig. 8.1b). Out of the 48 AMS samples Herrero-Bervera et al., (2001) measured from the cone sheets ( $n = 34$ ) and dykes ( $n = 14$ ), only 23 % (6 dykes and 5 cone sheets) may be projected back to the central foci. Instead,

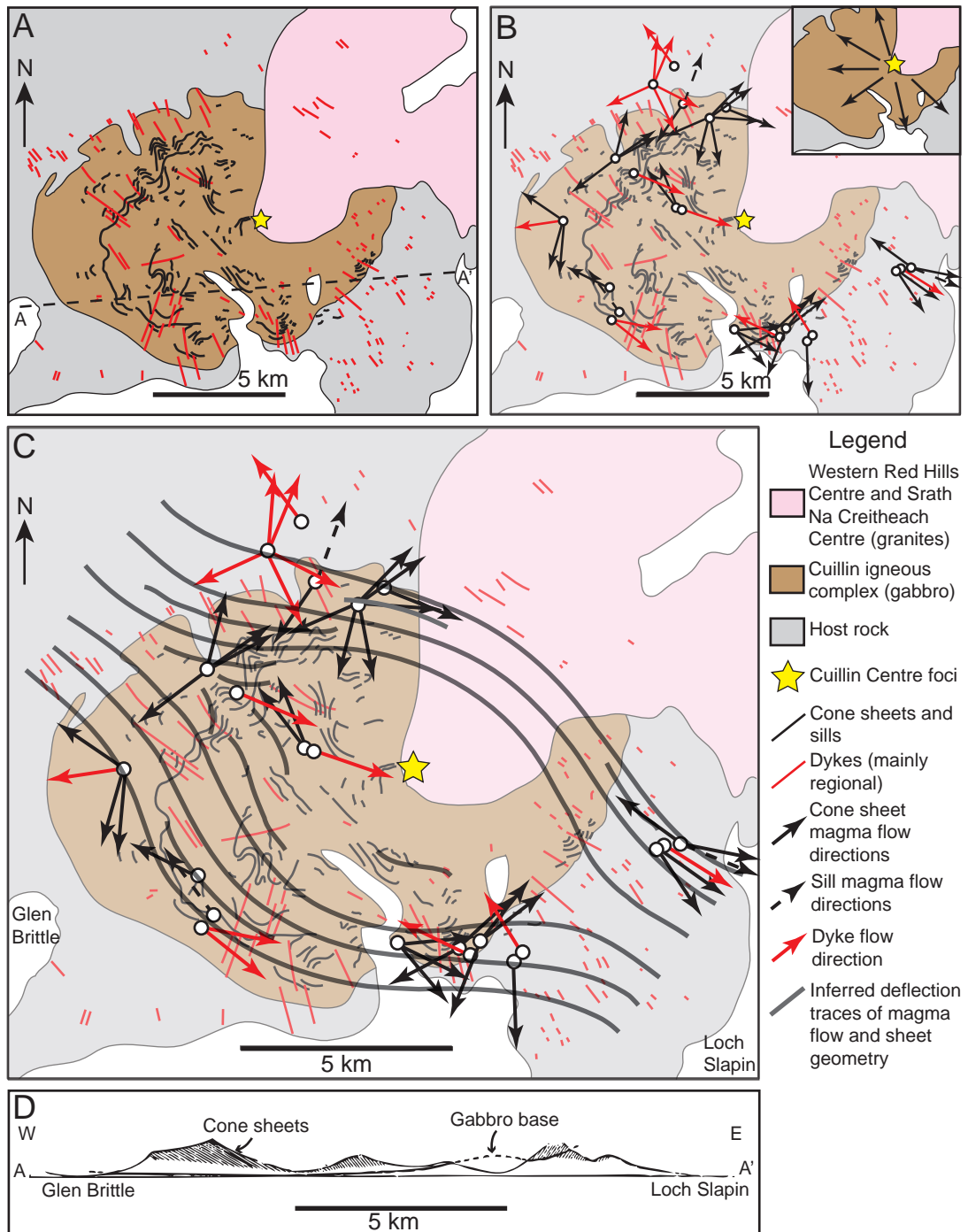


Fig. 8.1: A) Map of the cone sheets and regional dykes associated with the Cuillin igneous complex, Skye (after Walker, 1993; Bell, 2005). B) Magma flow directions in the cone sheets and regional dykes determined through AMS analysis (Herrero-Bervera et al., 2001; 2003). *Inset:* Generalised radial magma flow regime suggested by Herrero-Bervera et al., (2001; 2003). C) A potential re-interpretation of the Cuillin cone sheet and regional dyke magma flow regimes. Note that there is some disparity between the inferred deflection traces and the mapped cone sheet strikes due to the influence of the topography. D) Harker's (1904) cross-section of the Cuillin igneous complex depicting the limited extent of the cone sheets to elevations above 300 m. See (A) for cross-section position.

magma flow appears deflected from an underlying NW-SE trend around the igneous complex (Fig. 8.1c). This pattern is similar to that defined for the Ardnamurchan deflected regional dykes and suggests the Cuillin cone sheets were not centrally sourced, but represent deflected regional dykes (Fig. 6.13 and 8.1c). The magma flow directions determined by Herrero-Bervera et al., (2001; 2003) from imbricated fabrics possibly suggest the regional dykes primarily propagated from the NW. Harker (1904) suggested the Cuillin cone sheets “die out downwards”, to a lower limit of ~300 m elevation (Fig. 8.1d), which suggests the cone sheets do not extend to a central source and may support the proposal that they represent vertically restricted deflected regional dykes (Fig. 6.13b). It should be noted that Tibaldi et al., (2011) suggest this vertical distribution and an increase in mean sheet thickness with elevation is a result of the arrest of thin sheets at depth.

#### 8.2.1:2 *Mull*

Since Bailey et al., (1924) first described the cone sheets of Mull they have received little attention, particularly from a structural emplacement perspective (Mathieu and van Wyk de Vries, 2009). Evidence of regional dykes laterally propagating away from the Mull central complex to the SE (e.g. Macdonald et al., 1988; 2009; 2010; Jolly and Sanderson, 1995) and to the NW (this study) suggests Mull is an important regional magmatic source within the BIPI. Hence, the cone sheets local to Mull are more likely (or at least good candidates) to have a central source. The Mull cone sheets, which are typically >3 m wide (Bailey et al., 1924), are significantly thicker compared to the Ardnamurchan and Skye (~< 1 m average thickness; Walker, 1993; this study) deflected regional dykes, suggestive of a greater and more proximal magma supply. Although the distribution and abundance of the Mull cone sheets is poorly constrained, largely due to interruption by later major intrusions, Figure 8.2 suggests that cone sheet abundance is greater to the NE and SW of the central complex if the north-westwards intrusive centre migration is accounted for. This distribution is coincident with the contemporary regional  $\sigma_3$  principal stress axis intersection and implies a central source. Kerr et al., (1999) present a detailed geochemical analysis of a comprehensive range of intrusive

and extrusive igneous rocks on Mull, including the cone sheets, identifying a significant change in mantle source and partial melting depth during Centre 2 intrusion. This is reflected in all intrusions and supports a central source for the Mull cone sheets.

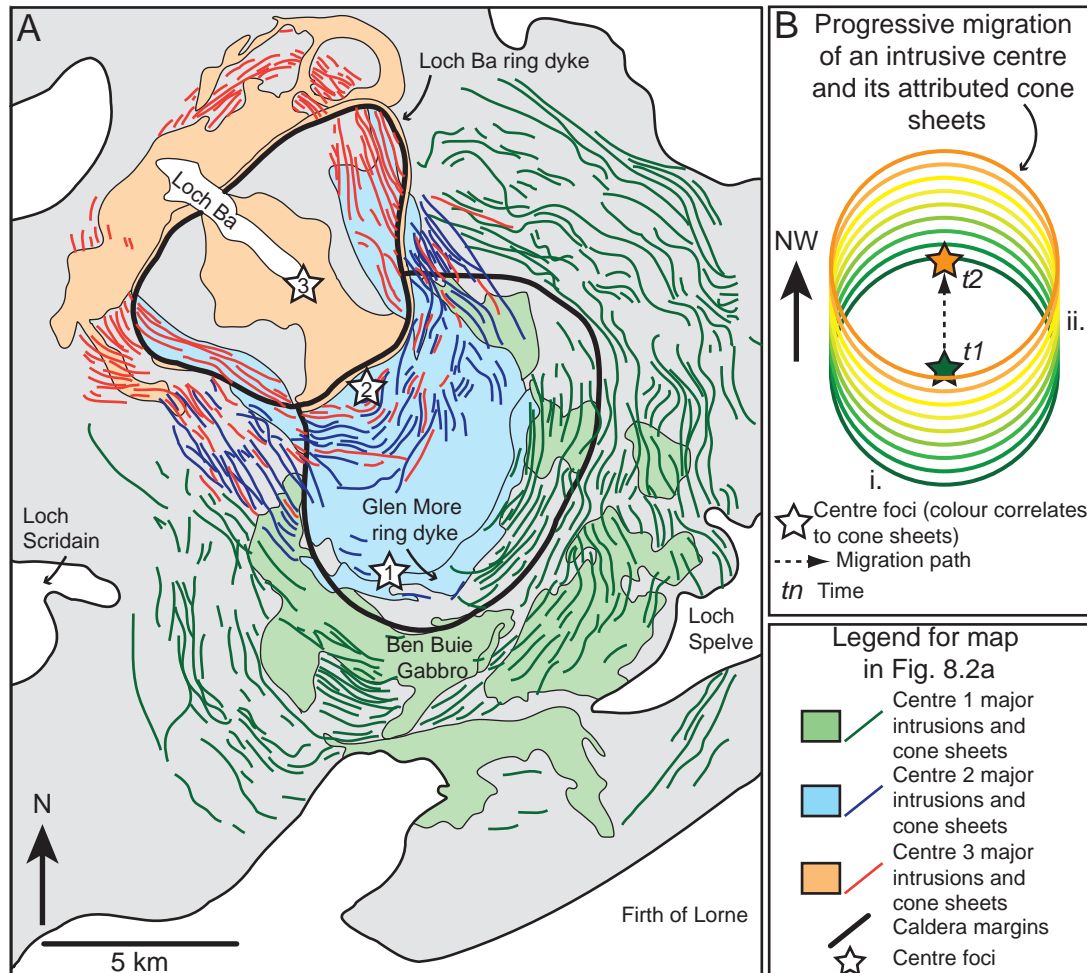


Fig. 8.2: A) Map of the Mull central complex showing numerous major intrusion components and the extent and distribution of the cone sheets associated with each Centre (redrawn from Kerr et al., 1999; Emeleus and Bell, 2005). B) Schematic sketch depicting how the north-westwards migration of an intrusive centre contemporaneous to cone sheet intrusion may produce an apparent increase in intrusion intensity to the SE or NW of the central complex.

### 8.2.1:3 Carlingford

The Carlingford central complex (County Louth, Northern Ireland) consists of a multitude of minor intrusions (e.g. cone sheets, dykes and outward dipping sheets), a large layered gabbro lopolith and major granophyre intrusions (Fig. 8.3a) (Le Bas, 1971; Halsall, 1974).

The Carlingford cone sheets, which may be divided temporally into three sets, have

similar thicknesses (0.25–1.5 m) and inward inclinations ( $\sim 45^\circ$  average dip) that decrease in angle with distance from the central complex (Le Bas, 1971; Halsall, 1974) compared to Ardnamurchan. A strong host rock control is also evident as many of the Carlingford cone sheets are parallel to fractures within the host rock and occasionally display ramp-flat structures (Fig. 8.3b) (Le Bas, 1971). Halsall (1974) determined the cone sheets were derived from three central sources, approximately ranging from 7.5–1.5 km depth, that were elongated parallel to the regional  $\sigma_1$  principal stress axis (i.e. NW-SE; England, 1988). Proportionally the Carlingford cone sheets are most abundant to the NE of the central complex, coincident with the zone of greatest doming (Fig. 8.3a) (Le Bas, 1971; Walker, 1975a). As the regional  $\sigma_3$  principal stress axis intersection occurs to the NE of the central complex, this may imply that the cone sheets are centrally fed. However, AMS analyses of the Eastern and Western Mourne Granites, conducted by Stevenson et al., (2007b) and Stevenson and Bennett (2011) highlights a source located subjacent to the SE; coincident with a geophysical anomaly interpreted to represent an unexposed mass of mafic material (Fig. 8.3c). As the geophysical anomaly extends westwards, Stevenson and Bennett (2011) postulated that intrusions within the Carlingford and Slieve Gullion central complexes may also be fed from the unexposed mafic body; implying the Carlingford cone sheets may be fed from the NE (Fig. 8.3c). This would also explain the greater abundance of cone sheets to the NE of the Carlingford central complex. A detailed study of the magma flow in these cone sheets would be a good test of this idea.

#### 8.2.1:4 *Determining magma source position*

Cone sheet-bearing central complexes within the BIPIP have here been used to test the application of cone sheet distribution, relative to the orientation of the active regional stress field during emplacement, as a method of highlighting potential cone sheet swarms that may not have a central source. Through utilising previous field observations, geochemical analyses and AMS data obtained from the Cuillin cone sheets (Skye) and associated intrusions it is suggested that increased cone sheet abundances to the NW and SE of the Cuillin central

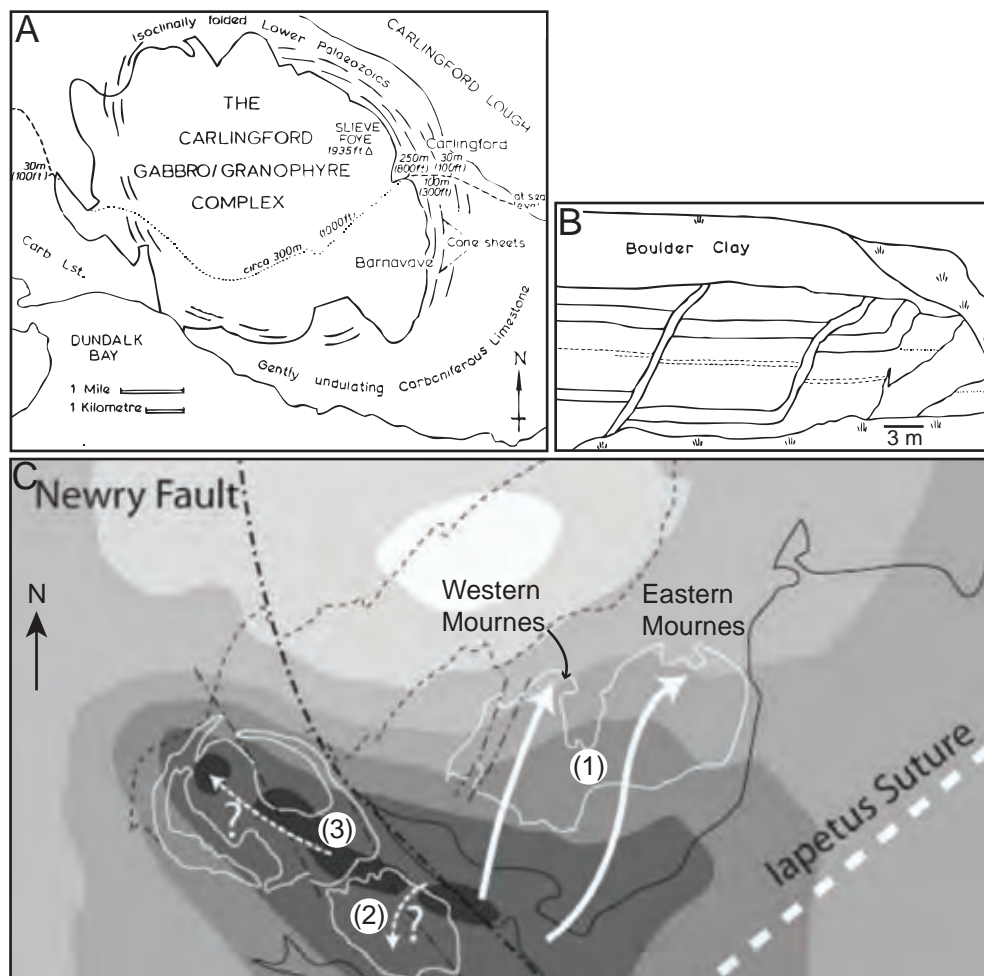


Fig. 8.3: A) Geological map of the Carlingford central complex showing the increase in cone sheet intensity to the NE (Le Bas, 1971). B) Carlingford cone sheets displaying a ramp-flat morphology. C) Sketch map of the Mourne (1), Carlingford (2) and Slieve Gullion (3) central complexes with inferred magma flow directions (white arrows) and Bouguer gravity anomalies superimposed (Stevenson and Bennett, 2011). The darker shades of grey represent the area of a proposed mafic body.

complex indicate a deflected dyke emplacement model. The Mull cone sheets, although poorly studied, display some structural (e.g. greater thicknesses) and geochemical trends, which coupled with an apparent increase in cone sheet abundance to the NE and SW of the Mull central complex, support a central source at depth. This is expected for the Mull cone sheets, given that the Mull central complex is a major source of regional dykes, rather than a focus for lateral propagating regional dykes sourced elsewhere. Overall, the evidence from the Cuillin and Mull cone sheets supports the use of cone sheet abundance distributions, in contemporaneous regional extensional settings containing regional dyke swarms present, as

a viable method for initially identifying possible laterally fed ‘cone sheets’. However, the Carlingford cone sheets highlight that there may be exceptions to this model.

### **8.2.2 Cone sheet-bearing complexes in regional extensional settings similar to the BIPIP**

Periods of volcanism associated with rifting and crustal extension are often manifested as a series of central volcanoes and regional dyke swarms (e.g. Iceland, Siler and Karson, 2009; BIPIP, Emeleus and Bell, 2005; Canary Islands, Schirnick et al., 1999; Gudmundsson, 2002). It is plausible that laterally propagating regional dykes, in volcano-tectonic settings similar to Ardnamurchan, may have been deflected into ‘cone sheet’ geometries by stress field interference. In the absence of detailed magma flow analyses, it appears possible to distinguish magma source position from the spatial distribution of areas of increased cone sheet abundance relative to the associated central complex and the sub-horizontal regional  $\sigma_3$  principal stress axes active during intrusion. Note that in the majority of extensional settings  $\sigma_1$  is oriented sub-vertically; the BIPIP is slightly different as coeval regional Alpine compression imparted a sub-horizontal  $\sigma_1$ . However, where  $\sigma_2$  is sub-horizontal (instead of  $\sigma_1$ ), the difference in magnitude between  $\sigma_2$  and  $\sigma_3$  will still likely be sufficient to control the positioning of areas of increased cone sheet abundance. This section provides several brief descriptions of cone sheet swarms in volcanic systems developed in extensional settings.

#### **8.2.2:1 *Iceland***

Iceland is situated on the divergent North Atlantic mid-ocean ridge and is the modern manifestation of the North Atlantic Igneous Province (Klausen, 2006). The neovolcanic rift zone, the area of current intrusive and extrusive activity, is oriented NE-SW (i.e. orthogonal to  $\sigma_3$ ) and bounded to either side by earlier volcanic products formed during the Neogene (Gudmundsson, 1995; Klausen, 2004). Similar to the BIPIP, the magmatic plumbing system primarily consists of NE-SW striking regional dykes and interspersed central complexes. The regional dykes (~4–5 m average width) of Iceland generally increase in intensity towards, and focus on, the central complexes. However, they are rarely observed to cross-cut the central

complexes, which are instead dominated by cone sheet swarms. Gautneb and Gudmundsson (1992) suggested this distribution of sheet intrusions relates to the entrapment of vertically ascending regional dykes, originating from an axial deep crustal reservoir (Burchardt et al., 2011), into an upper crustal magma chamber that fed cone sheets. The vast majority of regional dykes are assumed to have flowed vertically (Gautneb and Gudmundsson, 1992; Gudmundsson, 2002; Klausen, 2006; Kissel et al., 2010), although lateral magma flow regimes have also been defined (e.g. Paquet et al., 2007; Eriksson et al., 2011). Klausen (2006) further suggested some regional dykes may propagate towards the central complexes. Gautneb and Gudmundsson (1992) argue that the significant difference in average width and reduced intensity of the regional dykes compared to the cone sheets (~1 m average width) preclude a close genetic relationship, despite a broad petrological and geochemical (major and trace elements) similarity. However, Klausen (2006) provides a detailed study of the regional dykes surrounding the Birnadalstindur central complex (SE Iceland), which highlights a decrease in average dyke thickness to ~1–2 m within the central complex. Speight et al., (1982) and Jolly and Sanderson (1995) recognised similar average thickness ranges for the BIPIP regional dykes, but noted that proximal to the central complexes the regional dykes became thinner (~1–2 m). An increase in regional dyke intensity towards the central complexes was also observed (Jolly and Sanderson, 1995). A plausible alternative explanation to the regional dyke distribution may therefore be that laterally propagating regional dykes are deflected into ‘cone sheets’ within the vicinity of the central complex when a local compressive stress field is active. This may also explain the observed increase in thickness of the Centre 1 and Centre 2 ‘cone sheets’ with distance from the Ardnamurchan central complex.

Individual central complexes are often partially covered by glaciers, talus or scree (e.g. Siler and Karson, 2009), thereby limiting the accuracy of defining areas of high cone sheet intensity relative to the central complex and the coeval principal stress axes. Given the relative orientations of the regional sub-horizontal  $\sigma_1/\sigma_2$  (NE-SW) and  $\sigma_3$  (NW-SE) principal stress axes, it is suggested that Icelandic cone sheet swarms with greater abundances to the NW/SE of the central complex are likely to have been centrally fed whereas those with

increased intensities to the NE/SW may be fed by laterally propagating regional dykes. Siler and Karson (2009) report cone sheet dip parallel flow lineations and unpublished AMS data, in the Vatnsdalur cone sheet swarms (NW Iceland), suggestive of a central source. Although there is no quantitative observations on cone sheet abundance distribution, exposures of the Vididalsfjall cone sheet set to the SE and NE of the central complex account for 100 % and 80–100 % of rock outcrop (Siler and Karson, 2009). This implies cone sheets are most abundant to the SE of the central complex, consistent with a central source. Similarly, the small areal extent and close proximity of transects Klausen (2004) used to systematically measure cone sheet structure in the Thverartindur central complex tentatively suggests a greater abundance of cone sheets to the SE. Although this may reflect variations in exposure level, the implied central source is supported by the observed decrease in cone sheet thickness with increased elevation (Klausen, 2004). Unfortunately, the majority of studied cone sheet swarms in Iceland (e.g. Hafnarfjall, Gautneb et al., 1989; Kjalarnes, Gautneb and Gudmundsson, 1992; Birnudalstindur, Klausen, 2006; Geitafell and Dyrfjöll, Burchardt et al., 2011) contain no direct information pertaining to the magma source position or defined zones of increased abundance.

#### 8.2.2:2 *The Canary Islands*

Many regional dyke swarms in the Canary Islands are observed to focus on, and become more intense towards central volcanoes (e.g. Teno massif, Tenerife; Marinoni and Gudmundsson, 2000). Within the volcanic edifice however they are often poorly represented with sheet intrusions dominated by cone sheets (Schirnack et al., 1999). The Canary Islands are perhaps structurally more complicated in comparison to the BIPIP and Iceland, with several differently oriented regional dyke swarms attributed to spatially variable and temporally changing principal stress axes. Primarily, NW-SE striking regional dykes (i.e.  $\sigma_3$  oriented NE-SW) dominate in Tenerife and La Gomera whilst NE-SW striking regional dykes (i.e.  $\sigma_3$  oriented NW-SE) parallel the East Canaries Ridge in Lanzarote and Fuerteventura (Fig. 8.4a) (Marinoni and Gudmundsson, 2000; Marinoni, 2001). Many of the regional dykes

observed in Tenerife display sub-horizontal flow fabrics (Marinoni and Gudmundsson, 2000). Although several cone sheet swarms have been identified within the Canary Islands (e.g. Tejeda complex, Gran Canaria; Schirnick et al., 1999), no attention has been given to determining their magma flow regimes and a spatial variation in cone sheet abundance has only been recorded in the Vallehermoso cone sheet swarm on La Gomera (Ancochea et al., 2003; Rodriguez-Losada and Martinez-Frias, 2004). The felsic Vallehermoso cone sheets are more abundant to the NE and SW of their assumed central source and were emplaced contemporaneously with a felsic radial dyke swarm (Fig. 8.4b). Marinoni and Gudmundsson's (2000) recognition of a sub-horizontal, NE-SW oriented  $\sigma_3$  regional principal stress axis from the dykes on Tenerife is supported by distribution and curvature of the radial dykes on La Gomera (Fig. 8.4b), which is reminiscent of the Spanish Peaks (Ancochea et al., 2003). The distribution of the Vallehermoso cone sheets and radial dykes, therefore suggests they had a central source. This is corroborated by geochemical affinities with other local intrusions (Ancochea et al., 2003).

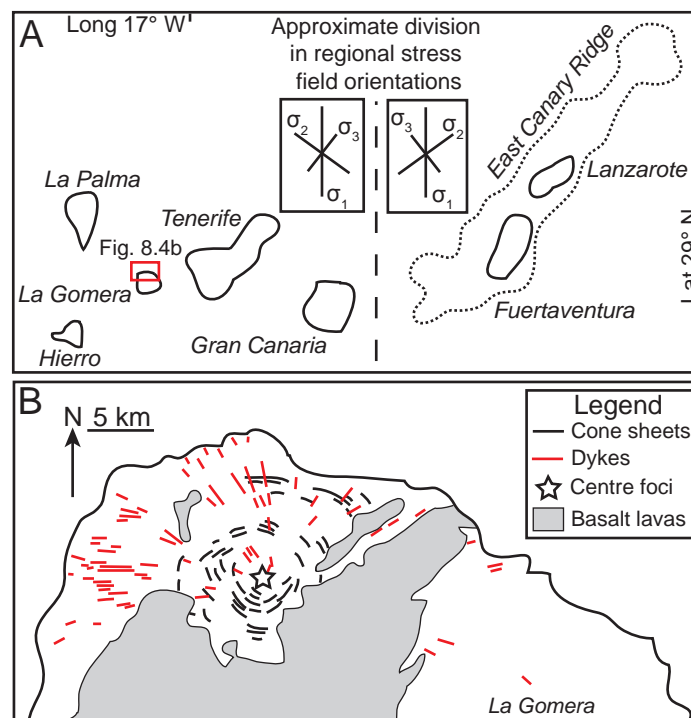


Fig. 8.4: A) Sketch map of the Canary Islands archipelago showing the approximate east-west division of the regional stresses active during regional dyke emplacement (after Marinoni and Gudmundsson, 2000). B) Map of the Vallehermoso cone sheet and radial dyke swarm of La Gomera (redrawn from Ancochea et al., 2003).

### 8.2.2:3 *Messum central complex, Namibia*

The Lower Cretaceous Messum central complex (Namibia), part of the Etendeka igneous province associated with the lithospheric impingement of the Tristan da Cunha mantle plume, contains several swarms of cone sheets and a contemporaneous NW-SE regional dyke swarm (Ewart et al., 2002). Along with other central complexes, Messum occurs in a NE-SW trending zone (Ewart et al., 2002), likely orthogonal to the regional  $\sigma_3$  axis during rifting. The cone sheets of the Messum central complex are more abundant to the NW and SE and are divisible into two swarms; the earlier Eastern gabbro cone sheets and the later Western gabbro cone sheets (Ewart et al., 2002). This distribution relative to the regional principal stress axes and the central complex suggest the cone sheets are centrally fed, consistent with the decrease in sheet thickness to the SW and NE of the central complex and some geochemical affinities with other major intrusions of the central complex (Ewart et al., 2002).

### 8.2.2:4 *Discussion*

Regional dykes with lateral propagation vectors are common in regionally extending (e.g. rifting) tectonic settings, particularly those associated with coeval mantle plume impingement (Ernst et al., 1995). The geometry and orientation of regional dykes in the vicinity of local volcanic systems is often variable. Regardless of the deflected regional dyke emplacement model, there is sufficient evidence highlighting the importance of stress field interference on magma emplacement dynamics. For example, regional dykes tend to focus in on central complexes by following locally deflected regional  $\sigma_1$  principal stress axis (Odé, 1957; Klausen, 2006). It therefore seems plausible that similar mechanisms may deflect the regional dykes into concentric strikes in the immediate vicinity of the central complexes. Sheet dip often appears to be fundamentally controlled by the pre-existing host rock structure and is exemplified by the occurrences of cone sheets intruding inwardly inclined fractures (e.g. this study; Le Bas, 1971), bedding (Johnson et al., 1999), magmatic layering (e.g. Tibaldi et al., 2011) or host rock foliations (e.g. Verner et al., 2008). These host rock and stress field controls will influence emplacement of centrally fed and laterally fed sheets in a similar

manner, producing virtually indistinguishable geometries. Whilst geochemical analyses may aid in defining separate magma sources, it has been shown that tracing the primary magma flow is a powerful alternative tool. Comparisons between the Ardnamurchan and Skye ‘cone sheets’ suggest that they are deflected dykes and that their lateral propagation may be defined from AMS and their increased abundances in areas where the regional  $\sigma_1$  principal stress axis intersects the central complex. Conversely, numerous cone sheet swarms with greater abundances in areas of regional  $\sigma_3$  intersections that suggest a central source provide other evidence that supports the inferred magma source position. It is likely that the source position of poorly studied or currently undiscovered cone sheet swarms may be approximately distinguished from abundance variations.

### **8.2.3 Cone sheet-bearing complexes in regional compressional settings**

An important consideration is how the results presented in this thesis may be applied to compressional tectonic settings, where the majority of active volcanoes are located. Although rare, some cone sheet-bearing central complexes were emplaced during contemporaneous regional compression. Importantly, regional dyke swarms do not develop in these tectonic settings as  $\sigma_3$  is often sub-vertical, limiting the potential sources for externally and laterally fed cone sheets. Two notable occurrences of cone sheets emplaced in a compressional regime belong to the Zarza central complex (Baja California, Johnson et al., 1999) and the Knížecí Stolec pluton (Czech Republic, Verner et al., 2008). Both cone sheet swarms display relatively steeper dips, compared to cone sheet swarms observed in extensional settings, as well as evidence of a strong host rock control on intrusion. The Zarza cone sheets dip inwards at  $\sim 65^\circ$  with those of the later cone sheet swarms oriented sub-parallel to folded bedding (Johnson et al., 1999). Mineral lineations plunging parallel to cone sheet dip imply a central source (Johnson et al., 1999). In contrast, the durbachitic cone sheets of the Knížecí Stolec pluton were emplaced at  $\sim 28$  km depth and apparently exploit inward dipping,  $55\text{--}80^\circ$ , host rock foliation planes. It is likely that cone sheets emplaced concomitantly to regional compression are centrally fed.

### 8.2.4 Major intrusions laterally fed by regional dykes

This thesis suggests that laterally propagating regional dykes may provide important regional magmatic connections between localised volcanic systems, feeding local intrusions (e.g. ‘cone sheets’ or stacked sheet intrusions such as the Ben Hiant Dolerite) and influencing edifice construction. Several studies have identified other laccolithic and sill-like intrusions that are fed by laterally propagating regional dykes (e.g. Ernst et al., 1995). Hyndman and Alt (1987) describe eight laccoliths fed by radial dykes originating from the Adel Mountains (Montana) volcanic pile, 8–23 km to the south (Fig. 8.5a). The individual laccoliths have length (0.5–5 km parallel to the flow direction axis) and thickness ranges (80–200 m) (Hyndman and Alt, 1987) similar to the sheets of the Ben Hiant Dolerite (<1.5 km length and ~70 thick). In contrast to the Ben Hiant Dolerite, which appears to be fed through intermediary primary magma tubes, Hyndman and Alt (1987) observed the Adel Mountain laccoliths formed by ‘roll-over’ of the radial dykes (Fig. 8.5b). Two other examples include: laterally propagating dykes of the MacKenzie dyke swarm (Canada) feeding sill-complexes 800–1500 km away from the plume head source (Ernst et al., 1995) and the Paraná sills in South America, which White (1992) similarly suggested were fed by extensive regional dykes. Transition of dykes into sills and laccoliths have also been recreated in analogue experiments (Rivalta et al., 2005; Kavanagh et al., 2006; Kervyn et al., 2009).

These examples suggest satellite intrusions and whole intrusive networks (e.g. ‘cone sheet’ and sill complexes) may have been emplaced at significant lateral distances from their magma source. Volcanic edifice construction is often assumed to result purely from intrusive activity related to a vertically stacked magmatic system with an upper crustal magma chamber (Callot et al., 2001; Acocella and Neri, 2009). Importantly, observations suggest that the interaction and interference between multiple, contemporaneous stress fields (e.g. the ambient stress field, a local stress field associated with intrusion expansion or a local stress field imparted by the volcanic edifice load (Kervyn et al., 2009)) influences edifice construction. Attributing the Ben Hiant Dolerite to the Mull central complex, rather than the Ardnamurchan

central complex, also implies close spatial relationships are insufficient in determining magma sources and that lateral magma transport between adjacent volcanic systems may be greater than previously considered.

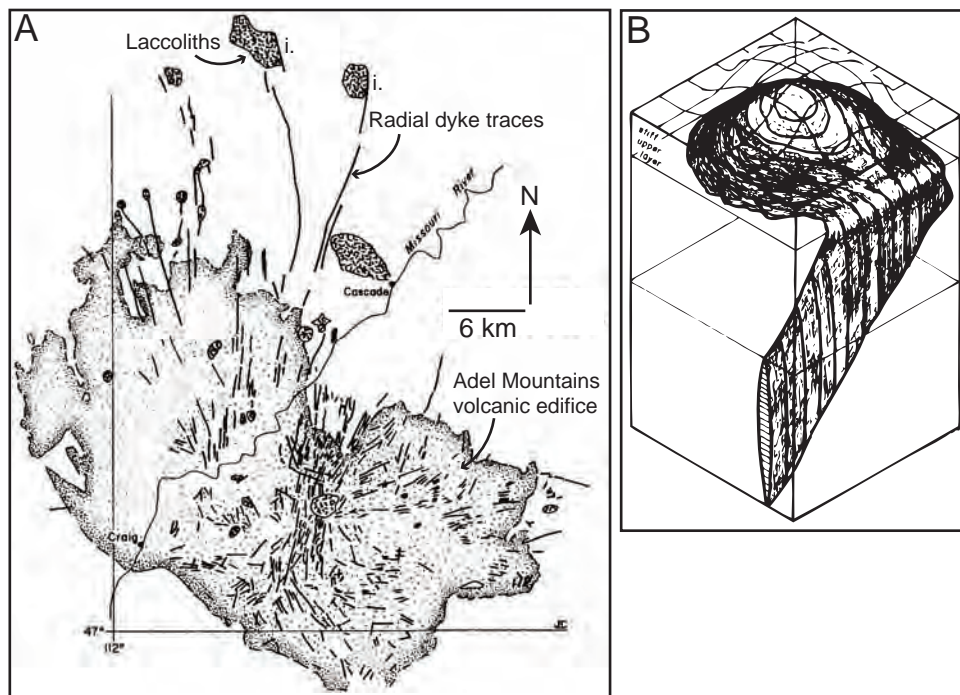


Fig. 8.5: A) Geological map of the Adel Mountain volcanic centre and the associated radial swarm that extends up to 30 km and is observed to feed several satellite laccoliths (Hyndman and Alt, 1987). B) Sketch of a gelatine analogue model showing roll-over of a dyke into a laccolith.

### 8.3 Conclusion

Generation of magmatic overpressure in a central magma reservoir and the consequent local compressive stress regime, which favours the formation and intrusion of inwardly inclined conical fractures, is a fundamental component of all previous cone sheet emplacement models and significantly influences volcano growth. The elegant simplicity of these models has allowed their successful application to explaining many geometrical relationships within cone sheet swarms emplaced throughout the geological record. Although quantifying the magma source position has been typically overlooked, there is sufficient evidence to conclude

that classic cone sheet emplacement does undoubtedly occur (e.g. the Otoge igneous centre cone sheets, Japan; Geshi, 2005). This thesis suggests that the influence of the pre-existing host rock structure and lithology as well as stress field interference on cone sheet intrusion may explain minor variations between individual cone sheets and whole cone sheet swarms. However, re-interpretation of the archetypal Ardnamurchan cone sheets importantly reveals a NW-SE oriented lateral magma flow regime that is inconsistent with a central source and is instead attributed to the deflection of laterally propagating regional dykes into a 'cone sheet' geometry. The proposed emplacement model also appears to be applicable to the formation of the Cuillin 'cone sheets' on Skye. Therefore, a central source to cone sheet swarms cannot immediately be assumed. Instead, detailed analyses of abundance variations, magma flow regimes and/or geochemical affinities are required. An important implication to all studies of ancient and active volcanic systems, particularly those developed in regional extensional settings, is that endogenous volcanic edifice construction and potentially eruption dynamics may be related to the emplacement of major and minor intrusions fed from laterally adjacent central volcanoes.

---

## APPENDICES

---

### APPENDIX A (on CD)

A tabulated synopsis of field observations and structural measurements of numerous cone sheet swarms, including those discussed in Chapter 1, emplaced throughout the geological record. The references the data is collated from are incorporated into the list of references.

### APPENDIX B

Details on the field and laboratory sampling method and a description of the procedure required to reorient block samples.

#### Sample collection

As the majority of the Ardnamurchan cone sheets are relatively thin and highly fractured, block samples approximately 10 x 10 x 10 cm were collected from areas containing as few fractures as possible. The aim of this strategy was to ensure at least five, preferably  $\geq 10$ , sub-specimens could be obtained from each block. Before the block was removed a strike bar and a dip bar was drawn on the smoothest surface. The dip bar represents the maximum inclination of the surface and the strike bar declination was always measured at the right-hand end (i.e. 90° anticlockwise from the dip direction). An arrow was marked at the right-hand end of the strike bar to aid with later reorientation. If overhanging surfaces were measured,

the recorded dip is  $>90^\circ$ . Having recorded the locality information, strike and dip the block sample was teased from the outcrop using a 4lb lump hammer and a chisel.

### **Lab preparation**

To obtain sub-specimens from the block samples, the sample were first drilled using a non-magnetic, diamond tipped drill-bit 24.5 mm in diameter. Prior to drilling, the strike bars were traced across the whole top surface of the block sample at 1.5 cm intervals. The block sample was then secured to the drill table with the marked surface facing upwards. The new dip of the surface was measured as well as the angle between the new strike declination (using the right-hand end) and the field strike declination (i.e. measuring from the lab strike, clockwise round to the field strike), which may range from  $0-360^\circ$  (cf. Owens, 1994). From the field strike, field dip, lab dip and lab pitch (i.e. to the field strike) the block sample can be reoriented. This reorientation data for the block samples measured in this thesis is provided on the CD and is labelled Appendix B1. Following these measurements, cores were drilled from the block sample ensuring the top surface displayed a field strike bar. After levering the cores out, the strike bar on the top surface was extrapolated vertically down the core and an upward facing tick marked on the strike projection comparable to the right-hand field declination (cf. Owens, 1994). Each core was then cut into 2 cm long sub-specimens with a non-magnetic grinding saw.

### **Measurement of the AMS samples**

Each sub-specimen was marked up according to the Agico KLY3-Kappbridge user guide (see [www.agico.com](http://www.agico.com) for details) and then individually placed into the sample holder of the KLY-3s spinning magnetometer in the University of Birmingham. The AMS of each sub-specimen was measured in three orientations and a bulk susceptibility measurement was also obtained. For each sample, the sub-specimen results are collated and output in a \*.ran and \*.asc file

format. Using the software provided in Appendix B2 on the CD, the AMS data may be reoriented into the field frame and manipulated to be output as lower hemisphere, equal area stereographic projections (see Owens, 1994; 2000).

## **APPENDIX C**

High-temperature, low-susceptibility experiments were conducted on selected specimens that were crushed to a fine ( $>0.5$  mm) powder. Approximately 2 g of the powder was funnelled into a test tube (provided by Agico), into which the CS-3 temperature sensor of the furnace apparatus was inserted. The CS-3 furnace was used to heat and cool the sample in a step-wise fashion, whilst measuring the samples bulk susceptibility. The raw data output, which for the samples measured in this thesis is provided in the Appendix C folder on the CD, may be opened in Microsoft Excel.

## **APPENDIX D (on CD)**

Structural measurements of the Ardnamurchan cone sheets, sedimentary bedding planes and conjugate fractures are tabulated and presented with locality data.

## **APPENDIX E (on CD)**

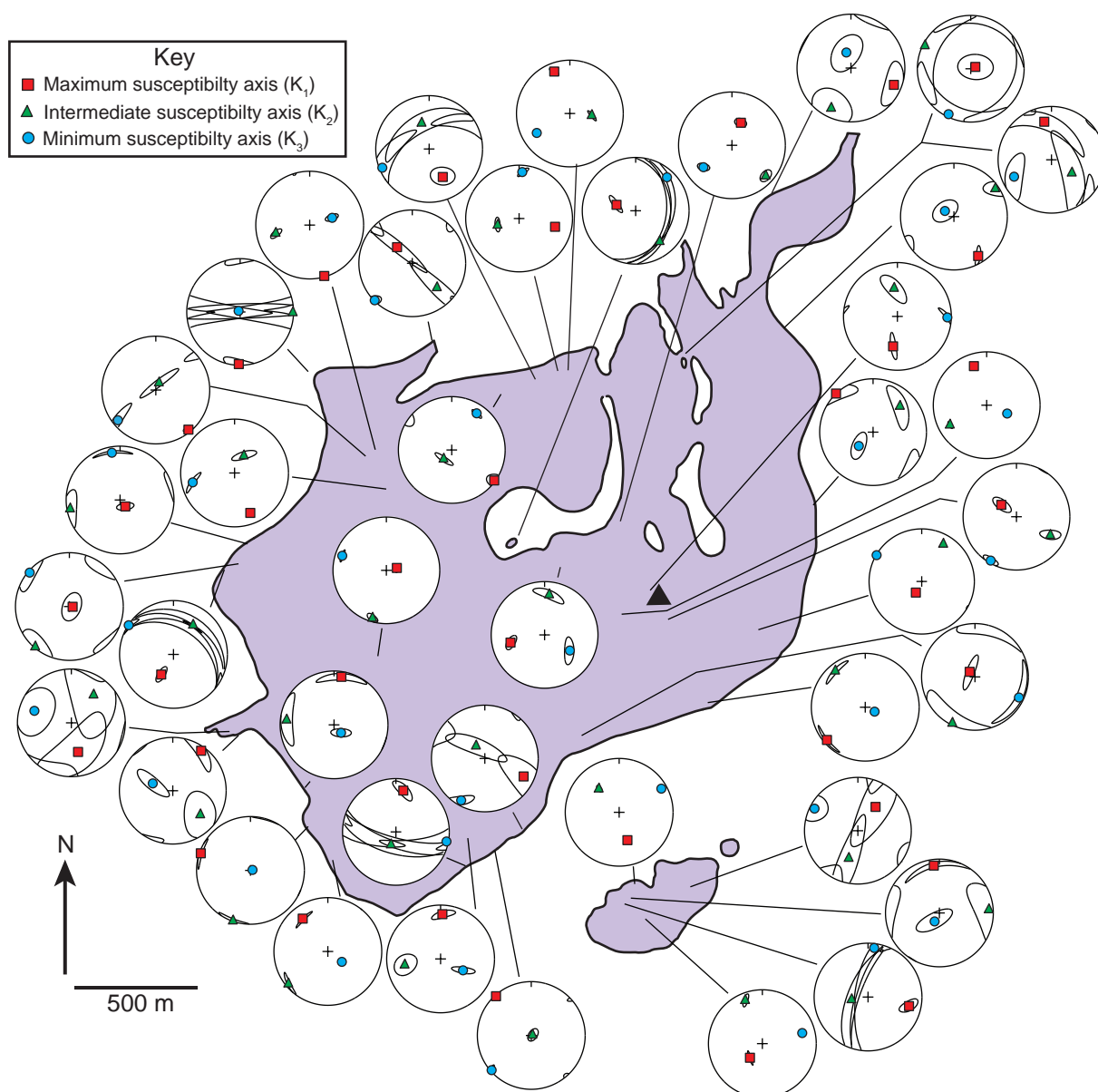
Reoriented AMS results for the Ardnamurchan cone sheets.

**APPENDIX F (on CD)**

Collated geochemical data from the Ardnamurchan cone sheets and several major intrusions (i.e. the Hypersthene Gabbro and the Centre 3 Layered Gabbro Lopolith) as well as cone sheets from Mull and Skye; regional dykes from Mull and southern Scotland-NE England; Loch Scridain sills from Mull and various intrusions on Rum. The references the data is gathered from are provided and are also incorporated into the list of references.

**APPENDIX G**

The AMS results for the Ben Hiant Dolerite samples are tabulated and presented on the CD. Figure AG1 displays the AMS lower hemisphere, equal area stereographic projections for the Ben Hiant Dolerite.



**Appendix G:** Map of raw anisotropy of magnetic susceptibility (AMS) results presented as lower hemisphere, equal area stereographic projections.

---

## LIST OF REFERENCES

---

- Abelson, M., Baer, G. and Agnon, A. (2001) Evidence from gabbro of the Troodos ophiolite for lateral magma transport along a slow-spreading mid-ocean ridge. **Nature**, 409: 72-75.
- Acocella, V. and Neri, M. (2009) Diike propagation in volcanic edifices: overview and possible developments. **Tectonophysics**, 471: 67-77.
- Allen, P. A. and Allen, J. R. (2005) **Basin analysis principles and applications**. Blackwell Publishing: 549 p.
- Ancochea, E., Brandle, J. L., Huertas, M. J., Cubas, C. R. and Hernan, F. (2003) The felsic dikes of La Gomera (Canary Islands): identification of cone-sheet and radial dyke swarms. **Journal of Volcanology and Geothermal Research**, 120: 197-206.
- André, A., Sausse, J. and Lespinasse, M. (2001) New approach for the quantification of paleostress magnitudes: applications to the Soultz vein system (Rhine graben, France). **Tectonophysics**, 336: 215-231.
- Anderson, E. M. (1936) Dynamics of formation of cone-sheets, ring-dikes, and cauldron subsidence. **Proceedings of the Royal Society Edinburgh**, 56: 128-157.
- Anderson, E. M. (1951) **The dynamics of faulting and dyke formation with applications to Britain**. Edinburgh: 206 p.
- Annen, C. (2009) Implications of incremental emplacement of magma bodies for magma differentiation, thermal aureole dimensions and plutonism–volcanism relationships. **Tectonophysics**, 500: 3-10.
- Annen, C., Leânat, J. F. and Provost, A. (2001) The long-term growth of volcanic edifices: numerical modelling of the role of dyke intrusion and lava flow emplacement. **Journal of Volcanology and Geothermal Research**, 105: 263-289.
- Arbaret, L., Diot, H. and Bouchez, J. L. (1996) Shape fabrics of particles in low concentration suspensions: 2D analogue experiments and application to tilting in magma. **Journal of Structural Geology**, 18: 941-950.
- Archanjo, C. J., Launeau, P. and Bouchez, J. L. (1995) Magnetic fabric vs. magnetite and biotite shape fabrics of the magnetite-bearing granite pluton of Gameleiras (Northeast Brazil). **Physics of the Earth and Planetary Interiors**, 86: 63-75.
- Aubourg, C., Giordano, G., Mattei, M. and Speranze, F. (2002) Magma flow in sub-aqueous rhyolitic dikes inferred from magnetic fabric analysis (Ponza Island, W. Italy). **Physics and Chemistry of the Earth**, 27: 1263-1272.
- Aubourg, C. and Geoffroy, L. (2003) Comment on paper: Magnetic fabric and inferred flow direction of dikes, conesheets and sill swarms, Isle of Skye, Scotland. **Journal of**

- Volcanology and Geothermal Research**, 122: 143-144.
- Aubourg, C., Tshoso, G., Le Gall, B., Bertrand, H., Tiercelin, J. –J., Kampunzu, A. B. and Modisi, M. (2008) Magma flow revealed by magnetic fabric in the Okavango giant dyke swarm, Karoo igneous province, northern Botswana. **Journal of Volcanology and Geothermal Research**, 170: 247-261.
- Baer, G. (1995) Fracture propagation and magma flow in segmented dykes: field evidence and fabric analysis, Makhtesh Ramon, Israel. In: Baer, G. and Heinmann, A. A., eds. **Physics and Chemistry of Dykes**. Rotterdam, Balkema: 125-140.
- Bahat, D. (1980) Hertzian fracture, a principal mechanism in the emplacement of the British Tertiary intrusive centres. **Geological Magazine**, 117: 463-470.
- Bailey, E. B., Clough, C. T., Wright, W. B., Richey, J. E. and Wilson, G. V. (1924) **Tertiary and post-tertiary geology of Mull, Loch Aline, and Oban**. Memoir of the Geological Survey of Great Britain, Sheet 44 (Scotland): 445 p.
- Bamford, D., Nunn, K., Prodehl, C. and Jacob, B. (1977) LISPB–III. Upper crustal structure of northern Britain. **Journal of the Geological Society, London**, 133: 481-488.
- Bascou, J., Camps, P. and Dautria, J. M. (2005) Magnetic versus crystallographic fabrics in a basaltic lava flow. **Journal of Volcanology and Geothermal Research**, 145: 119-135.
- Bell, J. D. (1982) Acid intrusions. In: Sutherland, D., ed. **Igneous rocks of the British Isles**. Chichester: 427-447.
- Bell, B. R., Claydon, R. V. and Rogers, G. (1994) The petrology and geochemistry of cone-sheets from the Cuillin igneous complex, Isle of Skye: evidence for combined assimilation and fractional crystallization during lithospheric extension. **Journal of Petrology**, 35: 1055-1094.
- Bell, B. R. (2005) **Skye Central Complex, bedrock and superficial deposits**. 1:25 000 Geology series. British Geological Survey, 1 sheet.
- Best, M. G. (2003) **Igneous and Metamorphic Petrology**. Blackwell Publishing: 729 p.
- Bonsor, H. C. and Prave, A. R. (2008) The Upper Morar psammite of the Moine Supergroup, Ardnamurchan Peninsula, Scotland: depositional setting, tectonic implications. **Scottish Journal of Geology**, 44: 111-122.
- Borradaile, G. J. (1987) Anisotropy of magnetic susceptibility: rock composition versus strain. **Tectonophysics**, 138: 327-329.
- Borradaile, G. J. (1988) Magnetic susceptibility, petrofabrics and strain: a review. **Tectonophysics**, 156: 1-20.
- Borradaile, G. J. and Henry, B. (1997) Tectonic applications of magnetic susceptibility and its anisotropy. **Earth-Science Reviews**, 137: 42-93.
- Borradaile, G. J. and Jackson, M. (2004) Anisotropy of magnetic susceptibility (AMS):

- magnetic petrofabrics of deformed rocks. *In*: Martin-Hernandez, F., Luneberg, C., Aubourg, C. and Jackson, M., eds. **Magnetic fabric: Methods and applications**. Geological Society of London Special Publication, 238: 299-360.
- Bott, M. H. P. and Tuson, J. (1973) Deep structure beneath the Tertiary volcanic regions of Skye, Mull and Ardnamurchan, North-west Scotland. **Nature Physical Science**, 242: 114-117.
- Bouchez, J. L. (1997) Granite is never isotropic: an introduction to AMS studies of granitic rocks. *In*: Bouchez, J.L., Hutton, D.H.W., Stephens, W.E., eds. **Granite: from Segregation of Melt to Emplacement Fabrics**. Kluwer, Dordrecht: 95-112.
- Brown, D. J. and Bell, B. R. (2006) Intrusion-induced uplift and mass wasting of the Palaeogene volcanic landscape of Ardnamurchan, NW Scotland. **Journal of the Geological Society, London**, 163: 29-36.
- Brown, D. J., Bell, B. R. and McLeod, G. W. (2006) A re-interpretation of the 'Centre 3 screens' of Ardnamurchan, NW Scotland. **Scottish Journal of Geology**, 42: 83-85.
- Brown, D.J. and Bell, B.R. (2007) Debris flow deposits within the Palaeogene lava fields of NW Scotland: evidence for mass wasting of the volcanic landscape during emplacement of the Ardnamurchan Central Complex. **Bulletin of Volcanology**, 69: 847-868.
- Brown, D.J., Holohan, E. P. and Bell, B.R. (2009) Sedimentary and volcano-tectonic processes in the British Palaeogene Igneous Province: a review. **Geological Magazine**, 146: 326-352.
- Burchardt, S. (2008) New insights into the mechanics of sill emplacement provided by field observations of the Njardvik Sill, Northeast Iceland. **Journal of Volcanology and Geothermal Research**, 173: 280-288.
- Burchardt, S. and Gudmundsson, A. (2009) The infrastructure of Geitafell Volcano, Southeast Iceland. *In*: Thordarsson, T., eds. **Studies in Volcanology: The Legacy of George Walker**. Geological Society of London Special Publication of IAVECI, 2: 349-370.
- Burchardt, S., Tanner, D. C., Troll, V. R., Krumbholz, M. and Gustafsson, L. E. (2011) Three-dimensional geometry of concentric intrusive sheet swarms in the Geitafell and the Dyrfjöll volcanoes, eastern Iceland. **Geochemistry, Geophysics, Geosystems**, 12: Q0AB09, doi: 10.1029/2011GC003527.
- Butler, R. F. (1992) **Palaeomagnetism: Magnetic Domains to Geologic Terranes**. Blackwell Scientific: 238 p.
- Byerlee, J. (1978) Friction of rocks. **Pure and Applied Geophysics**, 116: 615-626.
- Callot, J. P., Geoffroy, L., Aubourg, C., Pozzi, J. P. and Mege, D. (2001) Magma flow direction of shallow dykes from the East Greenland margin inferred from magnetic fabric studies. **Tectonophysics**, 335: 313-329.
- Callot, J. P. and Guichet, X. (2003) Rock texture and magnetic lineation in dykes: A simple

- analytical model. **Tectonophysics**, 366: 207-222.
- Cañón-Tapia, E. (2001) Factors affecting the relative importance of shape and distribution anisotropy in rocks; theory and experiments. **Tectonophysics**, 340: 117-131.
- Cañón-Tapia, E. (2004) Anisotropy of magnetic susceptibility of lava flows and dykes: A historical account. In: Martín-Hernández, F., Lüneburg, C. M., Aubourg, C. and Jackson, M., eds. **Magnetic fabric: Methods and applications**. Geological Society of London Special Publication, 238: 205-225.
- Cañón-Tapia, E. and Chávez-Álvarez, M. J. (2004) Implications for the anisotropy of magnetic susceptibility of dykes. In: Martín-Hernández, F., Lüneburg, C. M., Aubourg, C. and Jackson, M., eds. **Magnetic fabric: Methods and applications**. Geological Society of London Special Publication, 238: 227-249.
- Cartwright, J. and Hansen, D. M. (2006) Magma transport through the crust via interconnected sill complexes. **Geology**, 159: 816-830.
- Chadwick, W. W. and Dieterich, J. H. (1995) Mechanical modelling of circumferential and radial dike intrusion on Galapagos volcanoes. **Journal of Volcanology and Geothermal Research**, 66: 37-52.
- Chambers, L. M., Pringle, M. S. and Parrish, R. R. (2005) Rapid formation of the Small Isles Tertiary centre constrained by précised  $^{40}\text{Ar}/^{39}\text{Ar}$  and U–Pb ages. **Lithos**, 79: 367-384.
- Corazatto, C., Francalanci, L., Menna, M., Petrone, C. M., Renzulli, Tibaldi, A. and Vezzoli, L. (2008) What controls sheet intrusion in volcanoes? Structure and petrology of the Stromboli sheet complex, Italy. **Journal of Volcanology and Geothermal Research**, 173: 26-54.
- Correa-Gomes, L. C., Souza Filho, C. R., Martins, C. J. F. N. and Oliviera, E. P. (2001) Development of symmetrical and asymmetrical fabrics in sheet-like igneous bodies: the role of magma flow and wall-rock displacements in theoretical and natural cases. **Journal of Structural Geology**, 23: 1415-1428.
- Coward, M. P. (1983) The thrust and shear zones of the Moine thrust zone and the Scottish Caledonides. **Journal of the Geological Society, London**, 140: 795-811.
- Craig, J. R. and Vaughan, D. J. (1981) **Ore microscopy and ore petrography**. John Wiley & Sons, New York: 406 p.
- Creixell, C., Parada, M. A., Morata, D., Roperch, P. and Arriagada, C. (2009) The genetic relationship between mafic dike swarms and plutonic reservoirs in the Mesozoic of Central Chile (30°–33°45'S): insights from AMS and geochemistry. **International Journal of Earth Sciences**, 98: 177-201.
- Cruden, A. R. and Launeau, P. (1994) Structure, magnetic fabric and emplacement of the Archean Lebel Stock, S. W. Abitibi Greenstone Belt. **Journal of Structural Geology**, 16: 1481-1486.
- Cruden, A. R., Tobisch, O. T. and Launeau, P. (1999) Magnetic fabric evidence for conduit fed

- emplacement of a tabular intrusion: Dinkey Creek Pluton, central Sierra Nevada batholiths, California. **Journal of Geophysical Research**, 104: 10511-10530.
- Cruden, A. R. and McCaffrey, K. J. W. (2001) Growth of plutons by floor subsidence: Implications for rates of emplacement, intrusion spacing and melt-extraction mechanisms. **Physics and Chemistry of the Earth**, 26: 303-315.
- Curtis, M. L. and Riley, T. R. (2003) Mobilization of fluidized sediment during sill emplacement, western Dronning Maud Land, East Antarctica. **Antarctic Science**, 15: 393-398.
- Dagley, P., Mussett, A. E. and Skelhorn, R. R. (1984) The palaeomagnetism of the Tertiary igneous complex of Ardnamurchan. **Geophysical Journal of the Royal Astronomical Society**, 79: 911-922.
- Dagley, P., Skelhorn, R. R., Mussett, A. E., James, S. and Walsh, J. N. (2008) The Cleveland dyke in Southern Scotland. **Scottish Journal of Geology**, 44: 123-138.
- Day, S. J. (1989) **The geology of the Hypersthene Gabbro of Ardnamurchan Pont and its implications for its evolution as an upper crustal basic magma chamber**. PhD Thesis. University of Durham, Durham.
- Delaney, P. T. and Pollard, D. D. (1981) Deformation of host rocks and flow of magma during growth of minette dikes and breccias-bearing intrusions near Ship Rock. **New Mexico: US Geological Survey Professional Paper**, Report 1202: 61 p.
- Delaney, P. T., Pollard, D. D., Ziony, J. I. and McKee, E. H. (1986) Field relations between dikes and joints – emplacement processes and paleostress analysis. **Journal of Geophysical Research-Solid Earth and Planets**, 91: 4920-4938.
- Dickin, A. P. (1981) Isotope geochemistry of the Tertiary igneous rocks from the Isle of Skye, N. W. Scotland. **Journal of Petrology**, 22: 155-189.
- Dobson, K. J., Stuart, F. M. and Dempster, T. J. (2010) Constraining the post-emplacement evolution of the Hebridean Igneous Province (HIP) using low-temperature thermochronology: how long has the HIP been cool? **Journal of the Geological Society, London**, 167: 973-984.
- Dragoni, M., Lanza, R. and Tallarico, A. (1997) Magnetic anisotropy produced by magma flow: theoretical model and experimental data from Ferrar dolerite sills. **Geophysical Journal International**, 128: 230-240.
- Dunlop, D.J., and Özdemir, O. (1997) **Rock Magnetism: Fundamentals and Frontiers**. Cambridge Studies in Magnetism, 3, Cambridge University Press, New York: 573 p.
- Durrance, E. M. (1967) Photoelastic stress studies and their application to a mechanical analysis of the tertiary ring-complex of Ardnamurchan, Argyllshire. **Proceedings of**

- the Geological Association**, 78: 289-318.
- Ellwood, B. B. (1978) Flow and emplacement direction determined for selected basaltic bodies using magnetic susceptibility anisotropy measurements. **Earth and Planetary Science Letters**, 41: 254-264.
- Ellwood, B. B. and Whitney, J. A. (1980) Magnetic fabric of the Elberton Granite, Northeast Georgia. **Journal of Geophysical Research**, 85: 1481-1486.
- Emeleus, C. H. (2009) **Ardnamurchan Central Complex, bedrock and superficial deposits**. 1:25 000 Geology series. British Geological Survey, 1 sheet.
- Emeleus, C. H. and Bell, B. R. (2005) **British regional geology: the Palaeogene volcanic districts of Scotland 4<sup>th</sup> ed.** British Geological Survey, Nottingham: 214 p.
- England, R. W. (1988) The early tertiary stress regime in NW Britain: evidence from the patterns of volcanic activity. In: Morgan, A. C. and Parson, L. M., eds. **Early Tertiary volcanism and the opening of the NE Atlantic**. Geological Society of London Special Publication, 39: 381-389.
- England, R. W. (1992) The role of Palaeogene magmatism in the tectonic evolution of the Sea of the Hebrides basin: implications for basin evolution on the NW seaboard. In: Parnell, J., ed. **Basins on the Atlantic Seaboard: Petroleum Geology, Sedimentology and Basin Evolution**. Geological Society of London Special Publication, 62: 163-174.
- Ernst, R. E. (1994) Mapping the magma flow pattern in the Sudbury dyke swarm in Ontario using magnetic fabric analysis. In: **Current Research 1994-E**, Geological Survey of Canada, Ottawa: 183-192.
- Ernst, R. E. and Baragar, W. R. A. (1992) Evidence from magnetic fabric for the flow pattern of magma in the MacKenzie giant radiating dyke swarm. **Nature**, 356: 511-513.
- Ernst, R. E., Head, J. W., Parfitt, E., Grosfils, E. and Wilson, L. (1995) Giant radiating dyke swarms on Earth and Venus. **Earth-Science Reviews**, 39: 1-58.
- Eriksson, P. I., Riishuus, M. S., Sigmundsson, F. and Elming, S. A. (2011) Magma flow directions inferred from field evidence and magnetic fabric studies of the Streishvarf composite dike in east Iceland. **Journal of Volcanology and Geothermal Research**, 206: 30-45.
- Ewart, A., Milner, S. C., Duncan, A. R. and Bailey, M. (2002) The Cretaceous Messum igneous complex, S.W. Etendeka, Namibia: reinterpretation in terms of a downsag-cauldron subsidence model. **Journal of Volcanology and Geothermal Research**, 114: 251-273.
- Faithful, J. W. and Upton, B. G. J. (2006) Xenolithic insights into the deep geology beneath the Ross of Mull. **Scottish Journal of Geology**, 42: 37-41.
- Féménias, O., Diot, H., Berza, T., Gauffriau, A. and Demaiffe, D. (2004) Asymmetrical to symmetrical magnetic fabric of dikes: Paleo-flow orientations and Paleo-stresses

- recorded on feeder-bodies from the Motru Dike Swarm (Romania). **Journal of Structural Geology**, 26: 1401-1418.
- Ferrè, E. C. (2002) Theoretical models of intermediate and inverse AMS fabrics. **Geophysical Research Letters**, 29 (7): 31-1–31-4.
- Galland, O., Planke, S., Neumann, E. –R. and Malthe-Sørenssen, A. (2009) Experimental modelling of shallow magma emplacement: Application to saucer-shaped intrusions. **Earth and Planetary Science Letters**, 277: 373-383.
- Gautneb, H., Gudmundsson, A. and Oskarsson, N. (1989) Structure, Petrochemistry and evolution of a sheet swarm in an Icelandic central volcano. **Geological Magazine**, 126: 659-673.
- Gautneb, H. and Gudmundsson, A. (1992) Effect of local and regional stress fields on sheet emplacement in West Iceland. **Journal of Volcanology and Geothermal Research**, 51: 339-356.
- Geikie, A. (1897) **The ancient volcanoes of Great Britain**. Volume 2. Macmillan. London.
- Geldmacher, J., Haase, K. M., Devey, C. W. and Garbe-Schönberg. (1998) The petrogenesis of tertiary cone-sheets in Ardnamurchan, NW Scotland: petrological and geochemical constraints on crustal contamination and partial melting. **Contributions to Mineralogy and Petrology**, 131: 196-209.
- Geldmacher, J., Troll, V. R., Emeleus, C. H. and Donaldson, C. H. (2002) Pb-isotope evidence for contrasting crustal contamination of primitive to evolved magmas from Ardnamurchan and Rum: implications for the structure of the underlying crust. **Scottish Journal of Geology**, 38: 55-61.
- Geoffroy, L., Aubourg, C., Callot, J. P. and Moreira, M. (2002) Is the common use of AMS in mafic dykes scientifically correct? **Terra Nova**, 14: 183-190.
- Geshi, N. (2005) Structural development of dike swarms controlled by the change of magma supply rate: The cone sheets and parallel dike swarms of the Miocene Otoge igneous complex, Central Japan. **Journal of Volcanology and Geothermal Research**, 141: 267-281.
- Glazner, A. F., Bartley, J. M., Coleman, D. S., Gray, W. and Taylor, R. Z. (2004) Are plutons assembled over millions of years by amalgamation from small magma chambers? **GSA Today**, 14: 4-11.
- Graham, J. W. (1954) Magnetic susceptibility anisotropy, an unexploited petrofabric element. **Journal of Geophysical Research**, 54: 131-167.
- Gray, J. P. and Monaghan, J. J. (2004) Numerical modelling of stress fields and fracture around magma chambers. **Journal of Volcanology and Geothermal Research**, 135: 259-283.
- Grégoire, V., Blanquat, M., Nedelec, A. and Bouchez, J. (1995) Shape anisotropy versus magnetic interactions of magnetite grains – experiments and application to AMS in

- granitic-rocks. **Geophysical Research Letters**, 22(20): 2765-2768.
- Gribble, C. D. (1974) The dolerites of Ardnamurchan. **Scottish Journal of Geology**, 10: 71-89.
- Gudmundsson, A. (1995) Infrastructure and mechanics of volcanic systems in Iceland. **Journal of Volcanology Geothermal Research**, 64: 1-22.
- Gudmundsson, A. (1998) Magma chambers modelled as cavities explain the formation of rift zone central volcanoes and their eruption and intrusion statistics. **Journal of Geophysical Research**, 103: 7401-7412.
- Gudmundsson, A. (2002) Emplacement and arrest of dykes in central volcanoes. **Journal of Volcanology and Geothermal Research**, 116: 279-298.
- Gudmundsson, A. (2006) How local stresses control magma-chamber ruptures, dyke injections and eruptions in composite volcanoes. **Earth-Science Reviews**, 79: 1-31.
- Gudmundsson, A. and Phillip, S. L. (2006) How local stress fields prevent volcanic eruptions. **Journal of Volcanology and Geothermal Research**, 158: 257-268.
- Guglielmo, G. (1993) Magmatic strains and foliation triple points of the Merrimac plutons, northern Sierra Nevada, California: implications for pluton emplacement and timing of subduction. **Journal of Structural Geology**, 15: 177-189.
- Guglielmo, G. (1994) Interference between pluton expansion and coaxial tectonic deformation; three-dimensional computer model and field implications. **Journal of Structural Geology**, 16: 237-252.
- Hall, A. (1996) **Igneous Petrology**. Prentice Hall: 551 p.
- Halsall, T. J. (1974) **The minor intrusions and structure of the Carlingford complex, Eire**. PhD Thesis. University of Leicester, Leicester.
- Hansen, D. M. and Cartwright, J. A. (2006) Saucer shaped sill with lobate morphology revealed by 3D seismic data: implications for resolving a shallow level sill emplacement mechanism. **Journal of the Geological Society, London**, 163: 509-523.
- Hansen, J., Jerram, D. A., McCaffrey, K. and Passey, S. R. (2009) The onset of the North Atlantic Igneous Province in a rifting perspective. **Geological Magazine**, 146: 309-325.
- Hargraves, R. B., Johnson, D. and Chan, C. Y. (1991) Distribution anisotropy: the cause of AMS in igneous rocks? **Geophysical Research Letters**, 18: 2193-2196.
- Harker, A. (1904) **The tertiary igneous rocks of Skye**. Memoir of the Geological Survey of the United Kingdom: 481 p.
- Herrero-Bervera, E., Walker, G. P. L., Cañón-Tapia, E. and Garcia, M. O. (2001) Magnetic fabric and inferred flow direction of dikes, conesheets and sill swarms, Isle of Skye, Scotland. **Journal of Volcanology and Geothermal Research**, 106: 195-210.

- Herrero-Bervera, E., Cañón-Tapia, E. and Walker, G. P. L. (2003) Reply to comment made by Aubourg et al. **Journal of Volcanology and Geothermal Research**, 122: 145-148.
- Hills, E. S. (1963) **Elements of Structural Geology**, London.
- Hincks, G. (2004) **Earth Science Illustration Library** [online]. Available from <http://www.garyhincks.com> [Accessed 21<sup>st</sup> July 2011].
- Hirt, A. M. and Almqvist, B. S. G. (2011) Unravelling magnetic fabrics. **International Journal of Earth Sciences**. doi 10.1007/s00531-011-0664-0.
- Holdsworth, R. E., Harris, A. L. and Roberts, A. M. (1987) The stratigraphy, structure and regional significance of the Moine rocks of Mull, Argyllshire, W. Scotland. **Geological Journal**, 22: 83-107.
- Holland, J. G. and Brown, G. M. (1972) Hebridean tholeiitic magmas: a geochemical study of the Ardnamurchan cone sheets. **Contributions to Mineralogy and Petrology**, 37: 139-160.
- Hopkinson, J. (1889) Magnetic and other physical properties of iron at a high temperature. **Philosophical Transactions of the Royal Society of London A**, 180: 443-465.
- Horsman, E., Tikoff, B. and Morgan, S.S. (2005) Emplacement-related fabric in a sill and multiple sheets in the Maiden Creek sill, Henry Mountains, Utah. **Journal of Structural Geology**, 27: 1426-1444.
- Hrouda, F., Janak, F., Reil, L. and Weiss, J. (1971) The mimic fabric of magnetite in some foliated granodiorites, as indicated by magnetic anisotropy. **Earth and Planetary Science Letters**, 11: 381-384.
- Hrouda, F. (1982) Magnetic anisotropy of rocks and its application in geology and geophysics. **Geophysical Survey**, 5: 37-82.
- Hrouda, F. (2003) Indices for numerical characterization of the alteration processes of magnetic minerals taking place during investigation of temperature variation of magnetic susceptibility. **Studies in Geophysics and Geodesy**, 47: 847-861.
- Hutton, D. H. W. (2009) Insights into magmatism in volcanic margins: bridge structures and a new mechanism of basic sill emplacement – Theron Mountains, Antarctica. **Petroleum Geoscience**, 15: 269-278.
- Hyndman, D. W. and Alt, D. (1987) Radial dikes, laccoliths and gelatine models. **Journal of Geology**, 95: 763-774.
- Irving, E. (1970) The Mid-Atlantic ridge at 45° N. XIV. Oxidation and magnetic properties of basalt; review and discussion. **Canadian Journal of Earth Sciences**, 7: 1528-1538.
- Jaeger, J. C. (1969) **Elasticity, fracture and flow: With engineering and geological applications**. London: 268 p.

- Jackson, M. D. and Pollard, D. D. (1988) The laccolith-stock controversy: New results from the southern Henry Mountains, Utah. **Geological Society of America Bulletin**, 100: 117-139.
- Jeffrey, H. (1936) Note on fracture. **Proceedings of the Royal Society of Edinburgh**, 56: 158-163.
- Jelínek, V. (1978) Statistical processing of anisotropy of magnetic susceptibility measured on groups of specimens. **Studies of Geophysics and Geodesy**, 22: 50-62.
- Johnson, H. P. and Atwater, T. (1977) A magnetic study of the basalts from the Mid-Atlantic Ridge at 37°N. **Geological Society of America Bulletin**, 88: 637-647.
- Johnson, S. E., Paterson, S. R. and Tate, M. C. (1999) Structure and emplacement history of a multiple-center, cone-sheet-bearing ring complex, Baja California, Mexico. **Geological Society of America Bulletin**, 111: 607-619.
- Jolly, R. J. H. and Sanderson, D. J. (1995) Variation in the form and distribution of dykes in the Mull swarm, Scotland. **Journal of Structural Geology**, 17: 1543-1557.
- Jolly, R. J. H. and Sanderson, D. J. (1997) A Mohr circle construction for the opening of a pre-existing fracture. **Journal of Structural Geology**, 19: 887-892.
- Jones, S. M., White, N., Clarke, B. J., Rowley, E. and Gallagher, K. (2002) Present and past influence of the Iceland Plume on sedimentation. In: Doré, A. G., Turner, J. P. and White, N., eds. **Exhumation of the North Atlantic Margin: Timing, mechanisms and implications for petroleum exploration**. Geological Society of London Special Publication, 196: 13-25.
- Judd, J. W. (1874) The secondary rocks of Scotland. Second Paper. On the ancient volcanoes of the highlands and the relations of their products to the Mesozoic strata. **Quarterly Journal of the Geological Society**, 30: 220-302.
- Kavanagh, J. L., Menand, T. and Sparks, R. S. J. (2006) An experimental investigation of sill formation and propagation in layered elastic media. **Earth and Planetary Science Letters**, 245: 799-813.
- Kent, R. W. and Fitton, J. G. (2000) Mantle sources and melting dynamics in the British Palaeogene Igneous Province. **Journal of Petrology**, 41: 1023-1040.
- Kerr, A. C., Kempton, P. D. and Thompson, R. N. (1995) Crustal assimilation during turbulent magma ascent (ATA); new isotopic evidence from the Mull Tertiary lava succession, N. W. Scotland. **Contributions to Mineralogy and Petrology**, 119: 142-154.
- Kerr, A. C., Kent, R. W., Thompson, B. A., Seedhouse, J. K. and Donaldson, C. H. (1999) Geochemical evolution of the tertiary Mull volcano, NW Scotland. **Journal of Petrology**, 40: 873-908.
- Kervyn, M., Ernst, G. G. J., van Wyk de Vries, B., Mathieu, L. and Jacobs, P. (2009) Volcano load control on dyke propagation and vent distribution: Insights from analogue modelling. **Journal of Geophysical Research**, 114: B03401, doi:

10.1029/2008JB005653.

- Keunen, P. H. (1937) Intrusion of cone sheets. **Geological Magazine**, 74: 177-183.
- Khan, M.A. (1962) The anisotropy of magnetic susceptibility of some igneous and metamorphic rocks. **Journal of Geophysical Research**, 67: 2867-2875.
- King, R. F. (1966) The magnetic fabric of some Irish granites. **Geological Journal**, 5: 43-66.
- Kissel, C., Laj, C., Sigurdsson, H. and Guillou, H. (2010) Emplacement of magma in Eastern Iceland dykes: insights from magnetic fabric and rock magnetic analyses. **Journal of Volcanology and Geothermal Research**, 191: 71-92.
- Klausen, M. B. (2004) Geometry and mode of emplacement of the Thverartindur cone sheet swarm, SE Iceland. **Journal of Volcanology and Geothermal Research**, 138: 185-204.
- Klausen, M. B. (2006) Geometry and mode of emplacement of dike swarms around the Birnudalstindur igneous centre, SE Iceland. **Journal of Volcanology and Geothermal Research**, 151: 340-356.
- Knight, M.D. and Walker, G. P. L. (1988) Magma flow directions in dikes of the Koolan Complex, Oahu, determined from magnetic fabric studies. **Journal of Geophysics Research**, 93: 4308-4319.
- Kokelaar, B. P. (1982) Fluidization of wet sediments during the emplacement and cooling of various igneous bodies. **Journal of the Geological Society, London**, 139: 21-33.
- Krabbendam, M. and Leslie, A. G. (2010) Lateral variations and linkages in thrust geometry: the Traligill Transverse Zone, Assynt Culmination, Moine Thrust Belt, NW Scotland. In: Law, R. D., Butler, R. W. H., Holdsworth, R. E., Krabbendam, M. and Strachan, R. A., eds. **Continental Tectonics and Mountain Building: The Legacy of Peach and Horne**. Geological Society of London Special Publication, 335: 335-357.
- Kratinová, Z., Zavada, P., Hrouda, F. and Schulmann, K. (2006) Non-scaled analogue modelling of AMS development during viscous flow: A simulation on diapir-like structures. **Tectonophysics**, 418: 51-61.
- Lattard, D., Engelmann, R., Konty, A. and Sauerzapf, U. (2006) Curie temperatures of synthetic titanomagnetites in the Fe-Ti-O system: Effects of composition, crystal chemistry and thermomagnetic methods. **Journal of Geophysical Research**, 111: B12S28, doi:10.1029/2006JB004591.
- Launeau, P. and Cruden, A. R. (1998) Magmatic fabric acquisition mechanisms in a syenite: Results of a combined anisotropy of magnetic susceptibility and image analysis study. **Journal of Geophysical Research**, 103: 5067-5089.
- Le Bas, M. J. (1971) Cone-sheets as a mechanism of uplift. **Geological Magazine**, 108: 373-376.
- Lindline, J., Petronis, M. S., Pitrucha, R. and Sena, S. (2011) The late Oligocene Cieneguilla

- basanites, Santa Fe County: Records of early Rio Grande Rift magmatism. *In*: König, D. and Leuth, V., eds. **New Mexico Geological Society Fall Field Conference Guidebook #62 – Southern Tusas Mountains and Ojo Caliente**.
- Liss, D., Hutton, D. H. W. and Owens, W. H. (2002) Ropy flow structures – a neglected indicator of magma flow direction in sills and dykes. **Geology**, 30: 715-718.
- Liss, D., Owens, W. H. and Hutton, D. H. W. (2004) New palaeomagnetic results from the Whin Sill complex: evidence for a multiple intrusion event and revised virtual geomagnetic poles for the late Carboniferous for the British Isles. **Journal of the Geological Society, London**, 161: 927-938.
- Lundin, E. and Doré, A. G. (2005) NE Atlantic break-up: a re-examination of the Iceland mantle plume model and the Atlantic–Arctic linkage. *In*: Doré, A. G. and Vining, B. A., eds. **Petroleum Geology: North-West Europe and Global perspectives – Proceedings of the 6<sup>th</sup> Petroleum Geology Conference**. Geological Society of London: 739-754.
- Macdonald, R., Wilson, L., Thorpe, R. S. and Martin, A. (1988) Emplacement of the Cleveland Dike: Evidence from geochemistry, mineralogy, and physical modelling. **Journal of Petrology**, 29: 559-583.
- Macdonald, R., Baginski, B., Upton, B. G. J., Dzierzanowski, P. and Marshall-Roberts, W. (2009) The Palaeogene Eskdalemuir dyke, Scotland: long-distance lateral transport of rhyolitic magma in a mixed-magma intrusion. **Mineralogical Magazine**, 73: 285-300.
- Macdonald, R., Baginski, B., Upton, B. G. J., Pinkerton, H., MacInnes, D. A. and MacGillivray, J. C. (2010) The Mull Palaeogene dyke swarm: insights into the evolution of the Mull igneous centre and dyke-emplacement mechanisms. **Mineralogical Magazine**, 74: 601-622.
- Marinoni, L. B. (2001) Crustal extension from exposed sheet intrusions: review and method proposal. **Journal of Volcanology and Geothermal Research**, 107: 27-46.
- Marinoni, L. B. and Gudmundsson, A. (2000) Dykes, faults and palaeostresses in the Teno and Anaga massifs of Tenerife (Canary Islands). **Journal of Volcanology and Geothermal Research**, 103: 83-103.
- Marshall, M. and Cox, A. (1972) Magnetic changes in pillow basalts due to sea floor weathering. **Journal of Geophysical Research**, 77: 6459-6469.
- Martín-Hernández, F., Lüneburg, C. M., Aubourg, C. and Jackson, M. (2004) Magnetic fabric: methods and applications – an introduction. *In*: Martín-Hernández, F., Lüneburg, C. M., Aubourg, C. and Jackson, M., eds. **Magnetic fabric: Methods and applications**. Geological Society of London Special Publication, 238: 1-7.
- Mathieu, L., van Wyk de Vries, B., Holohan, E. P. and Troll, V. R. (2008) Dykes, cups, saucers and sills: Analogue experiments on magma intrusion into brittle rocks. **Earth and Planetary Science Letters**, 271: 1-13.
- Mathieu, L. and van Wyk de Vries, B. (2009) Edifice and substrata deformation induced by

- intrusive complexes and gravitational loading in the Mull volcano (Scotland). **Bulletin of Volcanology**, 71: 1133-1148.
- McKeagney, C. J., Boulter, C. A., Jolly, R. J. H. and Foster, R. P. (2004) 3-D Mohr circle analysis of vein opening, Indarama lode-gold deposit, Zimbabwe: implications for exploration. **Journal of Structural Geology**, 26: 1275-1291.
- McLeod, P. and Sparks, R. S. J. (1998) The dynamics of xenolith assimilation. **Contributions to Mineralogy and Petrology**, 132: 21-33.
- Menand, T. (2008) The mechanics and dynamics of sills in layered elastic rocks and their implications for the growth of laccoliths and other igneous complexes. **Earth and Planetary Science Letters**, 267: 93-99.
- Meyer, R., Nicoll, G.R., Hertogen, J., Troll, V.R., Ellam, R.M. and Emeleus, C.H. (2009) Trace element and isotope constraints on crustal anatexis by upwelling mantle melts in the North Atlantic Igneous Province: an example from the Isle of Rum, NW Scotland. **Geological Magazine**, 146: 382-399.
- Miller, C.F., Furbish, D. J., Walker, B. A., Claiborne, L. L., Koteas G. C., Bleick, H. A. and Miller, J. S. (2009) Growth of plutons by incremental emplacement of sheets in crystal-rich host: evidence from Miocene intrusions of the Colorado River Region, Nevada, USA. **Tectonophysics**, 500: 65-77.
- Mitchell, J. G. and Reen, K. P. (1973) Potassium-argon ages from the Tertiary Ring Complexes of the Ardnamurchan Peninsula, Western Scotland. **Geological Magazine**, 110: 331-340.
- Mitchell, W. I., ed. (2004) **The Geology of Northern Ireland. Our Natural Foundation**. Geological Survey of Northern Ireland, Belfast: 318 p.
- Molyneux, S. J. and Hutton, D. H. W. (2000) Evidence for significant granite space creation by the ballooning mechanism: The example of the Ardara pluton, Ireland. **Geological Society of America Bulletin**, 112: 1543-1558.
- Morgan, S., Stanik, A., Horsman, E., Tikoff, B., de Saint-Blanquat, M. and Habert, G. (2008) Emplacement of multiple magma sheets and wall rock deformation: Trachyte Mesa intrusion, Henry Mountains, Utah. **Journal of Structural Geology**, 30: 491-512.
- Moskowitz, B. M. (1981) Methods for estimating Curie temperatures of titanomagmaeomites from experimental Js-T data. **Earth and Planetary Science Letters**, 53: 84-88.
- Nesse, W. D. (2004) **Introduction to Optical Mineralogy**. Oxford University Press, Oxford: 348 p.
- Nicoll, G. R., Holness, M. B., Troll, V. R., Donaldson, C. H., Holohan, E. P., Emeleus, C. H. and Chew, D. (2009) Early mafic magmatism and crustal anatexis on the Isle of Rum: evidence from the Am M'am intrusion breccias. **Geological Magazine**, 146: 368-381.
- O'Driscoll, B., Troll, V. R., Reavy, R. J. and Turner, P. (2006) The Great Euclite intrusion of Ardnamurchan, Scotland: Reevaluating the ring-dike concept. **Geology**, 34: 189-192.

- O'Driscoll, B. (2007) The Centre 3 layered gabbro intrusion, Ardnamurchan, NW Scotland. **Geological Magazine**, 144: 897-908.
- O'Driscoll, B., Stevenson, C. T. E. and Troll, V. R. (2008) Mineral lamination development in layered gabbros of the British Palaeogene Igneous Province: A combined anisotropy of magnetic susceptibility, quantitative textural and mineral chemistry study. **Journal of Petrology**, 49: 1187-1221.
- O'Reilly, W. (1984) **Rock and Mineral Magnetism**. Blackie: Chapman and Hall, New York, USA: 220 p.
- Odé, H. (1957) Mechanical analysis of the dike pattern of the Spanish Peaks area, Colorado. **Geological Society of America Bulletin**, 68: 567-576.
- Orlický, O. (1990) Detection of magnetic carriers in rocks: results of susceptibility changes in powdered rock samples induced by temperature. **Physics of the Earth and Planetary Interiors**, 63: 66-70.
- Owens, W. H. (1974) Mathematical model studies on factors affecting the magnetic anisotropy of deformed rocks. **Tectonophysics**, 24: 115-131.
- Owens, W. H. (1994) Laboratory drilling of field-oriented block samples. **Journal of Structural Geology**, 16: 1719-1721.
- Owens, W. H. (2000) Error estimates in the measurement of anisotropic magnetic susceptibility. **Geophysical Journal International**, 142: 516-526.
- Owens, W. H. and Bamford, D. (1976) Magnetic, seismic and other anisotropic properties of rock fabrics. **Philosophical Transactions of the Royal Society of London A**, 283: 55-68.
- Özdemir, O. and O'Reilly, W. (1981) High temperature hysteresis and other magnetic properties of synthetic monodomain titanomagnetites. **Physics of the Earth and Planetary Interiors**, 25: 406-418.
- Özdemir, O. and O'Reilly, W. (1982) Magnetic hysteresis properties of synthetic monodomain titanomagemites. **Earth and Planetary Science Letters**, 57: 467-478.
- Palmer, H. C., Ernst, R. E. and Buchan, K. L. (2007) Magnetic fabric studies of the Nipissing sill province and Senneterre dykes, Canadian Shield, and implications for emplacement. **Canadian Journal of Earth Sciences**, 44: 507-528.
- Paquet, F., Dauteuil, O., Hallot, E. and Moreau, F. (2007) Tectonics and magma dynamics coupling in a dyke swarm of Iceland. **Journal of Structural Geology**, 29: 1477-1493.
- Park, R. G. (2005) The Lewisian terrane model: a review. **Scottish Journal of Geology**, 41: 105-118.
- Pasquarè, F. A. and Tibaldi, A. (2007) Structure of a sheet-laccolith system revealing the interplay between tectonic and magma stresses at Stardalur Volcano, Iceland. **Journal**

- of Volcanology and Geothermal Research**, 161: 131-150.
- Paterson, S. R. and Vernon, R. H. (1995) Bursting the bubble of ballooning plutons – A return to nested diapirs emplaced by multiple processes. **Geological Society of America Bulletin**, 107: 1356-1380.
- Petford, N. and Clemens, J. D. (2000) Granites are not diapiric! **Geology Today**: 180-184.
- Petford, N., Cruden, A. R., McCaffrey, K. J. W. and Vigneresse, J. L. (2000) Granite magma formation, transport and emplacement in the Earth's crust. **Nature**, 408: 669-673.
- Petrovský, E. and Kapička, A. (2007). On determination of the Curie point from thermomagnetic curves. **Journal of Geophysical Research**, 111: B12S27, doi:10.1029/2006JB004507.
- Petronis, M. S., Hacker, D. B., Holm, D. K., Geissman, J. W. and Harlan, S. S. (2004) Magmatic flow paths and palaeomagnetism of the Miocene Stoddard Mountain laccolith, Iron Axis region, Southwestern Utah, USA. In: Martín-Hernández, F., Lüneburg, C. M., Aubourg, C. and Jackson, M., eds. **Magnetic fabric: Methods and applications**. Geological Society of London Special Publication, 238: 251-283.
- Phillips, W. J. (1974) The dynamic emplacement of cone sheets. **Tectonophysics**, 24: 69-84.
- Philpotts, A. R. and Philpotts, D. E. (2007) Upward and downward flow in a camptonite dike as recorded by deformed vesicles and the anisotropy of magnetic susceptibility (AMS). **Journal of Volcanology and Geothermal Research**, 161: 81-94.
- Pinel, V. and Jaupart, C. (2004) Magma storage and horizontal dyke injection beneath a volcanic edifice. **Earth and Planetary Science Letters**, 221: 245-262.
- Pitcher, W. S. (1979) The nature, ascent and emplacement of granitic magmas. **Journal of the Geological Society, London**, 71: 259-305.
- Pollard, D. D. (1973) Derivation and evaluation of a mechanical model for sheet intrusions. **Tectonophysics**, 19: 233-269.
- Pollard, D. D. (1987) Elementary fracture mechanics applied to the structural interpretations of dykes. In: Halls, H. C. and Fahrig, W. F. eds. **Mafic dyke swarms**. Geological Society of Canada Special Paper, 34: 5-24.
- Pollard, D. D. and Johnson, A. M. (1973) Mechanics of growth of some laccolithic intrusions in the Henry Mountains, Utah, II: Bending and failure of overburden layers and sill formation. **Tectonophysics**, 18: 311-354.
- Pollard, D.D., Muller, O.H., and Dockstader, D.R. (1975) Form and growth of fingered sheet intrusions. **Geological Society of America Bulletin**, 86: 351-363.
- Potter, D. K. and Stephenson, A. (1988) Single-domain particles in rocks and magnetic fabric analysis. **Geophysical Research Letters**, 15: 1097-1100.
- Pressler, R. E., Schneider, D. A., Petronis, M. S., Holm, D. K. and Geissman, J. W. (2007)

- Pervasive horizontal fabric and rapid vertical extrusion: lateral overturning and margin subparallel flow of deep crustal migmatites, northeastern Bohemian Massif. **Tectonophysics**, 443: 19-36.
- Richey, J. E. (1928) Structural relations of the Mourne Granites (Northern Ireland). **Quarterly Journal of the Geological Society of London**, 83: 653.
- Richey, J. E. and Thomas, H. H. (1930) **The geology of Ardnamurchan, north-west Mull and Coll**. Memoir of the Geological Survey of Great Britain, Sheet 51 and 52 (Scotland): 393 p.
- Rickwood, P. C. (1990) The anatomy of a dyke and the determination of propagation and magma flow directions. *In*: Parker, A. J., Rickwood, P. C. and Turner D. H., eds. **Mafic Dykes and Emplacement Mechanisms**: 81–100.
- Rivalta, E., Bottinger, M. and Dahm, T. (2005) Buoyancy-driven fracture ascent: Experiments in layered gelatine. **Journal of Volcanology and Geothermal Research**, 144: 273-285.
- Roberts, J. L. (1970) The intrusion of magma into brittle rocks. *In*: Newall, G. and Rast, N., eds. **Mechanism of Igneous Intrusion**. Gallery Press, Liverpool: 287-338.
- Robson, G. R. and Barr, K. G. (1964) The effect of stress on faulting and minor intrusions in the vicinity of a magma body. **Bulletin of Volcanology**, 27: 315-330.
- Rocchi, S., Westerman, D.S., Dini, A., Innocenti, F., Tonarini, S. (2002) Two-stage growth of laccoliths at Elba Island, Italy. **Geology**, 30: 983-986.
- Rochette, P. (1987) Magnetic susceptibility of the rock matrix related to magnetic fabric studies. **Journal of Structural Geology**, 9: 1015-1020.
- Rochette, P., Jackson, M and, Aubourg, C. (1992) Rock magnetism and the interpretation of the anisotropy of magnetic susceptibility. **Review of Geophysics**, 30: 209-226.
- Rochette, P., Aubourg, C. and Perrin, M. (1999). Is this magnetic fabric normal? A review and case studies in volcanic formations. **Tectonophysics**, 307: 219-234.
- Rodriguez-Losada, J. A. and Martinez-Frias, J. (2004) The felsic complex of the Vallehermoso Caldera: interior of an ancient volcanic system (La Gomera, Canary Islands). **Journal of Volcanology and Geothermal Research**, 137: 261-284.
- Rubin, A. M. (1995) Propagation of magma-filled cracks. **Annual Review of Earth and Planetary Sciences**, 23: 287-336.
- Ryan, M. P. and Sammis, C. G. (1978) Cyclic fracture mechanisms in cooling basalt. **Geological Society of America Bulletin**, 89: 1295-1308.
- Saunders, A. D., Jones, S. M., Morgan, L. A., Pierce, K. L., Widdowson, M. and Xu, Y. G. (2007) Regional uplift associated with continental large igneous provinces: the roles of mantle plumes and the lithosphere. **Chemical Geology**, 241: 282-318.

- Saunders, A. D., Fitton, J. G., Kerr, A. C., Norry, M. J. and Kent, R. W. (1997) The North Atlantic Igneous Province. **Geophysical Monograph**, 1000: 45-93.
- Schirnack, C., van den Bogaard, P. and Schmincke, H. (1999) Cone sheet formation and intrusive growth of an oceanic island – The Miocene Tejeda complex on Gran Canaria (Canary Islands). **Geology**, 27: 207-210.
- Schofield, N. (2009) **Linking sill morphology to emplacement mechanisms**. PhD Thesis. University of Birmingham, Birmingham.
- Schofield, N., Stevenson, C. and Reston, T. (2010) Magma fingers and host rock fluidization in the emplacement of sills. **Geology**, 38: 63-66.
- Sigmundsson, F., Hreinsdóttir, S., Hooper, A., Árnadóttir, T., Pedersen, R., Roberts, M. J., Óskarsson, N., Auriac, A., Deciem, J., Einarsson, P., Geirsson, H., Hensch, M., Ófeigsson, B. G., Sturkell, E., Sveinbjörnsson, H. and Feigl, K. L. (2010) Intrusion triggering of the 2010 Eyjafjallajökull explosive eruption. **Nature**, 468: 426-430.
- Siler, D. L. and Karson, J. A. (2009) Three-dimensional structure of inclined sheet swarms: Implications for crustal thickening and subsidence in the volcanic rift zones of Iceland. **Journal of Volcanology and Geothermal Research**, 188: 333-346.
- Skelhorn, R. R. and Elwell, R. W. D. (1966) The structure and form of the granophyric quartz-dolerite intrusion Centre 2, Ardnamurchan, Argyllshire. **Transactions of the Royal Society Edinburgh**, 66: 285-306.
- Smallwood, J. (2008) Comment on: Determining magma flow in sills, dykes and laccoliths and their implications for sill emplacement mechanisms by Ken Thomson [Bulletin of Volcanology 70:183–210]. **Bulletin of Volcanology**, 70:1139-1142.
- Smythe, D. K. (1987) Deep seismic reflection profiling of the Lewisian foreland. In: Park, R. G. and Tarner, J., eds. Evolution of the Lewisian and comparable Precambrian high grade terrains. **Geological Society of London Special Publication**, 27: 193-203.
- Soper, N. J., Harris, A. L. and Strachan, R. A. (1998) Tectonostratigraphy of the Moine Supergroup: a synthesis. **Journal of the Geological Society, London**, 155: 13-24.
- Sparks, R. S. J. (2003) Forecasting volcanic eruptions. **Earth and Planetary Science Letters**, 210: 1-15.
- Speight, J. M., Skelhorn, R. R., Sloan, T. and Knaap, R. J. (1982) The dike swarms of Scotland. In: Sutherland, D., ed. **Igneous rocks of the British Isles**. Chichester: p. 449-459.
- Stacey, F. D. (1960) Magnetic anisotropy of igneous rocks. **Journal of Geophysical Research**, 65: 2429-2442.
- Stevenson, C. T. E., Owens, W. H. and Hutton, D. H. W. (2007a) Flow lobes in granite: The determination of magma flow direction in the Trawenagh Bay Granite, northwestern Ireland, using anisotropy of magnetic susceptibility. **Geological Society of America**

- Bulletin**, 119: 1368-1386.
- Stevenson, C. T. E., Owens, W. H., Hutton, D. H. W., Hood, D. N. and Meighan, I. G. (2007b) Laccolithic, as opposed to cauldron subsidence, emplacement of the Eastern Mourne pluton, N. Ireland: evidence from anisotropy of magnetic susceptibility. **Journal of the Geological Society, London**, 164: 99-110.
- Stevenson, C. T. E. and Bennett, N. (2011) The emplacement of the Palaeogene Mourne Granite Centres, Northern Ireland: new results from the Western Mourne Centre. **Journal of the Geological Society, London**, 168: 831-836.
- Storey, M., Duncan, R. A. and Tegner, C. (2007) Timing and duration of volcanism in the North Atlantic Igneous Province: implications for geodynamics and links to the Iceland hotspot. **Chemical Geology**, 241: 264-281.
- Strachan, R. A., Holdsworth, R. E., Krabbendam, M. and Alsop, G. I. (2010) The Moine Supergroup of NW Scotland: insights into the analysis of polyorogenic supracrustal sequences. *In*: Law, R. D., Butler, R. W. H., Holdsworth, R. E., Krabbendam, M. and Strachan, R. A., eds. **Continental Tectonics and Mountain Building: The Legacy of Peach and Horne**. Geological Society of London Special Publication, 335: 233-254.
- Sun, S. –s. and McDonough, W. F. (1989) Chemical and isotopic systematic of oceanic basalts: implications for mantle composition and processes. **Geological Society of London Special Publication**, 42: 313-345.
- Tarling, D. H. and Hrouda, F. (1993) **The magnetic anisotropy of rocks**. New York, Chapman and Hall: 217 p.
- Tauxe, L. (1998). **Paleomagnetic Principles and Practice, vol. 17 of Modern Approaches in Geophysics**. Kluwer Academic Publishers, Dordrecht, Boston, London: 299 p.
- Tauxe, L., Gee, J. S. and Staudgiel, H. (1998) Flow directions in dikes from anisotropy of magnetic susceptibility data: The bootstrap way. **Journal of Geophysical Research**, 103: 17775-17790.
- Tegner, C., Duncan, R. A., Bernstein, S., Brooks, C. K., Bird, D. K. and Storey, M. (1998)  $^{40}\text{Ar}$ – $^{39}\text{Ar}$  geochronology of Tertiary mafic intrusions along the East Greenland rifted margin: relation to flood basalts and the Iceland hotspot. **Earth and Planetary Science Letters**, 156: 75-88.
- Thomson, K. and Hutton, D. H. W. (2004) Geometry and growth of sill complexes: insights using 3D seismic from the North Rockall Trough. **Bulletin of Volcanology**, 66: 364-375.
- Thomson, K. (2007) Determining magma flow in sills, dykes and laccoliths and their implications for sill emplacement mechanisms. **Bulletin of Volcanology**, 70: 183-201.
- Thomson, K. and Schofield, N. (2008) Lithological and structural controls on the emplacement and morphology of sills in sedimentary basins. *In*: Thomson, K. and Petford, N., eds. **Structure and Emplacement of High-Level Magmatic Systems**. Geological Society of London Special Publication, 302: 31-44.

- Tibaldi, A. and Pasquarè, F. A. (2008) A new mode of inner volcano growth: The “flower intrusive structure”. **Earth and Planetary Sciences Letters**, 271: 202-208.
- Tibaldi, A., Pasquarè, F. A. And Rust, D. (2011) New insights into the cone sheet structure of the Cuillin Complex, Isle of Skye, Scotland. **Journal of the Geological Society, London**, 168: 689-704.
- Trewin, N. H., ed. (2002) **The Geology of Scotland**. The Geological Society, London: 576 p.
- Twiss, R. J. and Moores, E. M. (2007) **Structural Geology**. W. H. Freeman and Company, New York: 736 p.
- Uyeda, S., Fuller, M. D., Belshe, J. C. and Girdler, R. W. (1963) Anisotropy of magnetic susceptibility of rocks and minerals. **Journal of Geophysical Research**, 68: 279-291.
- Verner, K., Žák, J., Nahodilová, R. and Holub, F. V. (2008) Magmatic fabrics and emplacement of the cone-sheet-bearing Knížecí Stolec durbachitic pluton (Moldanubian Unit, Bohemian Massif): implications for mid-crustal reworking of granulitic lower crust in the Central European Variscides. **International Journal of Earth Science**, 98: 19-33.
- Vétel, W. and Cartwright, J. (2010) Emplacement mechanisms of sandstone intrusions: insights from the Panoche Giant Injection Complex, California. **Basin Research**, 20: 783-807.
- Walker, G. P. L. (1975a) A new concept of the evolution of the British Tertiary intrusive centres. **Journal of the Geological Society, London**, 131: 121-141.
- Walker, G. P. L. (1975b) Intrusive sheet swarms and the identity of Crustal Layer 3 in Iceland. **Journal of the Geological Society, London**, 131: 143-159.
- Walker, G. P. L. (1992) “Coherent intrusion complexes” in large basaltic volcanoes – a new structural model. **Journal of Volcanology and Geothermal Research**, 50: 41-54.
- Walker, G. P. L. (1993) Re-evaluation of inclined intrusive sheets and dykes in the Cuillins volcano, Isle of Skye. In: Prichard, H. M., Alabaster, T., Harris, N. B. W. and Neary, C. R., eds. **Magmatic processes and plate tectonics**. Geological Society of London Special Publication, 76: 489-497.
- Wall, M., Cartwright, J., Davies, R. and McGrandle, A. (2009) 3D imaging of a Tertiary dyke swarm in the Southern North Sea, UK. **Basin Research**, doi: 10.1111/j.1365-2117.2009.00416.x.
- Wartho, J., Kelley, S. P. and Blake, S. (2001) Magma flow regimes in sills deduced from Ar isotope systematic of host rocks. **Journal of Geophysical Research**, 106: 4017-4035.
- Wells, M. K. (1953) The structure and petrology of the hypersthene-gabbro intrusion, Ardnamurchan, Argyllshire. **Quarterly Journal of the Geological Society**, 109: 367-397.

- Westerman, D. S., Dini, A., Innocenti, F. and Rocchi, S. (2004) Rise and fall of a nested Christmas-tree laccolith complex, Elba Island, Italy. *In*: Breitzkreuz, C. and Petford, N., eds. **Physical Geology of High-Level Magmatic Systems**. Geological Society of London Special Publication, 234: 195-213.
- Wheeler, J., Park, R. G., Rollinson, H. R. and Beach, A. (2010) The Lewisian complex: insights into deep crustal evolution. *In*: Law, R. D., Butler, R. W. H., Holdsworth, R. E., Krabbendam, M. and Strachan, R. A., eds. **Continental Tectonics and Mountain Building: The Legacy of Peach and Horne**. Geological Society of London Special Publication, 335: 51-79.
- White, R.S. (1992) Magmatism during and after continental break-up. *In*: Storey, B.C., Alabaster, T. and Pankhurst, R. J., eds. **Magmatism and causes of continental break-up**. Geological Society of London Special Publication, 68: 1-16.
- White, R.S. and McKenzie, D. P. (1989) Magmatism at rift zones: The generation of volcanic continental margins and flood basalts. **Journal of Geophysical Research**, 100: 7685-7729.
- Woodcock, N. H. and Strachan, R. A. (2004) **Geological History of Britain and Ireland**. Blackwell Publishing, Oxford: 423 p.
- Žák, J., Paterson, S. R. and Memeti, V. (2007) Four magmatic fabrics in the Tuolumne batholiths, central Sierra Nevada, California (USA): Implications for interpreting fabric patterns in plutons and evolution of magma chambers in the upper crust. **Geological Society of America Bulletin**, 119: 184-201.
- Zellmer, G.F. and Annen, C. (2008) An introduction to magma dynamics. *In*: Annen, C. and Zellmer, G.F., eds. **Dynamics of Crustal Magma Transfer, Storage and Differentiation**. Geological Society of London Special Publication, 304: 1-13.

# Appendix A: Compilation of structural observations and measurements from studied cone sheet swarms

Reference(s)	Location	Approximate Age (Ma)	Dominant composition	Swarms (where individual data collected for)	Average dip	Dip range	Dip distribution (D = decreases with distance; B = bimodal; P = parallel)	Average or range of thickness (m)	Strike distribution	Areas of increased sheet intensity (with respect to central complex)	Mode of opening (D =dilatational; S = shear)
Harker (1904); Walker (1993); Herrero-Bervera et al., (2001;2003) Tibaldi et al., (2011)	Skye, NW Scotland	59	dolerite	-	30-50	5-89	D	0.69	concentric	NW/SE	D
Bailey et al., (1924)	Mull, NW Scotland	58	basic and acidic	-	38	-	-	3	horseshoe geometry	-	D
Richey and Thomas (1930)	Ardnamurchan, NW Scotland	58	dolerite	Centre 1	20	-	D	10	concentric	S/SE	D
				Outer Centre 2	40			2			
				Inner Centre 2	80						
				Centre 3	50						
Le Bas (1971); Halsall (Unpub. Thesis. 1974)	Carlingford, Ireland	60	mafic	-	45	0-65	D	1.5	-	E/NE	S?
Gautneb et al., (1989)	Hafnarfjall, Iceland	5	basaltic	-	65	-	B	<1.2	NE-SW strikes dominant	-	-

Gautneb and Gudmundsson (1992)	Reykjadalur, Iceland	5	dolerites	-	45	0-90	-	1	-	-	D
Gudmundsson (1995)	Hvalfjörður, Iceland	10	basaltic	-	-	5-90	B	0.03-11	concentric	-	-
Ritz et al., (1996)	Meugueur-Meugueur ring complex, Nigeria	400	troctolite	-	-	65-80	-	200-300	circular; 65 km diameter	-	-
Johnson et al., (1999)	Zarza ring complex, Baja California	116	anorthositic gabbro	2	65	-	P	0.1-10	individually arcuate	-	S
Schirnack et al., (1999)	Tejeda complex, Gran Canaria	9	trachytic - phonolitic	Older Younger	45	-	P	2.1 3.9	12 km diameter	-	S
Ewart et al., (2002)	Messum igneous complex, Namibia	130	cumulate gabbro; gabbro-norites	Western Outer	-	38-52	-	250-850	both originally concentric	-	-
				Western Inner	-	27-71	-	650-1575			
				Eastern	-	15-30	D	5-20			
Klausen (2004)	Thverartindur, Iceland	10	mafic	-	-	32-60	D	0.5-1	arcuate	SE	-
Ancochea et al., (2003); Rodriguez-Losada and Martinez-Frias (2004)	Vallehermaso, La Gomera, Canary Islands	10	trachytic - phonolitic	-	-	60-80	P	1-4	concentric	-	D
Geshi (2005)	Otoge igneous centre, Japan	13	alkaline basalt-andesite	-	45	15-80	D	2-3	-	E/W	-
Pasquarè and Tibaldi (2007); Tibaldi and Pasquarè (2008)	Stardalur, Iceland	1.7	basaltic	-	35	0-90	D	1.7	elliptical; 2.5-3.5 km diameter	-	D
Verner et al., (2008)	Knížecí Stolec, Czech Republic	340	durbachitic	-	-	55-80	-	-	arcuate	S/SE	S

Burchardt and Gudmundsson (2009); Burchardt et al., (2011)	Geitafell volcano, Iceland	5	mafic	4	60	-	D, B	0.64	concentric	-	-
Siler and Karson (2009)	Vatnsdalur, Iceland	10	mafic	Swarm 1a	-	20-80	P	<1	-	-	-
				Swarm 1b							
				Swarm 2	-	20-60					
				Swarm 3	-	20-60					

- = data not available

Source position and shape	Approximate source depth (km)	Evidence of source	Overall cone sheet swarm geometry (B = bowl-like; F = Fanning; N = nested parallel sheets; T = trumpet-like)
central	-	inward dip; radial AMS trend	T
central	-	inward dip	-
central; cupola (paraboloid of revolution)	5	inward dip	-
central	2	inward dip	-
central; spherical or prolate elliptical	-	inward dip	B

central; spherical	<5	inward dip; rare vertical flow lines	B
central	-	inward dip	-
central	>4	inward dip; steep/vertical flow lamination	B
central	2.5 1.25	inward dip	N
central laccolith	-	inward dip	N
central	-	inward dip	F
central; flattened sphere	1	inward dip; outward thinning of sheets	B, F
central	<1	inward dip	B
central	2	inward dip; radial magma flow regime	F
central	-	inward dip; central feeder zone	F
central	-	inward dip	-

central sill-like chamber	1.5	inward dip traced 'into' central gabbro (gabbro often cross-cuts cone sheets	T, B
central	1		
	5	inward dip; cone sheet dip-parallel hot slickenlines	N
	-		

**Appendix B: AMS block sample reorientation data**

Block sample*	Block sample field orientation	Block sample drill orientation relative to field orientation	Number of sub-specimens
CSA2	189/76	008/22	6
CSA4	145/63	200/33	4
CSC1	014/63	076/04	9
CSD1	353/73	284/13 (cores A-B); 104/10 (cores C-D)	11
CSD2	350/25	199/41	6
CSD3	028/64	049/27	3
CSE1	114/98	114/22	13
CSE3	266/64	270/08	15
CSF1	235/09	220/18	8
CSG1B	112/72	170/18	7
CSH1	337/59	024/21	6
CSH2	027/21	046/40	4
CSI1	345/85	104/40	6
CSJ1	158/72	124/05	7
CO1	049/61	092/44	9
CO2	023/91?	207/07	7
CSK1	083/61	115/16	6
CSL1	030/34	348/39	7
CSM1	140/89	239/04	4
CSN1	046/70	167/21	6
CSP1	159/71	282/22	6
CS100	146/100	149/05	8
CS105	075/108	196/21 (core A); 167/18 (core B); 145/07 (core C)	5
CS108	049/79	125/18	7
CS111	055/87	290/07	10
CS115	251/102	127/20	8
CS118	040/100	006/12	8
CS125	036/79	089/12	6
CS128	326/81	025/26	8
CS131	025/42	062/12	5
CS134	257/53	102/05	4
CS140	002/108	054/31	8
CS143	139/100	000/00	7
CS146	171/09	127/19	10
CS148	112/33	091/33	11
CS149	168/99	190/07	10
CS150	317/77	164/18	9
CS151	347/57	022/07	12
CS156	034/16	190/05	9
CS157	036/39	317/18	5
CS158	184/25	315/25	9
CS159	273/20	306/20	6
CS160	063/73	061/09	5
CS162	001/49	039/10	8

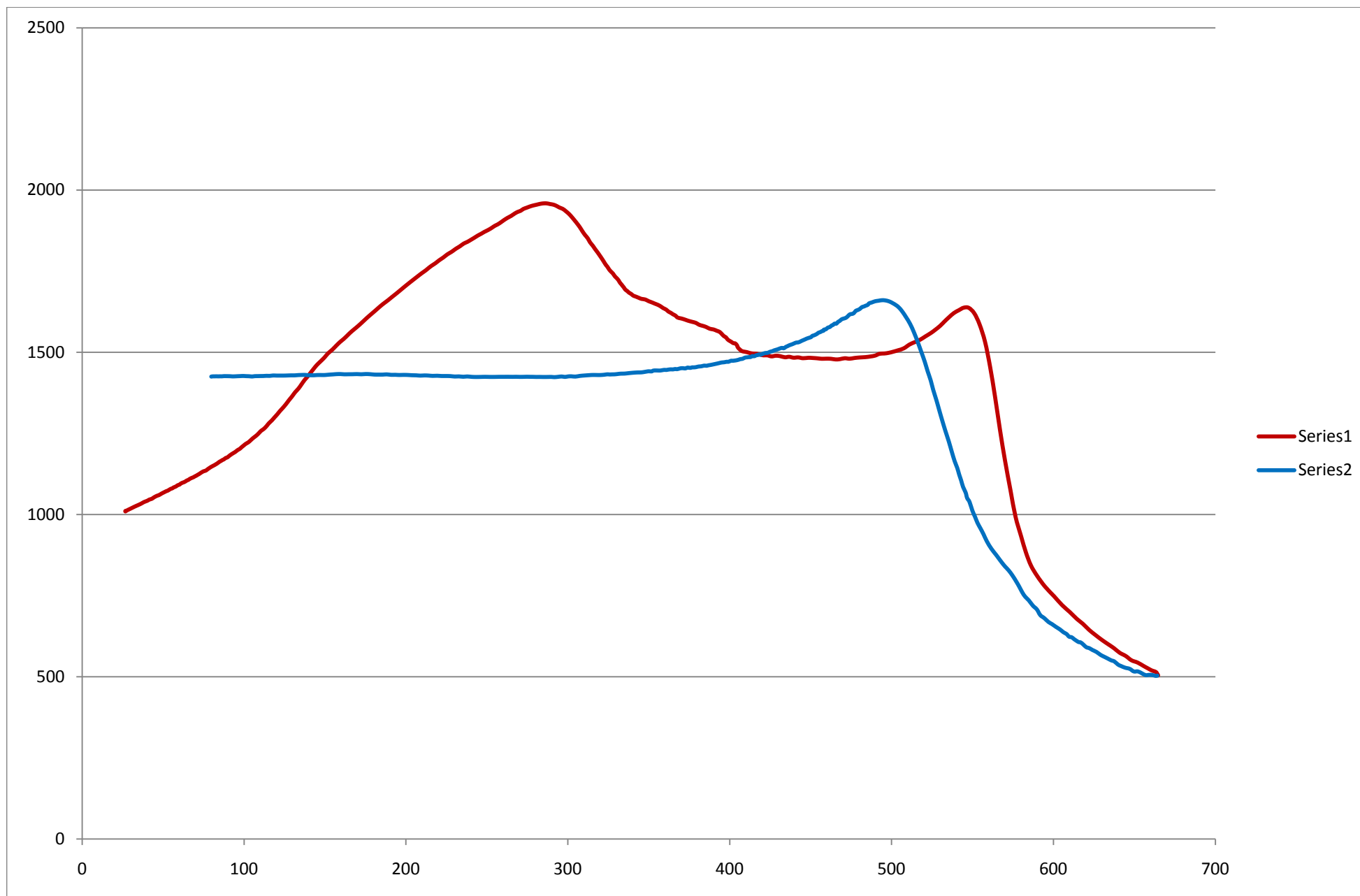
CS163	138/14	065/03	6
CS164	097/102	320/22	7
CS165	044/92	273/30	5
CS166	036/91	304/11	9
CS167	232/115	136/24	5
CS168	215/65	188/03	15
CS169	161/17	086/11	12
CS170	341/68	355/20	5
CS171	212/52	286/09	9
CS172a	142/77	147/07	6
CS172b	061/59	148/22	10
CS172c	124/84	078/36	4
CS172d	115/75	016/15	6
CS173	060/72	148/15	13
CS174a	269/30	286/13	5
CS174b	114/67	306/07	9
CS174c	066/78	120/24	6
CS175	311/32	171/04	11
CS176	340/32	135/08	9
CS177	202/68	042/08	8
CS178	340/36	125/15	6
CS179	125/41	146/07	5
CS180	238/57	247/29	7
CS182	005/74	358/22	5
CS183	020/64	180/22	5
CS184	019/87	032/11	8
CS185	127/105	065/13	6
CS186	096/51	156/42	4
CS187	105/69	293/29	8
CS188	125/97	030/06	4
CS208	313/100	156/15	6
CS223	342/53	000/10	6
CS226	005/91	180/07	6
CS227	089/39	318/22	4
CS255	104/125	254/11	6
CS257	166/94	101/06	7
CS261	127/15	074/09	5
CS265	082/27	220/13	6
CS268	166/22	002/26	5
<hr/>			
RD1	257/48	064/21	4
RD2	205/30	083/16	6
RD4	136/27	240/12	10
RD5	180/28	287/07	8
RD6	282/39	200/09 (core A); 154/09 (core B)	4
RD8	228/42	152/08	10
RD9b	028/019	013/10	7
RD14	160/12	270/36	7
<hr/>			

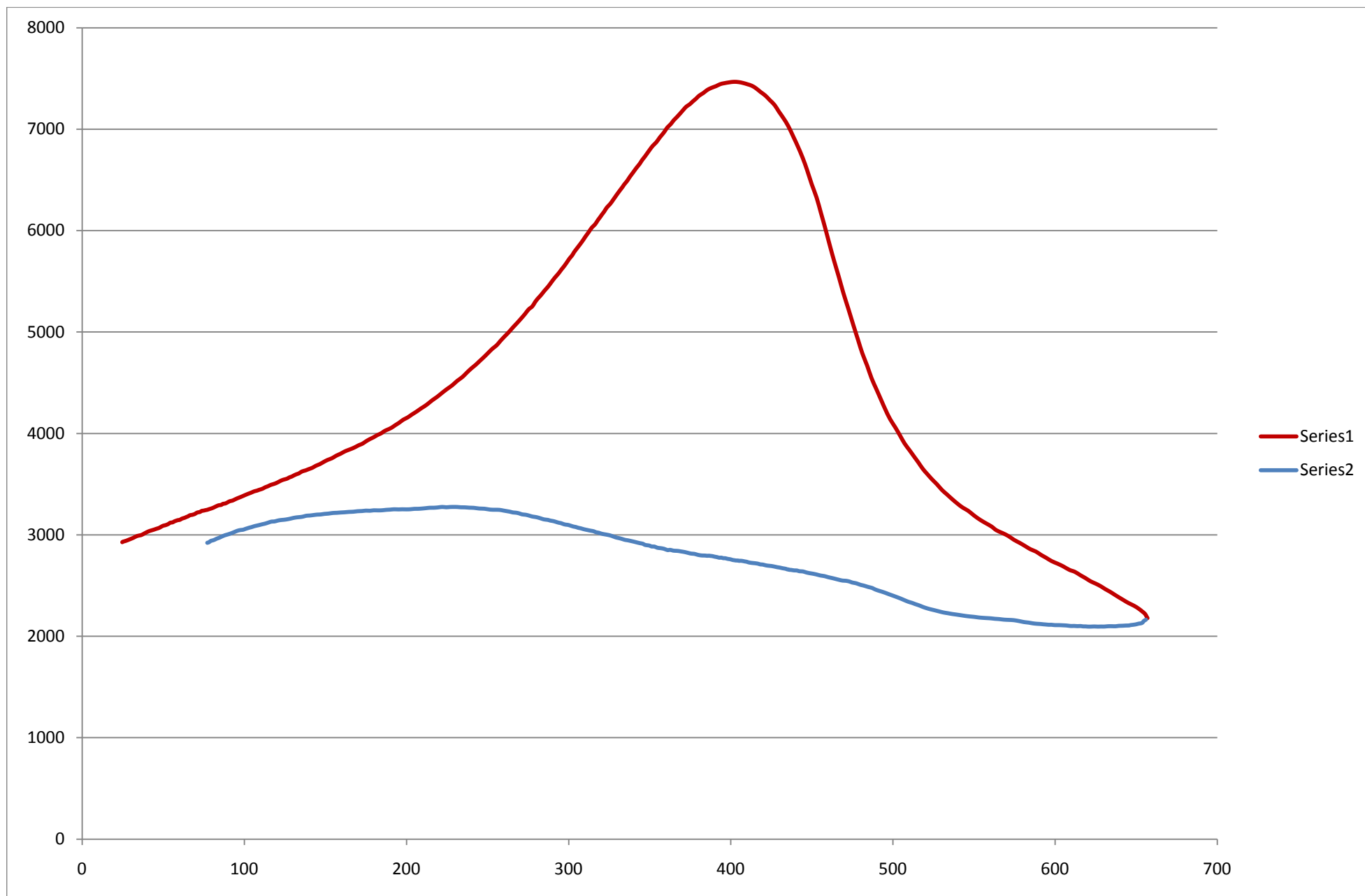
B-1	176/43	274/2 (cores A-C); 274/25 (cores D-E)	8
B-2	330/68	219/05	8
B-3	033/80	240/4	10
B-4	040/80	280/22	7
B-6	248/37	014/28	5
B-8	001/50	199/2	13
B-12	110/75	275/20	10
B-13	141/85	186/16	8
B-16	089/43	031/47	6
B-18	163/61	050/10	8
B-19	139/71	172/29	7
B-20	241/75	008/35	7
B-22	219/27	184/33	6
B-24	017/109	261/17	10
B-27	327/103	027/37	5
B-28	215/77	059/8	7
B-B	297/33	140/24	6
B-C	222/58	135/2	6
B-D	219/23	070/23	6
B-E	179/83	050/32 (cores A-D); 005/48 (core E)	9
B-100	087/15	320/12	7
B-101	109/20	350/10	4
B-102	330/73	076/10	8
B-103	304/63	117/12	8
B-104	140/81	242/43	6
B-105	287/81	114/03	14
B-106	196/58	274/09	12
B-107	290/103	015/15	8
B-108	350/53	147/07	4
B-109	335/74	019/44	4
B-115	286/87	067/23	7
B-116	067/64	123/08	12
B-117	164/77	165/28	4
B-118	342/87	245/11	15
B-119	097/28	087/10	10
B-120	164/59	151/34	4
B-121	175/70	162/37	10
B-122	170/93	033/08	5
B-123	025/62	299/05	13
B-125	137/80	194/29	5
B-126	037/39	052/10	6

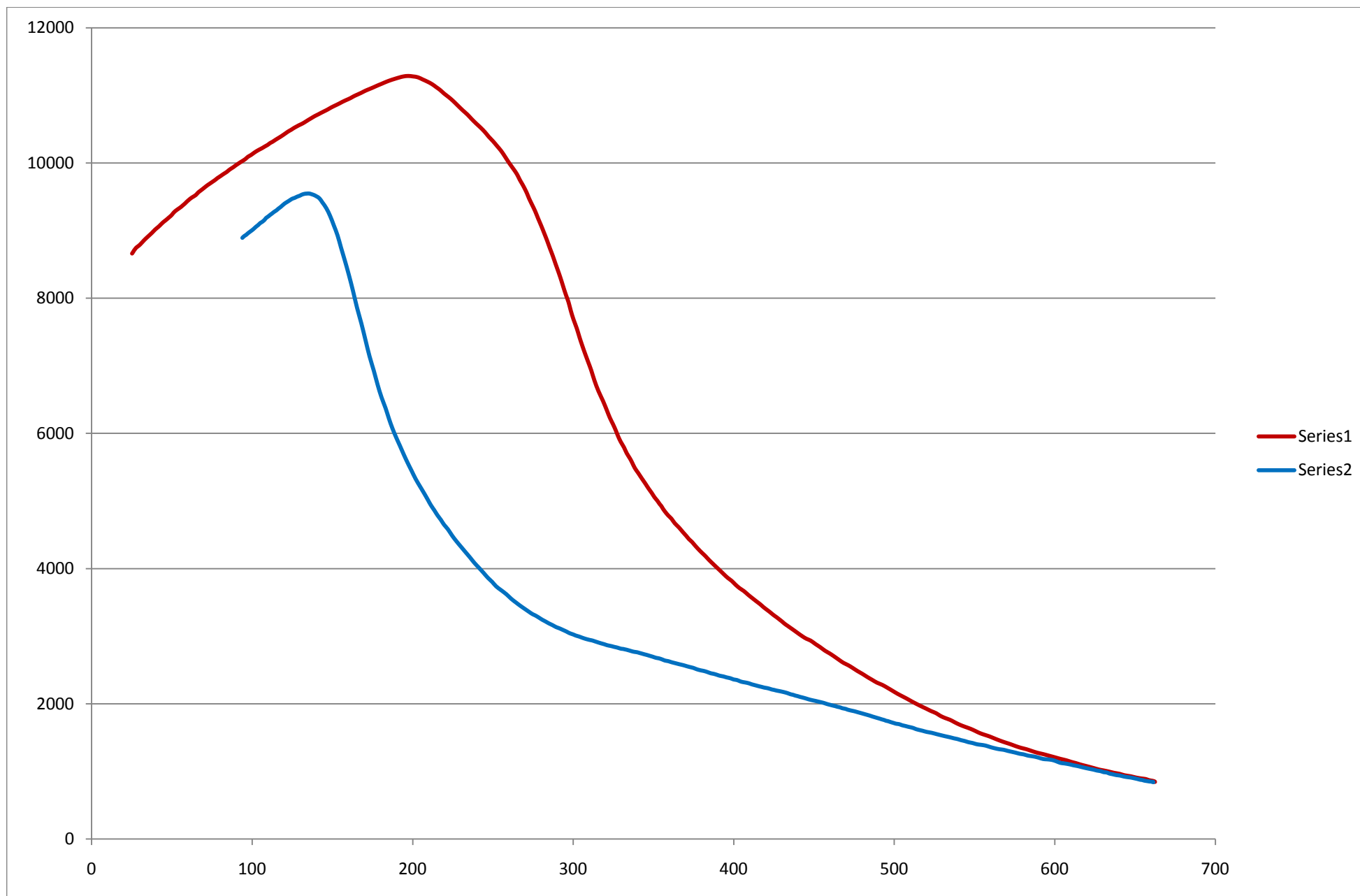
---

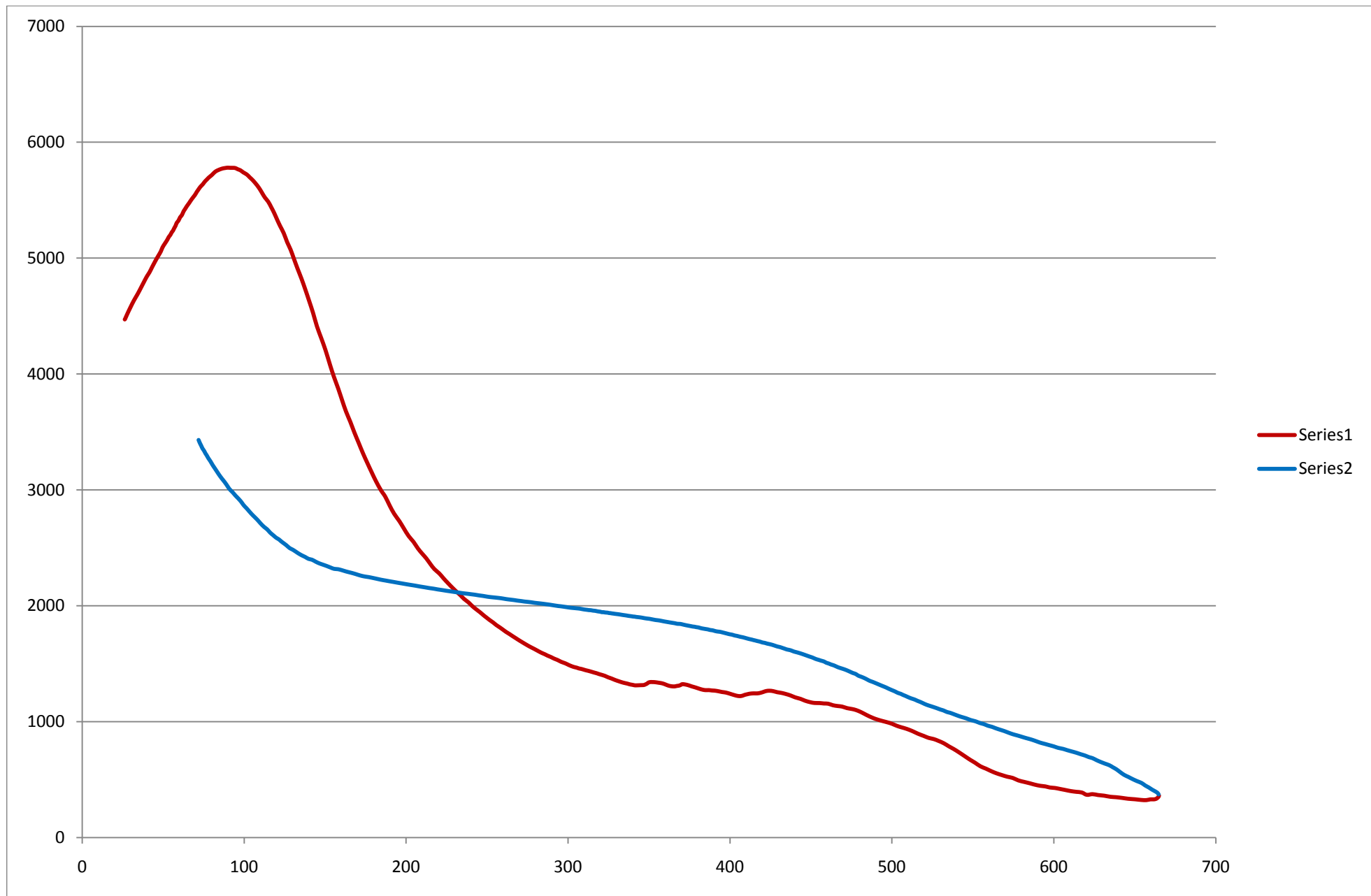
\* Two character prefix correlates to: CS = cone sheet; CO = composite cone sheet; RD = regional dyke; B- = Ben Hiant Dolerite

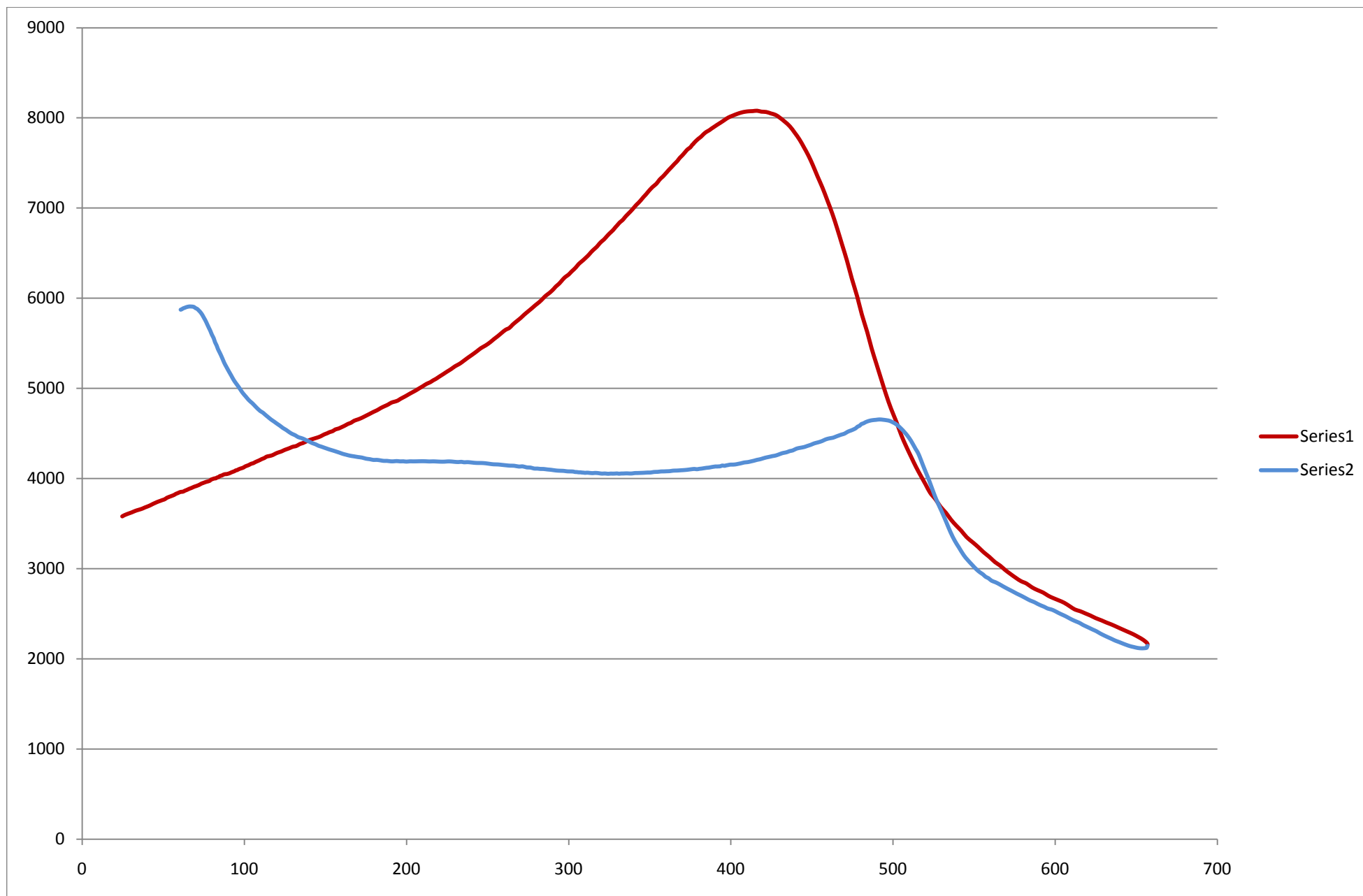
## **Appendix C**

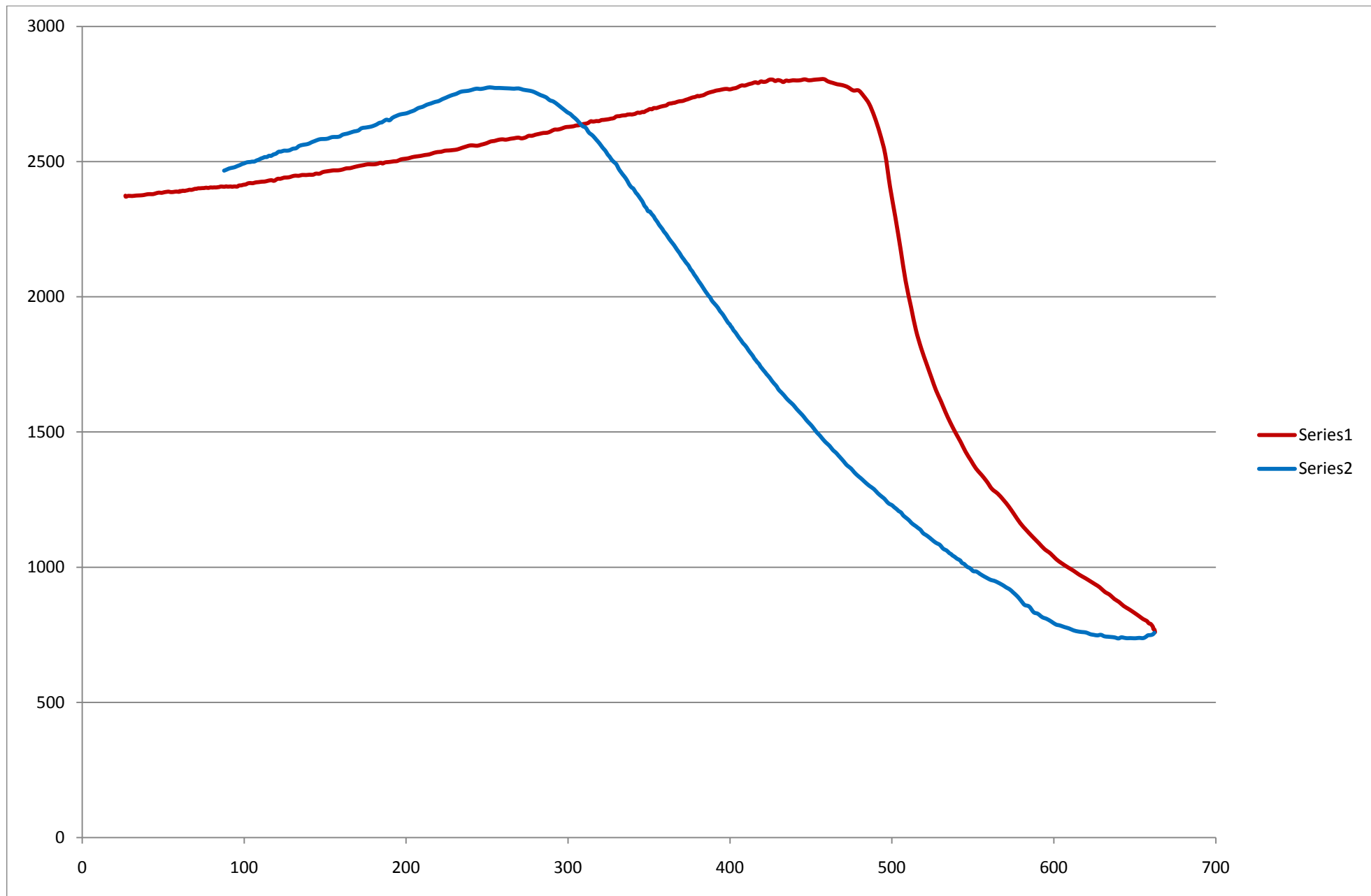


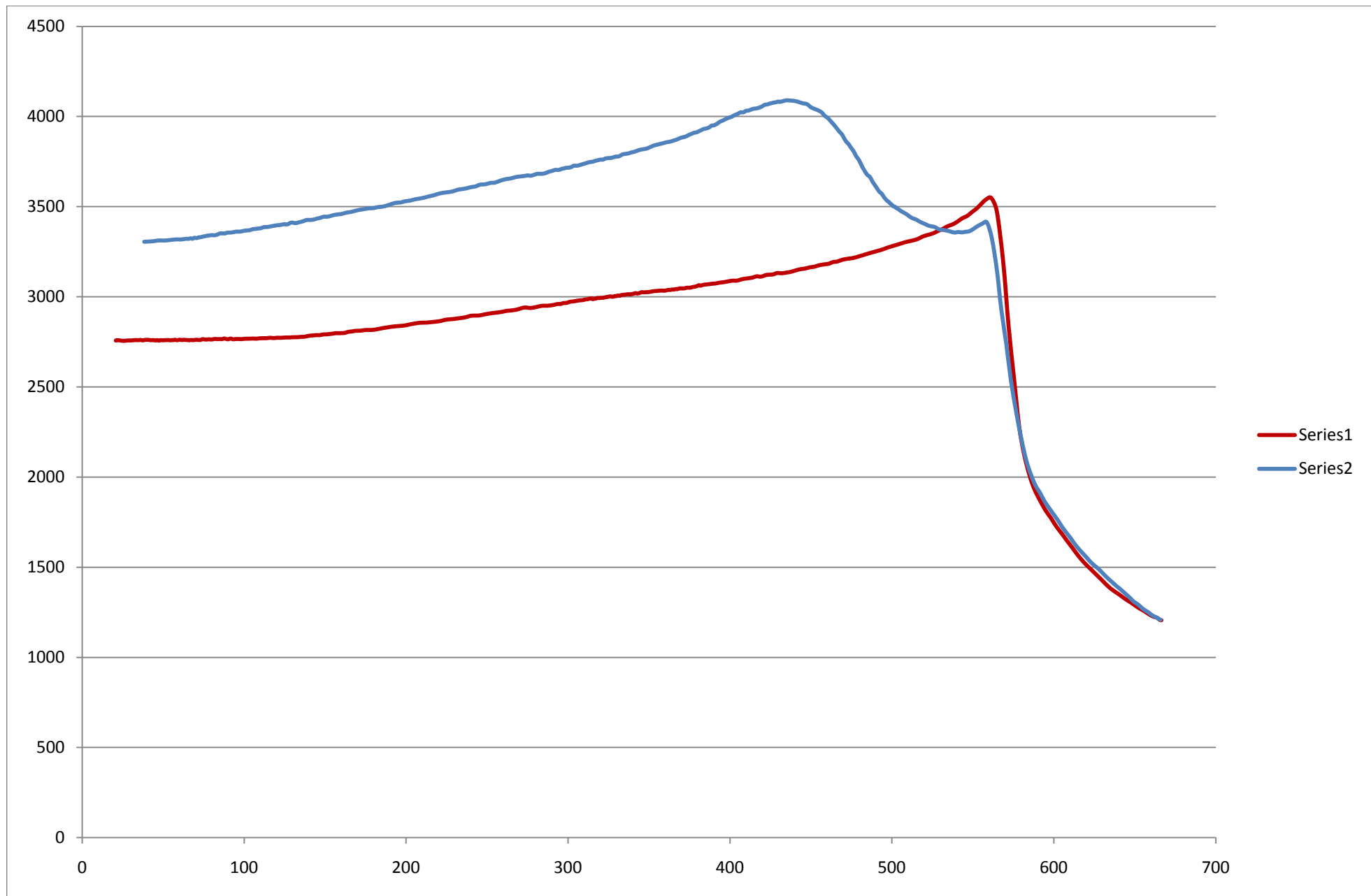


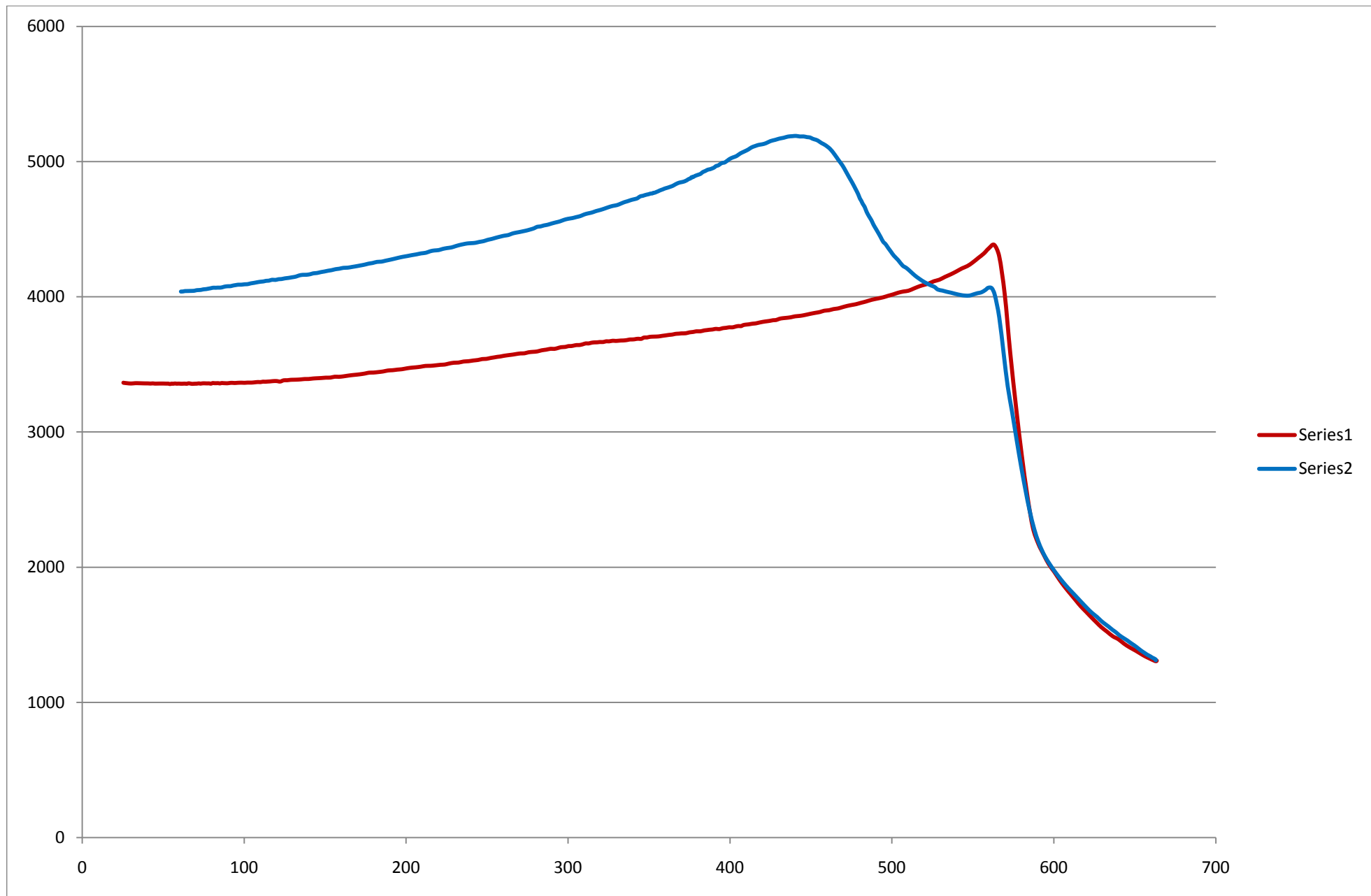


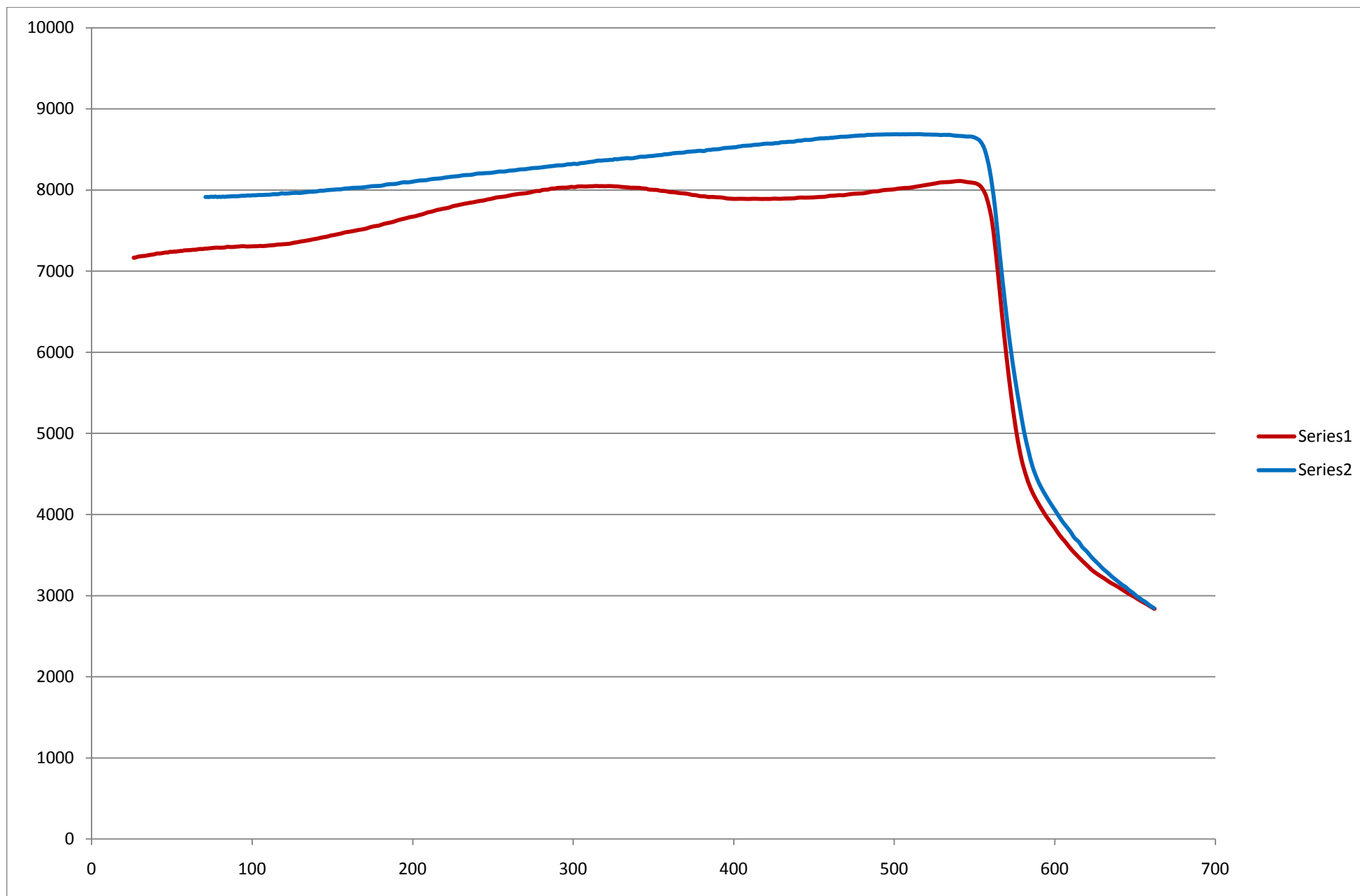


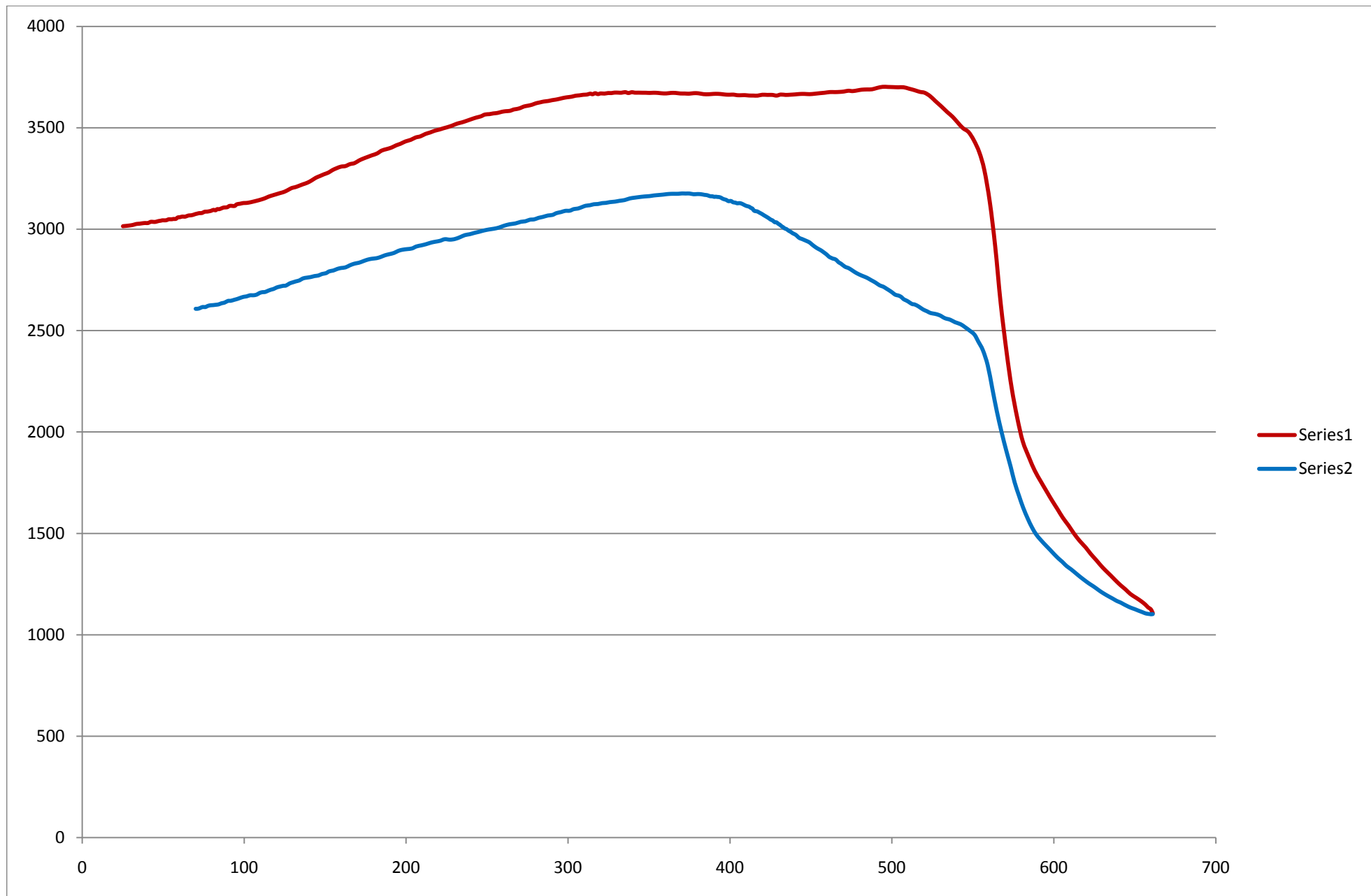


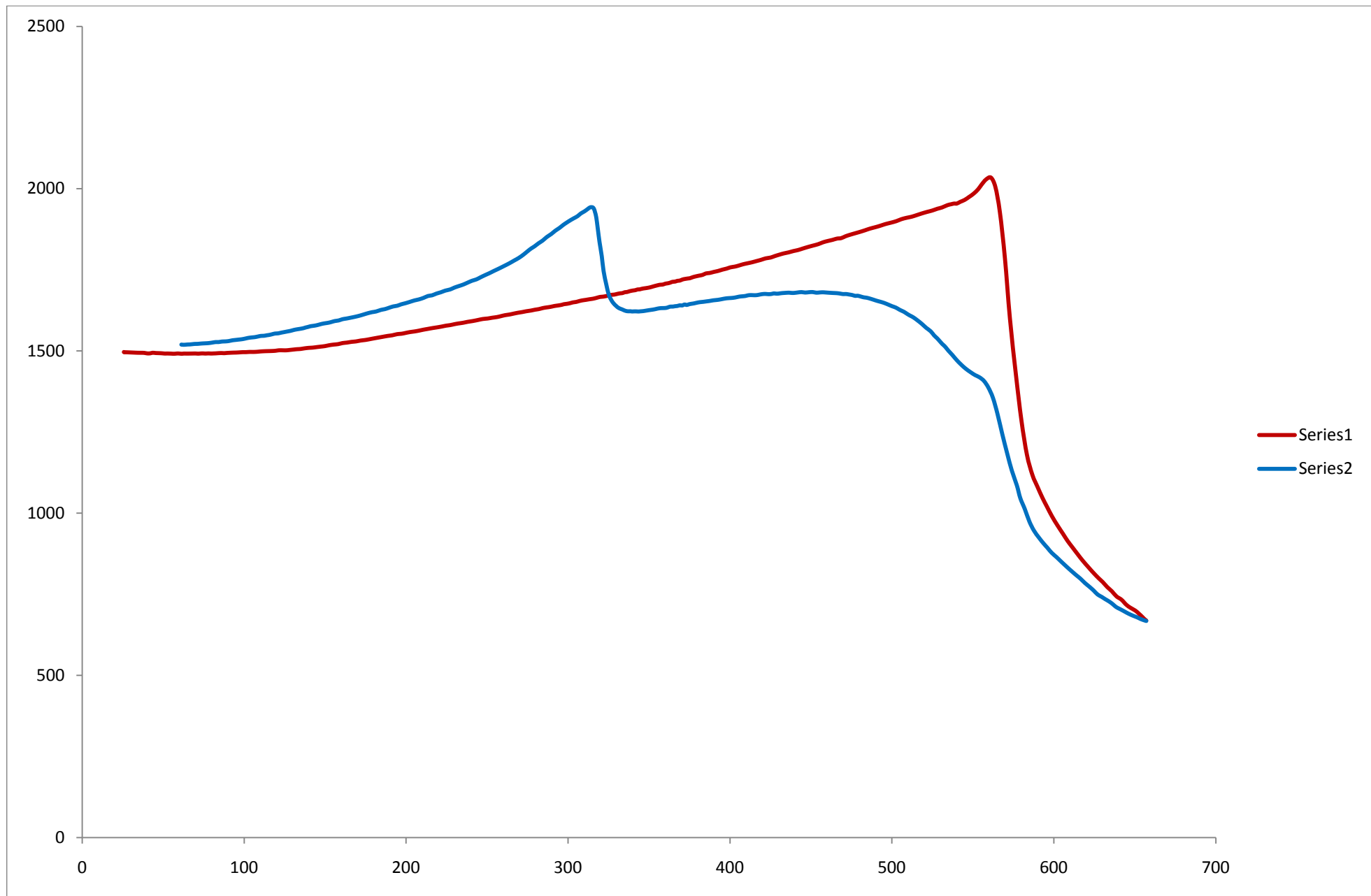


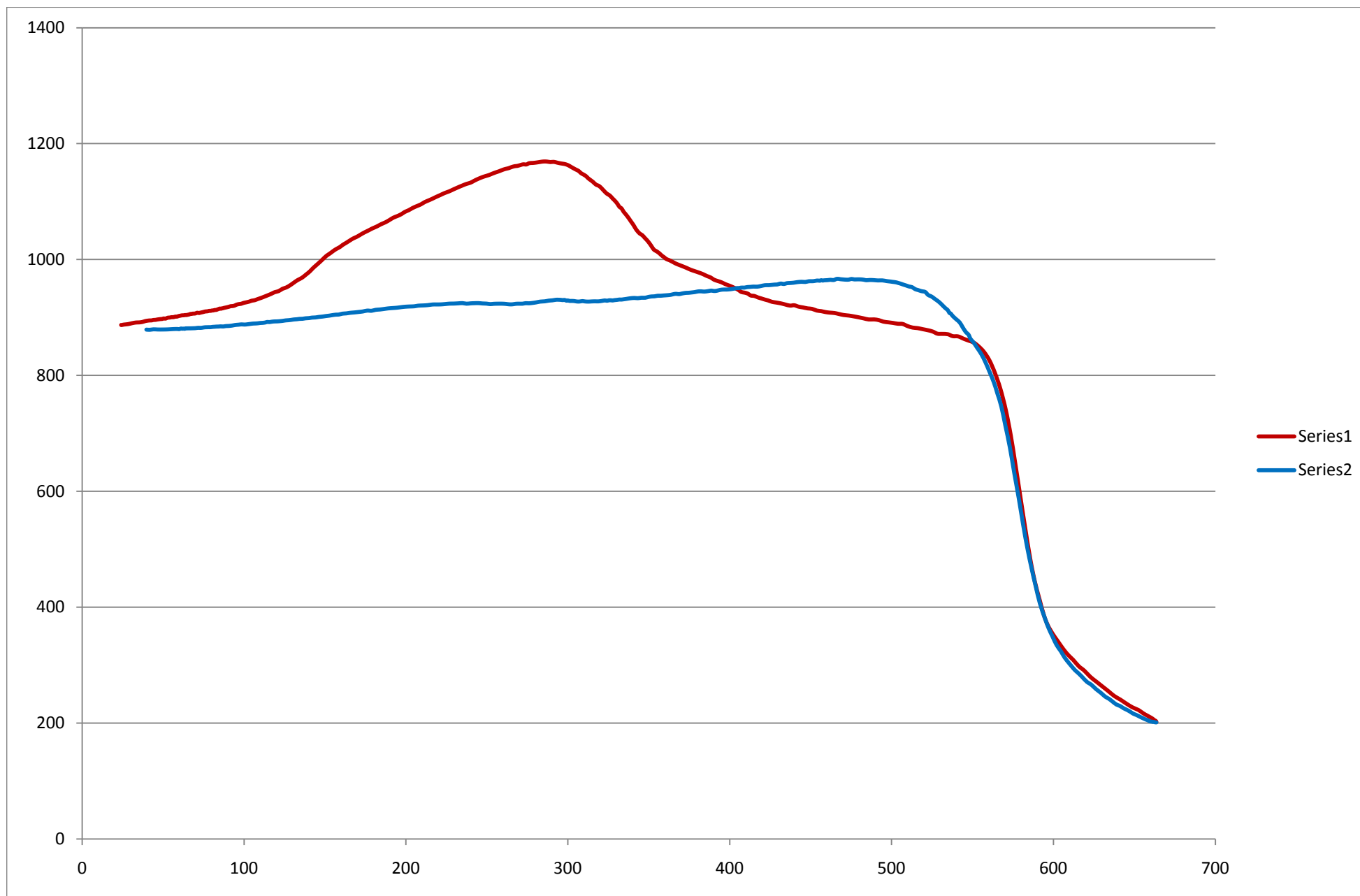


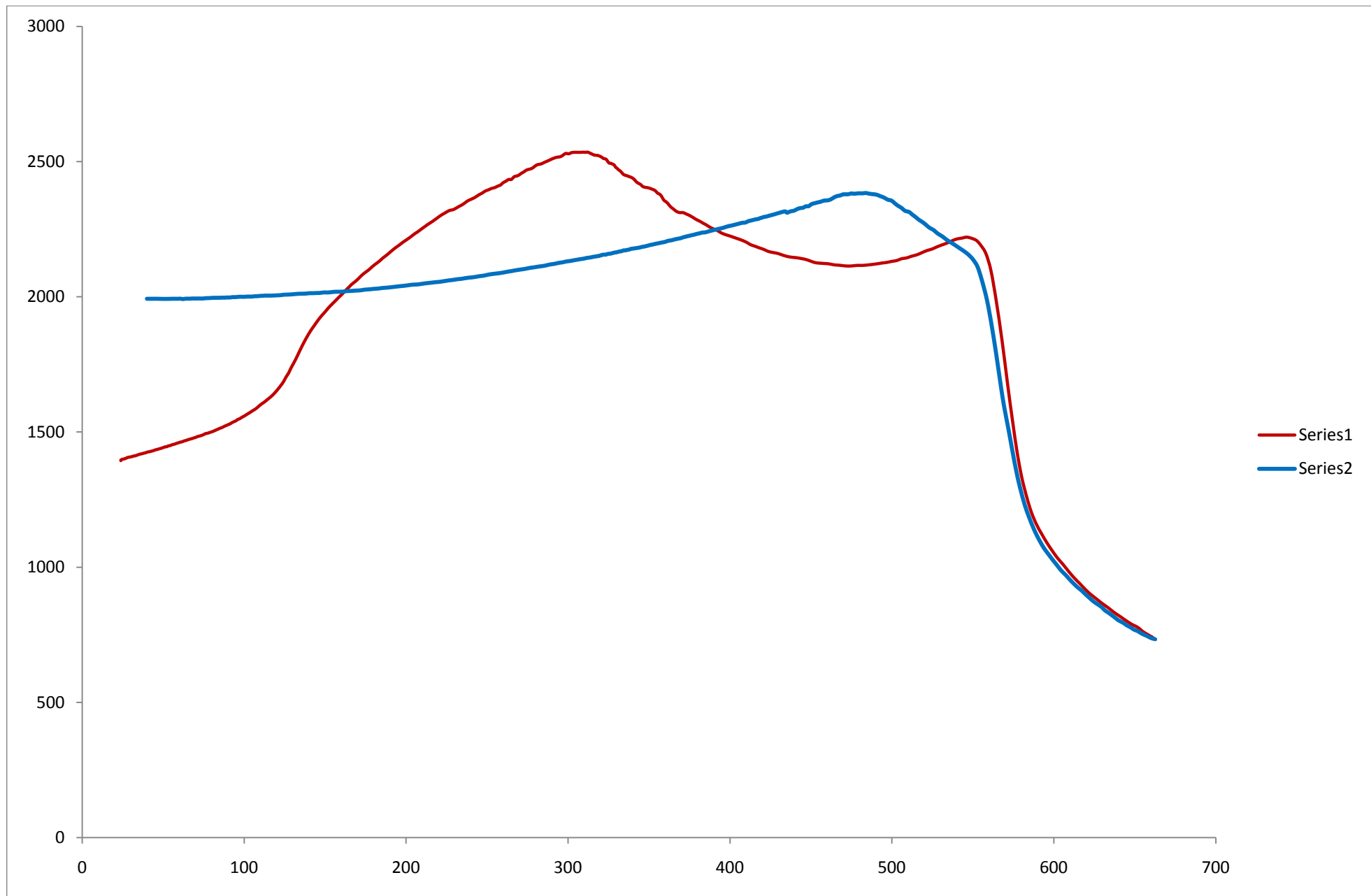


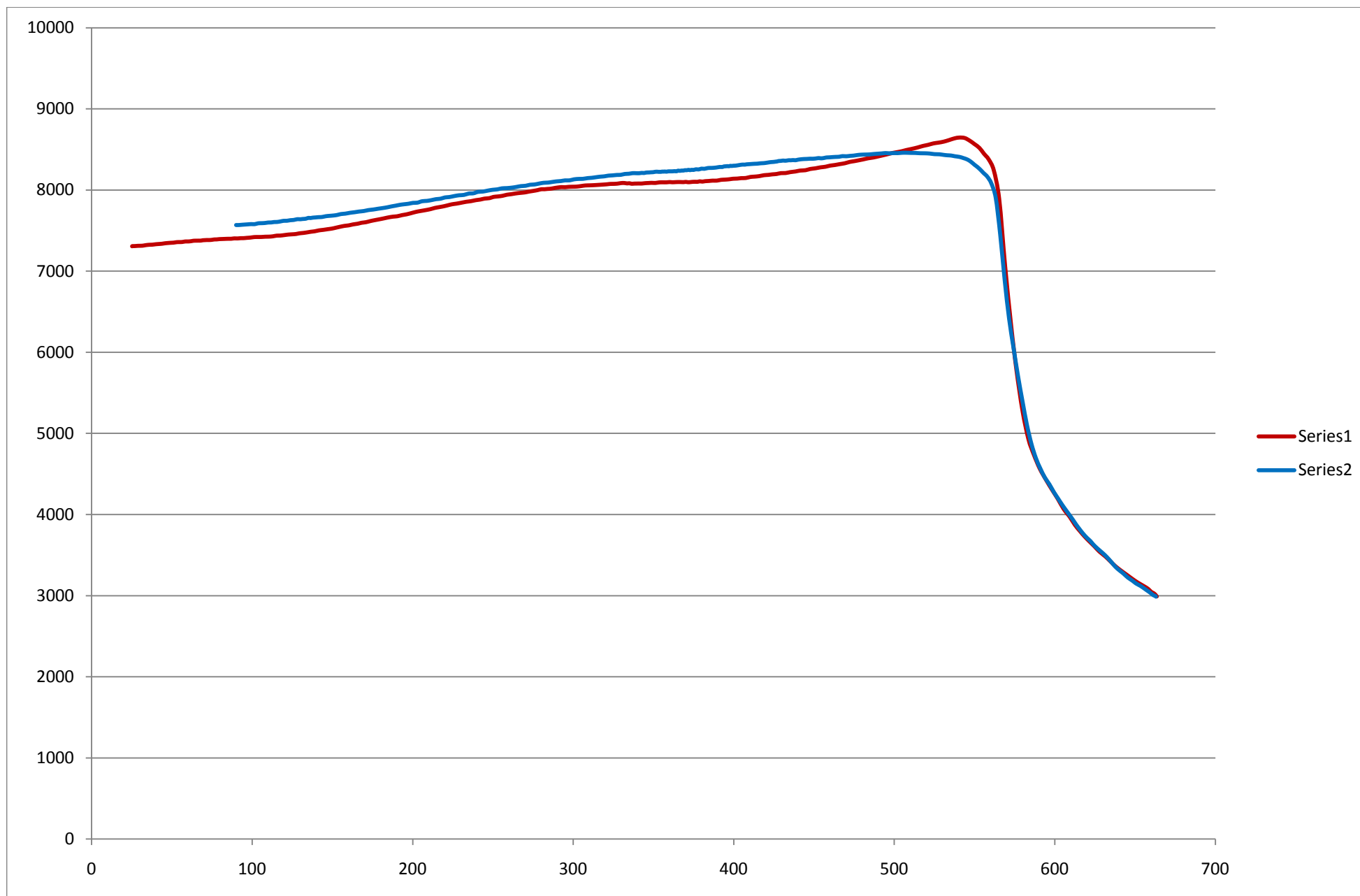


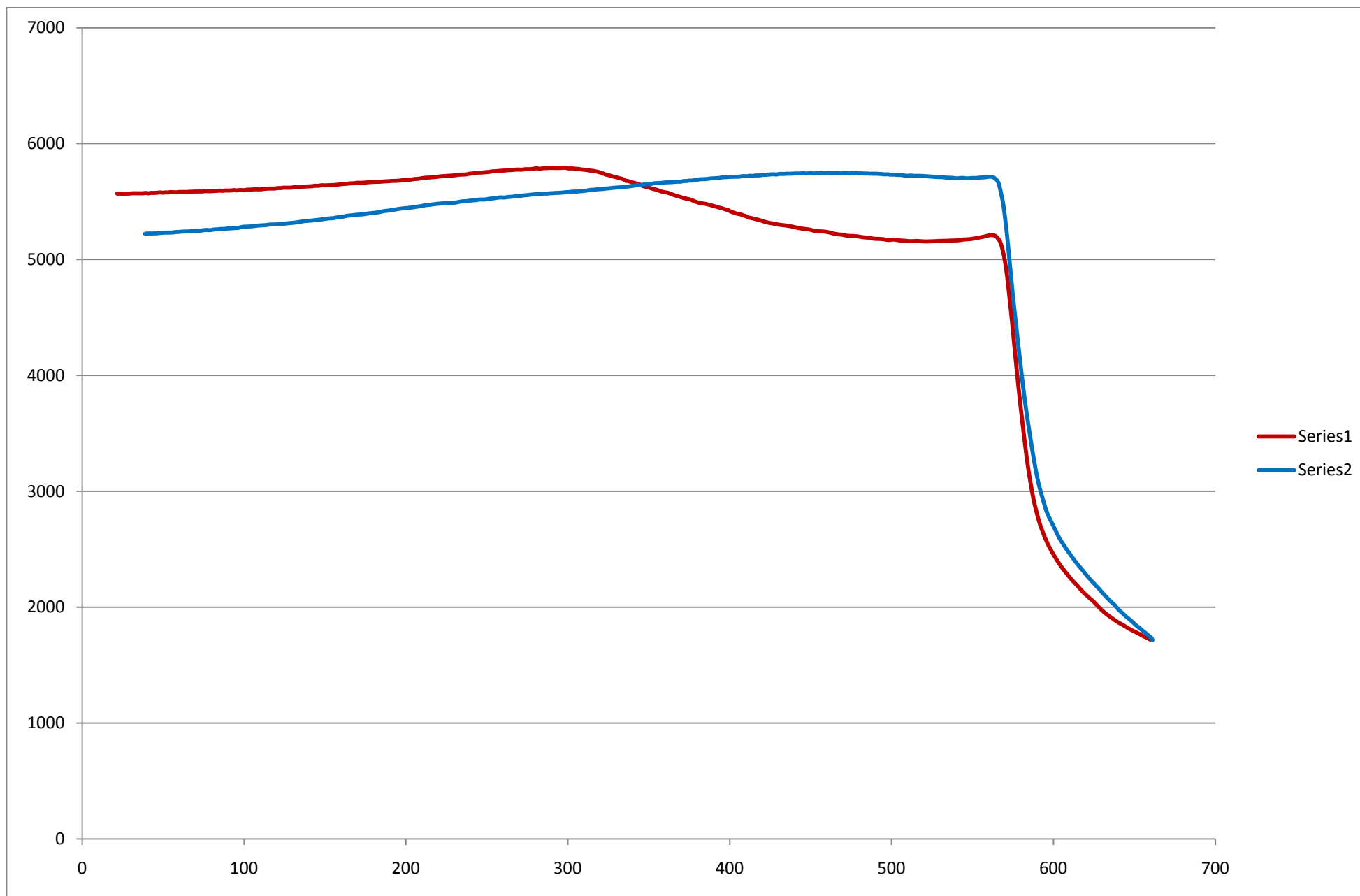


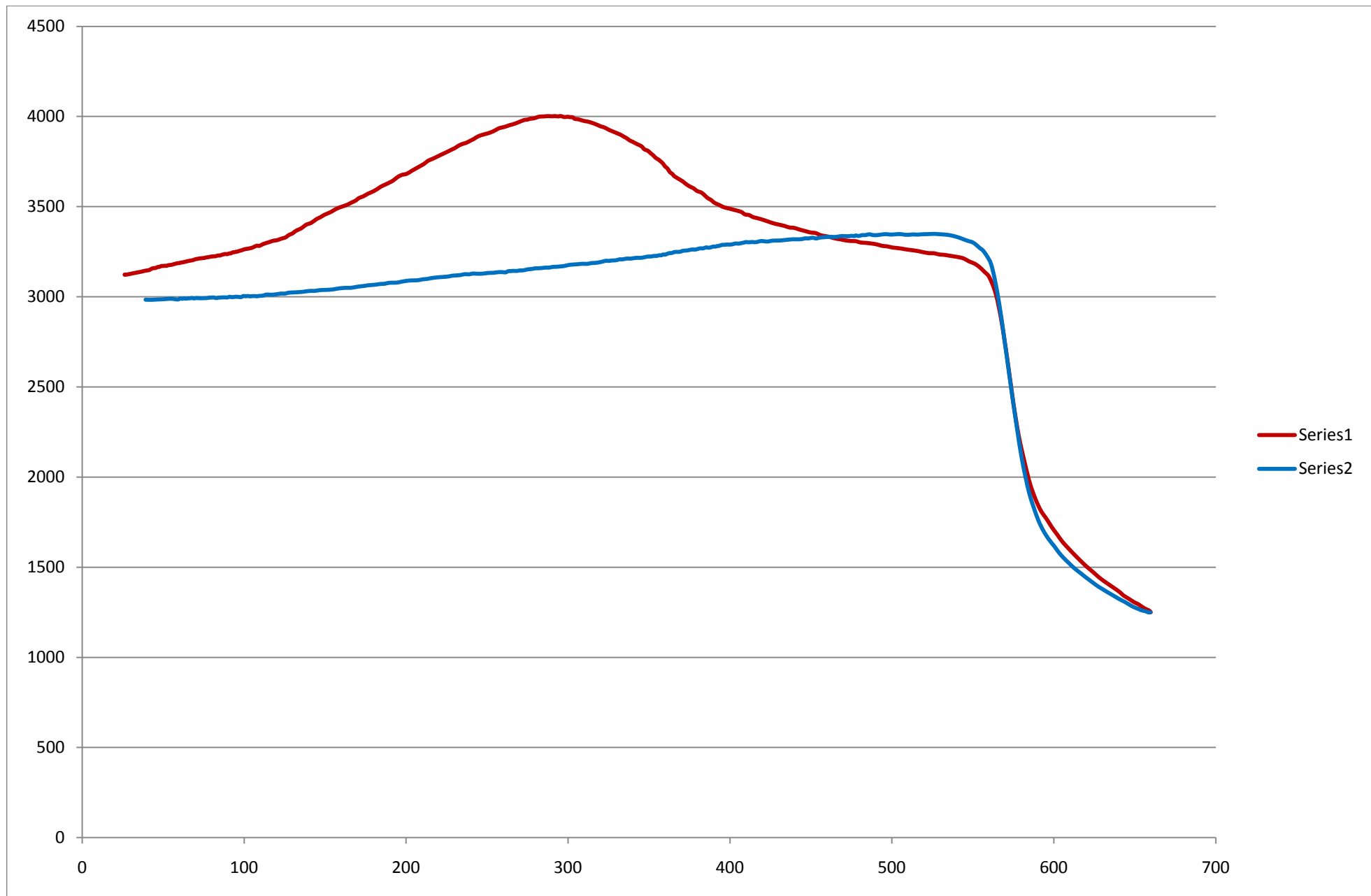












## Appendix D: Collected cone sheet structural measurements

Areas of cone sheet groups (see Fig. 4.1)	Approximate geographical location of cone sheet Areas and sub-groups*	Cone sheet swarm (1 = Centre 1; O2 = Outer Centre 2; I2 = Inner Centre 2; 3 = Centre 3)	Approximate distance to respective centre (km)	Approximate azimuth to respective centre (°)	Locality number	Individual cone sheet division (denoted by a line)	Grid Reference (NM) <sup>†</sup>	Closely associated AMS sample (if applicable)	Cone sheet strike (°)	Cone sheet dip (°)	Cone sheet dip direction	Cone sheet dip azimuth (°)	Cone sheet thickness (m)
Glas Eilean	O2		3.8	315	269	48333	62733	-	016	40	W	286	0.15
						48390	62896	CS 151	178	23	W	268	-
			3.8	315	270	48705	63153	-	039	29	NW	309	-
						48705	63153	-	061	38	NW	331	0.21
			4.3	315	110	49179	62839	-	017	39	W	287	-
			4.3	315	111	49177	62852	-	041	54	W	311	-
						49189	62858	-	001	78	W	271	-
						49164	62847	-	043	43	NNW	313	-
						49164	62847	-	024	47	WNW	294	-
			4.3	315	112	49175	62847	-	176	43	W	266	-
						49189	62858	-	049	64	NW	319	-
						49175	62847	-	071	24	SSE	161	-
						-	-	-	041	12	SE	131	-
			4.3	315	113	49189	62858	-	032	22	SE	122	-
						48971	63000	CO1 and CO2	092 040	19 37	N NW	002 310	- -
						4914	6282	CS 152	012	63	W	282	0.45
						4914	6282	-	033	63	NW	303	0.25
Between Glas Eilean and Mingary Pier	O2					4914	6282	CS 154	018	86	E	108	0.5
						4914	6282	-	168	61	SW	258	0.3
						4914	6282	-	161	72	SW	251	0.3
						4914	6282	CS 155	165	59	SW	255	0.3
						4914	6282	-	006	59	W	276	-
						4914	6282	CS 153	029	59	NW	299	-

4.3	315	334	4914	6282	-	071	60	NW	341	-			
			4914	6282	CS 156	025	62	NW	295	0.4			
			4914	6282	-	072	24	SE	162	-			
			4914	6282	-	066	28	SE	156	0.2			
			4914	6282	CS 157	080	24	SSE	170	0.2			
			4914	6282	-	066	28	SE	156	0.2			
			4914	6282	-	172	83	E	082	0.05			
			4914	6282	-	177	83	E	087	0.05			
			4914	6282	-	025	90		295	-			
			4914	6282	-	172	85	W	262	-			
4.5	315	45			CS163	036	48	W	306	-			
			49220	62696	-	036	40	NW	306	-			
					-	077	12	S	167	-			
			4.5	315	44	49208	62691	CS L1	019	40	W	289	-
			4923	6271	-	016	45	W	286	-			
			4.5	315	19			-	160	52	SW	250	-
			4923	6271	CS 162	123	15	SW	213	0.13-0.84			
			4.5	315	21	49235	62707	-	048	24	SSE	138	0.88
					-	072	16	SSE	162	-			
			4.5	315	22	49254	62722	-	047	34	NNW	317	-
4.5	315	23	49244	62705	-	020	40	W	290	-			
					-	020	49	W	290	-			
4.5	315	24	49237	62696	CS 164	040	48	NW	310	-			
4.5	315	49	49288	62685	-	030	43	NW	300	-			
4.5	315	27			-	114	33	NNE	024	0.25			
			49253	62704	-	001	42	W	271	0.25			
					-	154	08	SSW	244	0.25			
					-	162	53	SW	252	0.25			
					-	185	40	W	275	-			
4.5	315	28	49258	62746	CS 160	196	33	W	286	-			
					-	197	22	W	287	0.88			
4.5	315	25	49240	62694	-	059	42	NNW	329	-			

I

Mingary Pier	O2	4.5	315	25	49245	62690	-	035	02	NW	305	-
		4.5	315	26	49245	62690	CS M1	087	40	N	357	0.43
							-	061	50	NNW	331	-
		4.5	315	34	49270	62702	-	142	17	SW	232	-
							-	039	50	NW	309	-
		4.5	315	35	49276	62703	-	029	39	NW	299	-
		4.5	315	36	42980	62698	CS 158	132	19	SW	222	-
		4.5	315	29	49264	62724	-	128	20	SW	218	-
					49284	62711	-	140	10	SW	230	-
		4.5	315	31	49284	62711	CS N1	127	20	SW	217	-
							-	007	49	W	277	-
		4.5	315	32	49273	62724	-	105	15	SSW	195	0.9
		4.5	315	33	49261	62730	-	002	19	W	272	-
		4.5	315	37	49289	62706	-	012	50	NW	282	0.43
		4.5	315	39	49283	62691	CS 159	038	43	NNW	308	-
		4.5	315	40	49278	62690	-	044	51	NW	314	-
		4.5	315	51	49249	52650	CS 167	056	19	NW	326	-
							-	048	48	NW	318	-
		4.5	315	52	49271	62680	CS 166	154	10	WSW	244	-
							-	048	44	NW	318	-
		4.5	315	58	49278	62664	CS 169	161	18	SW	251	-
					49251	62667	-	131	08	SW	221	-
		4.5	315	62	49251	62667	-	130	07	SW	220	-
					49251	62667	-	116	49	NE	026	-
		4.5	315	59	49283	62666	-	140	13	SW	230	0.33
		4.5	315	47	49229	62690	CS K1	038	45	NNW	308	-
		4.5	315	42	49264	62687	-	048	41	NNW	318	-
					49229	62675	-	123	14	SSW	213	-
					49238	62679	-	139	23	SW	229	-
		4.5	315	50	49229	62671	-	109	15	S	199	-
					49236	62665	-	152	11	SW	242	-
					49244	62661	-	167	10	WSW	257	-
					49242	62666	-	177	08	W	267	-

4.5	315	53	49263	62684	CS 165	129	07	SW	219	0.7
					-	074	50	NNW	344	-
4.5	315	63	49271	62630	CS P1	126	12	SW	216	0.16
4.5	315	65	49286	62639	CS 105	167	05	NE	077	0.16
			49286	62639	CS 106	127	06	SSW	217	0.17
4.5	315	66	49285	62635	-	144	12	SW	234	0.21
			49286	62639	-	142	15	SW	232	1.55
4.5	315	65	49286	62639	-	018	55	W	288	1.28
			49286	62639	-	110	72	N	020	0.58
4.5	315	65	49286	62639	CS 108	086	10	S	176	0.32
4.5	315	66	49285	62635	CS 103	076	58	NW	346	0.85
4.5	315	65	49286	62639	CS 107	160	48	N	070	0.36
4.5	315	66	49285	62635	CS 104	128	23	NE	038	0.5
4.5	315	65	49286	62639	-	080	48	N	350	-
4.5	315	65	49286	62639	-	135	10	WSW	225	-
4.5	315	65	49286	62639	-	121	10	SW	211	0.23
			49368	62607	-	134	11	S	224	-
			49368	62607	-	134	11	S	224	-
			49368	62607	-	084	85	S	174	-
4.5	315	446	49368	62607	-	000	00		090	-
			49368	62607	-	008	12	W	278	-
			49362	62606	-	065	14	Nw	335	-
			49334	62597	-	004	18	W	274	-
4.5	315	447	49362	62606	-	-	-	-	-	-
4.4	308	150	49324	62834	CS 109/110	106	20	S	196	0.36
4.4	308	185			-	000	09	W	270	-
4.8	308	186	50268	63085	-	085	46	S	175	-
4.8	308	187	50244	63210	CS 117-119	040	42	NW	310	1
			4995	6315	-	160	22	W	250	0.35
			4995	6315	-	143	16	W	233	0.98
4.8	308	236			-	036	29	NW	306	-
			4995	6315	-	120	23	SW	210	0.8
4.8	308	237	49948	63126	CS 138	024	29	W	294	-

Mingary Pier to Mingary castle	O2	4.8	308	238	49937	63084	-	034	19	NW	304	-
		4.8	308	239	49933	63119	-	027	18	W	297	1
		4.7	308	240	49831	62999	-	002	71	W	272	2
		4.6	308	241	4983	6299	-	020	60	W	290	-
							-	038	60	W	308	-
							-	012	49	W	282	0.4
		4.5	308	242	49604	62981	-	175	61	W	265	-
		4.5	308	421	49429	62892	-	124	29	SW	214	-
		4.5	308	422	49722	62966	-	164	75	W	254	0.5
		5.4	308	102	50948	63150	-	253	30	SE	163	-
		4.9	308	96	50444	63023	-	167	49	W	257	-
		4.9	308	97	50449	63047	-	020	40	WNW	290	-
		4.9	308	98	50456	63057	-	022	35	WNW	292	-
		4.9	308	190	50628	62953	-	013	70	W	283	0.4
		5.2	308	191	50617	62920	-	057	71	NNW	327	-
		5.2	308	99	50618	62902	CSH1 and H2	001	52	W	271	-
		5.2	308	191	50617	62920	-	060	65	NNW	330	-
		5.3	308	100	50756	63106	CSI1	123	19	SSW	213	2
		5.3	308	101	50863	63128	-	058	43	N	328	-
East of Mingary castle	O2	4.9	308	90,95	50376	63118	CSJ1	024	32	W	294	-
		4.9	308	91	50363	63107	-	035	58	W (rotate	305	-
		4.9	308	92	50359	63106	-	038	07	NW	308	-
		4.9	308	94	50342	63093	-	020	46	W	290	-
		4.9	308	94	50342	63093	-	020	46	W	290	-

3	Sgeir nan Eun to Rubha Ailein	1 or O2?	4.9	308	184	5031	6309	-	030	58	NW	300	-
								-	027	14	NW	297	0.13
						5031	6309	-	003	60	W	273	0.68
						5031	6309	-	025	52	NW	295	0.65
						5031	6309	-	001	48	W	271	0.24
								-	172	02	W	262	0.21
						5031	6309	-	050	50	NW	320	-
						5031	6309	-	010	05	W	280	0.7
		O2	4.9	308	189			-	048	70	NW	318	0.6
						50634	63015	-	114	33	NNE	024	0.25
						51406	61322	CS 136	023	43	NW	293	-
						52234	62816	CS 135	068	45	NW	338	2.5
						52136	62889	-	068	28	NW	338	-
								-	055	28	SE	145	-
						49933	63127	-	008	50	W	278	-
						51466	63721	CS 134	057	37	NW	327	-
			5.6	339	232	51471	63557	-	092	23	N	002	-
						?	?	-	068	30	NW	338	-
4	East flank of Ben Hiant	1	5.2	310	208	54817	64073	-	060	52	NW	330	-
								-	104	34	N	014	-
						55173	64249	-	135	10	SW	225	-
								-	022	42	W	292	-
						551	642	-	012	58	W	282	-
						551	642	-	172	40	W	262	-
						551	642	CS 127	062	39	NW	332	-
						551	642	-	066	28	NW	336	-
						551	642	-	041	48	NW	311	-
								-	092	70	N	002	0.1
						49623	64124	-	092	70	N	002	0.1
						49635	64216	-	005	55	W	275	-
						49645	64196	-	114	78	NE	024	-
						49664	64392	-	030	37	NW	300	1
						49656	64396	-	008	36	W	278	-
						49687	64442	-	085	54	N	355	-

5	Glas Bheinn	O2	3.9	290	290	49705	64518	-	048	57	NW	318	-
			3.6	290	291	49561	64445	-	001	35	W	271	-
			3.7	290	293	49600	64154	-	072	52	NW	342	-
			3.8	290	294	49636	64548	-	025	41	W	295	-
			3.3	290	301	48751	64717	-	041	58	NW	311	-
			3.3	290	302	48731	64711	-	038	73	NW	308	2
						48731	64711	-	016	47	W	286	-
			3.2	290	303	48693	64708	-	011	50	W	281	-
						48646	64683	-	160	61	SW	250	-
			3.2	290	304	48646	64683	-	018	52	W	288	-
						48660	64689	-	043	43	NW	313	-
			3.2	290	306	?	?	-	120	57	NE	030	-
						?	?	-	077	76	NW	347	-
			3.3	290	308	48747	64727	-	078	49	N	348	2.5
						48747	64727	-	030	62	NW	300	1
			3.4	290	331	4912	6473	CS 185	026	46	NW	296	-
								CS 187	028	72	NW	298	-
						4912	6473	CS 186	009	58	W	279	-
								CS 188	014	37	W	284	-
			3.5	290	333	49391	64543	-	009	27	W	279	-
			4.4	290	311	50560	64612	-	178	33	W	268	-
			4.4	290	328	50222	64652	-	005	33	W	275	-
						50523	64637	-	072	22	NNW	342	-
			4.4	290	314	50522	64639	-	059	29	NW	329	-
	East of Allt Choire Mhuilinn	O2	5.7	290	250	52092	65330	CS 140	110	30	SW	200	-
			5.7	290	251	52047	65585	-	124	50	SW	214	-
			5.7	290	254	52261	65007	-	162	32	SW	252	-
			5.7	290	255	52177	65164	-	184	16	W	274	-
			5.7	290	256	52184	65168	-	156	32	SW	246	-
6	B8007 road junction with the northwards road to Achateny	O2	7.8	272	256a	52933	66659	-	071	32	S	161	-
			7.8	272	256b			CS 141	008	18	W	278	-
			7.8	272	257	52971	66545	CS 142	008	42	W	278	-
			7.8	272	258	52926	66668	CS 143	008	33	W	278	-

7	Garbh Rubha	1	3.7	234	260	53507	70513	CS 144-145	000	33	W	270	-
						53507	70513	-	005	22	W	275	-
			3.7	234	108/261	53796	70884	CS 149	157	28	W	247	-
								CS 146-148	166	12	W	256	0.7
			3.7	234	262	53741	71008	-	120	80	SW	210	0.7
								-	172	10	W	262	0.7
								-	113	50	SW	203	0.7
			3.7	234	263	53783	71058	-	036	17	NW	306	-
						53783	71058	-	002	25	W	272	0.1
						53783	71058	-	170	29	W	260	-
								-	000	17	W	270	-
						53763	71025	-	012	12	W	282	-
			2.7	234	265	53501	70778	-	045	23	SE	135	-
								-	024	03	NW	294	-
			2.7	234	266	53544	70783	-	120	11	SW	210	0.24
								-	160	12	W	250	-
								-	138	28	SW	228	-
			2.7	234	267	53612	70772	-	009	11	W	279	-
8	Kilmory coast	1	2.9	222	299a	52433	70950	-	115	43	NE	025	-
						52433	70950	-	113	32	NE	023	-
								-	122	30	NE	032	-
								-	137	40	NE	047	-
						52433	70950	-	120	39	NE	030	0.3
			2.9	222	299b	52433	70950	-	101	25	N	011	-
						52512	70816	CS 176	140	12	SW	230	-
			2.9	222	299c	52553	70616	CS 177	179	47	E	089	0.5
								-	165	47	E	075	-
			2.9	222	426b	52199	70685	-	162	20	W	252	-
			2.9	222	427a	52165	70710	-	102	72	S	192	-
						52165	70710	-	058	83	SE	148	-
			2.9	222	427b	52201	70747	-	146	55	S	236	-
			2.9	222	428a	52260	70727	-	142	27	S	232	-
			2.9	222	428b	52227	70732	-	051	23	NW	321	-

9	Fascadaile	O2	5	228	300a	49706	70709	-	001	63	W	271	-
			5.4	228	300b	50058	70889	CS 179	134	40	SW	224	-
			5.4	228	300c	50221	70872	CS 180	133	28	SW	223	0.8
			5.4	228				-	140	43	SW	230	-
10	Rubha Carrach	O2	3.7	199	404	46073	70792	-	084	56	S	174	-
						46073	70792	-	080	50	S	170	-
						46073	70792	-	106	64	S	196	-
						46061	70785	-	101	52	S	191	-
						46061	70785	-	142	58	SW	232	-
			3.7	199	405	46061	70785	-	112	70	S	202	-
						46061	70785	-	131	64	S	221	-
						46061	70785	-	105	44	S	195	-
						46061	70785	-	115	78	S	205	-
			3.7	199	406	46051	70742	-	109	71	S	199	-
						4605	7071	-	008	20	W	278	-
			3.7	199	407a	4605	7071	-	080	50	S	170	-
						4605	7071	-	094	42	S	184	-
			3.7	199	407b	46100	70500	CS 208	109	67	S	199	-
						46100	70500	-	120	63	S	210	-
								-	122	78	S	212	-
			3.7	199	408a	46341	70543	-	160	31	W	250	-
			3.7	199	408b	46053	70298	-	088	64	N	358	-
						46053	70298	-	094	68	N	004	-
	Port Eigin-aig	O2	5	207	419a	47082	70958	CS 223	098	40	S	188	-
						47082	70958	-	142	30	S	232	-
								-	130	40	S	220	-
						47082	70958	-	152	27	S	242	-
			5	207	419b	47113	70938	-	090	50	S	180	-
			5	207	420a	47111	70926	CS 226	092	48	S	182	-
			5	207	420b	47175	70883	CS 227	150	15	W	240	-
			3.6	99	423	41582	67363	-	176	02	W	266	0.3
								-	152	18	E	062	0.3
						41582	67363	-	179	78	E	089	-

11	Point of Ardnamurchan	O2	3.6	99	424a			-	027	81	E	117	-
						41579	67370	-	012	55	E	102	-
								-	008	49	E	098	-
								-	039	47	SE	129	-
			3.6	99	424b	?	?	-	030	90		120	-
								-	010	74	E	100	-
3.6	99	424c	41568	67367	-	029	61	E	119	-			
			41568	67367	-	025	60	E	115	0.05			
3.6	99	425	41587	67236	-	055	30	E	145	0.3			
12	Between Beinn nan Ord and Allt Garbh- dhalach	I2	1.2	50	273	4363	6608	-	174	81	W	264	-
						4363	6608	-	001	73	W	271	0.3
						4363	6608	CS 170	173	78	E	083	-
			1	50	434	44346	65605	-	172	90		262	-
						44346	65605	CS 261	162	90		252	-
			1	50	435	44342	65602	-	038	87	SE	128	-
			1	50	436	44346	65556	-	155	87	E	065	-
			1	50	437a	44405	65280	CS 265	162	70	W	252	-
			1	50	437b	44445	65251	-	154	85	E	064	-
			1	50	439	44495	65258	-	113	72	E	023	0.05
			1	50	440	44501	65259	-	132	62	W	222	-
								-	063	72	S	153	-
			1	50	441	44505	65329	CS 268	123	70	E	033	-
			1	50	442a	44508	65245	-	174	90		264	-
1	50	442b	4449	6525	-	140	78	E	050	-			
13	Port Choinnich	O2	3.3	37	409	42753	64032	-	178	33	W	268	-
			3.3	37	410a	42754	64020	-	160	71	E	070	-
			3.3	37	410b	4275	6402	-	159	62	E	069	-
			3.3	37	411	42737	64029	-	004	70	E	094	-
			3.3	37	412	42746	64014	-	173	81	E	083	-
			3.3	37	413	42732	64015	-	133	10	W	223	-
			3.3	37	414	42744	63999	-	150	62	E	060	-
			3.3	37	415	42778	63978	-	152	70	E	062	-
			3.3	37	416a	42636	64161	-	159	40	W	249	0.7

		3.3	37	416b	42636	64161	-	166	75	E	076	-
		3.3	37	417a	4239	6446	-	130	63	W	220	-
					4239	6446	-	145	79	W	235	-
		3.3	37	417b	42704	64090	-	140	50	E	050	-
		3.3	37	417c	42420	64141	-	150	72	W	240	-
Sron Bheag	O2	3.4	333	89	46007	62320	CS E1, E3, 172-174	062 048	18 20	NW NW	332 318	2 -
					46007	62320	-	100	61	N	010	-
		3.4	333	114	45994	62330	-	060	40	NW	330	-
		3.4	333	124	46005	62349	-	084 129	37 58	N NE	354 039	- -
		3.4	333	125	45893	62353	-	100	33	NNE	010	-
		3.4	333	126	45967	62378	-	089	40	N	359	0.4
		3.4	333	128a	45938	62397	-	088	63	N	358	-
		3.6	333	128b	46860	62513	CSF1	062	22	SE	332	-
		3.4	333	195	45445	63108	-	080	58	N	350	-
		3.4	333	279	45752	62524	-	074	43	NW	344	-
		3.4	333	202	45180	64109	-	089	58	N	359	-
		3.4	333	400	4605	6244	-	087	65	N	357	-
					4605	6244	-	075	44	N	345	-
		3.4	333	401	45772	62937	-	091	57	N	361	-
		3.4	333	402	46169	62891	-	072	45	N	342	-
		3.4	333	403	46175	62885	-	087	68	N	357	0.5
		3.4	333	203	46161	63680	-	-	-	-	-	-
		3.5	333	3	47109	62821	-	076	25	N	346	-
		3.5	333	5			-	016	42	W	286	-
		3.5	333	6	47121	62829	-	142	22	NE	052	-
		3.5	333	8	47132	62854	-	062	23	SSE	152	-
		3.5	333	4	47098	62819	-	055	24	NW	325	-
		3.5	333	10	47136	62855	-	042	38	WNW	312	-
		3.5	333	11	47140	62858	-	058	43	NW	328	-
		3.5	333	12	47149	62860	-	-	-	-	-	-
		3.5	333	13	47163	62878	CSC1	063	60	NNW	333	-

14	Ormsaigbeg	O2	3.5	333	17	47014	62718	-	039	30	NW	309	-
			3.5	333	54	47015	62643	CSG1B	163	41	E	073	-
						47015	62643	-	054	34	NW	324	-
								-	009	17	WNW	279	-
								-	110	15	N	020	-
						4701	6261	-	151	21	NE	061	-
			3.5	333	55			-	079	23	NNW	349	-
								-	020	22	WNW	290	-
						4701	6261	-	076	08	NW	346	-
								-	185	17	E	095	-
			3.5	333	56	46966	62580	-	063	35	NW	333	-
								-	-	-	-	-	-
			3.5	333	192	46527	62463	-	056	40	NW	326	1.4
			3.5	333	193	46444	62537		030	28	NW	300	-
								-	078	47	N	348	-
			3.5	333	309	46848	62467	-	027	68	NW	297	-
								-	102	40	N	012	-
			3.5	333	310	46838	62468	-	107	39	N	017	-
	Ormsaigmore coast	O2	3.2	333	220	47208	62997	-	036	13	SE	126	2
								CS 130	035	18	NW	305	-
						47229	62988	-	079	70	N	349	0.5
								-	068	57	NNW	338	-
			3.2	333	221	47229	62988	-	002	27	E	092	-
						47229	62988	-	146	41	NE	056	-
						47229	62988	-	064	25	SE	154	-
			3.2	333	222	47682	63378	-	047	28	NW	317	-
			3.2	333	223			-	054	45	NW	324	0.62
						4768	6335	-	046	40	NW	316	0.68
			3.2	333	224			-	080	62	N	350	0.49
						4772	6340	-	053	47	NW	323	0.86
			3.2	333	225			-	039	31	NW	309	0.39
						47285	63053	-	170	32	E	080	0.3
			3.2	333	226			-	084	47	N	354	-

‡ Host rock lithology codes: N = Neoproterozoic Moine metasedimentary rocks; M = Mesozoic metasedimentary rocks; M l = Mesozoic limestone where definable; M s = Mesozoic limestone where not definable; EP v = Early Palaeogene volcanoclastics; EP b = Early Palaeogene olivine basalt lava; Int. = Palaeogene Igneous intrusions of variable lithology (e.g. dolerite dykes).

[illegible]

[illegible]

[illegible]

Y	115-395	M I
Y	-	M I
Y	-	M I
Y	-	M I
Y	-	M I
Y	-	M I
N	-	M I
N	-	M I
N	-	M I
N	-	M I
N	-	M I
N	-	M I
N	126-306	M I
N	-	M I
N	-	M I
N	-	M I
N	-	M I
N	-	M I
N	-	M I
N	-	M I
N	-	M I
N	-	M I
N	-	M I
Y	-	M I
Y	057-237	M I
Y	-	M I
N	-	M I
N	-	M I
Y	-	M I
Y	-	M I
Y	-	M I
Y	-	M I
Y	-	M I

Y	043-223	M I
Y	-	Int.
N	-	M I
N	-	M I
N	-	M I
N	-	M I
N	-	M I
N	-	M I
N	-	M I
N	-	M I
N	-	M I
N	220/32	M I
N	-	M I
N	-	M I
Y	-	M I
Y	-	M I
Y	-	M I
Y	-	M I
N	-	M I
Y	-	M I
Y	-	M I
Y	-	M I
Y	095-275	M I
Y	-	M I
Y	-	M I
Y	-	M I
N	-	M I
Y	-	M I
Y	-	M I
Y	034-214	M I
Y	-	M I
Y	163-343	M I
Y	-	M I

N	-	M I
N	-	Int.
N	-	M I
N	-	M I
N	-	M I
N	-	M I
N	-	M I
N	-	M I
N	-	M I
N	-	M I
Y	-	M I
N	091-271	M I/N
N	021-201	N
N	-	N
N	-	N
N	-	N
N	-	N
N	035-215	N/int.
N	-	int.
N	-	EP v
N	-	EP v
N	-	EP v
N	094-274	EP v
N	-	EP v
N	-	EP v
N	-	EP b
N	-	EP b
N	149-329	EP b
N	-	Int.
N	-	N
N	-	N
N	-	N
N	-	N
N	-	Int.

N	133-313	N
Y	-	N
N	-	N
N	-	N
N	-	Int.
N	-	Int.
N	-	Int.
N	-	Int.
N	-	N
N	-	N
N	-	N
N	-	Int.
N	-	Int.
N	-	Int.
N	-	Int.
N	-	N
N	-	N
N	-	N
N	-	N
N	-	N
N	-	Int.
N	-	Int.
Y	-	N
Y	-	N
Y	-	Int.
N	-	Int.
N	170-250	Int.
N	-	Int.
N	-	Int.
N	-	Int.
N	-	N
Y	-	EP v
Y	-	N

N	-	M I
N	-	M I
Y	079-259	M I
N	-	M I
N	-	M I
N	-	M I
N	-	M I
Y	-	M I
N	-	M I
N	052-232	M I
N	112-292	M I
N	090-270	M I
N	-	M I
N	-	M I
N	092-272	M I
N	-	M I
N	058-238	M I
N	-	M I
Y	-	EP v
N	-	EP v
N	-	EP v
N	-	EP v
N	-	EP v
N	-	EP v
N	-	EP v
N	094-274	EP v
N	-	EP v
N	-	EP v
N	-	EP v
N	-	EP v
N	020-200	EP v
N	-	EP v
N	-	EP v

N	-	Int.
N	-	Int.
N	-	Int.
N	-	Int.
N	-	EP v
N	-	EP v
N	-	EP v
N	-	EP v
N	-	EP v
N	-	EP v
N	-	EP v
N	-	EP v
N	-	EP v
N	-	EP v
N	-	EP v
N	-	EP v
N	020/80	M s
N	146-326	M s
N		M s
N	-	EP v
N	-	M I
N	147-327	M I
N	-	M
N	-	M
N	-	M
N	-	M
N	-	M
N	-	M
N	-	M
N	-	Int.
N	-	Int.
N	-	Int.

[illegible]

N	-	M
N	-	M
N	-	M
N	-	M
N	-	M
Y	013-193	M s
Y	-	M s
N	-	M s
Y	-	M s
Y	-	M I
Y	-	M I
Y	061-241	M I
Y	030-210	M I
Y	-	M I
Y	-	M s
N	-	M I
N	-	M s
N	-	Int.
Y	-	M
Y	-	M
N	-	Int.
N	172-352	M
N	-	M
N	-	Int.
N	004-184	M s
N	-	M s
N	012-192	M s
N	-	M s
Y	141-321	M s
Y	-	M s
Y	155-335	M s
Y	150-330	M s
Y	-	M s

Y	155-335	M s
Y	152-332	M s
Y	-	M s
Y	-	M s
Y	-	M s
Y	-	M s
Y	-	M s
Y	-	M s
Y	-	M s
Y	-	M s
N	125-305	M s
N	131-311	M s
Y	131-311	M s
N	-	M s
N	-	M I
N	019-199	M I
N	-	M I
N	009-189	M I
Y	-	M I
N	152-332	M I
N	-	Int.
N	-	Int.
N	-	M I
N	-	M I/Int.
N	-	M I
Y	-	M I
Y	-	M I
Y	159-339	M I
Y	-	M I
N	-	M I
N	-	M I
N	-	M I
Y	-	M I

Y	-	M I
Y	010-190	M I
Y	-	M I
N	-	M I
N	-	Int.
N	-	Int.
N	-	Int.
N	-	Int.
N	-	Int.
N	000/23	Int.
N	-	Int.
N	-	Int.
N	-	N
N	-	N
N	-	Int.
N	-	Int.
N	-	Int.
N	-	Int.
N	-	Int.
N	-	N
N	-	N
N	-	Int.
N	-	Int.
N	-	Int.
N	-	Int.

= Mesozoic sandstone where  
 (gne sheets, gabbro)

## Appendix E: AMS results

Sample	Sheet ID	Grid reference	K <sub>1</sub>		K <sub>2</sub>		K <sub>3</sub>		K <sub>mean</sub> (10 <sup>-2</sup> )*	H	L <sup>†</sup>	F <sup>§</sup>
			Declination	Plunge	Declination	Plunge	Declination	Plunge				
		(NM)**	(°)	(°)	(°)	(°)	(°)	(°)	(SI units)	(%)	(%)	(%)
CSA2	1	50922 63157	198.40	32.80	018.30	57.20	108.40	00.00	05.29	02.90	2.25	0.66
CSA4	1	50915 63148	248.50	08.80	342.60	24.90	140.50	63.40	05.48	01.61	0.60	1.01
CSC1	2	47162 62878	302.60	40.00	041.90	11.00	144.30	47.90	05.63	03.16	1.30	1.86
CSD1	3	54821 64018	273.00	32.90	038.70	42.00	160.70	30.50	04.39	01.70	1.38	0.55
CSD2	3	54832 63993	000.80	06.20	099.10	53.10	266.20	36.20	04.30	01.93	1.17	0.54
CSD3	3	54826 63989	356.10	30.40	104.80	28.60	229.00	45.80	04.14	02.22	1.92	0.30
CSE1	4	46007 62320	157.10	03.90	265.20	77.60	066.30	11.70	04.38	02.01	1.52	0.49
CSE3	4	46009 62320	182.80	08.20	088.60	26.80	288.40	61.80	04.95	01.66	0.99	0.67
CSF1	5	46860 62513	116.50	47.20	215.90	08.60	313.60	41.50	00.19	02.52	1.60	0.92
CSG1B	6	47020 62641	057.00	27.60	316.40	19.40	196.00	55.20	00.18	03.22	1.21	2.00
CSH1	7	50618 62902	243.10	48.30	343.40	09.00	081.20	40.30	05.74	04.89	3.21	1.68
CSH2	7	50619 62902	227.50	46.80	327.60	09.40	066.10	41.70	06.41	06.52	3.85	2.67
CSI1	8	50749 63105	165.20	09.30	256.80	09.10	030.20	76.90	03.61	03.51	1.63	1.88
CSJ1	9	50379 63123	323.80	37.50	176.90	47.50	067.40	17.00	05.50	02.22	1.64	0.57
CO1	10	48981 62999	140.10	64.60	313.40	25.20	044.70	02.60	01.46	03.66	2.74	0.92
CO2	10	48968 63009	143.20	53.00	331.70	36.80	238.60	04.00	01.41	02.52	1.89	0.63
CSK 1	11	49228 62690	348.30	60.40	160.00	29.40	252.00	03.60	01.22	01.86	0.74	1.13
CSL 1	12	49213 62690	129.20	25.80	220.80	03.40	317.70	64.00	03.64	01.20	0.25	0.96
CSM 1	13	49246 62695	331.00	43.10	218.80	22.00	109.80	38.90	01.05	02.55	1.42	1.13
CSN 1	14	49283 62718	318.30	08.90	051.60	20.50	206.10	67.50	02.87	01.85	1.43	0.42
CSP 1	15	49272 62630	142.00	06.80	021.20	76.80	233.40	11.20	00.38	00.85	0.50	0.36
CS100	16	49347 62640	004.40	37.40	129.20	36.70	246.40	31.50	05.68	03.54	1.33	2.21
CS103	17	49338 62636	349.30	02.40	081.40	41.60	256.50	48.30	05.37	02.09	2.00	0.09

CS104	18	49295 62635	331.30	09.50	241.00	01.40	142.80	80.40	05.89	02.26	0.91	1.35
CS105	15	49287 62632	166.20	22.10	068.20	18.90	301.40	60.20	00.16	01.16	0.56	0.60
CS106	15	49289 62636	335.00	77.40	103.40	07.90	194.80	09.70	00.09	00.20	0.06	0.14
CS107	18	49281 62632	180.60	24.60	040.20	59.30	278.70	17.20	06.94	04.17	3.01	1.16
CS108	17	49287 62636	334.20	49.70	152.00	40.20	242.90	01.10	04.72	02.73	2.20	0.53
CS109	19	49324 62834	146.50	18.00	256.80	46.90	042.00	37.50	05.83	05.00	3.36	1.64
CS110	19	49324 62834	152.10	38.40	018.50	41.00	264.10	25.30	05.47	05.53	4.66	0.87
CS111	20	55427 64306	129.70	40.00	282.20	46.60	027.60	14.10	05.22	03.56	0.87	2.70
CS113	20	55364 64256	061.20	60.00	228.60	29.40	321.70	05.50	05.74	05.06	3.33	1.73
CS114	20	55300 64209	014.60	08.90	158.50	79.00	283.60	06.40	04.40	02.21	0.25	1.96
CS115	20	55300 64214	148.50	65.90	241.00	01.10	331.60	24.10	03.66	10.80	8.81	1.99
CS117	21	50294 63091	257.50	11.20	163.60	18.90	016.70	67.80	03.05	03.05	0.75	2.30
CS118	22	50306 63099	102.30	79.80	286.40	10.10	196.30	00.70	03.33	04.48	0.79	3.68
CS119	22	50300 63102	101.60	39.20	215.40	26.30	329.40	39.50	03.01	03.02	0.80	2.22
CS124	23	46134 63672	054.50	70.50	256.50	18.20	164.20	06.80	09.98	02.51	0.35	2.16
CS125	3	54651 63685	023.00	32.10	110.00	04.80	192.50	57.50	03.72	02.12	0.28	1.84
CS126	24	54732 63885	136.40	42.50	023.80	22.80	274.00	38.80	03.84	01.49	0.96	0.53
CS127	3	54737 63966	119.60	37.90	027.20	03.10	293.30	52.00	02.25	00.77	0.06	0.71
CS128	3	55840 64096	180.10	05.20	087.20	29.00	279.40	60.50	06.34	02.02	1.16	0.86
CS130	25	47215 62955	191.40	58.10	027.20	30.90	293.00	07.10	00.15	00.56	0.38	0.18
CS131	26	47698 63370	335.20	35.50	230.30	19.80	117.00	47.70	01.20	02.68	1.76	0.91
CS132	27	47259 63042	162.00	60.70	064.00	04.50	331.50	28.90	00.34	04.38	1.22	3.16
CS133	27	47265 63049	029.60	63.50	278.50	10.20	183.80	24.20	00.62	01.13	0.47	0.66
CS134	28	51431 63673	007.50	50.20	101.50	03.30	194.20	39.60	06.52	03.74	1.65	2.09
CS135	29	52235 62818	333.00	48.30	215.30	22.40	109.80	33.00	07.33	07.74	2.95	4.78
CS136	30	51400 63135	354.90	09.60	260.50	24.40	104.90	63.60	05.06	05.56	4.21	1.34
CS137	31	49959 63151	127.20	02.70	219.30	37.40	033.80	52.50	04.53	05.53	5.16	0.36
CS138	31	49953 63127	326.70	45.60	074.00	16.20	178.10	39.90	05.87	03.31	1.51	1.80
CS139	32	49568 62977	150.30	11.80	259.90	58.30	053.70	29.00	05.86	01.84	1.42	0.43

CS140	33	52092 65330	295.10	63.70	103.90	25.90	196.10	04.50	03.85	02.37	1.43	0.95
CS141	34	52839 66584	294.90	29.50	025.80	01.60	118.60	60.50	03.17	01.05	0.41	0.64
CS142	35	52933 66659	356.60	15.30	174.60	74.70	266.50	00.50	01.71	02.65	1.65	1.01
CS143	35	52926 66668	129.50	24.40	348.90	59.60	227.50	17.00	06.57	01.68	1.13	0.55
CS144	36	52505 70510	338.90	08.10	103.60	76.00	247.20	11.40	01.28	02.45	2.35	0.10
CS145	36	53540 70436	138.50	16.70	232.20	12.40	357.10	69.00	01.34	02.26	1.83	0.43
CS146	37	53738 71013	344.90	04.10	082.50	61.50	252.70	28.20	00.96	03.92	2.78	1.13
CS147	37	53738 71013	172.70	33.90	269.40	09.80	013.30	54.30	01.71	03.94	1.77	2.17
CS148	37	53738 71013	179.10	25.50	063.30	42.40	290.10	36.90	01.71	02.71	2.29	0.42
CS149	38	53797 70881	172.80	03.40	073.00	70.70	264.00	19.00	05.43	02.24	1.38	0.87
CS150	39	53604 70771	161.20	01.40	251.30	04.50	054.20	85.30	05.51	02.77	2.64	0.13
CS151	40	48390 62896	069.30	05.10	335.90	34.10	166.70	55.40	01.92	01.49	0.26	1.23
CS152	41	49146 62826	137.00	73.50	325.10	16.40	234.50	02.20	07.27	01.19	0.42	0.77
CS153	42	49148 62829	110.00	02.00	012.30	75.80	200.50	14.10	04.44	01.95	0.67	1.28
CS154	41	49151 62831	120.60	25.10	222.60	23.80	350.20	54.10	06.90	02.45	1.90	0.54
CS155	41	49152 62833	147.40	28.10	241.50	07.60	345.30	60.70	06.60	01.48	0.78	0.70
CS156	42	49152 62833	282.60	71.90	141.40	14.30	048.60	10.90	05.46	03.03	1.33	1.70
CS157	43	49150 62839	287.60	31.40	020.40	04.40	117.50	58.20	02.89	02.54	0.76	1.78
CS158	13	49282 62701	138.20	40.90	274.90	40.00	026.20	23.40	06.16	01.84	1.76	0.08
CS159	44	49298 62705	344.80	56.00	153.30	33.50	246.90	05.30	04.11	03.79	2.70	1.09
CS160	45	49257 62712	145.30	02.10	235.60	09.10	042.50	80.60	03.55	03.80	2.52	1.28
CS162	46	49234 62711	288.60	25.20	197.70	01.80	103.80	64.70	02.91	01.65	0.61	1.04
CS163	12	49227 62700	341.70	07.20	094.80	72.20	249.60	16.20	01.15	02.10	0.69	1.41
CS164	47	49235 62700	090.30	33.20	233.30	50.70	347.60	18.60	04.44	05.82	4.85	0.97
CS165	48	49263 62683	304.70	12.30	211.60	13.70	075.10	71.40	00.86	01.56	0.77	0.78
CS166	44	49267 62676	106.90	05.70	198.20	12.70	353.10	76.00	05.13	01.82	0.94	0.88
CS167	44	49250 62647	142.30	13.90	234.80	10.10	359.70	72.70	05.05	01.00	0.73	0.27
CS168	49	49267 62647	203.90	46.70	003.10	41.40	102.50	10.50	03.59	01.27	0.19	1.08
CS169	44	49278 62665	191.30	02.50	100.40	20.30	288.10	69.60	02.55	02.17	1.83	0.34

CS170	50	43649 66097	016.00	62.40	143.70	17.70	240.50	20.40	11.05	03.58	0.31	3.28
CS171	51	44492 65652	216.70	17.60	032.30	72.40	126.30	01.30	08.32	03.57	0.38	3.19
CS172a	4	45998 62322	359.30	06.00	263.80	42.40	095.70	47.00	03.88	01.82	1.28	0.55
CS172b	4	45998 62322	314.20	05.70	044.50	03.10	162.60	83.50	03.16	03.82	1.51	2.3
CS172c	4	45998 62322	332.10	21.20	158.30	68.70	062.90	02.10	04.79	01.77	1.58	0.19
CS172d	4	45998 62322	336.30	09.10	237.20	44.50	075.20	44.00	03.73	01.48	0.76	0.71
CS173	4	46005 62333	158.00	10.10	061.60	32.20	263.20	55.90	03.63	01.71	1.08	0.63
CS174a	4	45991 62321	317.10	35.50	221.10	08.40	119.70	53.20	03.09	02.62	0.55	2.07
CS174b	4	45991 62321	335.00	24.50	069.90	10.60	181.40	63.00	02.09	02.82	0.64	2.18
CS174c	4	45991 62321	122.00	01.40	213.90	54.70	031.00	35.20	01.26	00.83	0.45	0.38
CS175	52	52433 70933	333.10	18.90	234.20	24.10	097.20	58.50	03.31	02.55	2.01	0.54
CS176	53	52512 70816	334.00	00.20	067.20	87.00	244.00	03.00	04.56	02.74	2.16	0.58
CS177	54	52553 70616	248.00	53.10	006.70	19.90	108.60	29.70	09.64	00.96	0.37	0.60
CS178	55	49704 70698	121.30	39.50	346.40	40.60	233.40	24.60	08.97	04.63	2.89	1.73
CS179	56	50058 70889	330.50	10.80	227.30	50.20	069.00	37.70	09.89	00.98	0.14	0.84
CS180	57	50221 70872	359.90	30.70	231.00	46.60	107.80	27.40	08.75	02.34	1.90	1.16
CS182	58	52274 66643	297.80	05.70	101.30	84.00	207.60	01.70	00.85	00.88	0.33	0.54
CS183	58	52287 66690	307.90	16.00	080.40	67.00	213.20	16.10	01.30	01.79	0.70	1.09
CS184	58	52310 66953	293.50	03.20	202.30	20.20	032.00	69.50	01.16	03.01	2.12	0.89
CS185	59	49119 64733	124.80	47.60	252.70	29.30	252.70	29.30	05.40	01.91	1.54	0.36
CS186	60	49119 64733	121.30	50.50	243.20	23.50	347.50	29.60	05.96	01.16	1.07	0.09
CS187	59	49128 64737	078.40	55.20	213.40	26.20	314.40	21.20	05.16	01.96	1.41	0.54
CS188	60	49128 64737	024.30	78.70	156.50	07.60	247.60	08.30	06.59	02.02	1.12	0.90
CS208	61	46100 70500	297.80	47.60	158.70	34.70	053.00	21.30	08.94	02.07	0.95	1.12
CS223	62	47082 70958	001.20	31.90	076.20	22.50	137.50	49.20	05.45	01.96	0.99	0.97
CS226	63	47100 70877	187.60	24.90	305.70	45.40	079.30	34.20	06.19	02.40	1.00	1.40
CS227	64	47175 70883	281.70	04.90	185.80	50.30	015.80	39.30	04.14	02.17	1.04	1.13
CS255	65	48644 66029	130.60	03.80	039.00	22.80	229.50	66.90	12.67	00.89	0.35	0.54
CS257	66	48682 65459	011.30	53.80	192.50	36.20	102.10	00.60	09.31	01.08	0.74	0.33

CS261	67	44367 65577	119.90	83.50	016.70	01.50	286.60	06.30	13.20	03.96	0.06	3.90
CS265	68	44405 65280	189.00	77.60	048.60	09.60	317.20	07.80	17.62	02.47	1.00	1.46
CS268	69	44508 65239	157.90	82.20	256.40	01.20	346.60	07.70	23.49	02.02	0.66	1.36
RD1	70	46073 70792	013.10	41.50	178.90	47.60	276.80	07.10	05.41	00.99	0.74	0.26
RD2	71	47155 62907	093.80	77.00	327.60	07.70	236.20	10.30	03.54	03.66	1.70	1.96
RD4	72	50339 63103	289.60	10.40	195.70	20.20	045.20	67.10	00.05	01.15	0.25	0.90
RD5	73	50393 63085	126.60	42.50	005.00	29.80	253.10	33.00	04.36	04.21	1.49	2.71
RD6	74	47112 70877	016.80	55.20	247.60	23.70	146.30	23.90	03.57	00.85	0.41	0.44
RD8	75	52260 70727	294.00	47.60	030.30	05.70	125.40	41.80	09.01	02.64	1.69	0.96
RD9b	76	47734 67396	159.30	27.70	295.40	53.90	057.50	21.20	03.54	05.54	3.48	2.06
RD14	77	46894 62518	353.00	31.10	125.50	48.30	246.80	24.80	06.56	04.52	1.80	2.71

\*  $K_{\text{mean}} = (K_1 + K_2 + K_3) / 3$

†  $L = (K_1 - K_2) / K_{\text{mean}}$

§  $F = (K_2 - K_3) / K_{\text{mean}}$

# N.D. = not determined (no contact visible).

\*\* UK National Grid co-ordinates

Magnetic lineations not interpretable

Magnetic foliation not interpretable

$\mu$	Pj	T	Magnetic foliation	Magnetic foliation	Cone sheet		Field flow
			Strike	Dip	Dip azimuth	Dip value	Trend
			(°)	(°)	(°)	(°)	(°)
73.70	1.031	-0.54	018.40	90.00	138	22	N.D. <sup>#</sup>
30.80	1.016	0.26	050.50	26.60	138	22	N.D. <sup>#</sup>
35.00	1.032	0.18	054.30	42.10	333	14	105-330
65.40	1.020	-0.43	070.70	59.50	N.D. <sup>#</sup>	N.D. <sup>#</sup>	090-270
68.10	1.018	-0.37	176.20	53.80	N.D. <sup>#</sup>	N.D. <sup>#</sup>	N.D. <sup>#</sup>
81.10	1.024	-0.73	139.00	44.20	N.D. <sup>#</sup>	N.D. <sup>#</sup>	N.D. <sup>#</sup>
72.30	1.021	-0.51	156.30	78.30	328	30	N.D. <sup>#</sup>
56.20	1.017	-0.19	018.40	28.20	321	20	N.D. <sup>#</sup>
60.00	1.028	-0.33	043.60	48.50	152	22	N.D. <sup>#</sup>
31.20	1.034	0.29	106.00	34.80	068	32	N.D. <sup>#</sup>
62.40	1.051	-0.30	171.20	49.70	271	52	095-275
55.30	1.068	-0.16	156.10	48.30	280	49	095-275
40.80	1.036	0.08	120.20	13.10	N.D. <sup>#</sup>	N.D. <sup>#</sup>	N.D. <sup>#</sup>
70.80	1.023	-0.48	157.40	73.00	294	32	N.D. <sup>#</sup>
71.40	1.038	-0.49	134.70	87.40	310	37	N.D. <sup>#</sup>
71.60	1.027	-0.49	148.60	86.00	N.D. <sup>#</sup>	N.D. <sup>#</sup>	N.D. <sup>#</sup>
33.20	1.017	0.17	162.00	86.40	131	50	N.D. <sup>#</sup>
14.40	1.013	0.59	047.70	26.00	289	40	N.D. <sup>#</sup>
51.40	1.026	-0.13	019.80	51.10	357	40	133-313
73.50	1.020	-0.54	116.10	22.50	217	20	N.D. <sup>#</sup>
54.50	1.009	-0.11	143.40	78.80	221	08	N.D. <sup>#</sup>
30.90	1.036	0.28	156.40	58.50	N.D. <sup>#</sup>	N.D. <sup>#</sup>	164-344
87.40	1.024	-0.90	166.50	41.70	346	58	N.D. <sup>#</sup>

33.80	1.023	0.20	052.80	09.60	038	23	N.D.#
43.10	1.015	0.16	031.40	29.80	067	18	N.D.#
21.30	1.002	0.46	104.80	80.30	N.D.#	N.D.#	N.D.#
68.90	1.044	-0.43	008.70	72.80	N.D.#	N.D.#	N.D.#
76.50	1.029	-0.61	152.90	88.90	020	72	N.D.#
64.00	1.052	-0.34	132.00	52.50	192	32	N.D.#
79.40	1.061	-0.68	174.10	64.70	297	60	140-320
17.80	1.043	0.51	117.60	75.90	N.D.#	N.D.#	N.D.#
62.50	1.053	-0.31	051.70	84.50	N.D.#	N.D.#	N.D.#
07.40	1.025	0.70	013.60	83.60	N.D.#	N.D.#	N.D.#
77.30	1.119	-0.61	061.60	65.90	N.D.#	N.D.#	N.D.#
18.00	1.033	0.48	106.70	22.20	262	02	N.D.#
12.20	1.049	0.65	106.30	89.30	N.D.#	N.D.#	N.D.#
19.70	1.029	0.42	059.40	50.50	280	05	N.D.#
09.20	1.028	0.73	074.20	83.20	N.D.#	N.D.#	N.D.#
08.60	1.026	0.71	102.50	32.50	N.D.#	N.D.#	N.D.#
60.90	1.015	-0.28	004.00	51.20	N.D.#	N.D.#	N.D.#
04.90	1.009	0.84	023.30	38.00	332	39	N.D.#
53.30	1.020	-0.14	009.40	29.50	N.D.#	N.D.#	N.D.#
65.00	1.007	-0.36	023.00	82.90	305	18	152-322
62.60	1.036	-0.33	027.00	42.30	N.D.#	N.D.#	N.D.#
21.10	1.047	0.45	061.50	61.10	160	19	N.D.#
35.30	1.011	0.09	093.80	65.80	308	39	010-190
38.30	1.038	0.13	104.20	50.40	327	37	N.D.#
31.70	1.082	0.25	019.80	57.00	338	45	021-201
72.30	1.060	-0.51	014.90	26.40	N.D.#	N.D.#	N.D.#
86.00	1.063	-0.87	123.80	37.50	210	23	N.D.#
40.00	1.034	0.10	088.10	50.10	294	29	N.D.#
73.20	1.020	-0.51	143.70	61.00	277	22	N.D.#

56.40	1.024	-0.19	106.10	85.50	200	23	N.D.#
32.60	1.010	0.23	028.60	29.50	N.D.#	N.D.#	N.D.#
58.60	1.027	-0.24	176.50	89.50	N.D.#	N.D.#	N.D.#
64.10	1.018	-0.34	137.50	73.00	278	33	N.D.#
87.50	1.028	-0.92	157.20	78.60	N.D.#	N.D.#	N.D.#
76.80	1.025	-0.64	087.10	21.00	N.D.#	N.D.#	N.D.#
67.90	1.044	-0.46	162.70	61.80	262	10	N.D.#
39.20	1.041	0.03	103.30	35.70	N.D.#	N.D.#	N.D.#
79.60	1.031	-0.70	020.10	53.10	203	50	020-200
57.70	1.023	-0.21	174.00	71.00	247	28	008-188
87.10	1.032	-0.90	144.20	04.70	279	11	N.D.#
11.80	1.016	0.66	076.70	34.60	268	23	N.D.#
29.00	1.012	0.27	144.50	87.80	282	63	N.D.#
27.80	1.020	0.29	110.50	75.90	299	59	N.D.#
74.10	1.026	-0.55	080.20	35.90	N.D.#	N.D.#	N.D.#
47.80	1.015	-0.05	075.30	29.30	255	59	N.D.#
38.00	1.031	0.14	138.60	79.10	348	54	N.D.#
23.10	1.027	0.41	027.50	31.80	170	24	N.D.#
87.50	1.021	-0.92	116.20	66.60	222	19	N.D.#
68.10	1.040	-0.42	156.90	84.70	N.D.#	N.D.#	N.D.#
63.20	1.039	-0.33	132.50	09.40	N.D.#	N.D.#	N.D.#
30.50	1.017	0.26	013.80	25.30	N.D.#	N.D.#	N.D.#
26.10	1.022	0.34	159.60	73.80	167	12	N.D.#
78.70	1.064	-0.66	077.60	71.40	290	49	125-305
44.60	1.017	-0.02	165.10	18.60	228	15	115-295
47.00	1.018	-0.03	083.10	14.00	244	10	N.D.#
69.40	1.011	-0.47	089.70	17.30	318	48	N.D.#
09.90	1.015	0.10	012.50	79.50	N.D.#	N.D.#	N.D.#
79.60	1.024	-0.69	018.10	20.40	230	16	N.D.#

05.30	1.040	0.83	150.50	69.60	083	78	N.D.#
06.80	1.040	0.79	036.30	88.70	080	20	N.D.#
66.90	1.019	-0.39	005.70	43.00	328	30	N.D.#
33.30	1.040	0.21	072.60	06.50	328	30	N.D.#
83.10	1.019	-0.76	152.90	87.90	328	30	N.D.#
47.00	1.015	-0.09	165.20	46.00	328	30	N.D.#
60.00	1.017	-0.27	173.20	34.10	328	30	N.D.#
14.90	1.028	0.59	029.70	36.80	321	20	N.D.#
16.30	1.031	0.54	091.40	27.00	321	20	N.D.#
50.10	1.010	-0.22	121.00	54.80	321	20	N.D.#
75.10	1.027	-0.58	007.20	31.50	023	32	N.D.#
75.00	1.029	-0.57	154.00	87.00	230	12	N.D.#
31.70	1.011	-0.01	018.60	60.30	089	47	094-274
59.10	1.049	-0.21	143.40	65.40	N.D.#	N.D.#	N.D.#
09.20	1.011	0.72	159.00	52.30	N.D.#	N.D.#	N.D.#
79.60	1.025	-0.69	017.80	62.60	N.D.#	N.D.#	N.D.#
31.40	1.009	0.26	117.60	88.30	N.D.#	N.D.#	N.D.#
32.60	1.018	0.22	123.20	73.90	N.D.#	N.D.#	N.D.#
67.20	1.033	-0.37	122.00	20.50	N.D.#	N.D.#	N.D.#
76.80	1.020	-0.62	162.70	60.70	296	46	N.D.#
85.40	1.013	-0.86	077.50	60.40	279	58	N.D.#
68.90	1.020	-0.44	044.40	68.80	298	72	N.D.#
51.10	1.021	-0.10	157.60	81.70	284	37	N.D.#
40.20	1.021	0.10	143.00	68.70	212	78	146-326
45.80	1.020	-0.04	047.50	40.80	220	40	N.D.#
35.50	1.024	0.19	169.30	55.80	182	48	N.D.#
42.70	1.022	0.03	105.80	50.70	240	15	N.D.#
32.90	1.009	0.20	139.50	23.10	N.D.#	N.D.#	N.D.#
65.90	1.011	-0.37	012.10	89.40	341	62	N.D.#

00.90	1.047	0.96	016.60	83.70	072	90	N.D. <sup>#</sup>
34.50	1.025	0.19	047.20	82.20	252	70	N.D. <sup>#</sup>
26.00	1.021	0.35	076.60	82.30	033	70	N.D. <sup>#</sup>
70.80	1.010	-0.48	006.80	82.90	230	79	N.D. <sup>#</sup>
41.00	1.036	0.08	146.20	79.70	069	86	N.D. <sup>#</sup>
15.60	1.012	0.59	135.20	22.90	N.D. <sup>#</sup>	N.D. <sup>#</sup>	161-341
28.80	1.031	0.46	163.10	57.00	N.D. <sup>#</sup>	N.D. <sup>#</sup>	N.D. <sup>#</sup>
43.50	1.009	0.03	056.30	66.10	288	83	N.D. <sup>#</sup>
60.40	1.030	-0.25	035.40	48.20	140	80	N.D. <sup>#</sup>
59.30	1.058	-0.22	147.50	68.80	N.D. <sup>#</sup>	N.D. <sup>#</sup>	N.D. <sup>#</sup>
33.60	1.046646	0.22	156.80	65.20	N.D. <sup>#</sup>	N.D. <sup>#</sup>	155-335

---

**Appendix F:** Collated major, trace and rare earth element data from various intrusive for

Reference	Central complex	Intrusion type	Sample	SiO <sub>2</sub>	TiO <sub>2</sub>	Al <sub>2</sub> O <sub>3</sub>	FeO
Geldmacher et al., (1998; 2002)	Ardnamurchan	Cone sheets	ARG 4b	49.40	2.23	13.08	
			ARG 5	49.92	2.65	12.82	
			ARG 11b	48.73	1.14	19.90	
			ARG 17	49.38	0.72	22.48	
			ARG 18	48.72	1.14	19.54	
			ARG 19	50.06	1.94	13.47	
			ARG 20	49.91	1.39	16.84	
			ARG 22	49.66	2.16	13.02	
			ARG 23a	48.19	1.18	18.98	
			ARG 25	49.20	1.23	18.98	
			ARG 28	49.73	1.17	18.44	
			ARG 31	48.96	1.44	14.65	
			ARG 35	50.24	1.40	15.04	
			ARG 36	49.53	1.59	13.80	
			ARG 38	51.53	2.32	13.61	
			ARG 39	48.21	1.11	18.67	
			ARG 41	49.53	1.58	14.22	
			ARG 42	49.86	1.36	17.03	
			ARG 43	49.24	1.43	16.36	
			ARG 44	49.61	1.62	13.83	
			ARG 45	50.55	2.92	12.75	
			ARG 50a	60.17	1.42	14.39	
			ARG 53	50.43	2.03	13.40	
			ARG 55	50.36	1.81	13.21	
			ARG 56	49.77	1.54	14.69	
			ARG 57	50.28	1.87	13.66	
			ARG 58	49.45	1.61	14.08	
			ARG 59	50.34	1.75	13.85	
			ARG 61	50.38	2.70	12.68	
			ARG 6	49.67	1.66	14.42	
			ARG 7	59.81	1.17	13.44	
			ARG 8	70.23	0.82	12.84	
			ARG 9	69.74	0.80	12.73	
			11	49.49	1.40		
			11	49.64	2.06		
			Cone sheets	11	53.07	1.96	
			(Earlier than	11	49.52	2.36	
			emplacement of	11	50.45	2.71	
			the Hypersthene	11	52.08	2.54	
			Gabbro)	11	48.98	2.48	
			11	50.21	2.71		
			Cone sheets	12	54.68	1.89	
			(Later than	12	50.92	1.52	
			emplacement of	12	60.97	1.58	
			the Hypersthene	12	59.88	1.48	
			Gabbro)	12	51.43	2.70	

Day (1989)	Ardnamurchan	Marginal border group of the Hypersthene Gabbro	19	50.57	1.43	
			19	50.50	1.40	
			19	52.04	1.85	
			19	48.03	0.95	
			19	49.99	1.47	
			19	46.97	2.87	
			19	47.90	1.85	
		Inner series of the Hypersthene Gabbro	27	49.12	1.59	
			27	50.66	0.51	
			27	41.25	2.91	
			24	46.19	2.80	
			27	46.60	1.90	
			28	49.56	0.29	
			28	49.74	0.22	
			27	49.96	0.56	
			25	47.85	0.62	
			24	49.00	1.00	
			28	50.60	0.40	
			28	49.40	0.42	
Kerr et al., (1999)	Mull	Regional dykes	D145-3A	51.62	1.97	17.56
			D160-1B	49.60	2.26	17.28
			D186-3B	51.10	2.18	13.48
			D195-2A	47.08	2.84	16.81
			D300-1A	50.62	2.31	13.37
			D130-1B	48.29	1.60	14.56
			D221-2A	49.36	1.52	19.37
			D210-2A	46.33	2.05	15.30
			D285-3A	47.66	0.94	17.77
			D295-2B	47.87	0.76	17.51
			LB2	53.37	2.29	13.44
			LB4	45.96	2.39	14.38
			LB5	46.18	2.54	14.29
			LB7	46.57	3.43	12.24
			LB8	47.00	3.37	11.92
			LB6	46.92	1.50	15.67
			LB1C	47.61	1.42	16.23
		Cone sheets	B11-EB	49.49	0.99	15.43
			P2-EB	49.18	0.80	20.41
			V3-EB	48.81	1.10	17.67
			D4-EB	52.59	1.67	14.00
			D2-EB	48.16	0.97	17.14
			T20-EB	46.80	0.74	15.72
			E4-EA	61.29	0.82	14.66
			E9-EA	59.18	1.33	14.05
			E12-EA	72.11	0.27	13.83
			E18-EA	70.58	0.63	12.83
			C2-LB	61.54	1.64	14.12
			F15-LB	50.06	2.38	13.00
			G41-LB	61.36	2.57	13.04
			H21-LB	49.32	2.31	12.22

			A40-LA	56.79	1.68	13.29	
			T17-LA	56.35	1.73	14.22	
			G10-LA	51.95	2.47	12.99	
			G18-LA	59.49	1.54	13.63	
			H29-LA	53.64	2.60	12.49	
Preston et al., (1998)	Mull	Loch Scridain sills	SFB2	54.02	0.99	14.66	08.72
			RCB1	54.06	1.16	14.29	09.04
			RCB2	54.31	1.18	14.34	09.00
			ORB1	54.28	0.97	14.71	08.43
			TMB1	54.37	0.96	14.66	08.47
			SOB1	54.86	0.98	14.78	08.25
			SFB3	55.32	1.16	14.60	07.84
			PGB10	56.18	1.19	14.46	07.65
			ARB1	59.30	0.95	14.49	06.46
Bell et al., (1994)	Skye	Cone sheets	CS022	46.85	0.90	14.42	10.27
			CS015	46.86	0.95	13.92	11.00
			CS024	47.03	0.98	13.77	11.00
			CS027	47.14	0.99	13.68	11.15
			CS059	47.09	1.08	13.96	11.33
			CS028	47.36	1.05	14.20	11.28
			CS081	46.86	1.02	14.35	10.96
			CS089	46.81	1.12	14.11	11.27
			CS088	46.61	1.26	14.40	11.66
			CS017	47.37	1.03	13.72	11.67
			CS016	47.34	1.06	13.71	11.40
			CS029	46.39	1.22	13.86	12.45
			CS063	47.24	1.27	13.45	12.33
			CS007	46.92	1.39	13.47	13.00
			CS060	47.91	1.38	13.20	13.10
			CS057	47.11	1.37	13.25	13.13
			CS038	47.37	1.42	13.08	13.27
			CS039	47.77	1.45	12.93	14.20
			CS040	46.94	1.53	13.24	14.27
			CS041	47.67	1.78	12.70	14.80
			CS042	47.85	1.75	12.72	15.47
			CS043	47.91	2.24	12.16	16.13
Macdonald et al., (1988)	southern Scotland - NE England	Regional dykes	10B	58.80	1.23	13.71	10.15
			10F	58.30	1.21	14.03	09.95
			21B	58.60	1.16	13.76	09.47
Macdonald et al., (2009)	southern Scotland - NE England	Regional dykes	ESK-1B	49.50	0.94	14.78	
			ESK-2B	52.00	0.95	14.63	
			ESK-3B/A	55.46	0.89	13.95	
			ESK-4A	57.83	0.85	13.48	
			ESK-5A	59.14	0.83	13.44	
			ESK-6B/A	56.83	0.90	14.18	
			ESK-B	51.25	0.97	14.70	

ms emplaced throughout the BIPIP

Major element data

Fe <sub>2</sub> O <sub>3</sub>	MnO	MgO	CaO	Na <sub>2</sub> O	K <sub>2</sub> O	Na <sub>2</sub> O + K <sub>2</sub> O	P <sub>2</sub> O <sub>5</sub>	Mg no %
15.28	0.25	5.29	09.44	2.69	1.17	3.86	0.34	58.07
16.60	0.23	4.28	08.17	3.06	1.48	4.54	0.40	50.77
10.35	0.15	5.20	12.59	2.57	0.18	2.75	0.09	66.77
07.50	0.11	4.98	11.91	2.84	0.65	3.49	0.06	72.65
10.67	0.15	5.45	11.73	2.72	0.90	3.62	0.09	67.14
15.71	0.22	5.02	09.12	3.51	0.89	4.40	0.28	56.11
12.08	0.18	5.52	11.96	2.66	0.46	3.12	0.10	64.64
16.32	0.23	4.92	09.06	3.47	1.12	4.59	0.26	54.67
10.78	0.15	5.40	12.10	2.48	0.21	2.69	0.10	66.71
10.48	0.15	4.43	11.37	3.07	0.48	3.55	0.16	62.84
10.48	0.16	5.28	11.26	2.87	1.32	4.19	0.12	66.84
13.63	0.20	7.37	11.42	2.53	0.19	2.72	0.11	68.38
12.75	0.20	7.11	09.83	2.79	1.41	4.20	0.12	69.05
14.34	0.21	6.87	09.55	2.45	1.68	4.13	0.11	65.71
15.52	0.23	4.01	08.52	2.64	1.09	3.73	0.31	50.82
10.55	0.14	4.98	11.79	2.90	0.40	3.30	0.16	65.38
13.93	0.21	6.44	11.44	2.60	0.44	3.04	0.14	64.90
11.93	0.18	5.43	11.82	2.60	0.27	2.87	0.14	64.55
12.19	0.18	5.21	11.40	2.63	0.34	2.97	0.13	63.09
14.51	0.21	6.35	10.57	2.80	0.53	3.33	0.15	63.64
16.55	0.25	4.06	08.39	2.54	1.31	3.85	0.50	49.53
10.00	0.18	2.28	05.18	4.24	2.36	6.60	0.41	47.70
15.80	0.22	4.58	08.78	3.21	1.33	4.54	0.32	53.69
15.06	0.23	5.02	09.17	3.18	0.76	3.94	0.23	57.14
13.82	0.20	6.03	10.91	2.95	0.44	3.39	0.24	63.57
14.93	0.22	5.44	09.84	3.33	0.65	3.98	0.25	59.31
14.33	0.22	6.19	10.87	2.94	0.30	3.24	0.17	63.34
14.69	0.21	5.70	10.17	3.00	0.62	3.62	0.19	60.82
16.48	0.24	3.97	07.94	2.90	1.24	4.14	0.61	49.07
14.05	0.20	6.42	10.81	2.70	0.44	3.14	0.15	64.64
09.63	0.16	3.53	05.28	3.46	3.02	6.48	0.15	59.45
05.90	0.12	0.56	01.93	3.79	4.38	8.17	0.16	27.52
05.63	0.11	0.49	01.74	3.69	4.25	7.94	0.16	25.82
		5.76		2.83	0.47	3.30		
		5.28		2.89	1.16	4.05		
		4.13		3.16	1.38	4.54		
		4.78		2.69	1.28	3.97		
		3.94		2.85	1.28	4.13		
		3.45		3.22	1.89	5.11		
		4.96		2.67	1.20	3.87		
		3.83		3.33	1.76	5.09		
		3.93		2.20	1.85	4.05		
		6.64		2.67	0.55	3.22		
		2.33		3.04	2.34	5.38		
		2.69		3.07	2.49	5.56		
		2.92		3.13	1.77	4.90		

		6.35		2.80	0.55	3.35		
		6.69		2.84	0.58	3.42		
		4.59		3.50	1.53	5.03		
		7.69		2.57	0.24	2.81		
		6.44		2.94	0.54	3.48		
		5.34		2.52	0.73	3.25		
		6.59		2.55	0.35	2.90		
		6.98		2.59	0.23	2.82		
		9.11		2.24	0.16	2.40		
		6.64		2.33	0.16	2.49		
		5.35		2.89	0.63	3.52		
		7.32		2.49	0.34	2.83		
		3.98		2.95	0.29	3.24		
		1.03		3.49	0.43	3.92		
		8.00		2.64	0.17	2.81		
		9.65		2.06	0.23	2.29		
		6.26		2.72	0.23	2.95		
		0.91		3.93	0.54	4.47		
		6.65		2.94	0.25	3.19		
10.94	0.19	3.02	05.51	5.46	2.35	7.81	0.98	52.48
11.58	0.14	5.64	05.11	4.34	2.23	6.57	1.03	66.08
15.10	0.21	4.15	07.79	3.43	1.72	5.15	0.33	52.37
14.56	0.18	5.36	07.83	4.21	0.41	4.62	0.39	59.56
15.67	0.23	4.46	08.61	3.11	1.21	4.32	0.27	53.24
14.16	0.22	6.81	10.77	2.98	0.34	3.32	0.14	65.80
08.01	0.31	6.60	10.10	3.70	0.29	3.99	0.18	76.72
15.97	0.26	6.59	10.90	3.02	0.15	3.17	0.15	62.27
11.68	0.19	6.55	12.76	2.13	0.08	2.21	0.06	69.17
11.10	0.17	7.23	12.33	2.32	0.11	2.43	0.06	72.26
15.40	0.23	3.65	06.67	3.60	1.43	5.03	0.28	48.67
16.28	0.23	6.73	09.97	2.87	0.36	3.23	0.19	62.31
16.67	0.25	6.34	10.26	2.72	0.37	3.09	0.20	60.34
20.47	0.39	4.12	08.88	2.39	0.86	3.25	0.48	44.60
20.36	0.33	4.09	08.84	2.93	0.49	3.42	0.47	44.55
14.52	0.23	7.42	11.13	2.33	0.15	2.48	0.11	67.15
13.25	0.19	7.58	10.65	2.55	0.37	2.92	0.13	69.59
10.05	0.19	8.28	12.49	2.04	0.68	2.72	0.11	76.72
08.87	0.13	6.26	12.00	2.58	0.78	3.36	0.12	73.84
10.44	0.17	7.20	12.78	1.74	0.35	2.09	0.22	73.39
14.70	0.22	4.73	08.21	2.79	1.38	4.17	0.22	56.28
10.46	0.18	8.48	11.67	2.18	0.47	2.65	0.15	76.43
10.81	0.61	9.50	13.47	1.54	0.20	1.74	0.13	77.85
07.83	0.13	2.88	05.31	3.83	2.85	6.68	0.19	59.53
10.16	0.18	3.00	06.23	3.09	2.38	5.47	0.25	54.15
03.19	0.08	0.35	01.07	5.06	3.63	8.69	0.07	30.50
04.80	0.09	0.82	02.31	3.02	4.26	7.28	0.19	40.59
14.21	0.22	4.83	09.03	3.23	1.05	4.28	0.32	57.62
15.90	0.22	4.76	08.04	3.17	1.87	5.04	0.38	54.49
15.80	0.23	4.12	08.44	2.92	1.19	4.11	0.34	51.05
16.05	0.22	4.91	09.54	3.17	0.82	3.99	0.33	55.03

12.59	0.24	2.92	06.68	3.45	1.88	5.33	0.77	48.13
11.43	0.21	3.90	06.61	4.49	2.25	6.74	0.41	57.71
15.29	0.19	3.85	08.17	3.15	1.37	4.52	0.36	50.18
10.78	0.20	2.02	04.79	3.86	3.38	7.24	0.40	42.84
14.74	0.30	2.74	07.17	3.34	1.91	5.25	0.96	42.65
01.51	0.20	5.78	08.74	2.94	1.40	4.34	0.12	52.54
01.57	0.18	5.06	08.39	2.91	1.35	4.26	0.14	48.31
01.56	0.17	5.22	08.54	2.99	1.39	4.38	0.15	49.20
01.46	0.18	5.50	09.16	2.58	1.35	3.93	0.12	52.14
01.47	0.18	5.58	09.04	2.53	1.25	3.78	0.12	52.38
01.43	0.18	5.59	08.76	2.73	1.25	3.98	0.12	53.08
01.36	0.16	4.62	08.37	2.82	0.85	3.67	0.20	49.59
01.33	0.14	4.52	08.06	2.70	1.59	4.29	0.14	49.66
01.12	0.13	4.84	06.40	2.88	2.20	5.08	0.15	55.58
01.54	0.17	8.73	13.20	1.85	0.12	1.97	0.07	58.90
01.65	0.19	8.47	12.99	1.51	0.32	1.83	0.07	56.49
01.65	0.19	8.41	12.96	1.63	0.35	1.98	0.06	56.32
01.67	0.20	8.29	13.18	1.80	0.18	1.98	0.07	55.63
01.70	0.19	8.46	13.02	1.83	0.08	1.91	0.08	55.73
01.69	0.19	8.12	12.99	1.77	0.17	1.94	0.07	54.83
01.64	0.21	7.86	12.39	2.08	0.13	2.21	0.08	54.74
01.69	0.21	8.03	12.76	2.13	0.13	2.26	0.08	54.58
01.75	0.20	7.93	12.32	2.21	0.11	2.32	0.10	53.42
01.75	0.19	7.75	12.76	2.11	0.05	2.16	0.06	52.83
01.71	0.21	7.65	12.34	2.43	0.18	2.61	0.08	53.09
01.87	0.22	7.62	12.33	1.99	0.19	2.18	0.10	50.79
01.85	0.23	7.41	12.17	2.14	0.27	2.41	0.08	50.33
01.95	0.21	7.30	12.09	2.22	0.16	2.38	0.12	48.64
01.95	0.20	7.39	11.91	2.22	0.31	2.53	0.10	48.76
01.97	0.23	7.25	12.27	2.35	0.15	2.50	0.09	48.21
01.99	0.23	6.93	11.92	2.27	0.22	2.49	0.10	46.83
02.13	0.23	6.57	11.43	2.29	0.19	2.48	0.13	43.83
02.14	0.22	6.34	10.80	2.47	0.28	2.75	0.11	42.83
02.22	0.23	6.04	10.37	2.80	0.34	3.14	0.16	40.76
02.32	0.25	6.00	10.98	2.23	0.11	2.34	0.14	39.54
02.42	0.26	4.90	08.99	2.72	0.53	3.25	0.24	33.87
	0.18	4.10	05.54	2.78	2.12	4.90	0.23	42.10
	0.22	4.37	05.56	2.67	2.75	5.42	0.23	44.15
	0.16	4.06	06.24	2.03	2.40	4.43	0.20	43.56
11.02	0.15	7.25	10.18	2.62	0.81	3.43	0.10	72.46
10.07	0.16	6.29	09.63	2.09	1.13	3.22	0.12	71.42
09.38	0.15	5.09	08.79	2.11	1.69	3.80	0.14	68.46
08.89	0.13	4.55	06.95	2.39	2.51	4.90	0.15	67.18
08.33	0.13	4.02	07.05	2.21	2.23	4.44	0.13	65.87
08.80	0.13	4.59	07.44	2.12	2.01	4.13	0.15	67.60
10.60	0.16	6.49	10.17	2.11	1.01	3.12	0.12	71.01

[illegible]

	10	054	004
	14	129	006
	39	437	015
	19	193	014
	41	466	058
	46	366	225
	38	329	200
	47	466	180
	44	299	364
	42	267	546
	37	411	032
	29	410	136
	35	427	139
	37	366	025
	35	319	022
	38	340	137
	34	306	111
		307	295
		232	029
	38	235	237
	40	341	059
	36	228	254
	37	229	265
	21	121	048
	27	212	037
	05	008	005
	14	037	016
	40	370	025
	41	387	054
	38	411	042
	35	380	062

	24	073	040		021			
		220	010		035			
		397	010		041			
		103	007		000			
	30	083	047		026			
0.34	44	274	035		011	030	100	
0.30	43	209	043		014	032	104	
0.31	41	301	048		014	031	148	
0.34	41	256	039		012	023	109	
0.34	39	254	036		012	024	108	
0.35	45	258	039		012	026	096	
0.31	33	277	077		018	032	110	
0.31	36	261	090		022	038	163	
0.37	31	172	153		035	047	093	
0.43	37	235	350		130	137	059	
0.40	35	243	221		101	163	072	
0.40	32	243	184		098	173	071	
0.39	36	261	189		100	156	070	
0.39	36	256	313		117	158	070	
0.39	33	249	253		103	144	067	
0.38	41	237	136		101	152	080	
0.38	43	255	286		103	140	070	
0.37	39	273	259		108	130	077	
0.37	33	246	100		074	156	059	
0.37	33	244	115		074	144	074	
0.35	31	291	073		087	169	083	
0.34	35	295	142		089	178	080	
0.33	39	316	098		074	147	090	
0.33	39	331	121		074	193	079	
0.32	32	305	116		071	177	066	
0.31	35	313	108		064	185	071	
0.29	37	328	055		057	199	082	
0.28	39	363	075		053	186	096	
0.26	32	353	057		044	163	085	
0.25	38	375	036		040	164	085	
0.21	29	408	041		035	110	095	
			034		012			
			037		022			
			046		021			
	48	312	301	47	055	093	036	19
	44	285	239	41	043	071	047	18
	39	230	205	34	038	066	045	17
	35	207	171	31	027	060	049	17
	33	164	157	26	020	047	049	18
	36	216	178	32	034	055	044	19
	36	293	239	42	046	076	046	17

## Trace element data

Y	Rb	Cs	Sr	Ba	Zr	Hf	Nb	Ta
44	000	0.51	265	574	163	4.51	08.28	0.46
13	019	0.65	420	069	030	0.94	01.20	0.06
22	008	1.73	296	063	014	0.68	02.01	0.13
26	007	1.79	273	092	047	1.65	02.21	0.13
30	041	3.33	733	716	061	1.93	02.35	0.14
59	057	0.72	221	613	094	2.76	13.30	0.75
38	016	0.05	349	471	099	2.94	05.76	0.28
30	007	0.16	312	175	019	0.74	02.69	0.16
31	011	2.09	266	135	090	2.60	03.04	0.17
47	082	4.51	239	730	267	7.11	11.10	0.62
62	114	1.47	168	958	433	11.40	18.40	1.04

---

---

41	030	1062	1377	422	28.80
38	020	819	1200	305	21.00
44	041	342	610	202	10.00
35	005	652	144	243	12.50
43	030	244	376	178	08.90
31	006	274	151	078	03.00
17	001	483	205	082	02.00
38	002	192	057	102	03.70
27	001	108	024	051	01.90
19	001	152	038	038	01.20
58	052	222	404	224	10.90
37	007	228	155	129	07.20
38	006	209	173	133	07.60
84	028	160	202	250	10.30
82	016	198	194	248	10.30
29	005	171	047	074	02.80
27	005	252	244	084	04.70
28	035	113	052	047	03.00
20	009	360	071	041	06.00
29	005	158	089	081	
48	042	178	301	170	06.00
23	025	217	131	059	03.00
32	008	136	035	036	01.00
56	098	198	492	260	11.00
56	092	221	396	230	05.00
50	134	061	840	039	07.00
54	161	171	869	385	13.00
49	026	273	615	190	07.00
46	054	262	746	179	
40	034	207	386	180	
41	025	259	467	191	06.00

79	063		300	1025	292			
63	065		216	568	233		09.00	
	046		232	514	196			
58	111		183	578	304		12.00	
69	070		333	764	264		11.00	
32	031		202	425	133		07.30	
35	043		222	455	145		07.40	
35	043		226	404	146		07.90	
31	043		212	784	135		07.30	
32	042		211	356	132		06.70	
32	044		214	363	137		07.00	
29	049		411	504	149		09.00	
28	045		279	458	156		08.40	
34	074		216	560	200		11.00	
21	008		131	070	057		02.00	
23	010		126	091	055		02.00	
23	010		150	085	057		02.00	
22	009		125	075	058		04.00	
23	006		118	068	062		03.00	
22	010		133	064	063		03.00	
24	006		129	081	061		01.00	
24	006		129	057	064		03.00	
29	005		129	085	072		02.00	
21	005		153	087	058		02.00	
24	006		136	107	067		03.00	
26	008		131	078	069		03.00	
27	010		143	122	073		02.00	
29	011		139	112	083		04.00	
29	013		145	121	077		03.00	
27	008		146	097	072		02.00	
28	007		146	121	078		03.00	
33	008		139	116	089		04.00	
32	013		139	061	078		03.00	
41	013		150	084	113		03.00	
37	007		142	062	090		05.00	
52	018		146	142	151		06.00	
44	063		192	562	183			
43	076		212	491	178			
42	066		200	609	183			
30	034	2.20	192	213	104	3.20	05.30	0.40
34	047	2.20	188	256	133	4.20	07.00	0.40
35	063	4.40	172	371	164	4.60	08.50	0.50
37	112	4.90	194	464	192	5.60	09.90	0.60
35	081	2.90	167	528	207	6.20	09.90	0.70
38	077	2.70	175	440	196	5.50	09.50	0.60
32	041	3.20	180	246	120	3.60	06.00	0.40

			F					
Pb	Th	U	La	Ce	Pr	Nd	Sm	Eu
5.44	2.32	0.61	22.90	51.10	06.81	29.10	07.22	02.17
0.49	0.27	0.06	02.80	06.80	00.97	04.80	01.43	00.63
2.62	0.49	0.11	04.66	11.30	01.71	08.31	02.71	01.02
1.24	0.36	0.10	05.13	12.70	01.92	09.50	02.93	01.18
1.24	0.36	0.10						
1.76	0.61	0.15	06.06	14.70	02.20	10.80	03.40	01.27
8.95	3.64	0.85	33.70	74.30	09.72	40.40	09.62	02.55
4.54	0.80	0.20	18.80	43.30	05.97	26.40	06.29	02.05
1.61	0.41	0.10	07.29	17.50	02.62	12.50	03.63	01.39
2.11	0.92	0.24	07.51	18.00	02.63	12.40	03.71	01.39
9.94	5.58	1.38	29.90	65.30	08.24	33.10	07.42	01.78
17.70	10.00	2.44	50.70	109.00	13.50	52.30	11.20	02.33

4.00	4.00	39.80	117.80	11.90	53.00	11.43	03.56
4.00	3.00	41.20	116.20	11.90	59.90	11.45	03.51
10.00	8.00	17.80	45.00	05.10	21.30	04.80	01.47
4.00	5.00	12.40	33.10	05.60	27.00	07.15	02.52
1.00	8.00	19.40	42.20	05.90	25.50	08.57	02.11
7.00	5.00	06.10	14.60	02.20	10.30	03.34	01.39
4.00		05.60	15.70	02.70	12.40	03.10	01.17
3.00	4.00	04.40	11.40	02.30	11.80	04.28	01.86
	3.00	02.00	05.10	01.20	05.00	02.18	00.87
	2.00	01.80	04.30	01.10	04.10	01.75	00.68
8.00	8.00	24.70	50.50		31.80		
1.00	4.00				18.80		
2.00	3.00	04.00	05.60		13.30		
2.00	8.00	09.20	22.70		25.90		
3.00	8.00	09.30	29.80		29.20		
	2.00		04.20		10.40		
2.00	3.00	05.90	03.20		10.20		
		05.00	10.80	01.80	09.60	02.70	01.00
		04.80	10.90		07.60	02.10	00.80
		05.00	23.00				
		17.90	38.20	05.50	22.90	05.90	01.70
		02.40	05.90		05.70	01.90	00.80
		01.50	04.20	00.70	03.90	01.60	00.70
		24.90	52.00		28.40	06.50	01.50
		25.00	50.50	06.80		06.90	01.70
		20.00	54.00				
		42.40	58.30		40.90	08.10	01.40
		21.60	47.40	05.70	26.70	06.80	02.00
		15.50	36.80	04.50	23.20	06.20	01.90
		20.00	48.00	06.40	26.70	06.40	01.90
		17.30	40.70	05.00	25.50	06.90	02.20

			42.00	92.00			
			24.30	53.90	06.40	31.70	07.90 02.20
			19.10	45.20	05.40	26.80	07.10 02.10
			30.00	69.50	08.00	39.70	09.80 02.40
			35.00	78.00		51.80	11.80 03.50
7.60	6.10						
8.10	7.40		19.32	44.04	05.01	19.30	04.31 01.28
6.40	5.70		19.34	43.89	04.99	19.20	04.31 01.28
7.00	6.70						
7.10	5.80		17.15	39.37	04.46	17.40	03.87 01.14
7.70	7.00						
9.90	6.00		21.05	47.78	05.41	20.58	04.29 01.29
9.50	6.10						
12.60	8.10		27.55	62.42	06.97	25.18	05.23 01.31
6.00			02.86	07.73	01.13	06.05	01.88 00.76
5.00			02.17	06.30	01.03	06.19	02.02 00.84
5.00			02.14	07.00	01.04	07.00	02.25 00.99
6.00							
4.00			01.63	06.14	01.04	06.43	02.23 00.92
6.00			02.23	06.86	01.15	07.05	02.20 00.92
5.00							
2.00							
7.00							
5.00							
5.00			02.96	08.18	01.22	07.41	02.35 00.95
6.00			02.32	07.60	01.25	07.57	02.57 01.01
7.00			03.96	10.69	01.54	08.76	02.72 01.09
10.00			02.68	09.34	01.61	09.29	02.93 01.14
5.00			02.96	03.05	01.43	08.80	02.80 01.14
5.00			02.62	09.42	01.51	08.95	02.91 01.16
8.00			04.32	11.38	01.74	09.76	02.97 01.20
3.00			05.11	13.69	02.01	10.16	03.09 01.23
6.00							
8.00							
8.00			05.00	13.07	01.83	11.71	03.64 01.44
6.00			08.75	22.59	03.12	18.04	05.52 01.94
	6.51	2.10	26.00	60.40		34.40	06.99 01.78
	6.47	2.00	25.60	59.40		34.70	07.04 01.79
	6.91	2.10	26.60	61.80		36.00	07.15 01.79
3.20	3.80	1.00	13.60	28.50	03.69	14.70	03.97 01.13
1.80	4.90	1.30	18.40	38.50	04.87	19.40	04.77 01.23
2.20	6.60	1.70	22.20	48.20	05.90	23.90	05.37 01.21
6.90	8.00	2.00	26.20	56.10	07.02	27.40	05.93 01.27
3.00	7.30	2.40	29.40	59.90	07.59	30.40	05.93 01.26
2.40	8.20	2.40	25.30	57.00	07.00	26.70	05.81 01.31
1.80	4.40	1.20	15.80	34.70	04.44	17.30	04.31 01.22

Rare Earth Element data

Gd	Tb	Dy	Ho	Er	Tm	Yb	Lu
07.42	01.24	07.62	01.53	04.39	00.61	04.01	00.58
01.75	00.32	02.13	00.43	01.25	00.17	01.10	00.15
03.16	00.58	03.72	00.77	02.22	00.32	02.01	00.29
03.74	00.68	04.32	00.90	02.60	00.36	02.32	00.34
04.24	00.77	05.06	01.06	03.04	00.42	02.72	00.40
10.10	01.64	10.00	02.05	05.93	00.83	05.37	00.78
06.61	01.06	06.52	01.32	03.74	00.50	03.23	00.46
04.44	00.78	05.03	01.06	03.05	00.41	02.71	00.39
04.52	00.82	05.18	01.08	03.14	00.44	02.90	00.43
07.68	01.27	08.04	01.62	04.77	00.67	04.47	00.65
10.90	01.76	10.80	02.19	06.47	00.93	06.05	00.89


---



---

10.11	01.28	07.16	01.34	03.67	00.51	03.38	00.52
09.98	01.26	06.96	01.30	03.55	00.47	03.04	00.50
05.47	00.79	05.08	01.10	02.95	00.40	02.70	00.43
07.60	01.08	06.34	01.16	03.13	00.43	02.78	00.43
07.34	01.18	07.19	01.50	04.10	00.57	03.94	00.63
04.64	00.77	04.39	01.00	02.88	00.39	02.72	00.40
03.17	00.48	02.71	00.49	01.35	00.18	01.07	00.17
06.74	00.96	06.20	01.27	03.69	00.51	03.43	00.53
03.19	00.58	03.98	00.84	02.41	00.35	02.37	00.39
02.60	00.41	02.81	00.58	01.65	00.24	01.59	00.28

03.60	04.50	02.60	02.60	00.40
02.80	03.40	02.10	01.90	00.30
06.50	07.20	04.50	04.00	00.60
02.90	03.40	01.90	01.70	00.30
02.40	03.20	00.70	01.80	00.30
07.00	08.00	04.70	04.60	00.70
07.30	08.00	05.10	04.50	00.70
08.20	07.10	04.30	03.80	00.60
07.30	07.80	01.80	04.40	00.70
07.00	07.60	01.60	04.40	00.50
06.90	07.40	01.50	04.30	00.60
08.00	08.40	01.70	04.80	00.70

08.30		09.50	01.90	05.70		05.00	00.70
07.80		08.20	01.60	04.60		04.20	00.60
10.50		11.10	02.20	06.50		05.90	00.90
13.00		12.60	02.70	07.10		05.90	00.90
04.96		04.95	01.15	03.12		03.13	00.50
04.91		04.90	01.13	03.06		03.09	00.50
04.41		04.40	01.01	02.75		02.79	00.45
04.58		04.22	00.95	02.55		02.58	00.42
05.41		04.92	01.13	02.99		03.07	00.50
02.78		03.05	00.69	02.00		01.84	00.27
03.08		03.64	00.80	02.44		02.24	00.30
03.52		03.97	00.82	02.47		02.38	00.36
03.39		03.87	00.86	02.50		02.43	00.34
03.29		03.76	00.83	02.49		02.27	00.31
03.45		03.81	00.85	02.45		02.34	00.33
03.81		04.33	00.96	02.82		02.69	00.37
03.94		04.50	00.99	02.90		02.67	00.36
04.17		04.62	01.00	02.87		02.67	00.37
04.05		04.00	01.02	03.01		02.80	00.38
04.21		04.78	01.05	02.99		02.86	00.39
04.29		04.95	01.09	03.26		02.92	00.40
04.46		05.07	01.12	03.25		03.00	00.41
05.23		05.92	01.30	03.77		03.50	00.47
07.75		08.45	01.87	05.41		05.14	00.69
	01.21					04.51	00.73
	01.27					04.48	00.79
	01.19					04.49	00.76
04.40	00.85	05.02	01.09	03.44	00.52	03.19	00.50
05.22	00.96	05.76	01.21	03.51	00.56	03.42	00.52
05.46	01.00	05.80	01.21	03.61	00.57	03.56	00.55
06.23	01.04	06.32	01.29	03.77	00.59	03.72	00.59
05.89	01.05	06.75	01.38	04.01	00.62	03.87	00.48
05.95	01.09	06.44	01.32	03.99	00.60	03.88	00.58
04.79	00.93	05.51	01.15	03.38	00.54	03.26	00.50

# Appendix G: AMS results and block sample locations for the Ben Hiant Dolerite

Sample	Grid reference*	K <sub>1</sub>		K <sub>2</sub>		K <sub>3</sub>
	(NM)	Declination (°)	Dip (°)	Declination (°)	Dip (°)	Declination (°)
B-1	52568 62352	323.1	25.5	230.1	06.3	127.1
B-2	52500 62445	289.0	02.9	198.9	01.4	084.1
B-3	52480 62662	007.8	10.5	275.5	12.1	137.6
B-4	52171 62816	168.2	43.6	039.6	33.2	289.0
B-6	53747 63259	187.4	42.8	353.7	46.4	091.0
B-8	53700 62148	220.3	61.4	338.8	14.6	075.4
B-12	53075 62448	003.3	18.0	260.8	33.8	116.5
B-13	53168 62388	318.8	01.2	074.9	87.2	228.7
B-16	53900 62929	228.8	06.1	320.3	14.0	115.8
B-18	52286 63491	140.3	77.3	259.8	06.3	351.0
B-19	52265 63455	098.8	86.1	220.0	02.0	310.2
B-20	52210 63409	211.0	53.8	040.2	35.8	307.0
B-22	52572 63270	079.7	73.8	196.4	07.4	288.3
B-24	52816 63693	158.7	21.3	027.8	59.2	257.4
B-27	52749 63812	164.1	02.2	255.7	35.7	071.1
B-28	52711 63804	140.7	05.2	023.6	78.7	231.6
B-B	53660 62222	163.1	45.1	320.0	42.5	061.0
B-C	53637 62192	353.8	11.2	085.7	09.3	214.6
B-D	53169 62187	102.8	23.9	251.2	62.5	007.0
B-E	54168 64769	064.0	23.2	203.3	20.7	330.6
B-100	52234 62814	035.9	10.1	132.1	31.1	290.1
B-101	52582 64094	181.1	01.3	091.0	00.9	324.7
B-102	53267 64090	152.8	41.1	342.4	48.5	247.0
B-103	53037 64043	125.3	01.3	219.3	71.6	034.8
B-104	52926 64194	318.2	57.8	134.2	32.2	225.4
B-105	53383 64087	103.2	31.1	254.7	55.6	005.0
B-106	53422 64104	339.5	16.7	095.5	55.6	239.9
B-107	53831 64184	064.4	82.6	298.9	04.3	208.5
B-108	53824 64159	349.7	27.5	121.7	52.2	246.4
B-109	54171 64283	148.1	14.7	056.4	06.5	303.1
B-115	54283 63633	135.9	00.5	045.6	30.2	226.7
B-116	54076 63177	205.7	70.9	030.2	19.1	299.8
B-117	53757 63241	309.2	61.1	117.9	28.5	210.5
B-118	53552 63251	342.2	23.5	241.4	23.2	112.2
B-119	53400 63368	256.9	34.7	005.3	24.5	122.6
B-120	53207 63499	288.9	56.9	137.6	29.7	040.0
B-121	53567 63547	020.8	52.3	132.0	15.7	232.6
B-122	53870 62140	036.2	43.6	197.8	44.9	297.2
B-123	53050 62343	010.5	21.6	198.7	68.2	101.6
B-125	53214 62484	114.5	21.5	324.1	65.6	208.9
B-126	53451 62767	314.3	80.0	025.0	03.3	114.5

\* Grid references using UK National Grid co-ordinates

$$** K_{\text{mean}} = (K_1 + K_2 + K_3) / 3$$

$$^\dagger L = (K_1 - K_2) / K_{\text{mean}}$$

$$^\S F = (K_2 - K_3) / K_{\text{mean}}$$

K <sub>mean</sub> (10 <sup>-4</sup> )**		H	L <sup>†</sup>	F <sup>§</sup>	μ	Pj	T	Magnetic foliation strike (°)
Dip (°)	(SI units)	(%)	(%)	(%)	(%)			
63.6	11.043	02.90	0.57	2.33	13.8	1.03	0.61	37.1
86.7	10.418	02.99	0.63	2.36	14.8	1.03	0.58	174.1
73.9	11.551	00.85	0.26	0.60	23.2	1.01	0.40	47.6
28.2	05.449	00.79	0.30	0.49	31.3	1.01	0.27	19.0
06.9	03.276	01.15	0.46	0.69	33.6	1.01	0.20	1.0
24.1	10.098	07.86	1.68	6.18	15.3	1.09	0.57	165.4
50.5	09.782	01.67	0.62	1.05	30.5	1.02	0.27	26.5
02.5	14.522	02.37	1.35	1.02	52.8	1.01	1.00	138.7
74.7	02.359	03.23	0.80	2.44	18.1	1.03	0.52	25.8
11.0	06.792	01.08	0.55	0.53	46.1	1.01	-0.01	81.0
03.4	07.470	00.46	0.22	0.24	43.4	1.00	0.05	40.2
04.4	05.874	00.78	0.69	0.09	82.9	1.01	-0.80	37.0
14.3	02.812	06.46	2.68	3.78	35.3	1.07	0.19	18.3
21.2	02.278	00.80	0.55	0.25	65.4	1.01	-0.37	167.4
54.2	02.739	02.43	1.58	0.86	61.5	1.02	-0.29	161.1
10.0	04.523	01.54	1.32	0.22	80.4	1.02	-0.69	141.6
11.8	09.238	09.18	2.63	6.55	31.7	1.10	0.45	151.0
75.4	05.185	01.04	0.36	0.68	21.9	1.01	0.30	124.6
12.8	07.677	02.26	1.44	0.82	28.1	1.02	-0.20	97.0
58.0	02.581	01.68	0.84	0.84	44.9	1.01	-0.48	60.6
56.9	07.382	01.47	0.73	0.74	44.6	1.01	0.04	20.1
88.4	01.851	00.41	0.37	0.04	84.4	1.00	-0.83	54.7
04.8	07.539	00.82	0.73	0.09	82.6	1.01	-0.80	157.0
18.4	05.083	01.32	0.40	0.92	23.5	1.01	0.40	124.8
01.8	06.979	00.55	0.21	0.34	31.7	1.01	0.21	135.4
13.3	05.140	00.79	0.61	0.18	73	1.01	-0.54	95.0
29.1	05.239	01.03	0.39	0.63	31.9	1.01	0.24	149.9
06.0	14.909	00.72	0.48	0.24	63.1	1.01	-0.20	118.5
23.8	14.555	02.09	0.57	1.52	20.7	1.02	0.45	156.4
73.9	05.187	01.78	1.57	0.21	82	1.02	-0.77	33.1
59.8	04.988	00.64	0.21	0.42	26.9	1.01	0.32	136.7
01.4	19.134	09.03	4.22	4.81	41.3	1.09	0.09	29.8
04.8	05.725	11.35	3.39	7.96	23.1	1.13	0.43	120.5
55.9	04.513	02.18	1.29	0.89	55.5	1.02	-0.17	22.2
45.3	04.000	00.81	0.46	0.35	53	1.01	-0.16	32.6
13.2	03.984	02.94	1.18	1.76	33.9	1.04	0.21	130.0
33.3	05.402	01.05	0.56	0.50	48.2	1.01	-0.05	142.6
09.3	05.853	00.64	0.15	0.48	17.5	1.01	0.52	27.2
02.8	06.149	00.47	0.42	0.05	83.2	1.01	-0.81	11.6
10.9	06.001	01.21	0.23	0.98	13.5	1.01	0.65	118.9
09.4	09.739	00.99	0.54	0.45	50.5	1.01	-0.10	24.5

Magnetic foliation dip (°)
26.4
03.3
16.1
61.8
83.1
65.9
39.5
87.5
15.3
79.0
86.6
85.6
75.7
68.8
35.8
80.0
78.2
14.6
77.2
32.0
33.1
01.6
85.2
71.6
88.2
76.7
60.9
84.0
66.2
16.1
30.2
88.6
85.2
34.1
44.7
76.8
56.7
80.7
87.2
79.1
80.6